

“Saint-Petersburg OPEN 2015”

2nd International School and Conference on
Optoelectronics, Photonics, Engineering and
Nanostructures

St. Petersburg, Russia, April 6 – 8, 2015

BOOK of ABSTRACTS

**St. Petersburg
2015**

Copyright © 2015 by St.Petersburg Academic University, St.Petersburg Polytechnic University and individual contributors. All rights reserved. No parts of this electronic publication may be multiple copied, stored in a retrieval system or transmitted in any form or by any means, electronic, mechanical, photocopying, recording or otherwise, without the written permission of the publisher. Single photocopies of single articles may be made for private study or research.

ISBN 978-5-906433-08-4

2nd International School and Conference “Saint-Petersburg OPEN 2015” on Optoelectronics, Photonics, Engineering and Nanostructures carries on the tradition of annual conferences and schools organized at St.Petersburg Academic University for students, PhD students and young scientists. The School and Conference is established and chaired by Nobel Prize laureate in Physics academician Zhores Alferov.

More detailed information on the School and Conference is presented in spbopen.spbau.com

The Book of Abstracts includes abstracts of contributed works accepted for presentation at the Conference.

The volume was composed by St.Petersburg Academic University from electronic files submitted by the authors. Only minor technical corrections were made by the editors.

Chief Editor: Zhores I. Alferov

Editors: Alexey E. Zhukov, Vladimir V. Korenev

Published in Russian Federation

Organizers



St. Petersburg Academic University –
Nanotechnology Research and Education
Centre of the Russian Academy of Sciences



St. Petersburg State Polytechnical
University

SPIE. **STUDENT
CHAPTER**
SAINT-PETERSBURG
ACADEMIC UNIVERSITY
RUSSIAN ACADEMY
OF SCIENCES



St. Petersburg Academic University RAS
SPIE Student Chapter

Foundation for support of education and
science (Alferov's foundation)

Acknowledgments



The Optical Society

The Optical Society



The International Society
for Optics and Photonics



Skolkovo Foundation



Российский
научный
фонд

IOP Institute of Physics

Head of Program Committee

Zhores I. Alferov

Academician, Vice-President of the RAS, Chairman of St. Petersburg Scientific Centre of the RAS, Rector of St. Petersburg Academic University

Program Committee

Michael V. Dubina, corr. member of the RAS, Head of Nanobiotechnologies Laboratory and First Vice-rector on Science (St. Petersburg Academic University RAS, Russia)

Alexey E. Zhukov, corr. member of the RAS, Head of Nanophotonics Laboratory and Vice-rector on Education (St. Petersburg Academic University RAS, Russia)

Andrey A. Lipovskii (St. Petersburg State Polytechnical University, Russia)

Alexander V. Omelchenko (St. Petersburg Academic University RAS, Russia)

Robert A. Suris, academician, Head of Sector of Theoretical Bases of Microelectronics (Ioffe Physico-Technical Institute RAS, Russia)

Head of Organizing Committee

Alexey E. Zhukov (St. Petersburg Academic University RAS, Russia)

Organizing Committee

Andrey A. Lipovskii (St. Petersburg State Polytechnical University, Russia)

Alexander V. Omelchenko (St. Petersburg Academic University RAS, Russia)

Mikhail V. Maximov (Ioffe Physico-Technical Institute RAS, Russia)

Valentina V. Zhurikhina (St. Petersburg State Polytechnical University, Russia)

Vladimir V. Korenev (St. Petersburg Academic University RAS, Russia)

Yulia V. Kudashova (St. Petersburg Academic University RAS, Russia)

Ivan I. Shostak (St. Petersburg Academic University RAS, Russia)

Eduard I. Moiseev (St. Petersburg Academic University RAS, Russia)

Contents

Invited Speakers	18
1. New design concepts of semiconductor lasers V Shchukin, N Ledentsov, J Kropp, G Steinle, N Ledentsov Jr, S Burger, F Schmidt	19
2. All-optical control of ultrafast currents in graphene Yuri P. Svirko.....	22
Crystal Growth	23
3. Development of methods for ordered growth of nanowires R R Reznik, K P Kotlyar, G E Cirlin, A I Khrebtov, Yu B Samsonenko, I P Soshnikov, V Dyakonov, U M Zadiranov, E M Tankelevskaya and D A Kudryashov.....	24
4. Formation of structures with autocatalytic CdTe nanowires by magnetron sputtering deposition K P Kotlyar, R R Reznik, A A Semenov, P Yu Belyavskiy, S I Pavlov, A V Nashchekin, I V Shtrom, I P Soshnikov, G E Cirlin.....	26
5. InAlN/GaN based heterostructures grown by plasma-assisted and ammonia MBE V.V.Mamaev, A.N.Alexeev, D.M.Krasovitsky, S.I.Petrov, V.P.Chaly, V.G.Sidorov.....	28
6. A study of GaP(As)N dilute nitrides alloys lattice-matched to Si substrates A Lazarenko, E Nikitina, M Sobolev, E Pirogov, A Egorov.....	30
7. Influence of various processings on properties of diodes Shottk I. Pashayev.....	32
8. Acceptor states and carrier lifetime in heteroepitaxial HgCdTe–on–Si for mid–infrared photodetectors S V Zablotsky, N L Bazhenov, K D Mynbaev, M V Yakushev, D V Marin, V S Varavin and S A Dvoretzky.....	33
9. Surface defects formation in growth of GaN from a multicomponent vapor via chemical reaction: a model A V Redkov, A V Osipov, S A Kukushkin.....	35
10. InAsSb on GaAs (001): influence of the As molecules form on composition and epilayer crystalline perfection by MBE E.A. Emel'yanov, B. R. Semyagin, A. P. Vasilenko, A.A. Komanov, A.K. Gutakovskii, M. A. Putyato, V. V. Preobrazhenskii.....	37
11. Modeling of axial heterostructure formation in ternary III-V nanowires A A Koryakin, N V Sibirev and D Zeze.....	39
12. MBE growth of GaP epilayers on Si substrate M S Sobolev, A A Lazarenko, E V Nikitina, E V Pirogov, A S Gudovskikh, A Yu Egorov.....	42

13.	Modelling the growth process of porous aluminum oxide film during anodization E M Aryslanova, A V Alfimov, S A Chivilikhin.....	44
14.	Modelling of field desorption of monocrystal nanotip K A Nikiforov and A A Krasnova.....	46
15.	Synthesis of silicon carbide at room temperature from colloidal suspensions of silicon dioxide and carbon nanotubes D A Zhukalin, A V Tuchin, T V Kulikova, L A Bityutskaya.....	48
16.	Self-limited growth of Au catalytic nanoparticles N V Sibirev, Y Berdnikov, V G Dubrovskii, J H Kang and H Shtrikman.....	50
17.	Modelling polytypism in III-V nanowires: role of group V and nucleation patterns during the growth J Grecenkov, V G Dubrovskii.....	52
18.	Photoluminescence observation from zinc oxide formed by magnetron sputtering at room temperature D Kudryashov, A Babichev, E Nikitina, A Gudovskikh.....	54
19.	Study of initial stages of vacuum-thermal Ag thin film deposition. A Savitskiy, D Gromov, A Trifonov, V Rubcov, E Lebedev.....	56
20.	Modeling of the behavior and statistical analysis of compressibility in the process of Langmuir monolayer structurization H V Grushevskaya, G G Krylov, N G Krylova, I V Lipnevich.....	58
21.	MBE growth and optical properties of GaAs nanowires grown on Si(111) substrate using two-temperature steps regime R R Reznik, I V Strom, Yu B Samsonenko, A I Khrebtov, A D Bouravlev, I.P.Soshnikov, N.V.Kryzanovskaya and G E Cirlin.....	60
	Nanobiotechnology	63
22.	The influence of biocompatible coating on the magnetic properties and MRI relaxivity of γ -Fe ₂ O ₃ nanoparticles A Furasova, M Kozlova, O Osmolovskaya, M Osmolovsky, V Korzhikov, A Dobrodumov.....	64
23.	Combination of laser correlation and dielectric spectroscopy in albumin investigations E. Nepomnyashchaya, A. Cheremiskina, E. Velichko, E. Aksenov, T. Bogomaz.....	66
24.	Theoretical study of the amphoteric oxide nanoparticle surface charge during multi- particle interactions in aqueous solutions A V Alfimov, E M Aryslanova, S A Chivilikhin.....	68
25.	Activator-free luminescent nanocontainers for cancer tumor theranostics D A Eurov, S A Grudinkin, D A Kurdyukov, A V Medvedev, E Yu Stovpiaga and V G Golubev.....	70
26.	Dual color localization microscopy of FtsZ and DNA in <i>Escherichia coli</i> V V Gorbunov, A D Vedyaykin, I E Vishnyakov, G E Pobegalov, A S Melnikov, P.Yu. Serdobintsev, A V Sabantsev.....	72

27.	Technical solution for studying the peculiarities of pressure distribution on the surface of a human's feet E.A.Daminova.....	74
28.	Numerical modeling of the liquid front propagation in inhomogeneous nanoporous media D S Golovina and S A Chivilikhin.....	75
29.	Porous silicon nanoparticles for target drug delivery: structure and morphology A O Belorus, P A Somov, S S Tulenin, Yu M Spivak, V A Moshnikov.....	77
30.	Spectroscopy of peptides, proteins and oligonukleotides from solutions by ion mobility P S Koryakin, A N Arseniev, N V Krasnov, M Z Muradymov.....	79
31.	Molecular Beacon CNT-based Detection of SNPs A S Egorov, V P Egorova, H V Krylova, I V Lipnevich, T I Orekhovskaya, A A Veligura, M I Govorov, B G Shulitsky, L.Y. Fedotenkova.....	81
32.	The FNS-based analyzing the EEG to diagnose the bipolar affective disorder O Yu Panishev, S N Panisheva, S A Demin.....	83
33.	The photovoltaic tandem converter of solar energy Y Grib, A Stsiapanau, A Smirnov, E Mukha.....	85
34.	Effect of electric field applied upon Langmuir monolayers, decorated cells and nanocomposite microcapsules A V Ermakov, A S Chumakov, V P Kim, I A Gorbachev, I V Vidyasheva, D A Gorin, G B Khomutov, E G Glukhovskoy.....	87
35.	Microfluidic device for unidirectional axon growth E.Malishev, A.Pimashkin, A.Gladkov, Y.Pigareva A.Bukatin, V.Kazantsev, I.Mukhina, M.Dubina.....	89
36.	Modeling of the behavior and statistical analysis of compressibility in the process of Langmuir monolayer structurization H V Grushevskaya, G G Krylov, N G Krylova, I V Lipnevich.....	91
	Optoelectronics and Lasers	93
37.	Experimental research of changes of properties of white LEDs during long-term operation depending on the ambient temperature S N Markova, I S Mateshev, Y P Timonin, A N Turkin, K S Fedorenko.....	94
38.	Application of a LED-photodiode optocouple for the study of human respiratory function A G Malyshev, N K Zhumashev, G N Lukyanov, K D Mynbaev and A A Rassadina.....	96
39.	Calculation and simulation of colour characteristics of white LEDs S N Markova, I S Mateshev, Y P Timonin, A.N.Turkin, K S Fedorenko.....	98
40.	Investigation of defects influence on the luminescent properties of Si/Si _{1-x} Ge _x :Er/Si heterostructures A P Detochenko, A A Ezhevskii, M V Stepikhova and V G Shengurov.....	100

41.	The way to optimization of active region structure of InAs/InGaAs semiconductor quantum dot laser V V Korenev, A V Savelyev, A E Zhukov, A V Omelchenko, M V Maximov.....	102
42.	Increasing the noise immunity of optical-electronic systems based on video cameras with an optical converter M P Boronenko, P Yu Gulyaev, A E Seregin, K G Poluhina.....	104
43.	The new ultra high-speed all-optical coherent streak-camera R M Arkhipov, M V Arkhipov, V S Egorov, I A Chekhonin, M A Chekhonin, S N Bagayev.....	106
44.	Ultimate modulation bandwidth of 850 nm oxide-confined vertical-cavity surface-emitting lasers M A Bobrov, S A Blokhin, A G Kuzmenkov, N A Maleev, V M Ustinov.....	108
45.	Control of stress and threading dislocation density in the buffer layers AlN, grown on c-Al ₂ O ₃ D S Zolotukhin, D V Nechaev, V V Ratnikov, V N Jmerik, S V Ivanov.....	110
46.	Formation of elements of integrated acousto-optic cell based on LiNbO ₃ films by nanotechnology methods O A Ageev, E G Zamburg, A S Kolomiytsev, D O Suchkov, I A Shipulin and A V Shumov.....	112
47.	Improving the efficiency of emission extraction from nitride LED structures with a textured interfaces A S Evseenkov, I A Lamkin , S A Tarasov, A V Solomonov.....	114
48.	The research of the influence of the pollutants on water plants with the help of optical methods A A Asadova, E V Timchenko, P E Timchenko, L A Zherdeva, N V Tregub.....	116
49.	Raman spectroscopy for the control of the atmosphere bioindicators Shamina L.A., Timchenko E.V., Zherdeva L.A.....	117
50.	Tunable LD pumped Tm:KLuW laser O P Dernovich, N V Gusakova, S V Kurilchik, M P Demesh, V E Kisel, A S Yasukevich and N V Kuleshov.....	118
51.	Optical tomography in reacting flows based on Stokes Raman scattering D Sharaborin, L. Chikishev, V Dulin, D Markovich.....	120
52.	Development of non-contact laser vibrometer I Kononov, E Velichko, E Aksenov.....	122
53.	Monte-Carlo modeling of drift mobility in thin organic layers: lattice type influence V M Sukharev and V R Nikitenko.....	124
54.	Multifunctional optical processor for biological microobjects investigation K Domnin, E Aksenov.....	126
55.	Overview of optical and optical-electronic systems for alignment control Maksim Kleshchenok and Valery Korotaev.....	128

56.	A high stability reference for a «clock» laser used as a source for a frequency standard based on cold magnesium atoms M A Tropnikov, A M Shilov and A N Goncharov.....	130
57.	Diode pumped continuous-wave Tm,Ho:KYW microchip laser N V Gusakova, O P Dernovich, S V Kurilchik, M P Demesh, V E Kisel, A S Yasukevich and N V Kuleshov.....	132
58.	Pulse modulation of optical signals with high dynamic extinction ratio A. Petrov, A.V. Tronev V. Lebedev, E. Velichko, A.Shamray.....	134
59.	Pointed and traveling wave models for different laser regime simulations Liubou Krylova, George Krylov.....	135
60.	Application of GaN for photoelectrolysis of water A D Fomichev, M V Puzyk, A S Usikov, S Yu Kurin, I A Ermakov, D S Kovalev, B P Papchenko, H Helava and Yu N Makarov.....	138
61	Nanomaterial disordering in AlGaIn/GaN UV LED structures E I Shabunina, M E Levinshtein, M M Kulagina, S Yu Kurin, A E Chernyakov, V N Petrov, V V Ratnikov, I N Smirnova, S I Troshkov, N M Shmidt, A S Usikov, H Helava and Yu N Makarov.....	140
62.	Diode lasers with asymmetric barriers for 850 nm spectral range: experimental studies of power characteristics F I Zubov, A E Zhukov, Yu M Shernyakov, M V Maximov, E S Semenova, L V Asryan.....	142
63.	Microdisk lasers based on GaInNAsSb/GaAsN quantum well active region E I Moiseev, N V Kryzhanovskaya, Yu V Kudashova, M V Maximov, M M Kulagina, S I Troshkov, A A Lipovskii, V M Korpijärvi, H Karjalainen, T Niemi, M Guina, A E Zhukov.....	144
64.	The effect of the sulfide passivation on the luminescence of microdisk mesas with quantum wells and quantum dots Yu V Kudashova, N V Kryzhanovskaya, M V Lebedev, T V Lvova, I I Shostak, E I Moiseev, A E Zhukov, M V Maximov, M M Kulagina, A M Nadtochiy, S I Troshkov.....	146
65.	Modulation doping of quantum dot laser active area and its impact on lasing performance S S Konoplev, A V Savelyev, V V Korenev, M V Maximov, A E Zhukov.....	148
66.	The influence of mobile impurities on photoelectric properties of PbSe-based multiphase photosensitive structures A N Belenkov, V V Davydov, S B Boyko, Z N Petrovskaya and A Yu Karseev....	150

Photonics	152
67. Cyclometalated complexes of platinum metals – the new luminescent sensors M V Nikolaeva, E A Katlenok, M V Puzyk and K P Balashev.....	153
68. Optical properties of inorganic WS ₂ nanotubes and their composites with gold nanoparticles in suspensions and films AYu Polyakov, V A Lebedev, E A Goodilin, R Tenne.....	155
69. Electromagnetic properties of water on GHz frequencies for medicine tasks and metamaterial applications N D Pavlov and Y A Baloshin.....	156
70. Wood anomalies in the vicinity of 3D Bragg diffraction from hybrid opaline photonic crystals V S Nikolaev, M M Voronov, S A Yakovlev, A B Pevtsov.....	158
71. Photoluminescence of undoped InAs autoepitaxial layers D D Firsov, O S Komkov and A S Petrov.....	160
72. Numerical simulation of carpet cloaking device in terahertz frequency range V V Gill, A V Vozianova, M K Khodzitsky.....	162
73. Plasmonic properties of silver single nanoislands: size and shape effect E S Piliugina, S A Scherbak, F Heisler, A K Samusev, A A Lipovskii.....	164
74. Expressions for reflection and transmission coefficients for one-dimensional photonic quasicrystals M M Voronov.....	166
75. Influence of surface plasmon resonance on ZnO photoluminescence. Role of pumping level A P Tarasov, Ch M Briskina, M V Ryzhkov, S I Rumyantsev, V M Markushev....	168
76. Plasmon resonance in metal-semiconductor AsSb-AlGaAs metamaterials V I Ushanov, V V Chaldyshev, N A Bert, V N Nevedomskiy, N D Ilinskaya, N M Lebedeva, M A Yagovkina, V V Preobrazhenskiy, M A Putyato, B R Semyagin	170
77. 384x288 readout integrated circuit for MWIR and LWIR HgCdTe based FPA A V Zverev, Yu S Makarov and E A Mikhantiev.....	172
78. X-ray tube with photo cathode G A Timofeev, N N Potrakov.	174
79. Photoluminescence of Gd ₂ O ₃ :Er ³⁺ -based materials for conversion of solar energy Yu A Kuznetsova, A F Zatsepin.....	175
80. Features of collimation and focusing of few-cycle optical beams D Puzyrev and S Kozlov.....	177
81. Theoretical investigation of the correlation between perturbations of quantum optical circuit parameters and its performance A V Kozubov and S A Chivilihin.....	179
82. Temperature switching of resonator modes in microcrystals InN D R Kazanov, V H Kaibyshev, V U Davidov, A N Smirnov, V N Jmerik, N V Kyznetsova, S V Ivanov, T V Shubina.....	181

83.	Extracting S-parameters of bilateral electro-optic network for lightwave component analyzer calibration D Frolov, A Levchenko.	183
84.	Elimination of light coupling negative effect on the accuracy of external quantum yield determination in a MJ SC S A Kozhukhovskaia, E D Filimonov, M A Mintairov and M Z Shvarts.	186
85.	Low-temperature study of the rhodamin 6G phosphorescence in polymethylmethacrylate films in the presence of silver nanoparticles E I Konstantinova, R Yu Borkunov, M V Tsarkov, V A Slezhkin and V V Bryukhanov.	188
86.	Magnetic system design for investigation of magneto-optical properties of objects in strong magnetic field in terahertz frequency range S E Azbite, AKh Denisultanovand, M K Khodzitsky.	190
87.	Dielectric permittivity of artificial periodic structure and local field effects M N Anokhin, A A Tishchenko and M N Strikhanov.	191
88.	Spontaneous emission in metal-dielectric metamaterials including losses A R Gubaydullin, M A Kaliteevski.	193
89.	Spectral sensitivity characteristics simulation for silicon p-i-n photodiode S U Urchuk, S A Legotin, D S Elnikov, V P Astahov, O I Rabinovich, V P Yaromskiy and K A Kuzmina.	195
90.	Analysis of magnetic system with high-anisotropy localized magnetic field for terahertz-radiation generation S E Azbite and M K Khodzitsky.	198
91.	Photoionization of Rydberg States by Ultrashort Wavelet Pulses S Yu Svita, V A Astapenko.	199
92.	Tunable narrowband filters with cross-shaped resonators for THz frequency band V Y Soboleva, Yu D Nazarov, E A Sedykh and M K Khodzitskiy.	201
93.	Ultraviolet dosimeters based on bers with luminescence silver molecular clusters A Pshenova and A Sidorov.	203
94.	Reaction-diffusion optoelectronics based on dispersed semiconductors M A Gradova, O V Gradov	205
95.	Subminiature Eddy Current Transducers for Studying of the semiconductor material S F Dmitriev, V N Malikov, A M Sagalakov, L I Shevtsova, A O Katasonov.	207
96.	Dual-wavelength method and optoelectronic sensor for online monitoring of the efficiency of dialysis treatment A M Vasilevsky, G A Konoplev, O S Stepanova, A Yu Zemchenkov, R P Gerasimchuk, A Frorip.	209
97.	Resonant plasmon-stimulated nonlinear absorption in three-level systems. A Zasedatelev, T Dubinina, V Krasovskii, O Suprunova and A Chistyakov.	211
98.	Quantum walks of photon pairs in twisted waveguide arrays D N Vavulin, A A Sukhorukov.	213

Quantum Dots and Wells	215
99. Photoluminescence of GaAs/AlGaAs quantum ring arrays Yu D Sibirmovsky, I S Vasil'evskii, A N Vinichenko, D M Zhigunov, I S Eremin, O S Kolentsova, N I Kargin and M N Strikhanov.....	216
100. Local field effects and metamaterials based on colloidal quantum dots O V Porvatkina, A A Tishchenko and M N Strikhanov.....	218
101. Hot exciton relaxation in multiple layers CdSe/ZnSe selfassembled quantum dots separated by thick ZnSe barriers M Eremenko, G Budkin and A Reznitsky.....	220
102. Refraction index modulation induced with transverse electric field in double tunnel-coupled GaAs/AlGaAs quantum wells A A Shumilov, M Ya Vinnichenko, R M Balagula, L E Vorobjev, D A Firsov, P A Kasilovich, M M Kulagina, A P Vasil'iev.....	222
103. Dynamics of mid-infrared light absorption related to photoexcited charge carriers in Ge/Si quantum dots O I Kirilenko, R M Balagula, A N Sofronov, V Yu Panevin, L E Vorobjev, D A Firsov and A A Tonkikh.....	224
104. CV and GV characteristics for MISstructures with CdHgTe-based quantum wells under the wide temperature range (8300) K description D Gorn, A Voitsekhovskii.....	226
105. Observation of Rabi oscillations in microcavities N E Kopteva, R V Cherbunin, A V Mikhailov.....	228
106. Mid-infrared photoluminescence from structures with InAs/GaSb type II quantum wells A V Selivanov, I S Makhov, V Yu Panevin, A N Sofronov, D A Firsov and L E Vorobjev.....	230
107. Ballistic thermopower of suspended semiconductor structures with two dimensional electron gas E Yu Zhdanov, A G Pogosov, M V Budantsev, D A Pokhabov, A K Bakarov and A I Toropov.....	232
108. The luminescence properties of colloidal quantum dots I I Mikhailov, S A Tarasov, A V Solomonov, I A Lamkin.....	234
109. Estimation of the effective electron-capture cross section in the emission processes from arrays of vertically coupled InAs quantum dots in an n-GaAs matrix A Baklanov, A Gutkin, P Brunkov.....	235
110. Ion synthesis of GaN nanocrystals in silicon D S Korolev, A N Mikhaylov, A I Belov, V A Sergeev, V K Vasiliev, A E Smirnov, D E Nikolitchev, R N Kryukov, D V Guseinov, A S Markelov, V N Trushin and D I Tetelbaum.....	237

111. Visible light activated room temperature gas sensors based on nanocrystalline ZnO sensitized with CdSe quantum dots I V Krylov, A S Chizhov, M N Romyantseva, R B Vasiliev, D G Filatova, K A Drozdov, A M Abakumov, A M Gaskov.....	239
112 . Spin-dependent energy gap oscillations in the ultra-short carbon nanotube (5, 5) S V Popov, G I Glushkov, A V Tuchin.....	240
113. Purification non-aqueous solution of quantum dots CdSe-CdS-ZnS from excess organic substance-stabilizer by use PEHD membrane K Kosolapova, A Al-Alwani, I Gorbachev and E Glukhovskoy.....	242
114. Increasing of AlGaAs/GaAs quantum well robustness to resonant excitation by lowering Al concentration in barriers I A Solovev, V G Davydov, Yu V Kapitonov, P Yu Shapochkin, Yu P Efimov, Yu K Dolgikh, S A Eliseev, V V Petrov, V V Ovsyankin.....	246
Other Aspects of Nanotechnology	248
115 The measurements of doping density in InAs by capacitancevoltage techniques with electrolyte barriers D Frolov, G Yakovlev and V Zubkov.....	249
116. Dependence of microwave-excitation signal parameters on frequency stability of caesium atomic clock A A Petrov, V V Davydov, V A Vologdin, D V Zalyotov.....	251
117. Electropulse obtainment of metal-carbon structures on the basis of IGBT-switch A Tikhomirov, N Sobolev and Y Izotov.....	252
118. Nanopatterning of silicate glasses via thermal poling A V Redkov, A N Kamenskii, A A Lipovskii.....	254
119. Study of colloidal particles $Fe_mO_n-SiO_2$ synthesized by two different techniques S A Ionin, K G Gareev, N V Permyakov, V A Moshnikov.....	256
120. Cu/Diamond composite heat-conducting shims E N Galashov, A A Yusuf and E M Mandrik.....	257
121. Crystallite model of nanotube flow caused by soliton O A Rodygina, S A Chivilikhin, I Yu Popov, V V Gusarov.....	259
122 . The conductivity of a thin semiconductor wire in the longitudinal magnetic field O V Savenco, I A Kuznetsova.....	261
123. MEMS switch with the active contact breaking mechanism I V Uvarov, V V Naumov, O M Koroleva and I I Amirov.....	263
124. Fabrication technology of CNT-Nickel Oxide based planar pseudocapacitor for MEMS and NEMS I M Gavrilin, S A Gavrilov, D G Gromov, N E Gruzdev, A A Dronov, E P Kitsyuk, E A Lebedev, A A Pavlov.....	265

125.	Regimes of photon generation in dynamical Casimir effect under various resonance conditions A V Levchenko, A I Trifanov.....	267
126.	Force sensitive resistor on the base of metal-carbon structures A Tikhomirov and Y Izotov.....	269
127.	Influence of ion irradiation on the resistive switching parameters of SiO _x -based thin-film structures D S Korolev, A N Mikhaylov, A I Belov, V A Sergeev, D V Efimovikh, I N Antonov, E V Okulich, O N Gorshkov, A P Kasatkin and D I Tetelbaum.....	271
128.	Microwave vortex field D Poletaev.....	273
129.	Effect of carbon-doping on magnetic properties of Mn/Si interface M V Gomounova, G S Grebenyuk, I I Pronin, B V Senkovskiy.....	275
130.	Model of quantum dot and resonant states for the Helmholtz resonator A M Vorobiev and I Yu Popov.....	277
131.	On the spectrum discreteness of the quantum graph Hamiltonian with δ -coupling M O Kovaleva, I Yu Popov.....	279
132.	Hysteresis phenomenon of the field emission from carbon nanotube/polymer nanocomposite S V Filippov, E O Popov, A G Kolosko and P A Romanov.....	281
133.	Changes in the density of states of the quantum well in a polar solvent M I Zakirov.....	283
134.	Phase diagram calculation of AIIIBV binary solutions of the eutectic type in the generalized lattice model model G A Panov and M A Zakharov.....	286
135.	Generalized Thomson Problem and its Applications in Carbon Nanotube Structures Design A N Bondarenko, L A Kozinkin.....	288
136.	Electron mobility in fully-depleted SOI films E G Zaytseva, O V Naumova, B I Fomin, V P Popov.....	290
137.	Electrophysical properties of thin films on the basis of phase change memory materials on the pseudobinary line GeTeSb ₂ Te ₃ A O Yakubov and D Y Terekhovb.....	292
138.	Problems of the experimental implementation of MTJ L A Mazaletskiy, A S Rudy, O S Trushin, V V Naumov and A A Mironenko.....	294
139.	Design and long-term monitoring of DSC/CIGS tandem solar module M F Vildanova, A B Nikolskaia, S S Kozlov and O I Shevaleevskiy.....	296
140.	Equation of state for simulation of nanosecond laser ablation aluminium in water and air. R Davydov, V Antonov.....	298

141.	Features of nuclear magnetic resonance signals registration in weak magnetic fields for the express - control of biological solutions and liquid medium by nuclear magnetic spectroscopy method A Karseev, V Vologdin, V Davydov.....	299
142.	Nanoimprinting and self-arrangement of silver nanoislands on glass surface I Reduto, A Kamenskii, A Baklanov, S Chervinskii and A Lipovskii.....	301
143.	Modification of properties of silicon epitaxial films processing in hydrogen plasma O YuSmirnova, K A Solyanikova, A V Ermakov.....	303
144.	Excitation model of cardiac p cells of the cardiac conduction system M Grigoriev and L Babich.....	305
145.	Two-dimensional porous anodic alumina for optoelectronics and photocatalytic application L S Khoroshko, N V Gaponenko.....	307
146.	Mathematical modeling of sedimentation process of nanoparticles in gradient medium S I Ezhenkova, S A Chivilikhin.....	309
147.	Study of micro- and nanomechanical oscillators based on crystalline and amorphous C and W nanowhiskers S Yu Lukashenko, V V Lysak, I D Sapozhnikov, I S Mukhin, A O Golubok.....	311
148.	Reflectance anisotropy spectroscopy of plasmonic nanocluster arrays covering semiconductor surfaces A V Korotchenkov and V A Kosobukin.....	313
149.	Modeling, creation and study of highly efficient solar cells based on nitride nanowhiskers arrays grown on Si substrates D A Kudryashov, A M Mozharov, I S Mukhin, G E Cirlin, J C Harmand and M Tchernysheva.....	316
150.	Research of materials for porous matrices in sol-gel systems based on silicon dioxide and metallic oxides E V Maraeva, A A Bobkov, V Ph Markov, V A Moshnikov, S S Nalimova, L V Shaidadrov, A V Tretyakov.....	318
151.	Investigation of experimental field emission data and classical theory conformity in real-time mode P A Romanov, S V Filippov, E O Popov and A G Kolosko.....	320
152.	A theory of spectral properties of disordered metal-semiconductor nanocomposites N A Olekhno, Y M Beltukov and D A Parshin.....	322
153.	THz radiation under noncentral propagation of electrons through periodical channel A A Ponomarenko, A A Tishchenko, K V Lekomtsev and M N Strikhanov.....	324
154.	Spectral correlations of phase modulated entangled photons V O Sheremetyev, A I Trifanov.....	326

155.	The flow reactor system for in-line synthesis of semiconductor nanoparticles O A Ryzhov, L B Matyushkin.....	328
156.	The characteristics of semiconductor-to-metal transition in VO ₂ of different morphology Yu V Petukhova, O M Osmolovskaya, M G Osmolowsky.....	330
157.	Modelling of field emitter array characteristics in diode system K A Nikiforov and M F Sayfullin.....	332
158.	Theoretical investigation of sedimentation process for nanoparticles statistical ensemble K D Mukhina, S A Chivilikhin.....	334
159.	High Resolution Fourier Transform Spectrum of C ₂ H ₄ in the Region of 2500 - 3000 cm ⁻¹ Yu S Aslapovskaya, A L Litvinovskaya.....	336
160.	New type of high efficiency silicon multijunction solar cells I A Morozov, A S Gudovskikh, T N Berezovskaya, D A Kudryashov.....	338
161.	Light in moving medium S A Petrenko, A I Trifanov.....	340
162.	Modes of silver nanoisland film growth on the surface of ionexchanged glass A Kamenskii, I Reduto, J Kobert and A Lipovskii.....	342
163.	Single-walled carbon nanotubes: from synthesis to applications Evgenia Gilshteyn, Alexey Tsapenko, Albert G. Nasibulin.....	344
164.	Investigation of the dielectric properties of composites based on silicon dioxide with carbon nanotubes A A Goshev, M K Eseev, C S Osokin, S N Kapustin.....	346
165.	Atomic force microscopy of lead sulphide – cadmium sulphide solid solutions layers obtained by chemical bath deposition E V Maraeva, L N Maskaeva, V Ph Markov, V A Moshnikov, S S Tulenin, N A Forostyanaya.....	348
166.	Laser cutting of GaN/Al ₂ O ₃ structures O S Medvedev, O Khait, S Yu Kurin, A S Usikov, B P Papchenko, H Helava and Yu N Makarov.....	350
167.	Synthesis of luminescent ceramics from alumina nanopowder A N Kiryakov, D V Ananchenko, V S Kortov and S V Zvonarev.....	352
168.	Elastic moduli of alumina nanoceramics J A Perevozchikova, E A Buntov, A F Zatsépin and V S Kortov.....	354
169.	Specialized probes with nanowisker structures for high resolution magnetic force microscopy M V Zhukov, K I Belousov, A M Mozharov, I S Mukhin, A O Golubok.....	356
170.	Formation of metallic nanostructures on the surface of ion-exchange glass by focused electron beam F E Komissarenko, M V Zhukov, I S Mukhin, A O Golubok and A I Sidorov.....	358

171. Energetics of H ₂ generation from aqueous electrolytes using GaN electrodes A M Puzyk, M V Puzyk, A S Usikov, S Yu Kurin, I A Ermakov, D S Kovalev, B P Papchenko, Yu N Makarov, N M Shmidt	360
---	-----

Section

Invited Speakers

New design concepts of semiconductor lasers

V Shchukin¹, N Ledentsov¹, J Kropp¹, G Steinle¹, N Ledentsov Jr¹, S Burger²,
F Schmidt²

¹ VI Systems GmbH, Hardenbergstr 7, Berlin 10623, Germany

² Zuse Institute Berlin (ZIB), Takustr. 7, Berlin 14195, Germany

Abstract. Oxide apertures in oxide-confined vertical cavity surface emitting lasers (VCSELs) provide possibilities for engineering of the optical modes. Refractive index of the oxidized AlAs layer is approximately twice lower than that of the semiconductor converting a $\sim\lambda/2$ cavity into a $\sim\lambda/4$ layer of a distributed Bragg reflector (DBR) or, as opposite, a non-resonant $\sim 3/4\lambda$ section into a $\sim\lambda/2$ cavity. In the latter case the VCSEL modes of the non-oxidized core region can be coupled to the intentionally engineered modes of the oxidized periphery as the orthogonality between these modes is broken by the oxidation-induced optical field redistribution. Engineered VCSEL designs show that the overlap between the VCSEL mode of the core and the tilted mode at the periphery can reach $>30\%$ resulting in significant leakage for high-order transverse modes as confirmed by a three-dimensional modelling. A 850-nm GaAlAs leaky VCSEL based on this concept is designed, modelled and fabricated, showing single-mode lasing with aperture diameters up to 5 μm . Side mode suppression ratio $>20\text{dB}$ is realized at the current density of $10\text{kA}/\text{cm}^2$. In the case of the oxidation of a $\sim\lambda/2$ cavity layer a laser is designed in which a very high order optical mode at an effective mode angle beyond the angle of the total internal reflectance at the surface has a much longer photon lifetime as compared to the fundamental mode. A near field VCSEL is thus engineered where the light can be efficiently out-coupled directly to a fibre or polymer waveguide without exiting the crystal to the air.

1. Introduction

Vertical Cavity Surface Emitting Lasers (VCSELs) are key components for optical interconnects based on multimode fibre (MMF) for the applications in high performance computers and data centers. Recently there arose a significant interest in single mode (SM) VCSELs for extended distance transmission over MMF. It was shown that 25 Gigabit per second data transmission is possible at distances ~ 1 km over MMF as the chromatic dispersion, the key limiting factor in modern MMF, is drastically reduced [1]. Earlier approaches to SM VCSELs with large apertures [1–3] include challenging technological steps hardly compatible with the low-cost industrial production of VCSELs.

2 Single mode VCSEL via oxide aperture engineering of the leakage of the optical modes

A method [4] for SM VCSEL is based on the fact that the oxidation of GaAlAs layers with high Al content forms a structure in which an all-semiconductor core is surrounded by an oxidized periphery (Fig. 1(a)) having a lower refractive index. The vertical VCSEL optical mode of the core lies in a continuum spectrum of tilted optical modes of the periphery. Due to a strong modification of the

refractive index by the oxidation, the modes of the core and of the periphery having different number of nodes are no longer orthogonal enabling leakage. Figs. 1(b) through 1(e) illustrate a break of orthogonality and a possibility of engineering a strong overlap between the two modes.

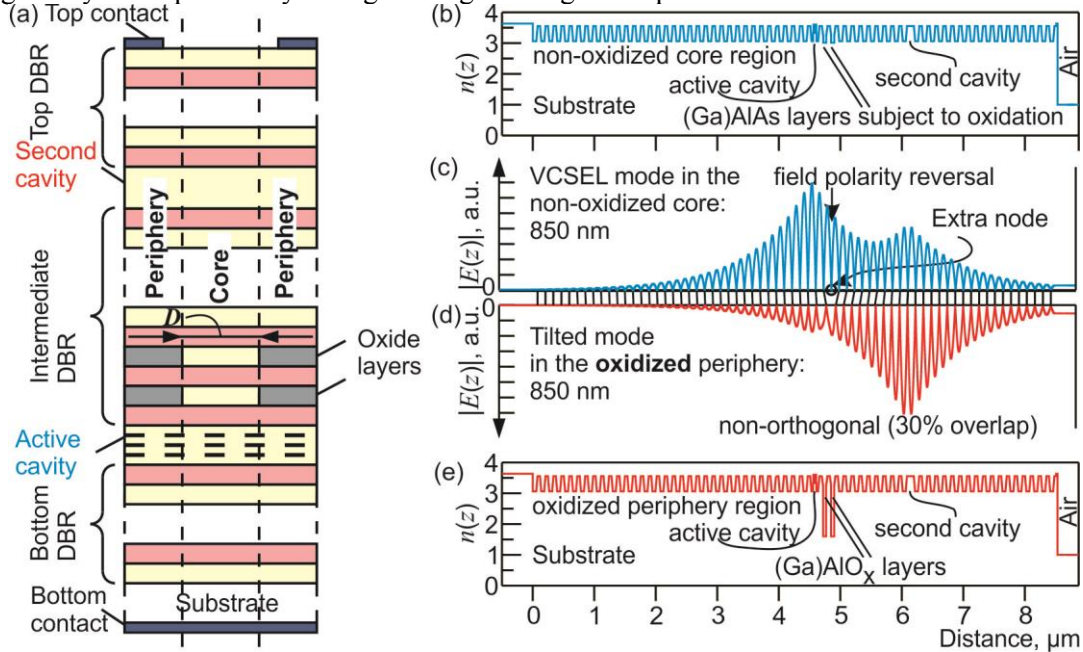


Fig. 1. (a) Schematic cross-section of a VCSEL with oxide apertures. (b) Vertical profile of the refractive index profile in the core. (c) VCSEL optical mode in the core. (d) Tilted optical mode at the periphery (d) Vertical profile of the refractive index at the periphery.

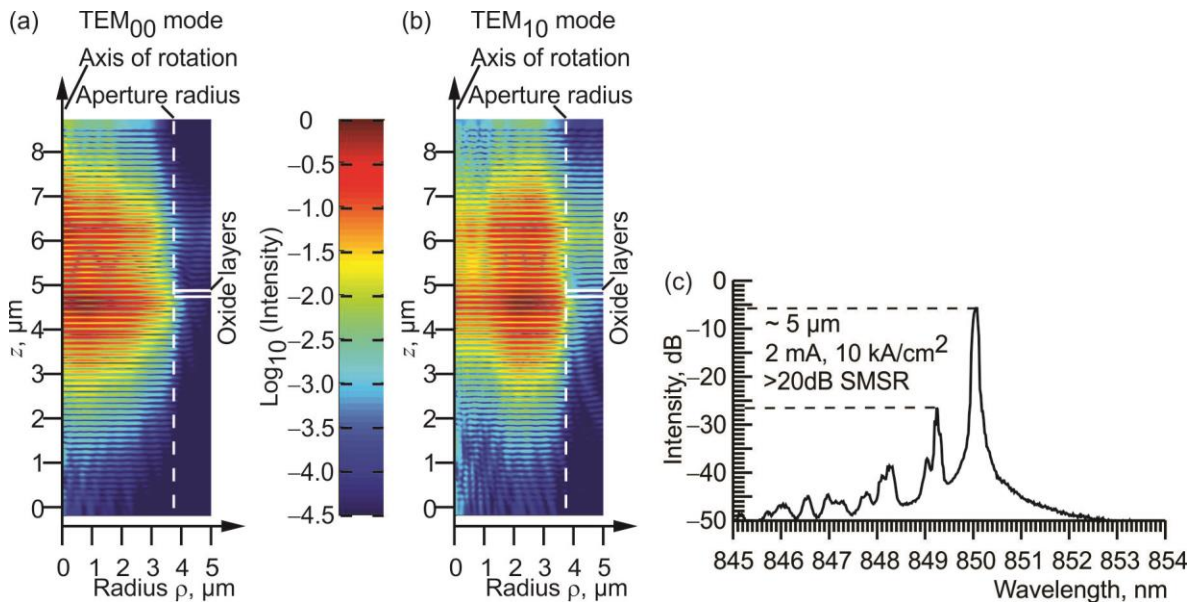


Fig. 2. Cross-sectional profiles of the TEM_{00} (a) and TEM_{10} (b) transverse optical modes in the VCSEL (c) Lasing spectrum of the VCSEL with 5 μm aperture diameter.

3D modelling of the transverse modes [5] show that the fundamental (TEM_{00}) mode (Fig. 2(a)) is located closer to the rotation axis and nearly does not interact with the periphery and a high-order (TEM_{10}) mode (Fig. 2(b)) is shifted closer to the periphery giving rise to a significant leakage indicated by yellow at the periphery opposite the second cavity. Higher leakage losses of the high-

order transverse modes support single transverse mode lasing, e.g. as observed at the VCSEL with the aperture diameter $5\mu\text{m}$ (Fig. 2(c)). At the current density 10 kA/cm^2 the side mode suppression ratio (SMSR) is $>20\text{ dB}$ [5]. To achieve SM lasing the approach does not require additional technology steps like surface patterning.

3. Near-field laser

Coupling and alignment of high-speed optical devices to optical waveguides is a critical challenge due to back reflections, reduced coupling efficiencies and difficulties to couple to a small diameter fibre or waveguide. Near-field coupling can overcome these problems [6]. If a surface emitting laser is generating laser light in an optical mode tilted with respect to the vertical axis (Fig. 3(a)) at an angle exceeding the angle of the total internal reflection at the semiconductor/air interface ($\sim 17^\circ$) the light can't exit the crystal. To ensure the operation in such a mode the cavity resonance is redshifted with respect to the gain spectrum, the top distributed Bragg reflector is of low reflectivity at angles close to the normal to the surface. The oxide apertures are configured such that an effective $\lambda/2$ layer is transformed by the oxidation into a $\lambda/4$ layer eliminating a cavity at the oxidized periphery thus suppressing leakage and creating a 3D "optical box" laser mode confinement. 3D modelling shows that the maximum Q-factor (~ 1000) is reached (Fig. 3(b)). If a polymer waveguide ($n\sim 1.5$) is attached, the Q-factor drops and the mode is efficiently coupled to the waveguide material (Fig. 3(c)).

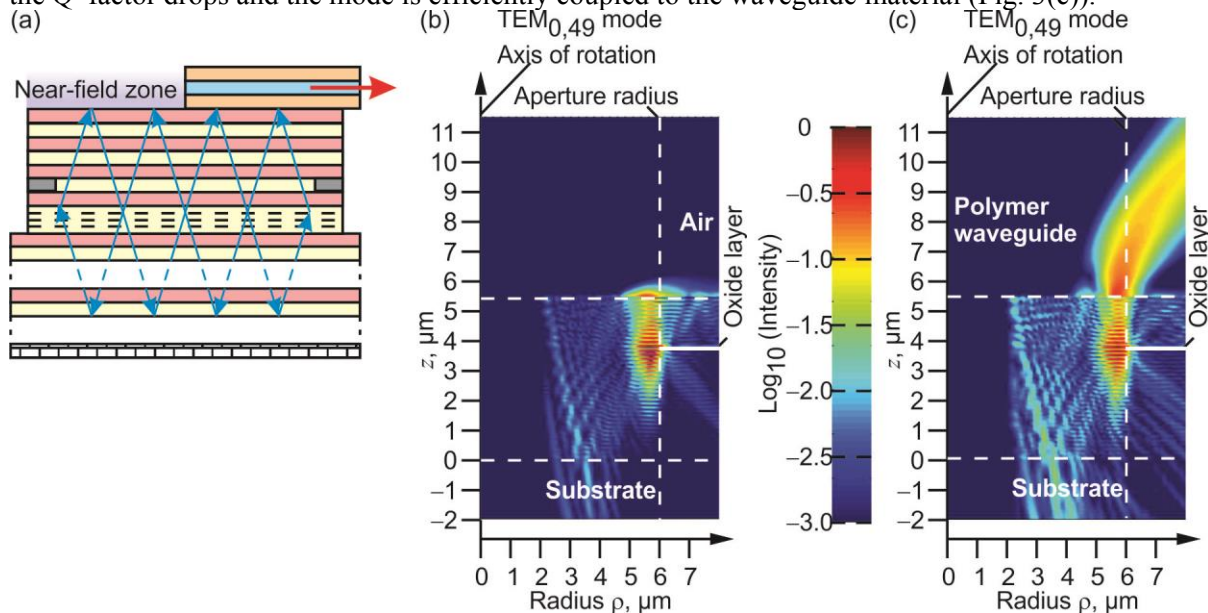


Fig. 3. (a) Schematic cross-section of a near-field laser. (b) Cross-section of a whispering gallery mode $\text{TEM}_{0,49}$ with a high Q-factor, the mode does not emit light to the air. (c) The whispering gallery mode $\text{TEM}_{0,49}$ efficiently coupled to the polymer waveguide.

The authors acknowledge support by ADDAPT project of the FP7 Programme of the European Union under Grant Agreement No. 619197.

- [1] Haglund E, et al., 2012 *Electron. Lett.* **48** 517
- [2] Chang-Hasnain C, et al., 1991 *IEEE J. Quant. Electron.* **27** 1402
- [3] Chen Ch, et al., 2009 *IEEE J. Sel. Topics Quant. Electron.* **15** 673
- [4] Ledentsov N, et al., 2012 *Proceedings of the Advanced Research Workshop on Future Trends in Microelectronics*, Corsica, France, June 25–29, 2012: *Future Trends in Microelectronics: Frontiers and Innovations*, S Luryi, J Xu and A Zaslavsky, eds., Wiley 142
- [5] Shchukin V, et al., 2014 *IEEE J. Quant. Electron.* **50** 990
- [6] Shchukin V, et al., 2015 *Proc. SPIE* **9381** 9381–30

All-optical control of ultrafast currents in graphene

Yuri P. Svirko²

Institute of Photonics, University of Eastern Finland, Joensuu, Finland

Strong and broadband light absorption in graphene allows one to achieve high carrier densities essential for observation of nonlinear optical phenomena making graphene a unique playground for studying many-body effects. Being of strong fundamental importance, these effects also open a wide range of opportunities in photonics and optoelectronics. Here, we make use of strong photon-drag effect to generate and optically manipulate ultrafast photocurrents in graphene at room temperature. Direction and amplitude of the drag-current induced in graphene are determined by polarization, incidence angle and intensity of the obliquely incident laser beam [1]. We also demonstrate that the irradiation of graphene with two laser beams of the same wavelength offers an opportunity to manipulate the photocurrents in time domain [2].

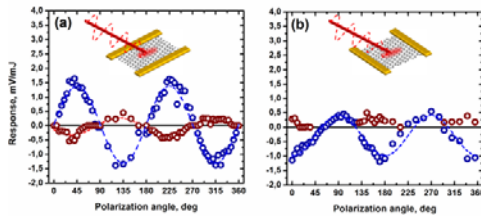


Fig. 1. The polarization dependence of the photocurrents in longitudinal (a) and transversal (b) geometries, correspondingly, at the incidence angle of $\alpha = 45^\circ$: Blue points correspond to the photon drag current, red points correspond to other contributions.

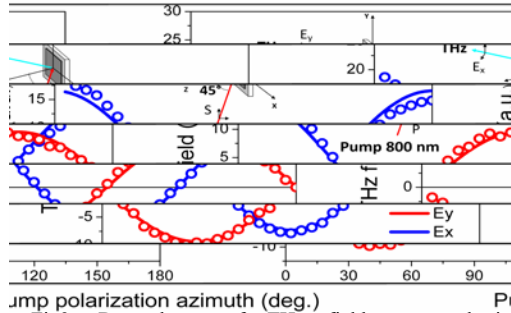


Fig2. Dependence of THz field generated in multilayered CVD graphene on the pump polarization

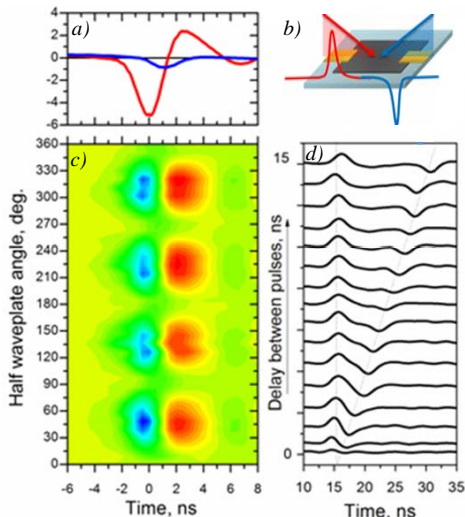


Fig.3. The photocurrent (a) induced by two 10 ns pulses arriving at the graphene simultaneously at mirror-reflection angles in transversal configuration (b) measured as a function of the polarization of the first pulse (c). Two pulses of the same intensity produce currents of opposite sign that cancel one another at zero time delay (d).

In the experiments, we used CVD graphene transferred to dielectric substrates and containing from 1 to 40 atomic layers [3]. Samples area was about 1 cm^2 . To induce photocurrents we employed a 1 kHz Ti:Sapphire femtosecond oscillator/amplifier (pulse width 120 fs, central wavelength of 790 nm) and optical parametric oscillator (pulse width 10 ns, a central wavelength tunable in the range from 1150 nm to 4000 nm). The light-induced current strongly depends on the polarization azimuth and vanishes at normal incidence. At a finite incidence angle, the photocurrent magnitude shows $\sin 2\phi$ - and $\cos 2\phi$ -like behavior (see Fig.1).

At the femtosecond excitation [4], the ultrafast currents results in the THz emission (Fig.2). Our analysis shows that the THz emission originates from the photon drag effect, i.e. from the, transfer of the photon momentum to free carriers .

All-optical control of photocurrent was demonstrated in the two-beam experiment when sample was irradiated with two mirror-reflected beams (see Fig.3b). At a zero time delay between the excitation pulses of the same intensity, the photocurrents completely compensate each other resulting in a zero net current. Since the drag current strongly depends on the polarization of the excitation beam, the net current was tuned by rotating the polarization plane azimuth of the first beam. The net current signal waveforms as a function of the first beam polarization azimuth obtained at nanosecond excitation is presented in contour plot on Fig.3c). The temporal profile of the net current can be controlled by varying time delay between excitation pulses (see Fig. 3d).

References

- [1] P. A. Obraztsov, G. M. Mikheev, S.V. Garnov, A.N. Obraztsov, Y. P. Svirko, "Polarization-sensitive photoresponse of nanographite". *Appl.Phys. Lett.* **98**, (2011) 091903.
- [2] P. A. Obraztsov, T. Kaplas, S. V. Garnov, M. Kuwata-Gonokami, A. N. Obraztsov, Yu. P. Svirko, "All-optical control of ultrafast photocurrents in unbiased graphene," *Scientific Reports*, **4**, 4007 (2014).
- [3] P. A. Obraztsov, G. M. Mikheev, S. V. Garnov, A. N. Obraztsov, and Yu. P. Svirko, "Broadband Light-Induced Absorbance Change in Multilayer Graphene," *NanoLetters* **11**, 1540-1545 (2011).
- [4] P. A., Obraztsov, N. Kanda, K. Konishi, M. Kuwata-Gonokami, S. V. Garnov, A. N. Obraztsov, Yu. P. Svirko, "Photon-drag-induced terahertz emission from graphen", *Physical Review B* **90**, 241416 (2014).

Section

Crystal Growth

Development of methods for ordered growth of nanowires

R R Reznik¹²³, K P Kotlyar², G E Cirlin¹²³⁴⁵, A I Khrebtov¹⁶, Yu B Samsonenko¹³⁴, I P Soshnikov¹³⁴, V Dyakonov⁷⁸, U M Zadiranov³, E M Tankelevskaya³ and D A Kudryashov¹

¹St-Petersburg Academic University – Nanotechnology Research and Education Centre RAS, Khlopina 8/3, 194021, St-Petersburg, Russia

²St-Petersburg State Polytechnical University – Nanotechnology, Polytechnicheskaya 29, 195251, St-Petersburg, Russia

³Ioffe Physical Technical Institute RAS, Politekhicheskaya 26, 194021, St-Petersburg, Russia

⁴Institute for Analytical Instrumentation RAS, Rizhsky 26, 190103, St-Petersburg, Russia

⁵Fock Institute of Physics, St-Petersburg State University, 198504 Petrodvorets, Russia

⁶Vavilov State Optical Institute, 199034, Birzhevaya line 12, St-Petersburg, Russia

⁷ZAE Bayern, Energieeffizienz Am Galgenberg 87, 97074 Würzburg, Germany

⁸University of Wuerzburg, Sanderring 2, 97070, Würzburg, Germany

Abstract. Developed a method of manufacturing substrates for self-catalyst/free-catalyst ordered growth of the nanowires. The experiments show the possibility of autocatalytic growth of ordered GaAs NWs on the produced during the research substrates.

1. Introduction

Nanowires are crystalline structures, the length of which considerably exceeds the diameter which is from 8 to 300 nm. Nowadays the interest in nanowires is caused by the prospects of their use in many applications, such as: chemical and biological highly sensitive sensors [1-3] emission cathodes and cantilevers for STM / AFM, fuel cells and batteries [4], in optoelectronics and one-particle electronics, in electromechanical devices (tensor sensors, microphones, piezoresistors).

The fabrication of device structures based on nanowires requires the development of methods and technologies for the synthesis of ordered semiconductor NWs and research of their features. We emphasize that developed by many researchers approach based on the creation of orderly catalytic growth centers of NWs [5] has a number of disadvantages, including the possibility of growth centers' shifting to their complete removal from the surface, branching of NWs, uncontrolled growth in other directions, uncontrolled alloying of catalyst by the material etc.

The aim of the work is to determine the possibility of producing A^3B^5 structures with ordered free-catalyst or self-catalytic NWs through inhibitory layer with ordered windows of growth. The initial goal is the formation of holes in the inhibitory ordered SiO_2 layers by electron lithography.

2. Experiments

Polished wafers Si (111) brand KDB-10 with SiO_2 layer about 50-100 nm thick previously synthesized by magnetron sputtering and / or thermal oxidation were used as the samples [ссылки на методики формирования (производства) слоев оксида кремния на кремнии] .

Electron resist layer 672 ARP (PMMA-polymethylmethacrylate 950 K) is coated using spinor (модель) on the sample surface and after that dried for 15 minutes at $T = 90^{\circ}C$. The thickness of the layer is about 70 nm. Then the sample was exposed in the electron microscope Zeiss SUPRA 25 with electron lithography unit Elphy Quantum Raith at electron energy 20 keV and. The developing is released in methylisobutylceton-isoprpanol 1:3 solution. The transferring lithographic images into

SiO₂ layer is released by etching with argon ion beam at energy of 0.5 keV and/or in SF₆ plasma. After that residual polymer is removed in O₂ plasma. At the final stage GaAs NWs is grown using MBE self-catalyst method [6].

3. Results

As a result of experiments, managed to get a substrate for the growth of nanowires with ordered holes for growth (fig. 1). The smallest diameter of the resulting stable windows was 40 nm, which is ideal for further growth, such as GaAs nanowires. The minimum spacing between the windows in the inhibitory layer was 2 microns.

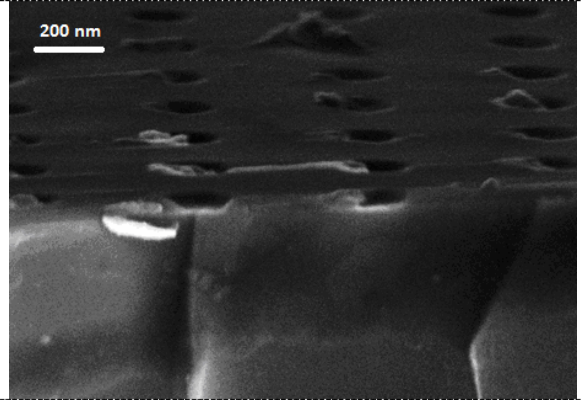


Figure 1. SEM image of sample with "Windows" in the SiO₂ layer on the Si substrate after ion etching

The Example of the sample with surface lithographic structure in the SiO₂ layer is shown in fig. 2. Nw is 1000 nm high and 30 nm in diameter. The growth of individual NWs with low density is observed off the field of lithographic picture, the arrangement of these NWs is disordered and random and apparently due to insufficient purity of the process.

There is SiO₂ flaking from the silicon surface in a number of cases after etching on the samples with SiO₂ layer applied by magnetron sputtering (figure 6). This happens due to the lack of adhesion of SiO₂ layer to the substrate during magnetron sputtering. No flaking of the inhibitory layer is observed on the samples with SiO₂ layer produced by oxidation of the substrate.

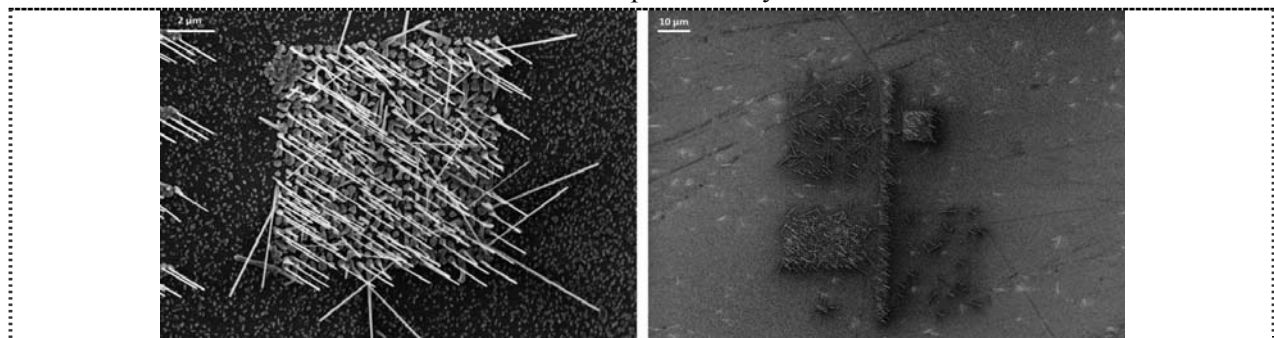


Figure 2. SEM image in geometry top view of ordered arrays of GaAs NW on substrates with a SiO₂ layer with a lithographic Windows.

- [1] Patolsky F, Zheng G and Lieber C M Fabrication of silicon nanowire devices for ultrasensitive, label-free, real-time detection of biological and chemical species *Nature Protocols* **1** no 4 1711-1724
- [2] Mathews M, Jansen R, Rijnders G, Lodder J C, and Blank D H A Magnetic oxide nanowires with strain-controlled uniaxial magnetic anisotropy direction *Phys. Rev. B* **80** no 6 064408
- [3] Markussen T, Ruruli R, Brandbyge M and Jauho A-P Electronic transport through Si nanowires: Role of bulk and surface disorder *Phys. Rev. B* **74** no 24 245313
- [5] Chan C K, Peng H, Liu G, McIlwrath K, Zhang X F, Huggins R A and Yi Cui High-performance lithium battery anodes using silicon nanowires *Nature Nanotechnology* **3** no 1 31-35
- [5] Persson A I, Fröberg L E, Samuelson L and Linke H The fabrication of dense and uniform InAs nanowire arrays *Nanotechnology* **20** no 22 225304
- [6] Soshnikov I P, Petrov V A, Proskuryakov U U, Kudryashov D A, Nashchyokin A V, Cirilin G E, Treharne R, Durose K Formation of structures with noncatalytic CdTe nanowires *Physics and Technology of Semiconductors* **47** no 7 865-878

Formation of structures with autocatalytic CdTe nanowires by magnetron sputtering deposition

K P Kotlyar¹, R R Reznik^{1,2}, A A Semenov⁵, P Yu Belyavskiy⁵, S I Pavlov³,
A V Nashchekin³, I V Shtrom^{2,4}, I P Soshnikov^{2,3,4}, G E Cirlin^{2,3,4}

¹St. Petersburg State Polytechnical University, 195251 St. Petersburg, Russia

²St. Petersburg Academic University - Nanotechnology Research and Education Centre of the Russian Academy of Sciences, 194021 St. Petersburg, Russia

³Ioffe Physico-Technical Institute of the Russian Academy of Sciences, 194021 St. Petersburg, Russia

⁴Institute for Analytical Instrumentation of the Russian Academy of Sciences, 190083 St. Petersburg, Russia

⁵Saint Petersburg Electrotechnical University "LETI", 197376 St. Petersburg, Russia

Abstract. In this work we experimentally studied the effect of substrate temperature on the growth of CdTe structures on the surface of the substrate Si (111) by magnetron sputtering deposition. The possibility of synthesis of autocatalytic CdTe nanowires with high crystalline perfection at a substrate temperature of 530°C. Typical dimensions obtained nanowires 20-50 nm in diameter and from 500 to 5000 nm in length with a density of 10^6 cm⁻².

1. Introduction

Cadmium telluride (CdTe) is a promising material for the production of low-cost efficient solar cells [1,2]. One of the possible ways to increase the efficiency of photoconversion is the transition from planar to three-dimensional morphology, for example nanowires (NWs).

Unfortunately, catalytic growth of NWs can be accompanied by uncontrolled doping by catalyst materials, that conduces noncontrollable alters of electrooptical characteristics of the structure. Therefore development of autocatalytic growth NWs is actual task.

In [3], the possibility of the growth of non-catalytic CdTe NWs on Si substrates using magnetron sputtering method (MSD) is demonstrated. But, measurements of photoluminescence (PL) of these structures did not contain of the emission band in the range important for optoelectronic applications. The absence of the PL emission can be associated with defects in the structure of the NWs. The work is an extension of these studies and aims to study the possibilities of synthesis of autocatalytic CdTe NWs with high crystalline perfection by MSD.

2. Experimental technique

Si (111) wafers are used as substrates. CdTe are deposited using MSD in VUP-7 chamber (Selmi Ukraine). The surface morphology of structure are studied using scanning electron microscope Zeiss Supra 25. The structure and composition of the samples are investigated photoluminescence and e-beam microanalysis.

3. Results and discussion

We find three morphologies of CdTe structures:

At temperatures below 250°C are grown polycrystalline films CdTe textured along the <111> direction. Amorphous layers of CdTe are grown at temperature in the range between from 300°C to 450°C. Forming of textured and amorphous films are typically for different materials [4,5]. Magnetron deposition of CdTe on the Si (111) substrate at the temperature about 530°C and a deposition rate about 0.1-0.3 nm/s leads to formation of two types of NWs (Fig. 1): short and long. Long NWs have typical sizes of 20-50 nm in diameter and from 500 to 5000 nm long at a density of 10^6 cm^{-2} . The characteristic diameter and length of short NWs amount 100-200 nm and 50-500 nm, respectively.

The structure of short NWs are multidomain. The long NWs have the morphology of a single crystal with preferential growth direction along the <111>. The presence of two morphologies suggests two mechanisms of generation and growth of NWs. During the SEM studies, we find significant fluctuations of NWs under the electron beam. These oscillations are associated with the charge at the object and suggest the possibility of significant piezoelectric effect.

E-beam microanalysis spectra show that the composition of all the samples is close to the CdTe stoichiometric.

Low-temperature PL spectra of the samples synthesized at the growth temperature below 250°C and the high temperature (530°C) comprises an emission line in the region of 1.4-1.6 eV. Samples formed in the temperature range between 300°C - 450°C do not contain the emission band in this range. Samples with polycrystalline structure have width line luminescence at low intensity. The high-temperature samples (Fig. 2) are a maximum of 1.58 eV and a full width at half maximum of about 19 meV. The result is evident the high crystalline perfection of NWs.

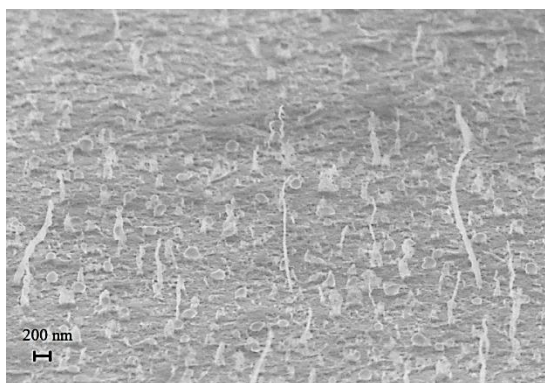


Figure 1. SEM image of the sample with CdTe/Si (111) structure grown by MSD at sample temperature 530°C.

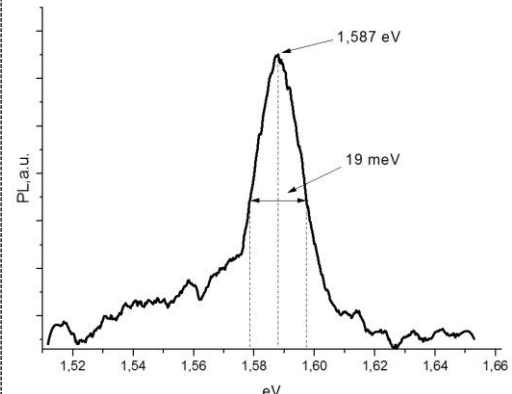


Figure 2. PL spectrum of sample with CdTe NWs.

4. Conclusion

We experimentally demonstrated the possibility of synthesis of autocatalytic CdTe NWs with high crystalline perfection at a substrate temperature of 530°C. Typical sizes of the grown CdTe NWs 20-50 nm in diameter and 500 to 5000 nm length at the density of 10^6 cm^{-2} . The grown structures with CdTe NWs can be applied for optoelectronic and piezoelectric devices.

References:

- [1] *CdTe and Related Compounds; Physics, Defects, Hetero and Nano-Structures, Crystal Growth, Surfaces and Applications*, Ed. by R Triboulet and P Siffert (Elsevier, Amsterdam, 2010).
- [2] *Semiconductor Nanomaterials for Flexible Technologies: From Photovoltaics and Electronics to Sensors and Energy Storage*, Ed. by Y Sun and J A Rogers (Elsevier, Amsterdam, 2010).
- [3] Soshnikov I P, 2013 *Semiconductors* **47** 875-878
- [4] Tang Zhiyong, 2006 *Science* **314** 274-278
- [5] Murray C B, 2000 *Annu. Rev. Mater. Sci.* **30** 545-610

InAlN/GaN based heterostructures grown by plasma-assisted and ammonia MBE.

V.V.Mamaev^{1,3,*}, A.N.Alexeev¹, D.M.Krasovitsky², S.I.Petrov¹, V.P.Chaly²,
V.G.Sidorov³

¹SemiTEq JSC, Saint-Petersburg, Russia

²Svetlana-Rost JSC, Saint-Petersburg, Russia

³ Saint Petersburg State Polytechnical University, Saint-Petersburg, Russia

Abstract. The results of use of STE3N MBE System for growth of GaN nanoheterostructures by both types of MBE (using plasma activation of nitrogen and ammonia) are presented. It is shown that the use of high-temperature AlN/AlGaIn buffer layers grown using ammonia at extremely high temperatures (up to 1150°C) allows to improve drastically the structural quality of the GaN layers and reduce dislocation density down to $9 \cdot 10^8 - 1 \cdot 10^9 \text{ cm}^{-2}$. On the other hand, unlike the ammonia MBE, which is difficult to use at $T < 500^\circ\text{C}$ (because of low decomposition efficiency of ammonia), PA-MBE is very effective at low temperatures, for example for growth of InAlN layers lattice-matched to GaN. The results of the growth of high quality GaN/InAlN heterostructures using both PA-MBE and NH₃-MBE (at extremely high ammonia flux) are shown.

At present time, an increasing number of researchers choose plasma-assisted MBE as it is simpler in service and also has a number of features, for example, such as possibility of low-temperature growth and absence of hydrogen on the growing surface. These features are very useful for growth of InN, InGaIn with high In content, InAlN and also effective p-doping. However unlike to ammonia MBE this method doesn't allow to increase noticeably the growth temperature, and thus improve the quality of the material by increasing the surface mobility of atoms.

One of the main problems in manufacturing GaN-based devices up to date is the lack of low cost lattice-matched substrates. Growth of III-Nitrides on mismatched substrates using different buffer layers usually yields high dislocation density, in the range of $10^9 - 10^{10} \text{ cm}^{-2}$ for MBE and 10^7 cm^{-2} for MOCVD using ELOG, which affect the device quality and reliability. Moreover, typical growth temperatures in MBE are much lower as compared with MOCVD. It leads to insufficient surface mobility of adatoms, worse coalescence of nucleation blocks, and, as a result, high dislocation density which limits carrier mobility. Typical values of room temperature electron mobility in GaN grown on sapphire are in the range 250-350 $\text{cm}^2/\text{V}\cdot\text{s}$ for MBE and 500-700 $\text{cm}^2/\text{V}\cdot\text{s}$ for MOCVD [1,2]. On the

other hand, MBE has several advantages: in-situ RHEED monitoring, sharper heterojunctions, higher purity etc.

In this paper we present the results of employing both types of MBE (plasma-assisted and ammonia), obtained in STE3N MBE System (SemiTEq). It is shown that the use of high-temperature buffer layers AlN/AlGa_xN grown by NH₃-MBE at extremely high temperatures (up to 1150°C) allows one to improve drastically GaN structural quality. The dislocation density in GaN grown by NH₃-MBE or PA-MBE on such buffer layer was reduced down to (9-10)×10⁸ cm⁻² that resulted in substantial increase in electron mobility up to 600-650 cm²/Vs in a 1.5-μm-thick GaN:Si (n=3-5×10¹⁶ cm⁻³) [3]. This result is comparable with a good quality MOCVD GaN and several times better than in conventional MBE. Importantly, growth of AlN at 1150°C is difficult to realize in PA-MBE since Al-rich mode is necessary for 2D-growth, while desorption of Al becomes significant at T>900°C.

Employing such a GaN layer in a double heterostructure (DH) with the cap Al_xGa_{1-x}N barrier layer (x=0.25-0.4) allowed us to vary the electron sheet density and mobility in a two dimensional electron gas (2DEG) in the range of (1.0-1.8)×10¹³ cm⁻² and 1300-1700 cm²/V's, respectively, providing control of a 2DEG channel sheet resistance in the range of 230-400 Ω/□.

On the other hand, unlike the NH₃-MBE which is difficult to use at T <500°C (because of low decomposition efficiency of ammonia), PA MBE growth is very effective at low temperatures, for example for InAlN layers lattice-matched to GaN. However, the results of the growth of InAlN lattice-matched to GaN by NH₃-MBE at extremely high flux of ammonia were published recently [4]. In this paper we show the results of growth of good quality GaN/InAlN heterostructures using both PA-MBE and NH₃-MBE. Also the results of heterostructures growth for test GaN-based UV photocathodes are presented.

[1] J.B. Webb et al., J. Crystal Growth **230**, 584 (2001).

[2] I. Akasaki and H. Amano, Jpn. J. Appl. Phys. **45**, 9001 (2006).

[3] S.I. Petrov, A.N. Alexeev et al, Phys. Status Solidi (c), 9 (3-4), 562 (2012).

[4] M.H. Wong, F. Wu, C.A. Hurni, S. Choi, J. S. Speck et al, Appl. Phys. Lett. 100, 072107 (2012)

[5] H.M. Ng et al., Appl. Phys. Lett. **73**, 821 (1998).

A study of GaP(As)N dilute nitrides alloys lattice-matched to Si substrates

A Lazarenko¹, E Nikitina¹, M Sobolev¹, E Pirogov¹, A Egorov²

¹ St.Petersburg Academic University, 8/3 Khlopina str., St.Petersburg, 194021, Russia

² Ioffe Physico-Technical Institute RAS, Saint-Petersburg 194021, Russia

Abstract. This article discusses the structural and optical properties of heterostructures with layers of GaP_{1-x}N_x ternary and GaP_{1-x-y}N_xAs_y quaternary alloys grown by molecular beam epitaxy on gallium phosphide and silicon substrates. Study of structures was carried out by methods of high resolution X-ray diffraction and photoluminescence in a wide temperature range 10-300 K. In the spectra of low temperature photoluminescence of dilute nitride alloys with small mole fraction of nitrogen (less than 0.007) clearly resolved narrow lines associated with localized states of nitrogen pairs and their phonon replica are observed.

Growing high-quality A³B⁵ compound semiconductors with a direct band-gap on Si substrates is the key to implementation of optoelectronic integrated circuits (OEIC), light-emitting diodes and solar cells on Si substrates [1,2]. A promising material for heteroepitaxy on silicon is gallium phosphide. The lattice mismatch between GaP and Si is rather small (0.37% at room temperature), and upon the addition of nitrogen during the epitaxial growth of GaP_{1-x}N_x on silicon, the crystal lattice parameters can be completely matched.

Even at a relatively low nitrogen fraction in nitrogen containing GaAs and GaPN alloys, substantial modification of the conduction band is observed. It was shown [3] that the conduction band of the nitrogen containing GaAsN and GaPN alloys was split into two subbands, E₊ and E₋, due to interaction of the localized energy level of nitrogen and the conduction band of the GaP and GaAs compounds. The addition of nitrogen to the GaP and GaAs materials yields a decrease in the band gap in combination with a decrease in the lattice constant, and the addition of nitrogen to the GaP material brings about the formation of the direct gap structure of the electron bands in the GaP_{1-x}N_x alloy.

In this work we investigate structural and optical properties of GaPN(As) layers grown on Si and GaP substrates by molecular-beam epitaxy (MBE). The structures were grown by MBE with VEECO GEN III system with a plasma source of nitrogen. Study of structures was carried out by methods of high resolution X-ray diffraction (XRD) and photoluminescence (PL) in a wide temperature range 10-300 K.

Comparison of the obtained experimental data from XRD curves to the values of nitrogen molar fraction calculated using the BAC model [3] (for the energy maximum coinciding with the experimentally observed PL peak) showed that the hybridization parameter is not constant and varies depending on the molar fraction of nitrogen in the solid solution. Figure 1 shows a plot of hybridization parameter V (used to calculate the energy position of conduction band in GaP_{1-x}N_x epilayers) versus nitrogen molar fraction x.

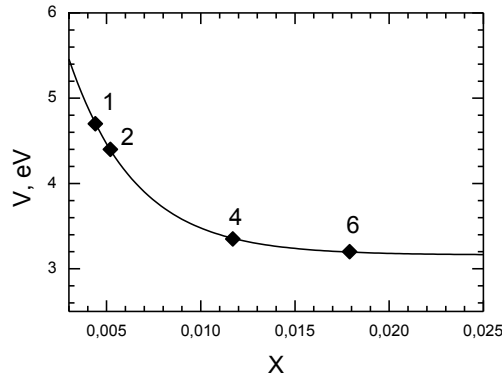


Figure 1. Dependence of the hybridization parameter on the molar fraction of nitrogen in $\text{GaP}_{1-x}\text{N}_x$.

In the low-temperature PL spectra of the samples with a low nitrogen content ($x < 0.007$), clearly resolved lines, associated with localized states of nitrogen pairs, and their phonon replicas are observed (figure 2). This effect is most clearly pronounced for the sample with the lowest molar fraction of nitrogen (black line). The energy positions of the levels of nitrogen pairs NN_i and individual nitrogen atoms in GaP and subband E_- of the conduction band of the GaPN alloy are also investigated.

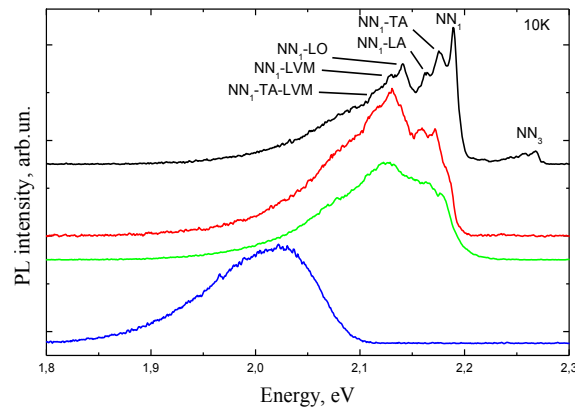


Figure 2. LT PL spectra of the $\text{GaP}_{0.918}\text{N}_{0.005}\text{As}_{0.077}/\text{GaP}$ (black line), $\text{GaP}_{0.993}\text{N}_{0.007}/\text{GaP}$ (red line), $\text{GaP}_{0.994}\text{N}_{0.006}/\text{Si}$ (green line) and $\text{GaP}_{0.937}\text{N}_{0.016}\text{As}_{0.047}/\text{GaP}$ (blue line) heterostructures at 10 K.

References

- [1] S. Y. Moon, H. Yonezu, Y. Furukawa, Y. Morisaki, S. Yamada, and A. Wakahara, *Phys. Status Solidi A* **204**, 2082 (2007)
- [2] A. V. Babichev, A. A. Lazarenko, E. V. Nikitina, E. V. Pirogov, M. S. Sobolev, and A. Yu. Egorov, *Semiconductors* **48**, 501 (2014)
- [3] B. Kunert, S. Reinhard, J. Koch, M. Lampalzer, K. Volz and W. Stolz, *Phys. Status Solidi C* **3**, 614 (2006)

Influence of various processings on properties of diodes Shottk

I. Pashayev

Sumgait State University, AZ 5000,
Sumgayit 43-quarter, Azerbaijan

Abstract

In the given work the reason of occurrence of a superfluous current near to temperature of crystallisation of amorphous metal alloy PbSb is studied and is simultaneously explained, influence ultrasonic processings (UP) on the properties, diodes Shottki made on technology (DSH) with a metal alloy a(PbSb)-nSi solar elements (SE). It is received, that occurrence of a superfluous current a(PbSb)-nSi DSH under action of thermoannealing is connected with changes of structure of an amorphous film of metal at transition in a polycrystalline condition. Influence UP on photo-electric properties a(PbSb)-nSi the sample SE depend on chosen mode UP.

The literature on the physics and technology of metal-semiconductor contact, extensively studied the role of semiconductor processes occurring in the contact, and it is believed that all these processes are associated with the semiconductor. The role of the metal in most cases neglected. The role of metal and its crystal structure on processes taking place not considered and poorly understood. To identify the role of the metal have been studied properties of Schottky diodes [1-3], depending on the structure and the metal contact region. Also investigated were the main parameters of the Schottky diode, such as saturation flux density, barrier height, the breakdown voltage, the ideality factor and not others, depending on the size of the contact area and thickness of the metal film. In recent years of the twentieth century, has increased interest in the Schottky diodes manufactured with the use of films of metals and metallic alloys, amorphous structure [1,2]. The reason for this interest is that the use of metal films with amorphous structure allows us to produce LH with important application properties. The advantage of using amorphous metal consists in the fact that due to the absence of grain boundaries and the grain structure in amorphous form has a uniform interface (GH) and, as a result, the DS should have the properties close to ideal. In addition, there are reports that the amorphous metal films serve as a good diffusion and electric barriers in microelectronic structures. This paper deals with the appearance of excess current aPbSb-nSi in DS near the crystallization temperature of amorphous metal alloy, and also examine the effect of the RCD on the properties of silicon solar cells aPbSb-nSi which are made by technology DS.

Since the ultrasonic treatment is an effective way to increase the internal energy of solids, depending on the absorption coefficient and the intensity of the ultrasound, various structural changes affecting the photoelectric and electrical properties of materials, as well as on the process of plastic deformation.

LH was used for manufacturing a silicon wafer n - type orientation (III) and a resistivity of 0.7 Om.sm. The matrix contains 14 diode area which varies in the range from 100 to 1400 mm². In this case, the contact area is equal to 1400 mm². Metal alloy a (PbSb) was deposited by electron-beam evaporation from two sources. Alloy (PbSb) was selected from those considerations that both components are widely used in microelectronics, and the alloy is well technologically. On the possibility of the alloy films with amorphous structure reported in [4]. Evaporation rate component is selected so that the composition of the alloy film corresponded Pb₅₂Sb₄₈, as in [4] reported that this alloy is prone to amorphization.

With the X-ray analysis revealed that the alloy films Pb₅₂Sb₄₈ before annealing has an amorphous structure, the appearance of excess current in a (PbSb) -nSi LH after annealing at temperatures above 180°S and due to a change of the interface DS. The experimental data show that the RCD affect the characteristics of a (PbSb) -nSi sample SE, to improve the photovoltaic parameters SE SE should be used RCD with a capacity of about $W_{uz} = 0,1Vt / cm^2$.

References

- [1]. B. Brodova, SG Bunchuk AN Lukyanov Technical Physics Letters, 2010, vol. 36 (4), pp.8-11.
- [2]. AN Gontaruk, D.V.Korbutyak, EV Korbut Technical Physics Letters, 1998, t.24 (15), pp.64-68
- [3]. IB Ermolovich, VV Milenin, RV Konakova et al. Technical Physics Letters, 1996, vol. 22 (6), pp.33-36.
- [4]. K. Suzuki, F. Hasim. "Amorphous metals." M. 1987,365 p.

Acceptor states and carrier lifetime in heteroepitaxial HgCdTe-on-Si for mid-infrared photodetectors

S V Zablotsky^{1,2}, N L Bazhenov², K D Mynbaev^{2,3}, M V Yakushev⁴, D V Marin⁴, V S Varavin⁴ and S A Dvoretzky⁴

¹Saint Petersburg Electrotechnical University "LETI", Popova 5, Saint-Petersburg 197376, Russia

²Ioffe Institute, Polytechnicheskaya 26, Saint-Petersburg 194021, Russia

³ITMO University, Kronverksky 49, Saint-Petersburg 197101, Russia

⁴Rzhanov Institute of Semiconductor Physics, Siberian Branch of RAS, ak. Lavrentieva 13, Novosibirsk 630090, Russia

Abstract. Heteroepitaxial HgCdTe-on-Si structures have been studied with the use of photoluminescence (PL) technique and carrier lifetime measurements. The study included that of as-grown samples and samples subjected to one- and two-stage annealing. Specific acceptor defects that were revealed with the PL studies have been shown to affect the values of carrier lifetime and its temperature dependence. The origin of these defects and its relation to mercury vacancy, one of the most frequent and important defects in HgCdTe, is discussed. The results of the studies are important for fabrication of HgCdTe-based infrared photodetectors, where big carrier lifetime is crucial for achieving maximum sensitivity and operating temperature of the device.

1. Introduction

Heteroepitaxial HgCdTe-on-Si technology provides almost ideal integration of photosensitive structures operating in the infrared part of the spectrum with silicon systems for signal pickup and processing in hybrid assemblies. At the same time, the large lattice mismatch between the films and the substrate results in the fact that such structures have a high density of defects that reduce carrier lifetime and cause excess dark currents in photodetectors, thus limiting their sensitivity and operating temperature [1]. For a long time, the main problem of HgCdTe-on-Si has been the high dislocation density. At the current stage of technology, the focus has shifted towards point defects and impurities. It has been shown that HgCdTe-on-Si structures contain both shallow and deep acceptor states [2], yet the effect of these states on the carrier lifetime and the performance of the photodetectors remained unclear. In this work, we address this problem by studying both carrier lifetime and defects in HgCdTe-on-Si structures grown with molecular beam epitaxy.

The structures were grown at the Institute of Semiconductor Physics of the Siberian Branch of RAS using ZnTe and CdTe buffer layers. HgCdTe chemical composition x in the photosensitive layers of the structures (with thickness of 5 to 6 μm) was 0.3 to 0.4, which corresponded to cut-off wavelengths of the photodetectors of 4.9 to 2.9 μm at the temperature $T=77$ K. Carrier lifetime τ was studied with the use of photoconductivity decay technique, and the defect structure was investigated with

photoluminescence (PL) measurements. The latter were performed in the temperature range from 4.2 to 300 K with excitation by a semiconductor laser and signal detection with a cooled InSb photodiode. Figure 1 shows low-temperature PL spectra of a HgCdTe-on-Si structure with $x=0.4$ for an as-grown sample and a sample after a two-step anneal (with both samples having n -type conductivity). The anneal included a high-temperature stage aimed at eliminating structural defects, and a low-temperature stage used to fill the mercury vacancies formed at the previous stage (a so-called ‘stoichiometric’ stage). One can see that the spectrum of the as-grown sample (line 1) consists of several bands, including that of exciton localized at compositional fluctuations (LE, band A), and those corresponding to transitions from the conduction band to shallow acceptor states c -A with the energy of the states $E_A \sim 14$ meV (B) and 28 meV (C) and to a deeper state with the energy $E_{DT} \sim 60$ meV (D). The spectrum of the annealed sample (line 2) contained only the LE band A' and the transition to the deep state D'. A similar sample annealed only at high temperature (which converted it into p -type, spectrum not shown) retained all the transitions typical of the as-grown sample, though the intensity of the transitions to the acceptor states substantially decreased as compared to that of the LE band. Figure 2 shows temperature dependencies of carrier lifetime $\tau(T)$ in a similar HgCdTe-on-Si structure with $x=0.3$. For the as-grown sample (curve 1), a complicated shape of the $\tau(T)$ dependence indicated the contribution of Shockley-Read recombination processes, with possible contribution from a number of recombination centres. Sample annealed in one stage into p -type conductivity (curve 3) showed a ‘classical’ shape of $\tau(T)$ dependence in HgCdTe [3]. Finally, sample subjected to the two-stage annealing (curve 2), showed a similar $\tau(T)$ dependence, yet with much higher carrier lifetime in the whole temperature range. This indicated that the p -type material contained a specific centre of Shockley-Read recombination. As the low-temperature stage of the annealing eliminates mercury vacancies, this centre can be related to this type of defect in HgCdTe. As can be seen, the results of the PL studies can be clearly related to those of the lifetime measurements. The presence of specific states in PL spectra is revealed in the temperature dependencies of the carrier lifetime. Thus the results obtained during the study can be used for PL-assisted identification of defects responsible for low carrier lifetime in HgCdTe-on-Si with the aim of undertaking technological steps to eliminate these defects completely.

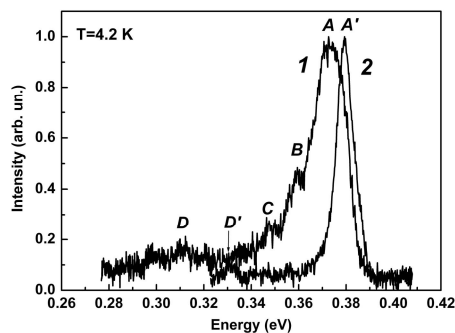


Figure 1. PL spectra of as-grown (1) and annealed (2) samples cut from a HgCdTe-on-Si structure

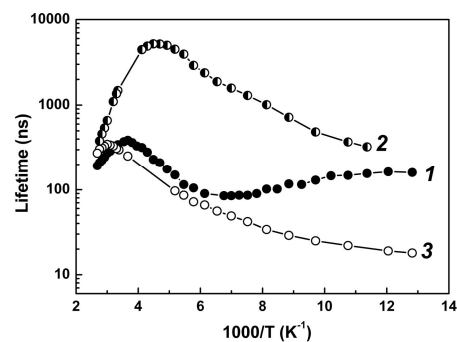


Figure 2. Carrier lifetime in HgCdTe-on-Si: 1, as-grown sample, 2, sample after two-stage anneal, 3, after high-temperature anneal only

1. Mollard L, Bourgeois G, Lobre C, Gout S, Viollet-Bosson S, Baier N, Destefanis G, Gravrand O, Barnes J P and Milesi F 2014 *J. Electron. Mater.* **43** 802
2. Mynbaev K D, Bazhenov N L, Yakushev M V, Marin D V, Varavin V S, Sidorov Yu G and Dvoretzky S A 2014 *Tech. Phys. Lett.* **40** 728
3. Krishnamurthy S, Berding M A and Yu Z G 2006 *J. Electron. Mater.* **35** 1369

Surface defects formation in growth of GaN from a multicomponent vapor via chemical reaction: a model

A V Redkov^{1,2*}, A V Osipov^{1,2}, S A Kukushkin^{1,2}

¹ Institute of Problems of Mechanical Engineering, Bolshoy pr. V.O., 61, Saint-Petersburg, 199178.

² Saint-Petersburg Academic University RAS, Khlopina str., 8/3, Saint-Petersburg, 194021

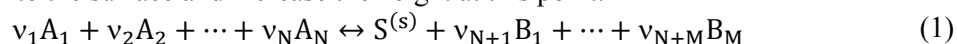
Abstract. We investigated in a general way the evolution of the elastic flat surface of the crystal during its growth from a multicomponent medium. The morphological instability of a planar growth front in the area, which is near the dislocation or other defects has been demonstrated. We have found growth conditions under which a multi-component film retains its shape and have analyzed different kinetic mechanisms which affect the stability.

1. Introduction

On the surface of epitaxial GaN layers during growth process often form so-called V-defects. Such defects generally are etching pits which have a crystalline faceting. Defects of this kind have a negative effect on the quality of heterostructures on the basis of the GaN. Understanding of the processes leading to their formation can help to find the parameters of growth, in which the concentration of defects is minimal, and therefore improve the quality of the semiconductor devices. At present time there is no quantitative theory of nucleation and growth of V-defects. In this work, it is assumed that one of the possible causes of the nucleation of V-defects is a violation of the ratio between the concentrations of III/V components near defects of the substrate (eg, dislocations). As a result of such violation an instability of the growth front [1-2] of the GaN film can appear. This instability can grow over time and lead to the formation of V-defects.

2. Model and results

Let us consider a plane front of the crystal of phase S which is growing from multicomponent medium in the reactor. The reactants are flow to the plane with constant rate (see. Fig. 1), and adsorb to the surface. They can diffuse through surface and react chemically (1) forming substance S, which incorporates directly into the surface and increase the height at this point.



Thermal desorption of the initial reactants and reaction products is also possible. Let's consider some defects below the surface like dislocations, pores, or substrate with a lattice parameter different from the growing phase S, or other defects that create stress field σ , which affects the lifetime of precursors in the surface.

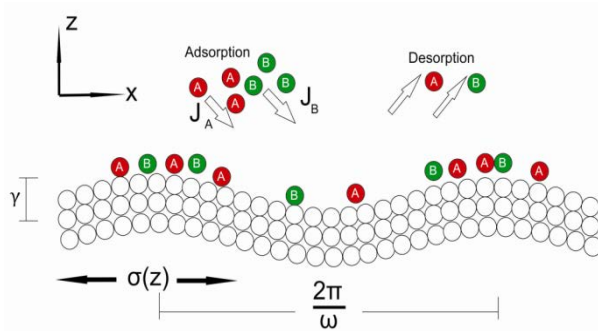


Figure 1. The perturbation of the surface, growing via reaction of the type $A + B \leftrightarrow S$. In general, the chemical reaction in the valleys and on the tops can occur with different rates.

The system which describes the concentrations of all reagents consists of several equations:

$$\left\{ \frac{\partial C_i}{\partial t} = D_i \frac{\partial^2 C_i}{\partial x^2} + J_i - K_p v_i \prod_{k=1}^N C_k^{v_k} + K_o v_i \prod_{k=N+1}^M C_k^{-v_k} - \frac{C_i}{\tau_i}, \quad i = A_1 \dots B_M \right. \quad (2)$$

Here C_i - the concentration of adatoms/molecules on the surface of substance i , which changes as a result of the incident flux, surface diffusion, chemical reaction and desorption. D_i - diffusion coefficient of substance i on the surface, K_p - the rate of direct chemical reaction of phase S formation, K_o - the rate of reverse chemical reaction. τ_i - the lifetime of the component.

Now let's made a small sinusoidal perturbation of surface Z with amplitude γ :

$$Z = z + \gamma \sin(\omega x) \quad (3)$$

Due to the changes of surface geometry local stresses also change, and thus, it affects lifetimes of adsorbed atoms on the surface, the equilibrium concentrations and rate of growth of the surface:

$$C_k|_{z+\gamma \sin(\omega x)} = C_k^0 (1 + \delta_k \sin(\omega x)) \quad (4)$$

So, if we now substitute into the system (2) all changed concentrations (4), and lifetimes, we will able to find the expression for growth rate of perturbation. It will be determined by the formula:

$$\frac{d\gamma}{dt} \sim \frac{K}{K^{eq}} - \Gamma_D \omega^2 \varepsilon_p^{os} + \frac{\varepsilon_p^{os}}{\varepsilon_o^{os}} \quad (5)$$

Where $K/K^{eq} - 1 = -A/kT$ - is the affinity of the chemical reaction, Γ_D is associated with the surface tension, stabilizing the surface [2], and averaged coefficients are defined as:

$$\varepsilon_p^{os} \sim \left(\sum_{k=1}^N \frac{v_k}{(\tau_o^i D_i \omega^2 + 1)} \right)^{-1}, \quad \varepsilon_o^{os} \sim \left(\sum_{k=N+1}^M \frac{v_k}{(\tau_o^k D_k \omega^2 + 1)} \right)^{-1} \quad (6)$$

It is evident that if the right-hand side (5) is greater than zero the perturbation increases over time. For each frequency there is a critical chemical affinity in which the surface becomes unstable. The coefficient of proportionality in (5) depends on the diffusion coefficients, the ratio of III / V, stress field σ , and the frequency of the disturbance. At certain ratios of III / V, it can be quite large, and the perturbation will grow quickly.

Thus, the criterion (5) allows to determine the mode of growth, in which the flat surface of the growing crystal is resistant to small distortions of form. So, if conditions of GaN growth by, for example, HVPE (which involves a chemical reaction) are in compliance with the criteria (5) the development of defects by this mechanism will not occur, and the GaN film will be of better quality.

References

- [1] W. W. Mullins and R. F. Sekerka 1963 *J. Appl. Phys.* **34**, 323
- [2] S.A. Kukushkin, A.V. Osipov and A.V. Redkov, 2014 *Physics of the Solid State* **56**, 2440

InAsSb on GaAs (001): influence of the As molecules form on composition and epilayer crystalline perfection by MBE

E.A. Emel'yanov, B. R. Semyagin, A. P. Vasilenko, A.A. Komanov,
A.K. Gutakovskii, M. A. Putyato, V. V. Preobrazhenskii
ISP SB RAS, pr. Lavrentieva 13, Novosibirsk, 630090, Russia

Abstract. The effect of molecular form As on the composition and crystalline perfection of solid solutions InSbAs by molecular beam epitaxy is experimentally investigated. A series samples was grown at different temperature values. The grown samples were investigated by HRXRD and TEM. The coefficients of the incorporation of arsenic As_4 and As_2 molecules were determined at different temperature values. It was found that coefficient of the incorporation of arsenic As_4 , unlike As_2 , has a less pronounced dependence on growth temperature, which is connected with the differences in As_4 and As_2 molecules interaction mechanisms with the growth surface at MBE. It was discovered that the transition layer, which helps reduce the threading dislocations density, is formed at low temperature of grown on the $InAs_xSb_{1-x}$ film interface.

1. Introduction

Solid $InAs_xSb_{1-x}$ solutions are attractive because of the possibility of creating optoelectronic device of the IR range sensitive to the wavelengths of order 12.4 μm . High electron mobility of this material can be used to create HEMT structures. However, there are some difficulties connected with obtaining high-quality $InAs_xSb_{1-x}$ epilayers. One of them is the absence of a proper substrate for the whole spectrum of solid $InAs_xSb_{1-x}$ solutions [1].

Another problem is epilayers growth with a set s composition in the sublattice of group V. The composition of the solid solution depends on both the amount of antimony and arsenic molecules flow and their incorporation rates S_{Sb} and S_{As} . The incorporation rates are the function of substrate temperature (T_s), molecular flows value and ratio for elements of groups III and V, molecular form of group V elements in a flow [2].

The aim our work was experimental investigation of the influence molecular form arsenic on the composition and crystalline perfection of the epilayers $InAs_xSb_{1-x}$ grown on GaAs (001) substrate by MBE.

2. Experimental methods

A series samples was grown at different T_s values. Each sample consisted of two layers. The first layer was grown using an As_2 molecules flow. After that, the growth was interrupted and the cracking temperature of arsenic source was decreased from 950 °C to 400 °C for As_4 molecules flow generation. Then a second layer was grown using the As_4 molecules flow which was equivalent the atomic As_2 flow in its atomic expression.

3. Results

The grown samples were investigated by HRXRD and TEM. S_{As_4} and S_{As_2} were determined at different T_s values. It was found that S_{As_4} , unlike S_{As_2} , has a less pronounced dependence on growth temperature, which is connected with the differences in As_4 and As_2 molecules interaction mechanisms with the growth surface at MBE [3]. It was discovered that the transition layer, which helps reduce the threading dislocations density, is formed at low T_s on the $InAs_xSb_{1-x}$ film interface (see Fig. 1).

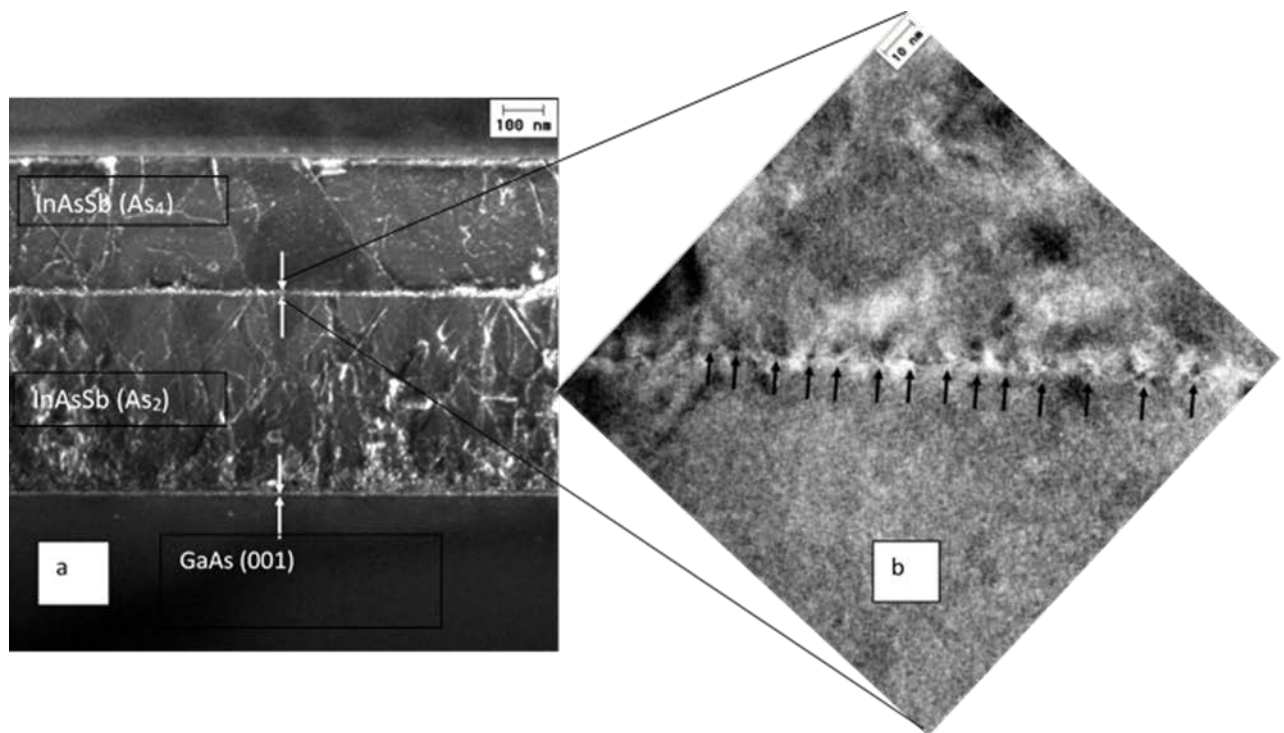


Figure 1. a – The cross-sectional TEM image (110) of the sample with two films InAsSb, lower grown with As_2 , top with As_4 , arrows indicate intense layers ($T_s = 319$ °C); b - HRTEM image border film - film, arrows denote the outputs of edge dislocations.

The work was carried out supported by grant RFBR – 14-02-31054

References

- [1] H. Gao, W. Wang, Z. Jiang, L. Liu, J. Zhou, H. Chen., J. Cryst. Growth, 308, 406, (2007).
- [2] A.N. Semenov, V.S. Sorokin, V.A. Solovyev, B.Ya. Meltser, S.V. Ivanov, SPE, 38, 3, 278,(2004) (in Russian).
- [3] E.A. Emelyanov, D.F. Feklin, A.V. Vasev, M.A. Putyato, B.R. Semyagin, A.P. Vasilenko, O.P. Pchelyakov, V.V. Preobrazhensky, Autometry journ, 47, 34, (2011) (in Russian).

Modeling of axial heterostructure formation in ternary III-V nanowires

A A Koryakin¹, N V Sibirev¹ and D Zeze²

¹ St. Petersburg Academic University, Khlopina 8/3, St.Petersburg, 194021, Russia

² School of Engineering and Computing Sciences, South Road, Durham, DH1 3LE, UK

Abstract. We have modeled axial heterostructure formation in ternary III-V nanowires grown by catalytic vapor-liquid-solid method. Our approach is based on the determination of chemical potential of a four-component liquid using the regular solution model and Stringfellow's scheme for computation of interaction coefficients of species in the droplet. The model allows the estimation of the heterojunction width dependence on the growth temperature that has not been analyzed in the previous works theoretically.

Heterostructure nanowires (NWs) have a wide range of potential applications in opto- and nanoelectronics and it is usually desirable to create an abrupt heterojunction for designing devices with high-performance characteristics. Among all growth techniques, vapor-liquid-solid growth (VLS) is the most often used to synthesize NWs at present. This growth method allows the formation of relatively sharp interfaces for materials with a group V element interchange (e.g. GaP/GaAs, InP/InAs, InAsP/InAs, GaAsP/GaP [1]) while for materials with a group III element interchange formation of abrupt interfaces is much more difficult (e.g. for AlAs/GaAs, GaInAs/InAs, InGaAs/GaAs [1]). Despite the variety of experimental data, there are very few studies that describe heterojunction formation in NWs theoretically (e.g. [2-4]) and, to the best of our knowledge, none of the existing model deals with ternary heterostructured NWs. The main question is to calculate the chemical potential of a four-component liquid (three components are NW growth materials and one component is a catalyst material) that is a driving force of VLS NW growth and determines NW growth rate and crystal structure [5]. In this paper, we build a model describing heterostructure formation in ternary III-V NWs grown by catalytic VLS method. Our approach is based on the determination of chemical potential of a four-component liquid using the regular solution model and Stringfellow's scheme for computation of interaction coefficients of species in the droplet [6]. Also in contrast to the previous works the model presented allows the estimation of the heterojunction width dependence on the growth temperature. In what follows, AlGaAs/GaAs NWs are considered as an example of ternary system and where the data presented in the literature [7] are used as a reference to compare our calculations with experimental results.

In the model proposed, we assume that NW growth proceeds in mononuclear layer-by-layer growth regime, in line with the case of NWs with small radii and under the usual conditions for molecular beam epitaxy NW growth [5]. Since the nucleus composition is unknown in the multicomponent

system, we consider an $Al_xGa_{1-x}As$ nucleus, where x is the Al molar fraction. The Gibbs free energy of island formation on the droplet-NW interface has the form $G(x) = a(x)i^{1/2} - \Delta\mu(x)i$, where i - the number of AlAs and GaAs pairs in the nucleus, $a(x)$ - a factor that depends on the surface energy of nucleus side walls, $\Delta\mu(x)$ - an average difference of chemical potentials for AlAs and GaAs pairs in the liquid droplet and in the $Al_xGa_{1-x}As$ NW. For a layer-by-layer growth, the NW growth rate dL/dt in monolayers equals to the number of nuclei that appear on the NW top facet per second [5] $dL/dt = \pi R^2 I$, where $I = A\sqrt{\Delta\mu/kT} \exp(-a^2/(4kT\Delta\mu))$ is the intensity of island formation, A - a prefactor that in general is a function of atomic concentrations of species in the droplet and temperature, T - the growth temperature, k - the Boltzmann constant, R - the NW radius. We also assume that the incorporation rate of Al and Ga atoms into the growing monolayer is proportional to the corresponding atomic concentrations, i.e. $v_{Al} = b_{Al}c_{Al}$ and $v_{Ga} = b_{Ga}c_{Ga}$, where c_{Al} and c_{Ga} atomic concentrations of species, b_{Al} and b_{Ga} - kinetic coefficients, b_{Al}/b_{Ga} is a slow varying function of temperature and equal to 1 in our consideration. Therefore, the Al and Ga molar fraction can be presented in the following form: $X_{Al} \equiv x = c_{Al}/(c_{Al} + c_{Ga})$, $X_{Ga} = c_{Ga}/(c_{Al} + c_{Ga})$. The material balance equations for material fluxes in and out of the droplet are subsequently introduced. The chemical potential difference of species is calculated below as a function of Al, Ga and As atomic concentrations since this quantity depends strongly on As concentration also [6]. Thus, three material balance equations for material fluxes of Al, Ga and As are considered:

$$\begin{aligned}\frac{dN_{Al}}{dt} &= \frac{1}{4} J_{Al} (R/H + H/R)^2 - \frac{1}{2} \frac{dL}{dt} X_{Al}, \\ \frac{dN_{Ga}}{dt} &= \frac{1}{4} J_{Ga} (R/H + H/R)^2 - \frac{1}{2} \frac{dL}{dt} X_{Ga}, \\ \frac{dN_{As}}{dt} &= \frac{1}{4} J_{As} (R/H + H/R)^2 - \frac{1}{2} \frac{dL}{dt} - (1 + H^2/R^2) \frac{c_{As}}{\tau_{As}},\end{aligned}$$

N_{Al}, N_{Ga}, N_{As} - the number of Al, Ga and As atoms in the droplet, J_{Al}, J_{Ga}, J_{As} - the vapor fluxes of Al, Ga and As atoms, H - the height of the droplet, τ_{As} - the desorption time for As atoms. Similar to the chemical potential calculation for ternary liquid used by Glas [6], we estimate the chemical potential difference of Al, Ga and As atoms in four-component solution and solid $Al_xGa_{1-x}As$ NW. We write $\Delta\mu$ in the form $\Delta\mu = x\mu_{Al}^L + (1-x)\mu_{Ga}^L + \mu_{As}^L - \mu_{AlGaAs}^S(x)$, where $\mu_{Al}^L, \mu_{Ga}^L, \mu_{As}^L$ - chemical potentials of Al, Ga and As atoms in the droplet, extracted by applying the Stringfellow formula, $\mu_{AlGaAs}^S(x) = x\mu_{AlAs}^S + (1-x)\mu_{GaAs}^S(x)$ is an average chemical potential of AlAs and GaAs pairs in the $Al_xGa_{1-x}As$ solid solution, i.e. a simple interpolation is used.

As a result, the model allows us to find the heterojunction width dependence on the growth temperature (figure 1).

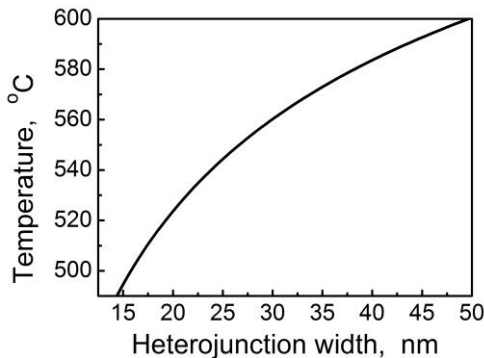


Figure 1. The AlGaAs/GaAs heterojunction width versus the growth temperature.

- [1] Messing M *et al.* 2011 *Nano Lett.* **11** 3899
- [2] Perea D, Li N, Dickerson R, Misra A, Picraux S 2011 *Nano Lett.* **11** 3117
- [3] Periwal P, Sibirev N *et al.* 2014 *Nano Lett.* **14** 5140
- [4] Li N, Tan T, Gosele U 2008 *Appl. Phys. A* **90** 591
- [5] Dubrovskii V 2014 *Nucleation Theory and Growth of Nanostructures* (Heidelberg: Springer)
- [6] Glas F 2010 *Appl. Phys.* **108** 73506
- [7] Kochereshko V *et al.* 2012 *Journal of Surface Investigation. X-ray, Synchrotron and Neutron Techniques* **6** 722

MBE growth of GaP epilayers on Si substrate

M S Sobolev¹, A A Lazarenko, E V Nikitina, E V Pirogov, A S Gudovskikh,
A Yu Egorov

¹St. Petersburg Academic University, St. Petersburg, Russia

Abstract. The possibility of creating a single-crystal GaP buffer layers on Si substrate by molecular-beam epitaxy is demonstrated. During the formation of GaP layer on silicon substrate p–n-junction is created between the p-Si substrate and near-surface layer of n-Si, which occurs as a result of diffusion of phosphorus in the substrate during epitaxial growth of GaP. This p–n-junction may be used as the first junction in silicon-based multijunction solar cells.

Academic interest and technological importance of dilute nitride semiconductors such as GaPN and GaAsN has been the subject of intensive research and technological development since their discovery. In recent decades, we have witnessed impressive progress in science and technology of dilute nitride semiconductors, as evidenced by the large number of papers on this topic [1-3].

GaP(As)N can be pseudomorphically grown on Si substrates while maintaining high structural quality [4]. Further, substitution phosphorous for a small amount of nitrogen in GaP (~ 0.5%) leads to formation of the direct band structure and opens the possibility of creating of novel efficient optoelectronic devices on its basis. Thus, dilute nitride alloys have a huge potential of creating optoelectronic devices integrated with silicon electronics, such as monolithic optoelectronic integrated circuits and efficient solar cells.

Unfortunately, the epitaxial growth of A³B⁵-N alloys directly on the silicon substrates is impossible. Therefore, it is necessary to precipitate the buffer layer the silicon surface. The best candidate for buffer layer is GaP, because the lattice mismatch between GaP and Si is less than 0.4%. However, the growth of GaP epilayer on Si substrate leads to generation of threading dislocations and stacking faults as well as anti-phase domains. On the (001) surfaces may be two possible phases differ by 90° in the plane of rotation. Between two anti-phase domains the anti-phase border is formed. This border can be electrically active, so it can be the centre of nonradiative recombination, which detrimental to the optoelectronic devices. To grow GaP initial layer on silicon substrates the migration-enhanced epitaxy (MEE) is used. Furthermore, Si substrate (100) with a vicinal surface misoriented by 4° towards the [001] direction is effective for the annihilation of anti-phase domains.

In this paper, we investigate GaP initial and buffer layers grown on silicon substrates by molecular beam epitaxy (figure 1). The structural quality of GaP layer has been studied. Furthermore, we present current-voltage and spectral characteristics of photodiode with p-n junction formed during epitaxy of thin layers of n-GaP on p-Si substrate to demonstrate the high quality of GaP epilayers grown on a silicon substrate by molecular beam epitaxy (MBE).

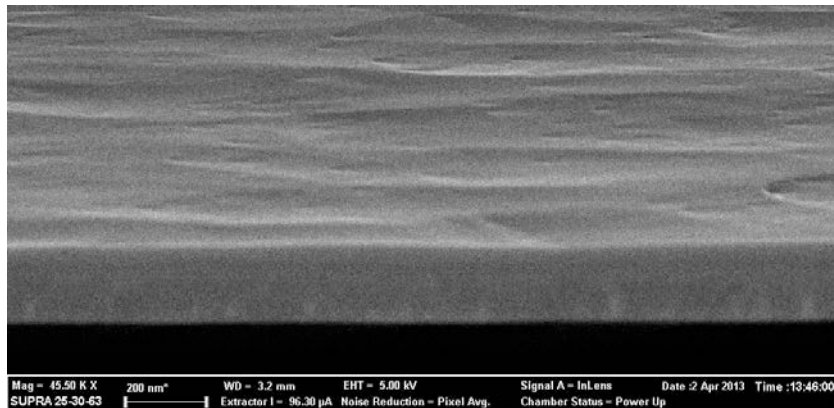


Figure 1. SEM image of GaP layer on Si substrate.

References

- [1] S.Y. Moon, H. Yonezu, Y. Furukawa, Y. Morisaki, S. Yamada, A. Wakahara. *Phys. Status Solidi A*, **204** (6), 2082 (2007)
- [2] Y. Furukawa, H. Yonezu, A. Wakahara, S. Ishiji, S.Y. Moon, Y. Morisaki, *J. Cryst. Growth*, **300**, 172 (2007)
- [3] T. Nguyen Thanh, C. Robert, W. Guo, A. Letoublon, C. Cornet, G. Elias, A. Ponchet, A. Rohel. *Appl. Phys. Lett.*, **112**, 053 521 (2012)
- [4] H. Yonezu, Y. Furukawa, A. Wakahara. *J. Cryst. Growth*, **310**, 4757 (2008)

Modelling the growth process of porous aluminum oxide film during anodization

E M Aryslanova¹, A V Alfimov¹, S A Chivilikhin¹

¹ITMO University, Kronverkskiy Ave, 49, St. Petersburg, 197101, Russia

Abstract. Currently it has become important for the development of metamaterials and nanotechnology to obtain regular self-assembled structures. One such structure is porous anodic alumina film that consists of hexagonally packed cylindrical pores. In this work we consider the anodization process, our model takes into account the influence of layers of aluminum and electrolyte on the rate of growth of aluminum oxide, as well as the effect of surface diffusion. In present work we consider those effects. And as a result of our model we obtain the minimum distance between centers of alumina pores in the beginning of anodizing process.

1. Introduction

Currently, the development of nanotechnology and metamaterials requires the ability to obtain regular self-assembled structures with different parameters [1-2]. One such structure are porous alumina films, which are self-organizing structures that consist of hexagonally packed cylindrical pores (Figure 1). Pore size and the distance between them can be varied depending on the anodization voltage, the electrolyte and the anodization time (pore diameter - from 2 to 350 nm, the distance between the pores - from 5 to 50 nm).

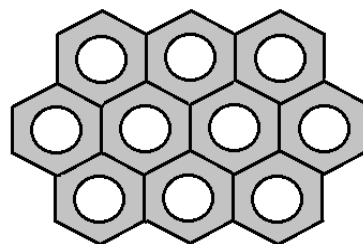


Figure 1. Hexagonal packing of the porous AAO

In this paper we describe an analytical model of the growth of anodic alumina. We consider the motion of the interfaces between the electrolyte- Al_2O_3 (dissolution) and between the Al_2O_3 -aluminum (oxidation) (Figure 2).

We consider the dynamics of moving boundaries and the change of small perturbations forms of these boundaries. In each of the areas under consideration Laplace equation for the electric potential is solved. The process of growth of porous alumina is described by the theory of small perturbations. In zero approximation boundaries are considered flat and the speed of their movement proportional to the

current density at these boundaries. The first approximation takes into account the small perturbations of the interface, which lead to small changes in the potentials and currents at these boundaries. The evolution of small perturbations of the interface is defined as a perturbation of the current density at the borders, and the process of surface diffusion.

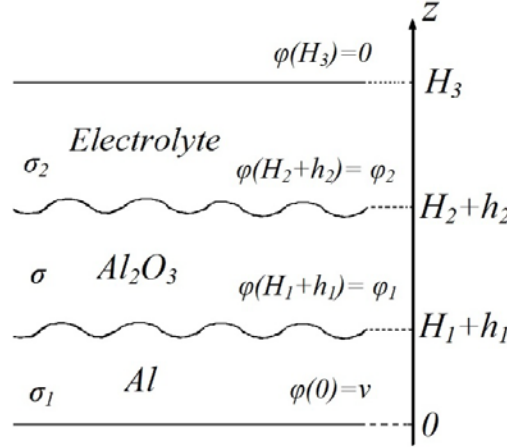


Figure 2. Inhomogeneous film with rough boundaries.

Using conditions of continuity of the current density at both interfaces (Al-Al₂O₃, Al₂O₃-electrolyte) we obtain the system of equations relating the potential disturbance on the interfaces:

$$\begin{cases} (-\sigma_2 sh(kH) - \sigma ch(kH)) \hat{\phi}_{2\bar{k}} + \sigma \hat{\phi}_{1\bar{k}} = \beta e^{kH} - \alpha \\ -\sigma \hat{\phi}_{2\bar{k}} + (\sigma_1 sh(kH) + \sigma ch(kH)) \hat{\phi}_{1\bar{k}} = \beta - \alpha e^{kH} \end{cases} \quad (1)$$

where $\alpha = v h_{1\bar{k}} / \mathcal{G}$, $\beta = v h_{2\bar{k}} / \mathcal{G}$, $\hat{\phi}_{\bar{k}}$ - the Fourier transform of the potential disturbance to the coordinates x, y , ϕ_1 - electrostatic potential of the aluminum layer on Al - Al₂O₃ interface, ϕ_2 - electrostatic potential of the aluminum layer on electrolyte - Al₂O₃ interface, σ_1 - conductivity of the aluminum, σ - conductivity of aluminum oxide, σ_2 - conductivity of the electrolyte, $\mathcal{G} = (H/\sigma + H_1/\sigma_1 + (H_3 - H_2)/\sigma_2)$, v - anodization voltage, H - thickness of aluminum oxide, $H_1 + h_1$ - thickness of the aluminum layer, $H_3 - (H_2 + h_2)$ - thickness of the electrolyte layer.

In this work we consider the solutions of the system (1) for different values kH . And add the influence of surface diffusion on the process.

As a result of the developed model we obtained the minimum distance $2\pi \sqrt[3]{\mathcal{G} D_1 / a_1 v}$ between centers of aluminum oxide pores in the beginning of anodizing process. The irregularities of porous structure contains in the spectral interval $k_2 < \sqrt[3]{a_1 k v / \mathcal{G} D_2}$.

References

- [1] Limonov A G 2010 *Matem. Mod.* **22** 97–108
- [2] Petukhov D I, Napolskii K S and Eliseev A A 2012 *Nanotechnology* **23** 335601

Modelling of field desorption of monocrystal nanotip

K A Nikiforov and A A Krasnova

Saint Petersburg State University, 7-9, Universitetskaya nab., St. Petersburg, 199034, Russia

Abstract. Mathematical and computer model of field desorption process from metal nanocrystal tip is proposed. The radius of curvature on the top of the emitter is about 50 lattice parameters. The model includes initial calculation of intersection between the crystal lattice and emitter shape for bcc and fcc crystal structures. Arbitrary axisymmetric shapes (figures of rotation) can be used for the emitter model. The algorithm for allocation of atoms being desorbed at given time step is based on an analysis of geometric environment with specified local electric field. Polyhedron nanostructured shape of emitter is obtained as result of evaporation. Computer program realization (Matlab stand alone application) is presented.

Field desorption microscopy and atom probe tomography are modern methods of investigation three-dimensional structure of solids [1]. The aim of the paper is to construct a model of the process of the field evaporation or field desorption (under the influence of a strong electric field) as well as simulation of final surface structure of desorbed emitter.

For a given value of the field strength at the surface of the emitter the outermost atoms primarily vaporize, having the greatest number of broken bonds with neighboring lattice atoms at given time step. According to [2], [3] detection of crystallographic faces and outermost atoms on emitter surface was carried out by the analysis of nearest neighbors up to the 5th order.

Figure 1 shows a model of a segment of a spherical top of the emitter (bcc crystal structure, radius is 50 lattice parameters), formed as result of the process of field evaporation (field strength is 48 GV/m, temperature 78 K). Area of some crystal faces increased on the surface of the emitter comparing to the original form.

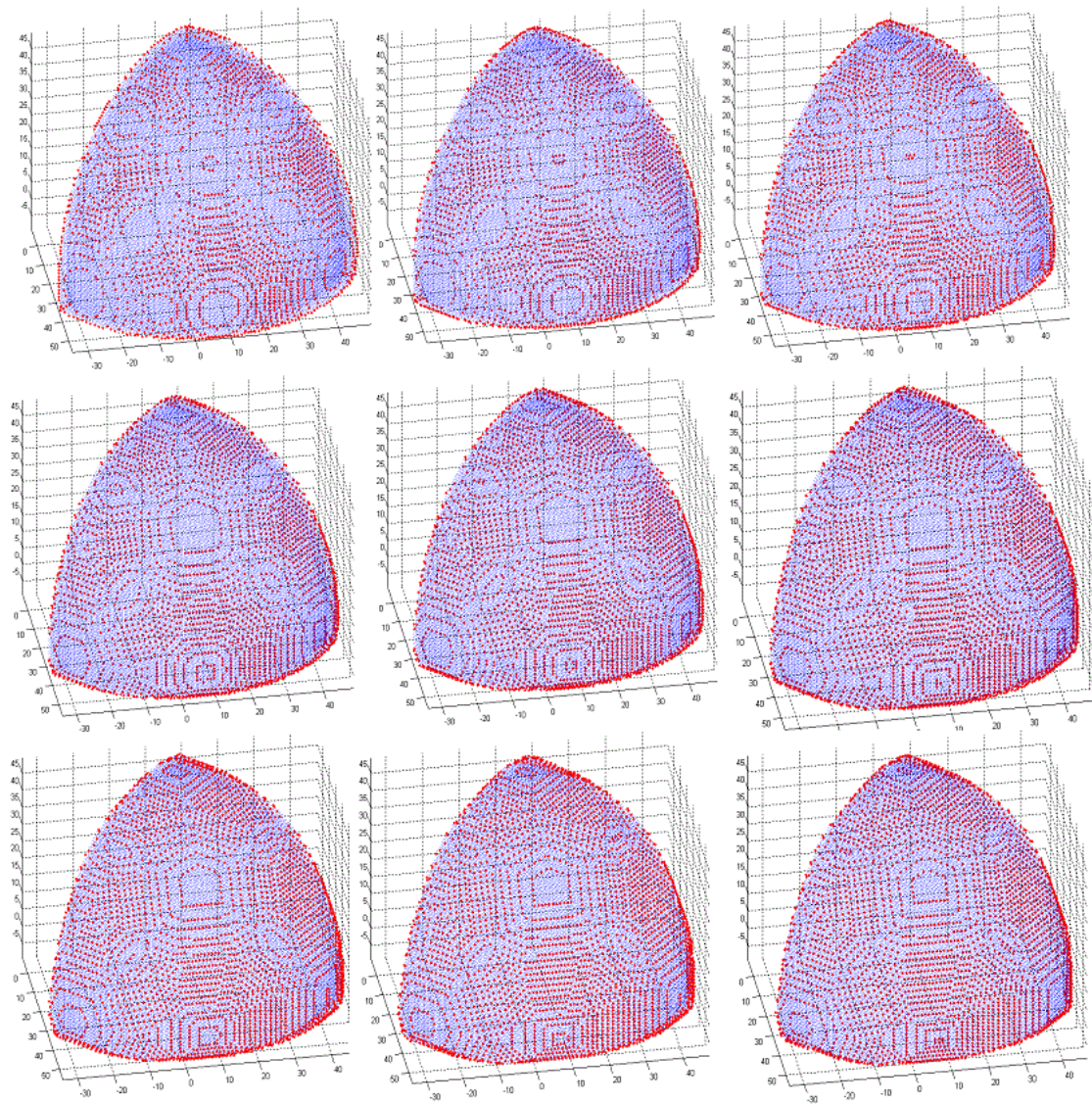


Figure 1. Several stages of field evaporation in the model of emitter tip. Emitter surface atoms are shown in blue, atoms desorbed at given stage are marked in red.

Acknowledgments

Financial support has been obtained from RFBR (13-01-00150) and partially from SPbSU (9.38.673.2013). Research was carried out using computational resources provided by Resource Center "Computer Center of SPbU" (<http://cc.spbu.ru/en>) and using experimental equipment of the Interdisciplinary Resource Center for Nanotechnology of St. Petersburg State University.

- [1] Gault B, Moody M P, Cairney J M, Ringer S P 2012 *Atom Probe Microscopy* (Berlin: Springer)
- [2] Nikiforov K A, Egorov N V, Shen C-C 2009 Surface reconstruction of a field electron emitter *Journal of Surface Investigation: X-Ray, Synchrotron and Neutron Techniques* **3** 833-9
- [3] Nikiforov K, Krasnova A 2014 Model of field electron emitter surface structure *2014 Tenth Int. Vacuum Electron Sources Conf. (Saint Petersburg)* (Piscataway: IEEE)

Synthesis of silicon carbide at room temperature from colloidal suspensions of silicon dioxide and carbon nanotubes

D A Zhukalin, A V Tuchin, T V Kulikova, L A Bityutskaya

Voronezh State University, 394006, Universitetskaya pl.1, Voronezh, Russia

Abstract. The formation of self-organized structures in colloid nanosystem aerosil – carbon nanotubes (SiO₂-CNT) were studied using numerical and natural experiments. Covalent interactions resulted in the formation of self-organized rodlike structures with diameter 250-300nm and length ~4μm. X-ray diffraction analysis of the obtained nanostructures revealed local formation of the silicon carbide phase at the room temperature.

1. Introduction

The use of carbon nanotubes (CNT) is commonly assumed while producing composite and hybrid nanomaterials as well as elements of nanoelectronics, sensors, energetic, microelectromechanical systems [1, 2]. There is a great interest to the local interactions of CNTs with oxygen-containing phases [3, 4]. Bolotov et al. [4] showed that during high-temperature annealing of composite SnO_{2-x}/multi-walled CNT in vacuum, there was transformation of its electronic structure along with local synthesis of tin oxycarbide. In addition to external high-energy CNT activation methods, it is important to consider the internal reserve of nanotubes themselves related to their size qualities, surface curvature and defects [5]. The uniqueness of carbon nanotubes is based on the dependence of the reactivity of carbon atoms from their topological positions: the increasing curvature is the reason of the decreasing activation energy of chemical reactions. Caps of carbon nanotubes have the greatest curvature, which allows considering its as an active center. Defects of the hexagonal structure define the local charge redistribution near the caps. The charged active center is the core of interactions between carbon nanotubes and second nanocomponents of same size. To achieve this goal, in our experiments we used amorphous SiO₂ of AEROSIL brand 300 particles 7 nm and an array of short CNTs (~0.5 μm) with the average diameter 20-40nm, obtained through arc discharge method. In the present work we investigated the mechanisms and conditions of aggregation and synthesis of self-organized structures in model nanosystem SiO₂-CNT using the methods of numerical and natural experiments.

2. Results and discussion

We conducted simulations of the local interaction between nanofragment SiO₂ and carbon nanotubes. Calculations were done using the DFT method in local spin density approximation LSDA. Calculations were performed using the program package Gaussian09 in the Supercomputer Center of Voronezh State University. Numerical experiments demonstrated the possibility of a formation of covalent bonds Si-C and O-C, as well as bridges C-Si-O-C. If the initial distance is greater than $r_{\text{Si-C}}^{\text{ct}}$, then the calculated value is $r_{\text{Si-C}} \sim 2.54 \text{ \AA}$, which is characteristic of Van-der-Waals interactions.

The investigation of interaction of aerosil with carbon nanotubes was conducted in homogeneous environment by mixing colloid solutions of SiO₂ and CNT using the drop method [5], with subsequent evaporation of dispersion medium – water. A drying drop is viewed as nanoreactor [6, 7] with dynamic walls.

During the interaction of amorphous SiO₂ with an array of short CNTs (~0.5 μm) at room temperature, we discovered 2 kinds of self-organized structures: rodlike and spherical. These structures differ not only by shape, but also by the ratio of atomic concentrations of Si:O – 4:1 for rodlike structures, and 1:2 for spherical structures, with high carbon concentration in both cases. It is known that the absorption band in the IR spectra in the region 1100 (SiO₂) - 980 - (SiO) - 943 cm⁻¹ (Si) linked to the stretching vibrations of the bridging oxygen Si-O-Si (stretching mode Si-O-Si) and used for determining the composition of the layers SiO_x. Displacement of oscillation mode to lower frequencies indicates the increasing concentration of silicon in the sample aerosil/short CNT. On the basis of IR spectroscopic studies and elemental analysis, we can conclude that composite on aerosil and CNTs is forming with a high content of silicon.

Based on the obtained data, it follows that there is a formation of silicone oxycarbide in the rodlike structures. The formation of oxycarbide phases during the interaction of SnO₂ with CNT, with the formation of O-C-Sn bond was convincingly shown in work [4]. The X-ray diffraction analysis of the obtained nanostructures revealed formation of the silicon carbide phase with a polytype 4H-SiC. The lattice parameters are a=b=3.081 Å, c=10.060 Å.

3. Conclusion

Therefore, during the study of interactions between nanomaterials in CNT-aerosil system at room temperature in drying drop, the formation of self-organized rodlike structures with diameter 250-300nm and length ~4μm was founded. X-ray diffraction analysis of the obtained nanostructures revealed formation of the silicon carbide phase at room temperature. Theoretical analysis confirmed that the mechanism of formation of such structures is due to the presence of charged active centre near caps of CNTs, which increases their reaction capability.

This work was supported by the project FP7-IRSES-295260 “ECONANOSORB“ under Marie Curie Actions of the 7th Framework Program of European Union and by RFBR, research projects N 14-02-31315 mol_a.

References

- [1] Chou S-L, Zhao Y, Wang J-Z, Chen Z-X, Liu H-K and Dou S-X 2010 *J. Phys. Chem. C* **114** 15862
- [2] Song J, Jensen D S, Hutchison D N, Turner B, Wood T, Dadson A, Vail M A, Linford M R, Vanfleet R R and Davis R C 2011 *Adv. Funct. Mater.* **21** 1132
- [3] Novikov L S, Voronina E N, Chirskaya N P 2013 *J. Adv. Mater.* **11** 12
- [4] Bolotov V V, Nesov S N, Korusenko P M, Povoroznyuk S N 2014 *Physics of the Solid State* **56** 1834
- [5] Zhukalin D A, Tuchin A V, Goloshchapov D L, Bityutskaya L A 2015 *Tech. Phys. Lett.* **41** 157
- [6] Su B, Wang S, Song Y, Jiang L 2011 *Nano Research* **4** 266
- [7] Barash L Yu 2015 *International Journal of Heat and Mass Transfer* **84** 419

Self-limited growth of Au catalytic nanoparticles

N. V. Sibirev¹, Y. Berdnikov¹, V.G Dubrovskii¹, J.H. Kang² and H. Shtrikman²

¹St. Petersburg Academic University, Khlopina 8/3, 194021 St. Petersburg, Russia

²Braun Center for Submicron Research, Department of Condensed Matter Physics, Weizmann Institute of Science, Rehovot 76100, Israel

Abstract. Employment of metal nanoparticles (Au) for catalytic growth of nanowires requires a narrow size distribution which is accessible when the nanoparticles assembly is limited by the elastic stress (for solid particles or nanoislands). Together with growth slowing down and stop the nucleation of new nanoislands was detected. At short deposition times the regime of “pulsing” nucleation of new islands leads to bimodal size distribution while at longer times the regime of slow growth of mean size with nucleation at low constant rate was observed. To describe such growth process, the standard form of island formation energy was modified by adding a new term corresponding to elastic energy. The newly developed model provided the description of experimentally observed growth features.

Narrow size distributions are usually required for applications of Au nanoislands, for example their usage as catalytic particles for nanowires growth. High size uniformity is accessible during solid islands formation in presence of lattice mismatch with substrate. In this case the growth is limited by elastic strain. During MBE deposition of gold on InAs substrate at 350 °C (which is below eutectic point) revealed the saturation of radial island size together with appearance and further evanescence of bimodal size distribution.

In a series of experiments the samples were removed from the MBE chamber after 0.25 - 5 minutes of deposition. After fast growth at short times, the mean island diameter changes slowly from 70 to 100 nm for deposition times from 0.5 to 2 minutes. At 2.5 minutes together with large island the small ones, newly nucleated, with the diameter around 10 nm were observed. Thus the mean island radius decreases. For this sample the island density was found to be higher than for the samples with shorter deposition.

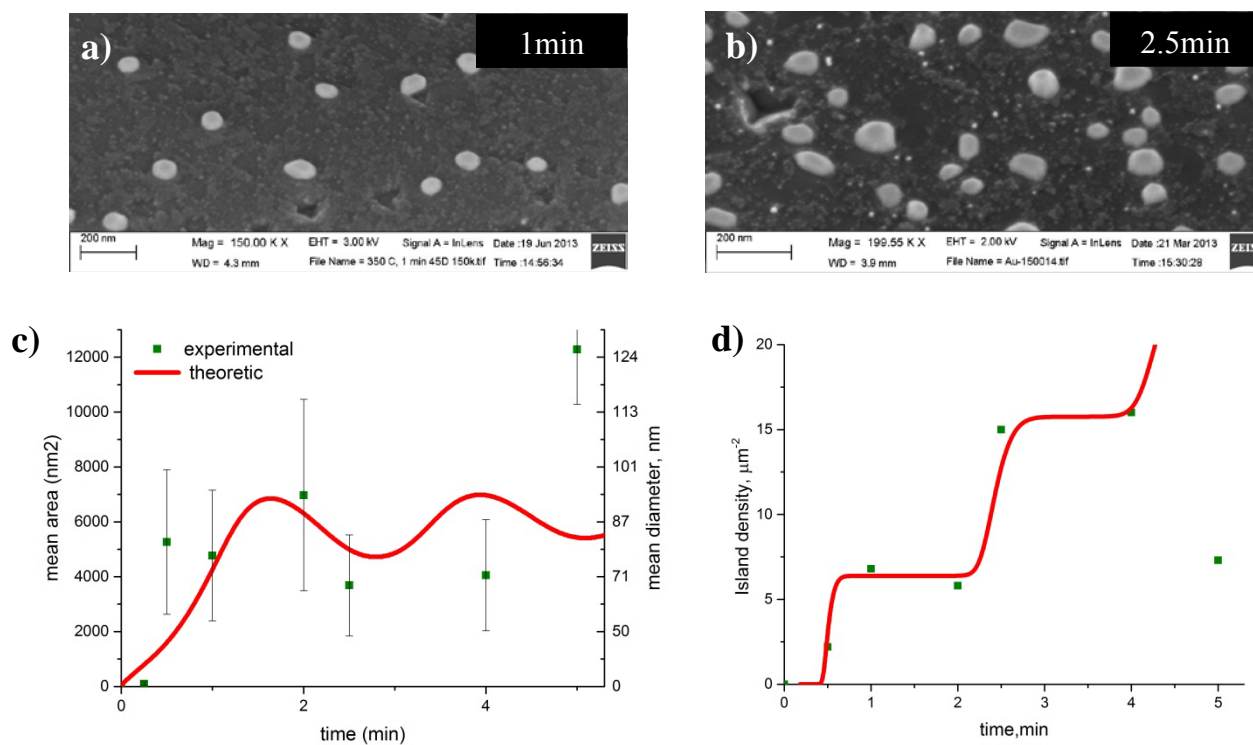


Figure 1. SEM images of Au nanoislands for a) 1min b) 2.5 min of deposition; plots for c) mean island size b) islands density variation with length of deposition

In order to describe theoretically the growth with second nucleation the classical form of island formation energy should be modified. Previously the increase of diffusion energy barriers was observed for self-limited growth of nanoislands [2] which should result in increase of formation energy. Our model assumes the elastic energy contribution to be proportional to r^4 (where r is the radius of nanoisland) Between short nucleation events when the number of islands is fixed the E_{int} could be expressed in terms of island radius as $E_{int} = d(N) r^3$ [4] where d is a constant which is linear to islands density N . The attachment of adatoms above the foot of nanoisland is obstructed due to Ehrlich-Schwoebel-like barriers for diffusion which results in increase of formation energy. The simplest way to model such a system is to add a new term of order of r^4 corresponding to elastic interactions inside the island. It could be written in the dimensionless form as:

$$F(r) = Ar^2 - (b(\zeta) + d(N))r^3 + Cr^4 \quad (1)$$

The shape of $F(r)$ varies considerably with density of islands N and supersaturation ζ . This variation is sketched on fig. 2.

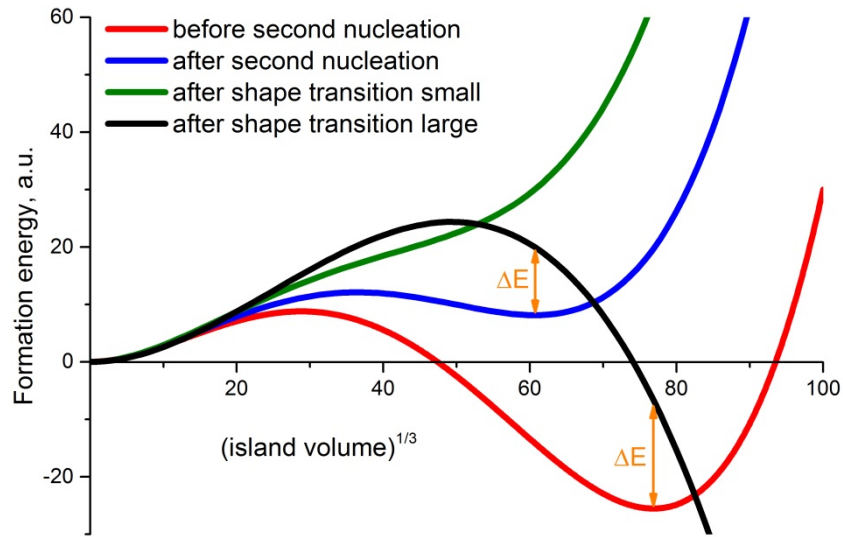


Figure 2 New island formation free energy at different stages of the growth

In conclusion the chain of effects were observed and described theoretically. Under constant material influx the growth stop results in new wave of islands nucleation. Nucleation of new islands leads to increase of the surface density. Increase of surface density results in increase of nucleation barrier and decrease of ΔE and thus causes the islands to change their shape with faceting. After shape transition islands continue growing which decrease the supersaturation and provoke coarsening of small islands.

References:

- [1] V. G. Dubrovskii, Nucleation Theory and Growth of nanostructures, Springer-Verlag, Berlin Heidelberg (2014).
- [2] Kratzer et al. Phys. Rev. B 73, 205347 (2006)
- [3] Medeiros-Ribeiro et al. Science, 279, 353 (1998)
- [4] Shchukin et al. Phys. Rev. Lett. 75, 2968 (1995)

Modelling polytypism in III-V nanowires: role of group V and nucleation patterns during the growth

J. Grechenkov¹, V.G. Dubrovskii^{1,2,3},

¹ St.Petersburg Academic University, Khlopina 8/3, 194021 St. Petersburg, Russia

² Ioffe Physical Technical Institute RAS, Politekhnicheskaya 26, 194021, St. Petersburg, Russia

³ ITMO University, Kronverkskiy pr. 49, 197101 St. Petersburg, Russia

Abstract. This theoretical work deals with polytypism in nanowires by utilizing nucleation theory and by modifying standard expression for nucleation rate. Polycentric and monocentric nucleation cases are also considered. Results show good agreement with experimental data.

1. Introduction

This is a theoretical work on describing wurtzite/zincblend polytypism that is present in III-V nanowires. Nanowires are usually grown by VLS (vapour-liquid-solid method), which means that after material is introduced into a MBE chamber it is absorbed by liquid catalyst droplet on top of the nanowire and only then incorporated into the solid body of the nanowire [1].

Nanowires are promising objects that may help to integrate silicon electronics with III-V optoelectronic devices in future.

2. The model

Material balance equations and nucleation theory are used to calculate concentrations inside the droplet. Comparing nanowire growth rate measured in experiment with the growth rate calculated with the help of Zeldovich formula nucleation rate yields the group III concentration inside the droplet and group V concentration is obtained through solution of material balance equations and careful calculation of chemical potential. Knowing the concentrations one can calculate wurtzite content in nanowire ensemble by comparing nucleation probabilities for islands of different crystal phases. [2]

It is speculated that the classical formula for nucleation rate must be modified due to the fact the calculation of nucleation barrier uses surface energies of nucleation islands, which is essentially macroscopic variable. Hence, for small nucleation islands consisting of just a couple of adatoms one has to make sure that the nucleation barrier is introduced correctly – nucleation probability should be zero for a nucleation island with the size of just one adatom. [3]

3. Results

Calculation results show good agreement with experimental data.[4] Fig. 1 depicts how wurtzite content is calculated. Scales in graph are set in such a way that the intercrossing of dotted and solid lines corresponds to group III concentration in catalyst droplet. Knowing this concentration one can refer to the solid line to see the wurtzite content.

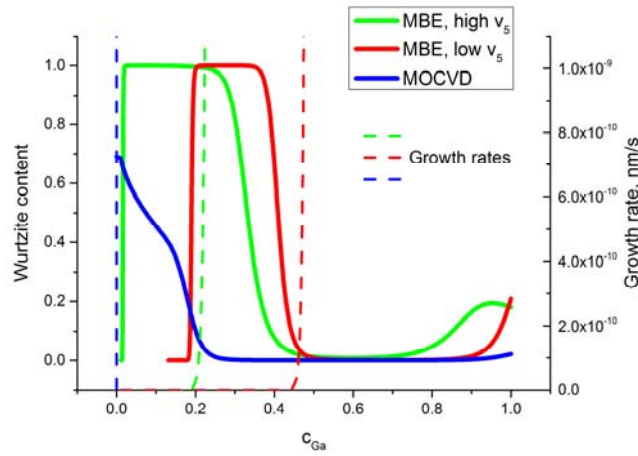


Fig.1 Growth rates and wurtzite percentage in GaAs nanowires as function of Gallium concentration in catalyst droplet. Intersections of same color corresponds to model prediction on Ga concentration inside the droplet and wurtzite percentage

The source of inconsistency of results of the model can be attributed to the fact that for higher group V flows polycentric nucleation may occur. Hence, for higher group V flows the model should be remastered to account also for polycentric nucleation case.

4. Conclusion

To conclude: the presented model uses modification of nucleation rate to describe zincblend/wurtzite polytypism in III-V nanowires. The correctness of this approach is backed by experimental results.

References

- [1] V. G. Dubrovskii, *Nucleation Theory and Growth of Nanostructures*, Springer (2014)
- [2] V. G. Dubrovskii, *Appl. Phys. Lett.* **104**, 053110 (2014)
- [3] V. G. Dubrovskii and J. Greckov, *Cryst. Growth Des.* 2015, 15 (1)
- [4] E. Gil et al, *Nanoletters* (2014)

Photoluminescence observation from zinc oxide formed by magnetron sputtering at room temperature

D Kudryashov¹, A Babichev¹, E Nikitina¹, A Gudovskikh¹

¹ St. Petersburg Academic University RAS 194021 St. Petersburg, Russia

Abstract: The photoluminescence (PL) of ZnO thin films grown by magnetron sputtering at room temperature has been observed. The PL spectra were measured using an instrument from Accent Optical Technologies with a solid state UV laser ($\lambda = 266$ nm) as the pumping source and at the temperature of 300 K. Samples grown at sputtering power of 100-200 W show a strong photoluminescence at wavelength of 377 nm and its intensity shows non-linear dependence with magnetron power. At values of sputtering power less than 100 W PL signal was not observed.

1. Introduction

Recently, there has been a growing interest in oxide photovoltaics. ZnO is a one of promising materials for wide-gap emitter in oxide heterojunction solar cells, for example AZO/ZnO/Cu₂O structure. Such structure has showed an efficiency value of 5.38% at AM1.5 [1]. Zinc oxide is a direct- and wide bandgap semiconductor with E_g of 3.3 eV [2]. Due to numerous of native point defects it has n-type doping. Defects have also influence on its optical and electrical properties [3]. Solar cell efficiency is determined primarily by a quality of structure's layers. The last can be directly determined by PL measurements. The aim of this work is to determine a ZnO thin films quality in dependence of its growth parameters.

2. Experimental

Deposition of Zinc Oxides thin films was carried out using RF magnetron sputtering setup (BOC EDWARDS Auto 500RF), located in the "clean room" of Academic University. Deposition of thin films performed at room temperature on Si(100)-wafers and glass slides. Pure argon (99.999 %) was used as working gas. Control of the oxide layers thickness was carried out using a profilometer AMBiOS XP-1. Refractive index was determined by ellipsometer HORIBA JOBIN YVON. Optical transmittance was measured by a spectrometer based on a monochromator Solar Laser Systems M266. SEM images were analyzed using a scanning electron microscope (SUPRA 25). The PL spectra were measured using an instrument from Accent Optical Technologies with a solid state UV laser ($\lambda = 266$ nm) as the pumping source and at the temperature of 300 K.

3. Results and discussion

SEM image of 500 nm ZnO thin films deposited on Si-wafer by magnetron sputtering is shown in figure 1. A small growth defects are observed on smooth surface. Figure 2 shows the PL spectra for ZnO thin films deposited at different values of magnetron power at room temperature. The PL intensity measurements show nonlinear RF power dependent behavior in the range of 100-200 W. It has maximum value at the magnetron RF power of 150 W. At power values of 50W and less no PL

signal was observed. Similar relations were obtained in [4] where authors shown changes in ZnO structure (grain size and Zn/O ratio) with increasing of rf-power. It was shown that at rf-power of 175W the Zn/O ratio has a maximum value of 1.11 and it decreases with further increasing of rf-power. The ZnO grain size is the lowest also at the magnetron power of 175W.

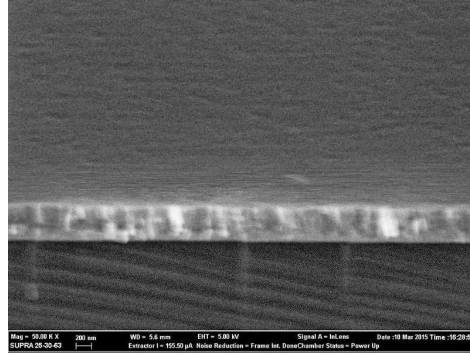


Figure 1. SEM image of rf-magnetron sputtered ZnO thin film deposited at 150 W on Si-wafer.

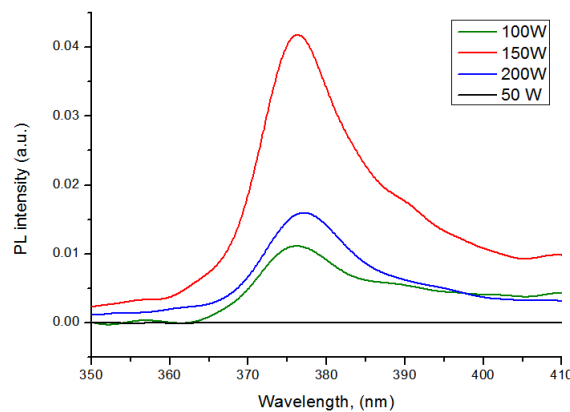


Figure 2. Room temperature PL spectra of ZnO thin films as a function of the RF power.

4. Conclusions

The photoluminescence of ZnO thin films grown by magnetron sputtering at room temperature has been observed. Samples grown at sputtering power of 100-200 W show a strong photoluminescence at wavelength of 377 nm and its intensity shows non-linear dependence with magnetron power caused by changes in Zn/O ratio and zinc oxide grain size.

5. Acknowledgment

The reported study was partially supported by RFBR, research project № 15-08-06645A and № 14-02-31485.

References

- [1] Tadatsugu Minami, Toshihiro Miyata, Yuki Nishi // Solar Energy, Volume 105, July 2014, Pages 206–217
- [2] Morkoç, H. and Özgür, Ü. (2009) General Properties of ZnO, in Zinc Oxide: Fundamentals, Materials and Device Technology, Wiley-VCH Verlag GmbH & Co. KGaA, Weinheim, Germany.
- [3] Anderson Janotti and Chris G Van de Walle 2009 Rep. Prog. Phys. 72 126501
- [4] A. Ismail, M.J. Abdullah // Journal of King Saud University – Science (2013)25, 209–215

Study of initial stages of vacuum-thermal Ag thin film deposition.

A. Savitskiy¹, D. Gromov¹, A. Trifonov², V. Rubcov¹, E. Lebedev¹

¹National Research University of Electronic Technology, 124498, Russia, Moscow, Zelenograd, Bld. 5, Pas. 4806

²Scientific Research Institute of Physical Problems named after F.V. Lukin, 124460, Russia, Moscow, Bld. 6, Pas. 4806, 6.

1. Introduction

The interest to nanoparticles arrangement has been associated with their wide range of applications. Metal nanoparticles are used for surface-enhanced Raman scattering, sensing, plasmonic and photonic [1-3]. In relation to the micro- and nanoelectronic applications arrangement of nanoparticles can be used in memory cell which is kind of next generation non-volatile memory that has attracted increasing attention in recent years as a possible replacement for flash memory [4-6].

2. Experimental

In the present work we investigated silver cluster array formation on non-heated thin film substrate of amorphous carbon using vacuum-thermal evaporation of small quantity of material. The distance between evaporator and deposition surface was 20 cm. The weight portion of evaporated silver determines the thickness of the film. In basic experiment weight portion ranged from 0.3 to 9 mg (corresponding thickness 0.5–15 nm). It should be noted that the indicated thicknesses are “virtual”, because 1–15 nm thick silver layer was deposited as particles array or discontinuous film. Thereafter samples were annealed in vacuum (residual pressure 1×10^{-5} Torr) at 250 °C during 30 min. The final samples were studied using transmission electron microscope FEI Tecnai G² 20 S-Twin equipped with EDAX X-ray energy-dispersive spectrometer. Then, obtained TEM images were analyzed: the number of particles per unit of the area was counted and their radii were measured. The histograms of particles size distribution were plotted.

3. Results

The investigation of the samples by TEM showed the significant dependence of the particle size and their surface density on the quantity of condensing Ag i.e. on the virtual film thickness. The obtained results formed the basis of the model which expands understanding of condensation processes, nucleation and growth of the crystalline phase from the gas phase.

References

1. N.G. Khlebtsov, "T-matrix method in plasmonics: An overview", *Journal of Quantitative Spectroscopy and Radiative Transfer*, 123, pp. 184-217, 2013.

2. N.C. Lindquist, P. Nagpal, K.M. McPeak, D.J. Norris, S.-H. Oh, "Engineering metallic nanostructures for plasmonics and nanophotonics", *Reports on Progress in Physics*, 75(3), art.no.036501, 2012.
3. J.Z. Zhang, C. Noguez, "Plasmonic optical properties and applications of metal nanostructures", *Plasmonics*, 3, pp. 127–150, 2008.
4. C.-P. Hsiung, H.-W. Liao, J.-Y. Gan, T.-B. Wu, J.-C. Hwang, F. Chen, M.-J. Tsai, "Formation and instability of silver nanofilament in Ag-based programmable metallization cells", *ACS Nano*, 4(9), pp. 5414-5420, 2010.
5. J.H. Jun, K. Cho, J. Yun, S. Kim, "Switching memory cells constructed on plastic substrates with silver selenide nanoparticles", *Journal of Materials Science*, 46(21), pp. 6767-6771, 2011.
6. N.J. Lee, B.H. An, A.Y. Koo, H.M. Ji, J.W. Cho, Y.J. Choi, Y.K. Kim, C.J. Kang, "Resistive switching behavior in a Ni-Ag₂Se-Ni nanowire", *Applied Physics A*, 102(4), pp. 897-900, 2011.

Modeling of the behavior and statistical analysis of compressibility in the process of Langmuir monolayer structurization

H.V. Grushevskaya, G.G. Krylov, N.G. Krylova, I.V. Lipnevich

Belarusian State University, 4 Nezavisimosti Ave., Minsk 220030, Belarus

Abstract. An approach has been developed to perform data processing for experiments on two-dimensional phase transition of the first order. The approach represents itself the two stage filtration with subsequent merging of processed data and comparison with simulation results based on geometro-thermodynamical methods. The approach has been successfully applied to description of the phase transition in compressed monolayers of steric acid.

1. Introduction

Development of formation methods for two-dimensional (2D) solid-state perfect structures, which can operate at room temperature, is an important problem of flexible electronics. Langmuir-Blodgett (LB) technique can be used to produce almost perfect two-dimensional structures, provided that the conditions on a phase boundary are under control [1].

When modeling the Langmuir monolayer compression by Monte Carlo methods a metastable state is excluded from consideration that does not allow for such a control. A compressibility κ , for $\tilde{\pi}-A$ isotherms being dependencies of surface tension $\tilde{\pi}$ on an area A per one molecule, presents itself a derivative from the dependence $\ln A(\tilde{\pi})$ over $\tilde{\pi}$. But, instead of it, the "apparent" compressibility $\kappa_{\text{app}} = 1/K'$ being an inverse elasticity of a Langmuir monolayer is calculated.

2. Data processing

To utilize LB monolayers as a material for nanoelectronics it is necessary to correlate structural changes in a metastable compressed monolayer with changes of phenomenological parameters of the monolayer (e.g., compressibility coefficient). This requires a statistical analysis of experimental dependences of the surface tension $\tilde{\pi}$ upon the area A per molecule, followed by compressibility calculation.

In this paper, we propose a method of statistical analysis when at first we smoothen 2D fluctuations of the vector $\vec{r}_i \equiv (\tilde{\pi}_i, A_i)$ over an interval of n_1 values of the surface tension $\tilde{\pi}_{i+j}$ and corresponding

to them values of the area A_{i+j} per one molecule: $\vec{r}_i \equiv (\tilde{\pi}_i, A_i) = \frac{1}{n_1} \sum_{j=-n_1/2}^{n_1/2} \vec{r}_{i+j}$. Then, a filtering

procedure based on the sliding mean with given window width m_1 is applied to the smoothed set, when an experimental value is to replace by a mean value obtained from the m_1 nearest points as:

$\tilde{\pi}_i \rightarrow \langle \tilde{\pi}_i \rangle = \frac{1}{m_1} \sum_{j=-m_1/2}^{m_1/2} \tilde{\pi}_{i+j}$. The filtering on the sliding mean was applied only to the readings of the

surface tension sensor, as its noise prevails over noise "inertial" position sensor. To find the compressibility $C(\tilde{\pi})$ of monolayer, the logarithmic derivative of the dependence $A(\tilde{\pi})$ obtained after the data processing with filtering parameters $\{n_1, m_1\}$ was calculated numerically. The existence of scale invariance property of phase transitions was accounted by merging several filtrations of original data.

3. Results and discussion

Typical compression $\tilde{\pi} - A$ isotherm is shown in Fig. 1a. The dependence $C(\tilde{\pi})$ is represented in Fig. 1a. It represents itself three sets of data which correspond to three filtration parameters: $\{n_1 = 3, m_1 = 3\}$, $\{n_1 = 4, m_1 = 5\}$, and $\{n_1 = 5, m_1 = 3\}$.

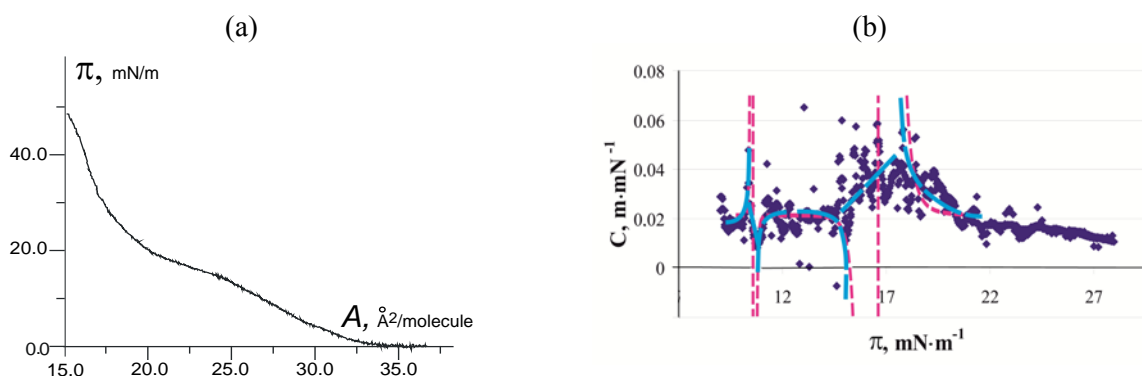


Figure 1. (a) $\tilde{\pi} - A$ -isotherm for a stearic acid monolayer. (b) The dependence of the compressibility C on $\tilde{\pi}$ in a first order 2D-phase transition in the monolayer. Symbols denote experimental data processing results, solid line is fitting, dashed line is the theoretical predictions.

We apply a geometrothermodynamics of the first order phase transitions in two-dimensional systems to the analysis of metastable compressed monolayers [2]. In this approach an electrocapillary contribution to compressibility κ is calculated by a following formula: $\kappa = -(B_c(r(\Delta t)) - B_c(r(t)))$ where B_c is the Berwald curvature of the compressed monolayer, which is the mean curvature of the trajectory of a particle under the action of electrocapillary forces.

Let $r(t)$ be a displacement of a particle during the time T_{pht} of phase transition: $t = T_{\text{pht}}$, $B_c(r(t)) \rightarrow B_c(r(T_{\text{pht}})) = \text{const}$. Then, we obtain κ as a quantity which is proportional to the mean curvature $B_c(r(\Delta t))$ of the monolayer element with a radius vector $\vec{r}(\Delta t)$ at an arbitrary time Δt (see dashed line in Fig. 1b). As one can see from Fig. 1b theoretical curve elucidate the origin of dispersion of compressibility.

Thus, the approach has been proposed that allows to describe the anomalous behaviour of compressibility at first order phase transition. The proposed approach is used to describe the formation of Langmuir monolayers of nanocyclic organometallic compounds.

References

- [1] Motschmann H, Möhwald H 2001 *Langmuir-Blodgett Films*. In: *Handbook of Applied Surface and Colloid Chemistry*. Ed. Holmberg K (John Wiley & Sons, Ltd)
- [2] Neagu M, Krylova N G, Grushevskaya H V 2013 *J. Math. Phys.* **54** 031508

MBE growth and optical properties of GaAs nanowires grown on Si(111) substrate using two-temperature steps regime

R R Reznik^{1,2}, I V Strom^{1,4,5}, Yu B Samsonenko^{1,3,4}, A I Khrebtov¹, A D Bourauvlev^{1,3,4,5}, I.P.Soshnikov^{1,3,4}, N.V.Kryzanovskaya¹ and G E Cirlin^{1,3,4,5}

¹St-Petersburg Academic University – Nanotechnology Research and Education Centre RAS, Khlopina 8/3, 194021, St-Petersburg, Russia

²St-Petersburg State Polytechnical University – Nanotechnology, Polytechnicheskaya 29, 195251, St-Petersburg, Russia

³Ioffe Physical Technical Institute RAS, Politekhnikeskaya 26, 194021, St-Petersburg, Russia

⁴Institute for Analytical Instrumentation RAS, Rizhsky 26, 190103, St-Petersburg, Russia

⁵St. Petersburg State University, 199034 St. Petersburg, Russia

Abstract. We report on the growth and optical properties of pencil-like GaAs nanowires (NWs) grown using an original two-temperature growth mode on Si substrate. Optically, the NWs array is active up to the room temperature. The low-temperature PL spectra is composed by the narrow bands corresponding to the direct, bound to surface states and bound to impurity excitons. After toluene treatment, the fine structure is disappeared in the spectra.

1. Introduction

Freestanding III-V NWs have recently attracted a rapidly increasing interest due to their unique growth, structural, transport and optical properties as well as a variety of promising applications as building blocks for future nanoelectronic [1] and nanophotonic [2] devices. Due to the ability to accumulate for strain in two dimensions [3], NW geometry is ideal for monolithic integration of semiconductor materials with different lattice mismatch. In particular, coherent, low temperature epitaxial growth of III-V compounds on silicon is of paramount importance for applications. It has been recently shown experimentally that coherent III-V NWs can be grown epitaxially on lattice-mismatched substrates by the vapor-liquid-solid (VLS) mechanism. In this paper we present MBE growth and optical examination of GaAs nanowires grown on Si(111) substrate using two-temperature steps regime allows one to obtain pencil-like NWs.

2. Experiments.

Growth experiments are carried out using Riber Compact21 MBE setup equipped with the effusion Au cell, on Si(111) substrates. Detailed procedure of NW growth is described in Ref. [4]. In brief, after the desorption of an oxide layer in the separate, vacuum-combined with the growth reactor, chamber. Then, to promote the NW formation by the growth catalyst, the deposition of $\sim 0.5\text{-}1$ nm thick Au layer is performed. The samples are then annealed in order to form liquid drops of alloy of Au with the semiconductor material of the substrate and transferred to the growth chamber. The MBE growth of GaAs NWs is carried out by the two-step temperature MBE technique. Firstly, the substrate temperature is set at 550°C and the growth of NWs is initiated. At the second stage, after 20 min. of the growth the substrate temperature is lowered to 530°C and next 40 min. of growth is performed. As a result, non-trivial, a pencil-like shape of the NWs is obtained. The process of NW nucleation and growth is monitored *in situ* by the reflection high energy electron diffraction (RHEED) technique. After several minutes of the growth, initially linear RHEED patterns are converted into the spots corresponding to the formation of wurzite-like crystallographic phase in the NWs. After the growth, the samples are studied by applying the scanning electron microscopy (SEM) and low-temperature photoluminescence (PL) techniques.

3. Results.

In Figs. 1 we present typical SEM image of GaAs NWs grown on the Si(111) substrate. The nanowires exhibit pencil-like shape having ~ 150 nm diameter at the base whereas ~ 25 nm at the top. This unconventional geometry is attributed to the two-step growth regime. At the first step, the NW diameter is dictated by the Au droplet size. At the second stage, at lower substrate temperature, the diffusion of the adatoms along the NWs sidewalls is suppressed. As a result, the formation of the nuclei at the sidewalls become significant and a lateral growth of the NWs is clearly observed.

Surprisingly, this NWs array is optically active up to the room temperature despite of the high density of the surface states typical for the NWs. The low temperature PL spectrum for as grown samples consists of a number of the narrow bands corresponding, to our opinion, to the direct, bound to surface states and bound to impurity excitons. To prove this observation, the NWs are subjected to the toluene treatment with consequent drying (which has to eliminate the surface-related excitons). After this procedure, the fine structure is disappeared in the spectrum (except of the lines corresponding to the cubic and/or wurzite bands) which supports the proposed origin of the narrow lines in the low-energy part of the PL spectra.

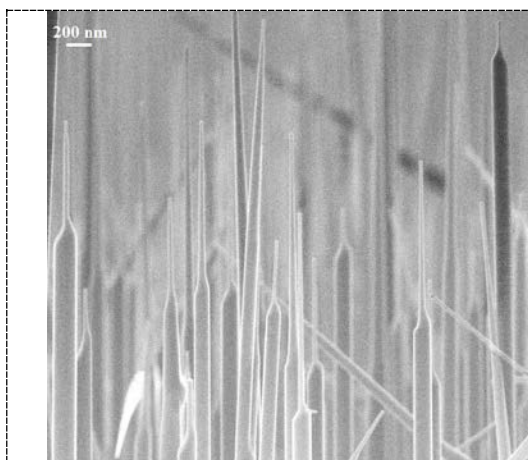


Figure 1. SEM image GaAs NWs grown on Si(111) substrate using two-step temperature mode.

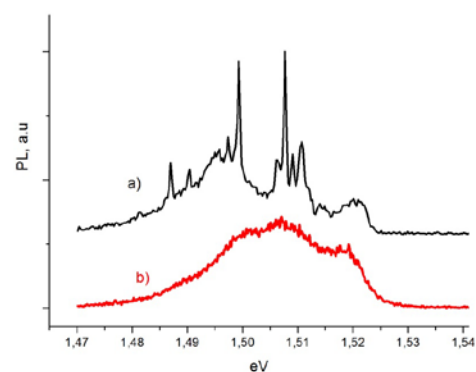


Figure 2. Low temperature PL spectra of GaAs NWs array taken at 10 K before (a) and after (b) toluene treatment.

References

- [1] Agarwal R and Lieber C M Semiconductors nanowires: optics and optoelectronics *Appl. Phys. A* **85** no 3 209-215
- [2] Chuang L C, Moewe M, Chase C, Kobayashi N P, Chang-Hasnain C and Crankshaw S Critical diameter for III-V nanowires grown on lattice-mismatched substrates *Appl. Phys. Lett.s* **90** no 7 043115
- [3] Cirilin G E, Dubrovskii V G, Soshnikov I P, Sibirev N V, Samsonenko Yu B, Buravlev A D, Harmand J C and Glas F Critical diameters and temperature domains for MBE growth of III-V nanowires on lattice mismatched substrates *Status Solidi RRL* **3** no 4 112-114
- [4] Samsonenko Yu B, Cirilin G E, Egorov V A, Polyakov N K, Ulin V P, Dubrovskii V G Specific features of formation of GaAs nanowire crystals during molecular beam epitaxy on different silicon surfaces *Semiconductors* **42** no 12

Section

Nanobiotechnology

The influence of biocompatible coating on the magnetic properties and MRI relaxivity of $\gamma\text{-Fe}_2\text{O}_3$ nanoparticles

A Furasova¹, M Kozlova¹, O Osmolovskaya¹, M Osmolovsky¹, V Korzhikov¹, A Dobrodumov²

¹Institute of Chemistry, Saint-Petersburg State University, Universitetskii pr. 26, Saint-Petersburg, 198504, Russia

² Institute of macromolecular compounds, Bolshoy pr. 31, Saint-Petersburg, 199004, Russia

Abstract. The superparamagnetic $\gamma\text{-Fe}_2\text{O}_3$ NPs were obtained by hydrothermal one-step synthesis via original approach. The surface modification of NPs were performed via adsorption using three different types of biocompatible coating. The magnetic characteristics (hysteresis loops, the blocking temperature and MRI relaxivity) of NPs were studied. It was shown that the nature of biocompatible coating are generally effected on NPs characteristics and can be used for regulation of MRI relaxivity.

1. Introduction

The main goal of modern medicine is the development and introduction of new products, which would allow both to simplify and make the most precise diagnosis of various diseases. That is why the method of magnetic resonance imaging (MRI) has been widely introduced into clinical practice. The difference between healthy and unhealthy tissues on the MRI picture is based mainly on variations in spin–lattice and spin–spin relaxation times of water protons.

To improve the precision of the analysis, the contrast agents were used. For T_1 mode agents based on chelating complex of paramagnetic metal are now successfully applied. Mixed valence magnetite Fe_3O_4 is used as biocompatible and non-toxic commercially available agents for T_2 mode. However, it hasn't found wide application in clinic. A number of studies indicate that magnetite could also be used as an agent for T_1 mode.

In this context, the goal of our investigation was to prepare magnetic nanoparticles (NPs) with stable magnetic characteristics based on $\gamma\text{-Fe}_2\text{O}_3$, to carry out the surface modification of NPs by different biocompatible coating, to study their magnetic behavior, and finally to evaluate their in vitro r_1 and r_2 relaxivity.

2. Experiment

The $\gamma\text{-Fe}_2\text{O}_3$ NPs were obtained by hydrothermal synthesis via original approach. The NPs morphology were determined by XRD, TEM, SSA estimation and DLS for aqueous suspensions. The surface modification of NPs were performed via absorption. The 10 mg of NPs were incubated at 25°C in 10 ml of biocompatible coating solution with different concentrations. The magnetic

properties of NPs were measured using FC-ZFC technic by VSM. The relaxivity measurement were conducted in microtomography probe Bruker Advance II 500 NMR spectrometer in the field value $11T$.

3. Results and discussion

The XRD has shown that the phase composition of the powder corresponds to $\gamma\text{-Fe}_2\text{O}_3$. The investigation of NPs size and shape using TEM has demonstrated the presence of only spherical particles with a diameter less of 10 nm. This data are fully consistent with the value obtained from the SSA. So the powder is monodisperse and has a narrow particle size distribution.

The surface modification of NPs were performed using three different types of biocompatible coating: (1) BSA – model protein for biomedical research, (2) dextran widely used at commercially available CA, and (3) synthetic polymer – oxidized poly-MAG.

At room temperature all NPs show superparamagnetic behaviour, at 7 K they becomes ferrimagnetic. The blocking temperatures depends on nature of biocompatible coating and are equal to 74 K for uncoated NPs and 50, 64, 52 K for BSA, dextran and pMAG coated NPs, correspondently. r_2 relaxivities of coated NPs at the T_2 mode increases in the series BSA – pMAG – dextran and are equal to 112, 145 and 308 $\text{sec}^{-1} \text{mM}^{-1}$ in the field of 11 T, respectively. r_1 relaxivities are 2.4, 1.0 and 0.9 $\text{sec}^{-1} \text{mM}^{-1}$ respectively. Relaxivity of uncoated NPs is not observed at the T_1 mode, and at the T_2 mode is 157 $\text{sec}^{-1} \text{mM}^{-1}$. So the nature of the biocompatible coating are generally effected on the magnetic characteristics and relaxivity of $\gamma\text{-Fe}_2\text{O}_3$ NPs. Thereby the regulation of MRI relaxivity of contrast agents based on $\gamma\text{-Fe}_2\text{O}_3$ NPs could be realized by variation the nature of biocompatible coating. The relationship between these parameters requires further study.

Acknowledgements

The work was financially supported by RFBR (grant № 13-03-00943). The authors express their gratitude to the Centre of X-ray Diffraction Studies, Center for optical and laser materials research and Innovative Technologies of Composite Nanomaterials (St. Petersburg State University).

Combination of laser correlation and dielectric spectroscopy in albumin investigations

E. Nepomnyashchaya¹, A. Cheremiskina¹, E. Velichko^{1,2}, E. Aksenov¹,
T. Bogomaz¹

¹Saint Petersburg State Polytechnic University, Saint Petersburg, Russia

²Saint Petersburg National Research University of Information Technologies,
Mechanics and Optics, St. Petersburg, Russia

Abstract. Joint use of laser correlation and dielectric spectroscopies for studies of biomolecular properties of albumin in water solution is considered. The conditions and parameters of the experiments are discussed. Similar behaviours of albumin molecular sizes and maximum frequency of peak of dielectric dissipation factor with increasing acidity were revealed. Using the suggested approach, biomolecular aggregation dynamics and changes in electrophysical properties on transition from one molecular structure to another may be investigated.

1. Introduction

Biomolecular objects attract an ever increasing attention of researches in different areas [1]. The interest is caused by a wide range of possible application of biomolecular technologies — from diagnostics and drug manufacturing in medicine to development of new elements and devices in molecular electronics.

One of the objects of research in our study is human serum albumin. Albumin is the globular protein which transports hormones, fatty acids, and other compounds, buffers pH, and maintains osmotic pressure, among other functions.

It is known that shift in pH cause conformational changes in protein molecules and their dysfunction. So, investigation of changes in molecular structure and dielectric features under the influence of different factors including pH can give valuable information. There are a lot of different methods of investigation of molecular structure and properties but electrophysical properties of proteins are understudied.

The goal of our study was to estimate molecular aggregation dynamics and to analyze the changes of electrophysical properties of albumin depending on solution acidity by using of combination of laser correlation and dielectric spectroscopies.

2. Methods and objects

We used combination of two methods — laser correlation spectroscopy (LCS) and dielectric spectroscopy in frequency range 20 Hz – 1MHz. Experimental setup and measure procedure of LCS was described in [2]. This method was used for evaluation of molecular size and dynamics of molecular aggregation in solution.

The dielectric spectroscopy (DS) method occupies a special place among the numerous modern methods used for physical and chemical analysis of material, because it enables investigation of dielectric relaxation processes. Intermolecular interactions and cooperative processes may be monitored by help of DS. Experimental setup consisted of a special liquid cell with two pole plates and LCR meter “MNIPI E7-20”.

The research objects in our study were water solutions of human serum albumin in concentration 0.01. To change the acidity of the solution buffers with acid and alkaline pH were used.

3. Results and discussion

The results of our study revealed similar behaviors of two characteristics: the size of the molecules in the solution (measured by LCS) and frequencies of maximum dielectric dissipation factor peaks of albumin (measured by DS) depending on acidity of solution. The obtained results are presented in figures 1 and 2.

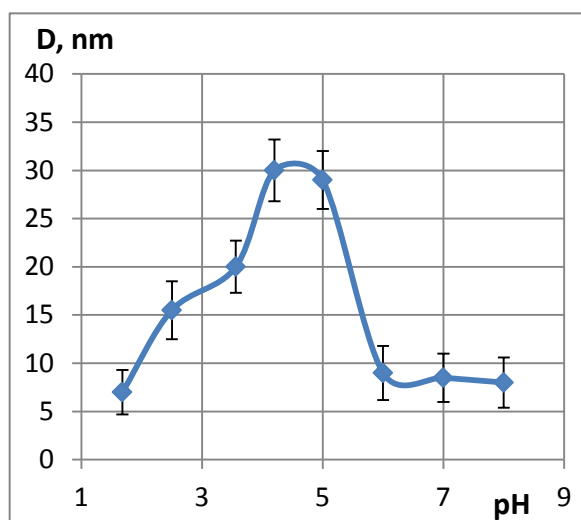


Figure 1. Dependence of molecular sizes of albumin on solution acidity.

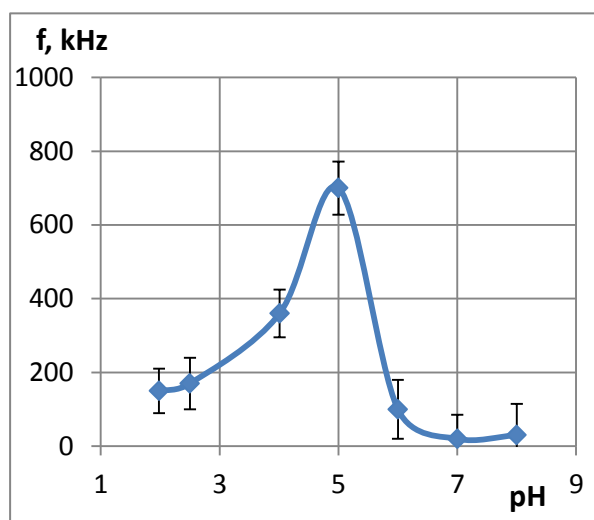


Figure 2. Dependence of frequencies of maximal dielectric loss angle tangent on acidity of albumin solution.

The maximal sizes of albumin molecules and maximal frequencies of dielectric loss angle tangent peaks were observed near the isoelectric point of albumin (pH = 4.8). This may be concerned with forming of special molecular structures in isoelectric solution.

4. Conclusion

Joint use of laser correlation and dielectric spectroscopies for studies of biomolecular properties is presented. Using the suggested approach, biomolecular aggregation dynamics and changes in electrophysical properties on transition from one molecular structure to another may be investigated.

References

- [1] www.scopus.com/results/results.url?sort=plf-f&src=s&st1=biomolecular+electronics 2015
- [2] Nepomnyashchaya E, Velichko E, Aksenov E and Bogomaz T 2014 *IOP Journal of Physics: Conference Series* **541** 012039

Theoretical study of the amphoteric oxide nanoparticle surface charge during multi-particle interactions in aqueous solutions

A V Alfimov, E M Arysanova, S A Chivilikhin

ITMO University, Kronverkskiy, 49, St. Petersburg, 197101, Russian Federation

Abstract. Nanoparticle surface charge plays an important role in many biological applications. In this study, an analytical surface charging model for the amphoteric oxide nanoparticles has been presented. The model accounts for the particle's electric double layer self-action on the charging process and the charge regulation during multi-particle interactions in aqueous solutions. The employment of the model allows to explicitly describe the nanoparticle agglomeration process and the accompanying agglomerate surface charge variation.

1. Introduction

Recent studies in the fields of nanotoxicology, nanobiotechnology and drug delivery suggest that the surface charge of a nanoparticle can significantly influence its interactions with biological matter. It has been shown that the cellular uptake, cytotoxicity and overall reactivity of amphoteric oxide nanoparticles are highly dependent on their charge [1, 2]. In the presence of agglomeration, the interparticle interaction and morphology of the agglomerates being formed are also governed by the nanoparticle surface charge and its redistribution [3].

The present study proposes an analytical model for the amphoteric oxide nanoparticle surface charging mechanism which accounts for the charge regulation during the multi-particle interaction in aqueous solutions and allows for the explicit description of the agglomeration process.

2. Results and discussion

The suggested surface charge model for amphoteric oxide nanoparticles accounts for a number of charging mechanisms including competitive protonation and deprotonation of the $[-OH]$ surface groups, chemical adsorption of H^+ and OH^- ions and van der Waals adsorption onto the particle

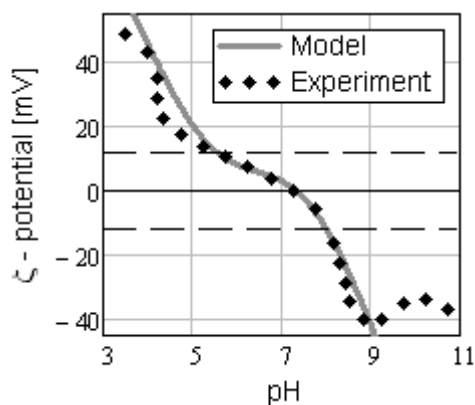


Figure 1. Comparison of the ZnO nanoparticle zeta-potential dependency on pH obtained using the proposed surface charge model with the experimental data from [2]. The dashed horizontal lines mark the range of zeta-potential values in which the local ion concentration dependency on the surface potential can be linearized.

surface and operates in the limit of non-saturated adsorption and desorption. The model also accounts for the external electric field effect and the nanoparticle's electric double layer self-action on the surface charging process. In figure 1 the pH dependency of a ZnO nanoparticle's zeta potential, obtained using the proposed model, is compared with the experimental data from [2]. It can be seen that the model provides an excellent agreement with the experiment except for the adsorption saturation effects at low and high pH-values.

Linearization of the potential-dependent H^+ and OH^- concentrations at the particle surface yields a simple expression for the nanoparticle surface charge density σ :

$$\sigma = \left\{ \sigma_0 + e \left[\beta_+ n_H \left(1 - \frac{e\varphi_\Sigma}{kT} \right) - \beta_- n_{OH} \left(1 + \frac{e\varphi_\Sigma}{kT} \right) \right] \right\} \cdot \left\{ 1 + \frac{e^2 [\beta_+ n_H + \beta_- n_{OH}]}{4\pi\epsilon\epsilon_0 \cdot kT} \left[\frac{1}{b(1+\kappa b)} + \frac{b-a}{ab} \right] \right\}^{-1}, \quad (1)$$

where σ_0 - constant portion of charge; n_H, n_{OH} - bulk H^+ and OH^- concentrations; a, b - physical and hydrodynamic particle radii; β_+, β_- - coefficients proportional to the sums of the rate constants for the adsorption processes involved; φ_Σ - potential of the external field; e - elementary charge.

The surface charge model can be implemented into the many-body nanoparticle interaction model, first introduced by the authors in [4]. The employment of the suggested charge regulation model allows to explicitly describe the multi-particle interactions during the agglomeration and to avoid the problem of the nanoparticle attachment probability declining to zero for the agglomerate size few orders smaller than the experimentally observed mean agglomerate size at neutral pH (see figure 2).

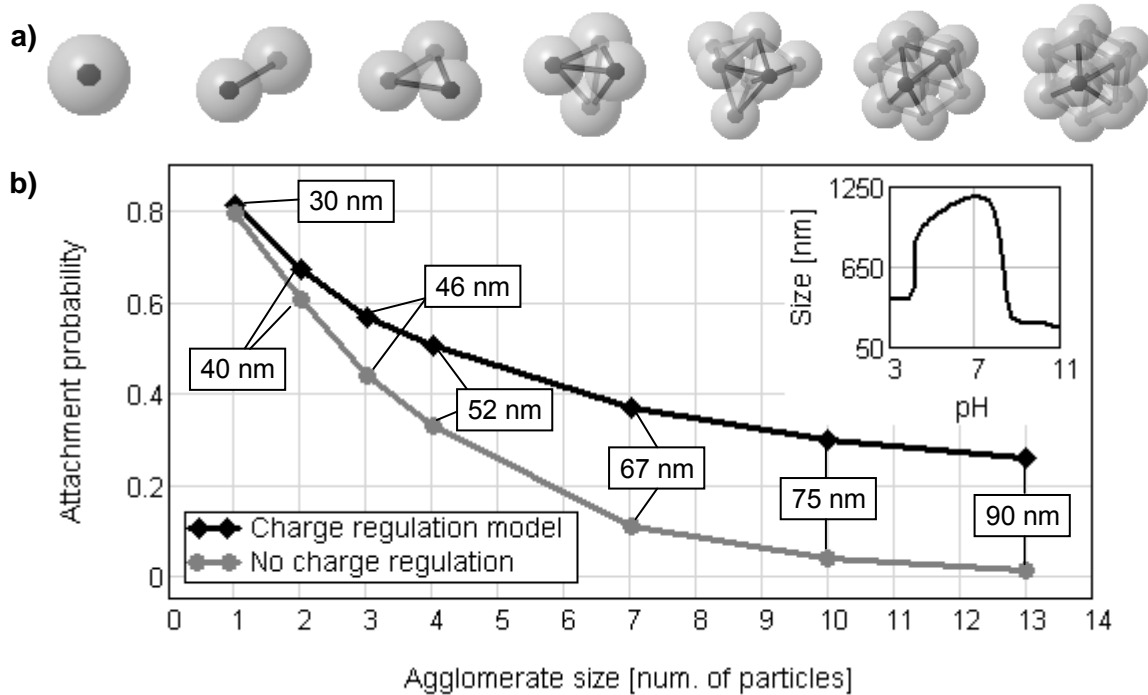


Figure 2. Probability of nanoparticle attachment to an agglomerate as a function of the agglomerate's size (as a number of constituent particles) at pH=7; (a) – considered agglomerate geometries; (b) attachment probabilities calculated with and without charge regulation model; the inset illustrates the experimental pH dependency of the mean agglomerate size taken from [2].

References

- [1] Barisik M *et al* 2014 *J. Phys. Chem. C* **118** (4) 1836
- [2] Berg J M *et al* 2009 *Nanotoxicology* **3** (4) 276
- [3] Chowdhury I *et al* 2013 *Environ. Sci.: Processes Impacts* **15** 275
- [4] Alfimov A V *et al* 2014 *J. Phys.: Conf. Ser.* **541** 012063

Activator-free luminescent nanocontainers for cancer tumor theranostics

D A Eurov, S A Grudinkin, D A Kurdyukov, A V Medvedev, E Yu Stovpiaga and V G Golubev

Ioffe Physical-Technical Institute, 194021 St. Petersburg, Russia

Abstract. We synthesized submicron monodisperse spherical mesoporous silica particles having visible broadband luminescence through one-step route. Obtained particles possess surface area of 550 m²/g and pore volume of 0.36 cm³/g, the average pore diameter is 3 nm. The synthesis procedure initiates chemically active inner surface that enables binding and retention of drugs loaded into the pores. The particles are very promising for the use in theranostics of cancer tumors as nanocontainers simultaneously acting as biomarkers.

1. Introduction

Monodisperse spherical mesoporous silica particles (MSMSPs) attract growing attention for their potential for creation of drug delivery systems into tumors [1]. Such particles exhibit several unique structural properties such as stable regular mesostructure, high surface area and pore volume that enables high loading capacity and offer the ability to protect pharmaceutical cargoes from premature release and degradation in harsh environments, and to reduce toxicity. Monodispersity of the particles provides them with similar hydrodynamic properties and therefore controllable time of drug delivery.

When using MSMSPs as drug delivery agents it is of great importance to have an ability of monitoring the process of their accumulation within cancer tumor. For this purpose usually one makes them luminescent by the incorporation of emission centers (activators) such as fluorescent dyes [2], rare earths [3] or semiconductor quantum dots [4]. Most of procedures allow reaching a strong photoluminescence emission but unfortunately requiring multiple processing steps and the use of expensive or toxic fluorophores. Furthermore, the incorporation of luminescence activators dramatically reduces pore volume and surface area that affects the efficiency of using MSMSPs as nanocontainers for toxic chemotherapeutics.

2. Results

In this work we developed the procedure for one-step synthesis of luminescent MSMSPs (L-MSMSPs). We used traditional approach of MSMSPs synthesis in the course of tetraethoxysilane (TEOS) hydrolysis [5]. In order to endow the particles with luminescent properties aminopropyl triethoxysilane (APTES) was added into the reaction mixture.

The obtained L-MSMSPs were annealed at 550°C in air for 8 h. The technology of synthesis allows to controllably vary the mean diameter of particles in the range 100–500 nm. Figure 1a shows typical microphotograph of obtained L-MSMSPs made with atomic force microscope (AFM). Standard deviation of the particles does not exceed 10%. Photoluminescence (PL) spectra of L-MSMSPs (figure 1b) reveal broad band with maximum at 480 nm and FWHM of 180 nm. Nitrogen adsorption-desorption

technique showed that synthesized particles possess high surface area ($550 \text{ m}^2/\text{g}$) and pore volume ($0.36 \text{ cm}^3/\text{g}$). The pore diameter is 3 nm.

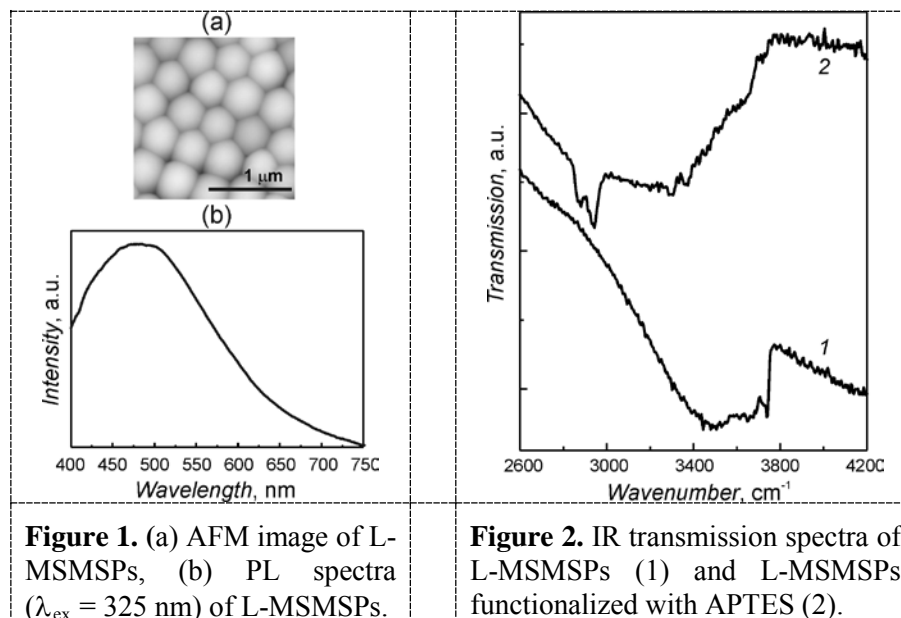


Figure 1. (a) AFM image of L-MSMSPs, (b) PL spectra ($\lambda_{\text{ex}} = 325 \text{ nm}$) of L-MSMSPs.

Figure 2. IR transmission spectra of L-MSMSPs (1) and L-MSMSPs functionalized with APTES (2).

Chemical activity of the particle's inner surface is provided by the presence of silanols. Figure 2 shows IR transmission spectra of bare MSMSPs (curve 1) and L-MSMSPs (curve 2). The narrow spectral band at 3745 cm^{-1} and bands in the $3650\text{-}3700 \text{ cm}^{-1}$ region are characteristic for isolated and terminal silanols, respectively, which indicates chemically active surface of the particles.

In order to confirm the activity of free silanols inner surface of L-MSMSPs were functionalized with APTES by capillary impregnation. It can be seen (figure 2 curve 3) that after functionalization narrow band at 3745 cm^{-1} almost disappeared. New bands in the $2850\text{-}3000 \text{ cm}^{-1}$ and $3280\text{-}3350 \text{ cm}^{-1}$ regions are characteristic for $-\text{CH}$ in the propyl group and $-\text{NH}$ in the amino group, respectively. It can be concluded that binding of APTES molecules with surface silanols of silica occurs which indicates high chemical activity of L-MSMSP's surface.

3. Conclusion

The technology developed in this study enabled synthesis of luminescent monodisperse spherical mesoporous silica particles through one-step route without using any luminescence activator. The particles possess broadband luminescence with maximum at 480 nm and FWHM of 180 nm. It is shown that surface of obtained L-MSMSPs is chemically active and can be easily functionalized that enables future application as nanocontainers for toxic chemotherapeutics in drug delivery systems. L-MSMSPs will simultaneously serve as luminescent biomarkers for monitoring of drug delivery and thus they might be applied in cancer theranostics.

References

- [1] He Q and Shi J 2014 *Adv. Mater.* **26** 391
- [2] Cho E-B, Volkov D O and Sokolov I 2011 *Adv. Funct. Mater.* **21** 3129
- [3] Moran C E, Hale G D and Halas N J 2001 *Langmuir* **17** 8376
- [4] Chan Y, Zimmer J P, Stroh M, Steckel J S, Jain R K and Bawendi M G 2004 *Adv. Mater.* **16** 2092
- [5] Trofimova E Yu, Kurdyukov D A, Yakovlev S A, Kirilenko D A, Kukushkina Yu A, Nashchekin A V, Sitnikova A A, Yagovkina M A and Golubev V G 2013 *Nanotechnology* **24** 155601

Dual color localization microscopy of FtsZ and DNA in *Escherichia coli*

V V Gorbunov¹, A D Vedyaykin¹, I E Vishnyakov², G E Pobegalov¹, A S Melnikov¹, P.Yu. Serdobintsev¹, A V Sabantsev¹

¹ Research Institute of Nanobiotechnologies, Saint-Petersburg State Polytechnical University, Saint-Petersburg, 195251, Russia

² Institute of Cytology, Russian Academy of Sciences, Tikhoretsky av. 4, Saint-Petersburg 194064, Russia

Abstract. Localization microscopy allows visualization of biological structures with resolution well below the diffraction limit. This is achieved by temporal separation of single fluorophore molecules emission and subsequent localization of them with the precision of few tens of nanometers in three dimensions. This method coupled with indirect immunocytochemistry was successfully used before to visualize FtsZ structures in dividing *Escherichia coli* cells. In this work we obtained super-resolution images of DNA distribution in *E. coli* cells using intercalating dye staining. The composite images (FtsZ + DNA) proved to be substantially more informative than the FtsZ images only.

FtsZ is one of the main cytoskeleton proteins in bacteria [1]. It is absent only in a few prokaryotic organisms thus being one of the most conserved bacterial proteins. FtsZ also plays a crucial role in the division of chloroplasts in plant cells [2]. This protein is one of the main components of the Z-ring, the structure that is responsible for the formation of the septum during cell division. It also forms spiral-like structures in bacteria. FtsZ is a tubulin homolog and possesses GTPase activity, but the filaments that it forms are more dynamic than microtubules. Exact mechanisms underlying the role of this protein in cell division remain largely unknown. In vitro experiments showed that FtsZ forms relatively short filaments up to 100 nm in length, and it is postulated that they are further organized by other proteins to form long-range structures like Z-ring.

High-resolution visualization of the structures formed by FtsZ in vivo can answer many current questions according to the role of this protein in bacterial division. In this work super-resolution localization microscopy was used to study the organization of FtsZ in bacterial cells [3]. It is known that FtsZ polymerization is controlled by nucleoid occlusion system that prevents the formation of the septum over nucleoid, preventing possible DNA damage that can arise from improper septum positioning. To visualize nucleoid position together with FtsZ dual-color localization microscopy was used. We have to admit that the obtained images are substantially more informative. Some visualized FtsZ and DNA structures are shown on Figure 1.

In this work TOP-10 *E. coli* strain was used, carrying pGEX4T2 plasmid to allow ampicillin selection. FtsZ was visualized by indirect immunocytochemistry whereas DNA was labeled with intercalating dye. Custom-built set up, incorporating laser-based fluorescence excitation and active

sample position stabilization was used to obtain data required for the reconstruction of super-resolution images, which was performed using an ImageJ [4] plug-in QuickPALM [5].

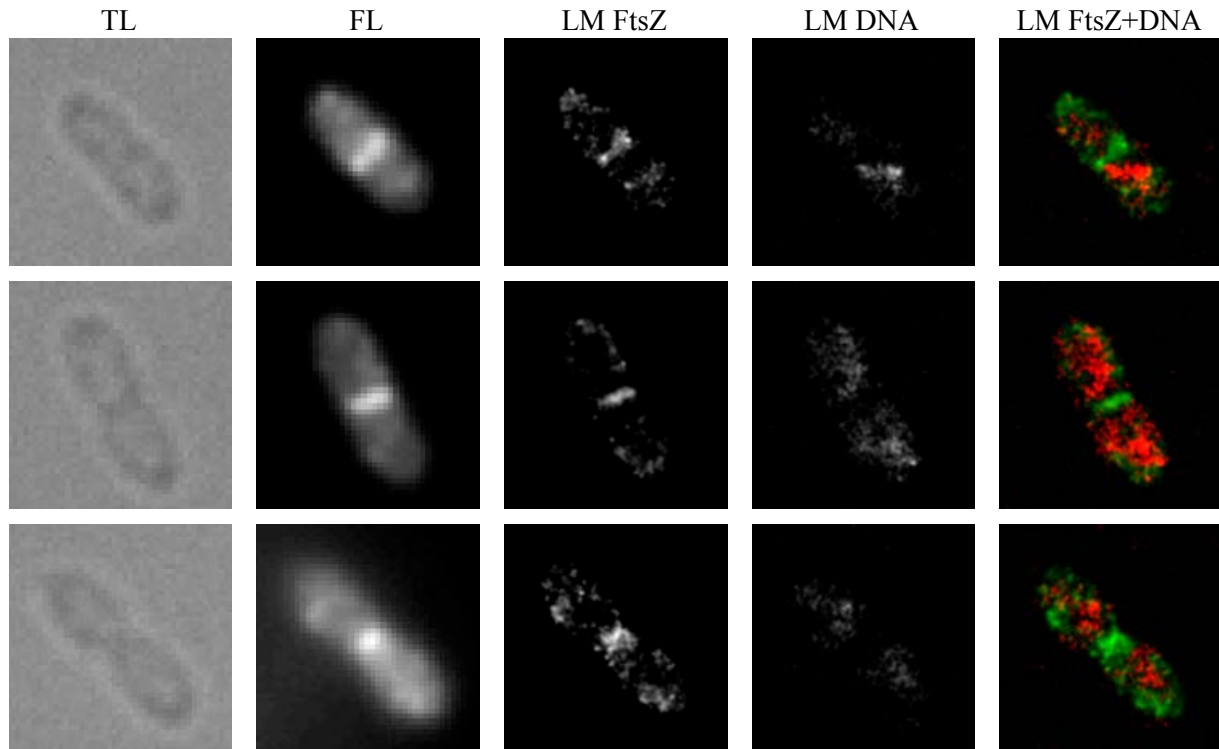


Fig. 1. FtsZ and DNA visualization in *E. coli* dividing cells. Different cells are shown in different lines. Transmitted light (TL) image, “conventional” fluorescent (FL) FtsZ image, localization microscopy images of FtsZ (LM FtsZ), DNA (LM DNA) and their composite (LM FtsZ+DNA) are shown.

References

1. Erickson, H.P., D.E. Anderson, and M. Osawa, *FtsZ in bacterial cytokinesis: cytoskeleton and force generator all in one*. *Microbiol Mol Biol Rev*, 2010. **74**(4): p. 504-28.
2. Strepp, R., et al., *Plant nuclear gene knockout reveals a role in plastid division for the homolog of the bacterial cell division protein FtsZ, an ancestral tubulin*. *Proc Natl Acad Sci U S A*, 1998. **95**(8): p. 4368-73.
3. Rust, M.J., M. Bates, and X. Zhuang, *Sub-diffraction-limit imaging by stochastic optical reconstruction microscopy (STORM)*. *Nat Methods*, 2006. **3**(10): p. 793-5.
4. Collins, T.J., *ImageJ for microscopy*. *Biotechniques*, 2007. **43**(1 Suppl): p. 25-30.
5. Henriques, R., et al., *QuickPALM: 3D real-time photoactivation nanoscopy image processing in ImageJ*. *Nat Methods*, 2010. **7**(5): p. 339-40.

Technical solution for studying the peculiarities of pressure distribution on the surface of a human's feet

E.A.Daminova

Ufa, Mingazheva 127-43, Russian Federation

Abstract. Device Implementation for spatiotemporal diagnosis of footstep rones is discussed, principle of simplified block scheme of this device are examined, description of sensor used in given.

As a vital necessity the musculoskeletal system suffers various diseases and pathologies that may be diagnosed with the help of specialized diagnostic tools and techniques, one of which is worked out in this developing device and this is just a spatiotemporal determination of feet zones.

The feet entirely perform bearing and movement functions, mitigates impetus during physical activity. With vaulted structure the feet acts as a buffer thus complementing the bending vertebral column, hip, knee and talocrural joints.

The pressure on feet produced by human's weight is very essential both during the quiescence and physical activity; that is why a variety of pathologies in feet functions, musculoskeletal structure lead to disturbances in the entire musculoskeletal system of a human, such as flatfoot – foot deformity, that is characterized by flattening its vaults. In addition, feet can reflect the other organs and systems condition, diabetes, for example. A man, who suffers the diabetes usually, has a diabetic foot syndrome.

The developing technical solution is an insole with installed strain transducers disposed in correspondence with the elements and belts of postural stimulation. Posturology especially focuses on the interconnection of accentual reactions with violation of vertical position of a human's body. The structure of this device consists of the following blocks: sensor unit represented by the insoles with installed sensors for the left and for the right feet; switching unit controlled by distributing signals of the microprocessor system which includes an analog-digital converter and a microcontroller; filter unit, which is necessary to clear up the informational signal from noise and interference; pre-amplification unit; the useful signal block, which informs the data about pressure; visualization block. The obtained information can be transferred to a Personal Computer, removable media, or shown on the visualization block display.

The suggested technical solution is set up on a modern cell base, meets the mobility requirements and also enables to determine and study pressure peculiarities and its distribution on the bearing surface of human's feet.

Numerical modeling of the liquid front propagation in inhomogeneous nanoporous media

D S Golovina and S A Chivilikhin

ITMO University, Kronverkskiy, 49, St. Petersburg, 197101, Russia

Abstract. In the last decade application of nanoporous materials in biology and medicine has been widely researched. One of the problems in this field are the transport processes in nanoporous media. The paper reports the numerical model, which simulates the motion of the liquid front, two-dimensionally permeating inhomogeneous nanoporous medium with altering porosity and pore size. Such model allows us to analyze the correlation between the inhomogeneities of the media and the shape and transition of a front. The evolutions of the liquid front profile for nanoporous media with various parameters have been obtained, using the program, written in C++.

1. Introduction

In recent years nanoporous materials have become a subject of various scientific researches. Considerable attention is given to their application in biology and medicine. For example, nanoporous materials can be used for drug delivery [1, 2], immunoisolation [3], tissue engineering [4], as biological sensors [5], etc.

One of the problems are the transport processes [6], which in case of nanoporous systems are considerably more complex, than in homogeneous phases or even in macroporous systems [7]. The purpose of our work is to numerically model the motion of the front of the liquid, two-dimensionally permeating inhomogeneous nanoporous medium with altering porosity and pore size. Such model allows us to analyze, how inhomogeneity of a medium influence the shape and the transition of a front.

2. Description of the numerical model

The presented model is based on the continuity equation for the incompressible flow and the approximation of Darcy's law. In two-dimensional case the combination of formulas $\nabla \vec{v} = 0$ and $\vec{v} = -\gamma \nabla P$ results in the linear differential equation (LDE):

$$\nabla(\gamma \nabla P) = 0 \quad (1)$$

which can be solved by classical numerical methods.

Here the coefficient $\gamma = \frac{\Omega D^2}{32\mu}$ [8], where Ω is the porosity of medium, D is the average pore diameter and μ is the coefficient of dynamic viscosity of the fluid. This coefficient describes the

medium. Making γ a matrix of the same size as the grid allows us to change γ in every grid node and, therefore, to take into consideration the inhomogeneity of the medium.

By solving the LDE (1) we obtain the distribution of pressure in the medium's part which has been permeated by liquid, and through that — the transition of a liquid front. Since a medium is inhomogeneous, the distribution of pressure in the front changes with its motion and must be recalculated after each iteration using a matrix, which comprises values of pressure in the medium (thus, also describes it) and also is of the same size as the grid.

3. Results

The program, which numerically models two-dimensional motion of the front of the liquid, permeating inhomogeneous nanoporous medium, has been written in C++. The evolutions of the liquid front profiles for nanoporous media with different parameters have been obtained (example can be seen at the figure 1).

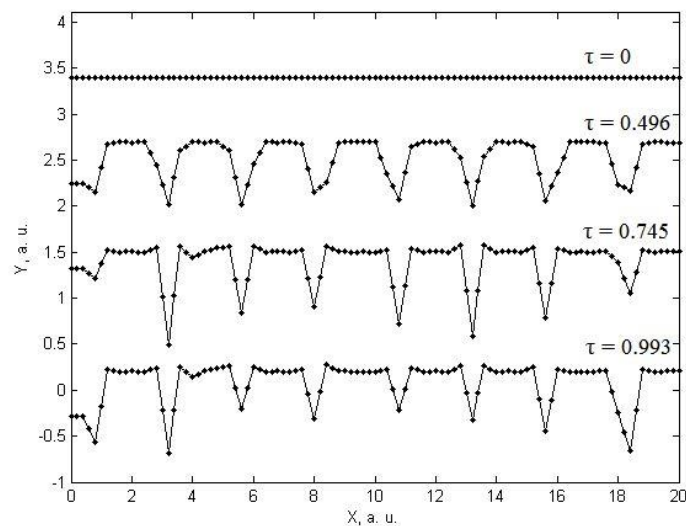


Figure 1. The evolution of the front profile in a nanoporous medium with perturbed parameters.

These numerical results allowed us to explore the correlation between the inhomogeneities of the media and the liquid front.

References

- [1] Sun CY, Qin C, Wang CG, Su ZM, Wang S, Wang XL, Yang GS, Shao KZ, Lan YQ and Wang EB 2011 *Adv. Mat* **23** 5629–32
- [2] Gultepe E, Nagesha D, Sridhar S and Amiji M 2010 *Adv. Drug Deliv. Rev.* **62** 305–15
- [3] La Flamme K E, Popat K C, Leoni L, Markiewicz E, La Tempa T J, Roman B B, Grimes C A and Desai T A 2007 *Biomaterials* **28** 2638–45
- [4] Cardea S, Pisanti P and Reverchon E 2010 *J. of Supercritical Fluids* **54** 290–95
- [5] Hu K, Lan D, Li X and Zhang S 2008 *Anal. Chem.* **80** 9124–30
- [6] Beckstein O and Sansom M S P 2004 *Phys. Biol.* **1** 42–52
- [7] Conner WC and Fraissard JP 2006 *Fluid Transport in Nanoporous Materials* (Dordrecht: Springer)
- [8] Scheidegger A E 1958 *The Physics of Flow Through Porous Media* (Toronto: University of Toronto Press)

Porous silicon nanoparticles for target drug delivery: structure and morphology

A O Belorus¹, P A Somov¹, S S Tulenin², Yu M Spivak¹, V A Moshnikov^{1,3}

¹ Saint Petersburg Electrotechnical University "LETI",
5th Prof. Popova Str., Saint-Petersburg, 197376, Russia

² Ural Federal University named after the first President of Russia B.N. Yeltsin, 19th
Mira street, Ekaterinburg, 620002, Russia

³ Peter the Great St.Petersburg Polytechnic University, 29, Polytechnicheskaya st.,
195251, St.Petersburg, Russia

Abstract. Nanoparticles of porous silicon were obtained by electrochemical anodic etching. Morphology and structure of the particles was investigated by BET adsorption, dynamic light scattering and scanning electron microscopy. The influence of technological conditions of preparation on geometrical parameters of the porous silicon particles (particle size distribution, pore shape and size, the specific surface area of the porous silicon) is discussed.

1. Introduction

Porous silicon and materials based on it have found their application in various fields of micro- and nanoelectronics, solar and hydrogen energy as well as in biomedical technology [1]. For example, ultrathin film of monodisperse nanoparticles of porous silicon, having the ability to photoluminescence can provide material, which improved efficiency of solar cells in the individual areas obtained by hydro-chemical deposition [2-4], and other methods for producing photovoltaic cells.

In recent years, in biomedicine and biotechnology are developing rapidly approaches to the visualization of the processes at the level of cells, tissues and organisms, drug delivery to sites of infection as well as the fight against cancer cells by methods of photodynamic therapy [1]. To date, special interest are porous silicon nanoparticles and composites based on them [5]. Such materials can potentially be used for applying *in vivo*. It does not produce allergic reactions, can be cleaved in the body and removed from it. In the pores of these materials can be placed and lock payload, drugs and cancer vaccines. The main advantage of these porous nanoparticles to more optically active materials (gold nanoparticles, semiconductor nanocrystals CbSe, CdTe, PbSe, PbS, carbon nanotubes) for use in *in vivo* applications is that such silicon nanoparticles are biodegradable and biocompatible. Important task in this case is to study the structure and morphology, determining the size of the nanoparticles, as well as the study of the influence of various dispersion media.

2. Experiment

In this work, the porous silicon nanoparticles were obtained by electrochemical anodic etching in a single-chamber electrochemical cell using an electrolyte solution based on hydrofluoric acid, using isopropyl alcohol as a dispersion medium. Then, the porous silicon layers ultrasonically milled, thus obtaining particles of porous silicon.

The structure, morphology and dimensions of such obtained nanoparticles were examined with a scanning electron microscope Tescan MIRA, particle size analyzer Photocor mini and equipment for the specific surface area measuring by the BET adsorption method and pore size distribution SORBI-MS and SORBI-PREP station.

3. Result

Comparing the data size of the nanoparticles obtained by scanning probe microscopy and dynamic light scattering showed that the particles obtained from single crystal silicon wafers with specific resistance $1 \Omega \cdot \text{cm}$, sustained in isopropyl alcohol for 1 year, the percentage particle size of about 200 nm - 74% 700 nm - 14.3%, 20 nm - 11.6%). For solutions that have been stored in isopropyl alcohol for a month, dynamic scattering method shows 100% of nanoparticles of 15 nm in size. For particles obtained from monocrystalline silicon wafers with specific resistance $0.3 \Omega \cdot \text{cm}$ study comparable two methods show the same trend in the percentage of particles and their sizes, as samples obtained from the silicon single crystal with specific resistance $1 \Omega \cdot \text{cm}$ at equal conditions.

Based on these data and the data of measurements of the specific surface area and pore size distribution for these materials [6] can be assumed that the porous silicon nanoparticles after the etching process have a size of about 15 nm. These porous silicon nanoparticles have an internal pore size distribution: 34.5% of the pores ranging in size from 3 to 5 nm, 21.2% with pore sizes ranging from 3 to 8 nm, 25.2% with pore sizes ranging from 8 to 11 nm, 19.1% with pore sizes from 40 to 70 nm [7]. In the aggregation going during storage of the nanoparticles in the dispersion medium after the exposure solutions within the time interval of one month or more. Over time aggregates are formed with typical dimensions of 200 nm and 700 nm. Presumably with increasing storage time, the formation of larger aggregates.

Acknowledgments

The reported study was this work was supported by project "Preparation and study of porous systems, functionalized nanomaterials, applications in photonics, sensor technology and medicine" (under the Russian Ministry of Education state task № 16.2112.2014 / K.

References

- [1] Belorus A O 2013 *Molodoi Uchenyi, in Russian* **8** 20720297
- [2] Chufarov A Yu, Ermakov A N, Samigulina R F, Zainulin Yu G, Forostyanaya N A, Maskaeva L N and Markov V F 2013 *Russian J. of Inorganic Chem.* **58** 1362–1369
- [3] Markov V F, Tulenin S S, Maskaeva L N and Kuznetsov M V 2014 *J. of Surface Investigation. X-ray, Synchrotron and Neutron Techniques.* **8** 659–665
- [4] Fedorova E A, Tulenin S S, Maskaeva L N Kuznetsov M V, Chufarov A Yu and Markov V F 2012 *Butlerov Communications.* **30** 144–149
- [5] Spivak Yu M, Maraeva E V, Belorus A O, Molchanova A V, Nigmatdzyanova N R 2013 *Smart Nanocomsite* **4** 115
- [6] Belorus A O, Maraeva E V, Spivak Yu M 2015 *Izvestia SPbGETU «LETI», in Russian* **2** 11
- [7] Belorus A O, Maraeva E V, Spivak Yu M, Moshnikov 2015 *Journal of Physics: Conference Series* **586** 012017

Spectroscopy of peptides, proteins and oligonukleotides from solutions by ion mobility

P. S. Koryakin^{1,2}, A. N. Arseniev¹, N. V. Krasnov¹, M. Z. Muradymov¹

¹Institute for Analytical Instrumentation of RAS, Saint-Petersburg, Russia

²St. Petersburg State Polytechnic University, Saint-Petersburg, Russia

The last decades for solving analytical problems in biochemistry, chemistry, pharmaceuticals, toxicology, forensic and environmental monitoring largely consists in the creation of instrument systems based on well-known previously separate powerful analytical methods already enshrined in the instruments. Such as, for example, gas chromatography (GC), liquid chromatography (HPLC), mass spectrometry (MS), ion mobility spectrometers (IMS). Setting targets for highly sensitive analysis of complex mixtures has led to the creation of instrument complexes GC-MS – to meet the challenges of chemistry and petrochemistry, HPLC-MS – to meet the challenges in biotechnology and medicine [1]. At the same time received a powerful impetus to the development of software for the control instrument complex, and processing of analytical information. A separate task was the question of connection of devices in complex with all their incompatibility operating conditions: for example, gas chromatography or liquid chromatography and vacuum system of the mass spectrometer and obtaining analytes ions: preferably basic and molecular fragments. Furthermore, their requirements imposed analytes (labile bioorganic) HPLC-MS. Nevertheless, improving the design of the ion source with electron impact and the development of a new method of producing ions of bioorganic substances from solutions will successfully carry out the combination of devices in the analytical system. Instrumental complexes GC-MS and HPLC-MS are universal devices with high analytical parameters. Such devices allow to solve complex analytical problems in various range of knowledge. But there are many problems for analytical chemistry, for which at first glance does not require expensive and universal devices. These tasks include monitoring of explosives, drugs, chemical hazards. Often these problems should be solved quickly in real time with a minimum of sample preparation and preferably using small devices at least in comparison with classical instrumental complex.

To solve these problems has been chosen another method of analytical chemistry – plasma chromatography method [2], hereinafter called the "Ion Mobility Spectrometry". Ion mobility spectrometry is a highly sensitive and fast method and, more importantly, a very small-sized. Devices that implement the method of ion mobility spectrometry working at atmospheric pressure. Therefore the need for methods of producing ions at atmospheric pressure ionization. Such methods include ionization at atmospheric pressure, for example, corona discharge or electrospray sample solution method. Development of devices based on ion mobility spectrometry developed initially in two directions: small size detectors for specific substances in the form of vapor or gas ionization at atmospheric pressure and a detector for gas chromatographs. Both directions are well developed and have achieved great success in terms of the development of instrument complexes GC-IMS [3], and as separate detectors for the analysis of air and the development of methods of analysis.

Direction associated with the use of ion mobility spectrometers as an independent detector for analysis of substances in solutions has developed only in the form of instruments for the analysis of swabs for search traces of explosives. When this method is used receiving the analyte ions in the electrospray solution modification method as "electrospray", namely in the form nanospray [4]. The idea of using ion mobility spectrometer as a detector for liquid chromatography never developed, i.e. a feed the sample solution in the ion sources ion

mobility spectrometer was about 0.02–1 $\mu\text{l}/\text{min}$, which does not correspond to the flow at the outlet of the capillary columns of liquid chromatographs (200–1000 $\mu\text{l}/\text{min}$) for implementing chromatographic methods for various classes separated substances. Chromatographic eluent flows cause difficulties in the process of electrospray and overload ion mobility spectrometer because of condensation eluent on the elements of the input path of the spectrometer and the drift zone. Nowadays the widely used instrument complex consisting of liquid chromatography, ion mobility spectrometer as additional ions analyzed separating device and the mass spectrometer as a highly sensitive detector. And in such instrument complex flow of the sample solution flowing into the electrospray ion source does not exceed the unit $\mu\text{l}/\text{min}$. [5]. Recent studies show that interest in creating ion mobility spectrometer with ion source with electrospray solutions retained by virtue of the need to expand the circle of detectors for liquid chromatography, for example, to enable the separation and detection of isomers of substances.

The result of the creation of such a device was the holding of the first test measurements, during which were examined the capability of producing an ion mobility spectra of peptides, proteins and oligonucleotides in positive and negative modes using an ion source with field desorption ion from solution under dynamic flow dividing spraying liquid at atmospheric pressure and normal conditions. As of the objects used solutions: aliphatic quaternary amines Me₄N and Et₄N, Arginine (175 Da), Reserpine (608,68 Da) in positive mode, macro biomolecules Human serum albumin (69367 Da), Hemoglobin Human (16 000 Da), Apoferritin (445000 Da), Myoglobin (17083 Da), Chymotrypsinogen A (25666 Da), and synthetic oligonucleotides Doditsela sodium sulfate (265 Da) in positive and negative modes. The studies were conducted on the prototype analytical complex ES-IMS (electrospray ion source — ion mobility spectrometer), developed at the request of FMBA of Russia under the Federal Target Program "National System of chemical and biological safety of the Russian Federation (2009–2014)".

Relevance of ion mobility spectrometer with electrospray ion source for the chromatographic eluent flow due to the fact that, having the advantages of relatively low cost, ease of use and low weight and size such a device significantly enhances performance liquid chromatography at solving specific analytical problems.

References

1. Arseniev A.N., Koryakin P.S., Krasnov N.V, Muradymov M.Z. [Spectroscopy of peptides, proteins and oligonukleotides from solutions by ion mobility]. *Nauchnoe Priborostroenie* [Science Instrumentation], 2015, vol. 25, no. 1, pp. 17–26. (In Russ.).
2. Cohen M.J., Karasek F.W. Plasma chromatography — a new dimension for gas chromatography and mass spectrometry // *J. Chrom. Sci.* 1970. Vol. 8, No. 6. P. 330–337.
3. Gas Chromatograph Detector. PCP, inc Ion mobility spectrometer // NASA SBIR Success. US.
4. Coy S.L., Krylov E.V., Nazarov E.G., Fornace A.Y.Jr., Kidd R.D. Differential mobility spectrometry with nanospray ion source as a compact detector for small organics and inorganics // *Int. J. Ion Mobil. Spec.* 2013. Vol. 16, No. 3. P. 217–227. DOI 10.1007/s12127-013-0136-3.
5. Hoiness H., Almirall J. Speciation effect of solvent chemistry on the abalysis of drugs and explosives by electrospray ion mobility mass spectrometry // *Int. J. Ion Mobil. Spec.* 2013. Vol. 16, No. 2. P. 237–246. DOI 10.1007/s12127-013-0136-2.

Molecular Beacon CNT-based Detection of SNPs

**A S Egorov¹, V P Egorova², H V Krylova^{3,5}, I V Lipnevich³, T I Orekhovskaya⁴,
A A Veligura², M I Govorov¹, B G Shulitsky⁴, L.Y. Fedotenkova²**

¹Institute of Physiology, Nat. Acad. Sci. of Belarus, 28 Akademicheskaya Str, 220072 Minsk, Belarus

²Belarusian State Pedagogical University, 18 Sovetskaya Str, 200005 Minsk, Belarus

³Physics Department, Belarusian State University, 4 Nezavisimosti Ave., 200030 Minsk, Belarus

⁴Belarusian State University of Informatics and Radioelectronics, 6 P. Brovki Str, 200013 Minsk, Belarus

Single Nucleotide Polymorphism (SNP) is the most common genetic variation in the genome. A large number of SNPs makes them unique genetic markers for preventive medicine and biomedical diagnostics. The use of molecular beacons tactics (MM) is one of the most sensitive methods for detecting SNPs. However, when using the MM for discriminating SNPs, substantial disadvantages of such types of probes have been identified (the presence of residual fluorescence and instability to intracellular nucleases), leading to the appearance of nonspecific signal in the sample. This problem can be solved by using nanostructured materials to modify the MM. It has been shown that the binding of few-layered carbon nanotubes (MWCNTs) to FAM-labeled oligonucleotides allows the carbon nanotubes to function as an effective nanotube fluorophore FAM [1].

In this study, we investigated the possibility of using this effect when designing a new approach to identify SNP-based fluorescence quenching by complexing the oligonucleotide with FAM-Munt, followed by the reduction of the fluorescence from hybridization of the oligonucleotide with FAM-target DNA sequences in solution.

The complexation performed by ultrasonic treatment of a mixture of MWCNTs and FAM-oligonucleotide suspended in TE buffer. The structural and functional properties of the resulting Munt / FAM-oligonucleotide complexes were characterized using scanning electron microscopy (SEM) and the method of analysis heterostructure (GA). Munt was uniformly distributed on the SEM images and fully covered by dense layers of self-assembled oligonucleotide. The method of HA demonstrated that the presence of the target sequence complementary to the solution leads to the dissociation of the MWCNT / FAM-oligonucleotide hybridization followed by homoduplex formation, as evidenced by the reduction in fluorescence of the fluorophore, the intensity of which is several fold higher than the fluorescence of FAM-free oligonucleotides. Furthermore, the presence of the target SNP oligonucleotide sequence leads to a fivefold reduction in the fluorescence intensity of the fluorophore and the reduction of the electrophoretic mobility of heteroduplexes containing a single mismatch.

Thus, MWCNT / FAM-oligonucleotide complexes may be used to create highly effective DNA biosensors operating according to the principle of molecular beacons for the purpose of detecting SNPs.

References

[1] A.A. Veligura Quenching of the fluorophore in the oligonucleotide layers of self-organized carbon nanotubes / Veligura A.A., Egorov A.S., Egorova V.P. [et.al.] // Scientific Bulletin of the Uzhgorod University. Series Physics. – 2013. V. 32. - P. 94-100.

The FNS-based analyzing the EEG to diagnose the bipolar affective disorder

O Yu Panishev^{1,2}, S N Panisheva^{1,2}, S A Demin^{1,2}

¹ Kazan Federal University, Institute of Physics, Kazan, 420008 Russia

² Kazan Federal University, Engelhardt Astronomical observatory, Zelenodolski region, st. Observatory, 422526 Russia

Abstract. Here we demonstrate a capability of method based on the Flicker-Noise Spectroscopy (FNS) in analyzing the manifestation bipolar affective disorder (BAD) in EEG. Generally EEG from BAD patient does not show the visual differences from healthy EEG. Analyzing the behavior of FNS-parameters and the structure of 3D-cross correlators allows to discover the differential characteristics of BAD. The cerebral cortex electric activity of BAD patients have a specific collective dynamics and configuration of the FNS-characteristics in comparison with healthy subjects.

Modern medical science has the powerful capabilities in solving many tasks in diagnosing and monitoring of the treatment quality. However, there are many difficulties connected with correct diagnosing in specific fields. First of all, it can be illustrated on example of the psychiatric disorders. The most disorders haven't the objective diagnostic criteria. At this rate, schizophrenia or a bipolar affective disorder are diagnosed based on criteria in either the American Psychiatric Association's fifth edition of the Diagnostic and Statistical Manual of Mental Disorders (DSM 5), or the World Health Organization's International Statistical Classification of Diseases and Related Health Problems (ICD-10). However in various papers [1, 2] it is shown that BAD and epilepsy are manifested in the specific behavior of synchronization effects and in spectral properties of alpha rhythm. In [3] on the basis of the flicker-noise spectroscopy (FNS) authors have formulated the criteria of degree of the susceptibility to schizophrenia in children/adolescents. In [4] it is demonstrated that the method based on the memory function formalism (MFF) can discover the susceptibility to schizophrenia by analyzing the collective phenomena in the cerebral cortex bioelectric activity. Bipolar affective disorder (earlier called manic-depressive illness) is a mental disorder characterized by periods of elevated mood and periods of depression. The elevated mood is significant and is known as mania or hypomania depending on the severity or whether there is psychosis. During periods of depression there may be crying, poor eye contact with others, and a negative outlook on life. In this paper within the framework of the flicker-noise spectroscopy [5, 6] we demonstrate a capability to formulate the objective diagnosing criteria for BAD using the analysis of EEG signals. The FNS method separates the analyzed signal into three components: low-frequency regular component corresponding to system-specific "resonances" and their interferential contributions, stochastic random-walk component at larger frequencies corresponding to dissipation effects, and highest-frequency inertial "spike" component corresponding to flicker noise. Also the method contains equations for describing the frequency-phase synchronization. We show here that the BAD existence leads to decreasing the resonance components and to increasing the chaotic components of the EEG-signal from the certain electrodes. Also we have discovered the crucial cerebral cortex areas for the BAD diagnosing. According to the hypothesis about dependence between the pathological abnormalities and the synchronization properties of bioelectrical activity we have revealed the characteristic features of the EEG collective dynamics in healthy people and BAD patients. It is shown that the cerebral cortex signals from healthy people are characterized by high degree of long-range synchronization, whereas EEG of BAD patients has a strongly pronounced short-range synchronization.

Acknowledgments

The work is performed according to the Russian Government Program of Competitive Growth of Kazan Federal University. This work was supported by the Russian Foundation for Basic Research, grant No 14-02-31385_mol_a.

References

- [1] Bhattacharya J, Kanjilal P P and Nizamie S H 2000 *IEEE Trans. Biomed. Engin.*, **46** 738
- [2] Bhattacharya J 2001 *Acta Neurobiol. Exp.*, **61** 309
- [3] Timashev S F, Panishev O Yu, Polyakov Yu S, Demin S A and Kaplan A Ya 2012 *Phys. A*, **391** 1179
- [4] Panishev O Yu, Demin S A, Kaplan A Ya and Varaksina N Yu 2013 *Biomed. Engin.*, **47** 153
- [5] Timashev S F 2007 *Flicker-Noise Spectroscopy: Information in Chaotic Signals* (Moscow: Fizmatlit) (in Russian)
- [6] Timashev S F, Polyakov Yu S, Yulmetyev R M, Demin S A, Panishev O Yu, Shimojo S and Bhattachatya J 2010 *Laser Phys.* **20** 604

The photovoltaic tandem converter of solar energy

Y Grib, A Stsiapanau, A Smirnov, E Mukha

Belorussian State University of Informatics and Radioelectronics (BSUIR), Minsk,
P. Brovkiy Str, 6, 220013, Belarus

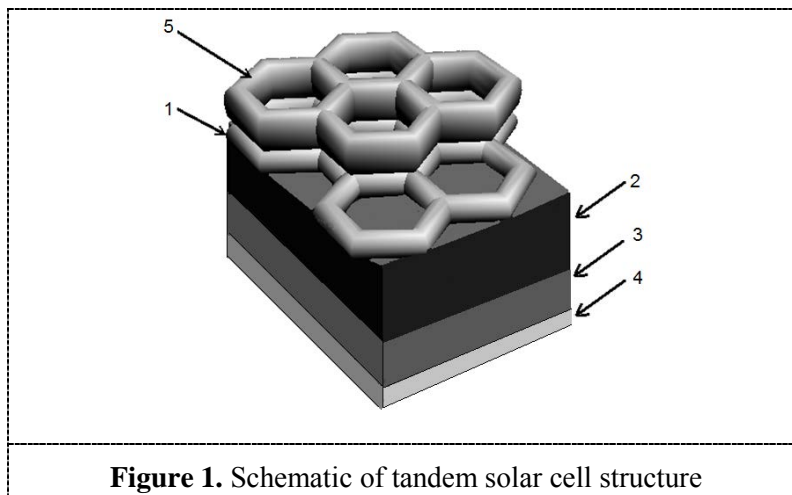
Abstract. This paper gives an overview of multijunction solar cell with aluminum nanoporous transparent top electrode. Al nanomesh was fabricated through electrochemical anodization of Al film in acid solution at low temperature condition.

1. Introduction

The primary sources for energy consumption are fossil fuels, which are known to be detrimental to the environment due to the excess emission of greenhouse gases from their use. An alternative that has been slowly gaining momentum as a viable alternative to the fossil fuel dependence is the use of Photovoltaic (PV) or solar cells. Better efficiencies are needed if solar technology is to become a larger contender in the movement toward alternative energy sources. Such mandated increases in efficiency have been seen in a class of PV known as multijunction (tandem) solar cells. The main principle being the use of multiple semiconductors arranged in a stack to more effectively capture electromagnetic radiation than the standard single junction cells [1].

2. The tandem structure of solar cell

The solar cell is delicately designed to efficiently absorb and convert light energy from the sun into electrical energy. Semiconductor solar cells are fundamentally simple devices. Semiconductors are able to absorb light and convert a percentage of the energy of the absorbed photons to electrical current. Figure 4 shows the physical structure of a tandem solar cell [2].

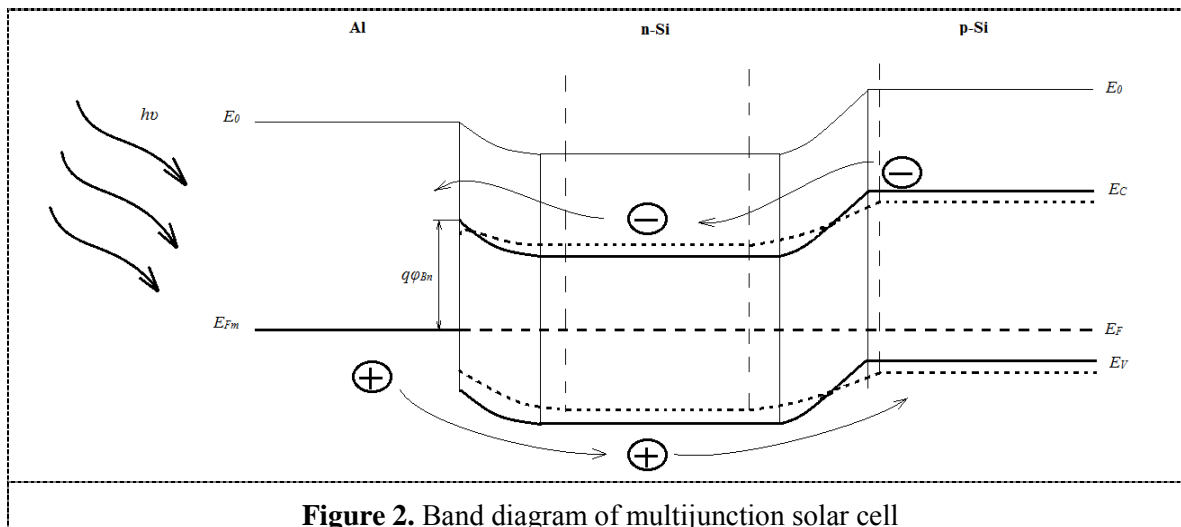


The Al nanoporous coating (1 in Fig.1) allows light to hit the semiconductor and be absorbed and converted into electrical energy. Al nanoporous electrode forms the contact Schottke with n-type silicon semiconductor (2 in Fig.1). Below the contact Schottke is a p-n junction.. A p-n junction is formed at the boundary between an n-type silicon and a p-type silicon (3 in Fig.1). The continuous contact is formed on the back side of device (4 in Fig.1). An antireflective top layer (5 in Fig.1) is fabricated on the Al nanoporous electrode to limit reflection and increase the amount of light absorbed by the cell.

3. Physics of tandem solar cells

The solar spectrum incorporates photons of different energy based on different wavelengths, so a single p-n junction solar cell will only have limited range for conversion efficiency where electrons move just beyond the conduction band and lattice heat loss is limited.

When designing a multijunction solar cell there are three basic design considerations: band gap differentiation, lattice constant matching, and current matching. Band gaps determine what wavelength of photons can be absorbed by a certain material and how much energy can be obtained by each photon. The difference between band gaps in multijunctions should be made as small as possible. This is because the amount of excess energy converted to light equalizes the photon energy and the band gap of the absorbing material [3]. The mechanism of operation is illustrated in Figure 2.



The junctions create the effective potential barriers for minority carriers and minimizes optical loss. In order for the multijunction to perform properly the band gap of the tunnel junction must be greater than the next cell [4].

4. Conclusion

Photovoltaic technology has advanced enough to where it has become a realistic option to help lower the world's dependency on fossil fuels. The developed tandem structure of solar cell has the number of advantages: the uniformity of the conversion increases, costly photolithography technology process is not required, use of low cost materials and the simplified fabrication process.

References

- [1] T. Katsuki. 2009. *Energies* 2(3) pp. 504-530.
- [2] B.Kazarkin, A.Stsiapanau, A.Tsybin, Y.Mukha, Y.Satskevich, A.Smirnov. 2014. *Abstracts of 1st Int.School and Conference "Saint-Peterburg OPEN 2014"*. P. 52-53.
- [3] T. Ameri, et al. 2011. *Solar Energy Materials and Solar Cells* 95(12) pp. 3256-3261.
- [4] W. Guter and A.W. Bett. 2006. *IEEE Transactions on Electron Devices* 53(9).

EFFECT OF ELECTRIC FIELD APPLIED UPON LANGMUIR MONOLAYERS, DECORATED CELLS AND NANOCOMPOSITE MICROCAPSULES

A. V. Ermakov^{1,2}, A. S. Chumakov^{1,2}, V. P. Kim³, I. A. Gorbachev^{1,2},
I. V. Vidyasheva², D. A. Gorin^{1,2}, G.B. Khomutov³, E.G. Glukhovskoy^{1,2}

¹ Saratov State University, Faculty of nano- and biomedical technologies, Saratov, 410012 Russia

² Saratov State University, Educational-Research Institute of Nanostructures and Biosystems, Saratov, 410012 Russia

³ M.V. Lomonosov Moscow State University, Faculty of Physics, Moscow, 119991Russia

Abstract. A new method of remote group control over permeability and integrity of nanocomposite microstructures of different nature is present in this paper. We investigate an electric field as a significant factor that able to affect the structures shell. The electric fields are carried out in quasi-two dimensional layers of the capsules. Such electro sensitive layers of micro containers will find a wide applicability in various fields.

1. Introduction

It was found in several works, that external electric field affects microcapsules shells. It is reported that the incorporation of molecules that align in electric fields into capsule's shells can be used as a sensitization of the capsule's permeability to the electric field. The structural degradation of the composite microcapsules with shells comprised of PVA/PAAc and multiwalled carbon nanotubes was demonstrated in presence of the electric field as well [1]. Nanocomposite microcapsules with ferroelectric liquid crystalline segments in PS-nylon shells are reported. This structure provided the possibility to control permeability through external electric fields [2]. In addition the possibility to employ rotating electric field as a method of measuring electro-physical characteristics of polyelectrolyte and hybrid lipid polyelectrolyte microcapsules [3] and also characteristics of living cells [4] are demonstrated.

2. Experiment

Our approach consists of using inorganic nanoparticles as a sensitizer of the capsules to an electric field. It's shown that nanocomposite polymeric microcapsules with magnetite nanoparticles in the shell and lipid covered with gold micro vesicles are sensitive to an external electric field of high intensity. Confocal microscopy allowed us to observe deformations of capsules shells and the decrease

of the vesicles concentration. The regularities of the lipid structures behavior are studied with Langmuir monolayers as models of the lipids membranes.

3. Results

The presence of an electric field has a significant influence on the formation of monolayers. Formation of liquid phase in a constant electric field portion of the isotherm corresponding liquid phase is strongly stretched, with an increase of about 25% by electric field, it does not depend on the direction of the electric field, and depended on the fact that field is applied.

4. Conclusion

Thus, a new approach for effect on the nanocomposite microcapsule and fibroblasts including opening microcapsule shell and membrane of biological cells by electric field was demonstrated. These results can be used for drug delivery systems controlled by electric field in the microfluidic devices and also for revise the data related to effect of electric field on the biological cells.

5. Acknowledgments

The work is supported by grant № 14-12-00275 of Russian Science Foundation and Saratov State University.

References

- [1] Yun, J.; Im, J. S.; Lee, Y.-S.; Bae, T.-S.; Lim, Y.-M.; Kim, H.-I. pH and electro-responsive release behavior of MWCNT/PVA/PAAc composite microcapsules, *Colloids Surf.* Pages 23–30 (2010)
- [2] Yoshida, M.; Matsui, T.; Hatate, Y.; Takei, T.; Shiomori, K.; Kiyoyama, S. J. Permeability Control in electro-sensitive microcapsules with immobilized ferroelectric liquid crystalline segments, *Polym. Sci., Part A: Polym. Chem.* Volume 46, pages 1749–1757 (2008)
- [3] Georgieva, R.; Neu, B.; Shilov, V. M.; Knippel, E.; Budde, A.; Latza, R.; Donath, E.; Kiesewetter, H.; Baumler, H.; Low Frequency Electrorotation of Fixed Red Blood Cells, *Biophysical Journal* Volume P. 2114–2120 (1998)
- [4] Cristofanilli, M.; DeGasperis, G.; Zhang, L.; Related to HER-2/ neu Over expression in MCF-7 Sublines Automated, *Clin Cancer Res*, V. 8 P. 615-619 (2002)

Microfluidic device for unidirectional axon growth

E.Malishev^{1*}, A.Pimashkin², A.Gladkov^{2,3}, Y.Pigareva², A.Bukatin¹,
V.Kazantsev^{2,4}, I.Mukhina^{2,3}, M.Dubina¹

¹ Saint-Petersburg Academic University - Nanotechnology Research and Education Centre of the RAS

² N.I. Lobachevsky State University of Nizhny Novgorod.

³ Nizhny Novgorod State Medical Academy

⁴ Laboratory of Nonlinear Dynamics in Living Systems, Institute of Applied Physics RAS, Nizhny Novgorod, Russia

Abstract. In order to better understand the communication and connectivity development of neuron networks, we designed microfluidic devices with several chambers for growing dissociated neural cultures. The chambers are connected with microchannels, which provide unidirectional axonal growth between “Source” and “Target” neural sub-networks. Experiments were performed in a hippocampal cultures plated in a polydimethylsiloxane (PDMS) microfluidic chip, aligned with a 60 microelectrode array (MEA). Axonal growth through microchannels was observed with optical microscope, and after 7 days *in vitro* electrical activity was recorded. Visual inspection and stimulus response analysis showed the predominant axonal growth in microchannels in a direction from “Source” chamber to “Target” Introduction.

1. Introduction

Microfluidic chips combined with microelectrode arrays are used in a wide range of electrophysiological studies of neural networks at subcellular, cellular and network-wide scale. Such devices provide a method to control morphology of the grown neural tissue in order to investigate memory, information coding and learning in the brain. Dissociated neural cultures can be grown in separated chambers connected with axons through microchannels [1]. Specific design of the microchannels can define axon outgrowth and a direction of electrical signal propagation through the neural network [2]. In this study we fabricated two types of asymmetric microchannels to investigate unidirectional axonal growth during culture development.

2. Methods

PDMS microfluidic chips containing an array of microchannels between two chambers were fabricated by two layer soft lithography (see Figure 1.a): first 5 μm -thick layer formed microchannels while second 50 μm -thick layer formed chambers. Microchannels' length varied from 200 μm to 1000 μm , and their structure was based on two types of segments, shown in figures 1.b and 1.c.

In order to investigate action potential propagation inside the microchannels, each PDMS chip was positioned and mounted onto the surface of a planar microelectrode array (MEA), so as to locate several electrodes in the microchannels(see figure 1.c,d). PDMS chip was adhered to MEA plate by heating them after mounting to 120°C for 20 minutes. Before cell plating the device was covered with polyethyleneimine or poly-d-lysine.

Dissociated hippocampal neurons were plated into separate subcompartments. Electrical activity was recorded after 7 days *in vitro* by USB-MEA system (Multichannel systems, Germany). Axons inside the microchannels were visualized with immunocytochemistry (Tau proteins marked by Alexa Fluor 647).

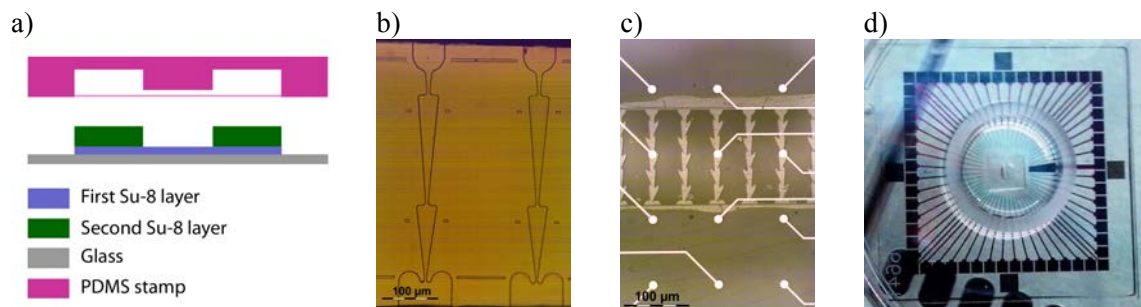


Figure 1. Fabrication of microfluidic device: a) SU-8 mold in section, b) optical light microscopy of 400 μm - length “Straight” microchannel, based on non rotated segments, c) optical light microscopy of “Zigzag” microchannels, based on rotated segments, mounted onto the MEA, d) complete device.

3. Results and Conclusions

In order to find optimal design of microchannels we studied axon growth dynamics varying microchannels’ length and shape of segment. Visual monitoring showed that in most cases axons, growing in “forward” direction of microchannels (from “Source” to “Target” chamber) reached their ends, while only several axons, growing “backward” passed more, than 2 segments (see figure 2.a,b). Similar results were shown by stimulus response analysis: spontaneous activity and stimulus responses propagate between chambers only from “Source” chamber into “Target”, but not vice versa (see figure 2.c).

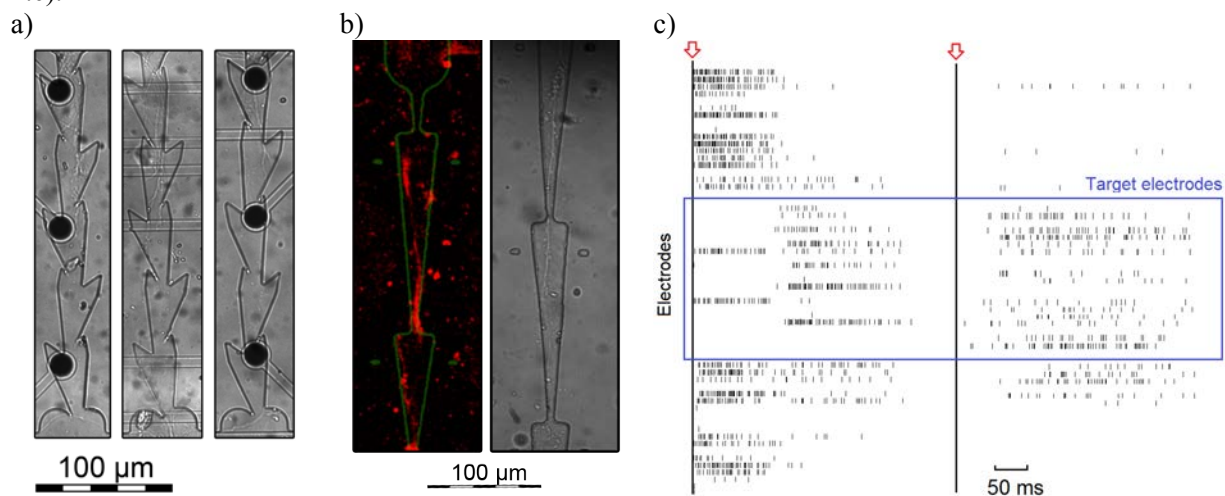


Figure 2. Axon growth direction monitoring: a) optical light microscopy of typical axon growth in microchannels with “Zigzag” segments b) immunocytochemistry image of 2 axons and optical light microscopy image of one axon in microchannels with “Straight” segments, c) Raster plot of spiking activity in response to stimulus (red arrow) applied to the electrode in “Source” chamber (left) and “Target” chamber (right). Each vertical line represents a spike timestamp.

4. References

1. Brewer, G. J., Boehler, M. D., Leondopulos, S., Pan, L., Alagapan, S., DeMarse, T. B., & Wheeler, B. C. (2013). Toward a self-wired active reconstruction of the hippocampal trisynaptic loop: DG-CA3. *Frontiers in Neural Circuits*, 7(October), 165.
2. Le Feber J., Postma W., Rutten W., De Weerd E., Weusthof M.. Two-Chamber MEA to Unidirectionally Connect Neuronal Cultures. *Proceeding of 9th Int. Meeting on Substrate-Integrated Microelectrode Arrays*, 2014. pp. 259-262.

5. Acknowledgements

This research was supported by the Russian Science Foundation (№ 14-19-01381)

Modeling of the behavior and statistical analysis of compressibility in the process of Langmuir monolayer structurization

H.V. Grushevskaya, G.G. Krylov, N.G. Krylova, I.V. Lipnevich
Belarusian State University, 4 Nezavisimosti Ave., Minsk 220030, Belarus

Abstract. An approach has been developed to perform data processing for experiments on two-dimensional phase transition of the first order. The approach represents itself the two stage filtration with subsequent merging of processed data and comparison with simulation results based on geometro-thermodynamical methods. The approach has been successfully applied to description of the phase transition in compressed monolayers of steric acid.

1. Introduction

Development of formation methods for two-dimensional (2D) solid-state perfect structures, which can operate at room temperature, is an important problem of flexible electronics. Langmuir-Blodgett (LB) technique can be used to produce almost perfect two-dimensional structures, provided that the conditions on a phase boundary are under control [1].

When modeling the Langmuir monolayer compression by Monte Carlo methods a metastable state is excluded from consideration that does not allow for such a control. A compressibility κ , for $\tilde{\pi}-A$ isotherms being dependencies of surface tension $\tilde{\pi}$ on an area A per one molecule, presents itself a derivative from the dependence $\ln A(\tilde{\pi})$ over $\tilde{\pi}$. But, instead of it, the "apparent" compressibility $\kappa_{\text{app}} = 1/K'$ being an inverse elasticity of a Langmuir monolayer is calculated.

2. Data processing

To utilize LB monolayers as a material for nanoelectronics it is necessary to correlate structural changes in a metastable compressed monolayer with changes of phenomenological parameters of the monolayer (e.g., compressibility coefficient). This requires a statistical analysis of experimental dependences of the surface tension $\tilde{\pi}$ upon the area A per molecule, followed by compressibility calculation.

In this paper, we propose a method of statistical analysis when at first we smoothen 2D fluctuations of the vector $\vec{r}_i \equiv (\tilde{\pi}_i, A_i)$ over an interval of n_1 values of the surface tension $\tilde{\pi}_{i+j}$ and corresponding

to them values of the area A_{i+j} per one molecule: $\vec{r}_i \equiv (\tilde{\pi}_i, A_i) = \frac{1}{n_1} \sum_{j=-n_1/2}^{n_1/2} \vec{r}_{i+j}$. Then, a filtering

procedure based on the sliding mean with given window width m_1 is applied to the smoothed set, when an experimental value is to replace by a mean value obtained from the m_1 nearest points as:

$\tilde{\pi}_i \rightarrow \langle \tilde{\pi}_i \rangle = \frac{1}{m_1} \sum_{j=-m_1/2}^{m_1/2} \tilde{\pi}_{i+j}$. The filtering on the sliding mean was applied only to the readings of the

surface tension sensor, as its noise prevails over noise "inertial" position sensor. To find the compressibility $C(\tilde{\pi})$ of monolayer, the logarithmic derivative of the dependence $A(\tilde{\pi})$ obtained after the data processing with filtering parameters $\{n_1, m_1\}$ was calculated numerically. The existence of scale invariance property of phase transitions was accounted by merging several filtrations of original data.

3. Results and discussion

Typical compression $\tilde{\pi} - A$ isotherm is shown in Fig. 1a. The dependence $C(\tilde{\pi})$ is represented in Fig. 1b. It represents itself three sets of data which correspond to three filtration parameters: $\{n_1 = 3, m_1 = 3\}$, $\{n_1 = 4, m_1 = 5\}$, and $\{n_1 = 5, m_1 = 3\}$.

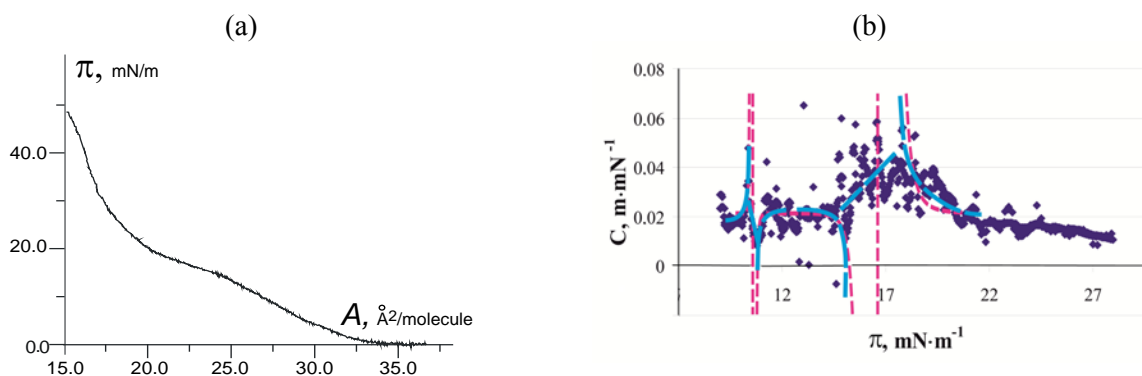


Figure 1. (a) $\tilde{\pi} - A$ -isotherm for a stearic acid monolayer. (b) The dependence of the compressibility C on $\tilde{\pi}$ in a first order 2D-phase transition in the monolayer. Symbols denote experimental data processing results, solid line is fitting, dashed line is the theoretical predictions.

We apply a geometrothermodynamics of the first order phase transitions in two-dimensional systems to the analysis of metastable compressed monolayers [2]. In this approach an electrocapillary contribution to compressibility κ is calculated by a following formula: $\kappa = -(B_c(r(\Delta t)) - B_c(r(t)))$ where B_c is the Berwald curvature of the compressed monolayer, which is the mean curvature of the trajectory of a particle under the action of electrocapillary forces.

Let $r(t)$ be a displacement of a particle during the time T_{pht} of phase transition: $t = T_{\text{pht}}$, $B_c(r(t)) \rightarrow B_c(r(T_{\text{pht}})) = \text{const}$. Then, we obtain κ as a quantity which is proportional to the mean curvature $B_c(r(\Delta t))$ of the monolayer element with a radius vector $\vec{r}(\Delta t)$ at an arbitrary time Δt (see dashed line in Fig. 1b). As one can see from Fig. 1b theoretical curve elucidate the origin of dispersion of compressibility.

Thus, the approach has been proposed that allows to describe the anomalous behaviour of compressibility at first order phase transition. The proposed approach is used to describe the formation of Langmuir monolayers of nanocyclic organometallic compounds.

References

- [1] Motschmann H, Möhwald H 2001 *Langmuir-Blodgett Films*. In: *Handbook of Applied Surface and Colloid Chemistry*. Ed. Holmberg K (John Wiley & Sons, Ltd)
- [2] Neagu M, Krylova N G, Grushevskaya H V 2013 *J. Math. Phys.* **54** 031508

Section

Optoelectronics and

Lasers

EXPERIMENTAL RESEARCH OF CHANGES OF THE PROPERTIES OF WHITE LEDs DURING LONG-TERM OPERATION DEPENDING ON THE AMBIENT TEMPERATURE

S.N. Markova¹, I.S.Mateshev¹, Y.P.Timonin^{1,2}, A.N.Turkin¹, K.S. Fedorenko¹

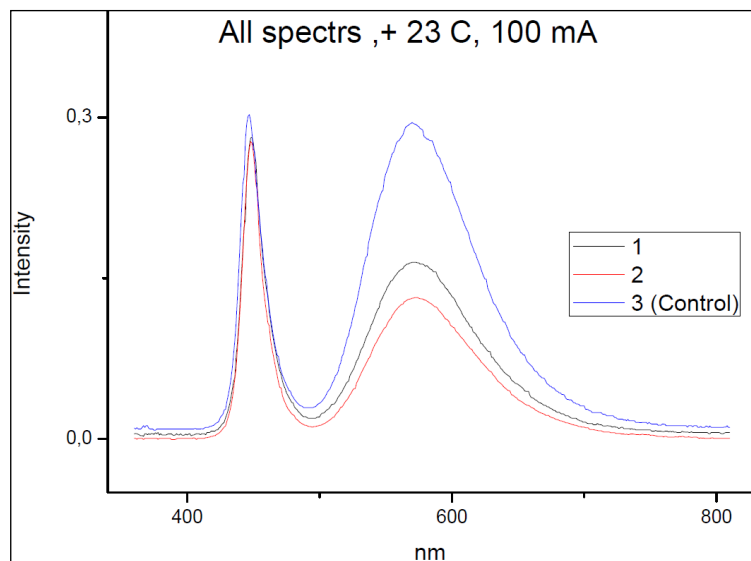
¹MSU Physics Faculty, Leninskie Gory, 119991, Moscow, Russia

Abstract. The paper is devoted to the research of changes in the characteristics of white LEDs, based on GaN crystal (electrical and spectral characteristics depending on the operation time and the ambient temperature). It has been found that the phosphor largely burnt out then crystal, and the color of LED light shifted in the blue region of the spectrum. Also it was observed an increase in resistance of the degraded samples compared with the new LED and an increase in the resistance of LEDs at low temperatures. The spectra of the LEDs at different temperatures were analyzed.

The paper is devoted to the research of changes in the characteristics of white LEDs, based on GaN crystal (electrical and spectral characteristics depending on the operation time and the ambient temperature). In this research we used LEDs based on a blue crystal covered with a phosphor; they were assembled in Russia. It was three samples: samples №1 and №2 were degraded (2160 hours), №3 was new (control sample). Ageing was carried out with the high current (120 mA), and at elevated temperature of the p-n junction (approximately 123 °C instead of the usual 83 °C).

As a result of ageing, the voltage-current characteristics of LEDs were changed: an increase in resistance of the degraded samples compared with the new LED caused, obviously, by increase in number of defects in the crystal.

The spectral characteristics (Pic. 1): there is a significant reduction in the height of the second peak, (the emission spectrum of the phosphor). Taking into account the CVC, we must conclude that the increase in the number of crystal defects is not the main factor in the deterioration of performance of lighting products based on white LEDs during operation, but such factor is the above-mentioned phosphor burning. The first peak (emission of the crystal) shifted slightly - this indicates that even after 2160 hours of operation at elevated current and temperature the wavelength is not changed substantially despite the degradation of the crystal. The second peak (emission of the phosphor) has shifted to longer wavelengths and demonstrated a tendency to the formation of a plateau. It's indicating that the phosphor largely burnt out, and the color of LED light shifted in the blue region of the spectrum.

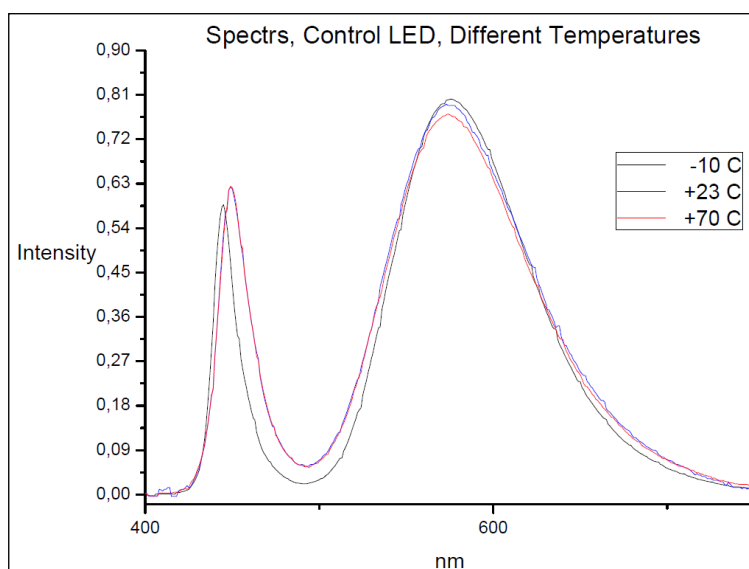


Pic.1. The emission spectra of aged (1, 2) and control (3) samples

In addition, as would be expected, there is a strong drop of luminous flux over time.

We proceed to the changes of the characteristics of the samples as a function of ambient temperature. It was found an increase in the resistance of LEDs at low temperatures, which is consistent with the theory of semiconductors. The spectra changed (Pic. 2) as follows: emission peak of the crystal is shifted to shorter wavelengths with the temperature decreases (449 nm at 70 ° C, 447 nm at room temperature and 445 nm at -10 ° C for a sample number 3); emission peak of the phosphor has a nonlinear dependence: 574 nm at 70 ° C, 570 nm at room temperature and 576 nm at -10 ° C (also sample number 3).

Photocurrent increases with decreasing of the temperature.



Pic.2. Emission spectra of control sample at various ambient temperatures

Application of a LED-photodiode optocouple for the study of human respiratory function

A G Malyshev¹, N K Zhumashev¹, G N Lukyanov¹, K D Mynbaev^{1,2} and A A Rassadina¹

¹ITMO University, Kronverksky 49, Saint-Petersburg 197101, Russia

²Ioffe Institute, Polytechnicheskaya 26, Saint-Petersburg 194021, Russia

Abstract. Application of a LED-photodiode optocouple for the study of human respiratory function is considered. The optocouple operating in the middle-infrared part of the spectrum (with the maximum of the LED emission peak at 4.1 μm) was applied for monitoring changes in CO_2 concentration during respiration of the human. Studies were carried out simultaneously with the measurements of pressure in the left and right halves of the nose cavity. The results of the study open possibilities for using LED-photodiode optocouple as a sensitive element in a compact and cheap sensor for detecting breath abnormalities associated with respiratory and other diseases.

Early diagnostics of respiratory diseases and development of its methods is one of the important trends in modern otorhinolaryngology. According to the data of The Ministry of Healthcare of Russian Federation (2013), nearly 39% of population suffers from respiratory diseases. Also, diagnosed are asthma (1%), allergic rhinitis (0.2%) and chronic obstructive pulmonary disease (0.6%). All these diseases are accompanied with nasal breath anomalies. At the present time, anterior active rhinomanometry is considered to be a clinically approved method of unbiased investigation of nasal breath [1]. Measured datum in this method is the nasal airway resistance that is the ratio of pressure difference to flow flux difference in the tube supplied to the organs of the respiratory system. Non-invasiveness of the measurements and the compactness of the equipment are the advantages of the method. However, the method distorts natural breathing because of using a tube, thus reducing the chances of early diagnostics. Besides that, operations with the diagnostic equipment demand high professional level of the staff and the equipment is quite expensive.

For early diagnosis of respiratory diseases, it is important to study natural breathing without additional tube. The results of the studies carried out earlier [2] showed a non-linear dynamic character of such diagnostic parameters of natural breathing as airflow velocity, temperature, and pressure. Therefore, the basic requirements for the sensor element are high sensitivity and fast response. The method described in [2] had a significant drawback: the quick response was achieved at the cost of the miniature size of the sensor (such as a thermistor). Such miniature elements are brittle and not suitable for further implementation in the production of diagnostic equipment. Replacement of the sensors described in [2] by optical sensors is more promising. For example, Russian company "LED Microsensor NT", Ltd., produces light-emitting diodes (LEDs) and photodiodes with fast times (dozens of nanoseconds), miniature size of the LED chip (0.3×0.3 mm), small angular divergence of

the LEDs ($\pm 3^\circ$), low power consumption (about 1 mW in a pulsed mode), long service life, and reasonably low cost. These optoelectronic devices are based on narrow-gap semiconductor nanoheterostructures (InAs(Sb,P) system) and can be applied in the mid-IR spectral region (3400 to 4300 nm wavelength).

This work presents the results of the study of the possibility of using a LED-photodiode optocouple ("LED Microsensor NT", Ltd.) as a sensor device for contactless measurement of the dynamic fluctuations of CO₂ concentration in the human breath. Carbon dioxide plays a leading role in the humoral mechanism of the regulation of respiration. It is known that the concentration of CO₂ changes during respiration: the proportion of CO₂ at inhalation is 0.03% and that at exhalation is 4.00%. This parameter is important in the breath diagnosis and is very informative.

The basic absorption band of CO₂ corresponds to the spectral region between 4200 and 4320 nm. Weaker absorption bands are located at 2700 nm and 2000 nm. In our study, we have used LEDs with dominating wavelength at 4.1 μm . The emission spectrum of the studied LED corresponded very well to the basic absorption band of CO₂. We studied the characteristics of the IR LED and carried out the research on the application of a LED-photodiode optocouple (figure 1). In particular, the sensitivity of the optocouple in the dynamic measurements of CO₂ concentration was studied simultaneously with the measurements of pressure in the left and right halves of the nose cavity using the sensor developed earlier [2]. The results showed the high sensitivity of the optocouple in respect to the changes of CO₂ concentration during respiration (figure 1(a)). The graphs of power spectral density revealed a coincidence of the main frequency peaks registered with the two methods (figure 1(b)). Thus, the results of our study open possibilities for using LED-photodiode optocouple as a sensitive element in the breath diagnostic sensor.

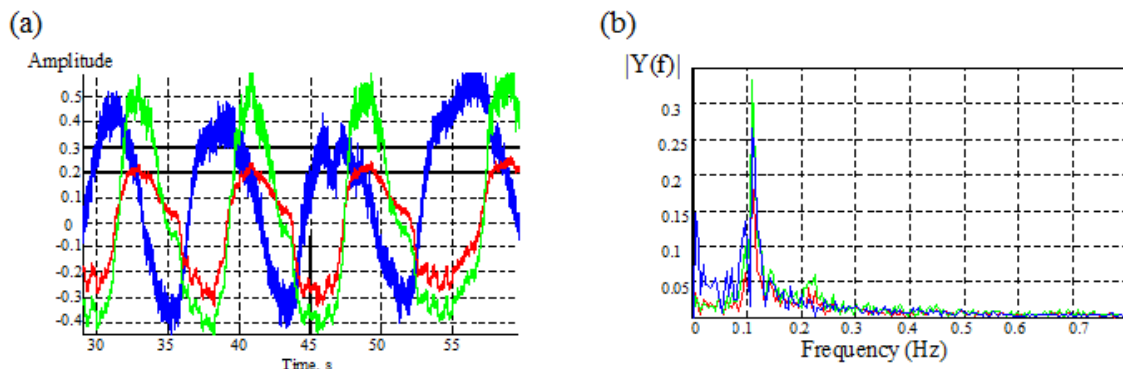


Figure 1. (a), the results of the measurements of respiration fluctuations. The colours show: blue, those obtained with the use of the optocouple, red, measured pressure in the left nasal cavity, green, measured pressure in the right nasal cavity. (b), graphs of the power spectral density. The colours show: blue, the concentration of CO₂, red, the results of pressure measurements in the left nasal cavity; green, those in the right nasal cavity.

To improve the parameters of the sensor, one needs to increase the quantum efficiency of the LEDs. Our studies showed that emission intensity of the LED at 77 K was much higher than that at 300 K. Such increase in the LED efficiency with temperature decreasing shows the dominating contribution of non-radiative (Auger) recombination in the LED structure at the room temperature. To increase the quantum efficiency of these LEDs, one needs to improve their design so the Auger recombination would be suppressed.

1. Clement P A 1984 Committee report on standardization of rhinomanometry *Rhinology* **22**(3) 151
2. Lukyanov G, Rassadina A and Usachev V 2005 Comparison and the analysis of processes of the movement of air through the human breathing system and its natural model *Proc. 2005 Intern. Conf. Phys. Control* IEEE Cat. No. 05EX1099C 872.

CALCULATION AND SIMULATION OF COLOUR CHARACTERISTICS OF WHITE LEDS

S.N. Markova¹, I.S.Mateshev¹, Y.P.Timonin¹, A.N.Turkin¹, K.S. Fedorenko^{1*}

¹MSU Physics Faculty, Leninskie Gory, 119991, Moscow, Russia

Abstract. The work is devoted to the calculation and simulation of characteristics of white LEDs based on GaN crystals after prolonged use, as well as at different temperatures. Color coordinates of CIE 1976 XYZ, normalized color coordinates, color rendering index (CRI), correlated color temperature (T_{cp}) and lumen equivalent of the spectrum have been obtained. The following changes in the characteristics of the LEDs were revealed: significant shift of color coordinates and correlated color temperature during cooling towards yellow glow and small displacements of characteristics during heating. Calculations were based on the experimental spectrums obtained at temperatures of + 23 ° C, + 70 ° C, -10 ° C. At the moment, work is underway on modeling the processes of degradation of LEDs on the basis of these characteristics.

The work is devoted to the calculation and simulation of characteristics of white LEDs based on GaN crystals after prolonged use, as well as at different temperatures. For the three experimental samples obtained color coordinates of CIE 1976 XYZ, normalized color coordinates, color rendering index (CRI), correlated color temperature (T_{cp}) and lumen equivalent of the spectrum. The calculations are based on spectrum of LEDs with following construction: crystal of blue glow coated with phosphor (produced in Russia), samples №1 and №2 were subjected to aging (2160 hours), №3 was not subjected to aging at all and was used as reference sample. Hours of aging were performed at high current (120 mA), and hence at an elevated temperature of the pn junction (approximately 123 ° C instead of the usual 83 ° C).

Produced calculations show different displacement of the color temperature and color coordinate toward blue emission and the reduction of the lumen equivalent of the spectrum in comparison with the reference sample (Table 1).

Table 1. Characteristics of samples number 1, 2 and 3.

Sample number		1	2	3
Color coordinates of CIE 1976	X	23,34	39,49	29,87
	Y	21,75	35,11	29,64
	Z	25,49	47,99	22,82
T_{cp}, K		5580	6230	4408
CRI		64	63	61
Lumen equivalent, Lm/W		330	319	372

Also characteristics of the samples were calculated according to the ambient temperature.

The following changes in the characteristics of the LEDs were revealed (Figure 1): significant shift of color coordinates and correlated color temperature during cooling towards yellow glow and small displacements of characteristics during heating. Calculations were based on the experimental spectrums obtained at temperatures of + 23 ° C, + 70 ° C, -10 ° C.

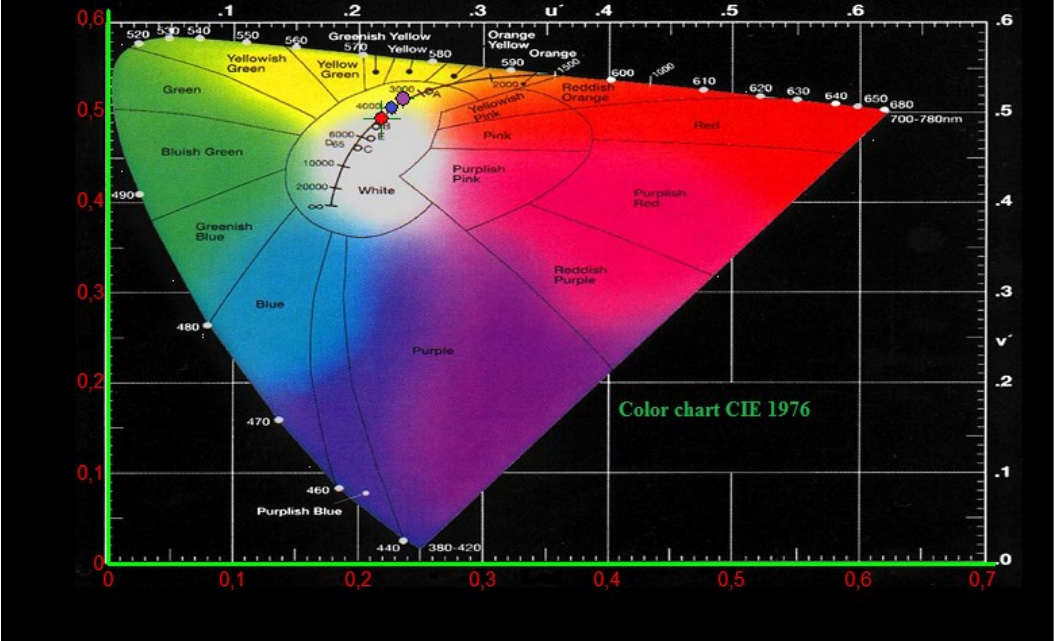


Figure 1. Color chart of the third sample at different temperatures: + 23 ° C (red dot), + 70 ° C (blue dot), -10 ° C (purple dot).

At the moment, work is underway on modeling the processes of degradation of LEDs on the basis of these characteristics. On the basis of the expected results is planned further study of the degradation of white LEDs to improve the LEDs construction and better selection of LED phosphors for greater resistance to aging and temperature changes.

Investigation of defects influence on the luminescent properties of Si/Si_{1-x}Ge_x:Er/Si heterostructures

A P Detochenko¹, A A Ezhevskii¹, M V Stepikhova² and V G Shengurov³

¹Lobachevsky State University of Nizhny Novgorod, Gagarin Ave. 23, Nizhny Novgorod, 603950, Russia

²Institute for Physics of Microstructures, Russian Academy of Sciences, GSP-105, 603950 Nizhny Novgorod, Russia

³Physico-Technical Research Institute, Nizhny Novgorod State University, Gagarin Ave. 23, 603950 Nizhny Novgorod, Russia

Abstract. In this contribution we discuss the results of investigations of Si/Si_{1-x}Ge_x:Er/Si structures with a high degree of heterolayer relaxation ($RES \leq 9\%$) by photoluminescence (PL) and electron paramagnetic resonance (EPR) methods. The obtained results of measurements carried out for such structure show a correlation between the intensity of the EPR line associated with dangling bond defects in silicon and the erbium photoluminescence intensity.

1. Introduction

One of the urgent tasks of semiconductor electronics is the development of silicon-based optoelectronic devices. The Er-doped silicon structures demonstrate unique emitting properties. However, a necessary condition for laser realization based on Si:Er is the development of waveguide structures with a high degree of localization of emission in the active layer. One of the options is structures such as Si/Si_{1-x}Ge_x:Er/Si. The optical confinement factor (Γ) in these waveguides can reach the value of 0.98 although this can be realized in the structures with relaxed Si_{1-x}Ge_x:Er layer, i.e. in the structures with the heterolayer thicknesses exceeding the critical value. Therefore, considerable interest is study the influence of structural defects on luminescence properties of Si/Si_{1-x}Ge_x:Er/Si structures.

2. Experimental

We present results of studying the luminescence properties of Si/Si_{1-x}Ge_x:Er/Si heterostructures with a high degree of relaxation of heterolayer ($RES \leq 9\%$) by methods of luminescence and electron paramagnetic resonance (EPR). In order to modify structure defects of heterolayer the structures were treated as follows: 1) ion implantation of phosphorus and subsequent annealing in inert atmosphere at 1000°C for 1 hour (implantation energy was 40 keV, implantation dose was $2 \cdot 10^{14} \text{ cm}^{-2}$); 2) annealing in hydrogen atmosphere (without implantation). The Si/Si_{1-x}Ge_x:Er/Si heterostructures studied here were grown by sublimation molecular beam epitaxy (MBE) in a germane (GeH₄) atmosphere at the temperature of growth 480°C. The procedure of growth was described in details elsewhere [2]. The PL spectra were studied using a BOMEM DA3 Fourier spectrometer, with the resolution as high as 0.1 cm^{-1} in the range of wave numbers from 5000 to 10000 cm^{-1} . For the excitation source, we used a Nd:YAG laser emitting at the wavelength 532 nm with the power 200 mW. The PL signal was detected with the germanium photoelectric detector, Edinburgh Instruments EO 817A cooled with liquid nitrogen. The EPR spectra were recorded using a Bruker EMX-plus 10/12 EPR spectrometer

equipped with an Oxford Instruments liquid helium cryostat and an ER 4112 HV temperature controller. The measurement were carried out at temperature $T = 4.2$ K.

3. Results and discussion

Analysis of EPR spectra of the $\text{Si}/\text{Si}_{1-x}\text{Ge}_x:\text{Er}/\text{Si}$ structures indicates the present of the line with $g = 2.005$ causing Si dangling bonds defects. This line with different intensity was observed in all structures that have not been exposed postgrowth treated. Post-growth treatments such as implantation of P ions and annealing in hydrogen atmosphere lead to a strong quenching or disappearance of the EPR lines of dangling bonds. This is obviously due to passivation by P impurity or saturation with hydrogen of dangling bonds, respectively. The disappearance of the line of Si dangling bonds accompanied by the appearance of the EPR line from the electrons localized on the phosphorus ($g = 1.998$).

Post-growth treatments of the $\text{Si}/\text{Si}_{1-x}\text{Ge}_x:\text{Er}/\text{Si}$ structures lead to change in their luminescent response. After treatments we found a decrease in the intensity or complete quenching of the PL signal associated with the optically active Er impurity. The Er luminescence lines are not observed in the samples where there were the EPR lines from electrons localized on the phosphorus. In the sample in which EPR line of dangling bonds exists after post-growth treatments the Er PL signal continued to be observed but its intensity was an order of magnitude smaller compared to the initial sample.

Thus the obtained results of measurements suggest that there is a correlation between the intensities of the EPR lines line associated with dangling bond defects in silicon and the erbium photoluminescence intensity.

4. Conclusion

The obtained results show there is a clear correlation between the intensities of the EPR lines associated with the Si dangling bonds and photoluminescence intensity of the Er impurity. A possible reason of the observed correlation is participation of the structural defects of heterolayer and doping impurities in the excitation and de-excitation of the rare-earth impurities.

References

- [1] M.V. Stepikhova, L.V. Krasil'nikova, Z.F. Krasil'nik, et al. // *J. Cryst. Growth*. 2006. V. 288, iss. 1. P. 65-69.
- [2] S. P. Svetlov, V. G. Shengurov, V. Yu. Chalkov, Z. F. Krasil'nik, B. A. Andreev, and Yu. N. Drozdov, *Izv. RAN. Ser. Fiz.* 65 (2), 203 (2001).

The way to optimization of active region structure of InAs/InGaAs semiconductor quantum dot laser

V V Korenev^{1,3}, A V Savelyev^{1,3}, A E Zhukov^{1,2,3}, A V Omelchenko^{1,3}, M V Maximov^{1,2}

¹Saint-Petersburg Academic University RAS, Saint-Petersburg 194021, Russia

²Ioffe Physico-Technical Institute RAS, Saint-Petersburg 194021, Russia

³Saint-Petersburg State Polytechnical University, 195251 Saint-Petersburg, Russia

Abstract. The task of energy consumption optimization in the case of quantum dot lasers emitting via the ground-state optical transitions is studied in details. It is shown that optimization of laser cavity sizes, the value of inhomogeneous broadening and number of QD layers forming laser active region allow us to achieve lasing spectrum of a given parameters at minimum injection current. In the case of multi-layered lasing structures optimal cavity length maximizing power conversion efficiency also minimizes injection current..

1. Introduction

Efficient semiconductor lasers having broadband emission spectra, which correspond to the transparency window of standard silicon optical fibre, can be used for the wide range of practical applications, such as optical coherence tomography and ultrafast data transmission [1 – 3]. Long-wavelength InAs/InGaAs quantum dot (QD) lasers, emitting via ground state (GS) optical transitions of QDs near 1.3 μm , allow one not only to overlap this practically useful wavelength range, but also to decrease operation current without significant impact on other device parameters [2 – 3].

The usage of multi-frequency emission of these compact diodes for the optical telecom purposes is a beneficial alternative to currently used distributed feedback lasers due to their cheapness and simplicity of fabrication [1 – 3]. Therefore, due to the possibility of usage of such semiconductor QD lasers as a part of data transmitting modules in compact portable devices, the task of optimization of its energy consumption plays an important role. To overcome the main obstacle of QD lasers optimization task we have developed its self-consistent analytical model in the explicit form.

2. Optimization of laser active region and laser power conversion efficiency

We consider an impact of those laser parameters, which can be varied at the epitaxial growth stage or during the device processing. They are laser cavity length (L), dispersion (σ) of the inhomogeneous broadening of the QDs ground-state optical transition, and number (Z) of QD layers in laser's active region [4 – 5]. In short cavities the output loss (α_{out}) is high. Therefore, gain saturation plays an important role. This, in its turn, leads to the increase of the required injection current. In case of long cavities, a total number of QDs in the active region increases due to the increase of its surface area. Therefore, high injection current is required to reach the population inversion that also results in the increase of I_{inj} . Therefore, there always exists an optimal cavity length (L_{opt}), which allows one to realize lasing spectrum of a given width (Ω) at minimum injection current (I_{opt}^L).

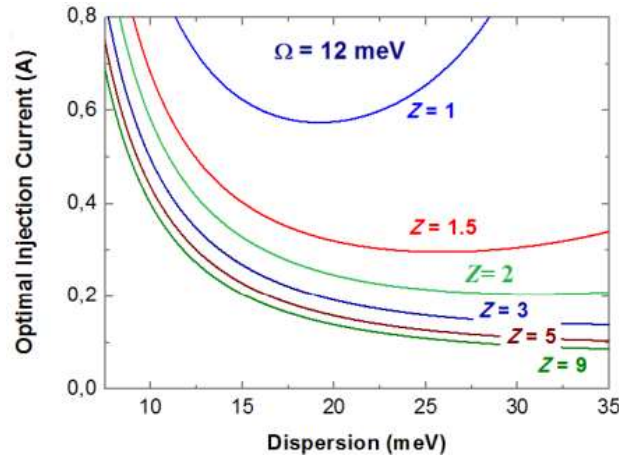


Fig. 1. The dependence of injection current optimized by laser cavity length (I_{opt}^L), realizing lasing spectrum of the given width ($\Omega = 12$ meV), on dispersion (σ) for different numbers of QD layers (Z).

In order to reveal the influence of dispersion (σ) on injection current we have calculated the dependence of injection current, optimized by the cavity length (I_{opt}^L), on σ – see Fig. 1. As it can be seen from the Fig. 1, there is always an optimal dispersion minimizing the optimal injection current (I_{opt}^L). Indeed, if dispersion is small (this means that QDs are uniform), lasing spectrum is always narrow. Therefore, it is hardly possible to reach sufficiently larger lasing spectrum width. In opposite situation, if σ is large, the gain saturation again starts to play an important role because the maximum gain (G_{max}) is inversely proportional to σ . As a result, there is always an optimal cavity length L_{opt} and dispersion (σ_{opt}) minimizing injection current for the given lasing spectrum width. As number of QD planes Z increase in multi-layered structures, the maximal gain G_{max} increases accordingly. This makes the gain saturation insignificant and shifts σ_{opt} to very high values.

Another important task is to elucidate the influence of the discussed laser parameters on the power conversion efficiency (PCE), which depends on all the key parameters of laser's active region, such as number of QD layers (Z) in it, dispersion of inhomogeneous broadening (σ) and laser cavity length (L). Using the model [5] we have shown it is logically to expect that the optimization of all the key parameters of laser active region (L , σ) will not only allow us to minimize injection current corresponding to the lasing spectrum of the given width ($I_{\text{opt}}^{L,\sigma}$), but also will correspond to high PCE.

3. Conclusion

It is shown that in a quantum dot laser there are optimal dispersion and laser cavity length corresponding to the minimum injection current required to achieve lasing spectrum of a given width. The increase of dispersion and number of QD layers also reduces the value of the injection current. However, too many layers of QDs in laser active region lead to only incremental decrease of injection current, while its efficiency decreases significantly.

Acknowledgements

This work is supported by Russian Foundation for Basic Research (grant 13-02-12016), by Committee for Science and Higher Education of the Government of St.Petersburg and by Dynasty Foundation.

References

- [1] A.E. Zhukov *et al*, *Quantum Electron.* **38**, 409 (2008).
- [2] C.F. Lam (*Elsevier, San-Diego, 2007*), 158.
- [3] A.V. Savel'yev *et al*, *Semicond.* **43**, 1597 (2009).
- [4] V.V. Korenev *et al*, *Appl.Phys.Lett.* **102**, 112101 (2013).
- [5] V.V. Korenev *et al*, *Semicond.* **46**, 684 (2012).

Increasing the noise immunity of optical-electronic systems based on video cameras with an optical converter

M.P. Boronenko, P.Yu. Gulyaev, A.E. Seregin, K.G. Poluhina

Ugra State University, Chehov st. 16, Khanty-Mansiysk, 628012 Russian Federation

Abstract. The luminophor coating of an electro- optical converter afterglow introduces an additional error to the measurement. The ratio that allows to calculate the intensity of spurious illumination at each subsequent frame have been determinate according to experimental data of luminescence kinetics. The proposed method increases the noise immunity of the electro-optical converter by eliminating luminophor afterglow.

1. Introduction

Application of optoelectronic systems based on video cameras with an electro-optical converters in scientific experiments [2], related to the problem of low sensitivity at high speed shooting and low exposures. The afterglow time of luminophor, covering the screen of OEC, presence is another problem. For some fields fast processes research the screen residual glow is the main limiting factor [1]. In different with low speed experiment where afterglow can be cleaned by several miniature lamp brief (5-10 seconds) screen backlight [4, 5] the proposals for solving this problem for high speed experiment without changing the hardware of the OEC were not found.

2. Experimental techniques

Experimental stand, which is composed of following equipment (fig. 1a): 1 - optical bench; 2 - sparkler; 3 – high speed camera VideoSprint based on 4 electron-optical converter (EOC); 5 – PC, was build for accomplish the task. Self-luminous sparkling fire was used as source of luminescence particles provoking glow luminophor. Flying glowing particles are shifted by a distance depending on their velocities during the accumulation of charge in the light-sensitive sensor area. Stroboscopic effect achieving by additional EOC shutter firing on the interval photocathode – micro channel substrate. At the same time on the EOC screen the number of images equal to the number of additional shutter releases N is forming. This track of moving particle is divided into N parts. The average brightness of each track part is forming with contribution of particles radiation which was absorbed by photosensitive element during the exposure time. It is obvious that in the filmed sequence of combustion particles frames, the brightness of the left track will fade gradually from frame to frame, if the time of luminophor afterglow is longer than frame interval. According to that it becomes possible to study the kinetics of luminophor afterglow.

3. Luminophor afterglow time measurement

To determine the decay time [3] the search for a sequence of frames, which was clearly evident gradual extinction of the moving object luminous trail registered in the image, was carried out. The study track must be chosen to avoid crossing with other particles tracks precipitating into the viewing area of camera. The luminescence intensity of the luminophor corresponds to the brightness of the pixels constituting the tracks. The measurements were carried out by the ImageJ program. The brightness measurement of photosensitive cells, which registering radiation one of the particle track part, is held in each frame where the track is still visible. The measured brightness was normalized by the maximum value. The coefficient, characterizing residual luminophor luminescence from frame to frame decreasing, is possible to determine by the plot.

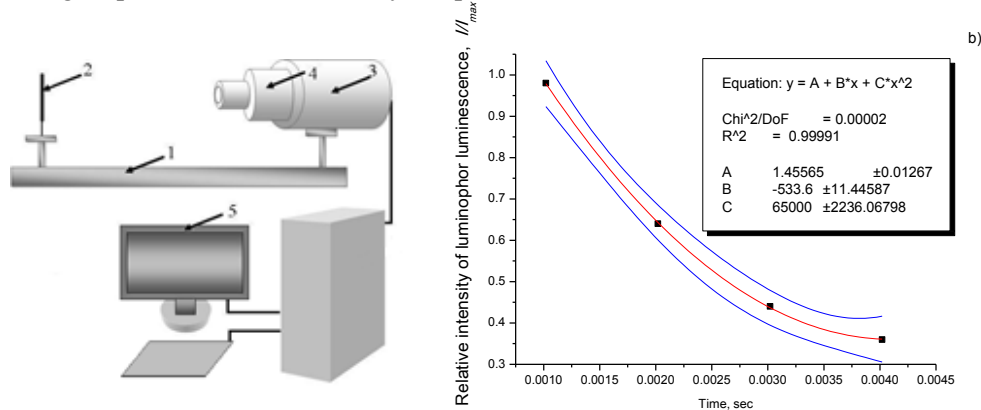


Figure 1. The experimental setup (a), the experimental data approximation (b).

4. Electro-optical converter noise immunity increasing method

In order to reduce the error introduced by the luminophor afterglow, it is necessary to subtract remaining afterflow background of previous frame from the study frame. Let registered by each detector brightness on the first frame I_1 has noise I_{noise} components and useful signal I_{01} :

$$I_1 = I_{noise} + I_{01},$$

Then the next frame is due to I_{noise} , I_{02} and afterglow of luminophor I_{1res} :

$$I_2 = I_{noise} + I_{02} + I_{1res},$$

And I_{1res} may be calculated from the calculated law of luminophor luminescence decay. Using inter frame subtraction, the accuracy of the tracks brightness measuring on the 30% can be achievable:

$$I_{1res} = \mu I_1,$$

$$I_2 = I_{noise} + I_{02} + I_{1res} - \mu I_1$$

where μ is the determined from the graph and depending on the type of luminophor afterglow decay coefficient.

5. Conclusion

The proposed method of increasing the noise immunity of the OEC allows to consider remaining afterglow in the study frame, subtract it, thereby increasing the accuracy of brightness temperature measurements up to 30% without changing the hardware. The method is limited to the specific type of the luminophor and the detected objects radiation intensity.

References

- [1] Antonenkov D. A. Sredstva poluchenija informacii o parametrah vzvesi, osnovannye na obrabotke fotoizobrazhenij //Vostochno-Evropejskij zhurnalпередovyh tehnologij. – 2014. – №. 4 (9). – P. 15-20.

The new ultra high-speed all-optical coherent streak-camera

R.M.Arhipov^{1,2}, M.V.Arhipov¹, V.S.Egorov¹, I.A.Chekhonin¹,
M.A.Chekhonin¹, S.N.Bagayev³

¹St.Petersburg State University, St.Petersburg, Russia

²Weierstrass Institute for Applied Analysis and Stochastics, Leibniz Institute
in Forschungsverbund Berlin e.V, Berlin, Germany

³Institute of Laser Physics, Novosibirsk, Russia

Abstract. The new type of all-optical coherent streak-camera was developed. It was shown that thin resonant film (quantum dots or molecules) radiates the angular sequence of retarded ultra short pulses under triangle-type spatial periodic distribution of the laser pump field.

The technology of laser coherent resonant holographic photonic crystals for developing of ultra high-speed ($\approx 10 \text{ deg}/10^{-11} \text{ sec}$) all-optical streak-camera and angular deflectors [1] is considered. The theoretical model of the resonant thin film Cherenkov radiation under triangle-type spatial gratings [2,3] of the laser pump field $E(t,x) = E(t) \cdot \text{saw}(x)$ was developed.

It was shown that thin resonant film (quantum dots or molecules) radiates the angular sequence of retarded ultra short pulses under triangle-type spatial periodic distribution of the laser pump field (Figure 1).

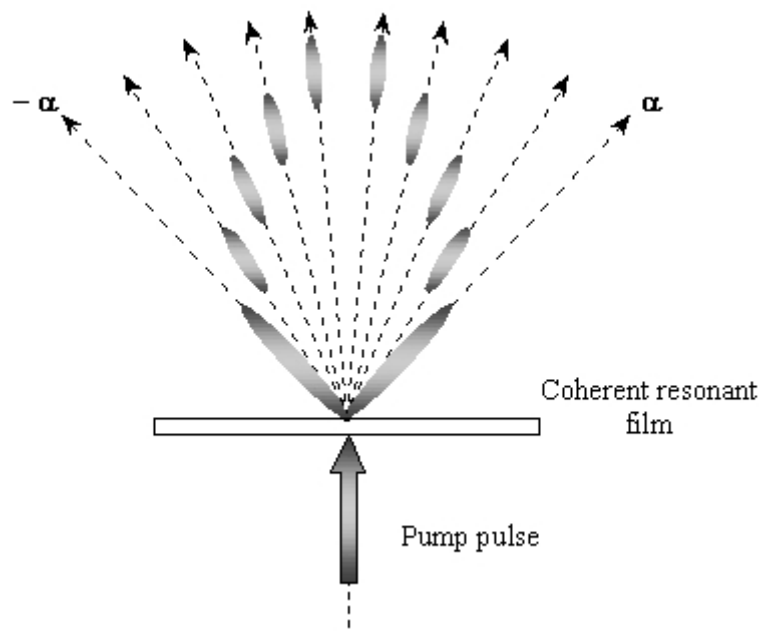


Figure 1. The temporal evolution of the high-speed angular deflector's far field interference pattern (self diffraction of the pump pulse)

The analytical and numeric solutions of the Bloch equations under two-level model of resonant medium were achieved. The new principle of ultra high-speed angular deflection of resonant pulse field due to coherent radiation of the transient spatial polarization pattern $P(t,x)$ [2,3] is developed. The effects of laser frequency detuning and medium relaxation processes in laser deflection effect were investigated in detail.

The principle of angular deflection of *nonresonant probe pulse radiation* due to diffraction on transient spatial population pattern $N(t,x)$ [2,3] is considered. Coherent nonlinear diffraction pattern is induced by control pump laser pulse. Possibility of operating of the probe pulse diffraction angle was investigated. The coherent resonant photonic crystal applications in laser beam control are discussed.

References

- [1] C.H. Sarantos, J.E. Heebner 2010 Opt. Lett. **35** (9) 1389-1391.
- [2] R.M.Arkipov, S.N.Bagayev, V.S.Egorov, I.A.Chekhonin, M.A.Chekhonin. Proceedings of the VI Intern. conf. HOLOEXPO-2009 81-86 Kiev Ukraine 01-02 July 2009.
- [3] R.M.Arkipov, M.V.Arkipov, S.N.Bagayev, V.S.Egorov, I.A.Chekhonin, M.A.Chekhonin Scientific notes of the Physics Department of Moscow State University 2013 **5** 135034 (1-4).

Ultimate modulation bandwidth of 850 nm oxide-confined vertical-cavity surface-emitting lasers

M.A. Bobrov, S.A. Blokhin, A.G. Kuzmenkov, N.A. Maleev, V.M. Ustinov
Ioffe Institute, Politekhnikeskaya 26, St. Petersburg, 194021 Russia

Abstract. Complex influence of photon lifetime (via mirror loss) and aperture size on the performance of 850 nm InGaAlAs oxide-confined vertical-cavity surface-emitting lasers (VCSELs) with fully doped AlGaAs-based distributed Bragg reflectors (DBR) was investigated. We find a tradeoff between photon lifetime and gain nonlinearity for maximizing the optical bandwidth, leading to the optimum aperture size close to 4-6 μm . In spite of the reduced photon lifetime (from 4 ps to 1 ps), the excess damping caused by the current-induced self-heating limits the ultimate modulation bandwidth for the given VCSELs design at 24-25 GHz.

Vertical-cavity surface-emitting lasers (VCSELs) emitting at 850 nm are widely used as low-cost high-performance light sources, in the mode of direct current modulation, for data communication systems over short distances and for the optical interconnects in high-performance computing systems [1]. The most important factor that limits modulation response is damping of the relaxation oscillation, which directly proportional to photon lifetime in optical microcavity, gain compression and inversely proportional to differential gain. To overcome damping limitation, the reduction of the photon lifetime was proposed [2]. In this work we have analyzed complex influence of photon lifetime together with aperture size on the high-speed performance of 850 nm InGaAlAs oxide-confined VCSELs and find the ultimate modulation bandwidth for the given VCSELs design.

A conventional VCSEL geometry with two doped distributed Bragg reflectors (DBR) was used. The VCSEL epitaxial structure consists of an n-doped GaAs contact/buffer layer, a bottom $\text{Al}_{0.15}\text{Ga}_{0.85}\text{As}/\text{Al}_{0.9}\text{Ga}_{0.1}\text{As}$ n-doped DBR, a 1.5λ -thick AlGaAs optical microcavity with a strained InGaAlAs-based active region, a top $\text{Al}_{0.15}\text{Ga}_{0.85}\text{As}/\text{Al}_{0.9}\text{Ga}_{0.1}\text{As}$ p-doped DBR, and a p-doped GaAs topmost contact layer. The details of the epitaxial and device VCSEL design are described in [3]. The photon lifetime was controlled by the mirror loss via a shallow etching the top mirror. By etching the surface of top DBR, the mirror loss can be adjusted within the range 0.3-1.8%, reaching a local maximum at 70 nm. Light power-current-voltage characteristics and small signal modulation response (S_{21}) of lasers were measured in the range current-aperture size from 1.5 μm to 10 μm .

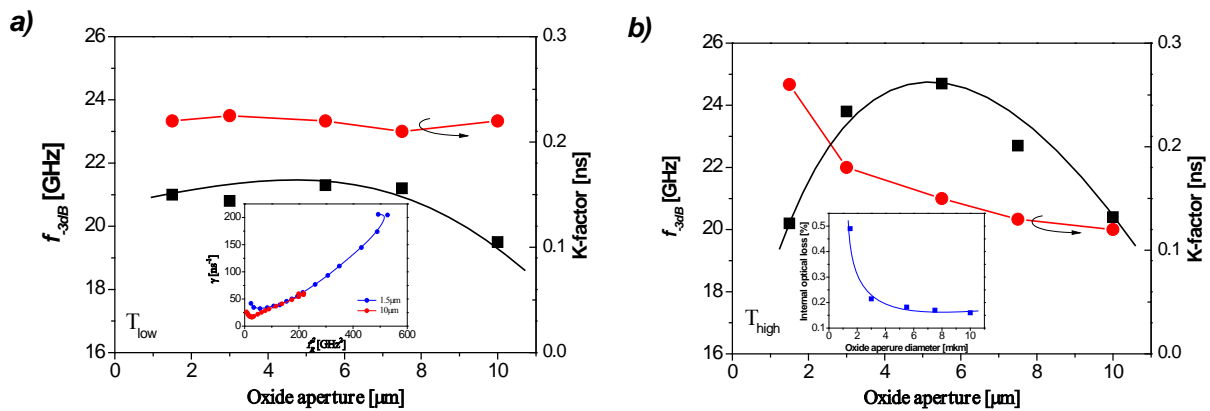


Fig.1. Measured 3dB modulation bandwidth and K-factor as function of the oxide aperture size for 850 nm InGaAlAs VCSELs with low (a) and high (b) mirror losses at 20°C. Insets: the damping coefficient versus the square of the resonance frequency for 1.5 μm device (a) show and the extracted internal optical loss as function of the oxide aperture size (b).

Fig. 1.a shows the maximum 3dB modulation bandwidth and the rate of damping rise (so called K-factor) as function of the aperture size for VCSELs with the low mirror loss ($\sim 0.3\%$). As expected, the 3dB modulation bandwidth increases with reducing the aperture size, but quickly saturates at 21 GHz for aperture diameters less than 7 μm . According to the S_{11} data and the equivalent circuit model electrical, the parasitic cut-off frequency of the investigated VCSELs was found to be about 24 GHz over the entire measured current range, which means that the electrical parasitic has no significant impact on the VCSEL's high speed performance. Hence, the saturation of the 3dB modulation bandwidth can be associated to the thermal effects and/or the damping. The resulting K-factor is hardly depended on the oxide aperture and be in the range of 0.21-0.23 ns, indicating the crucial role of the photon lifetime. However the dynamic characteristic of the large aperture VCSELs are mainly limited by the self-heating effect, while the higher photon density (e.g. the higher resonance frequency) and the excess damping caused by the current-induced self-heating sets the intrinsic limit of the reachable modulation bandwidth for smaller aperture VCSELs (see inset in Fig. 1.a).

The increase of the mirror loss up to 1.8% results in the reduction of the photon lifetime to 1-1.2 ps, however a twofold drop of the K-factor was revealed for the wide-aperture VCSELs (see Fig. 1.b). Moreover, the ultrasmall aperture VCSELs demonstrate a 20% increase of the resulting K-factor. It can be explained by the domination of the gain nonlinearity in the damping coefficient. The gain compression factor was estimated to be in the range $1.5\text{--}2 \times 10^{-17} \text{ cm}^3$ for all apertures size and the mirror loss. Hence, the complex behaviour of the K-factor can be attributed to the dramatic change in the differential gain. According to the dependences of the slope efficiency on the mirror loss, the internal optical loss increases significantly with the reduction of the aperture size: from 0.16% per round trip at 10 μm to 0.5% per round trip at 1.5 μm (see inset in Fig. 1.b), which means that the free carrier absorption loss are dominated in the wide-aperture VCSELs, while the optical scattering loss from the oxide aperture itself occurs in the smallest devices. Moreover, as the aperture size is reduced, the current injection efficiency decreases rapidly from 73% down to 35% (due to excessive carrier leakage at high current density). The dramatic increase of the threshold current density with decreasing aperture size (from 1.1 kA/cm^2 at 10 μm to 15 kA/cm^2 at 1.5 μm) leads to the significant reduction of the differential gain (from $9.72 \times 10^{-16} \text{ cm}^2$ at 10 μm to $4.1 \times 10^{-16} \text{ cm}^2$ at 1.5 μm).

As shown in Fig. 2.b, the decrease of the photon lifetime leads to the increase of the maximum 3dB modulation bandwidth for the wide-aperture lasers, while the maximum 3dB modulation bandwidth of the ultrasmall aperture VCSELs drops to 20 GHz. The competing effects of the reduced photon lifetime and the reduced differential gain results in the ultimate modulation bandwidth of 24-25 GHz at oxide current aperture in the range of 4-6 μm . The further enhancement of the modulation bandwidth can be done by minimizing self-heating (low heat generation and efficient heat removal from the active region) and optimizing design of the oxide aperture (tradeoff between the optical scattering loss and the mode volume).

This work was supported in part by the Ministry of Education and Science of the Russian Federation (grant № 14.607.21.0001, unique ID RFMEFI57714X0001), the Russian Foundation for Basic Research and the Basic research program of the Physical Science Branch of the Russian Academy of Sciences (project Sh-7). The authors would like to thank Vertically Integrated Systems GmbH (Federal Republic of Germany) and Connector Optics LLC (Russian Federation) for supporting VCSEL chips.

References

- [1] I. Kaminow, T. Li, and A.E. Willner, *Optical Fiber Telecommunications Volume VIA: Components and Subsystems*, Academic Press, 2013.
- [2] P. Westbergh, J.S. Gustavsson, B. Kögel, A. Haglund, A. Larsson, and A. Joel, "Speed enhancement of VCSELs by photon lifetime reduction," *Electron. Lett.*, vol. 46, no. 13, pp. 938-940, 2010.
- [3] L.Ya. Karachinsky, S.A. Blokhin, I.I. Novikov, N.A. Maleev, A.G. Kuzmenkov, M.A. Bobrov, J. A. Lott, N.N. Ledentsov, V.A. Shchukin, J.R. Kropp, and D. Bimberg, *Semicond. Sci. Technol.* 28, 065010, (2013).

Control of stress and threading dislocation density in the buffer layers AlN, grown on *c*-Al₂O₃

D.S. Zolotukhin*, D.V.Nechaev, V.V.Ratnikov, V.N. Jmerik, S.V. Ivanov

Ioffe Institute, Polytekhnicheskaya 26, St. Petersburg 194021, Russia

Abstract. Generation of the stresses and structural properties of three 390-nm-thick AlN buffer layers grown by plasma-assisted molecular-beam epitaxy (PA MBE) on *c*-Al₂O₃ with the different AlN nucleation layers have been studied. The strong dependence of the residual compressive stress and threading dislocation density (TDD) on size of the grains in the nucleation layers has been found. The lowest TDD of $1.9 \times 10^{10} \text{cm}^{-2}$ and largest compressive stress have been measured in the 390-nm-thick AlN buffer layer nucleated by using migration enhanced epitaxy at the substrate temperature 780°C.

1. Introduction

Semiconductor (Al,Ga)N compounds with maximum band gap of 6.1 eV are basic material system for compact ultraviolet (UV) optoelectronic devices working within spectral range of wavelength $\lambda = 360\text{--}210$ nm where there are many important applications on water and air UV disinfection, development of photo-sensitive technologies in medicine and biology, secure non line-of-sight optical communication etc. [1–3].

Absence of the commercial native substrates for growth of AlGa_xN heterostructures leads to usage of foreign substrates with the huge crystallographic and thermal mismatches (*c*-Al₂O₃, 6H-SiC, Si(111)) followed by generation of elastic compressive or tensile stresses in the heterostructures. Their relaxation occurs through an introduction of threading dislocations (TDs), transition to 3D-growth and development of the film's delamination or cracking.

Plasma-assisted molecular beam epitaxy (PA MBE) is one of the main technologies of AlGa_xN heterostructures with excellent opportunities on precise control of the epitaxial process. This paper describes the different kinds of the elastic stress and generation of the TDs during PA MBE of the AlN buffer layers nucleated on *c*-Al₂O₃ at the different growth conditions.

2. Experiment

Nucleation AlN layers with thickness (*d*) of about 30 nm were grown by conventional PA MBE and migration enhanced epitaxy on *c*-Al₂O₃ at the different temperatures of the substrate (*T_S*) of 550° and 770°C called as LT and HT respectively. The details of the growth have been reported in [4]. The main growth parameters are listed in Table 1. The subsequent 390-nm-thick AlN buffer layers were grown in all samples with the same slightly Al-rich growth conditions and substrate temperature *T_S*=770°C. Atomic force microscopy was used to measure the grain density in the nucleation layers. Radius of curvature (*R*) and the densities of screw and edge of TDs (*N_s* и *N_e*, respectively) were evaluated by X-ray diffraction (XRD).

3. Results

Table 1 contains measured and evaluated parameters of the studied AlN layers. The elastic stress at the end of growth of buffer layers (σ_g) before its cooling from growth temperature of 770°C down to room temperature were determined as the difference between residual (σ_r) and thermal stresses (σ_T). The former was determined from XRD data using Stoney formula while the later with value of ~ -1.1 GPa was calculated using data for heterostructure AlN/c-Al₂O₃ [5,6].

Parameters AlN nucleation layer	ρ_i (cm ⁻²)	R (m)	σ_r (GPa)	$\sigma_g = \sigma_r - \sigma_T$ (GPa)	N_s 10 ⁹ cm ⁻²	N_e 10 ¹⁰ cm ⁻²
LT ($T_s=550^\circ\text{C}$ d=130nm)	$4 \cdot 10^{11}$	+ 317	-0.17	0.55	10.9	9.6
HT ($T_s=770^\circ\text{C}$ d=30nm)	$2 \cdot 10^{11}$	+ 96	-0.56	0.54	7.2	2.5
HT MEE ($T_s=770^\circ\text{C}$ d=50nm)	$1 \cdot 10^{11}$	+ 26	-2.08	-0.98	2.5	1.9

This table shows that maximum and minimum residual compressive stresses are observed in HT-MEE and LT with the largest and smallest grain size of the nucleation layers, respectively. Therefore, this difference can be explained by the generation of tensile stress during coalescence of the islands in the nucleation layer which is inversely proportional to their diameters [7]. Thus, the LT- nucleation layer with high density of the nucleation grains is preferable to grow unstrained, flat AlN buffer layers. On the other hand, the maximum TD density is observed in the films with smallest grain size due to high generation rate of TDs at the grain boundaries [8]. Therefore, the AlN nucleation layers with a low density of the grains grown by MEE-HT allow one to decrease the TD densities.

Thus, we demonstrate an ability to control the residual elastic stress in AlN buffer layers grown on c-Al₂O₃ by low-temperature PA MBE using the different nucleation AlN layers with the grain size varied from several up to hundred nanometers through changing growth conditions. Also, we demonstrate that the HT-MEE nucleation layer provides the lowest density of TDs of $1.9 \cdot 10^{10}$ cm⁻² for 390-nm-thick buffer AlN layer.

References

- [1] H. Yoshida *et al.* H. Kan, Phys. Stat. Sol. A **208**, 1586 (2011).
- [2] S. Hwang *et al.* Appl. Phys. Express **4**, 032102 (2011).
- [3] D.G. Zhao *et al.*, J. Appl. Phys. **110**, 053701 (2011).
- [4] D. Nechaev *et al.* J.Cryst. Growth **378**, 378 (2013).
- [5] Iwanaga *et al.*, J. Mater. Sci. **35**, 2451 (2000).
- [6] R. Reeber, K. Wang, Mat. Res. Soc. Symp. **622**, T.6.35.1 (2000).
- [7] E. Chason *et al.* Appl. Phys. Lett. **74**, 356 (1999).
- [8] X.H. Wu *et al.*, J.Cryst. Growth **189/190**, 231 (1998).

Formation of elements of integrated acousto-optic cell based on LiNbO₃ films by nanotechnology methods

O A Ageev¹, E G Zamburg², A S Kolomiytsev³, D O Suchkov⁴, I A Shipulin⁵ and A V Shumov⁶

Southern Federal University, Institute of Nanotechnology, Electronics and Engineering, 347921, Taganrog, 2 Shevchenko st.

¹PhD, Professor, Directors of Institute of Nanotechnology, Electronics and Engineering, tel.: +7(8634) 371611,

² Reseracher, Department of Nanotechnology and MEMS, tel.: +7(8634) 371611,

³PhD, Assistant Professor, Department of Nanotechnology and MEMS, tel.: +7(8634) 371611.

⁴Student, Department of Radio-Technical Electronics, tel.: +7(8634) 371611,

⁵ Student, Department of Nanotechnology and MEMS, tel.: +7(8634) 371611,

⁶ Student, Department of Nanotechnology and MEMS, tel.: +7(8634) 371611,

Abstract. In the experiments we defined modes, and developed the technology of formation of elements of input-output laser emission and microlens of integrated acousto-optic cell by Pulsed Laser Deposition and Focused Ion Beams by using nanotechnology cluster complex, allowing controlled creation of elements in a single process cycle.

Acousto-optical devices are widely used in all kinds of radio-astronomy observatories, including terrestrial, airborne and space-based ones, as well as in atmospheric monitoring systems in many countries. Acousto-optic modulators and deflectors are used to control the amplitude, frequency, phase, polarization, direction of propagation of light beams. One of the budding directions is the development and study of the technology of forming elements of integrated acousto-optic cell, which allows to reduce the size of devices, reduces power consumption, increases sensitivity to vibrations, reproducibility of the parameters and provides for cost reduction in mass production [1]. One of the budding materials for the production of acousto-optic cell is LiNbO₃ [2, 3].

Cluster nanotechnological complex NANOFAB NFS-9 (NT-MDT, Russia) is one of the most budding systems as it combines several methods, including pulsed laser deposition (PLD), local nanoscale profiling by focused ion beam FIB, scanning probe microscopy (SPM), scanning electron and ion microscopy (SEM), diffraction of fast reflected electrons, and creates new opportunities for research, development of manufacturing technology, and the production of advanced micro- and nanoelectronics devices [4-7].

For forming LiNbO₃ films we used a Pulsed Laser Deposition (Neocera Inc., USA) module of complex NANOFAB, which provides for controlled deposition of films consisting of multicomponent oxides. The films were deposited at oxygen pressure of 50 Torr, with the energy density of the laser emission of 2.5 J/cm², the laser wavelength of 248 nm (KrF), and substrate temperature of 600°C. Film thickness - 400 nm. After the formation of LiNbO₃ films, the samples were passed through a vacuum transportation system to the modules of complex NANOFAB with Focused Ion Beams (Orsay Physics, France), which are used for local nanoscale operations, including local spraying, cutting, ion implantation, and local growth. Resolution of nano-profiling operations by means of ion beam is 10 nm. Etching was performed for each element at an accelerating voltage of 30 keV ion beam, the ion beam exposure time at each point of the pattern is 10 μsec, the total etching time of each element - 180

sec, the ion beam current is around 0.1 nA. Control of geometrical parameters generated structures was performed by SEM with built-in image processing software, as well as by semicontact AFM module SPM.

Figure 1 shows the SEM images of obtained elements of input-output laser emission and microlens in integrated version formed on LiNbO₃ film.

To sum up, as a result of experimental studies we identified modes and developed the technology of formation of elements of acousto-optic cell using nanotechnology cluster complex, allowing controlled creation of elements in a single process cycle.

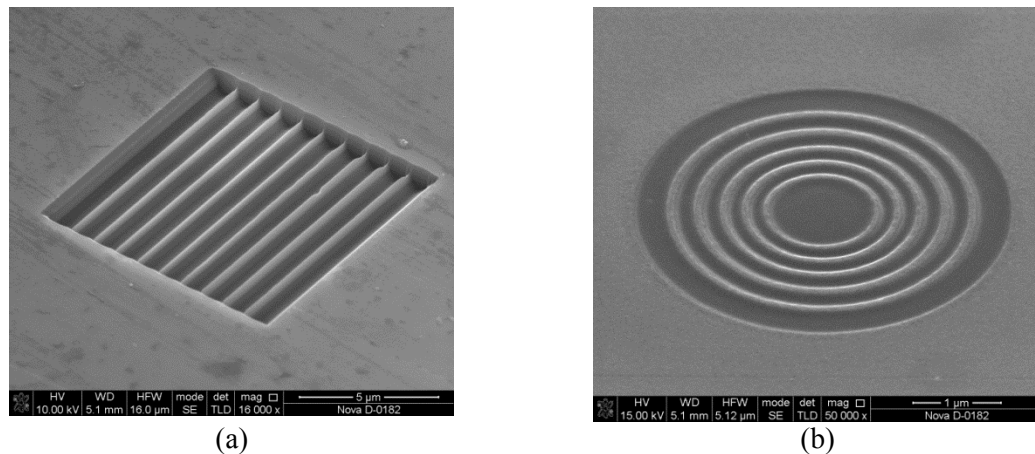


Figure 1. Element of input-output laser emission (a) and microlens (b) in integrated version.

The results were obtained by using the equipment of the Center for collective use "Nanotechnology" and the Research and Education Center, "Nanotechnologies" Southern Federal University.

This work was financially supported by the Ministry of Education and Science of the Russian Federation within the framework of the project stage of state contracts for scientific activities (job 16.1154.2014 / K), Federal Target Program "Scientific and Scientific-Pedagogical Personnel of Innovative Russia" for 2009-2013 (agreement №14.575.21.0045 , project's unique ID - RFMEFI57514X0045).

References

- [1] Волошинов В Б, Никитин П А, Трушин А С, Магдич Л Н 2011 *Письма в ЖТФ* **37** 22-28
- [2] Dostanko A P, Ageev O A, Golosov D A, Zavadski S M, Zamburg E G, Vakulov D E, Vakulov Z E 2014 *Semiconductors* **48** (9) 1242-1247
- [3] Zamburg E G, Ageev O A, Golosov D A, Alexeev A M, Vakulov D E, Vakulov Z E, Shumov A V, Ivonin M N 2014 *Applied Mechanics and Materials* **481** 55-59
- [4] Kolomiitsev A S, Konoplev B G, Ageev O A 2011 *Semiconductors* **45** 89-92
- [5] Ageev O A, Smirnov V A, Kolomiitsev A S, Serbu N I, Konoplev B G 2012 *Russian Microelectronics* **41** 41-50
- [6] Ageev O A, Vnukova A V, Gromov A L, Ilin O I, Kolomiytsev A S, Konoplev B G, Lisitsyn S A 2014 *Nanotechnologies in Russia* **9** 145-150
- [7] Ageev O A, Gusev E Y, Zamburg E G, Vakulov D E, Vakulov Z E, Shumov A V, Ivonin M N 2014 *Applied Mechanics and Materials* **475-476** 446-450

Improving the efficiency of emission extraction from nitride LED structures with a textured interfaces

A S Evseenkov¹, I A Lamkin¹, S A Tarasov¹, A V Solomonov¹

¹St. Petersburg Electrotechnical University “LETI”, 5 Prof. Popova Street, St. Petersburg 197376, Russia.

Abstract. The LED structures based on gallium nitride and grown on sapphire substrates were investigated. The basic parameters, namely the emission spectrum, power, current-voltage characteristic and temperature dependences have been received. Based on the parameters of the structures, the simulation output Monte Carlo method was conducted. On the basis of the simulation the best possible way to improve the structure by surface texturing and other possible modifications was revealed.

1. Introduction

One of the major problems now is the realization of the potential benefits of blue and white LEDs based on gallium nitride and its solid solutions in light sources. It requires considerable effort on their development and improvement. It is first necessary to significantly increase their power and external quantum efficiency, which is largely determined by radiation output of the LED structure.

Effective way to solve the problem of output light limiting is co-building surfaces that scatter light. When you create a specific shape roughness reduces the impact effect of total internal reflection, and the proportion of light output from the device is increased. To date, the texturing of substrates or epitaxial layers is used. In the LED industry two basic approaches are used: random texturing and patterned sapphire substrate (CAP). Random texturing of the top layer of *p*-GaN is not very expensive process and it does not require additional effort. Therefore, in this paper we consider the application of this method for the LED structures based on gallium nitride optimization.

2. The test samples

The authors studied the luminescence of the semiconductor nitride nanoheterostructures on the basis of solid solutions (Al, Ga, In)N having multiple quantum wells (MQW) and superlattices (SL), created by MOCVD method on the sapphire substrate. The investigated nanoheterostructures were identical except the last *p*-GaN epitaxial layer. The *n*-GaN buffer and contact layers were grown on the c-Al₂O₃ substrate having 4 μm thickness. Structures without SL were used as reference. The SL consisted of 15 In_{0,01}Ga_{0,99}N and In_{0,001}Ga_{0,999}N

layers each having 1 nm thickness and placed before the active region. The active region comprised one 2.5 nm width $\text{In}_{0,15}\text{Ga}_{0,85}\text{N}$ quantum well. Further the low-alloyed 50 nm thickness *i*-GaN layer was grown. The final *p*-GaN layer was of four types: the first type represented SL consisted of 9 pairs of $\text{Al}_{0,15}\text{Ga}_{0,85}\text{N}$ and GaN layers of 1.5 nm thickness, the second type - *p*-AlGaN layer with 15% aluminum fraction, the third type - *p*-AlGaN layer with 10% aluminum fraction and the fourth type - *p*-GaN layer. The final A, B, C, D layers thickness was 27 nm. Carrier concentration in these layers was $N = 3 \cdot 10^{17} \text{ cm}^{-3}$.

3. Experiment Conclusion

All the main characteristics were investigated: the emission spectrum, power, current-voltage characteristic and temperature dependences. Process modeling light output Monte Carlo was conducted based on the parameters of the structures. As a result of the simulation cycle structures of LED patterns were obtained of the boundaries between media layers. The introducing of the roughness on the relative radiation output from the structure were modeled. During the simulation the effect of modifying the structure on its parameters was investigated. In addition texturing the surfaces same other changes were simulated - for example adding lenses or decrease in the thickness of the semiconductor layer. It is found that the transmittance of the structure can be increased more than 3 times through the creation of the pyramids with an aspect ratio equal to 1, decreasing the layer of gallium nitride, and the creation of the lens on the sapphire interface.

The research of the influence of the pollutants on water plants with the help of optical methods

A A Asadova, E V Timchenko, P E Timchenko, L A Zherdeva, N V Tregub

Samara State Aerospace University (SSAU), Moskovskoye shosse 34, Samara

The growth of anthropogenic impact on the environment associated with the increase of industrial and agricultural emissions, such as synthetic surfactants (detergents), heavy metals and nitrates that have a significant impact on the functioning of living systems of hydrosphere. Due to the ability to accumulate various types of pollution the plants are effective markers of the state of ecosystems, which in contrast to traditional methods for measuring concentrations of pollutants express resistive functions of the biological environment to external influence, including the multiple factors and types of pollutants. The accumulation of anthropogenic load in plants is the integrative, i.e. plants contain a «history» of pollutant emissions.

The freshwater macrophages Elodea Brazilian (*Egeria densa*) was used as objects of study. The plants were divided separated into 4 groups: control groups, synthetic surfactants, agricultural emissions and heavy metals. The concentrations of heavy metals ranged from 0.1 MAC to 20 MAC. The control group of plants was in the medium of filtered tap water. These pollutants were introduced only once at the beginning of the experiment, i.e. a single salvo emission of pollutants with fixed concentration was practically simulated. The experiments were performed under laboratory conditions in reservoirs of water and it's excluding external influences. The uniform climatic conditions for all groups of the plants, as well as the regularity and constancy of the light flux influencing on the medium were provided.

Raman spectroscopy realized by experimental stand that included the high-resolution digital spectrometer Shamrock sr-303i with a built-in cooling camera DV420A-OE, RPB785 fiber-optic probe for Raman spectroscopy, combined with laser module LuxxMaster LML-785.0RB-04 (power - up to 500 mW, wavelength - 785 nm).

An inverted microscope Olympus IX71, confocal scanner Yokogawa CSU-1 with camera EMCCD iXon Andor were used for realization of confocal fluorescence microscopy. This system provides a resolution of 400 nm per pixel. Fluorescence was excited by a laser unit that ensures generation power up to 100 mW at a wavelength of 488 nm falls within the absorption band of chlorophyll.

The following results were produced as a result of this work:

- The dependence of the impact of pollutant concentration on the optical parameters of aquatic plants was experimentally established. Shown that the Raman intensity decrease by 70% at Raman bands 740 cm^{-1} and 1522 cm^{-1} , that responsible for C = C deformation vibration of chlorophyll and carotenoid occurs under the influence of pollutants on plant tissue. This feature corresponds to the "washing out of pigments" from plant cells and to changes in concentration of chlorophyll and carotenoids;

- Microscopically shown, that the degradation of chlorophyll occurs with presence of surfactants and associates with solubilization of membrane proteins and its permeability change;

- Dependence of influence of pollutant concentration on plant optical parameters with the exposure time was obtained;

- Optical coefficient that determines the impact of pollutants on plants and which defined as the ratio of intensities at Raman bands 740 cm^{-1} , 1522 cm^{-1} and 1435 cm^{-1} was introduced.

Raman spectroscopy for the control of the atmosphere bioindicators

Shamina L.A., Timchenko E.V., Zherdeva L.A.

Samara State Aerospace University (SSAU), Moskovskoye shosse 34, Samara 443086, Russia

In the world today the environmental concerns came to one of the top places by their social significance. One of the most perspective directions in modern science is the development of optical methods for the control of various types of pollutants. In view of ability to accumulate pollutants, plants are effective markers of ecological state of the atmosphere. The accumulation of anthropogenic load in plants is the integrative, i.e. plants contain a «history» of pollutant emissions.

These effects are invariably lead to a change in spectral properties of the medium. Therefore, by controlling the spectral changes, we not only can know the number of pollution, but also can measure their effect on living objects. Such control can be performed using the method of Raman spectroscopy, which has a high sensitivity and gives the most complete information about the state of a living system unlike other optical methods.

The following types of bioindicators were selected as research objects: silver birch (*Betula pendula*), dandelion (*Taraxacum*) and spruce (*РHcea бbies*). Collection of samples was carried out depending on the light level, age, and height of biological objects. Investigations were performed on more than 130 samples of plants. All objects of research were in the same climatic conditions, humidity and soil ph levels were identical to, that excluded impact on the optical properties of soil bioindicators.

The spectral characteristics of the samples were studied by experimental stand implementing the Raman spectroscopy. This stand includes a high-resolution digital spectrometer Shamrock sr-303i with a built-in cooling camera DV420A-OE, fiber optic probe RPB785 for Raman spectroscopy, combined with laser module LuxxMaster LML-785.0 RB-04 (power 150 mW, wavelength 785 nm).

As a result of our experiments:

- Spectral features of different types of bioindicators, depending on the light level were identified. Shown that the intensities ratio of Raman bands 730 cm^{-1} and 1600 cm^{-1} is not dependent on the level of illumination for two bioindicators - dandelion (*Taraxacum*) and silver birch (*Betula pendula*);
- Is established that the statistical scatter of optical parameters for wood bioindicators ranged from 9% to 14%, and vegetable plants - from 4% to 8.7%. On the basis of the obtained results, the dandelion (*Taraxacum*) was selected as a bioindicator of atmospheric emissions.

Tunable LD pumped Tm:KLuW laser

**O P Dernovich, N V Gusakova, S V Kurilchik*, M P Demesh, V E Kisel,
A S Yasukevich and N V Kuleshov**

Center for Optical Materials and Technologies, Belarusian National Technical
University, Minsk, Belarus

Abstract. Laser diode pumped Tm:KLuW laser was demonstrated in a three-mirror cavity configuration. Tunable laser emission was realized in a spectral range of 1826-1992 nm.

1. Introduction

Solid-state lasers at 2 μm wavelength based on Tm^{3+} -doped crystalline materials are of interest for a variety of applications in medicine, remote sensing and military technologies [1, 2]. It is attributed to high absorption of water and other atmospheric gases in this spectral range. In case of tunable operation of thulium laser they are attractive for using in spectroscopy, pumping of holmium lasers to obtain 2.0-2.1 μm radiation and optical parametric oscillator to achieve efficient conversion into mid-infrared region. In our work we have realized laser operation based on $\text{Tm:KLu}(\text{WO}_4)_2$ (Tm:KLuW) crystal in a three-mirror cavity configuration and obtained wavelength tuning over 165 nm wavelength range.

2. Experimental setup

The experimental setup of Tm:KLuW laser is shown in figure 1. Fiber-coupled AlGaAs laser diode emitting at 808 nm under room temperature was used as a pump source. The optical fiber diameter was 105 μm and numerical aperture was 0.15. To obtain good overlap between absorption band of Tm:KLuW crystal and emission of laser diode the later was cooled to 13°C. The pump radiation with M^2 of 20 was collimated and focused in active element in a spot of 120 μm diameter with two spherical lenses. The laser cavity consisted of plane input mirror M1, transmitting about 95 % of pump radiation and high reflecting at 1800-2000 nm spectral range, spherical mirror M2 with radius of curvature of -100mm and plane output coupler M3 with transmission of 1.8 % at laser wavelength. As an active element 2.5 mm long Ng-cut Tm:KLuW crystal with Tm^{3+} ions concentration of 5 at. % was used. The crystal faces were AR-coated for the pump and laser radiation. The Tm:KLuW crystal was wrapped by indium foil and mounted on analuminum heat-sink with two lateral sides in contact. No active cooling was applied to the laser crystal and the laser operated at standard room-temperature conditions. The maximum pump power incident on the active element was 3.06W. To achieve laser wavelength tuning BK7 glass prism was inserted into the cavity between spherical mirror M2 and output coupler M3 where cavity beam was close to collimated.

3. Results

Continuous wave laser emission at 1957 nm in the fundamental TEM₀₀ mode was realized in the setup shown in Fig. 1. The absorbed pump power at the laser threshold was 305 mW. The maximum output power of 600 mW was obtained with absorbed pump power of 2.45 W. The input-output characteristic of Tm:KLuW laser is shown in figure 2.

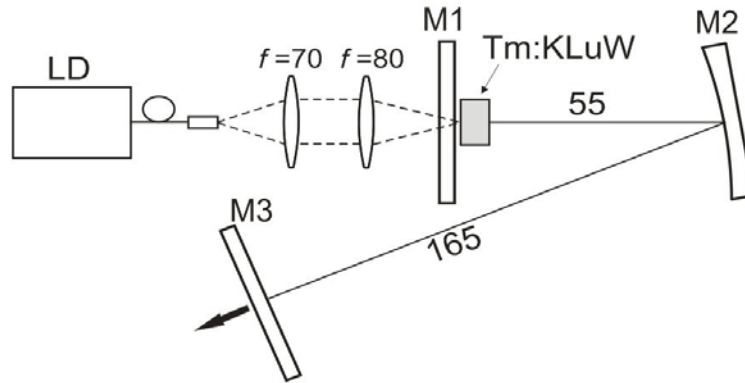


Figure 1. Experimental setup of Tm:KLuW laser.

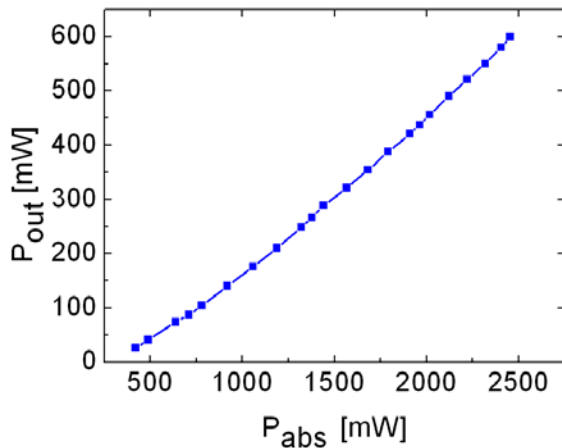


Figure 2. Input-output characteristic.

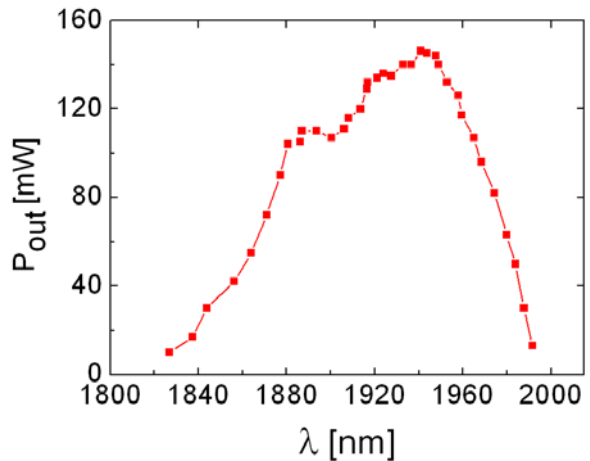


Figure 3. Laser wavelength tunability curve.

The laser output was polarized along Nm axis of the crystal, where amplification coefficient of the crystal was higher than one corresponding to Np polarization.

With the glass prism inserted in the cavity the laser wavelength was tuned in the spectral range of 1826-1992 nm. The tuning curve is depicted in figure 3. The entire tunability range of the laser was 165 nm.

References

- [1] Scholle K, Lamrini S, Koopmann P and Fuhrberg P 2010 2 μm laser sources and their possible applications *Frontiers in Guided Wave Optics and Optoelectronics* ed B Pal (Vukovar: Intech) p 471
- [2] Carrig T J 2004 Novel pulsed solid state sources for laser remote sensing *Proc. SPIE Int. Soc. Opt. Eng.* **5620** pp 187–198

Optical tomography in reacting flows based on Stokes Raman scattering

D Sharaborin^{1,2}, L. Chikishev^{1,2}, V Dulin^{1,2}, D Markovich^{1,2}

¹Kutateladze Institute of Thermophysics, 1 Ak. Lavrentyeva Avenue, Novosibirsk, 630090, Russia

²Novosibirsk State University, 2 Pirogova Str., Novosibirsk, 630090, Russia

Abstract. The paper reports on development of an optical system for tomographic imaging in reacting flows. The principles rely on registration of Stokes Raman scattering (rovibrational transitions for nitrogen), when a transparent object is illuminated by a laser sheet. The method allows for the local density and concentration evaluation.

Advances in optoelectronics provide devices for detection of a very weak emission and allows for non-intrusive measurements in reacting flows with high spatial resolution (hundreds of microns). Powerful lasers, efficient photocathodes with photo-multiplying tubes, and new optical filters can be combined into an optical system for registration of 2D images of Raman scattering, characterized by a very weak signal. The present paper reports on development of such system for local density and concentration measurements in flames based on detection of Stokes Raman scattering from nitrogen.

Scheme of the setup for 1D and 2D systems is displayed in Fig. 1. Third (355 nm) or second (532 nm) harmonic of a pulsed Nd:YAG laser (QUANTEL BrilliantB) could be used for the illumination of sampling volume. The energy of 6 ns laser pulses was monitored by an energy meter (Coherent LabMax-TOP). On average, the energy was 120 and 690 mJ for 355 and 532 nm, respectively, with RMS of variation below 5%. Fig. 1 shows the 2D image when a flame was illuminated by a laser beam. Orientation of linearly polarized laser light was controlled by half-wave plates. This was necessary to record Raman scattering for two perpendicular polarizations of the incident laser light. The images for the horizontal polarization were subtracted from those for the vertical polarization in order to minimize influence of the dark-current, reflections, and possible fluorescence (for UV).

1D system captured spectrum of the scattered light along the laser beam by using a Czerny-Turner spectrograph (Newport MS127i 1/8 m) equipped with a UV lens. The spectrometer alignment ensured the parallel orientation of the entrance slit and the laser beam. The used grating with 1 200 lines/mm provided the spectral resolution of 1 nm. The spectra along the beam were registered by a 12-bit ICCD camera (PCO DICAM Pro, photocathode type QE 20%, GEN II) mounted at the output of the spectrograph. To reduce noise, the scattered light from 100 laser pulses was collected during acquisition of each image. The collection time during each shot was 30 ns. For each measurement point, 10 frames were captured and averaged in order to reduce contribution of read-out noise. The image size of 1280 × 800 pixels corresponded to 108 nm on 105 mm.

A tunable optical filter (VariSpec LC), based on liquid crystals, was used to collect the emission for the desired wavelength, corresponding to the vibronic transition of nitrogen (607.3 nm when excited at

532 nm). For registration of the Raman signal, a 16-bit ICCD (Princeton instruments PI-MAX-4) was mounted after the tunable filter. A multi-notch holographic filter was also used to block the emission from Rayleigh scattering, which is about 10^4 times greater than the Raman scattering and was not blocked completely by the liquid-crystal filter. The scattered light from 200 laser pulses was collected during acquisition of each image with 8x8 pixels binning. The collection time was 200 ns.

Intensity of the Stokes lines depends on temperature and volume fraction of the molecules. Nitrogen line was used to evaluate ratio between the flame and ambient air temperatures. Dependence of the effective Raman scattering cross-section on temperature was taken into account in the same way as in [1]. This was done from calculations of the Raman spectra by using RAMSES code [3]. Smaller molar fraction of nitrogen in flames (combustion products) was taken into account. Comparison with results of thermocouple (type R) measurements showed good accuracy of the optical system for temperatures below 1800 K. For temperatures above 1800 K, a limited dynamic range of the CCD sensor limited accuracy.

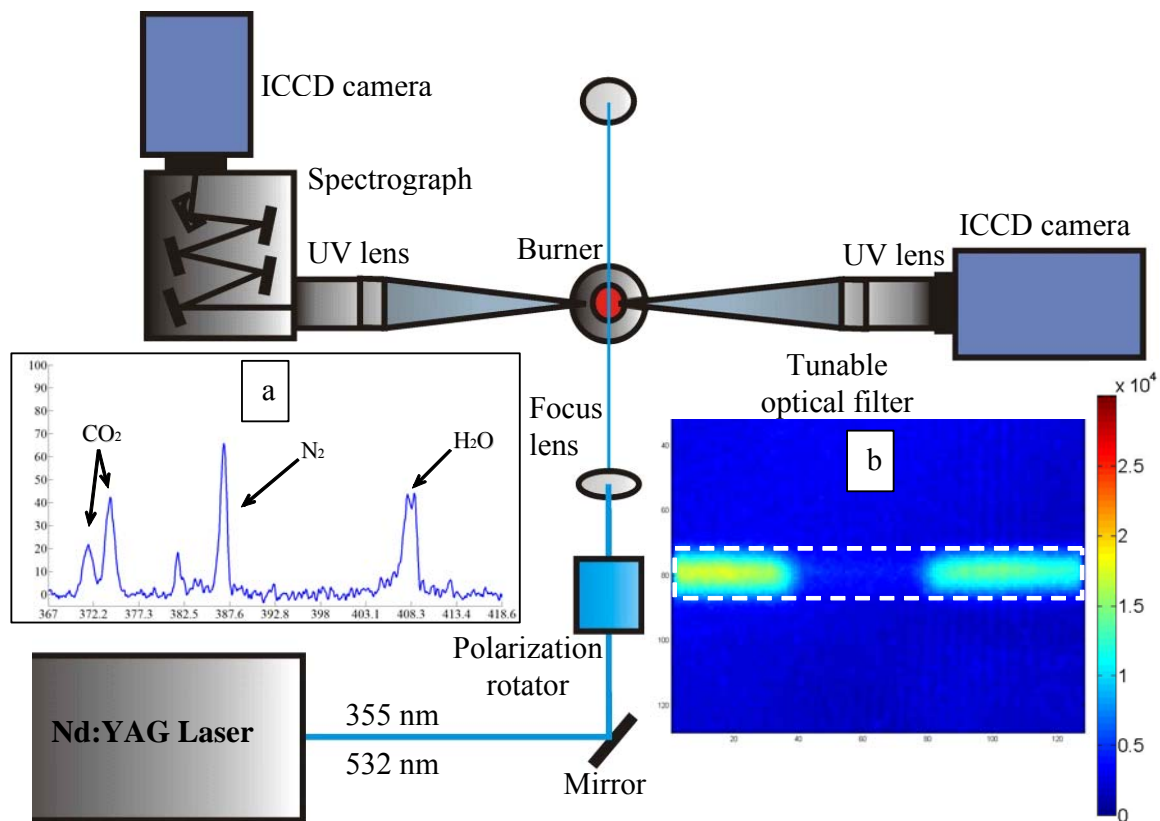


Figure 1. Scheme of the experimental setup for Raman thermometry and data example (a- Raman spectra, b- 2D distribution of Raman signal for N_2 vibronic transition) in flame.

Acknowledgments

Financial support has been obtained from RFBR (grant № 15-38-21003).

References

- [1] Rabenstein F and Leipertz A 1998 *J. Appl. Opt.* **37** 4937
- [2] Egermann J, Seeger T and Leipertz A 2004 *J. Appl. Opt.* **43** 5564
- [3] Hassel E P 1993 *J. Appl. Opt.* **32** 4058

Development of non-contact laser vibrometer

I. Kononov, E. Velichko, E. Aksenov

Saint-Petersburg State Polytechnic University

Abstract. Modified schemes of noncontact laser sensors for vibrometry are considered. The results of investigation of two laboratory models of laser speckle vibrometers are presented. Advantages and disadvantages of the vibrometer sensors are discussed.

1. Introduction

Development of methods and devices for nondestructive control of physico-mechanical properties of different objects is one of the important tasks of modern technique and machinery. There are a number of methods and devices for remote control of mechanical characteristics; however, the challenges and new tasks require the development of methods and devices of vibrational monitoring of different objects.

The laser-based optical methods of non-contact remote monitoring are in fact an extremely powerful tool for the study of the behavior of components during operation. One of the contactless optic methods is laser speckle-interferometry based on rather simple and cost-effective optical sensors. At the same time the method accuracy is comparable with the precision of more complex holographic systems.

The aim of our work was to develop methods and create laboratory models of laser speckle-vibrometry sensors for non-contact remote vibrometry of large- and small-scale objects. Vibration characteristics are important for evaluation of physical and mechanical parameters of different objects, such as bridges, dams, jet engines, electric motors, biological cells and tissues, etc.

2. Experiments

The several laboratory models of laser speckle vibrometers were developed and investigated. The characteristic features of these models were identified. Special attention was paid to non-contact registration of man's pulse shape of the radiocarpal artery. To solve this problem two laboratory models of speckle-vibrometers were developed: the first one was based on the point contactless sensing of skin and the second one was based on ringed light field sensing.

2.1. Point sensing

The scheme of the speckle-vibrometer model with point sensing is presented in figure 1.

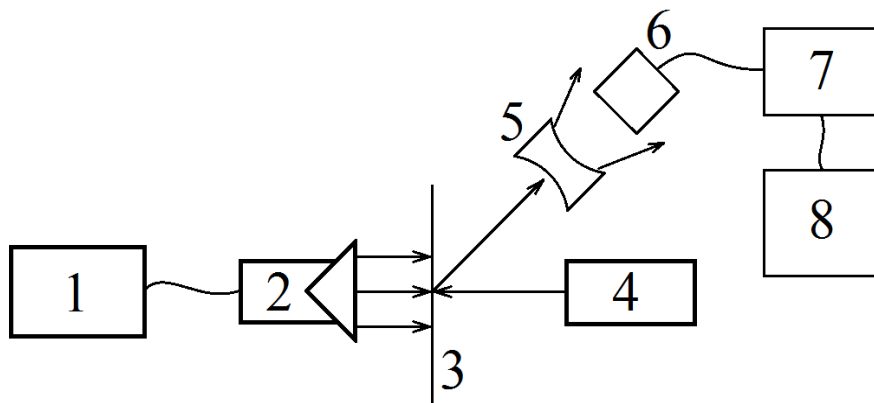


Figure 1. Speckle vibrometer scheme. 1 – sound frequency generator, 2 – speaker, 3 – target, 4 – semiconductor laser, 5 – diverging lens, 6 – photodiode, 7 – oscilloscope, 8 – computer.

We had revealed a number of limitations of the speckle-vibrometer model with point sensing:

- criticality to location of the sensing laser beam;
- detecting of signal from various light sources on photodetector and so the presence of pulse interferences;
- loss of signal in case of laser beam shifting from the artery.

2.2. Ringed light field sensing

To reduce the influence of sensor positioning on the signal it was proposed to use several infrared LEDs circumferentially. To create the circular illumination the optical system with axicon was developed (fig. 2). Vibrations with intended frequency were simulated by membrane which was excited by sound wave from generator of acoustic oscillations GZ-112.

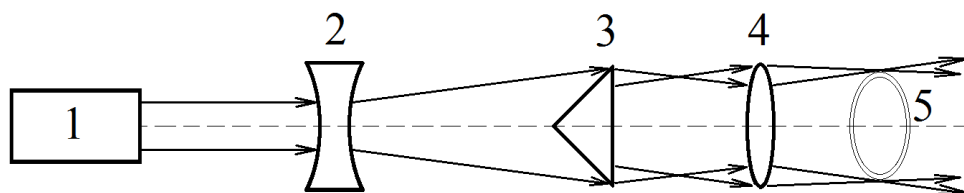


Figure 2. Optical system of ringed sensing. 1 – semiconductor laser, 2 – diverging lens, 3 – axicon, 4 – focusing lens, 5 – circular illumination.

3. Conclusion

The results of our experiments revealed efficiency of proposed laboratory model of the laser speckle-vibrometer. Details of the experiments are discussed in the report. The obtained results provide the basis for further investigation and development of laser vibrometer.

Monte-Carlo modeling of drift mobility in thin organic layers: lattice type influence

V M Sukharev and V R Nikitenko

National Research Nuclear University MEPhI, Moscow, Russia

Abstract. Hopping transport of charge carriers in thin (up to 100 nm) organic layers, which are suitable for organic light-emitting diodes and solar cells, is modeled in the framework of Gaussian disorder model. Drift mobility dependence within ranges of layer thickness, energy disorder and field strength is considered. Monte-Carlo simulations for small concentration case show fascinating behavior of drift mobility in dependence on type of lattice – simple cubic, body-centered and face-centered lattice. Results of this work are compared with the results obtained recently by Cottaar et al., done within balance equation approach. Additionally we take into account influence of image charge on injection in case of cubic lattice.

1. Introduction

Organic electronics devices consist of thin active layers. Predictive modelling of operation of such devices unavoidably needs correct characterization of charge transport in thin organic layers. Charge transport, being of hopping nature, can be described in the framework of Gaussian disorder model [1]. Values of mobility, which have been obtained from experiments for thicker layers (> 1 micrometer), are often used for modelling the light-emitting diodes. The recent review [2] combined all the results that had been published in this scientific area for the last few decades. As it was shown, lattice type of an organic volume does not have big influence on dynamic characteristics of a particle. It can be explained in terms of percolation theory [3]: correlation radius L is much bigger than lattice constant a_0 of a cell, so there is no difference what type of a lattice is. However, all main computing results, dedicated to dependence on lattice type, were obtained within balance equation approach to electron transport with periodic boundary conditions [4]. So it would be of interest to solve this problem to correct the obtained data or to improve it, using complete Monte-Carlo (MC) modeling, which is superior respective to balance equation approach.

2. Monte-Carlo procedure and scheme of modeling

In MC simulations we use the same approach that was applied in our previous work [5], but here we consider not only simple cubic lattice, but two more options: body-centered and face-centered lattice. A conventional model is used, where hopping centers are located at sites of a lattice. Number of sites along any transversal direction exceeds 10 times a number of sites along the electric field direction. Energies of sites are distributed randomly according to Gaussian distribution $g(E)$ with the variance σ . If an electron appears in the nearest to right electrode layer, event is over. Drift mobility is calculated from the average drift velocity. The analytic expression for drift mobility has the form [3, 6]:

$$\mu(T, c) = \frac{\mu_0}{c} \left(\frac{kT}{\sigma} \right)^\lambda \exp \left(\frac{\varepsilon_F(T, c) - \varepsilon^*}{kT} \right). \quad (1)$$

Eq. (1) was obtained in condition that field strength and relative carrier concentration, c , is small, $\sim 10^7$ V/m and $\sim 10^{-5}$, respectively). Parameters λ and ε^* are in charge of lattice type dependence [4, 6].

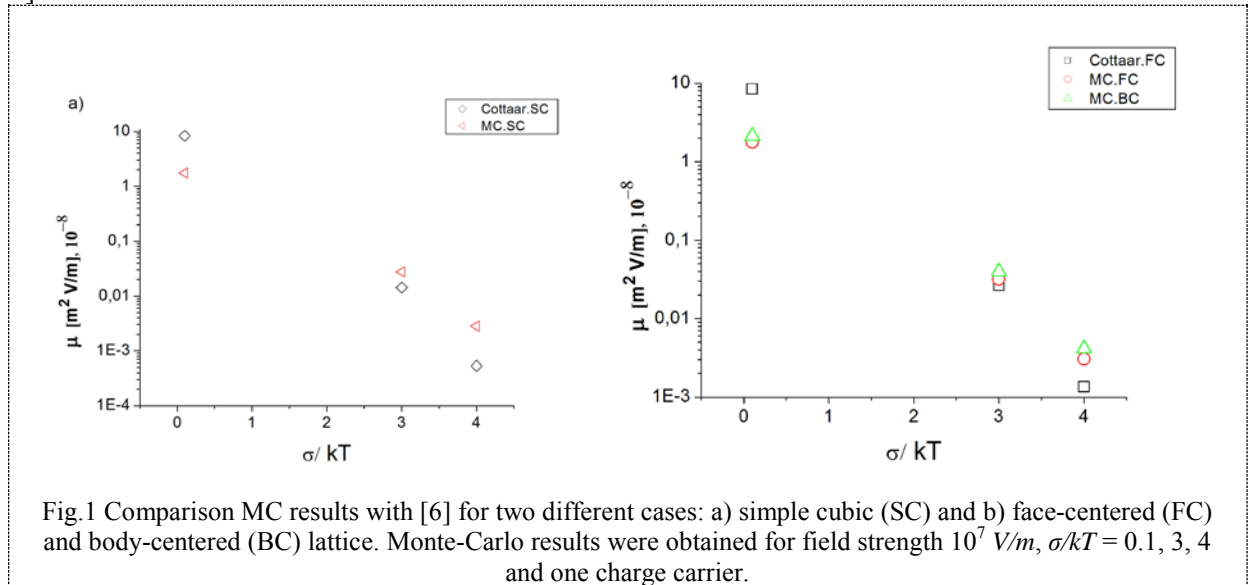


Fig.1 Comparison MC results with [6] for two different cases: a) simple cubic (SC) and b) face-centered (FC) and body-centered (BC) lattice. Monte-Carlo results were obtained for field strength 10^7 V/m, $\sigma/kT = 0.1, 3, 4$ and one charge carrier.

3. Discussion

Fig. 1 *a,b* shows that both MC and analytic results have only slight dependence on a lattice type, in accord with previous suggestions [3]. However, the difference increases along with the increase of disorder (it reaches 50% at $\sigma/kT = 4$, see Fig. 1*b*), so one has to take it into account in quantitative modelling. MC results exceed mobility from [6] at high disorder due to size effect on mobility in thin films [5]. Deviations in low-disorder limit result from absence of applicability of the analytic approach [6]. We also considered influence of image charge on injection of charge carriers. It is shown that this realistic effect strengthens thickness dependence of drift mobility, which has been reported in [5]. But for high disorder drift mobility becomes larger in case of coulomb interaction than without the influence of the electrode (dummy injecting electrode). This work was supported by Ministry of Education and Science of Russian Federation, Agreement No. 14.575.21.0002, ID RFMEFI57514X0002.

References

- [1] Bassler H Charge Transport in Disordered Organic Photoconductors a Monte Carlo Simulation Study 1993 *Phys. Status Solidi B* **175** 15
- [2] Baranovskii S D Theoretical description of charge transport in disordered organic semiconductors 2014 *Phys. Status Solidi B* **251** 487–525
- [3] Shklovskii B I and Efros A L Electronic Properties of Doped Semiconductors 1984 *Springer Berlin*
- [4] Cottaar J Coehoorn R and Bobbert P A Scaling theory for percolative charge transport in molecular semiconductors: Correlated versus uncorrelated energetic disorder 2012 *Phys. Rev. B* **85** 245205
- [5] Nikitenko V R Sukharev V M and Sannikova N A Drift mobility in thin organic layers: joint Monte-Carlo and analytic modeling 2014 *J. Phys.: Conf. Ser.* **541** 012028
- [6] Cottaar J Koster L J A Coehoorn R and Bobbert P A Scaling theory for percolative charge transport in disordered molecular semiconductors 2011 *Phys. Rev. Lett.* **107** 136601

Multifunctional optical processor for biological microobjects investigation

List the author names here K. Domnin¹, E. Aksenov¹

¹Saint Petersburg State Polytechnic University, Saint Petersburg, Russia

Abstract. The combination of two methods: diffractometry and polarimetry was considered. The optical processor device was realized on base of these methods. Biological objects and their phantoms investigations were carried out.

1. Introduction

Optical methods of investigation are usually used for studying of various objects, including bioobjects at the microlevel. These methods have a huge potential in noninvasive medical express diagnostics.

Changes in the pathological conditions of an organism give some deviations in morphological and chemical composition of blood. These deviations are caused by physiological shifts and the pathological processes in organ functions.

Changes in morphological composition of blood are expressed in reduction or increase of erythrocytes and leukocytes quantity, in change of uniform blood elements ratios and erythrocytes size and a form changes. At the physical, chemical and biological changes of blood properties may be observed viscosity change, violation of coagulability process, etc.

Erythrocytes (red blood cells) have a highest sensitivity to any pathologic changes in an organism therefore they are good objects for research and assessment of an organism physiological condition.

There are some optical methods for microobjects investigation. One of them is a laser diffractometry method, based on diffraction of the laser radiation on a single or multiple biological microobjects [1, 2]. This method is characterized by high precision, sensitivity, speed, the minimum invasivity, possibility of a large number of small particles simultaneous registration. Parameters of a diffraction picture are connected with microobject parameters, so it enables to determine their sizes, form, and internal structure.

The other method has a rather high potential for application in bioobjects researches – a laser polarimetry. Polarimetric diagnostics allows receiving information about optical anisotropy of biological tissues.

Optical methods usually allow one to solve problems which are insoluble or difficult for other methods. They are characterized by high sensitivity but makes great demands of experiment conditions and huge control because of method high sensitivity to external influences. Potential opportunities of optical processing are obvious: two-dimensions, real time working, high speed processing of big arrangement data, wide bandwidth of frequencies, etc. The theory describing operation of optical devices is well developed. So we determined the objectives of this work: to research biological microobject and its phantoms; to develop a multifunctional optical processor.

2. Experimental setup

To solve this problem the experimental setup was developed. It has two information channels: polarimetric and diffractometric, as well as control visual channel. The diffractometric channel includes laser, collimator, diaphragm, lens, object and CCD camera. The polarimetric channel includes laser; two polarizers: first of it is fixed, second is rotated; object and CCD camera.

The preliminary results were obtained. They are in well agreement with the theory results.

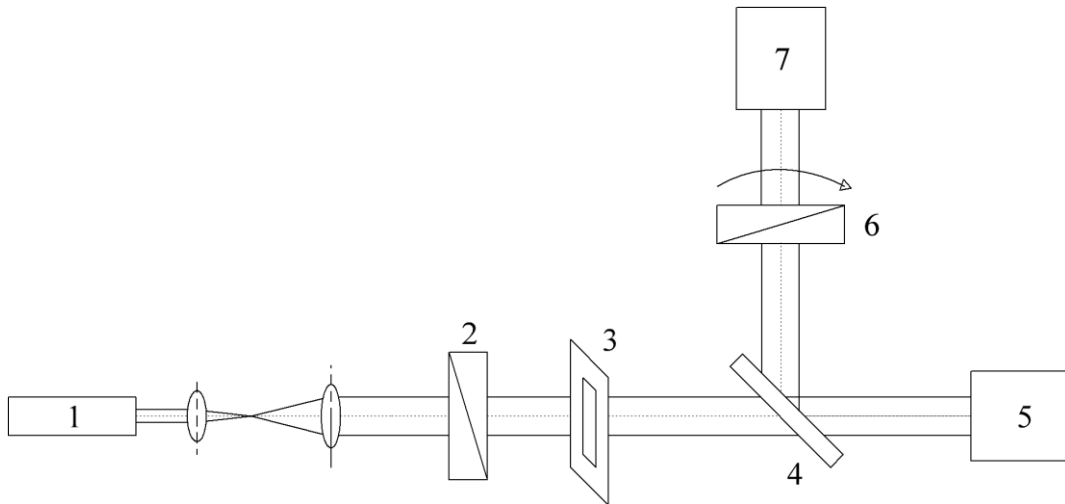


Figure1. Structural scheme of experimental setup. 1 – laser, 2,6 – polarizers, 3 – object, 4 – beam splitter, 5,7 – CCD cameras

References

- [1] Bessmeltsev S, Lendiaev A, Tarlykov V 2004 *Proc. SPIE* **5381** 151-156
- [2] Bessmeltsev S, Tarlykov V, Hodus I 2004 *Proc. SPIE* **5381** 146-150

Overview of optical and optical-electronic systems for alignment control

Maksim Kleshchenok and Valery Korotaev

Department of Optical-Electronic Devices and Systems, ITMO University, Kronverkskiy lane, 49 Saint-Petersburg 197101, Russian Federation

Abstract. In this paper, we show the analysis of existing technical solutions for control the alignment is carried out on the basic and necessary needs, which allowed to allocate a certain methods and systems specific advantages and disadvantages from the standpoint of these criteria. Presented the comparison systems for alignment control, depending on their range and measurement error. All types of systems are splitted for a four big groups (mechanic, optical, systems based on beam analysis and interference). The urgent task is to analyze the rational use of one or another measuring system in a given task. Comparison of these methods and principles offered directly implemented by the example of measuring systems which is quite obvious solution. The most progressive and hopeful type of the system is based on laser. Provided suggestions and improvements for future developing.

1. Introduction

Currently, optical-electronic devices and systems play an increasingly important role in the measurement of angular and linear displacement, positioning and motion control of working bodies in the industrial control systems of technological processes. This is because the rapid development of new, more advanced element base allows all of us to improve the quality of the contactless control due to new concepts. The desired improvement of the quality (accuracy, range, reliability) can also be achieved through the application of new algorithms for digital information processing, which determines the relevance of the research and development of appropriate multi-functional, in the sense of versatility, transducers, instruments and systems. Because such systems allow preventing (warn) technological disasters, the urgency of the problem increases in proportion to the technical progress of all mankind, to prevent the recurrence of tragedies have occurred, for example, the Bhopal disaster (1984), the Chernobyl disaster (1986), the Sayano-Shushenskaya power station accident (2009), pipeline spill in Israel (2014), which served as the impetus for the development of systems of this trend.

2. The choice of measurement scheme depending on the conditions and requirements of the technical problem

Analysis of existing technical solutions for control the alignment is carried out on the basis of the following criteria, which allowed to allocate to certain methods and systems specific advantages and disadvantages from the standpoint of these criteria (Table 1.8):

- Measurement range of laser systems is a major advantage (because of their large sizes (up to 20 mm)), which determines the popularity of their use in comparison with cross hairs systems (e.g., PPS-11 and Taylor and Hobson) and interferometers.
- The measurement error. Using the properties of coherent radiation in the interferometer provides a significant advantage, the latter is a high-tech optical components, the quality of the production and alignment, which fundamentally depend on the metrological properties of the system. Comparison of laser systems, OES systems and OEZ reflects similar accuracy characteristics.
- Working distance. All listed systems in the overview provide alignment control up to 10 m, however, systems of the active type (including OES, laser systems and interferometers) allow control at distances up to 50 m and more.
- Usability is often provided by the introduction of portable computing devices with databases and passive CE (OES, laser systems and systems with OEZ), which relieves the organization of communication and supply CE. High complexity, low level of automation and human factors eliminate mechanical methods and sighting systems.
- A common drawback all the above systems is the low level of adaptation to the existing technological process for alignment control.
- The resistance to impact of external conditions, such as vibration (the most critical mechanic methods), external exposure and the influence of the air tract [1] characterized by varying level of the system.

It should be noted that for different situations and the formulation of the technical problem the weight of the criteria varies. However, it is possible to formulate a generalized view on the ways of solving technical problems.

According to the review, the laser systems is able to partially provide the solution for today problems. However, a significant time of the output of such systems on the mode, temperature instability, the need to provide power at the point of control and increased requirements for safety limit their usage. The main feature of such systems is the linear increase of the measurement error with the increase of the measured offset (from 5 to 10 mm), due to the nonlinearity of the PSD (1-2%), which ultimately limits the performance of these systems.

Acknowledgments

The work is also financially supported by Government of Russian Federation, Grant 074-U01.

References

- [1] Anisimov A. G., Yarishev S. N., Timofeev A. N., Lashmanov O. and Korotaev V. V. 2011 *OSA Technical Digest. JWA24*

A high stability reference for a «clock» laser used as a source for a frequency standard based on cold magnesium atoms

M A Tropnikov^{1,2,4}, A M Shilov^{1,2} and A N Goncharov^{1,2,3}

¹ Institute of Laser Physics, Siberian Branch, Russian Academy of Sciences, pr. Acad. Lavrent'eva 13/3, 630090 Novosibirsk, Russia

² Novosibirsk National Research State University, Pirogova 2, 630090 Novosibirsk, Russia

³ Novosibirsk State Technical University, pr. Karla Marksa 20, 630092 Novosibirsk, Russia

Abstract. In this paper, the results of creation of a high stability reference for a radiation source at a wavelength of 457 nm based on a Nd:YVO₄ laser second harmonic with a diode pump are presented. Frequency stabilization by the reference passband allows achieving a laser system linewidth of less than 1 kHz. Thermostabilization of the reference with a PID controller which makes it possible to maintain the reference temperature with an accuracy of 1 mK was implemented. The radiation source can be used for precision spectroscopy of magnesium atoms and creation of a compact frequency standard based on cold magnesium atoms.

Frequency standards play an important role in fundamental research investigations, metrology, and navigation. The relative accuracy of a primary frequency standard based on a caesium fountain has probably reached its limit $\frac{\Delta\nu}{\nu} = 3 \cdot 10^{-16}$ [1]. Further increase in the accuracy of standards is associated

with transition from the microwave range of the spectrum to the optical range and, hence, with the creation of optical standards based on single ions or neutral atoms. Atomic standards have an advantage over ionic ones in terms of the signal/noise ratio. The alkali-earth metals are of great interest, in particular magnesium, which is most promising in this group: it has the narrowest intercombination transition, the simplest model structure of the atom, and whose frequency shift due to the thermal radiation is an order of magnitude less at the intercombination transition [2]. The existence of a clock transition $^1S_0 - ^3P_1$ with a natural width of 30 Hz and a fast closed transition $^1S_0 - ^1P_1$ allows effective cooling and trapping of magnesium atoms in a magneto-optical trap, which makes it possible to create a frequency standard with a relative accuracy of $10^{-15} - 10^{-16}$ [3]. A radiation source at a wavelength of 457 nm for this standard should have high frequency stability and a linewidth of order of 1 Hz.

At Institute of Laser Physics, a Nd:YVO₄ laser with frequency doubling was developed. The frequency stabilization of this laser by the reference passband allows achieving a laser spectral linewidth of 1 kHz. In this paper, the results of stabilization of a Fabri-Perot reference are presented. A

⁴ To whom any correspondence should be addressed.

reference with a base of an optic glass-ceramic was isolated from external thermal impacts by a thermal shield, and from acoustic impacts, by a vacuum chamber. Vibrational effects are suppressed by an anti-vibrational platform. Despite a low thermal expansion coefficient ($10^{-7} K^{-1}$) of the glass-ceramic its temperature change even by 1 K leads to a frequency change of 30 MHz. To suppress the influence of external temperature changes, a thermostabilization system of the reference with a PID controller developed with the NI LabVIEW software was implemented (figure 1).

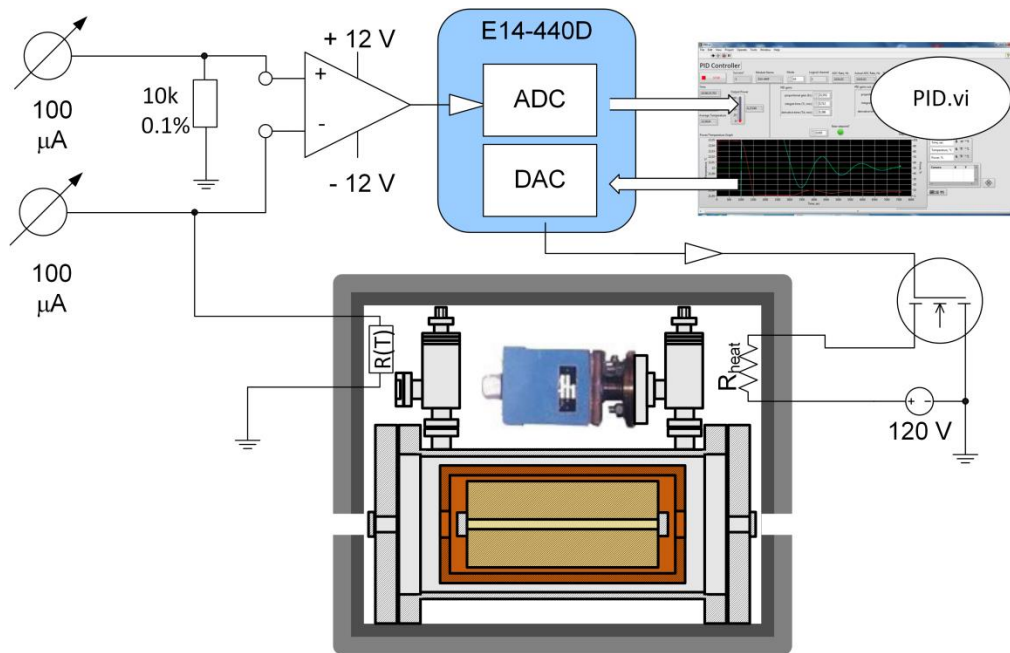


Figure 1. Reference thermostabilization scheme. The vacuum chamber with reference is in a metal case whose heater is an infrared thermofilm with 40 W power supply. The case is then isolated with polystyrene. R(T): thermistor ThorLabs TH10K, E14-440D: ADC/DAC external module (produced by L-Card).

The virtual instrument controls a key which locks the circuit of the heater power supply, and provides data visualization and registration. Power control is carried out with pulse-width modulation in the range from 0 % to 100 % with a 0,1 % step. The PID controller coefficients calculated with the Ziegler–Nichols tuning method allow one to maintain the reference case temperature with stability on a level of 1 mK. The obtained results will make it possible to decrease the laser system spectral linewidth and enhance the source frequency stability. In our further studies, possibilities of optimizing the stabilization parameters will be investigated.

References

- [1] <http://www.nist.gov/pml/div688/grp50/primary-frequency-standards.cfm>
- [2] Goncharov A N, Bonert A E, Brazhnikov D V, Shilov A M and Bagayev S N 2014 Precision spectroscopy of Mg atoms in a magneto-optical trap *Quantum Electronics* **44**(6) 521.
- [3] Bagayev S N, Baraulya V I, Bonert A E, Goncharov A N, Seidaliev M R and Farnosov S A 2001 A radiation source at 457 nm for high-resolution spectroscopy of a magnesium atom *Quantum Electronics* **31**(6) 495–499.

Diode pumped continuous-wave Tm,Ho:KYW microchip laser

**N V Gusakova*, O P Dernovich, S V Kurilchik, M P Demesh, V E Kisel,
A S Yasukevich and N V Kuleshov**

Center for Optical Materials and Technologies, Belarusian National Technical
University, Minsk, Belarus

Abstract. We report on a diode-pumped Tm,Ho:KY(WO₄)₂ microchip laser. Continuous-wave laser operation in the fundamental TEM₀₀ mode was obtained without active cooling of the crystal. Maximum output power of 77 mW at wavelength 2070 nm was achieved.

1. Introduction

Ho³⁺ doped solid state lasers operating at wavelength slightly above 2 μm are of interest for a variety of applications in remote sensing, medical treatment and for pumping of mid-IR optical parametric oscillators [1]. Using pulsed lamps as a pump sources of active elements limits overall efficiency and operation lifetime of such lasers [2]. Co-doping of laser crystals with Tm³⁺ ions allow to use commercially available AlGaAs laser diodes as pumping sources emitting around 800 nm. Cross-relaxation process in thulium ions and following nonradiative energy transfer to Ho³⁺ ions can provide effective population of holmium ⁵I₇ manifold [3,4]. Many previous studies have been reported for co-doped Tm,Ho crystals such as YAG [5], YLF [6], YVO₄ [7], and YAP [6]. Nevertheless the pump radiation at 790-800 nm in most cases was emitted by solid-state lasers that made the whole design bulky and quite costly. In our work we used fiber coupled laser diode as a pump source and demonstrated continuous-wave laser operation at 2070 nm with Tm,Ho:KY(WO₄)₂ (Tm,Ho:KYW) crystal in a microchip cavity configuration for the first time to our knowledge.

2. Experimental setup

Ng-cut Tm(5 at.),Ho(0.4 at.):KYW crystal with thickness of 2.98 mm was used as an active element. It was previously shown that such orientation of the crystal is favorable for arising the positive thermal lens in the crystal that enables stability of plane-plane microchip cavity configuration [8]. The experimental setup of Tm,Ho:KYW laser is shown in Figure 1. Fiber-coupled (d=105 μm, N.A.=0.15) AlGaAs laser diode (LD) with maximum available output power of 3 W at 802 nm and M²=20 was used as a pumping source. The LD radiation was collimated and focused in an active element to a spot of 120 μm diameter with two spherical lenses (f₁=70mm, f₂=80mm). The laser resonator was formed by two plane mirrors which were positioned in close proximity to the ends of the active medium. The HR plane input mirror was AR coated for pump radiation. The crystal faces were AR-coated for the pump radiation and the laser generation as well. The laser experiments were carried out for different transmission values of output coupler (T_{OC}=0.8%, 1.8%). The lateral sides of the laser crystal were in thermal contact with the aluminum heat sink, no active cooling of the laser crystal was provided.

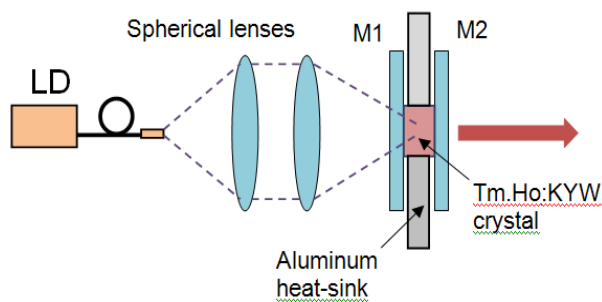


Figure 1. Experimental setup of Tm(5%), Ho(0.4%):KYW laser.

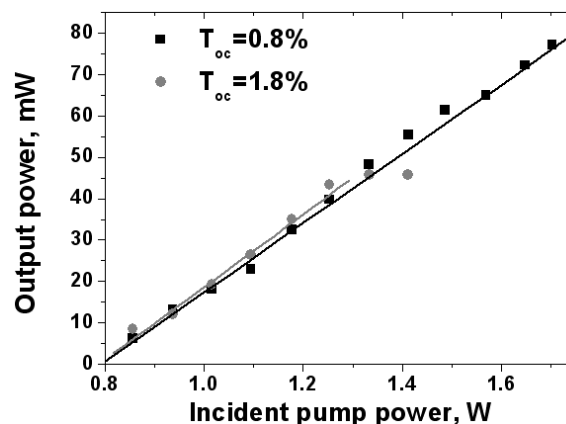


Figure 2. Input-output characteristics of Tm, Ho:KYW laser

3. Results

Continuous-wave operation was realized by using two output couplers with transmission of 0.8 and 1.8%. The laser performance characteristics are demonstrated in Figure 2. The highest output power of 77 mW at 2070 nm was obtained with 0.8 % output coupler. The corresponding slope efficiency of the laser with respect to incident pump power was estimated to be 8.5%. The laser threshold was about 0.8 W of incident pump power. The slope efficiency for output coupler $T_{oc}=1.8\%$ at low pump power was higher 9%, however maximum output power was limited up to 46 mW. It was observed in bending of input-output characteristic at higher pump power that can be caused by thermal stress inside the crystal. In the last case the laser wavelength shifted to 2058 nm that is attributed to higher level of cavity losses. In both cases the laser generated the fundamental TEM_{00} mode and the laser radiation was polarized along N_p principal axis of the crystal.

References

- [1] Scholle K, Lamrini S, Koopmann P and Fuhrberg P 2010 2 μ m laser sources and their possible applications *Frontiers in Guided Wave Optics and Optoelectronics* ed B Pal (Vukovar: Intech) p 471
- [2] Johnson L F, Boyd G D, Nassau K 1962 *Proc. IRE.* **50** p 87
- [3] Sudesh V, Asai K J. 2003 *Opt. Soc. Am.* **B 20(9)** pp 1829–1837
- [4] Sani E, Toncelli A, Tonelli M, Coluccelli N, Galzerano G, Laporta P 2005 *Appl. Phys. B* **81(6)** pp 847–851
- [5] Fan T Y, Huber G, Byer R L, Mitzscherlich P 1988 *IEEE J. Quantum Electron.* **24** pp 924–933
- [6] Elder I F, Payne M J 1998 *Optics Communications* **145** pp 329–339
- [7] Yao B Q, Li G, Meng P B, Zhu G L, Ju Y L, Wang Y Z 2010 *Laser Physics Letters* **7** pp 857-861
- [8] Gusakova N V, Yasukevich A S, Pavlyuk A A 2013 *540.WE-Heraeus-Seminar*

Pulse modulation of optical signals with high dynamic extinction ratio

A. Petrov^{1,2}, A.V. Tronev,³ V. Lebedev¹, E. Velichko^{2,3}, A. Shamray¹

¹Ioffe Physical Technical Institute, RAS, Saint Petersburg, Russia

²Saint Petersburg State Polytechnic University, Saint Petersburg, Russia

³Saint-Petersburg National Research University of Information Technologies, Mechanics and Optics, Saint-Petersburg, Russia

Abstract. The methods of extinction coefficient improvement based on saturable absorber are considered. The main principles and results are discussed. The statistical extinction coefficient was increased from 30 to 60 dB. The results are critical for impulse interrogators in multiunit systems of fiber optic sensors.

1. Introduction

The pulsed sources of optical radiation are widely used in modern systems of high-precision fiber-optic sensors. In time multiplexing interrogators and distributed systems based on coherent reflectometry, the extinction coefficient defines the noise level, dynamic range and sensitivity of the system. In such system the high characteristics of extinction coefficient are demanded. Optical impulses are formed by high coherent laser diode with distributed feedback in regime of continuous spectrum and external high frequency integrated optical modulator. The typical values of extinction coefficient are 20–30 dB but for practical uses the values 50–60 dB are needed.

In our work the methods based on saturable absorber are used for extinction coefficient improvement. The main principles and results are considered.

2. Results and discussion

The modulator based on Mach-Zehnder interferometer with extinction coefficient 30 dB was used as external integrated optical modulator. The saturable absorber was realized on optical fiber section doped with erbium. The base characteristics of saturable absorber, its minimal and maximal transmission factor were studied in static mode.

It was shown that static extinction coefficient may be increased to 60 dB. For dynamic extinction coefficient study the superconducting receiver of single photons was used. The transitional processes in dependence on saturable absorber parameters, maximal peak power, duration and frequency of impulses were also investigated. The results are critical for impulse interrogators in multiunit systems of fiber optic sensors.

Pointed and traveling wave models for different laser regime simulations

Liubou Krylova, George Krylov

Belarusian State University, Physics faculty, Nezaleznaŭski av. 4, Minsk 220030, Belarus

Abstract. We compare pointed dynamic laser model with spatially distributed one, $Nd : LSB$ laser is considered as a test example.

1. Introduction

Problems of optimization of laser systems are among the most substantial in laser physics. One usually uses the following approach to these problems. The dynamics of level populations is described via the balance (rate) equations. The intensity of the lasing is modeled either with a pointed dynamic model (when it is necessary to estimate dynamics features) or a steady-state spatially distributed (for example, when one needs to obtain power characteristics of the laser system with strong spatial inhomogeneity)[1, 2, 3, 4].

We focus on the possibility to use different models and appropriate constraints that are imposed on a system. On the one hand, concerning steady-state distributed model, its main constraint is the impossibility to study system dynamics. On the other hand, the pointed model is stated in terms of spatially-averaged values, thus it is poorly suitable for regimes with significant spatial inhomogeneities.

Thereby, it becomes necessary to use an equations system that unites the advantages of both pointed and distributed model. These so-called traveling wave model (also known as time-space distributed model) become widespread nowadays [5, 6, 7]. One of the main applications of this model is the case of Q-switched regime, where we fast intensity increase at the beginning of generation.

Being numerically simulated, it may lead to solution divergence. The decrease of integration step to may help to overcome this divergence, but this is not an option due to significant computation time increase and error accumulation. As it turned out, a proper units choice may solve the divergence problem to some extent. In paper [4] its authors propose dimensionless units. In this paper we use as an example of $Nd : LSB$ microchip laser with $Cr : YAG$ saturable absorber. All constants were taking from [8].

In order to use these units for the distributed model, they have to be rewritten in the following way: $G = gL_g$, $G_s = g_sL_s$

$$\frac{dD}{dt} = \frac{\tau_c}{\alpha_L} \gamma (1 - (1 + (u^+ - u^-))D)$$

$$\frac{dD_s}{dt} = \frac{\tau_c}{\alpha_L} \gamma_1 (-1 - (1 + \alpha(u^+ + u^-))D_s)$$

$$\frac{\alpha_L}{\tau_c} \frac{\partial u^+}{\partial t} - \frac{\partial u^+}{\partial x} = (-1 + AD + A_1 D_s)u^+ + R_{lum}(1 - D) \quad (1)$$

$$\frac{\alpha_L}{\tau_c} \frac{\partial u^-}{\partial t} + \frac{\partial u^-}{\partial x} = (-1 + AD + A_1 D_s)u^- + R_{lum}(1 - D)$$

$$D = \frac{(1 + \gamma_a \tau_g I) \cdot g}{N_T I \tau_g}, D_s = \frac{g_s}{N_0 \sigma_a}, u^\pm = \frac{\gamma_e \tau_g R^\pm}{1 + \gamma_a \tau_g I}, \tau_c = \frac{(L_g + L_s)n}{c} \quad (2)$$

$$g = \gamma_e N_2, g_s = (\sigma_e N_{2s} - \sigma_a (N_0 - N_{2s})), \alpha = \frac{\sigma^+ \tau_s}{\gamma_e \tau_g} (1 + \gamma_a \tau_g I)$$

$$\gamma = \frac{\tau_c (1 + \gamma_a \tau_g I)}{\tau_g \alpha_L}, \gamma_1 = \frac{\tau_c}{\tau_s \alpha_L}, R^\pm = u^\pm \frac{1 + \gamma_a \tau_g I}{\gamma_e \tau_g}$$

The boundary conditions are:

$$u^+(0, t) = r_1 u^-(0, t); u^-(1, t) = r_2 u^+(1, t); u^\pm(x, 0) = 0 \quad (3)$$

The above system is completely formulated in terms of local values and fits the requirements of distributed system. The proposed distributed model and the pointed one [4] should give matching results in the case of homogeneous value distribution over the resonator (for example, in cw regime) fig.1.

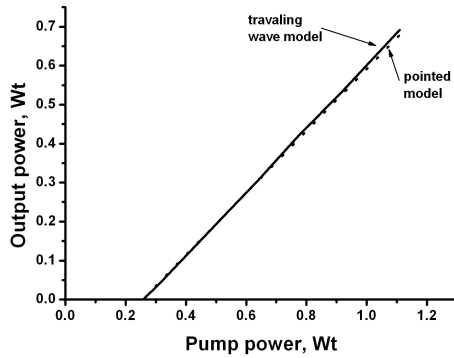


Figure 1. Generation power vs. the pump power for pointed (dash) and traveling wave (solid) models in cw regime.

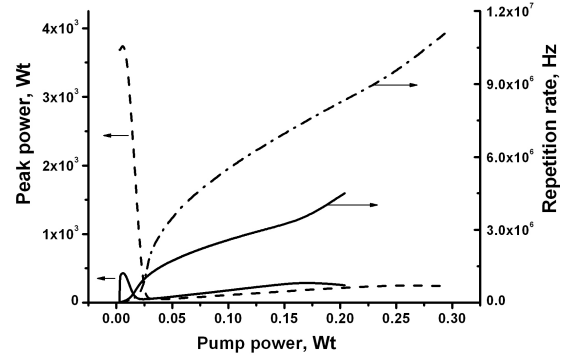


Figure 2. Generation peak power and repetition rate vs. the pump power for pointed (dash) and traveling wave (solid) models in Q-switched regime.

The models reveal significantly different results when spatial inhomogeneity is present (for example, when we introduce a saturable absorber into a transversely pumped resonator). Nevertheless, being compared to experimental data, our distributed model gives more realistic results.

Thus, the use of pointed model is limited to a few of use cases (cw-regimes with transverse or averaged longitudinal pumping).

The presence of considerable inhomogeneity of value distributions makes pointed model application in Q-switched regime rather dubious.

- [1] Feng S., Li S., Chen L., Chen W., Hu L. 2010 *Applied Optics*. **49** 3357
- [2] Agnesi A., Dell'Acqua S., Morello C., Piccinno G., Reali G. C., Sun Z. 1997 *IEEE J. Select. Topic Quant. Electron.* **3** 45
- [3] Degnan. J.J. 1989 *IEEE J. of Quant. Electr.* **25** 214
- [4] Peterson P., Gavrielides A., Sharma M.P., Erneux T. 1999 *IEEE J. Quant. Electron.* **35** 1247
- [5] Burov L.I., Krylov G.G., Krylova L. G. 2010 *Nonlinear Phenomena in Complex Systems* **4** 368
- [6] Kolpakov S.A., Barmenkov Y.O., Kiryanov A.V., Guzman-Chavez A.D., Cruz M.V., Andres J.L. 2012 *J. Opt. Soc. Am. B.* **29** 2453
- [7] Burov L. I., Krylova L. G. 2012 *J. Appl. Spectr.* **79** 397
- [8] S.V.Voitikov, A.A. Demidovich, L.E.Baaty, A.N.Kuzmin, M.B.Danilov. 2005 *Opt. Comm.* **251** 154

Application of GaN for photoelectrolysis of water

A D Fomichev¹, M V Puzyk², A S Usikov^{1,3}, S Yu Kurin⁴, I A Ermakov¹, D S Kovalev¹, B P Papchenko¹, H Helava³, and Yu N Makarov^{3,4}

¹University ITMO, Kronverkskiy pr. 49, St. Petersburg 197101, Russia

²Herzen University, Nab. r. Moyki 48, St. Petersburg 194186, Russia

³Nitride Crystals Inc., 181 E Industry Court, Suite B, Deer Park, NY 11729, USA

⁴Nitride Crystals Group Ltd., pr. Engel'sa 27, St. Petersburg 194156, Russia

Abstract. GaN layers n-type and p-type conductivity grown by HVPE on sapphire substrates were used as working electrodes for water electrolysis and photoelectrolysis and hydrogen gas generation. Specifics of water splitting process is discussed. Corrosion of the GaN materials are also considered.

Currently, there are several basic technologies used for the production of hydrogen: the conversion of methane, technologies for converting biomass into valuable fuel, and the decomposition of water. Semiconductor material immersed in an aqueous solution of electrolyte allows decomposition of water into molecular hydrogen and oxygen by solar irradiation of its surface. Required energy to split water molecule generates due to sunlight absorption in the semiconductor. This method of H₂ generation is a simple, low-energy consumption, carbon-free technology not demanding high temperatures and pressure. Another key benefit of this process is the high purity of the output hydrogen gas stream, an important requirement for its use in fuel cells.

The solar water splitting process may be spontaneous under illumination if electrochemical redox potentials of oxygen evolution reaction (OER) and hydrogen evolution reaction (HER) in an electrolyte bracket by the energy gap of a semiconductor [1]. This is fulfilled for GaN and InGaN materials [2]. A generic diagram of photoelectrochemical water splitting using GaN material and an alkaline electrolyte is given in figure 1.

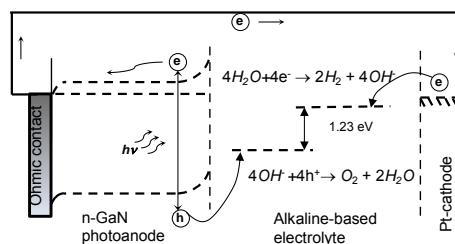


Figure 1. Schematic diagram showing photoelectrochemical water splitting using n-type GaN as a working electrode (photoanode).

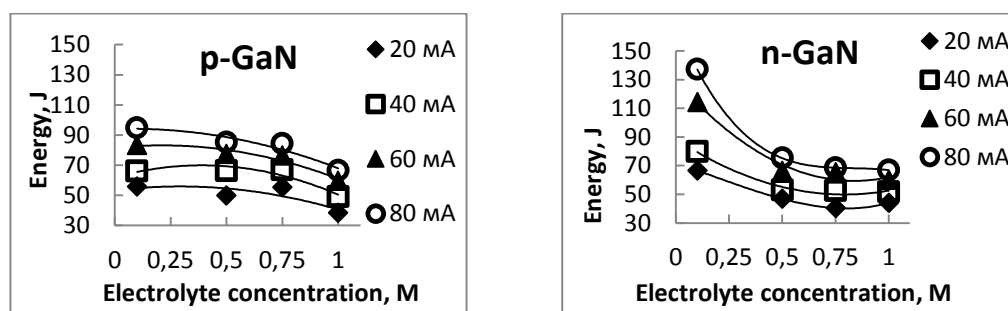


Figure 2. Energetics of a 1 ml H₂ generation during water electrolysis using n-GaN working electrode (cathode) depending on a concentration of Na₂SO₄-based electrolyte (0.1, 0.5, 0.75, 1.0 M).

The absorption of solar photon in a semiconductor material form an excited electron–hole pairs that split by a specific bend bending on the GaN electrode (anode) surface. Excited electrons come through external circuit to Pt-cathode and take place in HER that gives ions of OH⁻ (anion) and molecules of H₂. The anions come to the GaN-anode to participate together with exited holes leaving the semiconductor in OER that gives molecules O₂ and H₂O.

In this work we report on first results of electrolysis and photoelectrolysis of water using different electrolytes and n-type and p-type GaN layers as working electrodes. 5-7 μm thick GaN layers were grown on sapphire substrates by chloride hydride vapor phase epitaxy [3]. Sulfuric acid (pH = 1), sodium sulphate (pH = 7) or sodium hydroxide (pH = 14) were used as the electrolyte.

Energy required for a 1 ml H₂ generation depending on electrolyte concentration is given in figure 2. The process is more energy-consumed at lower electrolyte concentration and smaller currents on n-GaN electrode than on p-GaN one. It seems to reflect band bending at the n-GaN electrode surface that creates an additional energy barrier for electrons. At high concentration of electrolyte and high current the band bending effectively becomes lower and overall energy consumption for the process on the n-GaN electrode is somewhat lower than at the p-GaN electrode due to higher carrier mobility and better current spreading in the n-GaN material. It was also noted that the electrolysis takes place with the least energy consumption for n-GaN and p-GaN electrodes in the alkaline solution.

Hydrogen generation at n-GaN cathode started at low potential values depending on pH of the electrolyte. n-GaN layers found to be electrochemically inactive (no corrosion) at potentials from -1.5 V to +1.5 V in all aqueous electrolytes applied in this work. O₂ generation on the p-GaN anode (H₂ generation was observed on Pt-counter electrode in this case) began at potential more than +2V and accompanied by the p-GaN electrode corrosion.

Experiments on water photoelectrolysis were performed with Xenon light bulb (100 mW/cm²) or 365 nm UV LED and external power source. H₂ generation was observed on Pt cathode using n-GaN as photoanode. The experiments have shown that doping and crystalline quality of the GaN electrodes need to be optimized. The use of GaN/InGaN structures as working electrodes has to increase the photoelectrolysis productivity.

Acknowledgments

Work at University ITMO was supported by the Ministry of Education and Science of Russian Federation within the grant agreement 14.575.21.0054 (unique identifier of research activities is RFMEFI57514X0054).

References

- [1] Pinaud B A, Benck J D, Seitz L C et al. 2013 *Energy Environ. Sci.* **6** 1983-2002
- [2] Fujii K, Ohkawa K 2006 *Phys. Status Solidi C* **3** 2270–2273
- [3] Kurin S, Antipov A, Barash, I, Roenkov A et al. 2014 *Phys. Status Solidi C* **11** 813-816

Nanomaterial disordering in AlGaIn/GaN UV LED structures

E I Shabunina¹, M E Levinshtein¹, M M Kulagina¹, S Yu Kurin², A E Chernyakov³, V N Petrov¹, V V Ratnikov¹, I N Smirnova¹, S I Troshkov¹, N M Shmidt¹, A S Usikov^{4,5}, H Helava⁵, and Yu N Makarov^{2,5}

¹Ioffe Physical Technical Institute, Polytekhnicheskaya 26, St. Petersburg 194021, Russia

²Nitride Crystals Group Ltd., 27 Engels av., St Petersburg 194156, Russia

³Submicron Heterostructures for Microelectronics Research and Engineering Center RAS, Polytekhnicheskaya 26, St. Petersburg 194021, Russia

⁴University ITMO, Kronverkskiy pr. 49, St. Petersburg 197101, Russia

⁵Nitride Crystals Inc., 181E Industry Ct., Ste. B, Deer Park, NY 11729, USA

Abstract. It was demonstrated that disordering in AlGaIn/GaN LED structures is high and leads to shunt of the active region by an extended defect system. Conductivity of quasi-ohmic shunts localized in extended defect system is higher in AlGaIn/GaN structures than in InGaIn/GaN ones. As a result, carrier concentration participating in an radiative recombination in the active region of an AlGaIn/GaN LED reduces and it is one of the reasons behind low external quantum efficiency in the AlGaIn/GaN UV LEDs.

Development of high brightness InGaIn-based blue LEDs has demonstrated that structural quality is one of the important factors to get high external efficiency and long life-time of the LED lamps. However the structural quality mostly is not in strictly direct relation to threading dislocations (the lower dislocation density the better structural quality) but in connection with a nature of nano-structural arrangement (nanomaterial disordering) attributed to III-N materials. It was found that changes of nanomaterial disordering causing by different angles of tilt and twist of mosaic structure domains reflect in surface morphology. It allows examining the surface with a help of the atomic force microscopy for characterization of nanomaterial disordering quantitatively on the base of multifractal analysis [1]. It has been observed a correlation of nanomaterial disordering with multifractal parameters determined based on the surface morphology examination [1, 2].

Most of these correlations were observed in thick GaIn layers and relatively thin multilayer III-N structures. Quasi-ohmic shunts localized in extended system defects were observed in a 150- μm thick GaIn/sapphire template substrates with dislocation density of 10^6 cm^{-2} [3] and in InGaIn/GaN and AlGaIn/GaN light emitting diodes [2, 4]. The correlation between properties of UV AlGaIn/GaN LED structures and degree of disorder was not considered. In this paper we report on studies of AlGaIn/GaN structures with different parameters of nanomaterial disorder (degree of disorder - Δ_p and level of self-organization - D [4]) in relation with I-V characteristics of AlGaIn/GaN UV LEDs having different parameters of disorder conductivity of leakage paths (shunts) and values of a low-frequency noise.

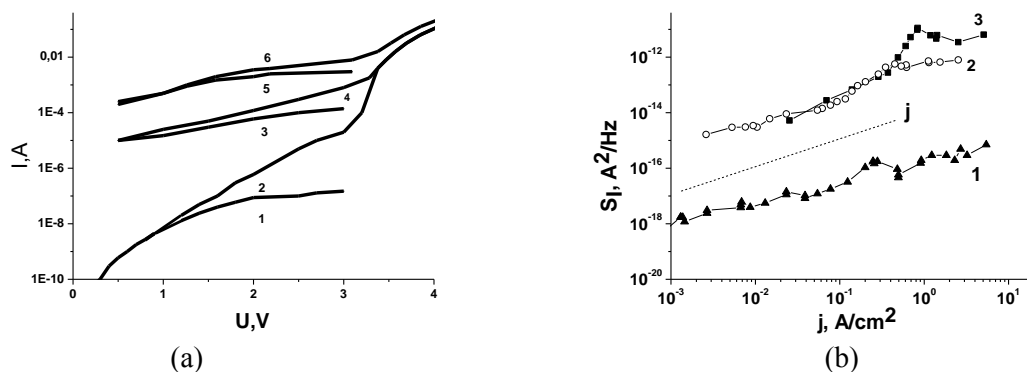


Figure 1. (a) I-V characteristics of AlGaIn/GaN UV LEDs having different parameters of disorder (Δ_p and D): curves 1,2 – 0.348 and 1.62; curves 3,4 – 0.37 and 1.78; curve 5,6 – 0.39 and 1.84. Curves 2,4,6 –direct current, curves 1,3,5 –reverse current. (b) The spectral noise density (S) in relation with current density (j). Curves 1, 2, 3 corresponds to I-V curves 1 and 2, 3 and 4, 5 and 6 in Figure 1(a), respectively.

Two type of LED were under comparison study. They are AlGaIn/GaN UV LEDs fabricated at the frame of this work and commercial available high- power InGaIn/GaN blue LEDs. The AlGaIn-based UV LED structures were grown by hydride vapor phase epitaxy HVPE on c-plane 2-inch sapphire substrates. Details of the structures growth and characterization can be found elsewhere [5]. The structures grown were processed to form mesas and deposit contacts. Fabricated chips had planar dimensions of $850 \mu\text{m} \times 850 \mu\text{m}$ with light extraction through the surface. Peak wavelength of electroluminescence (EL) was at 360-350 nm. Fabricated chips had external quantum efficiency (EQE) of 1.5%. Commercial available 450-460 nm blue InGaIn LED chips ($980 \mu\text{m} \times 980 \mu\text{m}$) having EQE of 40-45% were used for comparative studies. Evolution of I-V characteristics and external quantum efficiency were studied. The low frequency noise (LFN) methods were also used.

It has been shown that an increase in the parameters of nanomaterial disorder is accompanied by an increasing of direct and reverse currents at low voltage ($U < 3 \text{ V}$), conductivity of leakage paths (shunts) and values of low-frequency noise (see figure 1). These phenomena are similar to those in InGaIn/GaN structures. However, for AlGaIn/GaN structures with the lowest values of current the values of degree of disorder and shunt's conductivity are higher than that in InGaIn/GaN ones. In addition, all multifractal parameters (Δ_p and D) are larger too in AlGaIn/GaN structures and are typical for structures with low EQE values (less than 5%). The dependence of spectral noise density (S) on current density (j) has near monotonic tendency ($S(j) \sim j$) and is similar to the one in InGaIn/GaN structures, which is, to a large extent, related to processes in extended defect system shunting p-n-junction. The results obtained allow us to assume that high values of conductivity of quasi-ohmic shunts localized in extended defect system is one of the reasons behind low external quantum efficiency values in AlGaIn/GaN LEDs. More results and discussion will be presented.

Acknowledgments

Work at University ITMO was supported by the Ministry of Education and Science of Russian Federation within the grant agreement 14.575.21.0054 (unique identifier of research activities is RFMEFI57514X0054).

References

- [1] Shmidt N M et al. 2001 *Nanotechnology* **12** 471
- [2] Shmidt N M et al. 2015 *Phys. Status Solidi C* 1-4
- [3] Scajev P et al. 2012 *Journal of Applied Physics* **111** 023702
- [4] Pinos A et al. 2011 *Journal of Applied Physics* **109** 103108
- [5] Kurin S, Antipov A, Barash I, Roenkov A et al. 2014 *Phys. Status Solidi C* **11** 813-816

Diode lasers with asymmetric barriers for 850 nm spectral range: experimental studies of power characteristics

F.I. Zubov^{1,2}, A.E. Zhukov^{1,2}, Yu.M. Shernyakov^{3,1}, M.V. Maximov^{1,3,2},
E.S. Semenova⁴, L.V. Asryan⁵

¹ St. Petersburg Academic University, 194021, St. Petersburg, Russia

² St. Petersburg State Polytechnical University, 195251, St. Petersburg, Russia

³ Ioffe Physical-Technical Institute of RAS, 194021 St. Petersburg, Russia

⁴ DTU Fotonik, Technical University of Denmark, Kgs. Lyngby, DK-2800, Denmark

⁵ Virginia Polytechnic Institute and State University, Blacksburg, Virginia 24061, USA

Abstract. It is demonstrated that the use of asymmetric barrier layers in a waveguide of a diode laser suppress non-linearity of light-current characteristic and thus improve output power under high current injection. The results are presented for 850-nm AlGaAs/GaAs broad-area lasers with GaInP and AlInGaAs asymmetric barriers.

1. Introduction

It was proposed to use so-called asymmetric barrier layers (ABLs) on both sides of active region to improve temperature stability of diode lasers [1]. ABL that is closer to n -emitter should pass only electrons and another ABL, closer to p -emitter, should pass only holes. As a result, charge carriers in such laser coexist and, consequently, recombine only in the active region. Implementation of this concept is aimed at suppression of parasitic recombination in waveguide layers – the main problem of diode lasers with small localization energy of charge carriers in the active region, which in particular leads to decrease of efficiency of conversion of electrical energy into energy of laser radiation. Earlier [2] we have fabricated for the first time diode lasers with asymmetric barriers (LABs). Their experimental studies revealed that the introduction of ABLs leads to reduction in threshold current, increase in external differential quantum efficiency and decrease in internal optical losses near the lasing threshold, as well as increase in temperature stability.

2. Experiment

In this work, we fabricated 850 nm quantum well lasers with asymmetric barriers of optimized design and measured its power characteristics. Structures were grown by MOCVD on n^+ GaAs substrates. Here we used 7 nm-thick $\text{Ga}_{0.55}\text{In}_{0.45}\text{P}$ and $\text{Al}_{0.42}\text{Ga}_{0.38}\text{In}_{0.2}\text{As}$ ABLs located on the n - and p -side of the

quantum well, respectively. To reduce power density in ABLs, as well as to increase the output optical power of the device, we used a 800 nm wide waveguiding layer.

3. Results

The introduction of ABLs has not reduced the threshold of the catastrophic optical mirror damage (COMD) P_{COMD} . At the same time, it significantly improved linearity of light-current characteristic (Fig. 1). It is seen that light-current curve of LAB remain linear up to approximately 7 A whereas the test laser demonstrate a significant saturation of L-I curve starting from 4 A. As a result, a maximal optical power of about 9.2 W in LAB achieved by 60% lower pumping than in test laser of conventional design without ABLs.

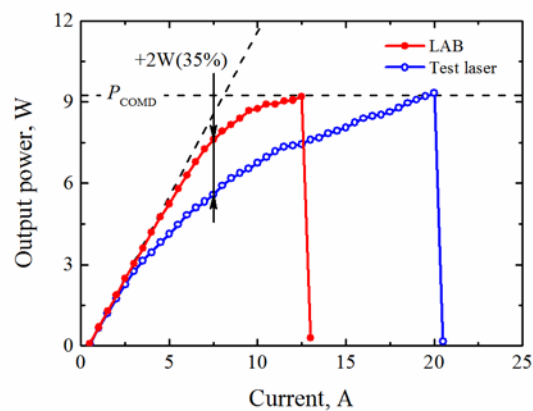


Figure 1. Output optical power versus pumping current in LAB and test laser without ABLs measured in pulse pumping regime at 20°C.

Acknowledgement

This work is supported by the Russian Scientific Foundation (project 14-42-00006 «A novel type of diode lasers with characteristics improved by using asymmetric barriers»).

References

- [1] Asryan L V and Luryi S 2003 *Solid-State Electron.* **47** 205.
- [2] Zhukov A E, Kryzhanovskaya N V, Zubov F I, Shernyakov Yu M, Maximov M V, Semenova E S, Yvind K and Asryan L V 2012 *Appl. Phys. Lett.* **100** 021107.

Microdisk lasers based on GaInNAsSb/GaAsN quantum well active region

E I Moiseev¹, N V Kryzhanovskaya¹, Yu V Kudashova¹, M V Maximov¹,
M M Kulagina³, S I Troshkov³, A A Lipovskii^{2,1}, V-M Korpijärvi⁴,
H Karjalainen⁴, T Niemi⁴, M Guina⁴, A E Zhukov¹

¹ St. Petersburg Academic University, Nanotechnology Center for Research and Education, Russian Academy of Sciences, St. Petersburg, 194021 Russia

² St. Petersburg Polytechnic University, St. Petersburg, 195251 Russia

³ Ioffe Physical–Technical Institute, Russian Academy of Sciences, St. Petersburg, 194021 Russia

⁴ Optoelectronics Research Centre, Tampere University of Technology, Tampere, Finland

Abstract. Microdisk lasers based on novel InGaAsNSb/GaAsN quantum well active region are developed and studied under optical pumping. Room temperature lasing at 1.5 μm in 4 μm in diameter microdisks with InGaAsNSb/GaAs QW is demonstrated.

1. Introduction

Semiconductors microdisk and microring lasers have been widely investigated as possible building blocks for photonic integrated circuits [1]. The circular symmetry of the cavity results in unique advantages such as low threshold, small foot-print, small mode volume, in-plane emission, control of emission wavelength from the device size, etc. [2]. The use of quantum dots (QDs) as active region in such lasers have the advantages of low threshold, high quantum efficiency, and high thermal stability of characteristics [3]. However since the ground state QDs optical gain is limited due to the finite number of the QDs the decrease of the resonator diameter to a limiting value results in lasing via excited states of QDs. Quantum well (QW) active region provides higher gain compare to QDs. Thus the use of QW active region may help to work out the problem of gain saturation when the laser's size are scaled down. In this work we have studied microdisk lasers based on single novel InGaAsNSb/GaAs(N) QW active region. Deep localization of carriers in these QWs results in improved temperature stability of lasing parameters due to the large conduction band offset between the GaInNAsSb QW and GaAs barriers [4]. We demonstrate single-mode lasing at room temperature in microdisk laser with diameter less than 4 μm .

2. Experiment

The epitaxial structure with InGaAsNSb/GaAsN QW was grown by MOCVD on n-doped GaAs substrate. The QW was inserted in the GaAsN strain compensating layer. Active region was placed in the middle of the GaAs layer confined from both sides with 10 nm thick $\text{Al}_{0.3}\text{Ga}_{0.7}\text{As}$ barriers to prevent carrier leakage. Total thickness of the waveguide layer was 240 nm. This waveguide layer was grown on the top of the 1500-nm-thick $\text{Al}_x\text{Ga}_{1-x}\text{As}$ layer that later forming a pedestal of the microdisks

($\chi=0.7-0.8$). Microdisks of different diameters from 1 to 6 μm were fabricated using photolithography and two step wet etching. Scanning electron micrograph of the 4 μm diameter microdisk laser is shown in Fig.1. The structures were investigated under optical pumping with YAG: Nd laser ($\lambda = 532\text{nm}$).

3. Results

The microphotoluminescence (μPL) spectra of the lasers were studied in a temperature range from 100 to 300K. The inset in Fig.2 shows temperature dependence of the threshold power of the microdisk laser with diameter $D = 4 \mu\text{m}$. The lasing on whispering gallery mode of the resonator was observed in temperature range from 130 K to 220K. At low temperature (130K) the threshold power is approximately 0.2 mW. The quality factor obtained from $(\lambda/\Delta\lambda)$ 20 000. When the temperature increases to 220K the threshold power increase and become 0.32 mW due to increase if the nonradiative processes in active region.

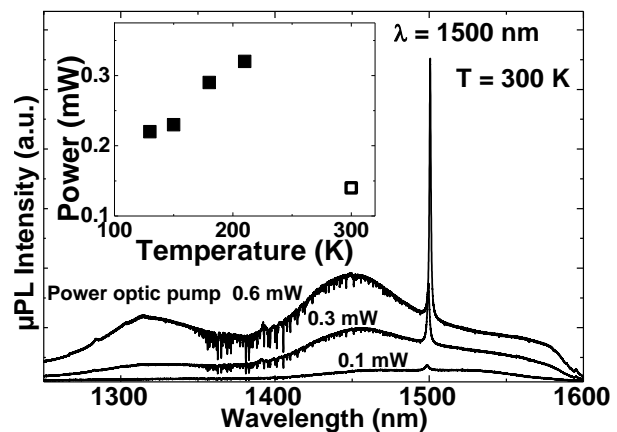
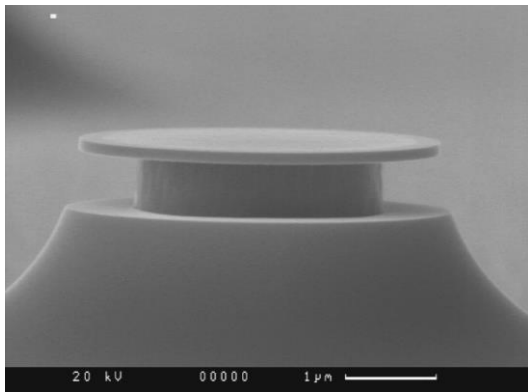


Figure 1. SEM image of a microdisk laser with $D = 4 \mu\text{m}$

Figure 2. Room temperature μPL spectra of 4 μm microdisk laser at different excitation power. Inset shows threshold power as a function of the temperature before (solid symbols) and after surface passivation (open symbols).

To obtain room-temperature lasing the structure with microdisk mesas was passivated in sulfur solution. The μPL spectra of the microdisk with diameter $D = 4 \mu\text{m}$ obtained at 300 K at different pump power are shown at fig.2. At the spectra we observe spontaneous emission from QW active region and a single narrow line corresponding to the whispering gallery mode of the microdisk resonator. The wavelength of the line is 1.5 μm . Increase of the pump power results in the rapid increase of the line intensity with threshold power 0.14 mW. To conclude, microdisk lasers with novel active region based on GaInNAsSb QW were investigated before and after passivation in a temperature range 100-300K. Room temperature single-mode lasing in microdisk laser with diameter 4 μm is demonstrated.

4. Acknowledgments

The work is supported by the Skolkovo Foundation (grant agreement for Russian educational and scientific organization no.4 dd. 25.12.2014).

References

- [1] S. Koseki et al, Applied Physics Letters, 94, 051110 (2009).
- [2] K. Srinivasan et al, Optics Express, 14 (3), 1094-1105 (2006).
- [3] Y. Arakawa, H. Sakaki, Appl. Phys. Lett. 40 939 (1982).
- [4] S. R. Bank et al, IEEE Journal of selected topics in QE, 11 (5), 1089–1098 (2005).

The effect of the sulfide passivation on the luminescence of microdisk mesas with quantum wells and quantum dots

Yu.V. Kudashova¹, N.V. Kryzhanovskaya¹, M.V. Lebedev², T.V. Lvova²,
I.I. Shostak¹, E.I. Moiseev¹, A.E. Zhukov^{1,3}, M.V. Maximov^{1,2},
M.M. Kulagina², A.M. Nadtochiy¹, S.I. Troshkov²

¹ St. Petersburg Academic University, Nanotechnology Center for Research and Education, Russian Academy of Sciences, St. Petersburg, 194021 Russia

² Ioffe Physical–Technical Institute, Russian Academy of Sciences, St. Petersburg, 194021 Russia

³ St Petersburg Scientific Center of RAS, 199034 St Petersburg, Russia

Yu.v.kudashova@mail.ru

Abstract. Sulfide passivation was used for reducing the surface recombination velocity of microdisk mesas based on (AlGaIn)As/GaAs heterostructures with active region formed either by ten GaAs/AlAs quantum wells or by 1 layer of InAs/In_{0.15}Ga_{0.85}As quantum dots. It was demonstrated that the sulfide passivation results in substantial increase of photoluminescence intensity in all types of the mesa-structures considered.

1. Introduction

Semiconductor lasers with ring and disk microresonators are good candidates for use in optical integrated circuits. Advantages of such microresonators are high quality factor of whispering gallery modes, small foot-print and low threshold current [1]. Recently InAs/InGaAs quantum dot based microdisk (MD) lasers as small as 2 μm in diameter were realized [2]. Further decrease of the MD diameter results in the switch of the lasing wavelength from the ground to excited state of QD array due to saturation of the QD modal gain. Quantum well (QW) active region provide higher gain compare to QDs but lateral localization of carriers is absent. In this work we develop the passivation method to reduce side-wall recombination in microdisk mesa-structures of different diameters and study microphotoluminescence intensity of QW and QD based microdisks before and after passivation [3].

2. Experiment

Two structures were grown by molecular beam epitaxy on semi-insulating GaAs (100) substrate. The active region in the first structure was formed by ten 10 nm-thick GaAs/AlAs QWs (MQW structure) and in the second structure by one layer of InAs/In_{0.15}Ga_{0.85}As QDs (QD structure). QDs were formed by Stransky-Krastanov method and the wavelength of ground state photoluminescence (PL) intensity maximum is 1280 nm at 300K. The wavelength of PL intensity maximum for structure with QWs is 850 nm 300K. Microdisk mesas with different diameters (from 2 to 6 μm) were formed using photolithography and wet etched by HBr:K₂Cr₂O₇:CH₃COOH solution. The structure were passivated by water solution of sodium sulphide (Na₂S:9H₂O) during approximately 4 minutes. Fig.1 shows

scanning electron microscopy (SEM) image of the microdisk mesa with 2.8 μm diameter after passivation. We observe that the passivation treatment does not affect the mesa. The microPL of the mesas was investigated under pumping with YAG:Nd laser ($\lambda = 527\text{nm}$) at room temperature before and after passivation.

3. Results

After passivation treatment the integral microPL intensity of both structures was increased. For example the microPL intensity increased in 35 times for 3.7 μm in diameter mesa of MQW structure and in 3 times for 3.9 μm in diameter mesa of QD structure. Fig.2 shows dependencies of normalized integral microPL intensities for both structures on the diameters of the mesas before and after passivation. The intensities were normalized on the intensity of the initial structures before mesa etching. After mesa etching the intensities of the both structures decreases. The intensity drop is stronger for the mesas with smaller diameters due to larger impact of the nonradiative recombination on the side walls and for the MQW structure compare to QD structure. This difference is due to the effective carrier localization in QDs.

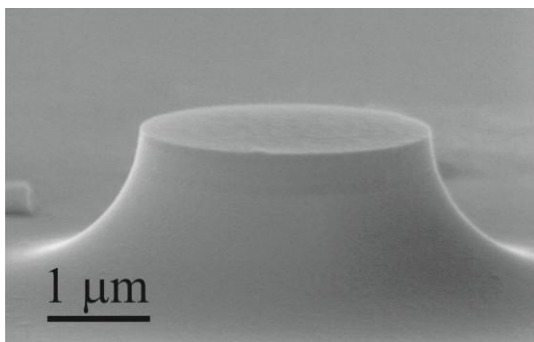


Fig.1 SEM image of the microdisk mesa with 2.8 μm diameter after passivation.

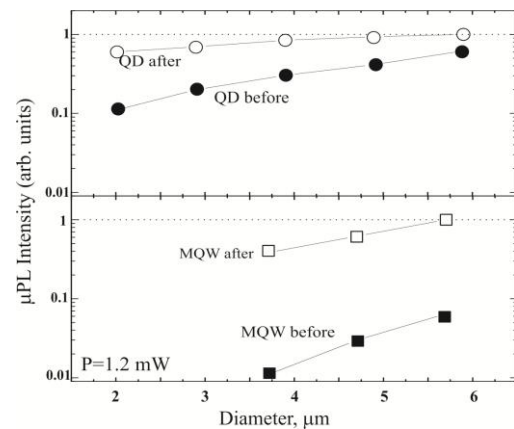


Fig.2 The normalized microPL intensity versus mesa's diameters for MQW(squares) and QD (circles) structures before (solid symbols) and after passivation (open symbols).

After surface passivation we observe increase of microPL intensity for all mesa diameters. In the mesa with largest diameters the intensity becomes nearly the same as in initial structures. The effect of passivation is more pronounced for MQW structure due to the larger diffusion length and smaller carrier localization energy compare to QD structure.

4. Acknowledgments

The work is supported by the Skolkovo Foundation (grant agreement for Russian educational and scientific organisation no.4 dd. 25.12.2014)

5. References

- [1] Baba T. and Sano D. IEEE J. Sel. Top. Quantum Electron 9, pp.1340 (2003).
- [2] Maximov M. V., Kryzhanovskaya N. V., Nadtochiy A. M., Moiseev E. I., Shostak I. I., Bogdanov A. A., Sadrieva Z. F., Zhukov A. E., Lipovskii A. A., Karpov D. V., Laukkanen J., Tommila J. Nanoscale Research Letters 9, pp.657 (2014).
- [3] Hobson W. S., Ren F., Mohideen U., Slusher R. E., Pearton S. J. J. Vac. Sci. Technol. A 13, pp. 642 (1995).

Modulation doping of quantum dot laser active area and its impact on lasing performance

S S Konoplev, A V Savelyev, V V Korenev, M V Maximov,
A E Zhukov

St Petersburg Academic University, St. Petersburg, 194021 Russia

Abstract. We present a theoretical study of modulation doping of active region in the quantum dot (QD) laser and corresponding issues of QD charge neutrality violation, band diagram of the laser and charge carriers distribution in the structure. Modulation doping is discussed as possible technique to control laser output characteristics. It was shown that modulation doping leads to increase of threshold current of lasing through excited QD optical transition together with power emission from QD ground state.

1. Introduction

The GaAs/AlGaAs semiconductor laser with InAs QD has several advantages compared to quantum well laser such as low threshold current and better temperature stability. The reason of such improvements is δ -like density of states in QD. However, when excited states (ES) of quantum dots are involved in lasing QD laser advantages become less pronounced. The major goal of this work is to study possibilities of suppression of ES lasing via modulation doping of thin layers near QD planes. It was shown earlier [1] that charging of QDs plays an important role in lasing though high-power lasing regime and ES emission were not discussed. Later, impact of charge redistribution between QDs and surrounding matrix was intensively discussed (see [2] and reference therein) on a phenomenological basis and experimentally [3]. The ration of holes to electron capture rates ('h-factor') was suggested as phenomenological parameter that is constant with respect to injection current. We present thorough theoretical study of laser band diagram in high injection regime in order to clarify origin of the non-unity value of the h-factor, its dependence on laser design and injection current. Finally, we study L-I curves in modulation doped structures and compare it with known experimental results.

2. Model and results

In order to address ES-lasing we choose three-level model of QD with two electron levels and one effective hole level. The lasing phenomenon was described on a basis of QD rate equations for localized carriers and photons in laser resonator. Drift-diffusion equation was solved in order to calculate band diagram of laser structure with modulation doping and charged quantum dots. Both analytical and numerical approaches to band diagram calculations were discussed. As a result, two-step approach was proposed to obtain accurate results with clear physical meaning: numerical modelling of emitter/active region boundary and following analytical calculation of QDs' properties.

It has been shown that h-factor is variable and depends on the carrier concentration near QD, doping and injection current. In the non-doped laser QDs become charged, ground electron state (GS) fully filled that suppress gain and lasing through GS in favor to ES emission. Our calculations demonstrate that p-type modulation layer lead to neutralization of QDs and increase of ground state gain. That, in turn, leads to an increase of threshold current for lasing via ES and increase power radiated from ground state. On the other hand, n-type doping leads to decrease of threshold current and can completely suppress GS lasing. An impact of doping on lateral transport of charge carries was also discussed and its importance for spatial hole burning in different type of lasers was demonstrated.

References

- [1] L.V. Asryan, R.A. Suris. Charge Neutrality Violation in Quantum-Dot Lasers *ieec journal of selected topics in quantum electronics*, vol. 3, no. 2, 1997
- [2] V.V. Korenev, A.V. Savelyev, A.E. Zhukov, A.V. Omelchenko, M.V. Maximov. The influence of charge carrier dynamics and temperature on double-state lasing phenomenon in semiconductor quantum 2013 dot lasers
- [3] I. C. Sandall, P. M. Smowton, J. D. Thomson, T. Badcock, D. J. Mowbray, H.-Y Liu, and M. Hopkinson, *Appl. Phys. Lett.* 89, 151118 2006.

The influence of mobile impurities on photoelectric properties of PbSe-based multiphase photosensitive structures

A N Belenkov¹, V V Davydov¹, S B Boyko², Z N Petrovskaya² and A Yu Karseev¹

¹ Saint Petersburg State Polytechnical University, Saint Petersburg, Russia

² JSC “NII “Giricond”, Saint Petersburg, Russia

Abstract. The PbSe-based photoelectric sensor technology is considered. The polycrystalline PbSe films are used for the production. The influence of mobile impurities in a material on the mechanism of photovoltaic effect is revealed and investigated. The experimental results of investigation of the photovoltaic effect are discussed.

Fire-fighting measures are very important for fire safety of all technological processes. Despite the significant progress in fire-fighting systems, the development of sensitive sensors for timely fire detection is still actual problem. Operating experience has demonstrated that optical systems were the most efficient devices for fire safety control of technological processes, but the main disadvantage of such systems is probability of false alarms caused by natural and industrial interferences. To eliminate false alarm rate in modern optical systems the method of spectral selection of registered signal is used.

To improve the fire-fighting optical systems based on the spectral selection it is necessary to increase the spectral sensitivity, response rate and operational reliability of integrated photodetectors. The advanced materials for improvement of characteristics of photovoltaic infrared sensors are considered to be polycrystalline PbSe films and PbSe–CdSe solid solutions.

A new photovoltaic sensor technology is developed in research laboratory of JSC “NII “Giricond”. We have used the thin-film polycrystalline structures based on A^4B^6 materials and A^4B^6 - A^2B^6 solid solutions. The main materials for polycrystalline structures are PbSe doping with group V impurities (e. g. Bi) and solid solutions of PbSe and CdSe. Conductivity of these materials is near to intrinsic (this is achieved by the doping with group V atoms). We can change the band gap of the material directionally between 0.2 and 0.6 eV by addition of CdSe to PbSe that allows us to control the spectral characteristics of the photoelectric sensors.

Although the mechanism of photovoltaic effect in these photoelectric sensors has not been fully investigated, it can be expected that photovoltaic effect was induced by the migration of the mobile impurities from the glass substrate to the photoelectric layer. It has been previously assumed that the barrier structure formation was caused by the diffusion of indium atoms from the indium contacts to the photosensitive layer during thermal treatment (conventional technology). To explain the mechanism of photovoltaic effect the photoelectric sensors based on $Pb_{0.96}Cd_{0.04}Se$ were investigated.

A scheme of the experimental setup for investigation of the impurity migration is presented in figure 1.

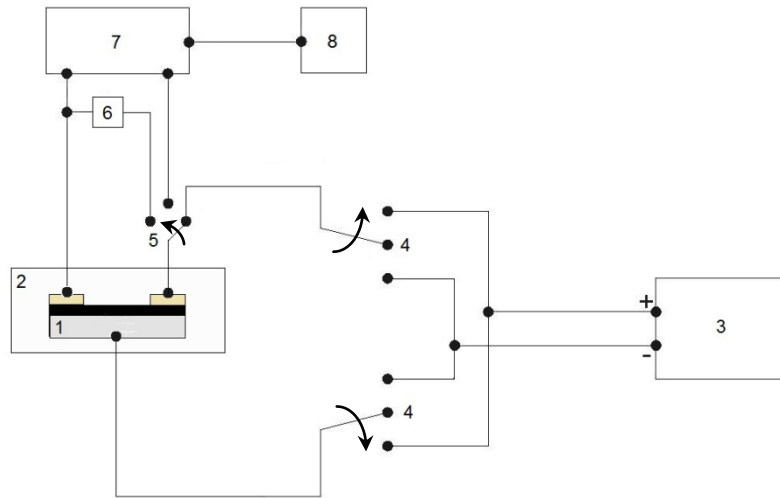


Figure 1. A scheme of the experimental setup: 1 – photoelectric sensor (photoresistor or photovoltaic cell); 2 – thermostat; 3 – voltage power supply; 4 – switches for changing direction of the electric field; 5 – the research mode switch; 6 – multimeter GDM 354 A; 7 – the device for automatic measurement of volt-ampere characteristics; 8 – PC.

The photoresistor and photovoltaic cell based on PbCdSe are affected by electric field and temperature (the temperature and the voltage are fixed: $T=150^{\circ}\text{C}$, $U=250\text{ V}$). Time dependence of the photosensitive layer resistance and the volt-ampere characteristic of the photovoltaic cell were obtained.

The results showed that there was outflow of positive ions Na^+ both from base area and electrode (In) sheath after applying a positive voltage to the photosensitive layer. Thereby the base area resistance decreases. The volt-ampere characteristic becomes practically linear. It means that the p-n-junction disappears. There is enhancement of base area and electrode sheath by positive ions after applying a negative voltage to the photosensitive layer. The base area resistance increases; the slope of the volt-ampere characteristic decreases. The possibility of the reverse conductivity type conversion indicates that diffusion of indium atoms had no dominant role in process of conductivity type conversion of electrode sheath of photosensitive layer.

Experimental data also indicates that the Fermi level of PbSe grain was shifted by the positive ions Na^+ accumulated near the boundary between grain and dielectric glass substance. Thereby the photosensitive layer resistance increases. Positive charge at the grain boundary increase and it causes conductivity type conversion. The p-n-junction is formed at the boundary between areas with different types of conductivity. Received data allow explaining the mechanism of photovoltaic effect as result of the migration of the mobile impurities. This enables to improve properties of developed photoelectric sensors by control of the migration of the mobile impurities.

Section Photonics

Cyclometalated complexes of platinum metals – the new luminescent sensors

M V Nikolaeva, E A Katlenok, M V Puzyk and K P Balashev

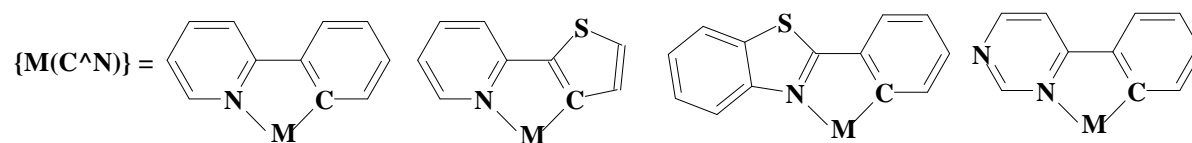
Department of Chemistry, Herzen State Pedagogical University, 48 Moika Embankment, St. Petersburg, 191186 Russia

Abstract. The influence of the environment on the cyclometalated Pt(II), Pd(II), Ir(III) complexes' optical properties in the presence of various organic and inorganic compounds in solution and the gas phase is studied. The feasibility of complexes' using as optical sensors for molecular oxygen, halide ions, hydrogen and Hg(II) cations in the liquid phase, as well as for water and some organic solvents' vapor in the immobilized state in the MF-4SK membrane.

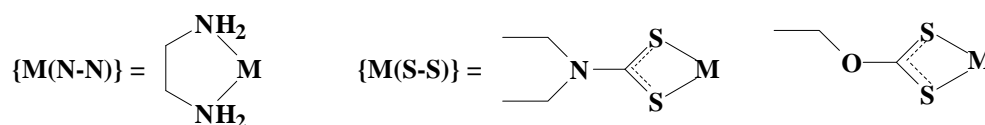
The specific structure of the cyclometalated Pt(II) and Ir(III) complexes with heterocyclic ligands, which characterized by intense and relatively long-lived phosphorescence in solutions and outer-sphere electron transfer reversible processes, determines the possibility of developing of these complexes-based optical sensors and chemosensors for the presence of various organic and inorganic compounds in the liquid and the gas phase, including in biosystems [1–5].

This work is aimed at studying the effect of the environment on the optical properties and the photoexcitation energy degradation efficiency of the cyclometalated Pt(II), Pd(II), Ir(III) complexes in homogeneous solutions and which immobilized on the surface of a MF-4SK cation-exchange membrane.

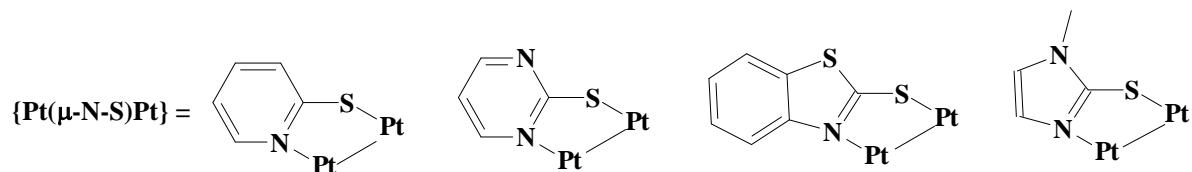
The investigation subjects are the mono- and binuclear Pt(II), Pd(II), Ir(III) complexes with metalated phenyl-substituted (C^N) imines:



chelating (N–N, S–S⁻) ligands:



and bridging 2-mercapto-derived (μ -N–S⁻) ligands:



The cumulative results of cyclometalated complexes' investigation by electronic absorption and emission spectroscopy, multinuclear one- and two-dimensional NMR resonance spectroscopy, X-ray crystallography and cyclic voltammetry [6–11] show:

1. Thermal quenching of the vibrationally structured complexes phosphorescence in liquid solutions as a result of competition between radiative and nonradiative processes of the photoexcitation energy degradation from electronically excited state with the metal-to-cyclometalated ligand charge transfer and ligand field state.

2. The phosphorescence quenching efficiency of Pt(II) complex solutions by halogenide ions ($\text{Cl}^- < \text{Br}^- < \text{I}^-$) is defined by external heavy atom effect due to increasing the spin-orbit interaction constant of the halogenide ion.

3. The dynamic character of phosphorescence quenching of the complexes by molecular oxygen in solutions with the near-diffusion rate constant determines the feasibility of complexes' using as luminescent sensors for the presence of molecular oxygen in solution.

4. The reversible effect of acidity on the phosphorescence intensity of Pt(II) and Ir(III) complexes' solutions is determined by the nitrogen atom protonation of the heterocyclic cyclometalated ligand.

5. Selective sensor optical properties of solutions of the mono- and binuclear Ir(III) and Pt(II) complexes with sulphur-containing donor atoms of the chelating or bridging ligands for Hg(II) cation are related to the specific complex formation of 'soft' S donor atom with 'soft' Hg(II) ion.

6. Vapochromic properties of the MF-4SK cation-exchange membranes modified by Pt(II) complexes for the vapor nature of methanol, water, ethanol, 2-propanol, n-butanol, acetonitrile or acetone are referred to complexes' phosphorescence quenching as a result of monolayer formation of the organic solvent in the membrane.

Increased reactivity of acetonitrile coordinated to the cyclopyridinated complexes and formation of the new amidine compounds in coordination with the organic amines are demonstrated.

Acknowledgments

The investigation was supported by the Ministry of Education and Science of the Russian Federation, state target no. 4.131.2014K.

References

- [1] Nikolaeva M V, Katlenok E A, Khakhalina M S, Puzyk M V and Balashev K P 2014 *J. Phys.: Conf. Ser.* **541** 012086
- [2] Zhao Q, Li F and Huang C 2010 *Chem. Soc. Rev.* **39** (8) 3007
- [3] Yang Y, Zhao Q, Feng W and Li F 2013 *Chem. Rev.* **113** (1) 192
- [4] Guerschais V, Fillaut J-L 2011 *Coord. Chem. Rev.* **255** (21–22) 2448
- [5] Wu Y, Jing H, Dong Z, Zhao Q, Wu H, Li F 2011 *Inorg. Chem.* **50** (16) 7412
- [6] Nikolaeva M V and Puzyk M V 2014 *Opt. Spectrosc.* **117** (4) 589
- [7] Katlenok E A and Balashev K P 2014 *Opt. Spectrosc.* **116** (1) 100
- [8] Katlenok E A and Balashev K P 2014 *Opt. Spectrosc.* **116** (2) 207
- [9] Katlenok E A and Balashev K P 2014 *Opt. Spectrosc.* **117** (3) 374
- [10] Katlenok E A, Zolotarev A A and Balashev K P 2015 *Rus. J. Coord. Chem.* **41** (1) 37
- [11] Khakhalina M S, Tikhomirova I Yu and Puzyk M V 2010 *Opt. Spectrosc.* **108** (5) 703

Optical properties of inorganic WS₂ nanotubes and their composites with gold nanoparticles in suspensions and films

A.Yu. Polyakov,¹ V.A. Lebedev,¹ E.A. Goodilin,¹ R. Tenne²

¹ Department of Materials Science, Lomonosov MSU, Moscow, Russia

² Department of Materials and Interfaces, Weizmann Institute, Rehovot, Israel

Abstract. Optical properties of inorganic WS₂ nanotubes (INT-WS₂) and Au-INT-WS₂ nanocomposites were studied using optical absorption spectroscopy, diffuse reflectance spectroscopy, optical microscopy in polarized light. Differences between absorption and extinction spectra are discussed. Au-INT-WS₂ nanocomposites are shown to be promising materials for light harvesting. Light polarization by INT-WS₂ thin films is also reported.

Composite nanomaterials based on layered transition metal disulphides and metal nanoparticles attract growing attention due to their unique optical and electronic properties which are not inherent in the individual components. Metal-semiconductor composites based on MoS₂ and WS₂ were shown to be promising materials for photocatalysis, light harvesting, field effect transistors, etc. [1].

Previously we developed a facile method for preparation of Au-INT-WS₂ nanocomposites by direct reaction of HAuCl₄ aqueous solutions with disulphide surface. It was shown that 3 min boiling of INT-WS₂ suspension in HAuCl₄ solution resulted in formation of gold nanoparticles on the nanotubes with no need in additional reduction agents and stabilizers. Preferential growth of gold nanoparticles near the surface defects (especially, steps and fractures) of the nanotubes indicated special role of these sites in heterogeneous gold nucleation. Different HAuCl₄/WS₂ molar ratios allow formation of gold nanoparticles with controllable diameter [2].

In this work we prepared not only suspensions but also thin films of INT-WS₂ and Au-INT-WS₂ nanocomposites. Films up to 2*2 cm² were deposited onto glass slides and Si wafers from liquid-liquid water-heptane interface. The films were characterized using scanning electron microscopy and X-ray diffraction. Optical properties of both suspensions and films were studied by optical absorption spectroscopy. For the films, diffuse reflectance spectra were also collected. Comparison of these spectra revealed a strong scattering impact in INT-WS₂ suspensions spectra. In addition, suppression of surface plasmon band in Au-INT-WS₂ nanocomposites containing < 10 nm gold nanoparticles was found. Optical microscopy study has shown that both INT-WS₂ and Au-INT-WS₂ nanocomposites are strong light polarizers.

References

- [1] Y. Shi, J.-K. Huang, L. Jin, Y.-T. Hsu, S.F. Yu, L.-J. Li, H.Y. Yang. Selective Decoration of Au Nanoparticles on Monolayer MoS₂ Single Crystals. *Scientific Reports* 2013, 3 : 1839.
- [2] A.Yu. Polyakov et al. Decoration of WS₂ Nanotubes and Fullerene-Like MoS₂ with Gold Nanoparticles. *J. Phys. Chem. C* 2014, 118, 4, 2161–2169.

Electromagnetic properties of water on GHz frequencies for medicine tasks and metamaterial applications

N D Pavlov¹ and Y A Baloshin²

¹ ITMO University, Kronverkskiy pr. 49, St.Petersburg 197101, Russian Federation

² ITMO University, Kronverkskiy pr. 49, St.Petersburg 197101, Russian Federation

Abstract.

Dielectric properties of fluids are of interest in modern radio physics and medicine. Dispersion characteristics of water in the GHz frequency band is necessary for diagnostics state of biological objects. Also in this frequency range, physical properties of fluids are required to investigate metamaterials in which liquids will serve as fillers. This work is devoted to study of liquids electromagnetic properties in the ultra-high frequency range (UHF).

1. Introduction

The knowledge about the electromagnetic properties of liquids in modern radio physics and medicine are important. The dispersion characteristics of fluids in the GHz frequency range required to research properties of metamaterials, when using these fluids as their fillers. Concerning of medical applications in such important tasks as diagnosis of the state biological object, the same dispersion properties plays an important role[1].

2. Methods of measuring the electromagnetic properties of liquids

For measurements of electrodynamic parameters of liquids are used two main techniques: Nicholson-Ross-Weir (NRW)[2] and the active near-field diagnostics [3]. These methods have similar physical principles of operation, but they differ in the practical execution and information that can be obtained from the test object. The NRW technique is based on the principle of extracting material parameters [2,4,5] from S-parameters reflection S_{11} and transmission S_{21} of the sample with thickness d , located in the waveguide section. Essential parameter for measurement of S-parameters is the change wave phase in passing through the sample. The phase imposes some restrictions on the shape of the sample surface, of which the sample necessary to give plane parallel shape, in order to avoid distortions in the phase of the wave. It is more difficult to achieve for the sample in the liquid state than in the solid, as the sample is placed into the waveguide. In contrast with active near-field diagnostic technique the advantage of NRW technique is the possibility of extracting the magnetic permeability. Active near-field diagnostic technique allows to define the material parameters by measuring the conductivity of the test sample and the impedance changes in the near field zone of antenna. Inability of magnetic permittivity measurements in this method is compensated by ease measurements of permittivity

and conductivity of liquids. In this case it is enough to locate the probe on the surface of liquid. Measurements of liquids were made by both techniques, the results are similar with each other in . Therefore, due to the complexity of measurements the NRW method particular number of measurements were made of the second method.

3. Results and discussions

Generally permeability value practically no changes in comparison with the dielectric permittivity and make its value by one. Since the method of active near-field diagnostics very comfortable in measuring permittivity and conductivity of liquids, it was preferred method of NRW for the most part of measurements. As a result of experimental studies we obtained the values of permittivity (real and imaginary part) of several different types of liquids, including salt mixtures.

References

- [1] Samoilov V O 2004 Medical biophysics *SpecLit* 496
- [2] Luukkonen O, Maslovski S I, Tretyakov S A 2011 A Stepwise NicolsonRossWeir-Based Material Parameter Extraction Method *IEEE antennas and wireless propagation letters* vol. **10** 1295-1298
- [3] Urasova N V 2006 The near-field UHF probing stratified medium *Nizhniy Novgorod* 113
- [4] Nicolson A M and Ross G F 1970 Measurement of the intrinsic properties of materials by time-domain techniques *IEEE Trans. Instrum. Meas.* **19** 377-382
- [5] Weir W B 1974 Automatic measurement of complex dielectric constant and permeability at microwave frequencies *Proc. IEEE* **62** 33-36

Wood anomalies in the vicinity of 3D Bragg diffraction from hybrid opaline photonic crystals

V S Nikolaev^{1,2}, M M Voronov¹, S A Yakovlev¹, A B Pevtsov¹

¹Ioffe Physical-Technical Institute, Politekhnicheskaya 26, St Petersburg, 194021 Russia

²St. Petersburg State Electrotechnical University LETI, St. Petersburg, 197376 Russia

Abstract. For hybrid chalcogenide/opal photonic crystals the optical reflection spectra demonstrating the interplay of diffraction resonances such as 3D Bragg diffraction and resonant Wood anomaly have been studied. The coupling coefficient of the Wood and Bragg waves has been estimated on the basis of the coupled-waves approach and the concept of the effective refractive index of the wave-guiding surface layer of the hybrid structure.

We consider the high contrast hybrid photonic crystals (HPCs)[1], which in our case are opaline photonic crystals covered with chalcogenide ($Ge_2Sb_2Te_5$) films of different thickness, and study the reflection spectra in which the resonant Wood anomalies and 3D Bragg diffraction can manifest themselves. Experimental reflection spectra for the structures considered with $Ge_2Sb_2Te_5$ films of the thicknesses $h = 40, 80$ and 150 nm at different light incidence angles ($11^\circ < \theta_0 < 66^\circ$) are shown in figure 1. The spectra show two kinds of features, one of which is a 3D Bragg diffraction peak moving to shorter wavelengths as the incidence angle increases, while the second is a Wood anomaly peak moving to longer wavelengths with an increase in the incidence angle. It is clearly seen that in the interaction region of the Bragg and Wood resonances the behaviour of the corresponding angular reflection spectra is different, showing a crossing of the lines, figures 1a,b (with the exception of a very narrow frequency region) in one case and a strong repulsion, typical for an anticrossing, figures 1e,f, in the second. The difference in intensity of the interaction is associated with different conditions for the propagation and scattering of light in the wave-guiding layer. In the hybrid structures being studied the above difference is determined by the thickness of the $Ge_2Sb_2Te_5$ film because the effective parameters (the effective refractive index \bar{n} and transverse wave vector component \mathbf{a}) of the quasi-guided mode invoked to describe the angular-dependent Wood anomalies, are strongly dependent on this thickness [2]. The figures 1c,d show the reflection spectra for a HPC with the $Ge_2Sb_2Te_5$ film thickness $h = 80$ nm. As is seen in figures 1c,d there are only two ridges of peaks, which are Wood anomalies corresponding to two different quasi-guided modes. A peculiarity of these spectra is the absence of the peaks of 3D Bragg diffraction on the (111) planes of the opal film.

Since the experimental reflection spectra corresponding to the Wood anomaly and 3D Bragg diffraction are fitted well by Lorentzian shape functions, one can expect that their spectral-angular dependence will be described by the coupled-mode theory. For this purpose we apply the two-coupled wave equation to the quasi-guided modes by analogy with the guided modes in dielectric waveguides [3]. A coupled-wave equation usually contains the wave vectors of the interacting waves, but since the wave vectors of the light propagating in the waveguide layer

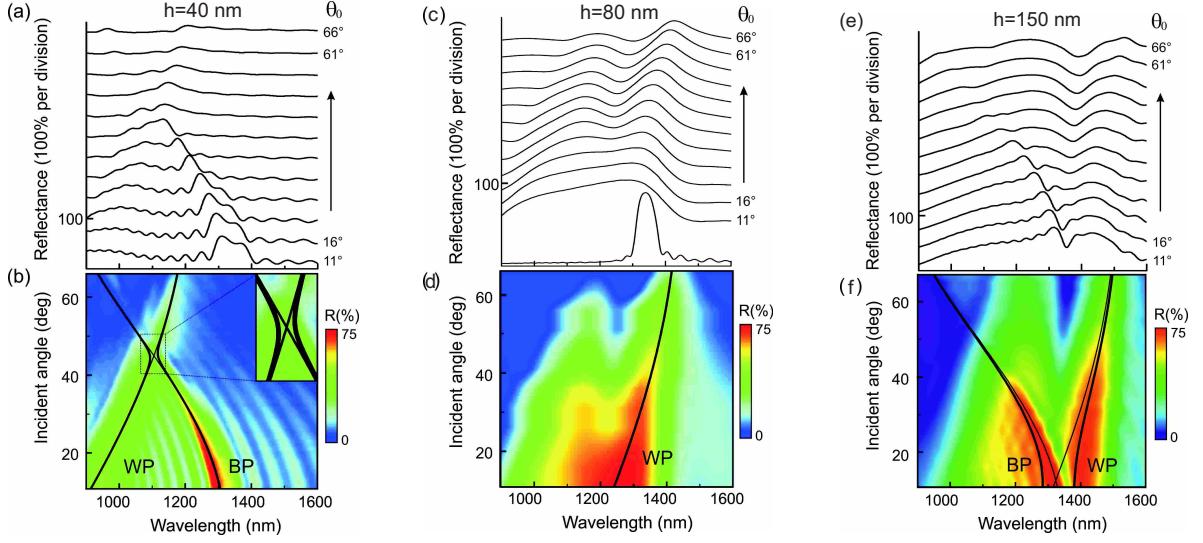


Figure 1. Experimental reflection spectra of hybrid opal/ $Ge_2Sb_2Te_5$ photonic crystals for different incident angles (θ_0) and $Ge_2Sb_2Te_5$ thicknesses (h). The spectra (a,c,e panels) are shifted vertically for clarity. The thick full curves (b,d,f panels) passing through the spectral maxima correspond to the coupled-waves modes of 3D Bragg diffraction (BP) and the Wood anomalies (WP) and are calculated by equation (1). The thin full curves (b,d,f panels) are calculated without interaction between the Wood and Bragg resonances.

attributed to the Wood anomaly and Bragg diffraction correspond to the certain outgoing angles of the light, θ , (in our case $\theta = \theta_0$) the equation for the coupled waves can be written as

$$(\omega - \omega_B(\theta))(\omega - \omega_W(\theta)) = \delta^2, \quad (1)$$

where $\omega_W(\theta) = 2\pi c/\lambda_W(\theta)$ and $\omega_B(\theta) = 2\pi c/\lambda_B(\theta)$ are the frequencies corresponding to the reflection spectrum maxima for the Wood anomaly [2] and 3D Bragg diffraction, taking into account an additional phase shift due to the thickness of the $Ge_2Sb_2Te_5$ film; δ is the effective coupling coefficient of the modes. If to consider δ to be a constant (equal to its value in the crossing point of the unperturbed lines), equation(1) will be quadratic relative to the frequency ω , whose roots $\omega_1(\theta) = 2\pi c/\lambda_1(\theta)$ and $\omega_2(\theta) = 2\pi c/\lambda_2(\theta)$ describe the behaviour of the coupled Bragg and Wood modes. The estimation of the coupling coefficient δ in the cases of the strong (figures 1e,f) and weak (figures 1a,b) interaction made with the help of equation(1) gives values $\approx 7 \cdot 10^{13}c^{-2}$ and $7 \cdot 10^{12}c^{-2}$, correspondingly. Such a large difference in the interaction intensity of the resonances is due to a difference in the interference conditions for 3D Bragg diffraction wave and the Wood anomaly wave in the surface waveguide layer. The effective parameters for the quasi-guided modes have been calculated as well: $\bar{n} = 1.85$, $\mathbf{a} = 0.38$ ($h=40$ nm); $\bar{n} = 3.11$, $\mathbf{a} = 1.04$ ($h=80$ nm); $\bar{n} = 3.25$, $\mathbf{a} = 1.01$ ($h=150$ nm).

Thus, in the frame of the coupled-waves approach we have studied the anticrossing phenomenon of the Wood and Bragg resonances in the reflection spectra of the hybrid opaline photonic crystals. From a comparison of the experimental data with the theoretical model calculations we have determined the effective parameters of the quasi-guided mode responsible for the appearance of the resonant Wood anomalies and the coupling coefficient between the modes of the Wood anomalies and 3D Bragg diffraction.

[1] Romanov S G, Regensburger A, Korovin A V, Peschel U, (2011) *Adv. Mater.* **23**, 2515

[2] Voronov M M, Pevtsov A B, Yakovlev S A, Kurdyukov D A, Golubev V G, (2014) *Phys. Rev. B* **89**, 045302

[3] Yariv A (1973) *IEEE J. Quantum Electron.* **9**, 919

Photoluminescence of undoped InAs autoepitaxial layers

D D Firsov^{1*}, O S Komkov¹ and A S Petrov²

¹Micro- and Nanoelectronics department, St. Petersburg Electrotechnical University “LETI”, Professora Popova Street 5, St. Petersburg 197376, Russia

²OJSC NRI “Electron”, Toreza ave. 68, St. Petersburg 194223, Russia

Abstract. Photoluminescence (PL) properties of undoped InAs autoepitaxial layers are studied at various temperatures (8-120 K) and excitation power. The studied structures have been grown on highly doped n⁺⁺-InAs substrates by the chloride-hydride vapour phase epitaxy method. PL spectra measurements were carried out with an FTIR spectrometer. The samples exhibit several luminescence peaks in the 2.9-3.3 μm range, which are attributed to free exciton transitions, deep donor bound excitons, and donor-acceptor pairs. Intensity of peaks exhibits a correlation with the free carrier concentration values obtained by independent measurements.

1. Introduction

Indium arsenide (InAs) autoepitaxial structures grown on highly doped substrates (n-InAs/n⁺⁺-InAs) are widely used [1] as materials for backside-illuminated infrared image detectors operating at wavelengths about $\lambda \sim 3 \mu\text{m}$. Such structures can selectively cover a broad spectral range due to variable transmission of differently doped n⁺⁺-InAs [2], while the epitaxial n-InAs acts as an active region. To obtain high sensitivity of such photodetectors, powerful diagnostic techniques are required to control optical properties and growth quality of fabricated [3] InAs epitaxial layers. One of the main methods for determining the quality of epitaxial layers is photoluminescence spectroscopy.

2. Experimental setup

The studied structures containing undoped autoepitaxial InAs layers were grown by chloride-hydride vapour phase epitaxy method on highly doped n⁺⁺-InAs substrates. Epitaxial layer thickness, determined from the interference pattern in infrared (IR) reflectance spectra [4, 5], is varied from 5 μm to 10 μm. Free carrier concentration in the layers, obtained with magnetoresistance measurements, was found to be in the $6 \cdot 10^{13} - 1 \cdot 10^{15} \text{ cm}^{-3}$ range.

The photoluminescence (PL) experimental setup was based upon a VERTEX 80 Fourier-transform infrared spectrometer (FTIR) operating in continuous scan mode. PL measurements were carried out in the 8-120K temperature range; excitation was performed with an 809 nm laser diode of variable power (1 mW - 300 mW).

3. Results and discussion

An example of the obtained low temperature PL spectra of a typical InAs autoepitaxial layer is shown on Fig. 1. The main PL peak at 3.0 μm (0.413 eV) is rather close to the direct band gap of InAs ($E_g = 0.415 \text{ eV}$ at 12 K [6]). Due to the relatively small exciton binding energy of InAs ($E_{ex} \approx 1 \text{ meV}$ [7]), the peaks observed at longer wavelengths of 3.1 μm (0.400 eV) and 3.25 μm (0.382 eV) can not

be attributed to bound exciton recombination. To determine their origin, we analyzed the dependence of peak intensity on laser excitation power, as shown on Fig. 2.

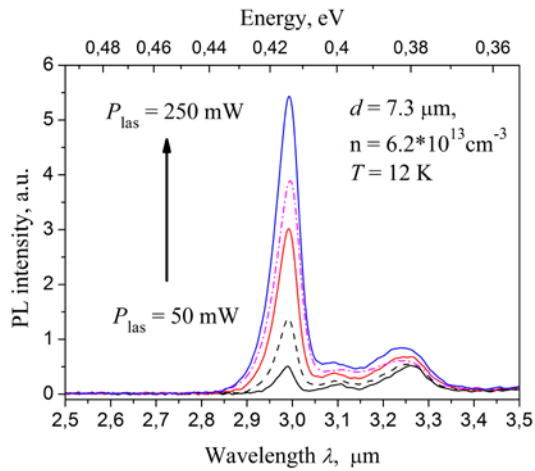


Figure 1. PL spectra of a typical n-InAs/n⁺⁺-InAs structure at various laser excitation power P_{las} .

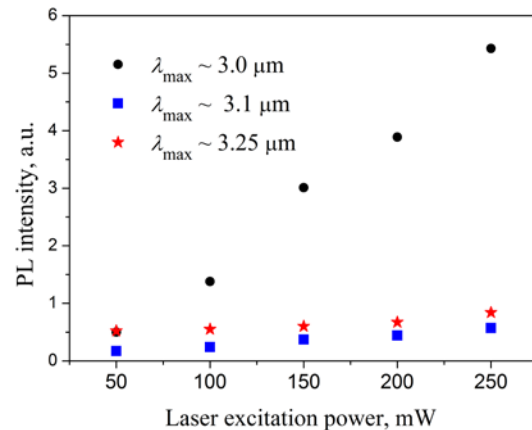


Figure 2. Dependence of PL intensity on excitation power for 3.0 μm (dots), 3.1 μm (squares) and 3.25 μm (stars) peaks, shown on Fig. 1.

The intensity of the main peak at 0.413 eV is demonstrating a linear increase proportional to laser power, which is characteristic of interband transitions [8]. The long wavelength peaks exhibit a much slower change in intensity, and therefore should be connected to impurity-based states [9]. As shown in [10], the peak at 0.382 eV originates from donor-acceptor pairs. The 0.4 eV peak can be attributed to excitons bound to deep donors in InAs (presumably carbon) [11].

It was also found that the donor-acceptor pair PL peak is most prominent in samples with the lowest electron concentration in the epitaxial layers. Therefore, it can be concluded that such structures have the highest degree of doping compensation.

References

- [1] Kovtonyuk N F, Misnik V P, Sokolov A V 2005 *Semiconductors* **39**(11) 1336
- [2] Komkov O S, Firsov D D, Kovalishina E A, Petrov A S 2014 *Prikladnaya Fizika* **4** 93
- [3] Grama D M, Petrov A S, Popov S D, Stepanov R M, Chilaeva E V 2008 *Izvestiya SPbGETU* **7** 13
- [4] Komkov O S, Semenov A N, Firsov D D, Meltser B Ya, Solov'ev V A, Troshkov S I, Pikhtin A N, Ivanov S V 2013 *Semiconductors* **47**(2) 292
- [5] Komkov O S, Firsov D D, Kovalishina E A, Petrov A S 2014 *Izvestiya VUZov. Materialy elektronnoi tekhniki* (3)
- [6] Fang Z M et al. 1990 *Journal of Applied Physics* **67**(11) 7034
- [7] Tang P J P, Pullin M J, Phillips C C 1997 *Physical Review B* **55**(7) 4376
- [8] Schmidt T, Lischka K, Zulehner W 1992 *Physical Review B* **45**(16) 8989
- [9] Tang P J P, Phillips C C, Stradling R A 1993 *Semiconductor science and technology* **8**(12) 2135
- [10] Lacroix Y, Watkins S P, Tran C A, Thewalt M L W 1994 *Appl. Phys. Lett.* **66** (9) 1101
- [11] Fang Z M et al. 1991 *Applied physics letters* **59** (12) 1446

Numerical simulation of carpet cloaking device in terahertz frequency range

V. V. Gill, A.V. Vozianova, M.K. Khodzitsky

ITMO University, Dept. of Photonics and Optical Information Technologies, 49
Kronverskiy pr. Saint-Petersburg, Russia, 197101

Abstract. This work is devoted to the numerical calculation of the effective constitutive parameters of the carpet cloaking device and to the numerical simulation of this cloak in COMSOL Multiphysics software for the terahertz frequency range.

1. Introduction

In recent years methods of design of composite structure called metamaterials are rapidly improving. Thereby there are unprecedented opportunities to manipulate of electromagnetic radiation. Transformation optics is new science of control of radiation [1], it is very powerful instrument for emission control. This approach is based on differential geometry and tensor analysis. Transformation optics shows that space can be arbitrarily curved according to predetermined manner [2]. The rays in such space will have special trajectories. The Fermat's principle is applied to control light by changing of the medium parameters. This is accompanied by a transformation from virtual space to physical space by coordinate transformations. The effective constitutive parameters of physical system which corresponds to wave propagation in virtual space were calculated.

One of the most interesting devices based on this principle are cloaks of invisibility. Special case of such devices is cover that crushes a cloaked object to a flat ground plane in virtual space [3, 4]. In fact there is an object and our cover is lying on the surface but to the observer it is perceived as the actual ground plane. This effect is achieved by coordinate transformations. The term "carpet cloak" was coined by Jensen Li and J.B. Pendry in [5] for such transformation.

The development of cloaking devices is very actual direction in spectroscopy, medicine, image analysis, etc. There are many implementations of devices based on various principles and working on the different frequency ranges [6, 7]. But operation of the cloak in the terahertz frequency range hasn't been clearly understood. A simulation of carpet cloaking device in terahertz frequency range was proposed.

2. Numerical solution and simulation

In this paper the carpet cloak for terahertz frequency range was proposed. For our problem the refractive index profile was calculated. The quasi-conformal mapping is used for transformation from virtual space (with coordinate (ξ, η)) to physical space (with coordinate (x, y)) because this mapping minimizes anisotropy [5]. A cloaking area was chosen as a symmetric domain. In virtual space it seems as rectangular domain divided into squares 1x1. Distortion function $f(x)$ for mapping in general case [8] looks like

$$f(\xi, \eta) = MF(\xi, \eta). \quad (1)$$

It was chosen a more simply case which corresponds to the quasi-conformal mapping where distortion function has the following form:

$$f(\xi, \eta) = M. \quad (2)$$

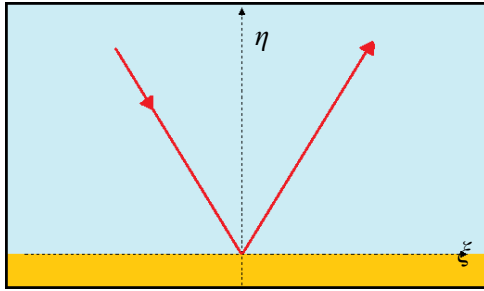


Figure 1. Virtual space.

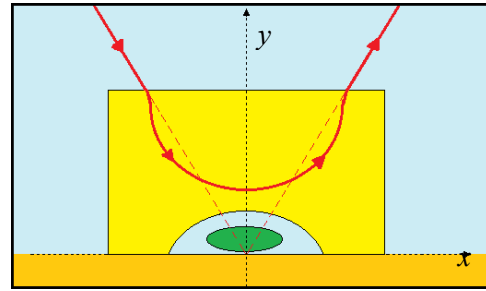


Figure 2. Physical space.

After mapping the required physical space was obtained. It is also rectangular domain but lower boundary is described by nonlinear function. This domain is divided into quadrangular cells. Refractive index profile is associated with grid's values using the following:

$$n^2 = \frac{1}{\sqrt{\det \mathbf{g}}} = \frac{1}{|\xi||\eta|}, \quad (3)$$

where \mathbf{g} is a metric in physical space. According to the optimal ratio [5] between refractive index and anisotropy (small enough value of anisotropy and not large enough value of refractive index), the refractive index was calculated.

For the transformation of grid by a quasi-conformal mapping a program in MATLAB software was obtained. For numerical simulation COMSOL Multiphysics software was used. The distribution of electromagnetic wave, which propagates through this cloak, was obtained.

References

- [1] Leonhardt U., Philbin T. Geometry and light: the science of invisibility // Dover Publication, Inc.—Mineola, New-York.—2010.
- [2] Gurvitz E. A., Vozianova A. V., Khodzitsky M. K. Simulation of beam-splitter made of metamaterials with angle distribution of constitutive parameters based on the transformation optics for terahertz frequency range // Journal of Physics: Conference Series. - 2014. - Iss. 541. - P. 012067 (1-5).
- [3] Zhang P., Lobet M., He S. L. Carpet cloaking on a dielectric half-space // Opt. Expr. 18, 18158–18163 (2010).
- [4] Ma H. F., Jiang W. X., Yang X. M., Zhou X. Y., Cui T. J. Compact-sized and broadband carpet cloak and free-space cloak // Opt. Expr. 12, 19947–19959 (2009)
- [5] Li J., Pendry J. B. Hiding under the Carpet: A New Strategy for Cloaking // Phys. Rev. Lett. 101, 203901-203904 (2008).
- [6] Silverinha M., Edwards B., Alu A. Experimental verification of plasmonic cloaking at microwave frequencies with metamaterials // Phys. Rev. Lett. – 2009. – V. 103. – P. 153901 (4)More references
- [7] Fan Zhou, Yongjun Bao, Wei Cao, Colin T. Stuart, Jianqiang Gu, Weili Zhang, Cheng Sun. Hiding a Realistic Object Using a Broadband Terahertz Invisibility Cloak // Scientific Reports.—2011.
- [8] J. F. Thompson, B. K. Soni, and N. P. Weatherill. Handbook of Grid Generation (CRC Press, Boca Raton, 1999).

Plasmonic properties of silver single nanoislands: size and shape effect

E S Piliugina¹, S A Scherbak¹, F Heisler^{2,3}, A K Samusev², A A Lipovskii^{1,4}

¹St. Petersburg Academic University, St. Petersburg 194021, Russia

²The International Research Centre for Nanophotonics and Metamaterials, ITMO University, St. Petersburg 197101, Russia

³Abbe Center of Photonics, Friedrich–Schiller–Universität Jena, Jena 07743, Germany

⁴St. Petersburg State Polytechnical University, St. Petersburg 195251, Russia

Abstract. We studied plasmonic properties of isolated silver nanoislands grown on the surface of silver ion-exchanged glass using out-diffusion growth method. The main attention is put on surface plasmon resonance dependence on nanoisland size and shape. The nanoislands were characterized with atomic force, scanning electron, and dark field microscopy. Experimental data was compared with the results of numerical modeling.

1. Introduction

Nowadays, ultrasensitive bio- and chemical sensors based on surface-enhanced Raman scattering (SERS) are under extensive studies. The key unit of these sensors is a substrate with a metallic nanostructure that provides the enhancement of Raman scattering due to the excitation of surface plasmon resonance (SPR). The SPR position strongly depends on structure parameters that determines the spectral range of SERS appearance [1,2,3]. Here we present the results of experimental studies and numerical modeling of the SPR properties of differently shaped isolated silver nanoislands grown on a glass substrate.

2. Experiments and modeling

Studied sample was fabricated using relatively new technique to manufacture 2D-patterned silver nanoisland structures that is out-diffusion growth of metal nanoisland film combined with thermal poling of the glass substrate with a profiled anodic electrode [4].

We used atomic force microscope (AFM) and scanning electron microscope (SEM) to characterize the shape and size of the nanoislands and dark field setup with Hitachi LaR MTM spectrometer to characterize spectral properties of the isolated nanoislands. In the dark field setup each nanoisland was lightened by the focused s-polarized beam from a halogen lamp, and the light scattered by the nanoisland was collected with an objective lens. Typical AFM and SEM images of a nanoisland and measured dark field spectrum of the nanoisland are shown in Figure 1a-c, respectively.

The numerical modeling of the spectra was performed in Comsol Multiphysics environment. Calculated spectrum is presented in Figure 1c, while the modeling geometry is illustrated in the inset in this Figure. The incident field was a plane wave with glancing angle 21.7° the same way as in the

dark field measurements. The scatterer considered was an extended silver hemiellipsoid with dielectric permittivity taken from Johnson and Christy work [5], and the substrate was a glass with dielectric permittivity 2.5. The modeled spectrum reasonably coincided with the experimental one.

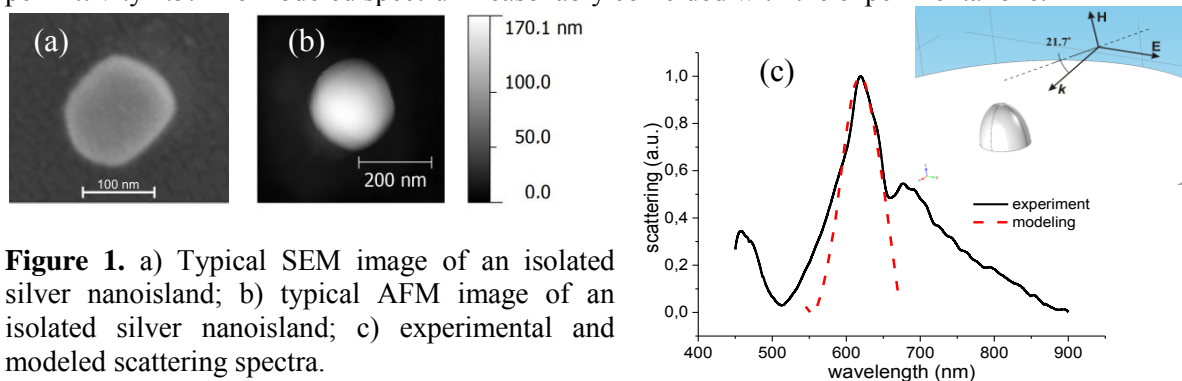


Figure 1. a) Typical SEM image of an isolated silver nanoisland; b) typical AFM image of an isolated silver nanoisland; c) experimental and modeled scattering spectra.

3. Results

In studied nanoislands, the SPR position varies from 450 nm to 730 nm, and it directly depends on the particle shape and size which vary from 100 to 180 nm in lateral plane and from 80-160 nm for height. The dependence of the SPR position on the lateral size is presented in Figure 2. X error bars correspond to SEM data with the account for the fact that after dark field studies the sample was covered with approximately 10 nm thick film of gold for the SEM measurements.

In so called quasistatic case, when the particle size is much less than the light wavelength, it was found from the calculations that the SPR position shifts towards shorter wavelength with an increase in the particle height (Figure 3a). Much smaller shift was found for bigger particles (see Figure 3b, where we have also plotted experimental data for several nanoislands of the same lateral size but differing in height). The lack of experimental data is because of the shortage in nanoislands of the same lateral size, and it is worth to note that even low ellipticity of the nanoparticles in lateral plane moves the SPR wavelength. Supposedly this is just the situation presented in Figure 3b.

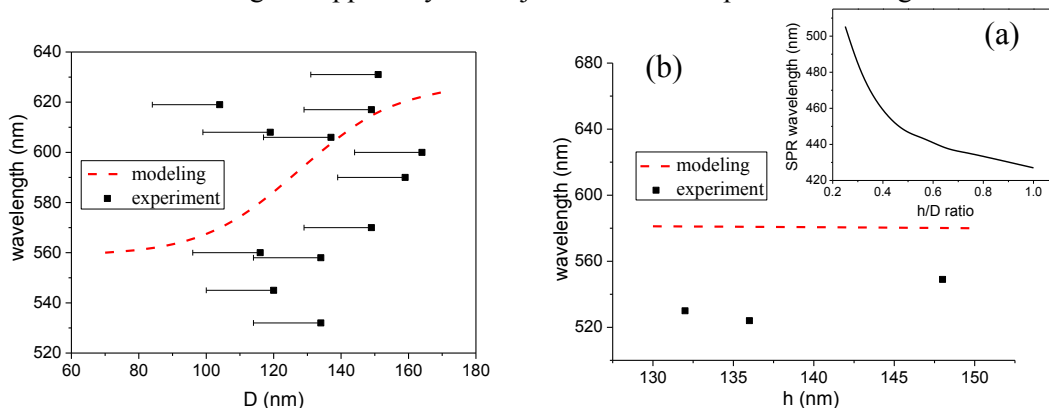


Figure 2. Dependence of SPR position on particle lateral size. The ratio of height to diameter is constant and about of 0.9.

Figure 3. Dependence of SPR position on particle height: a) quasistatic case, particle diameter is 20nm; b) experimental and numerical data, the average particle diameter is 140 nm.

References

- [1] Dieringer J A 2006 *Faraday Discuss.* **132** 9–26
- [2] Aroca R and Martin F 1985 *J. Raman. Spectrosc.* **16** 156–62
- [3] Klimov V V 2012 *Nanoplasmonics: Fundamentals and Applications (Singapore: PanStanford)*
- [4] Chervinskii S 2013 *J. Appl. Phys.* **114** 224301
- [5] Johnson P and Christy R 1972 *Phys. Rev. B* **6** 12

Expressions for reflection and transmission coefficients for one-dimensional photonic quasicrystals

M M Voronov

Ioffe Physical-Technical Institute, Politeknicheskaya 26, St Petersburg, 194021 Russia

Abstract. We theoretically study the propagation of light in one-dimensional (1D) photonic quasicrystals composed of dielectric layers in the framework of the so-called two-wave approximation. The approximate expressions for the light reflection and transmission coefficients as functions of the length of a quasicrystal are derived.

Quasicrystals belong to a wide class of aperiodic systems possessing long-range order and allowing coherent Bragg diffraction of electron or electromagnetic waves [1]. In the case of light waves such structures are called resonant or active photonic quasicrystals if the constituting materials produce dipole-like excitations; such systems are, for instance, multiple-quantum-well structures (MQWs). The theory of the propagation of electromagnetic waves in MQWs in the framework of the two-wave approximation was developed in work [2] and then generalized on the case of dielectric contrast [3]. It should be noted that in distinction from 1D periodic systems for which one can obtain analytically exact solutions, for 1D non-periodic systems it generally appears to be impossible and one has to resort to some approximations, in particular to that stated here. In this work we theoretically study the propagation of electromagnetic waves in 1D quasi-periodic media and consider the two-wave approximation in a general form to calculate the reflection and transmission coefficients for an all-dielectric photonic quasicrystal. The simplest photonic quasicrystal is the so-called Fibonacci quasicrystal, which can be constructed from layers A and B by the help of the substitution rule $A \rightarrow B$, $B \rightarrow AB$, thus, starting with a sequence $ABAABABA\dots$

Now we introduce the diffraction vectors G of a quasicrystal, which can be found from a sequence of the coordinates z_m , determining the positions of the scattering elements, which in our case are interfaces between the dielectric layers. For example, for 1D quasicrystals constructed from two constituent layers (A and B) the vectors G are given by two integer indices, h and h' , i.e. $G = G_{hh'}$ [1,2].

We consider a propagation (along z -axis) of electromagnetic waves in a 1D structure for which the modulation function $F(z)$, describing variation of the medium parameters (e.g. the dielectric permittivity) along z -direction, can be decomposed into the Fourier series $F(\omega, z) = \sum_G F_G e^{iGz}$. Besides periodic structures, which obviously satisfy this property, there are a number of the so-called deterministic aperiodic structures generating coherent Bragg diffraction, in particular, quasicrystals and incommensurate modulated crystals [1]. The frequency functions F_G depend on the system under consideration and require a separate calculation. For example, the function

$F_G(\omega)$ for highly doped MQWs is given in [4]. As long as the function $F(z)$ is almost-periodic [5] the electromagnetic field $E_K(z)$ with the wave vector K can be sought as a linear superposition $\sum_G E_{K-G} e^{i(K-G)z}$, and the wave equation is written as

$$-d^2 E_K(z)/dz^2 = F(\omega, z) E_K(z). \quad (1)$$

Hereafter we consider the situations where in RHS of the equation (1) only the components with vectors $G = 0$ and $\pm G$ are kept and one can take into account only two wave vectors, K and $K - G$, at the condition $|K - G/2| \ll G/2$. The last is valid if $|F_G| \ll |F_0|$, which allows neglecting the rest of vectors G . Thus, $E_K(z) \approx E_K e^{iKz} + E_{K-G} e^{i(K-G)z}$, where the wave vector magnitude K should be presented as $K = G/2 \pm Q$. Substituting the last expression for $E_K(z)$ into equation (1) and neglecting the other components except E_K and E_{K-G} we obtain

$$Q = \sqrt{(G/2)^2 + F_0 - \sqrt{G^2 F_0 + F_G F_{-G}}}. \quad (2)$$

By neglecting the absorption in the system one can get $F_G = F_{-G}^*$, and if the radicand (under the big root sign) is negative we find ourselves in the region of a pseudo-band gap. The latter resembles the typical band gaps in periodic structures; thus, a high reflectivity in the pseudo-band gap region is due to the constructive interference of the light waves competing with the effect of non-periodicity of the structure.

If a quasicrystal consists of layers characterized with non-frequency dependent dielectric susceptibilities one can find the Fourier-components $F_0 = (\omega/c)^2 \varepsilon_0$ and $F_G = (\omega/c)^2 \varepsilon_G$, where ε_0 and ε_G are Fourier-components of the dielectric profile function $\varepsilon(z) = \sum_G \varepsilon_G e^{iGz}$. The expression for ε_G can be easily derived from a given sequence of the layers in a quasicrystal. The edges of a pseudo-band gap calculated on the basis of the two-wave approximation are found from equation (2) under condition $Q = 0$: $\omega_{\pm} = (Gc/2)/\sqrt{\varepsilon_0 \pm \sqrt{\varepsilon_G \varepsilon_{-G}}}$. The value of the wave vector of the light propagating in the surrounding medium, q , must be chosen equal to $\omega\sqrt{\bar{\varepsilon}}/c$ because it leads to zero reflection coefficient when $F_G \rightarrow 0$; $\varepsilon_0 = \bar{\varepsilon} \equiv L^{-1} \int_0^L \varepsilon(z) dz$, where $\bar{\varepsilon}$ is the average dielectric constant and L is the length of a quasicrystal. Defining the field $E(z)$ in the same way as in [2], after a series of transformations the amplitude reflection coefficient of light for the photonic quasicrystal can be reduced to the following form

$$r_L = \frac{(F_G + Q^2 - (q + G/2)^2)(Q^2 - (q - G/2)^2)}{(F_G + Q^2 - (q - G/2)^2)((G/2)^2 - q^2 - Q^2 - 2iqQ \cot QL)} \quad (3)$$

and the amplitude transmission coefficient to

$$t_L = \frac{-2iqQ[F_G e^{iGL/2} + (Q^2 - (q - G/2)^2) e^{-iGL/2}]}{(F_G + Q^2 - (q - G/2)^2)((G/2)^2 - q^2 - Q^2 - 2iqQ \cot QL) \sin QL}.$$

A typical reflection spectrum $|r_L(\omega)|^2$ for a quasicrystal calculated by equation (3) in the vicinity of frequency $\bar{\omega} = Gc/2\sqrt{\bar{\varepsilon}}$ is almost symmetrical about $\bar{\omega}$ and resembles in much the reflection spectrum for an analogous periodic structure.

In conclusion, we have given the expressions for the reflection and transmission coefficients of 1D photonic quasicrystals and generalized the theory of light propagation in quasicrystals developed in works [2-4]. An analysis of the obtained expressions allows one to optimize the parameters of different 1D photonic quasicrystals to get pseudo-band gaps in the frequency range of interest.

- [1] Fujiwara T and Ishii Y 2008 *Quasicrystals* (Amsterdam: Elsevier)
- [2] Poddubny A N, Pillozzi L, Voronov M M and Ivchenko E L 2009 *Phys. Rev. B* **80** 115314
- [3] Poddubny A N and Ivchenko E L 2010 *Physica E* **42** 1871
- [4] Averkiev N S, Glazov M M, Voronov M M 2012 *Solid. St. Comm.* **152** 395
- [5] Corduneanu C 1989 *Almost-periodic functions* (New York: Chelsea)

Influence of surface plasmon resonance on ZnO photoluminescence. Role of pumping level

A P Tarasov^{1,2}, Ch M Briskina¹, M V Ryzhkov¹, S I Rumyantsev¹, V M Markushev¹

¹Kotel'nikov Institute of Radio Engineering and Electronics of Russian Academy of Sciences, Moscow 125009, Russian Federation

²Moscow Institute of Physics and Technology (State University), Dolgoprudny, Moscow Region 141700, Russian Federation

Abstract. The research of pumping level dependence of ZnO UV and visible luminescence was conducted. To describe the behavior of radiation intensity the model based on the set of rate equations was proposed. The simultaneous equations include the set of parameters which characterizes processes participating in exciton and defect-caused visible luminescence. The values of parameters were estimated using experimental dependence of luminescence intensity on pumping level. Proposed model can give the way for optimization of samples structure to maximize the effect of SP resonance influence on luminescence intensity.

1. Introduction

The report is devoted to investigation of dependence of ZnO luminescence intensity on the photoexcitation level. The samples investigated are ZnO microfilms with and without Ag cover. Luminescence excitation was carried out by the 3rd harmonics of Nd:YAG laser (355 nm, 10 ns) in the range of power of 5 – 200 uJ. Luminescence spectra were registered using photomultiplier.

2. UV radiation of ZnO

The research of dependence of UV (~380 nm) luminescence intensity of ZnO film on pumping level was conducted. In order to describe the behavior UV (exciton) radiation of ZnO film coated with Ag cover the simplified model was proposed. This model is based on simultaneous equations which contain the set of parameters. The parameters characterize processes such as zone-zone excitation (wherein electrons in conduction band (CB) and holes in valence band (VB) are formed), excitons formation and recombination in presence of plasmon field, photons formation caused by excitons recombination plasmon field formation in nanoscale interlayer between ZnO film and Ag cover, phonons formation caused by heat and losses i.e. due to conversion of part of photons caused by exciton recombination to heat through plasmons.

$$\left\{ \begin{array}{l} \frac{dn_1}{dt} = P e^{\frac{-(t-10)^2}{26,4}} - (M + B)n_1n_3 \\ \frac{dn_2}{dt} = Hn_4 + A(1 - L_A n_6)n_5n_4 - Cn_2 - Sn_2 \\ \frac{dn_3}{dt} = P e^{\frac{-(t-10)^2}{26,4}} - (M + B)n_1n_3 \\ \frac{dn_4}{dt} = Mn_1n_3 - Rn_4 - A(1 - L_A n_6)n_5n_4 \\ \frac{dn_5}{dt} = N_0(1 - L_N n_6)Sn_2 - N_0Sn_2W(1 + L_W n_6)n_2 - Tn_5 \\ \frac{dn_6}{dt} = \alpha P e^{\frac{-(t-10)^2}{26,4}} + Vn_2 + N_0Sn_2W(1 + L_W n_6)n_2 - En_6 \end{array} \right.$$

In these equations n_1 – concentration of electrons in CB, n_2 – concentration of photons appeared due to exciton recombination, n_3 – concentration of holes in VB, n_4 – concentration of excitons, n_5 – concentration of photons caused by plasmon vibration, n_6 – concentration of phonons, t – time, P – pumping level. Here are different parameters. Some of them (M , B , H , C , R , α) exist in case of uncovered ZnO film. Other parameters appear in presence of Ag cover.

The parameters values were estimated using experimental dependences of luminescence intensity on pumping level. Such dependence for uncoated ZnO film is linear (one can see it elsewhere [1]). In presence of Ag cover the dependence becomes essentially nonlinear.

Proposed theoretical approach was applied for analysis of above-mentioned dependence for ZnO film coated with Ag cover of 10 nm and 20 nm thicknesses. It was revealed that an increase of effective thickness of Ag cover leads to increase of heat losses and decrease of photons-to-plasmons transition possibility.

Thus, proposed model can give the way for optimization of samples structure to maximize the effect of impact of SP resonance on luminescence intensity.

This research partially overlaps with authors' paper [2].

3. Visible ZnO radiation

Similar simplified model based on simultaneous equations was considered for visible ZnO radiation. In this case the set of equations describes defect-caused visible radiation besides UV. For this consideration the process of filling energy levels in band gap was also taken into account. In [1] experimental dependence of visible radiation intensity on pumping level was shown. $I \sim P^{1/3}$ is a good approximation for that dependence.

During simulation it was revealed that only the assumption about donor-acceptor pairs as a cause of visible light can give $I \sim P^{1/3}$. In other words there are two energy levels in band gap. In presence of only one energy level in band gap one can get more sharp only dependence of $I \sim P^k$, where $1/3 < k < 1$.

Thus use of proposed model and experimental dependence $I(P)$ can give the way of receiving additional information about the nature of ZnO visible radiation. It seems that proposed simplified approach can be applied to other materials.

References

- [1] Studenkin S A and Cociverab M 2002 *J. Appl. Phys.* **91** 5060
- [2] Ryzhkov M V, Markushev V M, Briskina Ch M, Rumyantsev S I, Tarasov A P and Lyaskovskii V L 2014 *J. Nanoelectron. Optoelectron.* **9** 1-4

Plasmon resonance in metal-semiconductor AsSb-AlGaAs metamaterials

V I Ushanov¹, V V Chaldyshev¹, N A Bert¹, V N Nevedomskiy¹, N D Ilinskaya¹, N M Lebedeva¹, M A Yagovkina¹, V V Preobrazhenskiy², M A Putyato², B R Semyagin²

¹ Ioffe Physical-Technical Institute of the Russian Academy of Sciences, 26 Politekhnicheskaya, St Petersburg 194021, Russia

² Rzhanov Institute of Semiconductor Physics Siberian Branch of Russian Academy of Sciences, 13 pr. Lavrentieva, Novosibirsk 630090, Russia

Abstract. The optical extinction in metal-semiconductor metamaterial based on the AlGaAs matrix containing random arrays of plasmonic AsSb nano-inclusions is investigated. The metamaterial was grown by molecular beam epitaxy at low temperature. Annealing at temperatures of 400, 500 and 600°C provided a formation of a disordered arrays of the AsSb nano-inclusions of various sizes. The samples' microstructure was studied by the transmission electron microscopy. The average sizes of nano-inclusions were estimated of 6, 7 and 8 nm respectively to the corresponding annealing temperatures. In the experimental spectra of optical extinction of AsSb-AlGaAs metamaterial the resonant light absorption is observed. It was found that the plasmon resonance parameters of the metamaterial were almost independent of the size of AsSb nano-inclusions. The plasmon resonance energy was (1.47 ± 0.01) eV and its full width at half maximum was (0.19 ± 0.01) eV.

1. Introduction

The metal-semiconductor metamaterials are of great interest for the photonics due to its capability to provide enhanced light-matter interaction. This intensive interaction is represented via resonant light absorption and scattering by surface plasmons at metallic interfaces. The appearance of the plasmon resonance in such a composite medium is determined by the condition $\text{Re}(\varepsilon_m + 2\varepsilon_s) = 0$, where ε_s and ε_m are the permittivities of a semiconductor and a metal component respectively.

The purpose of this work was to develop and experimentally investigate new metamaterials based on the AlGaAs semiconductor matrix, containing random arrays of the AsSb metallic nano-inclusions.

2. Samples and experimental technique

The 1 μm thick AlGaAl(Sb) films were grown by molecular beam epitaxy at low temperature (200°C) on semi-insulating GaAs substrates with (001) orientation. The concentrations of the Al and Sb were 26% and 0.2% respectively, which provided the transparency window of AlGaAl(Sb) for light wavelengths of 700 nm and longer. The low growth temperature provided incorporation of the excess

arsenic into the epilayer in the form of antisite defects As_{Ga} with concentration of 1%. The grown samples were subjected to annealing at temperatures of 400, 500 and 600°C. The annealing provided a self-organization of the metallic AsSb nanoinclusions in the bulk of the AlGaAs epilayer. A volume fraction of nanoparticles was determined by measuring the concentration of arsenic antisite defects in the as-grown sample and was 0.17%. The microstructure of the samples was investigated by transmission electron microscopy (TEM). It was found that the average size of the AsSb nanoinclusions increased with annealing temperature and was about 6, 7 and 8 nm for 400, 500 and 600°C respectively. Figure 1 shows a dark-field TEM image of the sample subjected to annealing at 600°C.

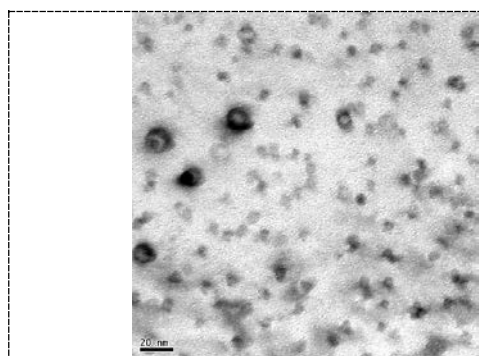


Figure 1. Dark-field TEM image of the random arrays of AsSb nanoinclusions in the AlGaAs matrix. Annealing temperature was 600°C.

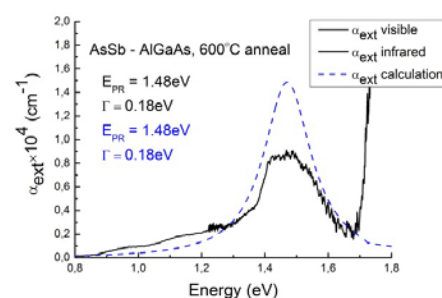


Figure 2. Dependences of the experimental (solid line) and calculated (dashed line) coefficients of optical extinction for the annealing temperature of 600°C.

3. Results and discussion

In optical extinction coefficient spectra, that we experimentally investigated, in the transparency window of the AlGaAs matrix a plasmon resonance for AsSb nanoinclusions was observed for all annealed samples. Resonant energies and FWHMs were 1.47 eV and 0.21 eV for the annealing at the temperature of 400°C, 1.47 eV and 0.20 eV for 500°C and 1.48 eV and 0.18 eV for 600°C respectively. Peaks' positions were almost independent of the size of the AsSb nanoinclusions, which is in a good agreement with the Mie theory for the case of particles that are small compared to the light wavelength [1].

A calculation of optical extinction coefficient spectrum was performed using Mie theory for a quantitative description of the experimental data for the sample annealed at 600°C. Plasma energy and a damping constant for the AsSb nanoparticles in vacuum were used in calculation as fitting parameters. They appeared to be equal to 7.38 eV and 3 fs respectively. A large dielectric constant of the semiconductor AlGaAs matrix shifts the plasmon resonance for the AsSb nanoinclusions down to energy of 1.48 eV. The FWHM of the calculated peak was 0.18 eV. The peak amplitude was not a fitting parameter. The calculated curves and experimental spectra appeared to be reasonably well consistent.

4. References

[1] Bohren C F and Huffman D R 1998 *Absorption and Scattering of Light by Small Particles* (New York: Wiley-Interscience)

384x288 readout integrated circuit for MWIR and LWIR HgCdTe based FPA

A.V. Zverev¹, Yu. S. Makarov² and E.A. Mikhantiev³

¹ Research scientist, The Institute of Semiconductor Physics SB RAS, Novosibirsk, Russia

² PhD Student, The Institute of Semiconductor Physics SB RAS, Novosibirsk, Russia

³ Engineer, The Institute of Semiconductor Physics SB RAS, Novosibirsk, Russia

Abstract. The review of architecture and characteristics of 384x288 silicon readout integrated circuit for MWIR and LWIR HgCdTe based FPA is presented.

1. Introduction

The main purpose of a silicon readout integrated circuit (ROIC) is a registration of an infrared flux intensity that is detecting by focal plane array (FPA) photodiodes and then a serial output of the accumulated information for imaging. The infrared flux intensity that is incident on the photodiode and proportion of useful information which contained in this flux are highly dependent from the wavelength range and from the surrounding background, which is supposed to detect the interests objects. The flux intensity in the mid-wavelength infrared (MWIR) band (3 – 5 μm) and long-wavelength infrared (LWIR) band (8 – 10 μm) is relatively high. However the useful signal is small in the LWIR band. A direct injection pixel cell architecture is suitable for the MWIR and LWIR bands. The main characteristic of this cell is its electron capacity. The extension of this capacity increases image integration time, that increases signal-to-noise ratio (SNR) [1]. More SNR is greater temperature resolution.

The modern ROIC should support the following features: integration then read (ITR) mode, integration while read (IWR) mode and subwindow readout mode. Additionally the number of power, reference and signal wires that should cross a cryostat border should be as small as possible.

2. Key features

The 384x288 ROIC with 25 μm pixel pitch for MWIR and LWIR HgCdTe photodiodes was developed and tested. The main characteristics of the ROIC: pixel cell electron capacity not less than 21 Me⁻, maximum output pixel rate per one video output 20 MHz, maximum dissipation power 100 mW.

The functional features of the ROIC:

- Provides built-in digital-to-analog converters (DAC), which can be used to set the offset voltage of photodiodes and to control Antiblooming and build-in testing system of the pixel cells.
- Provides a serial interface for controlling the functionality of the ROIC.
- Provides reception and accumulation of electric charge from each FPA photodiode simultaneously for a predetermined time by direct injection technique.
- Enables reading signaling information simultaneously on four video outputs, also using only one or two video outputs.
- Operates in the ITR or IWR modes.
- Allow selection of rectangular submatrix of any size and location which will be readout video information.
- Provides the ability to adjust the bias circuit of the analog part of the ROIC.

Figure 1 shows a schematic of the ROIC direct injection pixel cell. The ROIC operates in the snapshot mode. The PMOS transistors VTC1 and VTC2 are for accumulating charge during integration in both ITR and IWR modes. It is possible to disable the capacity of transistor VTC1 for reducing image integration time. It preserves the dynamic range where the average flux intensity is low enough, for example, when the ROIC is connected to MWIR FPA. PMOS transistor VTC3 used to read the accumulated charge in both ITR and IWR modes, and is also used for accumulating charge during integration in the ITR mode. In IWR mode charge accumulated at previous frame is transferred to capacity of transistor VTC3 and closed transistor VT6 prevents discharge of VTC3 capacity during the accumulation of photocurrent onto VTC1 and VTC2. NMOS transistor VT1 is used for Antiblooming and also can be used as an imitator of the current to test an array of pixel cells. It allows to evaluate performance of the ROIC before hybridization with a photodiode array. Pin PHDK of the cell is connected via indium bump to the cathode of the FPA photodiode with

common anode. NMOS transistor VT3 is direct injection transistor which used to set the offset voltage of photodiode.

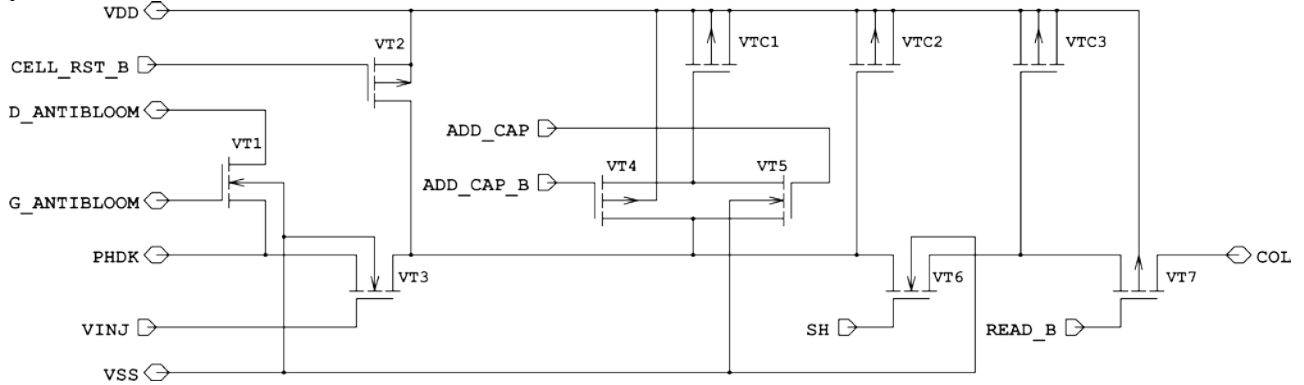


Figure 1. The schematic of the ROIC pixel cell. $C_{VTC1}=0,6$ pF, $C_{VTC2}=0,2$ pF, $C_{VTC3}=0,2$ pF.

The layout of the ROIC is presented in figure 2.

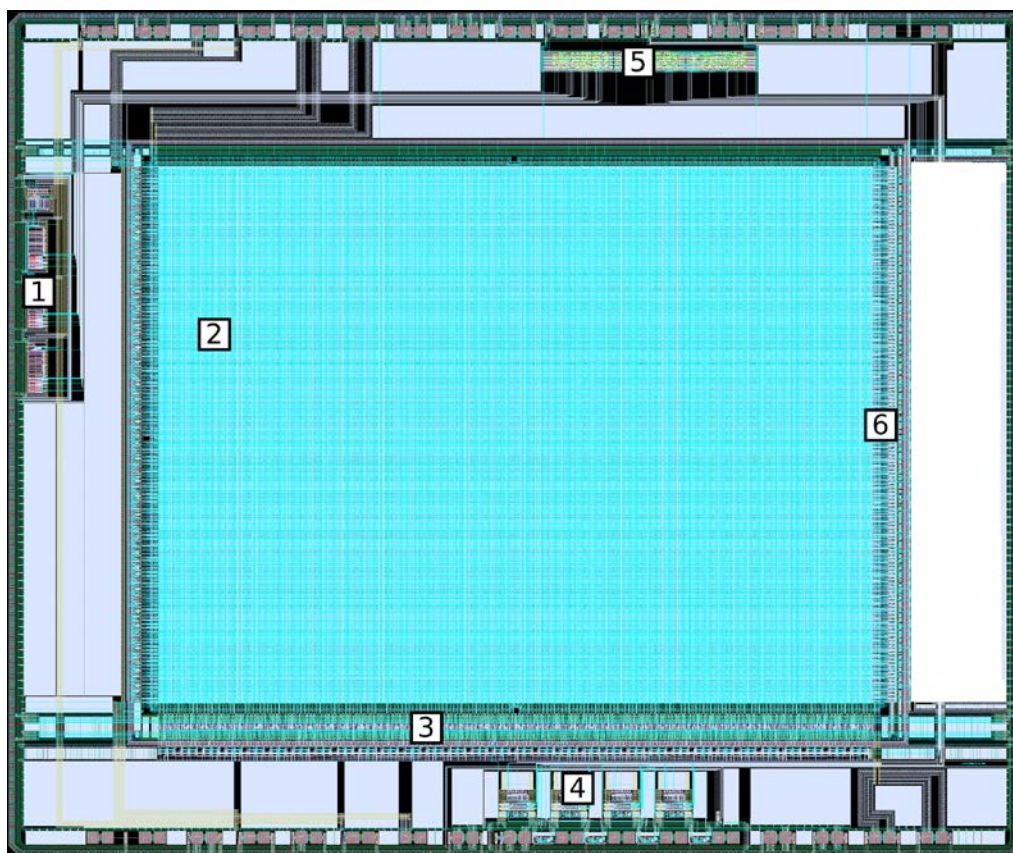


Figure 2. The layout of the ROIC. 1 – DACs block, 2 – array of pixel cells, 3 – column followers and decoder, 4 – preamplifiers and output buffers, 5 – digital block, 6 – row decoder.

3. References

[1] Rogalski A 2011 *Infrared Detectors – 2nd ed.* 662 876

X-ray tube with photo cathode

Timofeev G. A., Potrakov N. N.
Saint-Petersburg State Electrotechnical University,
Saint-Petersburg, Russia

It is known that X-ray tubes may have 3rd electrode called “grid” which is used for quickly turn on and turn off emitting flow of X-rays. But nowadays there was designed X-tube with cathode system based on photomultiplier tube (PMT). It consists of photocathode, dynode system and some focusing electrodes. Due to this construction, the intensity of X-rays can be controlled by intensity of falling on photocathode light. For example, light-emitting diode (LED) may be used for this purpose. When current flowing in LED is changing it will lead to changing intensity of its emitting light. So that kind of X-tubes give us the promising way for creating quickly-controlled X-rays sources.

Theoretically, this tube is almost inertia less. There were held some researches in aim to prove its frequency features in range from 1 kHz to 1MHz. For pulses generating was used LED with rise time 200-250ns. As X-rays detector was taken PMT-176 with crystal-scintillator NaI(Tl) which have relaxation time near 250ns. Researches were running at anode current values 200 and 800 mA with duty cycle at levels 2 and 4. X-tube experimental voltages were 30 and 60 kV. Results showed that at frequencies higher than 300 kHz the shape of signals was changed. It is caused by long rise time of LED and relaxation time of X-ray detector. To prove higher frequency characteristics of tube it is necessary to have better detector and better source of light.

In fact, X-ray tube with cathode based on photomultiplier tube can be used as an ordinary X-tube but its appliances are widely because of it provides more quick modulation. For example, it suitable for X-ray diffraction analysis or X-ray spectrometry analysis as well as special purpose devices. One of the promising ways of appliances that tube can be the opportunity to create information transmitter. The main purpose of such kind of invention is to improve signal-noise rate and secrecy of communication.

Photoluminescence of $\text{Gd}_2\text{O}_3:\text{Er}^{3+}$ -based materials for conversion of solar energy

Yu A Kuznetsova, A F Zatsepin

Ural Federal University named after the first President of Russia B.N.Yeltsin,
Yekaterinburg, Russia

Abstract. The spectral and luminescence properties of Er^{3+} activated Gd_2O_3 compacted powders have been investigated. There are several excitation channels of Er^{3+} luminescence: interband transitions, the energy transfer from Gd^{3+} ions and intracenter excitation. The quantum efficiency of the Er^{3+} ions luminescence under different excitation was calculated.

1. Introduction

Problems of modern energy, in particular, the growth of energy consumption and limited fossil resources, contribute to the development of alternative energy sources. Nowadays solar energy has broad prospects, therefore the majority of studies are focused on improving the efficiency of photovoltaic cells. One way is to use luminescent solar concentrators containing optically active centers [1]. The basic idea is better exploitation of the solar spectrum through the down-conversion and up-conversion mechanisms. Rare-earth ions are of interest as optical centers in luminescent energy converter materials due to specialty of their energy levels structure in the visible, ultraviolet and infrared regions of the spectrum. Rare earth oxides are used as the host materials because of their optical and chemical properties (broad band gap, low phonon energy) and the ability of being easily doped with rare earth ions in high concentrations. It is known that solar energy conversion efficiency is determined by the quantum efficiency of optically active ions photoluminescence [2]. In present work the quantum efficiency of the Er^{3+} ions luminescence in host lattice Gd_2O_3 under different excitation was determined.

2. Samples and Methods

Compacted powder samples of $\text{Gd}_2\text{O}_3:\text{Er}^{3+}$ were prepared by sol-gel method at the Institute of Physics Polish Academy of Sciences, Warsaw, Poland. The photoluminescence and excitation spectra and luminescence decay kinetics were obtained at room temperature using a fluorescence spectrometer PerkinElmer LS 55. The temperature luminescence intensity dependence was investigated using a spectrometer McPherson.

3. Results

Upon excitation 220 nm (interband transitions in host lattice Gd_2O_3) the emission spectrum of $\text{Gd}_2\text{O}_3:\text{Er}^{3+}$ demonstrates the intense lines at 522 and 544 nm attributed to the transitions of Er^{3+} ions. There are several excitation channels of Er^{3+} luminescence: interband transitions, the energy transfer from Gd^{3+} ions and intracenter excitation (figure 1, figure 2).

The mechanism of excitation energy transfer from Gd^{3+} ions to Er^{3+} optical centers are offered in accordance with the scheme (1).

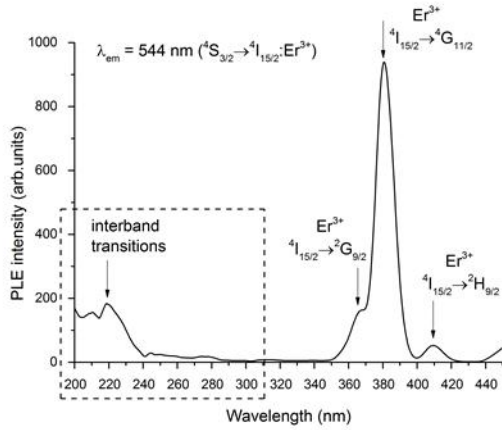
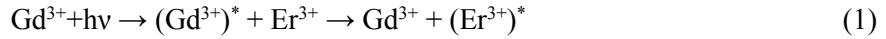


Figure 1. Excitation spectra at emission 544 nm ($^4S_{3/2} \rightarrow ^4I_{15/2}$: Er^{3+}) in the wavelength range from 200 to 450 nm.

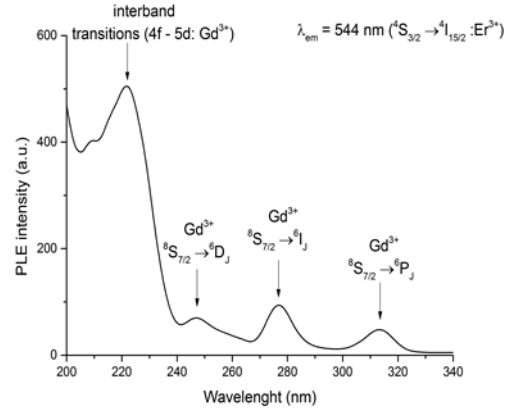


Figure 2. Excitation spectra at emission 544 nm ($^4S_{3/2} \rightarrow ^4I_{15/2}$: Er^{3+}) in the wavelength range from 200 to 340 nm.

The analytical expressions for calculating the quantum efficiency of the Er^{3+} ions luminescence under intracenter excitation (2) and excitation by Gd^{3+} ions (3) are obtained.

$$\eta_1 = \left(1 + \frac{C}{e^{-E/kT}}\right)^{-1}, \quad (2)$$

where η_1 – quantum efficiency under intracenter excitation;

C – quenching constant;

E – activation energy.

$$\eta_2 = \gamma_{\text{Gd-Er}} \cdot \eta_1, \quad (3)$$

where η_2 – quantum efficiency under excitation by Gd^{3+} ions;

$\gamma_{\text{Gd-Er}}$ – efficiency of the energy transfer from Gd^{3+} to Er^{3+} .

The parameters of temperature quenching of the Er^{3+} luminescence are determined as a result of quenching curve fitting according to Mott's law. On the basis of the obtained data the quantum efficiency of the Er^{3+} ions luminescence under intracenter excitation ($\eta_1=0,5$) and excitation by Gd^{3+} ions ($\eta_2=0,4$) are calculated.

4. Conclusion

The results indicate that the efficiencies of direct and indirect excitation of Er^{3+} ions luminescence are characterized by the same order. It is found that the most decay time of the Er^{3+} ions luminescence is observed under excitation by Gd^{3+} ions, however, the quantum efficiency in this case is less. It means that the major losses under indirect excitation take place at intermediate stages. So there is a reserve for minimizing these losses and the quantum efficiency of the Er^{3+} ions luminescence can be controlled by changes the defectiveness of host lattice Gd_2O_3 .

Acknowledgments

This research was carried out in the framework of state assignment of Russian Federation Ministry of Science and Education with partial support of the RFBR (project № 13-08-00568).

References

- [1] Strumpel C, McCann M, Beaucarne G et al 2007 *Solar Energy Materials & Solar Cells* **91** 238-249
- [2] Jiayue Sun, Guangchao Sun, Yining Sun and Liu Han 2014 *Optical Materials* **36** 1097-1100

Features of collimation and focusing of few-cycle optical beams

Danila Puzyrev and Sergey Kozlov

Department of Photonics and Optical Information Technology, ITMO University

Abstract. The paper reports theoretical features of collimation and focusing of few-cycle optical beams in transparent isotropic dielectric medium. It was showed, that a spatial collimation of such short waves results in a peculiar shaping of spatio-temporal structure with the central part moving faster than its outlying areas and collimated beam loses with distance half cycle of temporal electromagnetic field oscillation. In the focus of focusing mirror radiation number of oscillations in temporal field structure of beam depends on the focusing distance of the focusing mirror and temporal structure of collimated beam.

1. Introduction

Development of methods of generation terahertz radiation made it possible to obtain few-cycle (less than 10 field oscillations) electromagnetic waves [1]. Such radiation is widely applicable in spectroscopy, in drugs and explosive materials detection systems and for medical diagnostics [2]. Optical systems of emission, collimation and focusing initially few-cycle waves optimization is important problem in this area [3]. We consider initially Gaussian few-cycle waves propagation in homogeneous isotropic medium their collimation and focusing.

2. Collimation of few-cycle optical beams

In this paper we obtain analytical expressions which describes dynamics of collimated pulses emitted by few-cycle radiation source. For example, figure 1 illustrates these expressions for collimation of 1,5-cycle wave packet, which was emitted in the form of one-cycle optical beam. Red and blue areas correspond to maximum positive and minimum negative field respectively values of two-dimensional images. Here we take $\rho/\lambda_{\max} = 10$, where ρ is the initial transverse beam width, λ_{\max} is the wavelength corresponding to the maximum of input wave packet spectrum. For example, for terahertz single-cycle waves this value is usually $\lambda_{\max} = 300\mu m$.

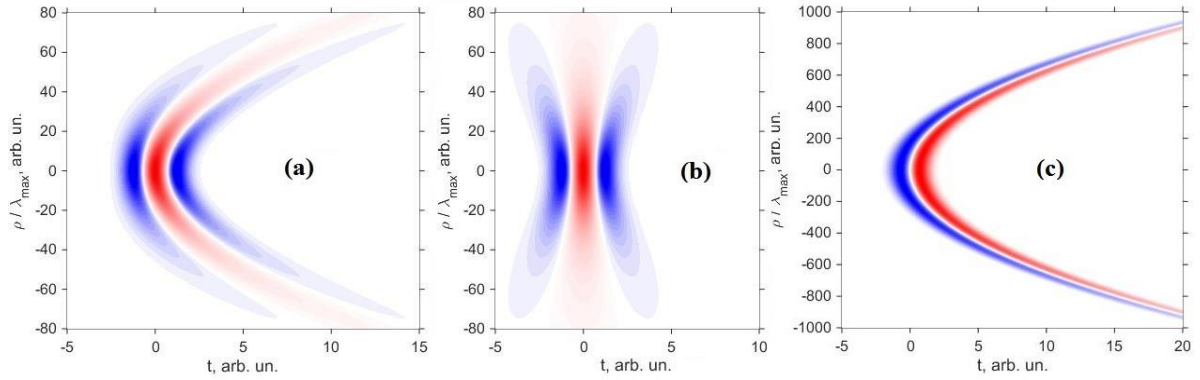


Figure 1. Electric field spatio-temporal structure of radiation before collimation (a), after collimation at the distance f_{col} (b) and $80f_{col}$ (c), where f_{col} is the focusing distance of collimation mirror.

Figure 1 shows that the central part of spatio-temporal structure of collimated beam moves faster than its outlying areas and loses half cycle of temporal electromagnetic field oscillation with distance.

3. Focusing of few-cycle optical beams

We have derived the expression described dynamics spatial distribution of the temporal spectrum

$$G_{foc}(\omega, x, y, z, z_f, f_{foc}) = \frac{iz_0^2 \left(z_{col}(\omega) f_{col} \left(1 - \frac{z}{f_{foc}} \right) + i \left(z_0 (z_f - f_{col}) - z (z_f - 2f_{col}) \right) \right)}{\left(z_{col}(\omega) f_{col} \left(1 - \frac{z}{f_{foc}} \right) \right)^2 + \left(f_{col} (z_f - f_{col}) - z (z_f - 2f_{col}) \right)^2} G_0(\omega) \times \exp \left(\frac{x^2 + y^2}{\rho^2} \frac{i \frac{f_{col}^3}{f_{foc}} + \frac{\rho^2 n(\omega) \omega}{2c} (z_f - 2f_{col})}{z_{col}(\omega) f_{col} \left(1 - \frac{z}{f_{foc}} \right) - i \left(f_{col} (z_f - f_{col}) - z (z_f - 2f_{col}) \right)} - ik(\omega) (f_{col} + z_f + z) \right) \quad (1)$$

where $z_{col}(\omega) = \frac{2cf_{col}^2}{\rho^2 n(\omega) \omega}$, x, y, z are coordinates of Cartesian axes (z axis coincides with wave

propagation direction and x, y — with transverse direction); $k(\omega) = \frac{\omega}{c} n(\omega)$ is the wave number,

$n(\omega)$ is the refractive index of medium, ω is the temporal frequency of electromagnetic wave, c is the speed of light in vacuum, f_{foc} is the focusing distance of focusing mirror, $G_0(\omega)$ is temporal spectrum at radiation source.

Analysis of expression (1) shows that number of oscillations in temporal field structure of focusing wave depends on distance f_{foc} and spatio-temporal structure at the input of focusing mirror.

References

- [1] Bespalov V G, Gorodetski A A, Denisyuk I Y, Kozlov S A, Krylov V N, Lukomski G V, Petrov N V and Putilin S E 2008 J. Opt. Technol. 75 636-642
- [2] Sakhnov S N, Leksutkina E V, Smolyanskaya O A, Usov A V, Parakhuda S E, Grachev Y V and Kozlov S A 2011 Optics and Spectroscopy 111 257-261
- [3] Puzyrev D., Drozdov A.A. Collimation and focusing of initially single-cycle paraxial optical beams. Journal of Physics: Conference Series. 2014. Vol. 541. No. 1. pp. 012065.

Theoretical investigation of the correlation between perturbations of quantum optical circuit parameters and its performance

AV Kozubov and S A Chivilihin

ITMO University, Kronverkskiy pr. 49, St.Petersburg 197101, Russian Federation

Abstract. In this paper described the operability of some quantum optical circuits which depends on perturbed parameters, such as reflectivity of beam splitters in the linear optical controlled-NOT gate in the coincidence basis or a Knill-Laflamme-Milburn CNOT gate.

1. Introduction

In the present there is an active development of such direction of quantum information as quantum teleportation [1]. Experimental and theoretical research of quantum teleportation, and its practical application, is one of the main directions in the field of quantum information. As a result, there were quite a number of experimentally realized schemes, ranging from those using photons [2] and the atoms [3], various hybrid systems and ensembles of particles [4]. The CNOT gate is one of the most important elements in quantum information theory and particularly in quantum computing. There are different realizations of this gate, both linear and non-linear. But all of them have one major problem – it operates with certain probability. However, furthermore its work is also influenced by inaccuracies of the constructions which may have a significant impact on the performance of the gate.

2. Methods

In this work we investigate how these quantum optical circuits work with some perturbed parameters such as reflectivity (transmittivity) of beam splitters. In the linear optical CNOT gate in the coincidence basis [5] circuit there are five beam splitters – two of them have the reflectivity of one-half and others have reflectivities of one-third.

In spite of this we want to see how it operates with the arbitrary values of reflectivity of the beam splitters. By using the Heisenberg equation for beam splitters

$$\begin{aligned} a_{out} &= \sqrt{\eta}a_{in} + \sqrt{1-\eta}b_{in}, \\ b_{out} &= \sqrt{1-\eta}a_{in} - \sqrt{\eta}b_{in}, \end{aligned} \tag{1}$$

where η ($1-\eta$) is the reflectivity (transmittivity) of the beam splitters, we can obtain the relation of control and target input modes to their corresponding output mode operators. It is necessary for calculating the output state of the system in the Schrödinger picture. We can calculate it through substituting input mode operators for the output operators, which we already derived. Thereby we

obtain the function of the output state for the circuit with the arbitrary beam splitter ratios. Thus we can analyze how this gate operates and what the error probabilities are.

Also in this work we have calculated the dependence of error probability from beam splitter ratios in Knill-Laflamme-Milburn CNOT gate [6]. There are different realizations of this gate with various type and amount of elements, in particular beam splitters, but despite this we can apply similar technique and methods to obtain the function of output states for these circuits.

3. Results and discussion

In the presented work, we have derived the analytical expression for the output state function of the system for several realized circuit of control-NOT gate, such as linear optical CNOT gate in the coincidence basis and Knill-Laflamme-Milburn CNOT gate. Also we have obtained an error probability for certain values of the deviations of the reflectivity in the beam splitters from the optimal values. Furthermore we have calculated and plotted dependence of the error probability in these circuits with arbitrary deviations in beam splitter ratios.

References

- [1] Bennett C Brassard G 1993 *Phys. Rev. Lett.* **70** 1895
- [2] D Bouwmeester J-W Pan K Mattle M Eibl H Weinfurter and A Zeilinger 1997 *Nat.* **390** 575
- [3] M D Barrett J Chiaverini T Schaetz J Britton W M Itano J D Jost E Knill C Langer D Leibfried R Ozeri & D J Wineland 2004 *Nat.* **429** 737
- [4] Alexey N Pyrkov and Tim Byrnes 2014 *Phys. Rev. A* **90** 062336
- [5] T C Ralph N K Langford T B Bell and A G White 2002 *Phys. Rev. A* **65** 062324
- [6] Ryo Okamoto Jeremy L O'Brien Holger F Hofmann Shigeki Takeuchi 2011 *Proc. Natl. Acad. Sci.* **108** 10067

Temperature switching of resonator modes in microcrystals InN

D R Kazanov*, V H Kaibyshev, V U Davidov, A N Smirnov, V N Jmerik, N V Kyznetsova, S V Ivanov, T V Shubina

Ioffe Physical-Technical Institute of the RAS, St.-Petersburg, 194021 Russia

Abstract. InN optical resonators, which can support whispering-gallery modes of low orders up to room temperature, were made by MBE on profiled substrates. The observed effect of mode switching with a temperature rise was ascribed to the change of optical parameters induced by the shift of an absorption edge and modification of its shape. The results of modelling taking into account variation of refraction index reproduce typical distribution of the intensity of electromagnetic field within the resonators.

1. Introduction

The complexity of the production of planar Bragg microcavities with dielectric or semiconductor mirrors causes interest in the 3D resonators - microcolonies, disks and crystals, which can support whispering gallery modes (WGM) [1]. We recently demonstrated the possibility of the creation of such resonators based on InN microcrystals with diameters up to 2.2 microns by molecular beam epitaxy (MBE) on profiled substrates [2]. The specific shape of the crystals in the form of an inverted truncated hexagonal pyramid is realized by the difference in the lateral and vertical components of the growth rate. Insertion of radiating dipoles in the resonator cavities can be applied for microlasers and source of single photons using the Purcell effect by means of amplification of low-intensity optical transitions. In this paper, we analyze the changes in the content of the optical modes induced by temperature variation.

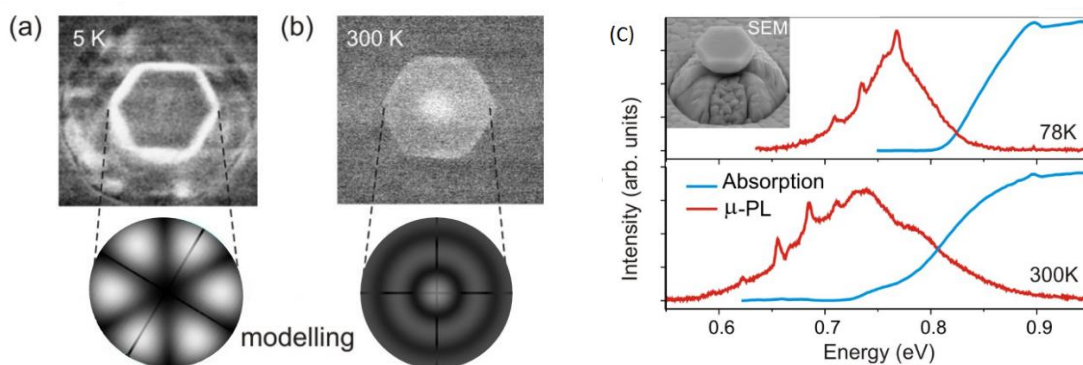


Figure 1. (top a,b) Change of the dominant type of modes from azimuthal (a) to radial (b), which is observed by μ -CL at different temperatures. (bottom a,b) Modelling of typical electromagnetic distribution of intensity taking into account different refractive index. (c) Image of an InN microcrystal and a μ -PL spectrum at different temperatures shown together with absorption spectra of the structure.

2. Experiment and modelling

Micro-photoluminescence (μ -PL) and micro-cathodoluminescence (μ -CL) measurements demonstrated the existence of low order WGM in the microcrystals and the possibility of amplification of radiation up to the room temperature (Fig.1). By μ -CL studies, it was found out in addition that optical modes switch from azimuthal to radial while temperature rising (Fig.1c). In the simplest cylindrical approximation it is well known that the frequency of a resonator mode of m -order appears to be $\omega \propto mc/Dn$, where D - diameter, n - refractive index, c - speed of light. Therefore, while D is constant, only n can change the type of modes. To determine the n variation the integral spectrum of transmission and refraction were measured at different temperatures. Complex dielectric function in the vicinity of the absorption edge was found by Kramers - Kronig relations. The result of temperature dependence of refractive index is shown in Fig. 2. Numerical modelling of those modes distribution (Fig.1a,b) using obtained optical parameters was done by solving Maxwells equations in the Comsol Multiphysics software with following approximations: microcrystals were considered to be truncated cones, boundaries were chosen in order to make the rapid decay of wave outside the crystal. The simulated energy distributions in the characteristic modes are in reasonable agreement with experimentally observed μ -CL images (Fig. 1 a,b).

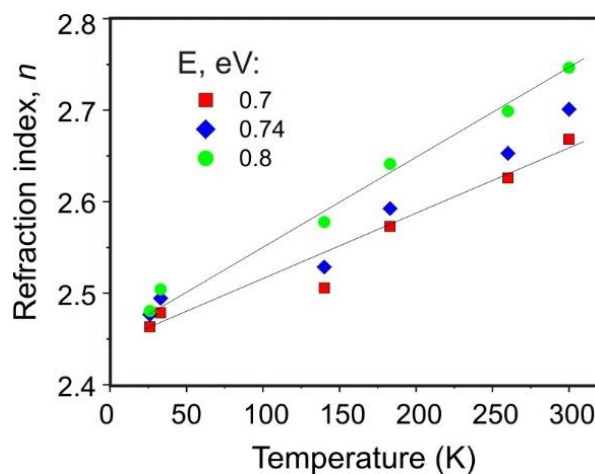


Figure 2. Temperature dependence of refractive index for three different energies in InN emission band.

In general, the effect of temperature-induced mode switching should be taken into account while designing the devices, which uses selective amplification of definite radiative frequencies by means of whispering gallery modes.

Acknowledgments

This work has been supported by Russian Science Foundation, grant № 14-22-00107

References

- [1] K. J. Vahala // Nature, V. 424, 839 (2003).
- [2] T V Shubina et al., XVIII Symposium "Nanophysics & Nanoelectronics", 686 (2014)

Extracting S-parameters of bilateral electro-optic network for lightwave component analyzer calibration

D. Frolov¹, A. Levchenko

Kuban State University, 149 Stavropolskaya st., Krasnodar, Russia

Abstract. In this paper we theoretically propose a new method for extracting E/O and O/E S-parameters of a bilateral electro-optic network (BEON) based on measuring reflection coefficients from three optical loads: an absorber and two mirrors. This technique includes two series of reflections measurements: first when loads are connected to optical port of BEON directly and second when loads are connected in series with optical waveguide with calibrated length. Using two BEONs and this calibration technique allows to make calibrated lightwave measurements with a standard microwave network analyzer without using additional electro-optical equipment such as lightwave component analyzer or optical heterodyne techniques.

1. Introduction

A bilateral electro-optic network (BEON) and its use for lightwave network analysis measurements was first reported by Pollard [1]. Unlike majority E/O and O/E components that are not reciprocal in nature BEON is a network in which forward (electrical to optical) and reverse (optical to electrical) transmission is allowed. Using BEONs in lightwave network analyzers instead of single laser diodes and photodetectors allow to use an optical analogue of various microwave two-port calibrations such as TRL. This allows to measure full S-matrix of O/O components. However it sacrifices the ability to perform E/O and O/E measurements.

A two-tier calibration of the electro-optic analyzer was reported by Pollard [2]. However in this calibration BEON is treated as a blackbox whose S-parameters are measured with a HP8703A or other lightwave component analyzer, that uses the optical heterodyne technique [3] to measure the frequency response $S_{21}^{O/E}$ of its photodetector. This technique uses two Nd:YAG lasers, one passing through the modulator, the other functioning as a local oscillator to convert one of the sidebands of the modulated carrier to IF frequency. This IF frequency can be swept by sweeping the wavelength of laser beam, thus the wavelength can be controlled by varying the temperature of YAG crystal.

However these measurements are conducted with complex optoelectronic system that includes lasers, spectrum analyzer, temperature control system, different lenses and polarization control devices. This can be a serious disadvantage in case if one needs to characterize an unknown photodetector or a BEON that is operated in O/E mode because it is impossible to make such measurements with a standard lightwave component analyzer like HP8703A.

2. Description of measurement procedure

The process of extracting scattering parameters of BEON can be done with a standard VNA. First it is needed to calibrate vector network analyzer (VNA) with one of known techniques [4,5,6]. After calibration BEON electrical port should be connected to one of VNA's ports and six S11 measurements with optical loads should be done as it is shown in figures 1 and 2.

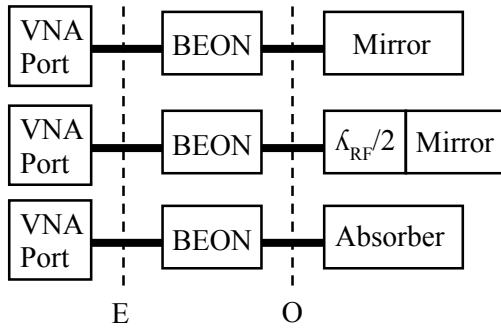


Figure 1. VNA measures complex reflection coefficients of BEON's electrical port with three type of loads: first mirror (equivalent to short load at RF), second mirror placed $\lambda_{RF}/2$ far (open load) and absorber (matched load at RF).

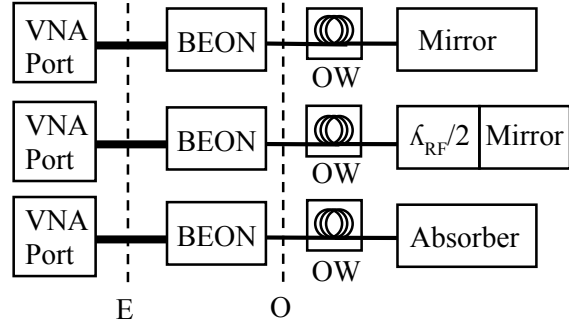


Figure 2. VNA measures complex reflection coefficients of BEON's electrical port with the same loads, but connected in series with optical waveguide (OW) of calibrated length (equivalent to air line at RF).

As a result we have six complex reflection coefficients that can be presented as a system of six equations – three equations (1-3) for reflections without optical waveguide and three with it (4-6)

$$S_S = S_{11}^{E/E} + \frac{S_{21}^{E/O} S_{12}^{O/E} \Gamma_S}{1 - S_{22}^{O/O} \Gamma_S} \quad (1)$$

$$S_O = S_{11}^{E/E} + \frac{S_{21}^{E/O} S_{12}^{O/E} \Gamma_O}{1 - S_{22}^{O/O} \Gamma_O} \quad (2)$$

$$S_L = S_{11}^{E/E} + \frac{S_{21}^{E/O} S_{12}^{O/E} \Gamma_L}{1 - S_{22}^{O/O} \Gamma_L} \quad (3)$$

$$S_S^/ = S_{11}^{E/E} + \frac{S_{21}^{E/O} S_{12}^{O/E} \Gamma_S^/}{1 - S_{22}^{O/O} \Gamma_S^/} \quad (4)$$

$$S_O^/ = S_{11}^{E/E} + \frac{S_{21}^{E/O} S_{12}^{O/E} \Gamma_O^/}{1 - S_{22}^{O/O} \Gamma_O^/} \quad (5)$$

$$S_L^/ = S_{11}^{E/E} + \frac{S_{21}^{E/O} S_{12}^{O/E} \Gamma_L^/}{1 - S_{22}^{O/O} \Gamma_L^/} \quad (6)$$

Using analogue with (1-6) for $\Gamma_S^/, \Gamma_O^/, \Gamma_L^/$ we also have three equations:

$$\Gamma_S^/ = S_{11}^{OW} + \frac{S_{21}^{OW} S_{12}^{OW} \Gamma_S^/}{1 - S_{22}^{OW} \Gamma_S^/} \quad (7)$$

$$\Gamma_O^/ = S_{11}^{OW} + \frac{S_{21}^{OW} S_{12}^{OW} \Gamma_O^/}{1 - S_{22}^{OW} \Gamma_O^/} \quad (8)$$

$$\Gamma_L' = S_{11}^{OW} + \frac{S_{21}^{OW} S_{12}^{OW} \Gamma_L^{OW}}{1 - S_{22}^{OW} \Gamma_L^{OW}} \quad (9)$$

where S_{11}^{OW} , S_{12}^{OW} , S_{21}^{OW} and S_{22}^{OW} are S-parameters of optical waveguide.

Values S_S , S_O , S_L , S_S' , S_O' , S_L' are known from the measurements, all other values: $S_{11}^{E/E}$, $S_{21}^{E/O} S_{12}^{O/E}$, $S_{22}^{O/O}$, Γ_S^{OW} , Γ_O^{OW} , Γ_L^{OW} , S_{11}^{OW} , $S_{21}^{OW} S_{12}^{OW}$, S_{22}^{OW} are unknown. So we have system with six equations and eight unknown values.

But in some frequency points that we shall call reference points, influence of S_{11}^{OW} and S_{22}^{OW} parameters will be very small and it can be observed when the equivalent RF length of optical waveguide will provide 180° difference between RF waves reflected from the ends of the optical waveguide. In these reference points reflected waves will eliminate each other so reflection coefficients $S_{11}^{OW} \approx S_{22}^{OW} \approx 0$. And this condition is true only for defined number of frequencies. So in several reference points there are only six unknown values and six equations and it is possible to find a solution for the system of equations. But even having only several reference points it is possible to find a solution for all frequency range by using Hermite polynomials [7].

3. Conclusion

In this paper we theoretically describe a simple method for extracting full S-matrix of a BEON both in E/O and O/E directions that is based on using only one port of standard microwave VNA three optical loads and a light waveguide of calibrated line.

References

- [1] Iezekiel S, Elamaran B and Pollard R 2000 Recent developments in lightwave network analysis *Eng. Sci. and Educ. J.* **12** 247
- [2] Pollard R 2002 Developments in lightwave S-parameter measurement techniques *IEE Proc.-Sci. Meas. Technol.* **149** 6 345
- [3] Tan T, Jungerman R, Elliott S 1989 Optical Receiver and Modulator Frequency Response Measurement with a Nd:YAG Ring Laser Heterodyne Technique *IEE Trans. Microw. Theory Tech.* **37** 8 1217
- [4] Kruppa W and Sodomsy K 1971 An explicit solution for the scattering parameters of a linear two-port measured with an imperfect test set *IEEE Trans. Microw. Theory Tech* **19**, 122–123
- [5] Rehnmark S 1974 On the calibration process of automatic network analyzer systems *IEEE Trans. Microw. Theory Tech.* **22** 457–458
- [6] Heuermann H and Schiek B 1994 Robust algorithms for Txx network analyzer self-calibration procedures *IEEE Trans. Instrum. Meas.* **43** 18–23
- [7] Digital Library of Mathematical Functions. National Institute of Standards and Technology. URL: <http://dlmf.nist.gov/18.18.E20> Retrieved 30 January 2015

Elimination of light coupling negative effect on the accuracy of external quantum yield determination in a MJ SC

S A Kozhukhovskaia, E D Filimonov, M A Mintairov and M Z Shvarts

Ioffe Physical-Technical Institute, St. Petersburg, 194021, Russia

Abstract. This paper presents a new technique allows to eliminate negative effect of light coupling and to determine true value of external quantum yield of a multijunction solar cell.

1. Introduction

The light coupling (LC) observed inside monolithic semiconductor heterostructures and discussed actively during recent years, which results in appearance of induced current in a p-n junction (subcell) owing to absorption of luminescence from the adjacent wideband p-n junction, can lead to such positive effects as the rise of the short circuit current, of the open circuit voltage and, as a result, of the efficiency of a GaInP/GaAs/Ge multijunction solar cell (MJ SC). The processes mentioned above complicate methodology of the experimental study of MJ SCs and can substantially affect the accuracy in determining spectral and I-V characteristics.

It is known that, in investigating MJ SC spectral characteristics, an abnormal photo-response out of typical spectral sensitivity range of the subcell under study is fixed. So a Ge subcell can demonstrate a high sensitivity in the short wavelength spectrum region, radiation from which is absorbed completely in photoactive GaInP and GaAs layers located above. In this case, the absolute photosensitivity values of the Ge subcell being registered appear to be low. In the majority of cases, the registered abnormal photoresponse of modern MJ SCs appears to be as a result of a complex negative effect of fundamental (LC) processes and of properties of p-n junctions (low shunting resistance) inherent in the semiconductor structure on the photosensitivity spectral dependences being determined by standard methods. This highlighted the need to improve corresponding experimental procedures [1, 2].

2. Experimental details

In the work, a new approach to determining true values of photosensitivity of narrowband (NB) subcells in a MJ SC based on study of spectral characteristics only with application of sources of frequency modulated radiation ensuring also a light bias for the wideband (WB) subcells, is presented. The procedure has two stages. At the first one, the dependence of the photocurrent induced by luminescence in the NB subcell (J_{LC}^N) on the photocurrent generated in the neighboring emitting WB subcell (J^W) (Fig.1) is measured. At the second stage, at a chosen level of illumination of the WB subcell and a corresponding bias voltage V_{BIAS} , registration of the NB subcell photocurrent values is performed: J_0^N – induced by luminescence and $J_1^N + J_\lambda^N$ – at additional monochromatic illumination of a preset wavelength (λ). It should be noted that the value of $J_1^N + J_\lambda^N$ will be less than the expected value of $J_0^N + J_\lambda^N$ due to change of the photocurrent flowing through the WB p-n junction and causing luminescent radiation [2]. It is easy to establish graphically (Fig.2) the following correlation for photocurrent values in the point at V_{BIAS} :

$$\Delta J + J_0^N = J_i^N + J_{\lambda}^N, i = 1, 2 \quad (1)$$

$$QE = (\Delta J/J_{ref}) QE_{ref}, \quad (2)$$

where ΔJ – registered increment of the photocurrent caused by monochromatic radiation and used in standard measurement procedures for determining the external quantum yield of the photoresponse (expression 2); J_{ref} – photocurrent of a reference SC at its illumination by chopped monochromatic radiation; QE_{ref} – external quantum yield of the reference SC at chosen wavelength.

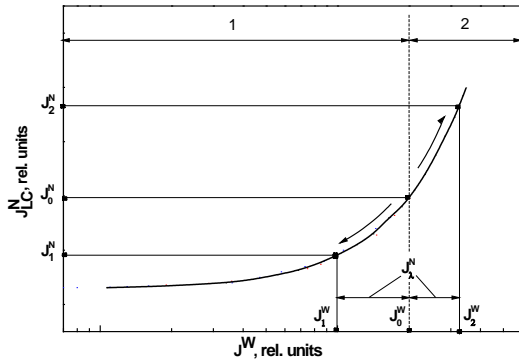


Figure 1. The dependence of the photocurrent induced by luminescence in the NB subcell (J_{LC}^N) on the photocurrent generated in the neighboring WB subcell (J^W): 1 and 2 designate the zones for J_{λ}^N determination, when λ is within the NB (1) or WB (2) subcell photosensitivity range.

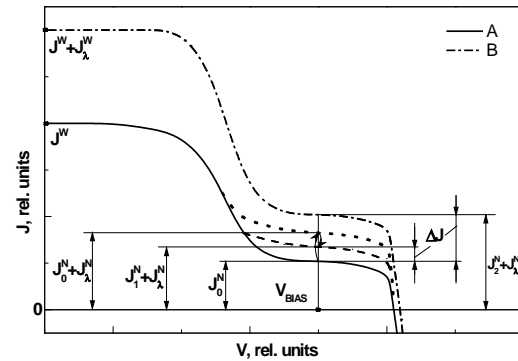


Figure 2. Graphical representation of photocurrent values for I-V curves, obtained under various conditions of illumination by chopped monochromatic light in the NB (A) and in the WB (B).

The sought-for value of J_{λ}^N is determined graphically by subtraction. Consistently stepping left (zone 1, Fig.1) from the value of J_0^W (J_0^W – is set using light bias sources and controlled accurately at measurement sequence) by some value of J_{λ}^N , search for a pair of values (J_1^N , J_{λ}^N), at which the equality (1) will be valid, was carried out. The obtained value of J_{λ}^N is free from a light coupling negative influence and allows calculating the true value of the external quantum yield of photoresponse for the NB subcell within its spectral sensitivity in substituting ΔJ for J_{λ}^N in the expression 2. In the short wavelength range beyond the main sensitivity range of the NB subcell [3], the procedure for evaluating J_{λ}^N is similar to that pointed out above with the only difference that the search of the pair of (J_2^N , J_{λ}^N) values is carried out right from the J_0^W value (zone 2, Fig.1).

3. Conclusion

The proposed procedure has been realized on an installation for recording spectral dependencies of MJ SC photoresponse, in which an optical chopper was placed in front of the tested specimen thereby modulating fluxes of monochromatic radiation and light shift.

References

- [1] Shvarts M Z, Mintairov M A, Emelyanov V M, Evstropov V V, Lantratov V M and Timoshina N Kh 2013 Method for direct measurements of luminescent coupling efficiency in concentrator MJ SCs *AIP Conf. Proc.* **1556** 147
- [2] Lim S H, Li J J, Steenbergen E H and Zhang Y H 2011 Luminescence coupling effects on multi-junction solar cell external quantum efficiency measurements *Progress in PV: Research and Applications* **21** 344
- [3] Kozhukhovskaia S A, Filimonov E D and Shvarts M Z 2015 Experimental model of multi-junction solar cell: IV curve tailoring and photoresponse artifact simulation *Journal of Physics: Conference Series* **586** 012014

Low-temperature study of the rhodamin 6G phosphorescence in polymethylmethacrylate films in the presence of silver nanoparticles

E I Konstantinova¹, R Yu Borkunov², M V Tsarkov³, V A Slezhkin⁴ and V V Bryukhanov⁵

¹ – Department of Physics, Kaliningrad State Technical University, 1 Sovietsky prospect, 236022, Kaliningrad, Russia

^{2,3} – Institute of Physics and Technology, Immanuel Kant Baltic Federal University, 14 A, Nevskogo street, 236041 Kaliningrad, Russia

⁴ – Department of Chemistry, Kaliningrad State Technical University, 1 Sovietsky prospect, 236022, Kaliningrad, Russia

⁵ – Centre for Laser Nanotechnologies and Information Biophysics, Immanuel Kant Baltic Federal University, 14 A, Nevskogo street, 236041 Kaliningrad, Russia

Abstract. In this paper by the methods of femtosecond laser photoexcitation in the wide range of temperatures the rhodamine 6G (R6G) phosphorescence in thin polymethylmethacrylate films with the ablated silver nanoparticles has been investigated. The nonmonotonic character of the lifetimes change of phosphorescence including interval including the interval as descending and of increasing has been found. The effect of silver nanoparticles on the main processes was determined.

The study of the temperature dependence of the various characteristics phosphorescence (phosphorescence spectra, quantum yield, durationexcited states, etc.) is of great importance both for determining the nature of the emitting centers, as well as for the study of molecular interactions in condensed media. This study method of the phosphorescences processis widely used in practice and is generally accepted.

Low-temperature researches of phosphorescence of R6G molecules in films polymethylmethacrylate (PMMA) on the original automated fluorescent installation (figure 1) which based on the femtosecond continuous laser and the electronic low-temperature nitric cryostat were conducted.

Films were produced by filling on glass of solution of R6G and PMMA in chloroform. Ablated nanoparticles of silver were produced by the technique described in article [1]. The silver nanoparticles sizes were investigated on the correlation FotoCor-Complex installation and their average size made 40 nm. Films with silver prepared similarly, to solution of R6G and PMMA adding silver nanoparticles. Concentration of R6G in the film made $C=5 \cdot 10^{-4}$ M, silver nanoparticles - $C=0,85 \cdot 10^{-9}$ M. Thickness of a film is 40 microns.

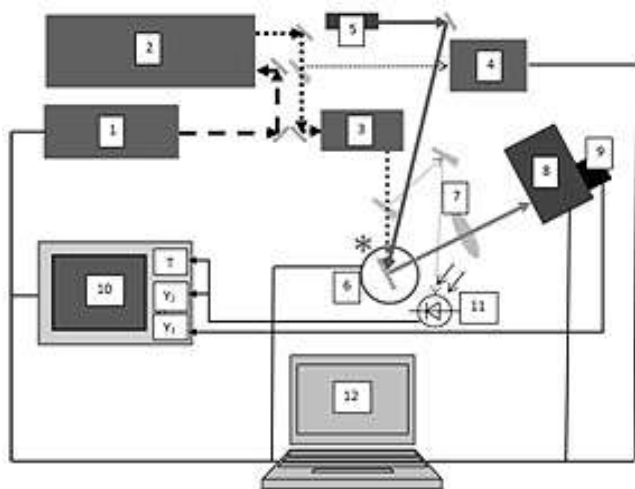


Figure 1. The block diagram of the installation: 1 – femtosecond pulses generator "TETA-25", Avesta; 2 – femtosecond laser pulses compressor "Compulse", Avesta; 3 – the 2nd harmonica generator, Avesta; 4 – femtosecond single-pulse autocorrelator "ASF-20", Avesta; 5 – solid-state continuous laser Laser-export co.ltd "LCS-DTL-317"; 6 – "Optistat DN2-V" cryostat, Oxford instruments with a sample; 7 – lens; 8 – monochromator "ML-44", Solar; 9 – PEM "m-h10720", Hamamatsu; 10 – high-speed digital oscillograph "DPO4104B", Tektronix; 11 – high-speed avalanche photo diode; 12 – computer.

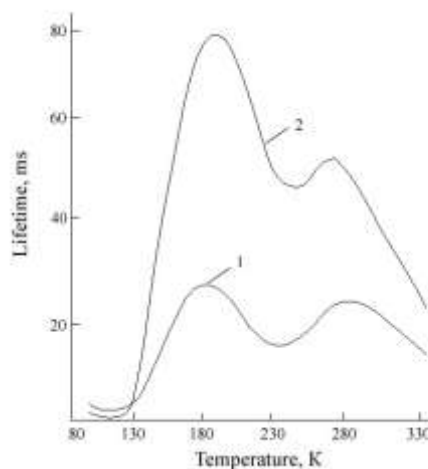


Figure 2. The temperature quenching of the rodamine 6G phosphorescence: 1 – without silver nanoparticles, 2 – with silver nanoparticles.

Lifetimes of phosphorescence were calculated from the oscillograms of signal processed in the standard way (exponential image of the curve decay was picked up and was produced by convolution of signal and the response function of PMT and oscilloscope [2]). In figure 2 temperature dependence of the lifetimes of phosphorescence R6G with silver nanoparticles and without them is presented. Apparently from drawing, all studied temperature interval can be broken into five areas including an interval decrease and increase.

The temperature phosphorescence quenching derived as result of β -relaxation process propagation to the neighboring region of the polymer with the dye molecules. In addition, there is the diffusion quenching acceleration of the triplet states of molecules and impurities particles. In addition, there is an acceleration of the diffusion quenching of the triplet states of molecules and impurities particles. Figure 2 shows that in the presence of silver nanoparticles (curve 2) increases the phosphorescence lifetime. It is can be explain by influence of the plasmons energy on the R6G molecules T-states.

The results have been obtained in the accord with the state task of the Education and Science Ministry of the Russian Federation No. 3.809.2014/K.

References

- [1] Bryukhanov V V et al 2014 Peculiarities of the femtosecond laser photoexitation of fluorescence and phosphorescence of rhodamine 6G molecules in the polymethylmethacrylate films with silver nanoparticles *KGTU izvestia* 6 34
- [2] Lakovich J 1986 Principles of fluorescent spectroscopy Moscow 76

Magnetic system design for investigation of magneto-optical properties of objects in strong magnetic field in terahertz frequency range

S E Azbite, AKh Denisultanov and M K Khodzitsky

Department of Photonics and Optical Information Technologies, ITMO University,
49 Kronverksky av., St. Petersburg, Russia

Abstract. A strong localized magnetic field system at room temperature was proposed for application in terahertz magneto-optics, magneto-resonance spectroscopy and magneto-tunable devices.

1. Introduction

At the present moment in terahertz spectroscopy there are some tasks, which need strong magnetic fields for their solution, such as investigation of optical properties of objects under magnetic field, terahertz magnetic resonance spectroscopy and new magnetically controlled equipment development [1]. For example, it was theoretically assumed, that graphene monolayer has magneto-dependent optical properties, such as permittivity and conductivity, under strong magnetic fields over 2 Tesla in terahertz frequency range [2]. This feature may be used for design of magneto-tunable terahertz devices, e.g. narrow band and broadband filters, polarizers, beamsplitters, generators, etc.

2. Results

Today electromagnets and superconducting magnets are used to obtain a strong magnetic field. Such types of magnetic systems have cumbersome construction and need additional equipment. Usually permanent magnets give a small magnetic field. In this paper permanent magnet based on giant magnetic anisotropy material SmCo₅ was proposed and investigated. Optimal design of this magnetic system was developed and calculated. It needs to be made as a semi-sphere that comprised segments, separated by radial planes cones. This magnetic system geometrical configuration was calculated that gives a strong localized magnetic field gradient along radial component. Such magnetic system affords an opportunity to work with different magnetic field strength values.

3. Conclusions

The magnetic system with strong localized magnetic field was simulated in software COMSOL MultiPhysics using AC/DC Module. The magnet radius value at the predetermined magnetic field strength allocation and sample size were obtained by the iteration algorithm. The magnetic field strength distribution was calculated analytically [3].

References:

- [1] Kamaraju Net. al. 2015 Appl. Phys. Lett. 106, 031902
- [2] Denisultanov A et al. 2014 J. Phys.: Conf. Ser. 541 012058
- [3] Samofalov V, Belozorov D and Ravlik A 2013 Physics -Uspekhi 56 pp 269-288.

Dielectric permittivity of artificial periodic structure and local field effects

M N Anokhin, A A Tishchenko and M N Strikhanov

National Research Nuclear University MEPhI, Moscow, Russia

Abstract. In this work we study dielectric properties of an artificial periodic structure on the base of the local field theory. We generalize Clausius-Mossotti relation for case of an infinite material. Limiting cases are studied.

1. Introduction

Artificial periodic structures based on different kinds of materials are of interest of researchers[1]. Of particular interest is a changing of dielectric properties. Periodicity is responsible for its special electromagnetic properties[2]. This structures are of importance for an application in resonators, signal dividers and metamaterials.

2. Macroscopic and local fields

Let us consider the infinite periodic structure composed of anisotropic molecules. Let all the molecules of the material have the polarizability $\alpha_{ij}(\omega)$. Let the external field \mathbf{E}^0 act upon this material.

We use dipole approximation as all the atomic electrons is non-relativistic. Using linearity of Maxwell's equations we obtain the Fourier transform of the solution of Maxwell's equations in a medium[3]:

$$E_i^{mic}(\mathbf{r}, \omega) = E_i^0(\mathbf{r}, \omega) + \frac{1}{2\pi^2} \int d^3l S_{ij}(\mathbf{l}, \omega) \alpha_{jk}(\omega) \sum_b E_k^{mic}(\mathbf{R}_b, \omega) \exp\{-i\mathbf{l}(\mathbf{R}_b - \mathbf{r})\} \quad (1)$$

Let $r = R_a$ in Eq. (1). In this case we have a system of N equations for acting on the a-th molecule field. We can solve this system only approximately for the reason that $N \gg 1$:

$$E_i^{mic}(\mathbf{R}_a, \omega) = E_i^0(\mathbf{R}_a, \omega) + \frac{1}{2\pi^2} \int d^3l S_{ij}(\mathbf{l}, \omega) \alpha_{jk}(\omega) \sum_b E_k^{loc}(\mathbf{R}_b, \omega) \exp\{-i\mathbf{l}(\mathbf{R}_b - \mathbf{R}_a)\} \quad (2)$$

We find a local field by averaging over the location of other molecules:

$$E_i^{loc}(\mathbf{R}_a, \omega) = E_i^0(\mathbf{R}_a, \omega) + \frac{1}{2\pi^2} \int d^3l S_{ij}(\mathbf{l}, \omega) \alpha_{jk}(\omega) \int d^3R_{ba} N w(\mathbf{R}_{ba}) E_k^{loc}(\mathbf{R}_a + \mathbf{R}_{ba}, \omega) \exp\{-i\mathbf{l}\mathbf{R}_{ba}\} \quad (3)$$

where $w(\mathbf{R}_{ba})$ is the probability density of finding the b -th molecule at the distance $\mathbf{R}_{ba} = \mathbf{R}_b - \mathbf{R}_a$ ($k = \overline{1, N-1}$):

$$w(\mathbf{R}) = \frac{1}{N} \sum_{m=1}^N \delta(\mathbf{R} - \mathbf{R}_m) \quad (4)$$

We obtain the macroscopic field by averaging over the coordinates of all the molecules:

$$E_i(\mathbf{R}, \omega) = E_i^{loc}(\mathbf{R}, \omega) + \frac{1}{2\pi^2} n \int d^3R' S_{ij}(-\mathbf{R}', \omega) \alpha_{jk}(\omega) E_k^{loc}(\mathbf{R} + \mathbf{R}', \omega) \quad (5)$$

A connection between the macroscopic field \mathbf{E} and the local field \mathbf{E}^{loc} in the coordinates (\mathbf{q}, ω) is obtained:

$$E_i(\mathbf{q}, \omega) = E_i^{loc}(\mathbf{q}, \omega) + 4\pi n S_{ij}(\mathbf{q}, \omega) \alpha_{jk}(\omega) E_k^{loc}(\mathbf{q}, \omega) - \frac{1}{2\pi^2} \sum_{m=1}^N \exp\{i\mathbf{q}\mathbf{R}_m\} S_{ij}(-\mathbf{R}_m, \omega) \alpha_{jk}(\omega) E_k^{loc}(\mathbf{q}, \omega) \quad (6)$$

Equation which connects the Fourier transforms of the local and macroscopic fields[4]:

$$t_{ik}(\mathbf{q}, \omega) E_k^{loc}(\mathbf{q}, \omega) = E_i(\mathbf{q}, \omega) \quad (7)$$

where

$$t_{ik}(\mathbf{q}, \omega) = \delta_{ik} + 4\pi n S_{ij}(\mathbf{q}, \omega) \alpha_{jk}(\omega) - \frac{1}{2\pi^2} \sum_{m=1}^N \exp\{i\mathbf{q}\mathbf{R}_m\} S_{ij}(-\mathbf{R}_m, \omega) \alpha_{jk}(\omega) \quad (8)$$

3. Discussion

In the long-wave approximation we obtain generalized Clausius-Mossotti relation. In the limiting cases it goes into known results

This work was supported by Ministry of Education and Science of Russian Federation, Agreement No. 14.575.21.0002, ID RFMEFI57514X0002.

References

- [1] Silin R A Electromagnetic waves in artificial periodic structures 2006 *Phys. Usp.* **49** 542
- [2] Pisarenco M, Setija I D On the complexity of aperiodic Fourier modal methods for finite periodic structures 2014 *Journal of Computational Physics* **261** 130
- [3] Anokhin M N, Tishchenko A A, Ryazanov M I and Strikhanov M N Permittivity of anisotropic dielectric near surface with local field effects 2014 *Journal of Physics: Conference Series* **541** 012023
- [4] Ryazanov M I and Tishchenko A A Clausius-Mossotti-type relation for planar monolayers 2006 *JETP* **103** 539 [*ZhETF* **130** 621]
- [5] Ryazanov M I, Strikhanov M N and Tishchenko A A Local field effect in diffraction radiation from a periodical system of dielectric spheres 2008 *Nucl. Instr. and Meth. B* **266**, 3811

Spontaneous emission in metal-dielectric metamaterials including losses.

A. R. Gubaydullin^{1*}, M. A. Kaliteevski^{1,2}

¹St. Petersburg Academic University, St. Petersburg 194021, Russia

²Department of Physics, Durham University, Durham DH1 3BH, United Kingdom

Abstract. We study the emission rate enhancement of the dipole emitter centred in the stratified metal-dielectric metamaterial, characterized by the hyperbolic isofrequency surface. We find out a limited enhancement of the Purcell factor in the layered metamaterial. We demonstrate that the radiative decay rate is strongly depends on a ratio of the thickness of layers and is affected by the level of losses in metal.

1. Introduction.

Metamaterials constructed from periodic metal-dielectric multilayer system are generally known as a simple realization of the so-called hyperbolic media [1]. Such hyperbolic metamaterial (HMM) systems have attracted great scientific interest over the past decade due to their special optical properties emanating primarily from hyperbolic dispersion of isofrequency surface, which for the metal-dielectric stratified media is given by:

$$\frac{k_x^2 + k_y^2}{\varepsilon_{\parallel}} + \frac{k_z^2}{\varepsilon_{\perp}} = \left(\frac{\omega}{c}\right)^2.$$

and can be hyperbolic when one of the principal components of the effective permittivity tensor ε_{eff} of the diagonal form is opposite in sign to the other two principal components [2].

$$\varepsilon_{eff} = \begin{pmatrix} \varepsilon_{\perp} & 0 & 0 \\ 0 & \varepsilon_{\perp} & 0 \\ 0 & 0 & \varepsilon_{\parallel} \end{pmatrix}$$

The hyperbolic dispersion relation for eigenmodes of such structures depends strongly on frequency, and can be obtained only for a certain ratio of the layer thicknesses.

The density of photonic states in HMM diverges [3], affording an enhancement of the spontaneous emission which is known as the Purcell effect. This effect provides a means to tune the emission properties of the light source, potentially useful for a variety of applications. For a point dipole-emitter embedded in the hyperbolic medium ultra-high values of the Purcell factor have been reported [4,5]. However, structures with metallic layers are also characterized by losses, which should be accurately taken into account. Therefore, we need to clarify how losses affect the electromagnetic properties of the multilayered HMM and the Purcell factor.

2. Results and discussion.

We study electromagnetic properties of layered metal-dielectric structures by means of isofrequency contours and dispersion diagrams. To retrieve effective parameters of metal-dielectric stratified media we apply an approach based on the Bloch-mode analysis of periodic structures. To explore the outlined questions we calculate the dependence of Purcell factor on the frequency varying the thickness of metal layers and changing the level of losses.

We study the Purcell factor for a point dipole emitter embedded in the central dielectric layer of the stratified media. We assume that the dipole-source is enclosed between two identical distributed Bragg reflectors formed by semi-infinite metal-dielectric periodical system. Therefore the system can be treated as a cavity, and to calculate the Purcell factor we apply an approach based on the quantum theory of the spontaneous emission (SpE) from an active microcavity [6]. Reflectivity and transmittance through layered media were calculated by applying the transfer matrix approach with an emphasis to losses in metal layers and loss compensation by modeling the effect of gain in dielectric layers [7]. We have obtained that for the full compensation of losses the value of gain should be calculated for each frequency in some particular direction.

Our results show the increase of the molecular decay rates for particular frequencies related to the region when the real part of the permittivity of metal layers is negative. We have observed that ultra-high values of the Purcell factor are significantly dependent on the ratio of the layer thicknesses and affected by the level of losses.

Acknowledgements. The work was supported by FP7 ITN NOTEDEV network.

References

- [1] I. I. Smolyaninov and E. E. Narimanov, "Metric signature transitions in optical metamaterials," *Phys. Rev. Lett.* 105, 067402 (2010).
- [2] D. Smith and D. Schurig, "Electromagnetic wave propagation in media with indefinite permittivity and permeability tensors," *Phys. Rev. Lett.* 90, 077405 (2003).
- [3] Z. Jacob, J. Kim, G.V. Naik, A. Boltasseva, E.E. Narimanov, V.M. Shalaev, "Engineering photonic density of states using metamaterials," *Applied Phys. B: Lasers and Optics* 100 (2010) 215.
- [4] A. N. Poddubny, P. A. Belov, and Y. S. Kivshar, "Spontaneous radiation of a finite-size dipole emitter in hyperbolic media," *Phys. Rev. A* 84, 023807 (2011).
- [5] I. Iorsh, A. Poddubny, A. Orlov, P. Belov, and Y. S. Kivshar, "Spontaneous emission enhancement in metaldielectric metamaterials," *Physics Letters A* 376, 185187 (2012).
- [6] F. De Martini, M. Marrocco, P. Mataloni, L. Crescentini, R. Loudon, "Spontaneous emission in the optical microscopic cavity," *Phys. Rev. A* 43 (1991) 2480.
- [7] Roman S. Savelev, Ilya V. Shadrivov, Pavel A. Belov, Nikolay N. Rosanov, Sergey V. Fedorov, "Loss compensation in metal-dielectric layered metamaterials," *Phys. Rev. B* 87, 115139 (2013)

Spectral sensitivity characteristics simulation for silicon p-i-n photodiode

S.U. Urchuk¹, S.A. Legotin¹, D.S. Elnikov¹, V.P. Astahov¹, O.I. Rabinovich¹,
V.P. Yaromskiy² and K.A. Kuzmina¹

¹National university of science and technology "MISiS" 119049, Leninskiy pr., bl.4,
Moscow, Russia

²JSC "Scientific-manufacturing plant for testing equipment", 141070, Pioneer st.,
bl. 2, Korolev, Moscow region, Russia

Abstract. In this paper the simulation results of the spectral sensitivity characteristics of silicon p-i-n-photodiodes are presented. The analysis of the characteristics of the semiconductor material (the doping level, lifetime, surface recombination velocity), the construction and operation modes on the characteristics of photosensitive structures in order to optimize them was carried out.

1. Introduction

During different equipment types which uses the yielding the radiation detector, in most cases, defines the basic parameters of optical systems. Modern development of optical receivers is characterized by the further parameters improvement and radiation characteristics detectors: sensitivity, speed, the spectral sensitivity range, reliability and etc. [1]

Silicon photodiodes have a long life usage, mechanical strength and compact size. P-I-N photodiodes have high bandwidth at low bias voltage, which makes them ideal detectors for use in high speed photometry of optical communication lines [2].

At the same time, the effective multilayer photodetector structures creation requires consideration of factors that affect the photosignal formation. Simultaneous optical radiation absorption consideration, the transfer of photogenerated charge carriers and their recombination, including recombination at the layer boundaries and surface requires computer simulation that allows a detailed analysis of the structure design influence and electrical characteristics of individual regions with the lowest material cost.

2. Results and discussion

In order to optimize physical and topological structure of multilayer silicon structures simulation program for spectral characteristics was developed. Simulating photosensitivity silicon of photosensitive structures was performed by solving the basic system of equations: Poisson equation, the continuity and the electrons and holes transfer [3]. The simulation program was developed using the language Borland Delphi 7. The program allows to recreate the simulated layers structure, specifying the of layers quantity, the material, the conductivity type, doping level and the each layer thickness.

For determination of the spectral dependence of the photosensitivity it was given its spectral range and in every area of monochromatic spectral range by the photocurrent was determined. Moreover, in order to analyze the physical processes occurring in the structure, and then optimize the design of the structure separately the photocurrents generated separately p- and n- regions and the space charge region were determined. As a result, the spectral sensitivity distribution of the units in A/W was achieved. As an initial structure for simulation it was adopted the structure shown in figure 1.

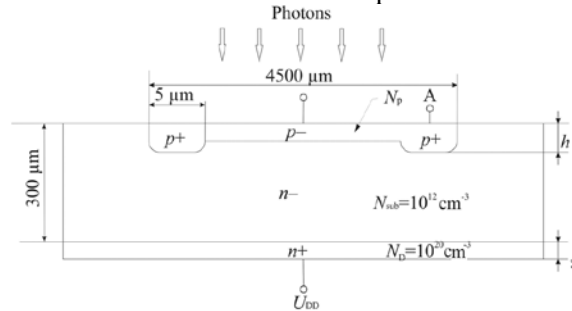


Figure 1. The initial silicon p-i-n-structure chosen for simulation

Figure 2 shows an example of calculated p-i-n-structure spectral characteristics.

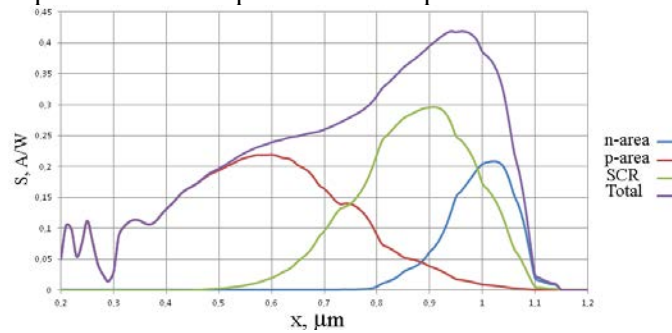


Figure 2. Estimated the multilayer p-i-n structure spectral characteristics

The program also allows you to estimate the lifetime impact, recombination rate, thickness and doping level in various areas, consider the effect of changing the doping level without changing the lifetime and mobility. It may seem strange, but the total spectral sensitivity is not too dependent on the doping level of the lightly doped n-region (if not to take into account the change in mobility and lifetime) (fig. 3). Although the space charge region varies considerably.

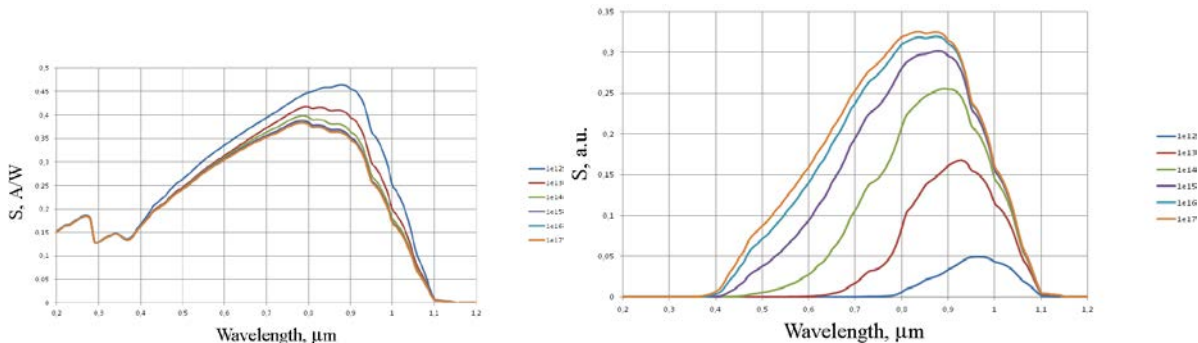


Figure 3. Effect of the doping level of the lightly doped n-region on the spectral sensitivity characteristics (left) and contribute to the spectral sensitivity characteristics of the space charge region (right) ($N_d = 10^{12} \div 10^{17} \text{ cm}^{-3}$).

At the same time, an increase in the p-region doping level does not lead to a significant change in the photosensitivity spectral characteristics, but there is a slight increase in sensitivity of the long waves part. This is due to the fact that the space charge region is expanded slightly by increasing the contact potential difference, which leads to an increase in the contribution of the space charge region. The n-region contribution slightly reduced due to a decrease in the area where photons are absorbed, by expanding the SCR. The top p-layer contribution in the spectral response curve is not changed (taking into account reducing the lifetime and the electron mobility with increasing doping level the p-region contribution should decrease).

3. Conclusions

It was carried out the various factors influence: the electrons and holes lifetime and mobility, surface recombination velocity on the spectral sensitivity characteristics of p-i-n-structures. In order to optimize the photodetector structure parameters it was calculated the parameters when changing the top layer depth of p-doping levels and changing doping areas of the structure. To expand the spectral sensitivity characteristics of silicon photodetector structures toward shorter wavelengths it is required the maximum achieving space charge region to the surface. At the same time, action is required to ensure the improvement of the surface properties to reduce the surface recombination velocity and the simultaneous use of anti-reflection coatings.

Acknowledgements

This study was supported by the Federal Targeted Program “Research and development on priority directions of scientific-technological complex of Russia for 2014—2020, state contract № 14.575.21.0018 (unique identifier for applied scientific research (project) RFMEFI57514X0018).

References

- [1] Baranochnikov M.L. 1985 *IR photodetectors*. (M. Review)
- [2] Volkov D.L., Karmanov D.E., Murashev V.N., Legotin S.A., Mukhamedshin R.A. and Chubenko A.P. 2009 *Instruments and Experimental Techniques*, **52(5)**, 655-664
- [3] MOS SBIS. 1988 *Simulation of elements and technological processes*. (M.: Radio & communication)

Analysis of magnetic system with high-anisotropy localized magnetic field for terahertz-radiation generation

S E Azbite and M K Khodzitsky

Department of Photonics and Optical Information Technologies, ITMO University,
49 Kronverksky av., St. Petersburg, Russia

Abstract. Four permanent magnetic systems with different configuration characterized by strong localized magnetic field were considered and analysed for application in terahertz devices.

1. Introduction

At the present time scientific researches in terahertz frequency range attract more interest. Terahertz radiation may be applied for biomedicine, non-destructive examination, security system, spectroscopy, etc. For efficiency of terahertz radiation generation from semiconductors, a magnetic system is necessary. Currently, superconductor and permanent magnetic systems are used. Strong magnetic field superconductor systems need cooling and power source whereas permanent magnetic systems operate at room temperatures and produce small magnetic fields [1]. This paper represents the compact permanent magnetic system with strong magnetic field at room temperature.

2. Results

In this paper four magnetic systems were considered. These systems have various segmental configuration based on the material with giant magnetic anisotropy (e.g. SmCo₅, NdFeB) such as cylinder with hole, semi-sphere, Halbach cylinder and two magnets with a gap [2]. The following characteristics were analyzed for these magnetic systems: magnetization, magnet dimension, gap between plates and infrared radiation (IR) pump area. Due to use this material a strong localized magnetic field can be obtained at room temperature. Magnetic field strength distribution depends on magnet geometrical parameters. The semi-sphere system was selected on the results of comparative analysis. The design of this system has optimum parameters, like size and configuration, for obtainment of known beforehand magnitude and magnetic field strength distribution of the system. Furthermore, the system consisting of two same uniaxial magnets with opposite magnetic field strength direction allows giving twofold magnetic field strength compared to one magnet case.

3. Conclusions

Each of four systems was simulated by COMSOL MultiPhysics software using AC/DC Module. SmCo₅ magnet properties were selected for simulation. The dimensional parameters were calculated for an operating terahertz pulsed spectrometer consistent with design compactness and strong localized magnetic field capability. The dependence of magnetic field strength on magnet characteristics (like magnetization, magnet dimension, gap between plates and IR pump area) was analytically calculated. Consequently, it was shown the possibility of optimum system development on basis of this analytical estimation and simulation.

References:

- [1] Bespalov V *et al.* 2008 *J. of Opt. Tech.* **75** pp 636-642.
- [2] Samofalov V, Belozorov D and Ravlik A 2013 *Physics -Uspekhi* **56** pp 269-288

Photoionization of Rydberg States by Ultrashort Wavelet Pulses

S Yu Svita, V A Astapenko

Moscow Institute of Physics and Technology, 141700, Institutskii per.9,
Dolgoprudnyi, Russia

Abstract. Photoionization of Rydberg atomic state by the ultra-short wavelet pulses (USWP) is calculated in the frame of perturbation theory with the use of Kramers ionization cross-section. Two simplest types of USWP are considered, namely, cosine and sine pulses. Analytical expressions containing scaling functions for photoionization probability are derived for above-mentioned USWP.

1. Introduction

Atoms in highly excited (Rydberg) states are important nanoobjects both from theoretical point of view and for different applications in nanophysics particularly in nanophotonics. Rapid development of ultra-short pulse generation technology makes it urgent to investigate the peculiarities of the USWP-Rydberg atom interaction.

2. General formulas for radiation absorption probability

The present work is devoted to theoretical description of atomic Rydberg states photoionization by USWP within the frame work of perturbation theory. We consider two types of USWP cosine- and sine ones. Fourier transforms of these pulses are given by the following expressions:

$$E_{\cos}(\omega) = 2\sqrt{\frac{2}{3}} \sqrt[4]{\pi} E_0 \omega^2 \tau^3 \exp(-\omega^2 \tau^2 / 2), \quad (1)$$

$$E_{\sin}(\omega) = 2i \sqrt[4]{\pi} E_0 \omega \tau^2 \exp(-\omega^2 \tau^2 / 2), \quad (2)$$

here E_0 is the amplitude of electric field strength in the pulses and τ is pulse duration parameter.

For the calculation of Rydberg state photoionization probability during all time of USWP action we use the formula obtained in paper [1]

$$W_{ph} = \frac{c}{4\pi^2} \int_{I_m/\hbar}^{\infty} \sigma_{ph}(\omega') \frac{|E(\omega')|^2}{\hbar \omega'} d\omega' \quad (3)$$

here $\sigma_{ph}(\omega)$ is photoionization cross section for which we use Kramers formula:

$$\sigma_n(\omega) = \frac{8\pi}{3\sqrt{3}} \frac{Z_{eff}^4}{n^5 c \omega^3}. \quad (4)$$

Here n is principal quantum number of Rydberg state and Z_{eff} is effective charge of atomic core. Using equalities (1), (3) – (4) we obtain the following expression for photoionization probability of Rydberg states by cosine pulse ($I_{nZ_{eff}} = Z_{eff}^2 / 2n^2$ is ionization potential of Rydberg state):

$$W_n^{(cos)}(\tau) = \frac{2^8}{9\sqrt{3}} \left[\frac{E_0}{E_{sc}} \right]^2 f_c(\tilde{\tau} = \tau I_{nZ_{eff}}), \quad (5)$$

$$E_{sc}(n, Z_{eff}) = \frac{Z_{eff}^3}{n^{5/2}}, \quad (6)$$

$$f_c(\tilde{\tau}) = \tilde{\tau}^5 \operatorname{erfc}(\tilde{\tau}). \quad (7)$$

Here $f_c(\tilde{\tau})$ is scaling function of dimensionless time $\tilde{\tau} = \tau I_{nZ_{eff}}$, $\operatorname{erfc}(x)$ is complimentary error function ($\operatorname{erfc}(x) = 1 - \operatorname{erf}(x)$).

For sine pulse we have

$$W_n^{(sin)}(\tau) = \frac{2^8}{3\sqrt{3}} \left[\frac{E_0}{E_{sc}} \right]^2 f_s(\tilde{\tau} = \tau I_{nZ_{eff}}), \quad (8)$$

here

$$f_s(\tilde{\tau}) = \tilde{\tau}^5 \left[\frac{\exp(-\tilde{\tau}^2)}{\sqrt{\pi} \tilde{\tau}} - \operatorname{erfc}(\tilde{\tau}) \right]. \quad (9)$$

Plots of function (7) and (9) are shown in fig.1.

3. Results and conclusions

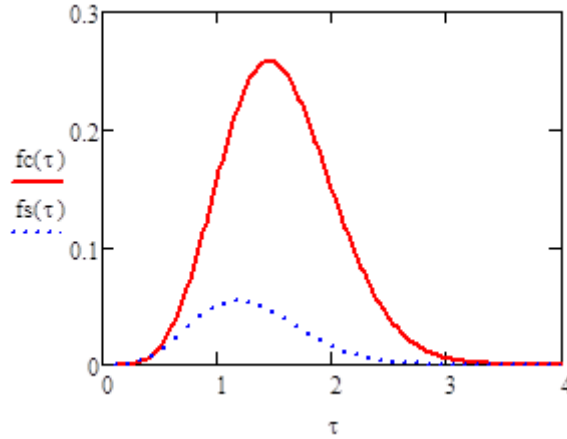


Figure 1. Solid curve - $f_c(\tau)$, dotted curve - $f_s(\tau)$, abscissa is dimensionless time.

Thus in the framework of used model we obtain general expressions for total photoionization probability of Rydberg states with given principal quantum number and effective core charge as a function of wavelet pulse duration for electric strength amplitude satisfied the conditions of perturbation theory

References

- [1] Astapenko V A 2010 *Phys. Lett. A* **374** 1585

Tunable narrowband filters with cross-shaped resonators for THz frequency band

V.Y. Soboleva, Yu. D. Nazarov, E.A. Sedykh and M.K. Khodzitskiy
Department of Photonics and Optoinformatics, ITMO University, 49 Kronverksky
Ave. 197101, Saint-Petersburg, Russia

Abstract: Tunable narrowband filter for terahertz frequency range comprised of cross-shaped metallic resonators deposited on semiconductor substrate was proposed and investigated.

Introduction

Terahertz radiation is an intensely researched field which strives to find applications in our everyday life: from medicine and security to nondestructive evaluation. Special interest is paid to terahertz spectroscopy and communication at terahertz frequencies. It is important to develop elementary base for terahertz frequency communication devices. Such elements as low-pass, high-pass, bandstop and bandpass filters are required to control the frequency of generated THz radiation, providing the opportunity to implement frequency modulation in THz frequency range. These devices can be implemented using arrays of resonators of various shapes placed on substrate with controlled material parameters. Another important field is terahertz spectroscopy, which can be used to study and identify organic molecules which have energy transition with energies that of photon of terahertz frequency associated with rotation and vibration degrees of freedom. [1]

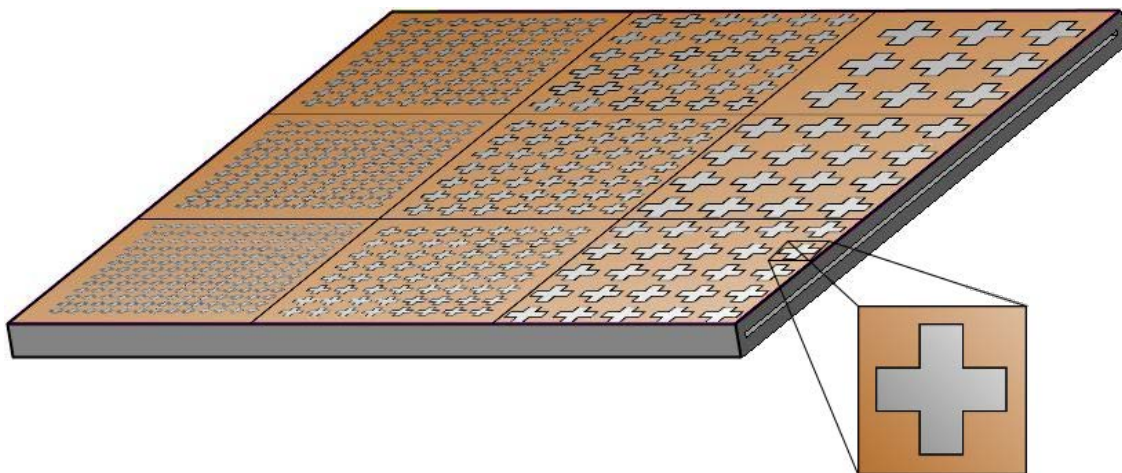


Figure 1: Tunable narrowband filters with cross-shaped resonators for THz frequency band. Slit dimensions are varied between arrays.

Results

This work is devoted to numerical simulation of transmission spectra of tunable narrowband bandpass terahertz filter implemented using cross shaped resonator arrays [2]. Filter is composed of 9 arrays with varying resonator geometry placed on the semiconductor (Si substrate). Coarse tuning of the transmission band is achieved by selecting an array with appropriate resonator dimensions (by varying width, length, corner curvature of the cross-shaped resonator and its period one can define position and width of the resonant peaks of absorption), and fine tuning of the resonance frequency is achieved by varying substrate

permittivity. It can be changed by applying electric or magnetic field, varying temperature or optically pumping the substrate.

According to the simulation results experimental prototype with varying resonator geometry will be designed and fabricated. This filter will be used in laboratory terahertz time domain spectroscopy setups in order to irradiate studied samples with narrowband terahertz radiation. It can also be used in THz photometer setup in order to limit the frequency band influencing the studied cell cultures.

References

1. Yun-Shik Lee, Principles of Terahertz Science and Technology 2009
2. Voisiat B, Bičiūnas A, Kašalynas I and Račiukaitis G, Band-pass filters for THz spectral range fabricated by laser ablation 2011, *J. Appl. Phys A* **104** 953 - 8

Ultraviolet dosimeters based on fibers with luminescence silver molecular clusters

Alisa Pshenova and Aleksandr Sidorov
Optical Informatics, Technologies and Materials Dept.
ITMO University, 197101, 49 Kronverkskiy pr., Saint-Petersburg,
Russian Federation

1. Introduction

Detection and dosimetry of ultraviolet (UV) radiation are in demand in many branches of industries, medicine and biology. For these purposes photodiodes based on aluminum nitride or silicon carbide can be used, but they are expensive, insufficiently reliable and can not work in zones of high electromagnetic interference. Fiber sensors do not have these disadvantages. However, process of capture and transmission of UV radiation to the photodetector by fiber in the form of wave modes is ineffective. Efficiency can be improved by using luminescent fibers which transform UV radiation into the visible range of the spectrum. In this case, inexpensive silicon photodiodes may be used as photodetectors. The purpose of this study is to investigate the possibility of using fibers with luminescent molecular clusters of silver as sensitive elements in UV dosimeters.

2. Experimental

In experiments we were using multimode fibers made from the following types of glasses:

- 1) Photo-Thermo-Refractive glass with neutral molecular clusters of silver Ag_n ($n=2-4$) [1].
- 2) Silicate glass with neutral molecular clusters of silver formed by ion exchange method [2].

Glasses were synthesized in the ITMO University. We have previously shown [1,2] that these glasses have intense luminescence in the visible range of the spectrum under illumination of UV radiation (Fig. 1). The advantage of these glasses is the stability of their luminescent properties in UV range. Fibers were stretched out from the molten glass. Model of the sensor contained luminescence 5 cm-length fiber, cylindrical quartz lens for collecting UV radiation to the fiber, standard multimode transmission fiber and silicon photodiode in a photogalvanic mode.

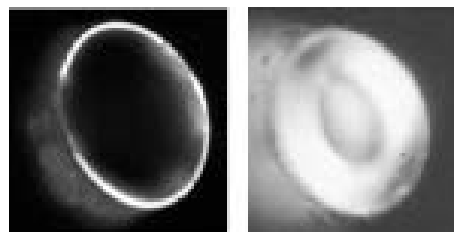


Figure 1. Luminescence of the edges of fiber with neutral molecular clusters of silver formed by ion exchange method

3. Results

Experiments have shown that the fibers made from glass mentioned above, converse UV radiation from the spectral range 240-390 nm to spectral range 450-650 nm with significant efficiency. The sensor allows detecting UV radiation in the range of illumination from 0.2 W/m^2 to 7.0 W/m^2 and has a linear power characteristic in this range.

4. Conclusions

Current research demonstrated fundamental possibility of using of fiber with neutral molecular silver clusters as a sensitive element of UV dosimeter. This engineering solution decreases the cost of a final product. We should also note that using of fiber-based structure allows to locate electrical part of the dosimeter outside the field of negative influences, such as high temperature, electromagnetic interference, etc.

5. References

- [1] A. Tervonen, B. R. West, S. Honkanen // Opt. Eng. 2011. V. 50. 071107.
- [2] V. D. Dubrovin, A. I. Ignatiev , N. V. Nikonorov, A. I. Sidorov, T. A. Shakhverdov, D. S. Agafonova // Opt. Mater. 2014. V. 36. P. 753.

Reaction-diffusion optoelectronics based on dispersed semiconductors

Gradova M.A.¹, Gradov O.V.²

¹Semenov Institute of Chemical Physics, Russian Academy of Sciences, Moscow, Russia

²Institute for Energy Problems of Chemical Physics, Russian Academy of Sciences, Moscow, Russia

Abstract. Since many dispersed semiconductors are capable of light energy conversion and possess photocatalytic and luminescent properties, and any discreet light-sensitive medium can be applied for the positional-sensitive light flux registration (similar to pixels and voxels in semiconductor-based image recording), the use of chemically active dispersed semiconductors allows to perform a direct signal / image registration based on light-sensitive reaction-diffusion redox systems without conventional CCD / CMOS devices. The image capturing in this case will correspond to the formation of the metastable dissipative structures in the active medium, with their morphological properties determined by the flux gradient and provided by the corresponding dispersed semiconductor medium sensitivity.

1. Prerequisites

Many dispersed semiconductors are known to be effective light energy converters, photocatalysts and photoluminescent nanoparticles [1-4]. At the same time a dispersed, i.e. a discreet photosensitive medium can be used in a position-sensitive light flux registration, and hence can be applied for the image recording similar to the CCD with the pixel function performed by the discrete semiconductor elements. The above mentioned chemical activity of the dispersed semiconductors allows to perform the charge transport and the image fixation based on the chemical principles. There are several light-sensitive autocatalytic reactions, such as Kuhnert reaction [5] which is a special case of the self-oscillatory Belousov-Zhabotinsky reaction where the redox processes occur in accordance with the light flux gradient. There also have been developed a number of advanced systems for image registration and neural network processing based on light-sensitive BZ-type reactions and other reaction-diffusion systems, including the biomolecular ones [6-10]. However, the lack of the semiconductor properties of the active medium prevents from the direct image capturing, directional data recording and transduction in such systems without using conventional optoelectronic devices (CCD or CMOS positional-sensitive sensors).

2. Our proposals

We propose to use self-oscillatory systems with the redox-catalysis / photocatalysis on the surface of the dispersed semiconductor nanoparticles involved as the redox-agents in the autocatalytic and reaction-diffusion processes. The image recording process in this case will correspond to the formation

of the metastable dissipative structures in the dispersed medium, with their morphological properties determined by the flux gradient and provided by the corresponding dispersed semiconductor medium light-sensitivity, as well as by the reversibility of the photoredox processes similar to those occurring in the photographic process where the silver halide micro / nanoparticles are also both dispersed semiconductors and photocatalysts [11]. The charge nature of the processes in the active medium makes it possible to perform a direct registration according to the principles of the "direct optoelectronics" without using CCD or CMOS active pixel sensors as the secondary image converters in the framework of the above approach [12,13].

References

- [1] Vasil'tsova O.V., Parmon V.N. Organized photocatalytic systems based on lipid vesicles and semiconductor nanoparticles // *Kinetics and Catalysis* - 1999 - Vol. 40, Issue 1 - pp. 62-70.
- [2] Savinov E.N., Gruzdkov Yu.A., Parmon V.N. Suspensions of semiconductors with microheterojunctions - a new type of highly efficient photocatalyst for dihydrogen production from solution of hydrogen sulfide and sulfide ions // *International Journal of Hydrogen Energy* - 1989 - Vol. 14, Issue 1 - pp. 1-9.
- [3] Gruzdkov Yu.A., Savinov E.N., Korolkov V.V., Parmon V.N. Mixed suspensions of semiconductors forming microheterojunctions. A new type of highly efficient photocatalysts: photocatalytic production of dihydrogen from a water solution of sulfide ions in the presence of plasence of platinized $ZnyCd1-y/CuxS$ suspension // *Reaction Kinetics and Catalysis Letters* - 1988 - Vol. 36, Issue 2 - pp. 395-400.
- [4] Bavykin D.V., Savinov E.N., Parmon V.N. Surface effects on regularities of electron transfer in CdS and CdS/CuxS colloids as studied by photoluminescence quenching // *Langmuir*. - 1999. - Vol. 15, Issue 14 - pp. 4722-4727.
- [5] Kuhnert L. A New Optical Photochemical Memory Device in a Light Sensitive Chemical Active Medium // *Nature* – 1986 – Vol. 319 – pp. 393-394.
- [6] Rambidi N.G., Kuular T.O.-O., Machaeva E.E. Information processing capabilities of chemical reaction-diffusion systems. Belousov-Zhabotinsky media in hydrogel matrices and on solid supports // *Advanced Materials for Optics and Electronics* – 1998 – Vol. 8 – pp. 163-171.
- [7] Rambidi N.G., Maximychev A.V. Neural networks based on biomolecular nonlinear dynamic media. Image processing operations // *Optical Memory and Neural Networks* – 1996 – Vol. 5 – pp. 129-143.
- [8] Gritsenko O.V., Sidelnikov D.I., Simonova A.P., Chernavskii D.S., Rambidi N.G. Towards a biomolecular computer. 3. Information processing features of the distributed biochemical systems functioning in the mode of dissipative structure formation // *Journal of Molecular Electronics* – 1991 – Vol. 7 – pp. 155-166.
- [9] Rambidi N.G., Maximychev A.V. Optical neural networks based on nonlinear dynamic media: state of art and some potentialities // *Proceedings of SPIE* – 1998 – Vol. 3402 – pp. 434-440.
- [10] Rambidi N.G. Biologically inspired information processing technologies: reaction-diffusion paradigm // *International Journal of Unconventional Computing* – 2005 – Vol. 1, pp. 101-121 (2005).
- [11] Jiang J., Li H., Zhang L. New insight into daylight photocatalysis of AgBr@Ag: synergistic effect between semiconductor photocatalysis and plasmonic photocatalysis // *Chemistry* – 2012 – Vol. 18, Issue 20 – pp. 6360-6369.
- [12] Gradov O.V., Gradova M.A. Synchronization of Photochemical Processes and Photoinduced Self-Organization in Dispersed Semiconductors under Optical Pumping // 3-rd Int. Symp. "Molecular Photonics" – 2012 – p. 156.
- [13] Gradov O. Reaction-diffusion optical soft matter lab-on-a-chip. Preprint, 2015 (in press).

Subminiature Eddy Current Transducers for Studying of the semiconductor material

S F Dmitriev¹, V N Malikov¹, A M Sagalakov¹, L I Shevtsova², A O Katasonov¹
Altai State University, Lenina avenue, 61,[656049](#), Barnaul, Altai region
Novosibirsk State Technical University, 20 K.Marx Prospekt, Novosibirsk Oblast

Abstract. Based on an eddy-current transducer (ECT), a probe has been designed to study the semiconductor material. The structural diagram of the probe is given and the basic technical data are stated (the number of windings is 10–130 turns, and the value of the initial permeability of the core $\mu_{\max} = 500$). Due to the high confinement of the magnetic field, it is possible to acquire data from small areas of semiconductor plates. Response versus ECT positioning diagram is also provided.

1. Introduction

The demand for improvement and development of semiconductor material production technology brings up a concern of efficient quality control. Production of materials for microelectronics requires implementation of high-precision measuring methods and instruments in the industry, adoption of modern nondestructive inspection techniques[1].

Today, diagnostics of semiconductor plates is mainly performed using the 4-point probe technique. This technique has a number of disadvantages. The nondestructive inspection (NDI) using the eddy-current method (ECM) is based on registration of variations in the eddy-current electromagnetic field, which are induced by the exciting coil of eddy-current transducer (ECT) in the electrically conducting unit under inspection. The advantage of electromagnetic inspection is the possibility to perform measurement without a contact between the transducer and the object of measurement. Interaction between them usually takes place at narrow intervals (0.1-2mm). That's why this technique can yield good results, when the unit under inspection is moving.

One more advantage of ECM is the relative simplicity of the transducer's design. Coils are placed into a protective case and then encapsulated in a compound. As a result, they are resistant to mechanical and weather stresses, and they are able to work harsh environments with wide ranges of temperature and pressure.

The results of the experiment and their discussion.

An experimental installation for electromagnetic diagnostics of semiconductor plates through eddy-current method was created at the premises of the Altai State University. Information gathering system in the form of eddy-current probe is the installation's main module. In order to test the device, a series of measurements was performed for electrical conductivity of reference semiconductors with a-priori known conductivity values. Response versus ECT positioning diagram is shown in Fig. 1.

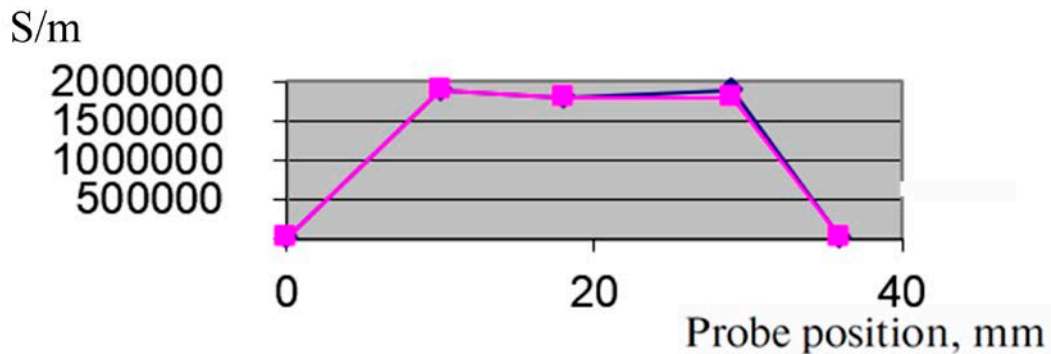


Fig.1. Response versus ECT positioning diagram. InAs

By means of reference semiconductor plates with known values of specific conductivity, the response was plotted against specific conductivity. Gallium-arsenide plate conductivity versus the probe's position above the plate is plotted in Fig. 2.

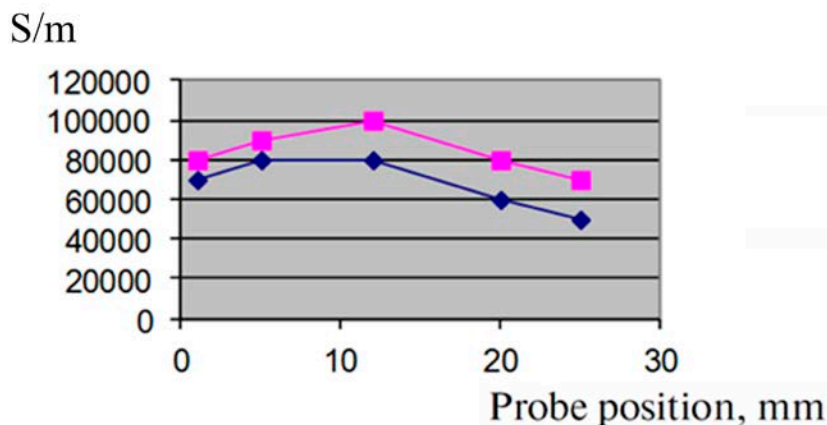


Fig.2. Response versus ECT positioning diagram. GaAs

On the presented diagram, we can note sufficient variations in the conductivity depending on the probe's position above the object. This fact provides the evidence of the semiconductor's structural discontinuity and (consequently) of the low quality.

Conclusions.

Semiconductor conductivity measurement results gathered during the research show the potential of the eddy-current method for quality control of semiconductor materials.

Due to the high confinement of the magnetic field, it is possible to acquire data from small areas of semiconductor plates, which allows for the conclusion about semiconductor impurity distribution in small areas. Therefore, this method offers exciting possibilities for evaluation of quality of semiconductor plates.

References

[1] S. F. Dmitriev, A. V. Ishkov, V. N. Malikov, A. M. Sagalakov Subminiature eddy current transducers for studying metal-dielectric junctions. *Instruments and Experimental Techniques*. November 2014, **Volume 57, Issue 6**, pp 751-754

Dual-wavelength method and optoelectronic sensor for online monitoring of the efficiency of dialysis treatment

A.M. Vasilevsky¹, G.A. Konoplev¹, O.S. Stepanova¹, A.Yu. Zemchenkov², R.P. Gerasimchuk², A. Frorip³

¹ St. Petersburg Electrotechnical University, St. Petersburg, 197376 Russia

² Mariinsky Hospital, St. Petersburg, 194104 Russia

³ LDIAMON AS, Tartu, 51014 Estonia

Abstract. The absorption spectra of spent dialysate in the ultraviolet region were investigated. A novel dual-wavelength spectrophotometric method for uric acid determination in effluent dialysate and an optoelectronic sensor based on UV LED were developed. Clinical trials of the proposed sensor were carried out in the dialysis unit of St. Petersburg Mariinsky Hospital. The relative error of measurement for the concentration of uric acid does not exceed 10%.

1. Introduction

Hemodialysis (HD) is an extracorporeal method of blood purification by means of a dialysis machine for patients suffering from renal failure. During this life-supporting medical procedure low molecular weight waste products of metabolism and excessive water are removed from patient's blood circulating through a dialyzer to dialysis fluid (dialyzate) via semi-permeable membranes. HD treatment is carried out 3 times a week; every session lasts 3-5 hours. It is important to be able to control the efficiency of the dialysis treatment online.

Existing monitoring systems of spent dialysate in the outlet of the dialysis machine have several drawbacks. The most promising approach is to use ultraviolet (UV) spectrophotometry in narrow wavelength regions.

In clinical practice uremic markers such as urea, creatinine and uric acid are used. Based on prior knowledge of the spectral characteristics of uremic markers and recent developments in UV light-emitting diodes (LEDs), uric acid was selected as a parameter in the quantifying of HD dose.

2. Experiment

Experimental studies of the spectral absorption of samples of spent dialysate during HD have proved the validity of spectrophotometric method for HD control. However, additional research work is required to make possible the quantitative control of uremic toxins using UV spectrophotometry.

The maximum of spectral absorption of urea lies in the range of wavelengths shorter than 200 nm, the absorption maxima of uric acid located in the region 238 and 293 nm, creatinine - 217 and 234 nm. Analysis of the profiles of the absorption spectra of the dialysate samples from different patients suggests that the usage of the wavelength of 293 nm for quantitative analysis of uric acid in dialysate (so-called single wavelength method) leads to significant errors, since at this wavelength not only uric acid influence the dialysate absorption but also other components. Therefore it is necessary to define additional informative ranges and to evaluate the contribution of other components.

The study of features of the shape of the absorption spectra of samples of dialysate over 300 patients allowed to propose a classification of spectra with informative signs in the 260 ... 290 nm: type "A" assigned to the type of the absorption spectra, the shape of which is described with a function $dk/d\lambda > 0$ maximum at 290 nm (~ 15% of total patients); type "B" - spectra, which are characterized by the dependence $dk/d\lambda \approx 0$ without the distinct maximum (~ 70% of the total number of patients); type "C" - the shape of the spectrum have a slope in the said range, wherein $dk/d\lambda < 0$ (~ 15% of total patients). It should be noted that the shape of the absorption spectrum of the dialysate per patient remained virtually unchanged throughout the whole period of the research (more than two years).

In the wavelength range of 260 ... 290 nm the absorption spectral shape are dominated by uric acid and the set of components, which include tryptophan, hippuric acid, pseudouridine, adenosine and a number of others, partly unidentified components. The concentrations of these components are low, but their combination, conventionally called pseudocomponent (pseudo-NK), is associated apparently with individual metabolic processes, and determines the shape of the absorption band in this range. Decomposing of pseudo-NK is of scientific interest for further research.

Spectral analysis in the wavelength range 260 ... 320 nm of dialysis fluid samples from patients assigned to different types, and simultaneous biochemical tests for uric acid made it possible to find the profile of the absorption spectrum for the pseudo-NK.

3. Results

The results of experimental studies and modeling of the spectra in the range of 260...350 nm showed:

- The spectral absorbance of the dialysate in 285 ... 295 nm is mainly due to uric acid;
- At shorter wavelengths range absorption due to both uric acid and pseudocomponent NK. The region of 260 ... 270 nm is optimal for estimating of the absorption of pseudo-NK, where the absorption of uric acid is minimal.
- A novel dual-wavelength spectrophotometric method for uric acid determination in effluent dialysate and an optoelectronic sensor based on UV LED were developed.

The mathematical basis of the method is the law of Bouguer-Lambert for the two-component medium. The proposed method is implemented as a compact optical sensor using UV LEDs at the wavelengths 262 and 287 nm, which was designed and manufactured by LDIAMON AS (Tartu, Estonia) in collaboration with Saint-Petersburg Electrotechnical University (Saint-Petersburg, Russia).

4. Conclusion

Clinical trials of the proposed sensor carried out in the dialysis unit of St. Petersburg Mariinsky Hospital. The results of spectral measurements are presented as time profiles of dialysate spectral transmission at two wavelengths and uric acid concentration in the course of a HD session. The relative error of measurement for the concentration does not exceed 10% (for more than 100 samples).

References

- [1] Vasilevsky A, Konoplev G, Stepanova O, Rubinsky A, Gerasimchuk R, Frorip A, Nephrol. Dial. Transplant. 29, 461 (2014)

Resonant plasmon-stimulated nonlinear absorption in three-level systems.

A.Zasedatelev¹, T. Dubinina^{2,4}, V. Krasovskii^{1,3}, O. Suprunova¹, and A. Chistyakov¹.

¹National Research Nuclear University «MEPhI», Moscow, Russian Federation

²Department of Chemistry, M.V. Lomonosov Moscow State University, Moscow, Russian Federation

³Prokhorov General Physics Institute of the Russian Academy of Sciences, Moscow, Russian Federation

⁴Institute of Physiologically Active Compounds, Russian Academy of Sciences, Chernogolovka, Russian Federation

Abstract. Present investigation is devoted to the mechanisms of resonant nonlinear absorption in the hybrid exciton-plasmon systems. We used novel substituted subphthalocyanines (SubPc) as excitonic 3 – level systems, and 50 nm gold nanoparticles (AuNp) as plasmonic structures. We succeeded to define mechanisms of resonant nonlinearities and to show that local field factor (LFF) and Purcell factor (PF) lead to dramatic enhancement (more than 10-fold) in SubPc nonlinearity.

The unique optical properties of hybrids based on metal nanoparticles and chromophore molecules are very promising in nonlinear optics. Such exciton-plasmon systems can be used in optical modulators and switchers, nanolasers [1], high-sensitive spaser sensors [2], harmonic generation materials, optical limiters etc. The tight “mixing” of plasmonic properties of metal structures with excitonic properties of chromophore is the key feature of resonant nonlinearity, it leads to dramatic changings in optical nonlinear properties in the whole exciton-plasmon system. The local field factor i.e. the enhancement of the near field intensity would result in increase of the nonlinear responses, on the other hand enhancement of the decay rate of excited states would lead to acceleration of the rate in the radiative relaxation process. In spite of very different time scales of the processes in uncoupled regime, when the chromophore and plasmon structures don't interact, in the tightly “mixing” exciton-plasmon regime both processes could have the similar time scales. Therefore it is very difficult to predict a character of nonlinear properties in general, without full description of the exciton-plasmon system's dynamics.

The subject of our research is the study of plasmon-stimulated nonlinear absorption in three-level systems for the strong exciton-plasmon coupling regime. By the reason of their 14 π -electron nature [3] subphthalocyanines were chosen as the excitonic systems. We demonstrated that in the case of resonant short-pulse (<500 ps) excitation, SubPc molecules can be treated as 3-level quantum systems. In order to tune the parameters of three level systems, novel SubPc complexes bearing different axial ligands (bromine- or chlorine-) and peripheral substituents (phenyl- or phenoxy-) were used. The cores of obtained hybrid structures possess 50 nm average size gold nanoparticles. Linear optical properties investigations were performed using UV-Vis spectroscopy, decay rates of the first excited electronic state were determined by time correlated single photon counting (TCSPC) method, and resonant nonlinearities were studied by Z-scan technique [4]. In this study, in order to obtain the absorptive nonlinearity we performed open-aperture Z-scan measurements, using a frequency doubled Nd³⁺:YAG laser at 532 nm provided 350-ps mode locked pulses at a repetition rate of 5 Hz to prevent heating processes. We showed that nonlinearity of “free” SubPc molecules operates by their electronic states populations. The systems dynamics were considered by rate equations. We obtained excellent

coincidence of FDTD simulated results with experimental data for all studied compounds. In the case of hybrid structures, SubPc molecules formed the outer shell of gold core. Nonlinear response of gold particles was successfully described by effective 3-order Kerr susceptibility. According to our study, the chromophore's impact on the nonlinear response of the gold particles can be neglected due to small outer shell thickness (<5nm). In thin shell approximation, the exciton-plasmon interactions consists of 2 factors: the first is the LFF, i.e. influence of the enhanced electric field on the 3-level systems which stimulates excitation processes; the second is the PF, i.e. the strong increase of first excited state radiative decay rate due to exciton-plasmon coupling, which stimulates relaxation process. That leads to dramatic redistribution of electronic states populations. FDTD numerical simulations of resonance plasmon-stimulated absorption in the 3-level systems resulted more than 10-fold enhancement in comparison with "free" systems. The calculations results are proved by Z-scan curves of experimental samples.

References:

- [1] Demonstration of a spaser-based nanolaser, M.A. Noginov et al., *Nature* 460: 1110–1112, (2009).
- [2] Spaser spectroscopy with subwavelength spatial resolution, Yurii E. Lozovik, Igor A. Nechepurenko, Alexander V. Dorofeenko, Eugeny S. Andrianov, Alexander A. Pukhov, *Physics Letters A* 378 (2014) 723–727.
- [3] Subphthalocyanines: Singular Nonplanar Aromatic Compounds-Synthesis, Reactivity, and Physical Properties, C. G. Claessens, D. González-Rodríguez, T. Torres, *Chem. Rev.* 2002, 102 (3), 835–854.
- [4] Z-Scan Measurements of Optical Nonlinearities, M. Sheik-Bahae, A.A. Said, T.-H. Wei, D.J. Hagan, E.W. VanStryland, *The Journal of Quantum Electronics* 26 (1990) 760-769.

Quantum walks of photon pairs in twisted waveguide arrays

D N Vavulin¹, A A Sukhorukov²

¹ITMO University, 49 Kronverksky Ave., St.Petersburg, 197101, Russia

²Nonlinear Physics Centre, Research School of Physics and Engineering, Australian National University, Canberra, ACT 2601, Australia

Abstract. We consider an array of closely spaced optical waveguides, which are twisted around a central axis along the propagation direction. We derive Schrodinger-type equation of the biphotonwavefunction, taking into account the waveguide bending through the appearance of additional phase in the coupling coefficients. We present an example of the evolution of quantum photon-pair state.

1. Introduction

Quantum walks involving several particles can be used to implement quantum algorithms, which can perform faster than classical analogues. Of particular interest are quantum walks, where interference of several walkers can be used to realize various simulations, including database search [1]. Quantum walks of photons can be implemented in arrays of coupled waveguides. In particular, coherent quantum phenomena can be potentially simulated in closed-loop arrangements of waveguides [2]. Recently, a new type of coupled waveguides with a twisted geometry were demonstrated in a photonic-crystal fiber [3]. In this work, we study the effect of twist on quantum walks of photons.

2. Discussion

We consider an array of closely spaced optical waveguides, which are twisted around a central axis along the propagation direction. Such structure composed of three waveguides is schematically shown in Fig. 1(a). We derive Schrodinger-type equation of the biphotonwavefunction, taking into account the waveguide bending through the appearance of additional phase in the coupling coefficients [4]. We present an example of the evolution of quantum photon-pair state in Figs. 1(b-d). We consider an input condition in the form of Einstein-Podolsky-Rosen (EPR) entangled state, where two photons are present together with equal probability in any of the waveguides, but photons cannot be in different waveguides, see correlation plot in Fig. 1(b). As the state evolves, the correlation properties can become reversed, and the photons are most likely to appear in different waveguides after a certain propagation distance, see Fig. 1(c). Interestingly, at a longer propagation distance the input state can be almost exactly restored, see Fig. 1(d). These features can be controlled by the amount of twist. We also analyse integrated photon generation and quantum walks [5], implemented through spontaneous four-wave mixing in optical fibers. Such system can further tailored to produce entangled optical-angular-momentum states, which have applications for quantum communications and imaging.

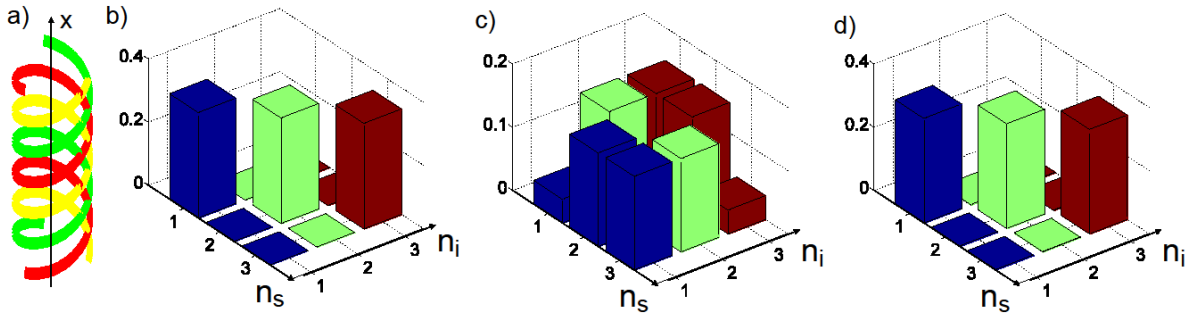


Figure 1. a). Scheme of coupled twisted waveguides. (b-d) Two-photon correlations ($|W|^2$) (W - biphoton wavefunction) between different waveguides at (b) $z = 0$, (c) $z = L/2$, (d) $z = L$.

References

- [1] Hamilton C S, Kruse R, Sansoni L, Silberhorn C, and Jex I 2014 Driven Quantum Walks. *Phys. Rev. Lett.* **113**, 083602-5
- [2] Owens J O et al. 2011 Two-photon quantum walks in an elliptical direct-write waveguide array. *New J. Phys.* **13**, 075003-13
- [3] Xi X M, Wong G K L, Frosz M H, Babic F, Ahmed G, Jiang X, Euser T G, and Russell P St.J 2014 Orbital-angular-momentum-preserving helical Bloch modes in twisted photonic crystal fiber. *Optica* **1**, 165-169
- [4] Garanovich I L, Longhi S, Sukhorukov A A, and Kivshar Yu S 2012 Light propagation and localization in modulated photonic lattices and waveguides. *Phys. Rep.* **518**, 1-79
- [5] Markin D M, Solntsev A S, and Sukhorukov A A 2013 Generation of orbital-angular-momentum entangled biphotons in triangular quadratic waveguide arrays. *Phys. Rev. A* **87**, 063814-5

Section
Quantum Dots and
Wells

Photoluminescence of GaAs/AlGaAs quantum ring arrays

Yu.D. Sibirmovsky¹, I.S. Vasil'evskii¹, A.N. Vinichenko¹,
D.M. Zhigunov², I.S. Eremin¹, O.S. Kolentsova¹, N.I. Kargin¹ and
M.N. Strikhanov¹

¹ National Research Nuclear University "MEPhI", 115409, Moscow, Russia

² Lomonosov Moscow State University, 119992, Moscow, Russia

Abstract. Epitaxial samples with GaAs/AlGaAs quantum rings (QRs) of different shapes were grown by molecular beam epitaxy. Photoluminescence (PL) spectra of the samples were measured at 20 - 90 K and 300 K, intense peaks attributed to the QR layers were observed. The peaks were identified by comparison of as-grown and selectively etched samples and by the calculation of the ground state energy for charge carriers in GaAs QRs. FWHM narrowing with the temperature increase was observed below 70 K.

Quantum rings (QRs) are novel nanostructures similar to quantum dots but with unique electronic and optical properties, especially in magnetic fields [1]. Photoluminescence spectra of GaAs/AlGaAs quantum rings were studied in several works [2,3], though the temperature dependence of the spectra has not been investigated in detail. Also, QR layers are usually overgrown and annealed before the PL experiments, so the spectrum of as-grown surface layers of QRs was not studied so far.

Two samples were investigated in the present work, containing one layer of single QRs (A1) and two layers of double QRs (A2), formed by droplet epitaxy [4]. Both samples were grown on GaAs(001) substrate with GaAs buffer layer and Al_{0.28}Ga_{0.72}As barrier layer. For A2 sample one QR layer was overgrown by Al_{0.28}Ga_{0.72}As, and another (identical) QR layer was grown on the surface. For more information on the growth procedure see [5].

The mean diameter and height of the rings were measured using atomic force microscopy and scanning electron microscopy. The outer/inner diameter of the QRs were 53±12/22±6 nm for A1, 56±9/28±3 nm for A2 inner rings and 140±24/100±23 nm for A2 outer rings. The height was 4.5±0.5 and 4.3±0.3 nm for A1 and A2, respectively.

For PL measurements 488 nm Ar⁺ laser was used with intensity of 100 mW/cm². Spectra were measured at 20-90 K and at room temperature. PL peaks of QR layers were identified by comparing their energy with GaAs band gap (1.52 eV at 20 K) and Al_{0.28}Ga_{0.72}As band gap (1.87 eV at 20 K). The reference spectra of the etched samples without QR layers were also measured (Fig. 1).

The A2 low temperature PL spectrum has an additional peak at lower energy which is attributed to the buried QR layer. Calculation using simple quantum well (QW) model shows that the ground state energy is much higher for surface QW than for buried QW. The temperature dependences of QR peak energy and full width at half-maximum (FWHM)

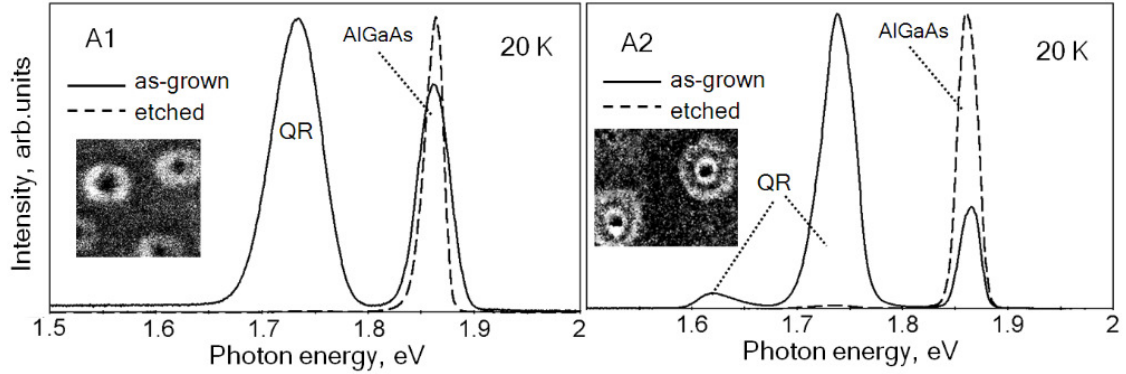


Figure 1. Normalized PL spectra of the samples A1 (left) and A2 (right) at $T=20$ K. As-grown (solid line) and etched (dashed line) samples are compared.

presented in Fig. 2. The FWHM narrowing with the temperature increase was observed below 70 K. This phenomenon in disordered systems has been noticed before and is usually explained by carriers' relaxation into global minima of the potential (larger QRs in this case) instead of local minima. The peak energy also decreases more rapidly with the temperature increase than GaAs bulk band gap (Fig. 2), which is in good agreement with the proposed model.

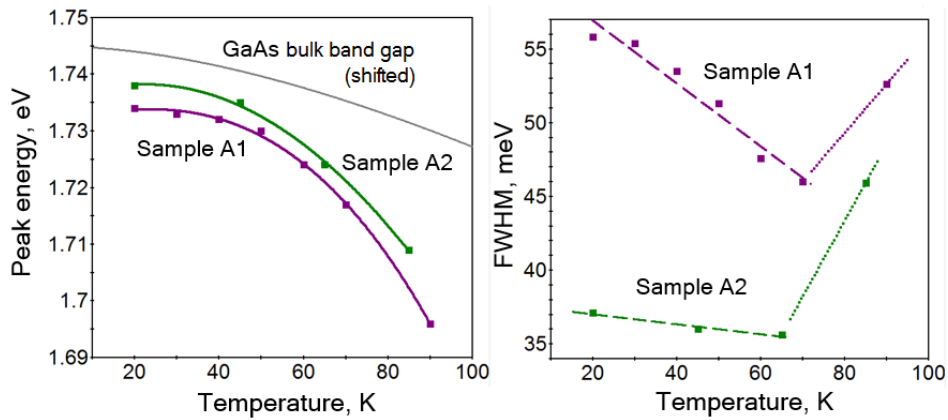


Figure 2. Temperature dependence of the energy (left) and FWHM (right) of QR peaks for samples A1 and A2. GaAs bulk band gap (Varshni relation) is shown shifted to higher energy for comparison.

Finally, the ground state energy of QRs was calculated. The results are in good agreement with the experiment, including the low temperature shape of the peaks, determined by the QRs size distribution.

References

- [1] F. Ding, N. Akopian, B. Li et al. Phys. Rev., B 82 (7), 075309 (2010)
- [2] T. T. Kuroda, T. Mano, T. Ochiai et al. Phys. Rev., B 72 (20), 205301 (2005)
- [3] Z.Y. AbuWaar, Y.I. Mazur, J.H. Lee. J. Appl. Phys., 101 (2), 024311 (2007)
- [4] N. Koguchi, S. Takahashi, T. Chikyow. J. Cryst. Growth, 111 (3), 688 (1991)
- [5] Yu. D. Sibirmovskii, I. S. Vasilevskii, A. N. Vinichenko et al. Bull. Lebedev Phys. Inst., 41 (9) 243 (2014)

Local field effects and metamaterials based on colloidal quantum dots

O V Porvatkina, A A Tishchenko and M N Strikhanov

National Research Nuclear University MEPhI, Moscow, Russia

Abstract. Metamaterials are composite structures that exhibit interesting and unusual properties, particularly negative refractive index and artificial magnetism. In this article we consider metamaterials based on colloidal quantum dots (the multiphase colloidal semiconducting nanocrystals). We investigate such structures taking into account local field effects and theoretically analyze expressions for permittivity and permeability of metamaterials based on colloidal quantum dots, particularly, colloidal quantum dots CdSe. Also we investigate how the values of dielectric polarizability and magnetic polarizability depend on the dots radius and properties the material the quantum dots are made of.

1. Introduction

Metamaterials demonstrate new properties, some with no analog in conventional materials, for example, artificial magnetism and near-field focusing. Unusual electromagnetic response of these materials could lead to a range of applications including OLEDs, ultrafast LEDs and nanoscale lasers [1,2]. In our work we consider metamaterials based on spherical colloidal quantum dots (CQDs). CQDs are organic nanocrystals with semiconductor core (for example, CdSe) that have organic ligands bound to surface. CQDs have tunability and atomic-like optical emission, therefore they are very interesting for studying interaction between light and metamaterial based on them.

2. Dielectric and magnetic properties of metamaterials based on colloidal quantum dots

We consider homogenous magnetic medium which consists of N anisotropic CQDs described by dielectric polarizability tensor $\alpha_{ij}^e(\omega)$ and magnetic polarizability tensor $\alpha_{ij}^m(\omega)$. In our previous work [3] we obtained the dependence of permittivity tensor $\varepsilon_{ik}(\omega)$ from dielectric polarizability tensor $\alpha_{ij}^e(\omega)$ and permeability tensor $\mu_{ij}(\omega)$ from the magnetic polarizability tensor $\alpha_{ij}^m(\omega)$. We also take into account local field effects and use a long-wave limit. Local field is an effective field calculated by averaging over the positions of all colloidal quantum dots in respect to the one considered [4]. It is well known that permittivity and permeability are complex values (for metamaterials real parts of permittivity and permeability are negative $\varepsilon' < 0$, $\mu' < 0$). Taking into account that dielectric and magnetic polarizability are also complex values, using the results of work [3] we obtain equations for real parts of permittivity and permeability:

$$\varepsilon' = \frac{1 - 32/9 \pi^2 n^2 \left((\alpha_e')^2 + (\alpha_e'')^2 \right) + 4/3 \pi n \alpha_e'}{1 + 16/9 \pi^2 n^2 \left((\alpha_e')^2 + (\alpha_e'')^2 \right) - 8/3 \pi n \alpha_e'} \quad (1)$$

$$\mu' = \frac{1 - 32/9 \pi^2 n^2 \left((\alpha_m')^2 + (\alpha_m'')^2 \right) + 4/3 \pi n \alpha_m'}{1 + 16/9 \pi^2 n^2 \left((\alpha_m')^2 + (\alpha_m'')^2 \right) - 8/3 \pi n \alpha_m'} \quad (2)$$

Combining conditions $\varepsilon' < 0$, $\mu' < 0$ with Eqs. (1),(2) one can obtain limits for the multiplication of the concentration of CQDs and dielectric/magnetic polarizability of CQDs:

$$0.1 < n \alpha_{e,m} < 0.16. \quad (3)$$

The resulting ratio allows defining the concentration of colloidal quantum dots which is necessary to create metamaterials (and vice versa). We consider metamaterial consisting of colloidal quantum dots CdSe ($\varepsilon = 10$). In [5,6] equations for real and complex parts of dielectric and magnetic polarizability were obtained. Using these equations, we obtain dependence of the dielectric and magnetic polarizability of the QDs on the radius quantum dots. Notice that we can control the color of the light emitted by the dots by changing their size. So, OLEDs with metamaterials based on QDs can produce any color of light.

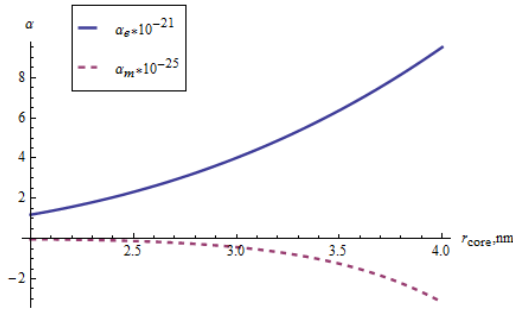


Figure 1. Dependence of the dielectric and magnetic polarizability of the QDs on the radius QDs.

3. Discussion

Permittivity and permeability of metamaterials based on CQDs were investigated. Eqs. (1), (2) show the possibility of creation metamaterials with simultaneously negative permittivity and permeability. Eq. (3) determines the limits of concentrations of QDs and dielectric/magnetic polarizability.

This work was supported by Ministry of Education and Science of Russian Federation, Agreement No. 14.575.21.0002, ID RFMEFI57514X0002.

References

- [1]Pendry J B Negative refraction makes a perfect lens 2000 *Phys. Rev. Lett.* **85** 39
- [2]Agranovich V M and Gartsstein Yu N Spatial dispersion and negative refraction of light 2006 *Physics-Uspokhi* **49** 1029 [*UFN* **176** 1051]
- [3]Porvatkina O V, Tishchenko A A and Strikhanov M N Local field effects in anisotropic metamaterials 2014 *Journal of Physics: Conference Series* **541** 012024
- [4]Ryazanov M I and Tishchenko A A Clausius-Mossotti-type relation for planar monolayers 2006 *JETP* **103** 539 [*ZhETF* **130** 621]
- [5]Shalaev V M, Wenshan C, Chettiar U K, H-K Yuan, Sarychev A K, Drachev V P and Kildishev A V Negative index of refraction in optical metamaterials 2005 *Optics Letters* **30** 33
- [6]Morokhov I D, Petinov V I, Trusov L I, Petrulin V F Structure and properties of fine metallic particles 1981 *Sov. Phys. Usp.* **24** 295 [*UFN* **133** 653]

Hot exciton relaxation in multiple layers CdSe/ZnSe self-assembled quantum dots separated by thick ZnSe barriers

M Eremenko, G Budkin and A Reznitsky¹

Ioffe Institute, Politekhnikeskaya 26, St. Petersburg 194021, Russia

Abstract. We have studied optical spectra of two samples of MBE grown CdSe/ZnSe multilayer heterostructures with CdSe self-assembled quantum dots. Sample A was grown at $T=280^{\circ}\text{C}$ and includes two CdSe quantum wells (QWs) with nominal thicknesses 2.7 and 1.4 ML separated by ZnSe barrier of 14 nm thickness. The sample B was grown at $T=340^{\circ}\text{C}$ and included 15 QWs with nominal thickness of each CdSe layer of 3 ML separated by ZnSe barriers of 12 nm thickness. Photoluminescence (PL) and PL excitation (PLE) spectra of these samples were studied at $T=2\text{K}$. It was found that PLE spectra of the states forming short wavelength side of the PL spectra of the sample B and that of PL spectra of shallow QW of the sample A revealed pronounced oscillating structure with energy period of ZnSe LO phonon under excitation with photons in a wide energy range both in the regions of quantum-dot states and in that of free states in the ZnSe barrier. Creating of excitons with kinetic energies more than 0.3 eV, which considerably exceed the exciton binding energy (appr. 0.03 eV), was observed. It has been concluded that oscillating structure of PLE spectra arises due to cascade relaxation of hot excitons.

The numerous structural and spectroscopic studies carried out so far have shown that under certain conditions epitaxy of several CdSe monolayers into a ZnSe matrix leads to formation of a quantum well (QW) from an inhomogeneous ZnCdSe solid solution with nanosize objects, many properties of which are of 0D nature. Depending on the growth conditions, and primarily on temperature, such self-assembled quantum dots (QD) may be of 2D or 3D nature. The most complex topological structure is observed for 2D objects obtained at $T = 280^{\circ}\text{C}$. At this temperature the coherent CdSe insertions in ZnSe with CdSe nominal thickness in the range of 1 - 3 ML are known to generate planar CdSe-enriched QDs incorporated into the body of ZnCdSe QW [1, 2]. Low-temperature CdSe deposition at $T=230^{\circ}\text{C}$ followed by thermal activation stage at temperatures typically more than 310°C results in three-dimensional QDs on a thin wetting layer [2, 3].

In this communication, we discuss the PL and PLE spectra of two multilayer ZnSe/CdSe/ZnSe heterostructures, samples A and B, grown at $T=280$ and 340°C and separated by rather thick ZnSe barriers of 14 and 12 nm, respectively. As it was shown previously, in multilayer samples with so thick ZnSe barriers at low temperatures there was no evidence of exciton tunneling between QD states in adjacent QW layers [4]. It was found that the main features of the PLE spectrum of heterostructures with planar nanoislands are the following: (i) the oscillating character of PLE spectra for states on the short-wavelength side of the PL band reflecting exciton cascade relaxation with emission of LO

phonons, which practically disappears from the PLE spectrum above a certain photon energy E_{ME} , which is related to the region of transition from states localized within QDs to those distributed over all the QW plane; and (ii) increasing of the PL signal more than an order of magnitude under excitation by photons with energy exceeding the energy gap of the barrier material [5]. It can be concluded that both abovementioned features of PLE spectra reflect main role of two channels of the population of the emitting states, namely, (i) direct capture of e-h pairs or excitons from the barrier states to the QD states and (ii) excitons or pairs capture from the barrier states to QW states with the following diffusion along QW states and consequent capture in QD states.

Let us suppose that due to some reasons excitation channel of the QD emitting states through QW states is not effective. Then the only possible excitation channel of QD states is the direct capture of e-h pairs from the barrier states. One can expect that cascade relaxation of hot excitons with the emission of LO phonons would be the most effective way of the population of the emitting QD states. We have found distinct oscillating structure of PLE spectra of the states forming short-wavelength side of the PL spectrum of the sample A (see figure 1, right panel). At the spectral range above ZnSe fundamental absorption edge we have detected up to 10 maxima in PLE spectra which are separated by the energy 31.5 meV of ZnSe LO(Γ)-phonon. Moreover, in this spectral range effectiveness of the energy transfer to the emitting states exponentially decrease with the increase of exciton kinetic energy. Hot exciton nature of the structure observed in PLE spectra is the most clearly manifested when the excitation spectra are detected in polarized light. Figure 1, right panel, shows two PLE spectra obtained under excitation by linearly polarized light and recording in the parallel (solid curve Y1) and crossed (dash curve Y2) orientations of the polarizer and analyzer. The same figure presents a spectrum of the degree of polarization $Y3 = (Y1 - Y2) / (Y1 + Y2)$ (curve Y3 with symbols).

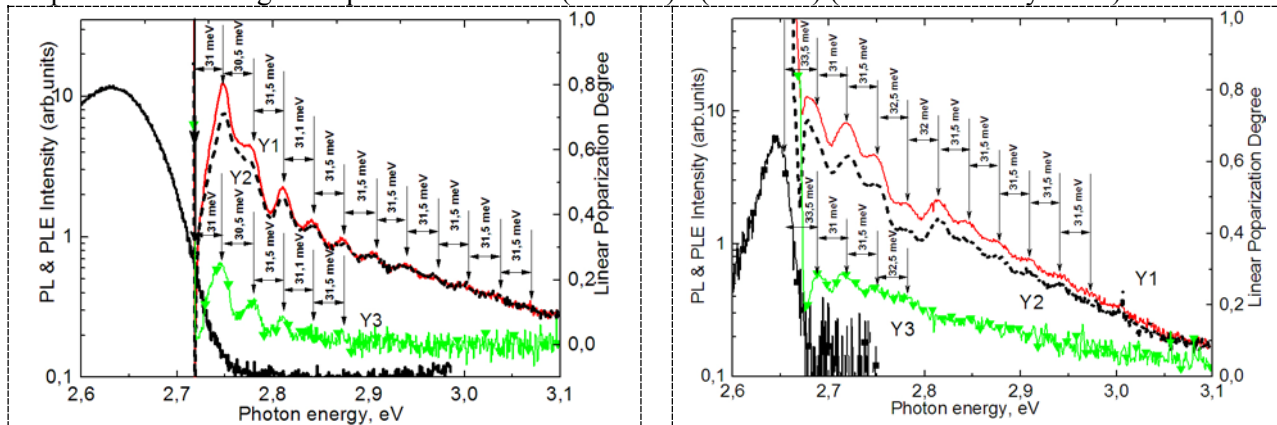


Figure 1. Black solid lines show the PL spectra of samples A and B (right and left panels, respectively). Thin solid (Y1) and dashed (Y2) curves represent linearly polarized PLE spectra of the same samples in polarizations with parallel and crossed orientations of polarizer and analyzer, respectively (left log axes). Solid lines with symbols Y3 (green in colour) indicate spectra of the linear polarization degree (right linear axes) (see text).

Similar features of PLE spectra we have found for the emission states forming high energy side of the PL spectrum of the sample B, grown in Stranski-Krastanov regime (Figure 1, left panel). In both samples oscillating structure of the PLE spectra was found not only within QD states but also in the energy region far above the fundamental edge of ZnSe barrier. We discuss the model which explains these experimental findings.

References

- [1] Peranio N *et al.* 2000 *Phys. Rev. B* **61** 16015
- [2] Schikora D *et al.* 2000 *Appl. Phys. Lett.* **76** 418
- [3] Litvinov D *et al.* 2002 *Appl. Phys. Lett.* **81** 640
- [4] Reznitsky A *et al.* 2009 *Phys. Status Solidi C* **9** 2695
- [5] Reznitsky A *et al.* accepted for publication in *Phys. Status Solidi B*

Refraction index modulation induced with transverse electric field in double tunnel-coupled GaAs/AlGaAs quantum wells

A A Shumilov¹, M Ya Vinnichenko¹, R M Balagula¹, L E Vorobjev¹, D A Firsov¹,
P A Kasilovich¹, M M Kulagina², A P Vasil'iev²

¹ Peter the Great St. Petersburg Polytechnic University, St Petersburg, Russia

² Ioffe Physical-Technical Institute, St Petersburg, Russia

Abstract. Modulation of refraction index under transverse electric field in the spectral range corresponding to intersubband light absorption was studied in structures with multiple tunnel-coupled GaAs/AlGaAs quantum wells. Refraction index modulation was calculated using Kramers-Kronig relation and experimentally determined spectra of intersubband light absorption in equilibrium conditions and under transverse electric field.

1. Introduction

Quantum cascade lasers (QCL) are efficient radiation sources. They cover wide spectral range, and now can be used in data transmission systems. In order to their performance to be efficient an effective and easy to implement modulation system should be introduced [1]. In case of GaAs/AlGaAs-based QCL there is a way to create frequency modulation system by introducing the layers with tunnel-coupled quantum wells (QW) into the waveguide. Application of transverse electric field to the tunnel-coupled QW system can induce intersubband absorption modulation, which, in turn, will produce refraction index modulation. Temperature variation can have the same effect in the lesser extent. Here we present the results of the investigation of GaAs/AlGaAs tunnel-coupled QW system response on the transverse electric field and calculation of refraction index modulation in these conditions.

2. Sample and experiment

The investigated structure contains 100 pairs of tunnel-coupled QWs GaAs/AlGaAs. It was grown using molecular beam epitaxy on semi-insulating GaAs substrate. The narrow and wide quantum wells have widths of 4.5 and 6.6 nm, respectively; the barrier is 3 nm thick. Structure was selectively doped in the wider QWs. The investigated structure contains three electron levels of size quantization. The energy of the $e1-e3$ transition is about 125 meV, energy of $e2-e3$ transitions is about 95 meV. In order to apply transverse electric field mesa was etched on the surface of structure at the stage of post-growth processing. For detailed information about postgrowth processes (mesa etching, contacts coating, sample processing in multipass geometry) see [2]. Vacuum Fourier transform spectrometer Bruker Vertex 80v with different photodetectors (MCT, pyroelectric, silicon bolometer) was used to obtain equilibrium intersubband absorption spectra. Closed cycle cryostat Janis PT407RM with operational temperature range of 4–320 K and a temperature setting accuracy of 0.1 degrees was used in the experiment. Spectra under transverse electric field were obtained in step-scan mode with addition of boxcar integrator and current preamplifier to the experimental setup configuration.

3. Results and discussions

In earlier work [2] we presented the results of intersubband absorption investigation without electric field and studied the influence of temperature variation on the absorption spectra. These spectra contained one distinct peak at the energy corresponding to the $e1$ - $e3$ electron transitions. This peak widened and slightly shifted with the temperature variation. Here we present the intersubband absorption modulation spectra when transverse electric field is applied to the structure (see figure 1). The dip in these spectra corresponds to the decrease in absorption. Its energy position is in good agreement with $e1$ - $e3$ transition energy. Observed absorption decrease is associated with electron redistribution between first two subbands $e1$ and $e2$ (see inset in figure 1). One can see that spectra for voltage $U = 20$ V and $U = 25$ V are almost identical. It can indicate that $U = 20$ V corresponds to complete depletion of $e1$ subband. This also corresponds to our numerical estimations.

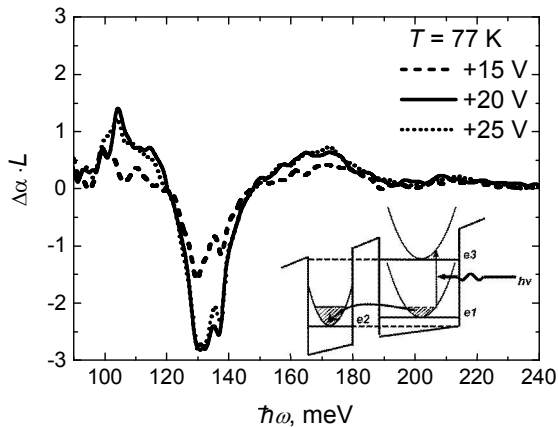


Figure 1. Absorption modulation spectra for p -polarized light at $T = 77$ K. Inset shows schematically electron redistribution under transverse electric field. L - optical length.

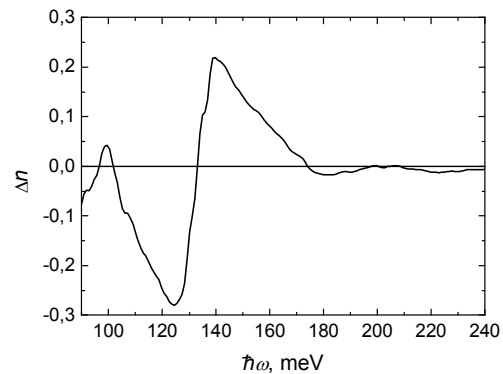


Figure 2. Spectrum of refraction index variation Δn under transverse electric field corresponding to applied voltage $U = 20$ V at $T = 77$ K.

Spectra of refraction index change $\Delta n(\omega)$ were calculated from the obtained intersubband absorption modulation spectra using Kramers-Kronig relation (see figure 2). Results of calculation show that in maximum the change of refraction index is approximately 10% of the whole refraction index of GaAs ($n = 3.27$), so efficient modulation of infrared radiation is possible with tunnel-coupled QW structures in transverse electric field.

4. Conclusion

The obtained results confirm the feasibility of tunnel-coupled QW-based infrared modulators. Experimental results show that low voltage value is enough to significantly change the energy spectrum of structure and provide the electron distribution between QW.

Acknowledgments

This work has been supported by the Russian Foundation for Basic Research (Projects № 14-02-31489, 14-02-00336) and the Ministry of Education and Science of the Russian Federation.

References

- [1] Luryi S, Gouzman M 2006 *International journal of high speed electronics and systems* **16**(2), 559-566.
- [2] Rybalko D A, Vinnichenko M Ya, Vorobjev L E, Firsov D A, Balagula R M, Panevin V Yu, Kulagina M M, Vasil'iev A P 2014 *Journal of Physics: Conference Series* **541**, 012081

Dynamics of mid-infrared light absorption related to photo-excited charge carriers in Ge/Si quantum dots

O I Kirilenko¹, R M Balagula¹, A N Sofronov¹, V Yu Panevin¹, L E Vorobjev¹, D A Firsov¹ and A A Tonkikh^{2,3}

¹Peter the Great St.Petersburg Polytechnic University, Polytechnicheskaya 29, St.Petersburg 195251, Russia

²Max Planck Institute of Microstructure Physics, Weinberg 2, Halle (Saale) 06120, Germany

³Institute for Physics of Microstructures RAS, GSP-105, Nizhny Novgorod 603950, Russia

Abstract. Mid-infrared optical absorption spectra of Ge/Si quantum dot structures in polarized light were obtained under conditions of interband optical excitation. Mid-infrared absorption changes in comparison to equilibrium conditions for certain light polarization in spectral range of 0.25 – 0.6 eV. The sign of the effect is found to be different in various spectral ranges. Transients of photoinduced absorption contain fast and slow components. The fast decay component of the absorption is related to the direct recombination of localized holes and electrons in quantum dots while a slow component is determined by significantly less probable processes of indirect in real space recombination.

1. Introduction

Nanostructures with quantum dots are being studied by a number of scientific groups around the globe. Intensive studies of optical and photoelectric properties of Ge/Si quantum dots are motivated by a possibility to develop mid- and near-infrared optoelectronic devices based on these structures. Lately a noticeable progress has been made in technology aspects of Ge/Si quantum dots growth [1]. There is a number of papers dedicated to studies of near-IR photoluminescence dynamics [2,3], and the results contain a lot of original information explaining recombination processes in quantum dots. The present work is focused on the optical properties of Ge/Si quantum dots in the mid-infrared spectral range under conditions of non-equilibrium population of the dot states with photo-excited charge carriers and also presents recent results on photoinduced absorption dynamics in GeSi quantum dot structures.

2. Experimental setup and samples

Structure with self-assembled MBE-grown Ge/Si quantum dots (QD) on Si (001) substrate was studied. Structure contains 10 periods of quantum dot layers formed in growth regime similar to one described in [4]. Quantum dots have a pyramidal shape with the average height of 2.7 nm, and the average base size of 14 nm. No intentional doping was performed.

The absorption spectra in mid-infrared range were measured with an automated experimental setup based on a prismatic monochromator with a global as a source of broadband infrared radiation that acted as a probe radiation. CW YAG:Nd laser was used as a source of pump radiation to create non-equilibrium charge carriers. During steady-state spectral measurements pump and probe radiation were simultaneously mechanically chopped at different frequencies. Photodetector signal was measured concurrently with two SR830 Lock-In amplifiers. The first one measured a signal proportional to the equilibrium optical transmittance T of the sample. The second one measured a signal proportional to the variation of the optical transmittance ΔT related only to non-equilibrium photo-excited charge carriers. Dynamics of photoinduced absorption was registered at the certain wavelength of probe radiation with digital oscilloscope LeCroy WaveSurfer 24MXs-B. Pumping was performed with 10 ns pulsed YAG:Nd laser.

3. Experimental results

Experimental steady-state photoinduced absorption spectra demonstrate that the presence of nonequilibrium charge carriers leads to the increase of optical absorption for z-polarized light in a wide spectral range with the centre at 0.3 eV and to the decrease of absorption at photon energies of about 0.45 eV. Absorption at photon energy of 0.3 eV is related to optical hole transitions from the ground state of quantum dot to continuum of states above the barrier. The spectral position of this absorption feature correlates well with previously measured mid-infrared photoconductivity spectra in similar doped structure [5]. Decrease of absorption at 0.45 eV can be related to the dynamic analogue of Burstein-Moss effect. Indirect optical transitions of electrons from the dot's localized states to the vicinity of QD in the Si conduction band become impossible due to the depopulation of the QD caused by pump radiation.

A set of absorption relaxation curves after an excitation with short laser pulses was measured at different temperatures. At the low temperature ($T = 90$ K) as well as at the intermediate temperature ($T = 190$ K) relaxation decay consists of fast and slow components. The fast component has a characteristic time of few μs and its value slightly increases with temperature, while for the slow component time value is tens of μs and decreases with the temperature increase. At the room temperature relaxation curve does not demonstrate two-stage behavior. Earlier such kinetics was observed in interband photoluminescence studies [2,3]. The fast decay component is related to the direct recombination of localized holes and electrons inside quantum dots, a slow component is determined by indirect in real space recombination that is significantly less probable.

4. Conclusion

In conclusion, in this work photo-induced mid-infrared absorption spectra were measured in Ge/Si quantum dot structures. Polarization-dependent dynamic analogue of the Burstein–Moss effect is observed. Dynamics of photoinduced light absorption was studied under conditions of pulse interband optical excitation. Two distinct components of absorption decay with significantly different characteristic times were isolated.

Acknowledgments

This work has been supported by the Russian Foundation for Basic Research (Project № 13-02-12203) and the Ministry of Education and Science of the Russian Federation.

References

- [1] Tonkikh A A, Zakharov N D, Novikov AV, Kudryavtsev KE, Talalaev V G, Fuhrmann B, Leipner H S and Werner P 2012 *Thin Solid Films* **520** 3322
- [2] Julsgaard B, Balling P, Lundsgaard Hansen J, Svane A and Nylandsted Larsen A 2011 *APL* **98** 093101
- [3] Kamenev B V, Tsybeskov L, Baribeau J-M, Lockwood D J 2005 *Phys. Rev. B* **72** 193306-1-4
- [4] Tonkikh A, Zakharov N, Talalaev V and Werner P 2010 *Phys. Status Solidi RRL* **4** 224-226
- [5] Panevin V Yu, Sofronov A N, Vorobjev L E et al 2013 *Semiconductors* **47** 1574-77

C-V and G-V characteristics for MIS-structures with CdHgTe-based quantum wells under the wide temperature range (8-300) K description

D Gorn, A Voitsekhovskii

Department of Quantum Electronics and Photonics, Nanoelectronics and Nanophotonics Laboratory, Tomsk state university, Lenina Av. 36, 634021 Tomsk

Abstract. Description of theoretical model for energy-band spectrum calculation for the heteroepitaxial CdHgTe (MCT) structures grown by molecular-beam epitaxy (MBE) method with the single quantum wells (QW) is presented in this work. This computation model allows to calculate different electro-physical properties of this structures and allows to explain features of their C-V and G-V characteristics in the wide temperature range, i.e. from ³helium^o till room temperatures.

At present, experimental methods of low-temperature ($T \sim 8$ K) semiconductor heterostructures research including structures with quantum wells by the impedance spectroscopy method are increasingly available. One of the impedance spectroscopy methods is the method of capacity-voltage characteristics [1, 2].

Results of experimental research of admittance (total conductivity) for metal-insulator-semiconductor structures based on Cd_xHg_{1-x}Te grown by MBE with single quantum wells are presented in [3]. In this scientific work describes results of admittance research for MIS-structures based on MBE MCT with QW under the range temperature from 8 till 300 K. After the comparison results of these investigations with structures without quantum wells authors have made the following conclusion: quantum well may cause the essential influence on complex conductivity structure under the near-³helium^o temperatures. Hence, it is too difficult to interpret the influence of quantum well on the structure electro-physical parameters. The cause of this is absence of theoretical model at present which allows to carry out precise quantitative estimation for influence of dimensional quantization on heteroepitaxial MBE MCT structures properties [4, 5].

There are brief description of basic principles of self-consistent electrostatic potential theoretical model for semiconductor heterostructure in this work. This model are based on joint decision of Poisson and Schrödinger equations for heterostructure comprising a quantum well. Similar theoretical model have been used by us for a infrared photoluminescence spectra calculation for MCT structures comprising potential and quantum wells [6].

At the formulation of the problem we have taken into account the fact that all structures under consideration were grown by the molecular-beam epitaxy method on the ³Ob'-M^o MBE-equipment in the Institute of semiconductor physics (Novosibirsk).

In structures comprising a quantum wells spatial distribution of electrostatic potential defines also by the concentrations of 2D-electrons and 2D-holes in the dimensional quantization subband in a quantum well. It is necessary to now dimensional quantization levels energies and envelope wave function to define values of these concentrations. Dimensional quantization levels energies and envelope wave functions can be obtained by the Schrödinger equation solution.

Poisson equation solution have been obtained by finite difference method with the use of quasi-linearization [7]. Schrödinger equation have been solved in terms of in the approximation of the asymmetric rectangular potential well with a barrier of finite height [5].

Figure 1 provides an example of using presented method to calculate the energy structure of the QW of the MCT with the composition in a well 0.27 and 0.36 mole fractions and a 10 nm thick.

The capacity-voltage characteristics of the MIS-structure based on MCT QW can be calculated from the voltage balance equation for the structure.

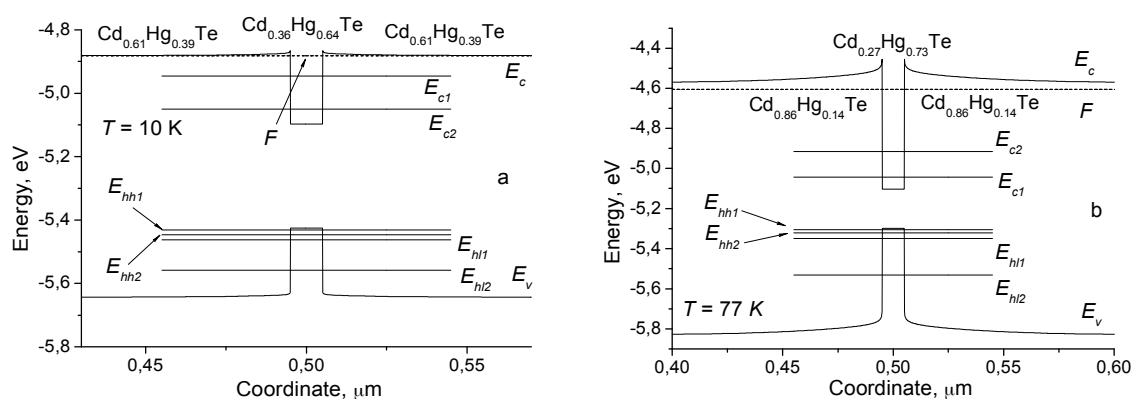


Figure 1. Energy-band diagram profile for structures with QW $\text{Cd}_{0.61}\text{Hg}_{0.39}\text{Te}/\text{Cd}_{0.36}\text{Hg}_{0.64}$ (a) и $\text{Cd}_{0.86}\text{Hg}_{0.14}\text{Te}/\text{Cd}_{0.27}\text{Hg}_{0.73}\text{Te}$ (b) with the QW width 10 nm under the 10 K (a) and 77 K (b).

Thus, this study is devoted to building of physical and mathematical model to carry out numerical calculations of the electrical parameters of the MBE MCT structures, including quantum wells. The model account for the presence of the dimensional quantization levels of the electrons, light and heavy holes in the quantum well.

References

- [1] Zubkov V.I. 2006 *Peterburgskii jurnal elektroniki* **4** 52
- [2] Zubkov V.I. 2007 *FTP* **41** (4) 331
- [3] Dzyaduh S.M., Voitsekhovskii A.V., Nesselov S.N., Dvoretiskii S.A., Mikhailov N.N. and Gorn D.I. 2013 *Izv. vuz. Fizika* **56** 50
- [4] Shik A.Ya., Bakueva L.G., Musihin S.F. 2001 *Physics of low-dimensional systems* (SPb.: Nauka)
- [5] Vorobov L.E., Ivchenko E.L., Firsov D.A. 2001 *Optical properties of nanostructures* (SPb.: Nauka)
- [6] Voitsekhovskii A.V., Gorn D.I., Izhnin I.I., Izhnin A.I., Goldin V.D., Mikhailov N.N., Dvoretiskii S.A., Sidorov Yu.G., Yakushev M.V., Varavin V.S. 2012 *Izv. vuz. Fizika* **55** 50
- [7] Amosov A.A., Dubinskii Yu.A., Kopchenova N.V. 1994 *Computation methods for engineers*. ± (M.: Vyssh. shk.)

Observation of Rabi oscillations in microcavities

Kopteva N. E.¹, Cherbunin R. V.¹, Mikhailov A. V.¹

¹ Spin Optics laboratory, Saint Petersburg State University, Saint Petersburg, 198504, Russia

Abstract.

In this work we observe Rabi oscillations in a semiconductor microcavity with embedded quantum wells in the strong coupling regime. The optically induced time-resolved Kerr rotation technique was used for researching this effect. In Kerr rotation signal some periods of Rabi oscillations was observed. Influence of the dark excitons reservoir on lifetime of Rabi oscillations is studied.

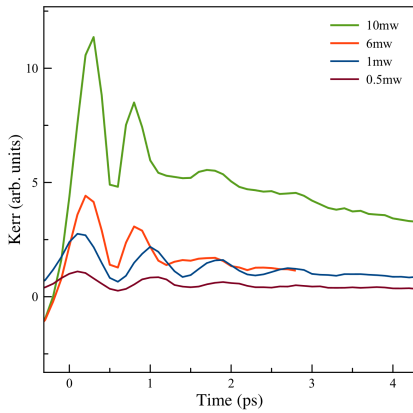


Figure 1. Rabi oscillations in a Kerr rotation signal. Different curves correspond to different power of the pump pulse.

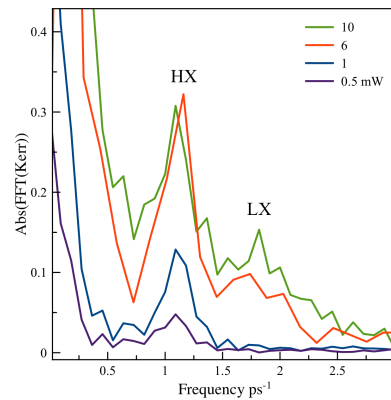


Figure 2. Fast Fourier transform of Kerr signal. HX (LX) calculated frequency of the transition of heavy (light) hole exciton and photon.

Rabi oscillations are quantum beats in a mixed exciton-photon system in a microcavity. In the microcavity operating in the strong coupling regime between an exciton and a photon, the anticrossing of exciton-polariton branches is observed. If we excite two exciton-polariton branches in point of zero detuning by a shot laser pulse, system initially in a purely photonic state goes in a pure exciton state [1]. It is called vacuum-field Rabi oscillations.

In this work we represent observation of Rabi oscillations in a signal of Kerr rotation dynamics. We used a pump-probe Kerr rotation technique for investigations of the exciton-polariton dynamics after excitation of system by shot pump pulses. The pump pulses were circularly polarized. The time-delayed probe pulses were linearly polarized in vertical plane. Its

rotation after reflection of a sample as a function of the pump-probe delay in the femtosecond scale is detected. Sample under study is a high quality *GaAs/AlGaAs* microcavity containing a quantum wells. The sample was wedge shaped, so that the detuning between photon and exciton modes can be changed.

We detect reflection spectra in a different point of the sample correspond to different detunings. An analysis of these spectra shows that in our sample a strong coupling regime is realized, because we observe an anticrossing of upper and lower polariton branches. It means that Rabi oscillations should present in this sample. In dynamics of Kerr rotation we observe a periodical changes of an amplitude in decay signal of a polariton polarization (fig. 1). Frequency of these oscillations correspond to the energy of Rabi splitting in a point of a zero detuning (fig. 2). We associate the fast decay of the amplitude of this oscillations with a small coherence time of the ensemble of excitons created in the system. This time can be changed if reservoir of dark excitons is present [2]. We observed influence of additional cw-pumping creating the reservoir on a decay time of Rabi oscillations.

References

- [1] A. Brunetti, M. Vladimirova, D. Scalbert, M. Nawrocki, A. V. Kavokin, I. A. Shelykh, and J. Bloch. Observation of spin beats at the rabi frequency in microcavities. *Phys. Rev. B*, 74:241101, Dec 2006.
- [2] S. Demirchyan, S. Yu. Chestnov, I. P. Alodjants, A. M. Glazov, M. and V. Kavokin, A. Qubits based on polariton rabi oscillators. *Phys. Rev. Lett.*, 112:196403, May 2014.

Mid-infrared photoluminescence from structures with InAs/GaSb type II quantum wells

A V Selivanov, I S Makhov, V Yu Panevin,
A N Sofronov, D A Firsov and L E Vorobjev

Peter the Great St. Petersburg Polytechnic University, Politechnicheskaya str., 29, St. Petersburg, 195251, Russia

Abstract. The results of experimental investigations of interband photoluminescence spectra from quantum well nanostructures based on InAs/GaSb type II heterojunctions in mid-infrared spectral range in the wide temperature range from 10 K to the room temperature are presented. The calculated effective bandgap of quantum well is in good agreement with the spectral position of interband photoluminescence line.

1. Introduction

Quantum wells (QW) and superlattices (SL) based on InAs/GaSb type II heterojunctions allow to create the photodetectors operating in mid-infrared spectral range [1-3], which are compete with HgCdTe-based devices. In the type II QWs the spectral position of the interband absorption edge or the luminescence line is determined by the effective bandgap E_g^{eff} - energy gap between the ground electron and hole states, which are separated in the real space. Using the calculations of the electron and hole energy levels, one is able to design the necessary band profiles for devices operating in mid-infrared spectral range. Unfortunately the total error in E_g^{eff} corresponding to mid-infrared range could be the same order of magnitude as E_g^{eff} itself because of large dispersion of band structure parameters of the hetero pair components in the reference data. In these conditions the experimental investigation of the effective bandgap is important task. In the present work, the effective bandgap value for InAs/GaSb type II QW is obtained from the study of the interband photoluminescence spectra in the mid-infrared spectral range at the different lattice temperatures.

2. Samples and experimental setup

Sample for optical studies with type II QWs was MBE grown on GaSb substrate on a 500 nm GaSb buffer layer. Sample contains 20 periods GaSb/InAs/GaSb layers forming QWs for electrons and holes, separated with 20 nm $\text{Al}_{0.35}\text{Ga}_{0.65}\text{As}_{0.03}\text{Sb}_{0.97}$ lattice-matched barriers. Each period contains 4 nm InAs layer, forming QW for electrons. 25 nm GaSb layers are located on both sides of InAs layer forming QWs for holes. The structure contains a 25 nm undoped GaSb cap layer.

The energy spectrum for our structure was calculated using the Schrödinger equation for the envelope function by transfer matrix method taking into account the mechanical stress in InAs layer. The values of material parameters were taken from paper [4], interpolation formula for parameters of

alloys was taken from paper [5]. According to energy spectrum calculations, the effective bandgap is $E_g^{\text{eff}} = 182 \text{ meV}$ at the temperature $T = 77 \text{ K}$.

For experimental studies the sample was mounted into the low vibration closed cycle cryostat based on the pulse tube thermodynamic cycle. Sample temperature can be varied from 10 K to 320 K. Interband optical excitation of the sample was attained with the solid state pulsed laser ($\lambda = 1.064 \mu\text{m}$, pulse duration $0.25 \mu\text{s}$, repetition rate 8 kHz, maximum average power about 60 mW). The mid-infrared photoluminescence spectra were studied using vacuum Fourier transform infrared spectrometer operating in step scan mode. The photoluminescence intensity was measured by liquid nitrogen cooled HgCdTe-photodiode equipped with the preamplifier. In order to block the pumping light, the high resistance Ge optical filter (transmittance of about 40 % in the mid-infrared spectral range) was set in the front of the HgCdTe-photodiode. The photoresponse of HgCdTe-detector was measured by gated integrator SR250.

3. Experimental results and discussion

The photoluminescence spectra were studied in the spectral range 70 – 400 meV at the different temperatures of the sample (from 10 K to the room temperature). Obtained spectra show a luminescence band lying in the spectral range from 180 meV to 260 meV, near the effective bandgap calculated value (182 meV). We associate above mentioned luminescence band with the indirect in the real space radiative recombination of photoexcited electrons and holes in type II InAs/GaSb QWs. The comparison of photoluminescence spectra for the different temperatures of the sample demonstrates the decrease of the interband luminescence intensity as well as weak shift of the luminescence band to the lower energies with the temperature increase. The decrease of the interband luminescence intensity could be connected with the internal quantum efficiency decrease with the temperature increase. The shift of the luminescence band could be connected with the change of the band offsets on the heterointerfaces of the QW with the sample temperature change.

Summary In the present work, the interband photoluminescence spectra from quantum well nanostructures based on InAs/GaSb type II heterojunctions in mid-infrared spectral range and its temperature dependence were investigated. The quantum well nanostructure effective bandgap calculated value is in satisfactory agreement with the spectral position of interband photoluminescence line. It is shown, that the emission band observed at high temperatures right up to the room temperatures. This work is partially supported by RFBR (Grant 13-02-12203) and the Ministry of Education and Science of Russian Federation.

References

- [1] Haugan H J, Brown G J, Szmulowicz F, Grazulis L, Mitchel W C, Elhamri S, Mitchell W D 2005 *Journal of Crystal Growth* **278** 198
- [2] Rehm R, Walther M, Schmitz J, Fleißner J, Fuchs F, Ziegler J, Cabanski W 2006 *Opto-Electronics Review* **14** 19
- [3] Plis E A 2014 *Advances in Electronics* 2014 246769
- [4] Vurgaftman I, Meyer J R, Ram-Mohan L R 2001 *Journal of Applied Physics* **89** (11). 5815
- [5] Donati G P, Kaspi R, Malloy K J 2003 *Interpolating Journal of Applied Physics* **94**(9) 5814

Ballistic thermopower of suspended semiconductor structures with two dimensional electron gas

E Yu Zhdanov^{1,2}, A G Pogosov^{1,2}, M V Budantsev¹, D A Pokhabov^{1,2},
A K Bakarov¹ and A I Toropov¹

¹Institute of Semiconductor Physics, SB RAS, Novosibirsk, Russia

²Novosibirsk State University, Novosibirsk, Russia

Abstract. We study ballistic electron transport in suspended semiconductor nanostructures containing high mobility two dimensional electron gas structured with periodical square lattice of artificial scatters — antidots. Longitudinal magnetoresistance and ballistic thermopower demonstrates commensurability oscillations originating from geometrical resonances both in suspended and non-suspended samples. We found differences between suppression of commensurability oscillations in longitudinal magnetoresistance by dc current in suspended and non-suspended Hall bars while commensurability oscillations of thermopower doesn't demonstrate drastic differences.

1. Introduction

Recently, semiconductor nanostructures detached from the substrate containing two dimensional electron gas (2DEG) attract significant attention due to the influence of additional mechanical degrees of freedom [1] and peculiarities of heat transport [2,3] on electron transport in these systems.

In the present work we investigate ballistic electron transport and thermopower in suspended 2DEG structured with periodical lattice of antidots.

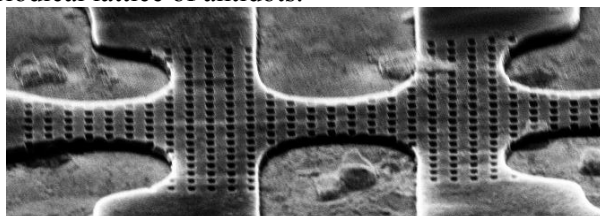


Figure 1 Image of the suspended hall bar covered with periodical lattice of antidots which was made by electron microscopy at an angle of 60 degrees.

2. Experimental details

Experimental samples were fabricated by photolithography from AlAs/GaAs heterostructures containing high mobility two dimensional electron gas. 2DEG density was $n_s = 5 \times 10^{11} \text{ cm}^{-2}$ and a mobility $\mu = 2 \times 10^6 \text{ cm}^2/\text{Vs}$ measured at liquid helium temperature. Heterostructures were grown by means of molecular-beam epitaxy above 400 nm thick $\text{Al}_{0.7}\text{Ga}_{0.3}\text{As}$ sacrificial layer. Then samples were covered with periodical square lattice of antidots by electron lithography. Diameters of antidots

were varied from 100 to 200 nm and periods of the lattices from 500 to 800 nm for different samples. The sacrificial layer was removed by means of selective wet etching in HF based etchant (see Figure 1). Magnetotransport measurements were performed at low temperatures 0.5÷4.2 K.

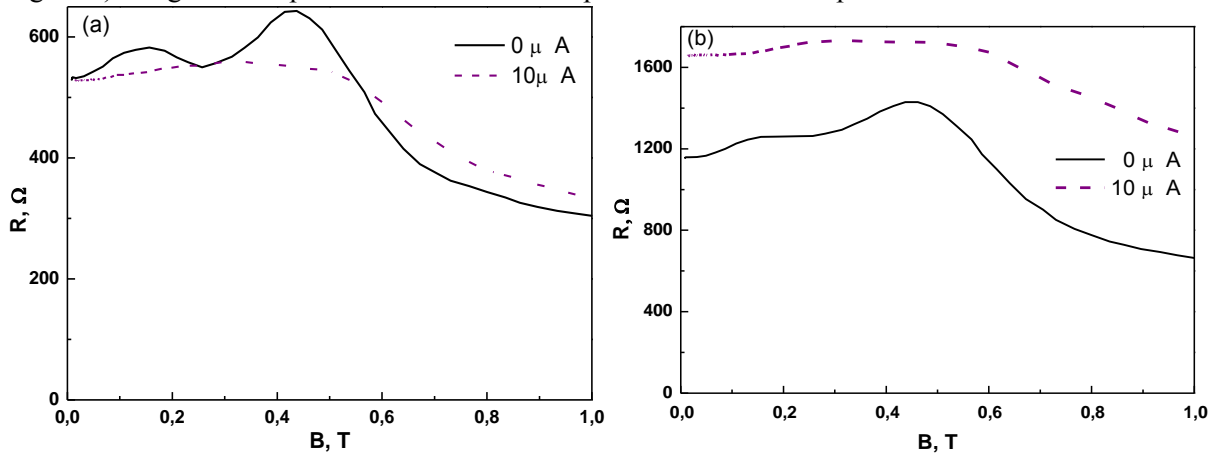


Figure 2 Dependence of the magnetoresistance on applied dc current (a) non-suspended sample; (b) suspended sample.

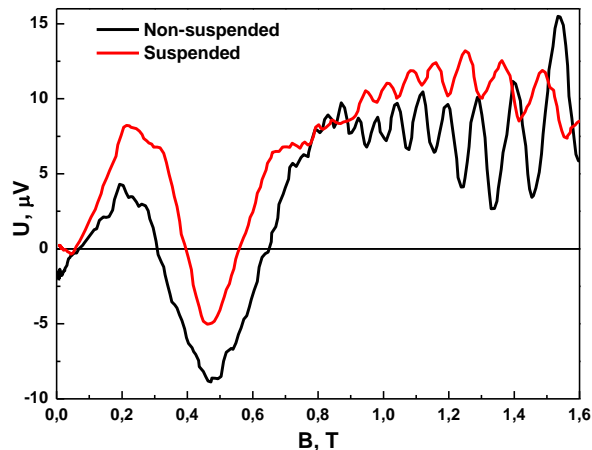


Figure 3 Ballistic thermopower of non-suspended and suspended Hall bars with antidot lattice.

3. Experimental results

We found that commensurability oscillation (CO) originating from geometrical resonance are well pronounced both in magnetoresistance and in magnetic field dependence of thermopower which means that the electron mobility in 2DEG remains high after suspension. The study of suppression of CO in magnetoresistance by dc current shows different behavior for suspended and non-suspended samples (see Figure 2). However, a comparative study of CO in thermopower doesn't demonstrate drastic differences (see Figure 3).

The work is supported by RFBR (grants 13-02-01153, 14-02-31585) and Russian Academy of Sciences.

References

- [1] Ekinci K L and Roukes M L 2005 *Rev. Sci. Instrum.* **76** 061101
- [2] Pogosov A G, Budantsev M V, Zhdanov E Yu, Pokhabov D A, Bakarov A K and Toropov A I 2012 *Appl. Phys. Lett.* **100** 181902
- [3] Zhdanov E Yu, Pogosov A G, Budantsev M V and Pokhabov D A 2013 *AIP Conf. Proc.* **1566** 211
- [4] Baskin E M, Gusev G M, Kvon Z D, Pogosov A G and Entin M V 1992 *JETP Letters* **55** 678

The luminescence properties of colloidal quantum dots

I.I. Mikhailov, S.A. Tarasov, A.V. Solomonov, I.A. Lamkin

Saint Petersburg Electrotechnical University «LETI» (ETU)

Abstract. In this paper were investigated colloidal quantum dots based on CdSe and CdS. Were studied their photoluminescence spectra. And it was revealed the influence of surface defects on the photoluminescence spectra.

For the last decade colloidal quantum dots (CQDs) have become an object of particularly intensive studying. CQDs are semiconductor particles of nanometer scale synthesized in liquid media and characterized by unique properties which substantially differ from bulk material properties. One of the most important advantages of CQDs is facility of geometric size tunability through technological parameters variation (time, temperature etc.) and that synthesis procedures don't require expensive equipment and materials. CQDs is promising material for a high-performance LED and laser structures creation, as well as photosensitizers in solar cells or luminophores in micro-devices for optical tomography of biological tissues.

In order to investigate properties and characteristics of CQDs, methods of non-invasive optical spectroscopy were applied. These techniques are based on the utilizing of photoluminescence effects and allow obtaining information regarding particle size, crystal structure quality, quantum yield and other CQDs parameters.

In the first part of the work CdSe CQDs were prepared in aqueous medium with the use of thioglycolic acid (TGA) acting as surfactant. Absorption onset and photoluminescence peak shift to long-wavelength region with time which indicates that average nanoparticle size increases in the process of the reaction. Further experiment was held where CdSe cores were coated with the shell of wider bandgap material CdS. Photoluminescence intensity for this sample increased twofold compared to uncoated nanoparticles, indicating that CdS shell provides surface defects passivation, hindering non-radiative recombination and thus increasing quantum yield.

The synthesis of colloidal CdSe quantum dots in organic medium was carried out in the second part of the work. The spectra reveal two radiation regions: a high intensity peak on the left side of the characteristics and a broad plateau of a lower intensity on the right. This plateau was formed due to surface defects. Intense narrow peak was formed due to the interband energy transition.

Synthesized nanoparticles are planned to be used as luminophores for microdevices of optical tomography of biological tissues.

We thank L.B. Matyushkin and D.S. Mazing for providing the samples.

Estimation of the effective electron-capture cross section in the emission processes from arrays of vertically coupled InAs quantum dots in an n-GaAs matrix

A. Baklanov¹, A. Gutkin², P. Brunkov^{1,2}

¹ St. Petersburg State Polytechnical University, 29 Polytechnicheskaya, St. Petersburg, 195251 Russia

² Ioffe Physical-Technical Institute, 26 Polytechnicheskaya, St. Petersburg, 194021 Russia

Abstract. In the paper we investigate the processes of electron emission from arrays of vertically coupled InAs quantum dots in the space charge region of the Schottky barrier in the matrix of n-type of GaAs. We developed a model of thermally activated tunneling of charge carriers, which allows to calculate the parameters that characterize the processes of electron emission. The temperature dependence of the activation energy of the carriers, the ground state energy carrier in the quantum dot at different reverse bias voltage of the Schottky barrier, and the dependence of the electron-capture cross section on the binding energy of the quantum dot ground state were obtained. The comparison of the values performed for samples with different number of layers of quantum dots: 3, 6 or 10 layers.

1. Introduction

The study of the emission processes of charge carriers in heterostructures that contain arrays of self-assembled quantum dots (QDs) is an important part in the design and optimization of devices and active elements which are based on these structures [1]. It is important to study the mechanisms of this emission and different factors affecting the value of its rates. In this paper it is assumed that the electron emission from arrays of vertically coupled QDs to conduction band of the semiconductor matrix is in the form of thermally activated tunneling process with the involvement of virtual states. For such a process implemented a model that describes the experimental data of the temperature dependence of the emission rate which obtained by admittance spectroscopy. These processes are studied in [2-4], but their dependence of the effective carrier capture cross sections on the ground state energy of the electrons in the QDs were not conducted.

2. Experiment

The investigated structures were Schottky barriers based on epitaxial layers of Si-doped GaAs ($n \approx 2 \times 10^{16} \text{ cm}^{-3}$), which contained 3, 6 or 10 InAs QDs layers. The emission rate of charge carriers from the QDs was determined by the method of admittance spectroscopy at different reverse-bias voltages [4]. The frequency (f) of the Probe AC voltage was varied within the limits of $10^4 - 10^6$ Hz. Whereas the differential conductance reaches a maximum peak when the emission rate is $e_n \approx \pi f$ (Fig. 1) (in the figure for the sample with 10 layers QDs). The experimental dependence approximated using a previously

proposed model [4], which describes the process of thermally activated tunneling of charge carriers (Fig. 1, b).

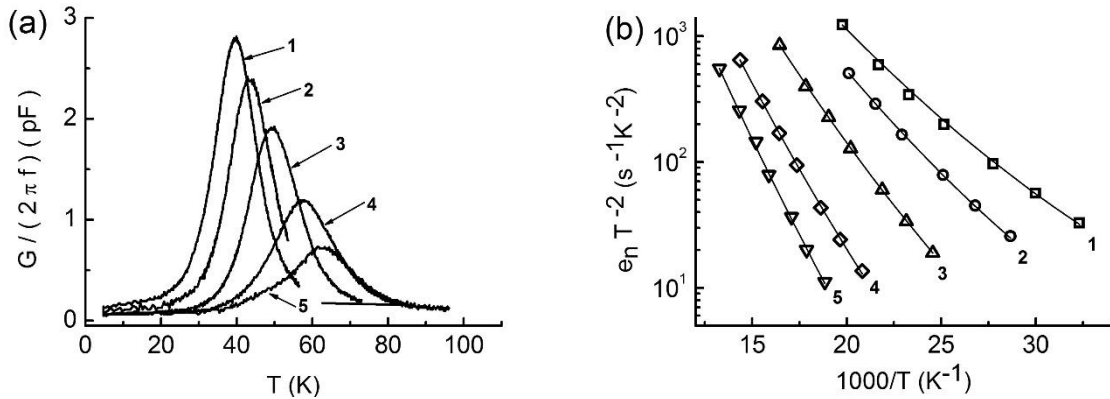


Fig. 1. Temperature dependences at a frequency of 0.1 MHz at different reverse-bias voltages: (a) of the differential active conductivity G of the Schottky barriers, (b) of the rate of electron emission from the QD ground state (Dots represent the experimental data and solid lines represent the results of the approximation). (V_{rev} : -0.60 V (1), -1.00 V (2), -1.40 V (3), -1.80 V (4), -2.00 V (5)).

3. Results

As a result of analysis of the experimental temperature dependence of the emission rate at different reverse-bias voltages were calculated activation energy and the binding energy of the carriers in quantum dots (Fig. 2 a) (in the figure for the sample with 10 layers QDs). Were also evaluated in the effective electron-capture cross section (Fig. 2, b): the capture cross section increases with the energy of the electron in the QD. Thus it is possible to obtain estimates for the effective electron-capture cross section by analyzing experimental data.

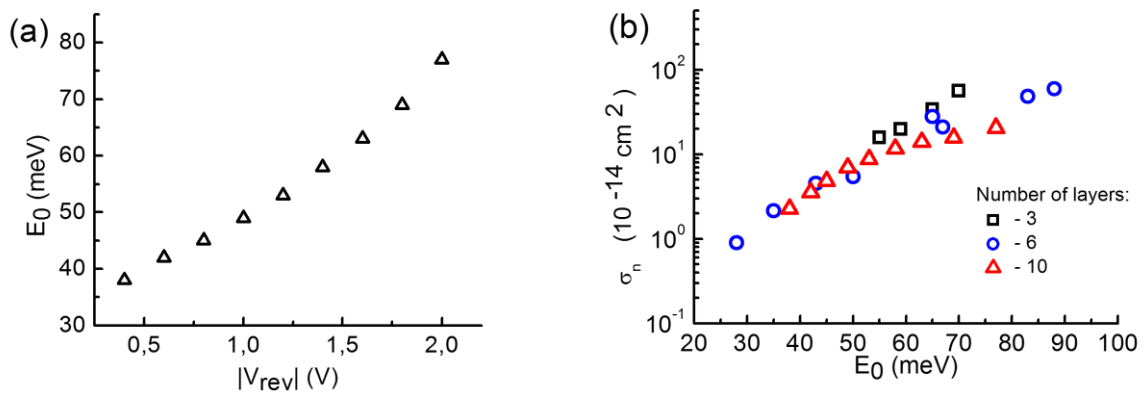


Fig. 2. (a) Binding energies E_0 of the ground state of QDs probed at different reverse-bias voltages V_{rev} . (b) Dependence of the effective electron-capture cross section on the binding energy E_0 of the QD ground state for samples with 3, 6 or 10 layers of QDs.

References

- [1] Zhiming M. Wang 2012 Quantum Dot Devices (Berlin: Springer)
- [2] Brunkov P. et al 1999 *J. Electron. Mat.* **28** 486
- [3] Gutkin A. et al 2007 *Semiconductors* 41 1353
- [4] Gutkin A. et al 2008 *Semiconductors* 42 1104
- [5] Baklanov A. et al 2014 *Semiconductors* 48 1186

Ion synthesis of GaN nanocrystals in silicon

D S Korolev, A N Mikhaylov, A I Belov, V A Sergeev, V K Vasiliev, A E Smirnov, D E Nikolitchev, R N Kryukov, D V Guseinov, A S Markelov, V N Trushin and D I Tetelbaum

Lobachevsky State University of Nizhni Novgorod, 23/3 Gagarin prospect, Nizhni Novgorod, 603950, Russia

Abstract. The structure and composition of a subsurface silicon layer subjected to a double implantation of Ga and N ions with subsequent annealing have been investigated using X-ray photoelectron spectroscopy (XPS), electron spin resonance (ESR), X-ray diffraction (XRD). The results indicate a possibility of ion-beam synthesis of GaN composite nanostructures in silicon-based materials.

1. Introduction

Gallium nitride attracts great attention as a source of short-wave optical emission (LEDs and lasers) for the new-generation optoelectronic devices. However, epitaxial growth of gallium nitride on silicon wafers is difficult due to high lattice mismatch and differences in thermal expansion coefficients of the two materials. Therefore, a topical problem is to investigate the possibility of synthesis of GaN nanoinclusions in silicon. In the present work, the possibility of synthesis of GaN phase in Si by the double gallium and nitrogen ion implantation with subsequent annealing is studied.

2. Experimental

Samples of *n*-type Si were implanted with Ga⁺ (80 keV) and N₂⁺ (40 keV) ions with different doses in the range of $2.5 \cdot 10^{16} - 1 \cdot 10^{17} \text{ cm}^{-2}$. Energy and dose of ions were selected in such a way that the depth distribution of Ga and N were the same. Implanted samples were annealed at 900 °C (30 min) in N₂ flux. Structure, chemical composition of the implanted layers was analyzed by ESR, XPS and XRD.

3. Results and discussion

The ESR data show that ion implantation into the Si surface layer transform it into amorphous state (with the concentration of dangling bonds in the range of $5 \cdot 10^{17} - 6 \cdot 10^{18} \text{ cm}^{-3}$ depending on the order and dose of ion implantation). After annealing at 900 °C the defect concentration is reduced, but remains still noticeable, indicating incomplete recrystallization process.

XPS spectra acquired with depth profiling of the Si implanted layer give the distributions of Ga and N similar to the ion profiles calculated by SRIM (www.srim.org). The amount of nitrogen atoms bound to silicon is found to be ~13 at. % even without annealing, probably due to the stronger Si-N bonding in comparison with that of Ga-N. Ga atoms are predominantly in an unbound state (~10 at.%), and the concentration of Ga-N bonds is less than 3% at. After annealing, a part of Ga atoms is reduced (figure 1) due to their evaporation, however about 1-2 at. % of GaN phase is still revealed in Si

subsurface layer. Thus, high-temperature annealing leads to the loss of a small quantity of the GaN phase, formed during the ion implantation process.

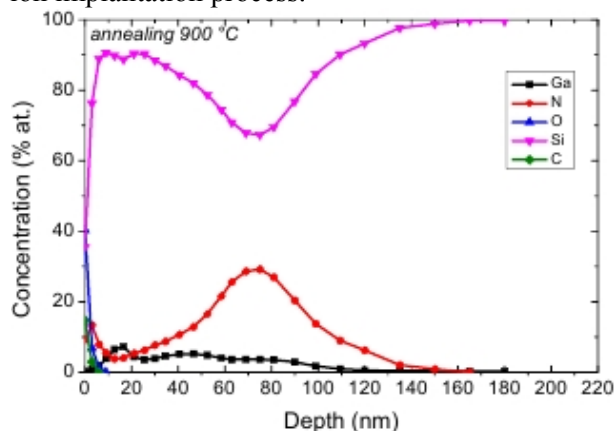


Figure 1. Depth distributions of chemical species in Si implanted with Ga^+ ($5 \cdot 10^{16} \text{ cm}^{-2}$) and N_2^+ ($2.5 \cdot 10^{16} \text{ cm}^{-2}$) ions and annealed at $900 \text{ }^\circ\text{C}$.

The absence of crystalline phase in Si implanted layer before annealing is established by XRD. For the small dose after annealing the reduction of defect concentration and partial crystallization are confirmed by the appearance of the Si (111) peak (figure 2). However, the intensity of GaN peak is too small to indicate the presence of crystalline phase of gallium nitride.

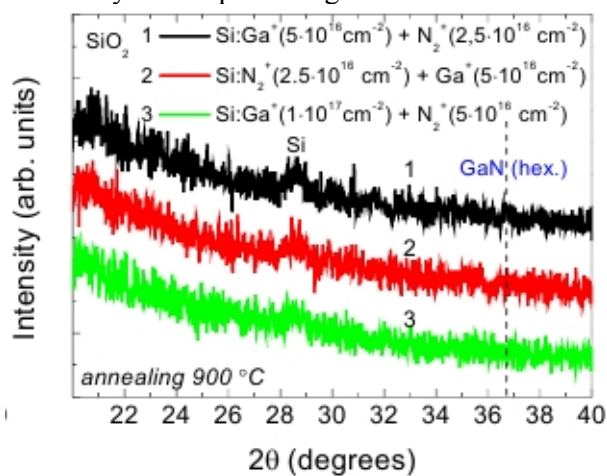


Figure 2. XRD spectra of Si implanted with Ga^+ and N_2^+ ions in different conditions and annealed at $900 \text{ }^\circ\text{C}$.

The reported data is not an evidence of the absence of GaN nanoparticles in the implanted Si layers, rather said about their amorphous state or about small volume fraction.

4. Conclusions

Thus, the co-implantation of gallium and nitride ions into silicon leads to the formation of Ga-N bonds in silicon even without annealing. After annealing at $900 \text{ }^\circ\text{C}$, the concentration of Ga-N bonds is reduced, but several percent of amorphous GaN phase is present. The optimization of annealing conditions is required to prevent the partial loss of implanted gallium.

The work is supported by the Ministry of Education and Science of the Russian Federation (RFMEFI58414X0008).

Visible light activated room temperature gas sensors based on nanocrystalline ZnO sensitized with CdSe quantum dots

I.V. Krylov³, A.S. Chizhov¹, M.N. Rumyantseva², R.B. Vasiliev^{1,2},
D.G. Filatova², K.A. Drozdov³, A.M. Abakumov², A.M. Gaskov²

¹*Department of Materials Science, Moscow State University, Leninskie Gory 1-21, Moscow 119991, Russia*

²*Chemistry Department, Moscow State University, Leninskie Gory 1-3, Moscow 119991, Russia*

³*Physics Department, Moscow State University, Leninskie Gory 1-2, Moscow 119991, Russia*

One of the major disadvantages of currently available semiconductor gas sensors are relatively high operating temperature and power consumption, which limits their use in a miniaturized gas analyzers and fire detectors. In recent years, several reports on the use of photoactivation to increase gas sensitivity of a metal oxide semiconductor (MOS) appeared. The vast majority of publications is devoted to the study of MOS sensor properties under UV illumination. However, using the powerful UV radiation cannot significantly reduce the power consumption of the semiconductor gas sensor. Regarding the solar spectrum it seems to be more effective to use the radiation in the visible range. In order to increase MOS sensitivity to the visible light it is necessary to modify the structure by implementing appropriate photosensitizers – colloidal semiconductor nanocrystals or quantum dots (QDs).

In this work we investigated the optical, photoelectric and sensor properties of nanocrystalline zinc oxide (ZnO) thin films with CdSe colloidal quantum dots. Nanocrystalline ZnO was synthesized by the precipitation method. Colloidal CdSe quantum dots were obtained by high temperature colloidal synthesis.

Absorption spectra were obtained for powder structures ZnO, CdSe QDs solution and powder ZnO structures with CdSe QDs in the visible range. Zinc oxide does not show noticeable absorption for visible light with $\lambda > 425$ nm. The QDs exhibit absorption in the visible spectral range with a sharp low-energy excitonic transition at $\lambda = 535$ nm. For the ZnO/CdSe structure photoconductivity spectrum was obtained. Photoconductivity and absorption spectra demonstrate clear correlations. The maximum of photoresponse curve for ZnO/CdSe nanocomposite matches well the maximum in absorption spectrum of the CdSe nanocrystals for ZnO/CdSe samples. This suggests that effective charge transfer between QDs and oxide semiconductor is achieved.

Room temperature electrical resistance of ZnO-based samples under periodic green light illumination ($\lambda_{\text{max}} = 535$ nm) depending on oxygen content in the gas phase were investigated. It was found that with the oxygen concentration growth values of the resistance in darkness and under illumination increases, which is accompanied by an increase in the effective photoresponse. The data obtained can be explained by the model proposed by Hou et al. [1] The obtained results indicate that nanocrystalline semiconductor oxides sensitized with CdSe QDs can be used for NO₂ detection under visible light illumination at room temperature without any thermal heating.

References

1. D. Hou, A. Dev, K. Frank, A. Rosenauer, T. Voss, Oxygen-controlled photoconductivity in ZnO nanowires functionalized with colloidal CdSe quantum dots, *J.Phys. Chem. C* 116 (2012) 19604–19610.

Spin-dependent energy gap oscillations in the ultra-short carbon nanotube (5, 5)

S V Popov, G I Glushkov, A V Tuchin

Voronezh State University, 394006, Universitetskaya pl.1, Voronezh, Russia

Abstract. Results of the numerical simulation of an electronic structure of an ultrashort single-walled carbon nanotube (5, 5) at singlet and triplet states were presented. An antiphase energy gap oscillation on the length of the ultrashort nanotube (5, 5) in singlet and triplet states was revealed. It was found that the ground state of the nanotube is singlet, however the energy of the singlet-triplet transition corresponds to the energy value of visible and IR-radiation.

1. Introduction

Lots of theoretical researches of carbon nanotubes demonstrate that decreasing tube length less than 10 nm causes great changes in electronic structure and fundamental parameters such as energy gap between the lowest unoccupied (LUMO) and the highest occupied (HOMO) molecular orbitals (ELH), ionization potential (IP), electron affinity (EA). Rochefort et. al researched the electronic structure of armchair single-walled carbon nanotube us-SWCNT (6,6) with length $L < 2.4$ nm. It was found out that this ultrashort CNT is semiconductor, but infinite tube must have zero energy gap according to “3k” rule [1-5]. Size-dependent effects caused the oscillations of energy gap, the oscillations magnitude decreases with the tube length increment. Cioslowski et al. by DFT/B3LYP with 6-311*G basis set researched us-SWCNT (5,5) with $L < 2.5$ nm and found energy gap oscillations for singlet state, but triplet states and singlet-triplet transitions were not well described. Triplet states are perspective for spintronics, optoelectronics and molecular electronics applications. The aim of this work is theoretical study of electronic structure of us-SWCNTs (5, 5) on singlet and triplet states.

2. Computational details

The numerical simulations of electronic structure of armchair ultrashort single-walled carbon nanotubes us-SWCNT (5,5) were carried out by DFT (density functional theory) method with B3LYP (Becke, Lee, Yang, Parr) exchange functional in 6-31G basis sets respectively. The half of fullerene C_{60} cut perpendicular to C_5 axis acts as a cap of finite nanotube. The finite closed CNT structures were produced by sequential adding of ring segments (10 carbon atoms) between tube caps. The sequential incrementation of j causes rotation of hats on $\pi/5$ relatively to each other, thus the symmetry vs segment number can be $D_{5h}(j=2m+1)$ or $D_{5d}(j=2m)$ $m=0, 1, 2 \dots$

3. Results and discussion

The energy gap E_{LH} of us-SWCNT extremely exceeds energy gap of infinite CNTs (5,5) $E_g=30$ meV due to quantum effects and caps influence. The dependence of energy gap between the highest occupied molecular orbital (HOMO) and the lowest unoccupied molecular orbital (LUMO) versus

segments number in finite closed CNT(5,5) in singlet and triplet states is shown in figure 1. All armchair CNTs (with caps or without them) can be divided into three groups for number of segments j aliquot to $3m$, $3m+1$, $3m+2$.

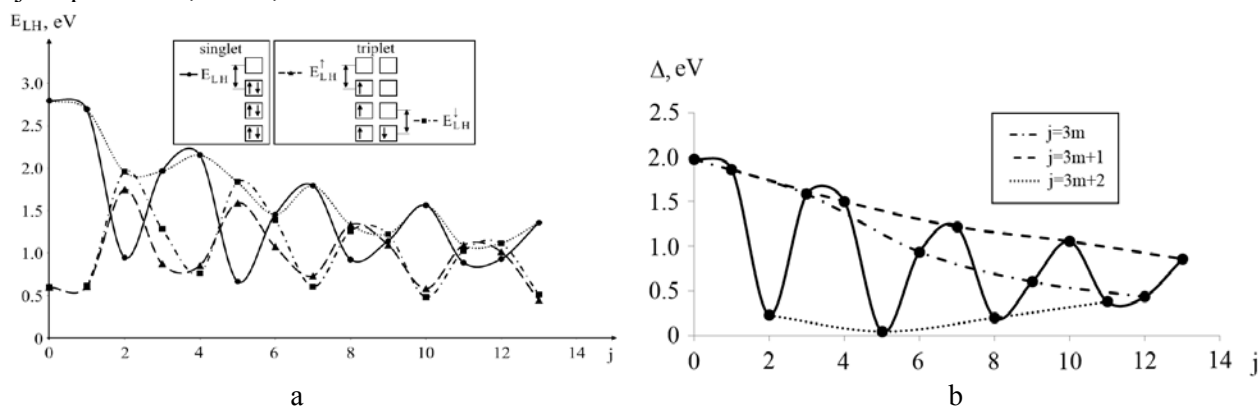


Figure 1. The Energy gap E_{LH} of singlet and spin-dependent E_{LH}^{\uparrow} and E_{LH}^{\downarrow} of triplet states of us-SWCNT(5, 5) versus the number of segments i (a). An maximum gap E_{LH} is shown by the dotted line. The energy of the singlet-triplet transition of us-SWCNT (5, 5) (b)

Energy gap indicates the stability of the system, so for $(3m+2)$ tubes the ground state corresponds to uncompleted electronic orbital that is contrary to [6,7]. The difference of triplet and singlet states is positive. It indicates that ground state corresponds to closed electron shell in researched length range and corresponds to near (for $3m$ and $3m+1$) and far (for $3m+2$) infrared (IR). For singlet CNTs with the number of sections $j=3m+1$, $3m$ and $3m+2$ ($k=0, 1, 2, \dots$) ΔE_{LH} possesses the maximum, average and minimal values that corresponds to the introduced classification based on the calculations of the dependency of the gap LUMO-HOMO vs the nanotube length. It was found out that for singlet this dependence is works in antiphase: $3m+1$ corresponds to minimum, $3m$ – average and $3m+2$ maximum energy.

4. Conclusions

The size confinement in closed armchair us-SWCNT (5, 5) causes to non-zero size-dependent energy gap oscillation between the lowest unoccupied and the highest occupied molecular orbitals. There are three types of us-SWCNTs (5, 5) with the number of segments $i=3m$, $3m+1$, $3m+2$ that have the intermediate, maximal and minimal energy gap at the singlet state the intermediate, minimal and maximal energy gap at the triplet state of nanotubes. The energy of the singlet-triplet transition corresponds to the energy value of visible and IR-radiation that makes us-SWCNTs promising materials for optoelectronics and spintronics.

References

- [1] Saito R, Fujita M, Dresselhaus G and Dresselhaus M 1992 *Appl. Phys. Lett.* **60** 2204
- [2] Minitmire J 1995 *Carbon* **33** 893
- [3] Tuchin A V, Ganin A A, Zhukalin D A, Bitytskaya L A and Bormontov E N 2014 *Recent Adv. In Biomedical & Chem. Eng. and Mat. Sc.* **1** 40
- [4] Rocherfort A, Salahub D R and Avouris 1999 *J. Phys. Chem. B* **103** 641
- [5] Liu L, Yang C, Zhao K, Li J, and Wu C 2013 *Nature Comm.* **4** 3989
- [6] Fowler P, Batten R, Manolopoulos D 1991 *J. Chem. Soc. Faraday Trans.* **87** 3103

Acknowledgments

This work was supported by RFBR, research projects N 14-02-31315 mol_a.

Purification non-aqueous solution of quantum dots CdSe-CdS-ZnS from excess organic substance-stabilizer by use PE-HD membrane

K Kosolapova¹, A Al-Alwani², I Gorbachev^{2,3}
and E Glukhovskoy²

¹Faculty of Nano- and Biomedical Technologies, Saratov State University, Russia

²Department of Educational and Research Institute of Nanostructures and Biosystems, Saratov State University, Russia

³Department of Colloids and Interfaces, Max Planck Institute of Colloids and Interfaces, Germany

Abstract. Recently, a new simple method for the purification of CdSe-CdS-ZnS quantum dots by using membrane filtration, the filtration process, successfully separated the oleic acid from quantum dots through membranes purification after synthesis; purification of quantum dots is a very significant part of post synthetical treatment that determines the properties of the material. We explore the possibilities of the Langmuir-Blodgett technique to make such layers, using quantum dots as a model system. The Langmuir monolayer of quantum dots were then investigated the surface pressure-area isotherm. From isotherm, we found the surface pressure monolayer changed with time.

The interest of nanoparticles – semiconductor quantum dots, – it was continued to increase in last decades. Quantum dots have a scientific interest due to unique physical properties. Purification of quantum dots – it's very important process after synthesis. Purified quantum dots (QDs) are the foundation for the creation of light-emissive devices.

Nanoparticles rectify it's very difficult due to small size (2-5nm). As well it's difficult due to a small selection of suitable solvents, irreversible adsorption with other materials, aggregation. Aggregation nanoparticles lead to a change in the size of the system elements. Change in the size of the system to make difficult selection of membrane with pore to a certain size.

Is now used many methods of purification [1]. In this work presented the results of studied that show the possibility of purification by membrane filtration solutions QDs in chloroform and toluene. Present results of experimental use one of low-cost materials for the membrane. This filter with nanopores - its high density polyethylene. It was used for separation of organic molecules of the stabilizer (oleic acid) from initial solution QDs.

Purification of QDs, stabilized oleic acid, was carried out with using a specially assembled unit (see. Fig. 3) for 168 hours. Isotherm compression of the external solution were removing for observation and diffusion control during this time.

A series of pilot experiments to select a suitable membrane. There were three options materials – cellulose dialysis membrane, plastic films of low and high density (LD-PE and HD-PE). As a result of the experiments was chosen high density polyethylene.

Cellulose dialysis membrane and low density polyethylene film were excluded for various reasons. Firstly, they have pores too large: there through QDs permeate. Secondly, the dialysis membrane is most convenient for the filtration of aqueous solutions. In organic solvents, dialysis membrane retains fragility, resulting in the formation of microcracks at the bend and the loss of functionality.

The solution of colloidal quantum dots stabilized oleic acid in chloroform to about 10^{-6} M concentration of 125 μ l was placed in a dialysis bag which was immersed in the box with chloroform. The internal volume of the solution in the package was 125 μ l (Fig. 1a), the volume of the external solution in a bank – 50 ml (Fig. 1b).

As a vessel for carry through a membrane filter was taken jar reagent plastic screw cap 100 ml.

[1] Kowalczyk B., Lagzi I., Grzybowski B.A., Nanoseparations: Strategies for size and/or shape-selective purification of nanoparticles // Current Opinion in Colloid & Interface Science. 2011. Vol. 16. P. 135–148.

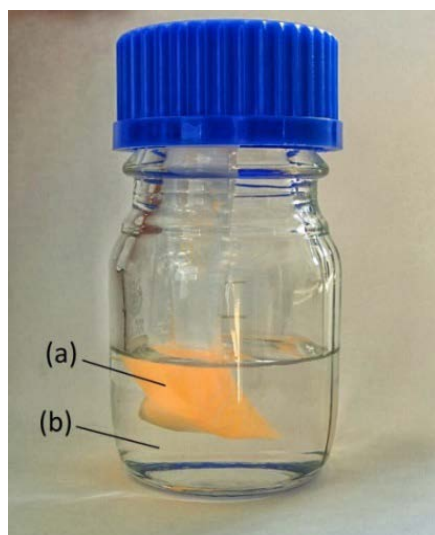


Figure 1. Chemical reaction apparatus for carrying out the process of separation: QD membrane solution bag (a), chloroform (b).

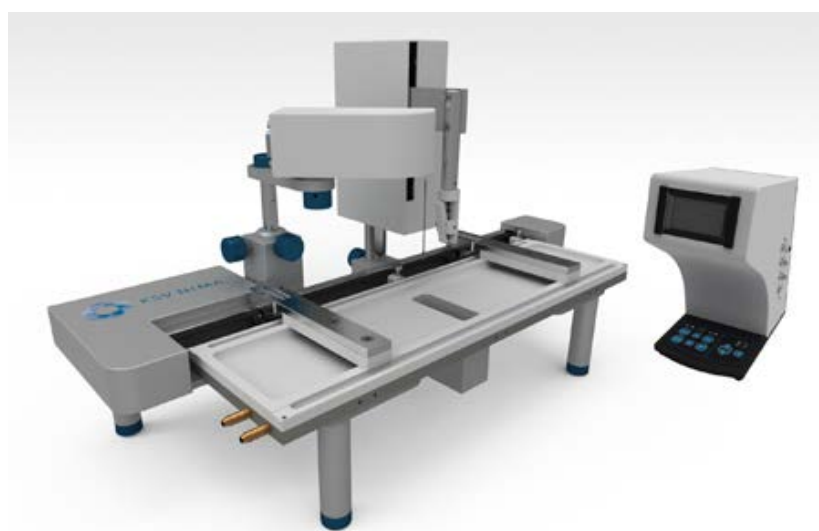


Figure 2. KSV Nima LB Trough KN2002.

Control and monitoring the diffusion of the surfactant through the membrane was done by measuring the surface pressure (isothermal compression) of the external solution. To measure the surface pressure setting used KSV Nima LB Trough KN2002 (Fig. 2) [2].

Compression isotherms were recorded every 24 hours. For cleanliness before each measurement surface degreasing bath and purified with chloroform. As subphase used deionized water with a resistivity of $18 \text{ MOhm} \times \text{cm}$. On the surface of the water each time make the same amount of material from the outer volume (of the solution in a glass container) – $800 \mu\text{l}$.

After evaporation of the solvent (8 minutes) and the monolayer was compressed isothermally movable barriers at a constant rate – $8 \text{ cm}^2/\text{min}$.

The data obtained during the compression isotherm measurement shown in (Fig. 3). It is noticeable that the increases of maximum surface pressure with increasing filtration time, (Fig. 4). Obviously the Reducing of length of gas phase of external solution is due to increase the number of surfactant molecules in the external volume of the solution. This growth is due to the process of diffusion of unbound molecules of oleic acid through polyethylene membrane.

[2] Kim T., Organic-solvent resistant ultrafiltration and nanofiltration membrane modules for separation and purification of nanoparticles // Diss. PhD in Chemistry. Oregon State University. 2011. 107 p.

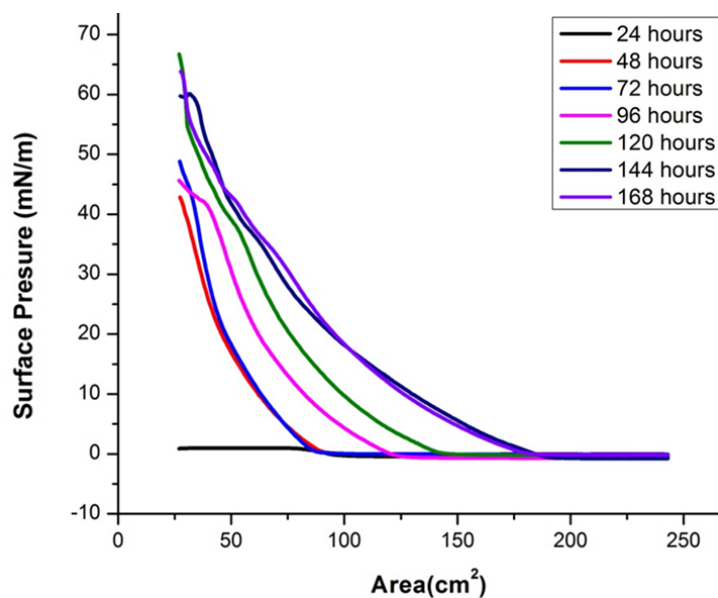


Figure 3. Compression isotherms surfactants of external solution.

When comparing images obtained by the method of Brewster angle microscopy, it can be seen that with increasing filtration time increases the amount of surfactant in the external volume. Monolayers were formed from solutions past 48 hours (Fig. 5) and 168-hour filtration (Fig. 6).

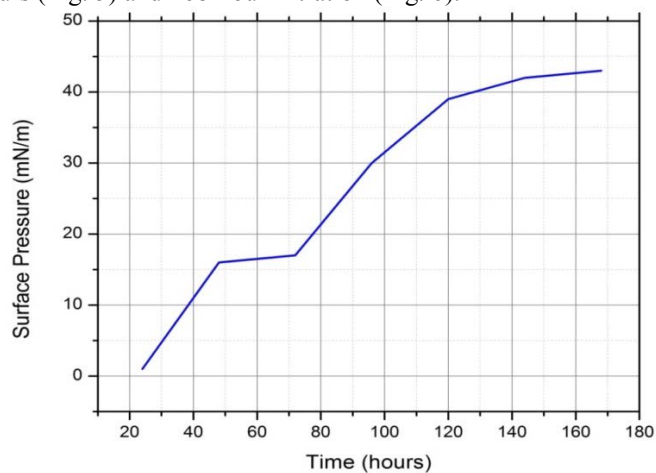


Figure 4. The growth of surface pressure over time.

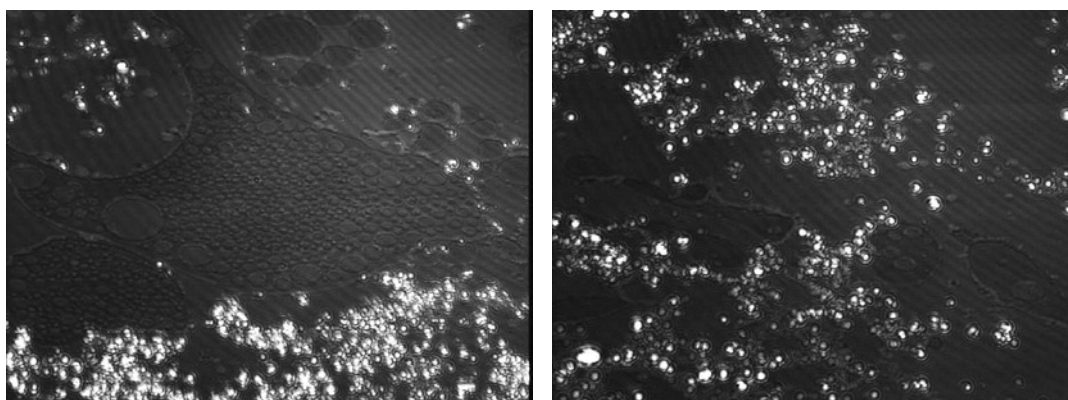


Figure 5. Images BAM outer monolayer of the solution after filtration of the solution to RT for 48 hours.

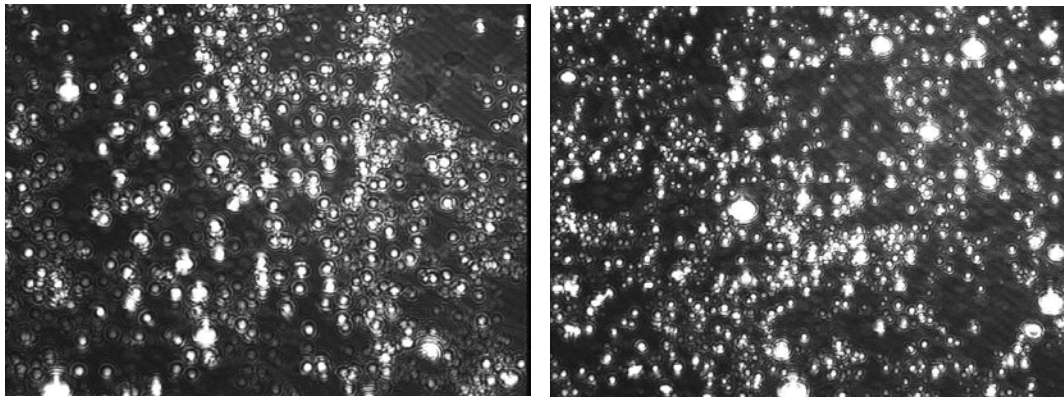


Figure 6. Images BAM outer monolayer of the solution after filtration of the solution at RT for 168 hours (right).

Thus, a method of purifying a solution of quantum dots, CdSe-CdS-ZnS by membrane filtration of unbound molecules from the excess oleic acid [2, 3].

To investigate the changes in the number of surfactant in the external volume of the solution used Langmuir-Blodgett technique. In the process of compression isotherms were taken the outside solution during the membrane filtration of the solution of quantum dots. In the solution the unbound surfactant molecules leaving from a stock solution of QDs. Isotherms obtained at significantly increasing the maximum surface pressure and reduce the length of the gas phase in monolayers with increasing time filtering solution QDs scan, which shows an increase in surfactant concentration on the surface of the water surface.

The work is supported by grant № 14-12-00275 of Russian Science Foundation and Saratov State University.

[3] Munir A., Dead end membrane filtration. / Instructor: Dr. Syed A. Hashsham // Michigan State University. Laboratory Feasibility Studies in Environmental Engineering. ENE 806. - Spring, 2006, 36 p.

Increasing of AlGaAs/GaAs quantum well robustness to resonant excitation by lowering Al concentration in barriers

I.A Solovev, V.G. Davydov, Yu. V. Kapitonov, P. Yu. Shapochkin, Yu. P. Efimov, Yu.K. Dolgikh, S.A. Eliseev, V.V. Petrov, V.V. Ovsyankin

St. Petersburg state university, St. Petersburg, Russia

Abstract. The robustness of AlGaAs/GaAs quantum well to high resonant excitation is studied. It was found that lowering Al concentration in barriers does not influence spectral quality of the sample whereas decrease parasitic broadening of the resonance by an additional optical pumping.

1. Introduction

A3B5 semiconductor heterostructures with quantum wells (QW) are very attractive for research because of theoretical possibility to use them as an all-optical logic element [1]. We have demonstrated that the molecular beam epitaxy technique (MBE) allows one to produce high-quality samples with the inhomogeneous broadening comparable to the radiative linewidth of excitonic resonance for both $\text{In}_{0.02}\text{GaAs}_{0.98}/\text{GaAs}$ [2] and $\text{GaAs}/\text{Al}_{0.3}\text{Ga}_{0.7}\text{As}$ [3] QWs. There are limitations of direct use of $\text{GaAs}/\text{Al}_{0.3}\text{Ga}_{0.7}\text{As}$ structures in optical information processing due to the bleaching effect manifested itself as broadening of excitons spectral lines under high resonant excitation.. The effect has characteristic time longer than $1\mu\text{s}$. In this work we have shown, that the bleaching effect can be reduced through lowering Al concentration in barriers from 30% to 3% while maintaining the same spectral quality of the sample.

2. Experimental

The sample T670 grown by MBE techniques contains 14 nm GaAs QW with $\text{Al}_{0.03}\text{Ga}_{0.97}\text{As}$ barriers. We use the reflection spectroscopy to investigate coherent optical properties of excitons with heavy holes (HH-exciton). The p-polarized probe pulse of light is incident on the sample surface at the Brewster angle [2,3]. In this case the reflection spectrum could be described by the Lorentz curve:

$$K_R(\omega) = \frac{\Gamma_R^2}{(\omega - \omega_0)^2 + (\Gamma_R + \Gamma_{NR})^2} \quad (1),$$

Where ω_0 – frequency of HH-exciton resonance, Γ_R – radiative width, Γ_{NR} - nonradiative broadening and K_R is the reflection coefficient measured experimentally. Sample temperature was 8K. Probe light was weak enough to guarantee the linear regime. Spectra were recorded using spectrally wide probe fs-pulse and spectrometer with multichannel CCD-detector.

In order to study the bleaching effect we use an additional monochromatic pump light which was tuned to HH-exciton resonance. Fig.1 illustrates the dependence of the resonant reflection (RR)

spectra $K_R(\omega)$ on pump intensity I_{pump} . It should be noted that there is no significant shift of spectral line so thermal broadening is negligible. Fitting the spectral lines by Eq. (1) taking into account weak nonresonant background lets us obtain Γ_R and Γ_{NR} .

3. Discussion

It has been experimentally established that radiative width remains constant in wide range of pump intensity and equals 36 ± 3 μeV . This value is similar to that obtained for the E296 sample (QW 13 nm, GaAs/Al_{0.3}Ga_{0.7}As) which was investigated in previous work [2]. Observed ratio $\Gamma_{NR}/\Gamma_R = 0.46$ in linear mode ($I_{\text{pump}}=0$) proves the high quality of the sample T670 (for comparison in E296 the ratio is $\Gamma_{NR}/\Gamma_R = 0.46$ also). However significant nonradiative broadening appears only for pump intensities above 10^{18} photon/cm²s (Fig. 1b) which are by 2 orders of magnitude higher than in the e296 sample (Fig. 1b). We attribute such behavior to the weaker charge effects in this system. An indirect proof of this fact is an absence of the spectral features at energies slightly lower than the HH-exciton resonance that correspond to the creation of charged excitons (trions) by excitation of an exciton near the free charge carrier, which were observed in E296 sample. Nevertheless we couldn't fully exclude charge effects from consideration due to the observed small decrease of Γ_{NR} at low pump intensities (see inset Fig.1b) typical for photovoltaic phenomena [4].

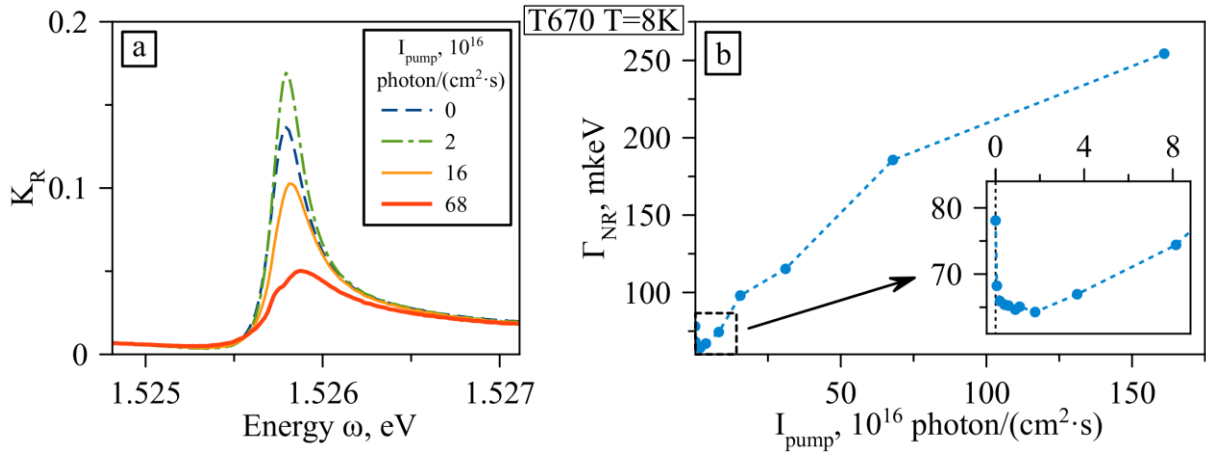


Figure 1. RR spectra with different I_{pump} (a), dependence Γ_{NR} on I_{pump} (b).

4. Conclusion

We have investigated resonant reflection spectra from QW with additional resonant pumping. We demonstrate here that lowering Al concentration in barriers lets us to decrease the bleaching effect with remaining high spectroscopic qualities of the sample

5. Acknowledgements

The reported study was partially supported by RFBR, research project № 15-52-12016 nnio_a. This work was carried out on the equipment of the SPbU Resource Center “Nanophotonics” (photon.spbu.ru)

References

- [1]. I.Ya. Gerlovin, V.V. Ovsyankin, B.V. Stroganov and V S Zapasskii, Nanotechnology **11** (2000) 383–386
- [2]. S.V. Poltavtsev et al., Solid State Communications 199 (2014), 47–51
- [3]. S. V. Poltavtsev and B. V. Stroganov, Physics of the Solid State, 2010, Vol. 52, No. 9, pp. 1899–1905
- [4] Sh. Glasberg et al., Physical Review B Vol. 59, № 16

Section

**Other Aspects of
Nanotechnology**

The measurements of doping density in InAs by capacitance-voltage techniques with electrolyte barriers

D Frolov, G Yakovlev and V Zubkov

Department of micro- and nanoelectronics, St. Petersburg Electrotechnical University “LETI”, Prof. Popov str. 5, St. Petersburg 197376, Russia

Abstract. The doping densities in n-InAs structures were studied by means of capacitance-voltage technique using electrolyte to form Schottky-like contact. It was shown that in heavily doped InAs ($> 10^{18} \text{ cm}^{-3}$) depletion approximation can be used. Concentration in low doped InAs can be estimated by simulation (using modified Thomas-Fermi approximation to take into account surface accumulation). Measured doping densities were compared with concentration obtained by Hall measurements. The difference between CV and Hall results in undoped samples was explained.

Capacitance-voltage (CV) profiling is widely used to characterize semiconductor materials and structures. Conventional CV measurements are performed by forming metal Schottky contact on semiconductor surface. However, in some semiconductor materials like InAs and InN the formation of reliable Schottky contact is difficult due to surface accumulation, in this case an electrolyte can be used to form rectifying contact [1,2]. Another advantage of electrolyte barriers which are used in electrochemical capacitance-voltage (ECV) profiling technique is the ability to perform controlled dissolution of the semiconductor [3,4].

Gopal et al. [5] have reported first on the possibility of ECV profiling of n-InAs. In their paper they noted that measured carrier concentration in highly doped InAs corresponds well to Hall measurements, but in undoped InAs layers the measured concentration was much higher in comparison to Hall concentration. The purpose of the present work is to explain the mismatch between CV and Hall results in undoped samples and to determine the optimal parameters of CV measurements for doping density extraction in n-InAs.

Undoped InAs epi layers were grown by HVPE process on n^+ -InAs substrates. Dopant densities were studied in undoped layers and in n-type substrates. Capacitance-voltage measurements were performed using ECVPro profiler (Nanometrics) with LCR meter Agilent E4980A connected directly to electrochemical cell. The solution of 0.2 M H_2SO_4 was used to form electrolyte barrier with nominal contact area of 0.1 cm^2 . CV characteristics were simulated by modeling of potential and carrier distribution using Poisson equation with modified Thomas-Fermi approximation (MTFA) [6,7]. Doping densities used in the simulation were obtained from magnetoresistance (for epi structures) and Hall effect measurements (for substrates) performed at 77 K.

Experimental and simulated capacitance-voltage curves are shown in Figure 1. The main feature of the measured characteristics comparing to CV of classical Schottky barriers is the deviation of C^{-2} vs. V plot from linear, which behave very similar to metal-oxide-semiconductor (MOS) structures. At lower biases, in the region of low positive slope, the potential bents downwards which causes formation of

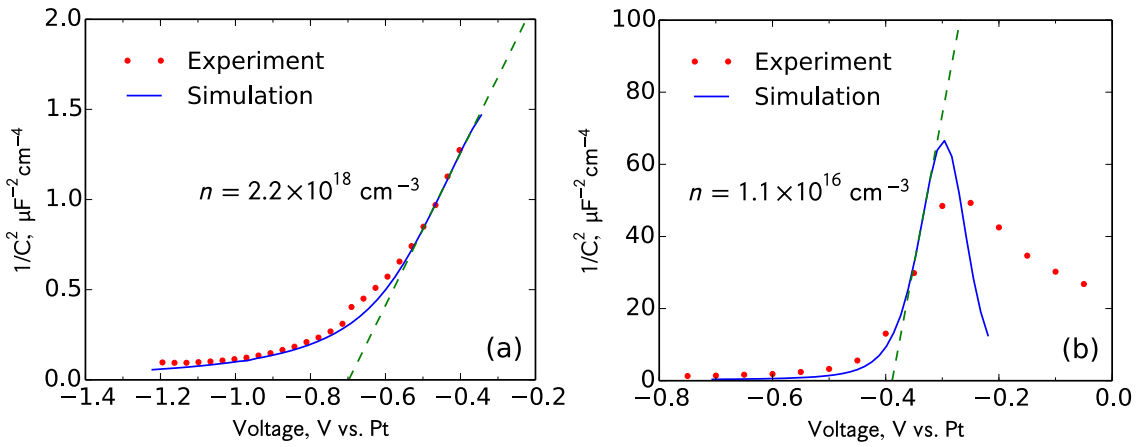


Figure 1. Mott-Schottky plot of experimental data and simulation for: (a) n-InAs substrate with $N_D = 2 \times 10^{18} \text{ cm}^{-3}$ and (b) unintentionally doped epi layer ($1 \times 10^{15} \text{ cm}^{-3}$). Electron densities calculated from linear fitting (dashed line) are also shown.

accumulation layer and growth of carrier density. At higher positive voltages a depletion takes place with the slope on the Mott-Schottky plot proportional to the doping density. Further increase of bias leads to inversion which is characterized by a negative slope. The transition from depletion to inversion affects the accuracy of doping density measurements.

For n⁺-InAs substrate (Figure 1-a) the measured CV has a good agreement with simulation results. The concentration of $2 \times 10^{18} \text{ cm}^{-3}$ was used for heavily doped n-InAs in simulation. The electron concentration calculated from linear approximation in depletion region gives $2.2 \times 10^{18} \text{ cm}^{-3}$. The difference between the dopant concentration used in the simulation and the calculated electron density is due to the small bias range, which corresponds to the depletion region. This difference is much higher for epi-layer with doping level of $1 \times 10^{15} \text{ cm}^{-3}$ (Figure 1-b) because the Fermi level shifts toward the center of forbidden energy gap, and the inversion starts earlier.

To conclude, in heavily doped n-InAs ($N_D > 10^{18} \text{ cm}^{-3}$) the range of biases, in which the depletion occurs, is wide enough to use the depletion approximation for doping density estimation with 10 % accuracy. At the lower doping levels simulation of capacitance-voltage characteristics should be used to estimate doping density.

References

- [1] Yim J W L, Jones R E, Yu K M, Ager J W, Walukiewicz W, Schaff W J and Wu J 2007 *Phys. Rev. B* **76** 41303
- [2] Vasheghani Farahani S K, Veal T D, Mudd J J, Scanlon D O, Watson G W, Bierwagen O, *Phys. Rev. B* **90** 155413
- [3] Blood P 1986 *Sernicond. Sci. Technol* **1** 7–27
- [4] Zubkov V, Kucherova O, Frolov D and Zubkova A 2013 *Phys. Status Solidi C* **10** 342–5
- [5] Gopal V, Chen E-H, Kvam E P and Woodall J M 2000 *J. Electron. Mater.* **29** 1333–9
- [6] Veal T D, Piper L F J, Schaff W J and McConville C F 2006 *J. Cryst. Growth* **288** 268–72
- [7] Paasch G and Übensee H 1982 *Phys. Status Solidi B* **113** 165–78

Dependence of microwave-excitation signal parameters on frequency stability of caesium atomic clock

Petrov A.A., Davydov V.V., Vologdin V.A., Zalyotov D.V.

Saint-Petersburg State Polytechnical University, Saint-Petersburg, Russia

Abstract. The theoretical calculations and experimental research of the new scheme of the microwave – excitation signal for the caesium atomic clock showed decrease step frequency tuning by several orders and improvement the spectral characteristics of the output signal of frequency synthesizer. A range of generated output frequencies is expanded, and the possibility of detuning the frequency of the neighboring resonance of spectral line that makes it possible to adjust the C-field in quantum frequency standard is implemented. Experimental research of the metrological characteristics of the quantum frequency standard on the atoms of caesium - 133 with new design scheme of the microwave – excitation signal showed improvement in daily frequency stability on $1.2 \cdot 10^{-14}$.

Currently caesium atomic clocks are the main devices allowing the formation and reproduction with the high accuracy of physical units of time and frequency.

With the development of scientific - technical progress operating conditions of caesium atomic clock are constantly changing. Therefore new requirements for measurement accuracy, reliability and weight - dimensional characteristics are produced to frequency standard. This leads constantly upgrade existing and develop new models of caesium atomic clocks. For this aims it is reasonable to carry out research, develop new methods and find a new design solutions based on the latest appearing electronic components and discovered physical phenomena.

One of the main metrological characteristics of beam atomic clocks is the Allan variance. The microwave – excitation signal of atomic transition generated at the out of frequency synthesizer has a significant influence on the metrological characteristics of the quantum standard.

In present work a dependence of parameters of microwave – excitation signal on the frequency stability of quantum frequency standard on atoms ^{133}Cs has been studied. A new implementation of a digital frequency synthesizer for atomic clocks is presented.

Experimental study of frequency synthesizer showed improvement parameters of the microwave-excitation signal, such as the step of frequency tuning, time of the frequency tuning, range of generated frequencies, phase stability and spectral characteristics. Experimental research of the metrological characteristics of the quantum frequency standard on the atoms of caesium - 133 with new scheme of the microwave – excitation signal showed improvement in daily frequency stability on $1.2 \cdot 10^{-14}$.

Electropulse obtainment of metal-carbon structures on the basis of IGBT-switch

A Tikhomirov¹ and N Sobolev² and Y Izotov³

¹ Petrozavodsk State University, Department of Physics- Engineering, Researcher, Lenin Avenue 33, Russia.

^{2,3} Petrozavodsk State University, Department of Physics- Engineering, Undergraduate student, Lenin Avenue 33, Russia.

Abstract. The opportunity of obtainment of metal-carbon structures on the basis of electropulse erosion discharge has been investigated. The analysis of the obtained powders of metal-carbon structures has been carried out. The average size structures of metal-carbon powders is in range of hundred nanometers.

1. Introduction

Methods of obtainment of nanostructures on basis of electric discharge have significant perspectives. The electrical discharge in this application has some advantages such as energy efficiency, quality of the process. The use of non-conducting liquid in the electropulse discharge has great importance for extracting the structures obtained in it. The cone geometry of discharge leads to the mixture of liquid under the influence of pressure gradient. The aim of this work is to obtain powders in electropulse discharge and investigate their structure.

2. Experimental set-up

Solid switch has been applied in this work to get short high-voltage pulses. Presently the area of IGBT-devices is developing very fast and characteristics of abovementioned semiconductor devices allow bringing together transistors consequentially and paralleling in the integrated. Experimental set-up is presented on the figure 1.

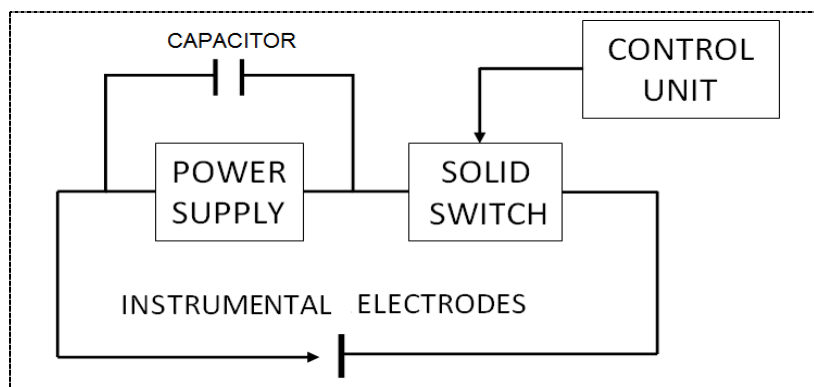
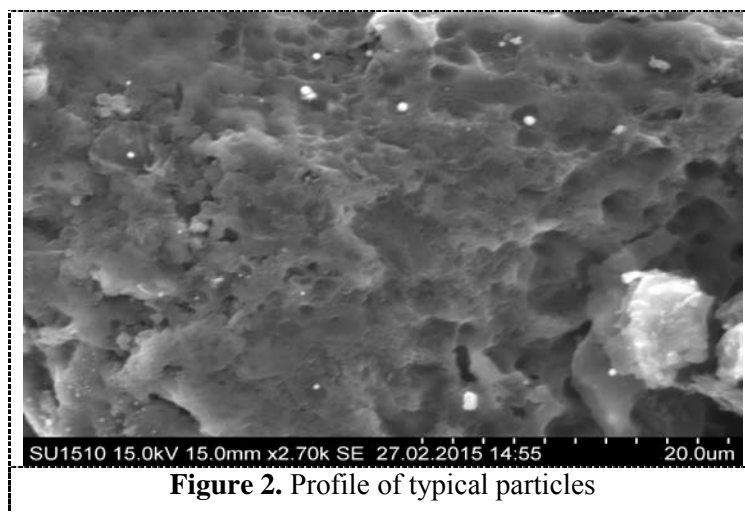


Figure 1. Schematic representation of the experimental set-up

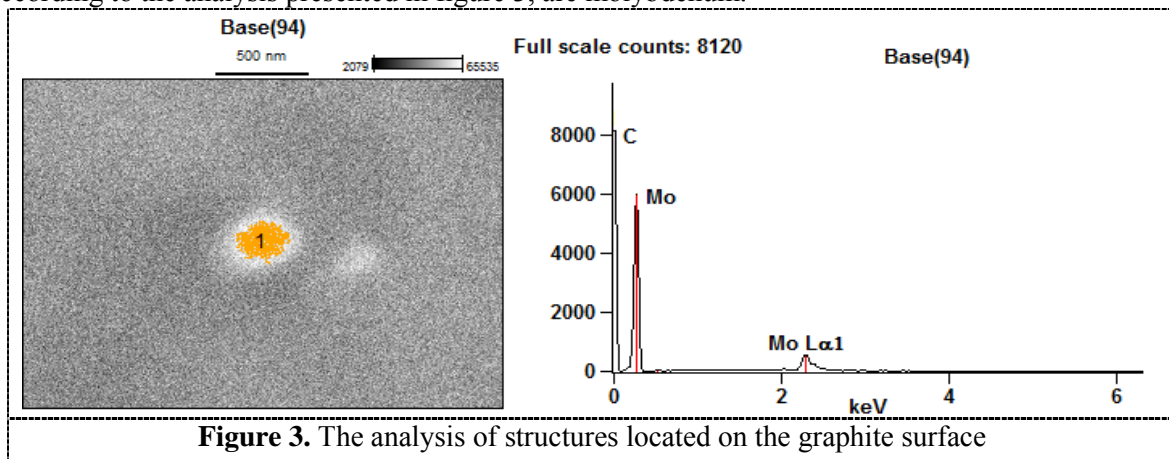
Instrumental electrodes used to obtain metal-carbon powders present a graphite core with a diameter of about 6 mm (anode) and molybdenum plate (cathode), that get into contact being acted on by the proper weight of a graphite core. As working liquid distilled water was used. The result of the impact of electro-pulse discharge in working liquid is suspended material from metal-carbon structures that is poorly deposited. The extraction of metal-carbon structures from liquid phase was done by evaporation in the furnace at the temperature of 660 degrees.

3. Results and Discussion

The obtained powders have been investigated on the scanning electronic microscope Hitachi SU1510 (figure 2). It should be mentioned that one can notice bigger particles as well. As a rule, they have the stretched forms. But the thorough analysis of this profile showed that it is multiple groups of smaller particles.



To great extent, the powder obtained in electropulse discharge consists of graphite particles having the size of about 100 micrometers and spherical particles located on their surface. The latter ones, according to the analysis presented in figure 3, are molybdenum.



References:

- [1] Abu Zaid OA (1997) On the effect of electro-discharge machining parameters on the fatigue life of AISI D6 tool steel. *J Mater Process Technol* 68: 27-32
- [2] Ho KH, Newman ST (2003) State of the art electrical discharge machining (EDM). *Int J Mach Tool Manufac* 43:1287–1300

Nanopatterning of silicate glasses via thermal poling

A V Redkov^{1-3*}, A N Kamenskii³, A A Lipovskii^{2,3}

¹Institute of Problems of Mechanical Engineering, Bolshoy pr.V.O., 61, Saint-Petersburg, 199178.

²Saint-Petersburg Academic University RAS, Khlopina str., 8/3, Saint-Petersburg, 194021

³Saint-Petersburg State Polytechnical University, Polytechnicheskaja str., 29, Saint-Petersburg, 195251

Abstract. We studied formation of nanoscale surface relief on the anodic surface of an alkali-silicate glass in the course of thermal poling in open anode configuration and related structural/compositional changes in the subanodic region of the glass. The surface of poled glass beneath an anodic electrode goes down relatively to the unpoled glass area and a step between poled and unpoled regions arises. The step height dependence on the density of electric charge transferred in poling is analyzed. The applicability of thermal poling for nanopatterning of glass surface is demonstrated.

1. Introduction

Thermal poling of glasses involves heating of a glass plate placed between two electrodes up to a temperature sufficient to activate the glass conductivity and applying a DC voltage to the electrodes [1]. For conventional alkali-silicate glasses this temperature is about 250–300 °C that is essentially below their glass transition temperature, and the voltage is about several hundred volts. Formed electric field induces the migration of positive alkali and alkali earth ions from the anodic surface of a glass towards cathode that results in compositional/structural changes of the subanodic glass region. These changes are the subject of present study.

2. Experimental

In the experiments we used 1 mm thick slides of soda-lime glass. We poled the slides in air atmosphere at 250 °C using high quality polished $1 \times 1 \text{ cm}^2$ n-silica plates as the electrodes. Eight samples processed in the range of voltages 100–1700V differed in transferred charge density. Morphology of the poled glass surface was studied with optical profilometer Zygo New View, whereas structural/compositional studies were performed via the analysis of micro-Raman spectra registered with Witec Alpha 300R spectrometer equipped with confocal optical microscope. We also poled the series of glass samples using grating-like profiled electrode with the period of 400 nm. These samples were characterized with atomic force microscope (AFM) Veeco Dimension 3100.

3. Results and discussion

Performed experiments show that the surface of the glass beneath the anodic electrode goes down under poling, and a step between poled and unpoled regions near the electrode edge arises. The dependence of the step height on transferred electric charge density is presented in Figure 1. The reason of the step formation is the removal of alkali and alkali earth cations from subanodic region of the glass in thermal poling and their full or partial replacement by smaller hydrogen ions from atmospheric water vapours. The replacement of intrinsic ions of the glass by smaller ones, accompanying structural changes of the glass matrix and its partial relaxation result in the decrease in the poled glass volume under the anodic electrode. The deformation of the volume mainly occurs in the direction perpendicular to the surface of the glass. According to micro-Raman spectrometry compositional/structural changes of the glass, in particular increasing the glass network connectivity, take place in 1-5 μm thick subanodic layer of the poled glass [2]. Poling with the transferred charge density below 180-200 mC/cm^2 does not damage the glass surface while higher charge densities induce defects and channels directed into the bulk of the glass, the depth of the channels being about the same as the depth of the step near the electrode edge.

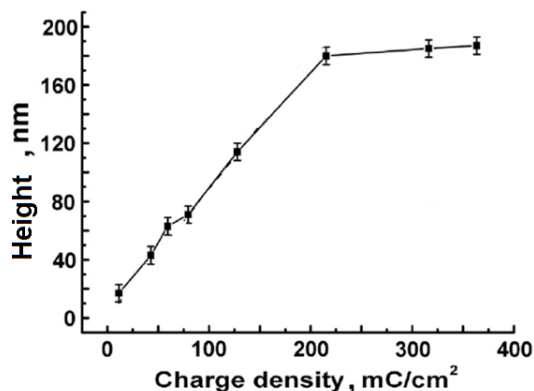


Figure 1. Height of the formed step vs transferred charge density

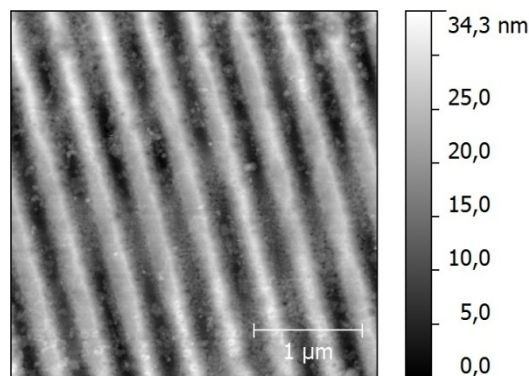


Figure 2. AFM image of the glass surface poled with nanoprofiled electrode

Poling of a glass sample with a nanoprofiled grating-like anodic electrode allowed us to manufacture a relief grating of 400nm periodicity on the surface (Figure 2). The height of the relief in this case is quite small, $\sim 30\text{nm}$, however subsequent chemical etching of the sample with an appropriate agent, e.g. $\text{HF}:\text{NH}_4\text{F}$, can increase the depth because of different etching rates of poled/unpoled glass regions.

4. Conclusions

We showed that thermal poling of the soda-lime glass results in the formation of surface relief up to 200 nm in height. The main origin of this phenomenon are structural changes in the glass matrix, which result in increasing the glass connectivity and decreasing its volume. Thermal poling is a prospective approach to make substrates with nanoprofiled surface for needs of biology, chemistry, and optics. Obtained results allow evaluating the maximal depth of relief structures which can be formed on the surface of the glasses using poling-induced surface profiling.

References

- [1] Carlson D E, Hang K W and Stockdale G F, 1972, *J. Am. Ceram. Soc.* **55** 337
- [2] Redkov A V, Melehin V G, Statcenko V V and Lipovskii A A, 2015 *J. Non-Cryst.Sol.* **409** 166

Study of colloidal particles $\text{Fe}_m\text{O}_n\text{-SiO}_2$ synthesized by two different techniques

S A Ionin, K G Gareev, N V Permyakov, V A Moshnikov

Saint Petersburg Electrotechnical University "LETI",
5th Prof. Popova Str., Saint-Petersburg, 197376, Russia

Abstract. Colloidal solutions $\text{Fe}_m\text{O}_n\text{-SiO}_2$ were obtained by two different techniques based on sol-gel process: silica cores coated by iron oxide layer and iron oxide cores coated by silica. Dried layers were investigated by atomic force microscopy and size distribution was plotted. Resistivity's change under the influence of magnetic field was measured using LCR-meter.

1. Introduction

Composite magnetic colloids could be applied for solving biomedicine problems such as MRI diagnostics [1] or blood vessel controlled occlusion [2], including oncology [3]. Synthesis of superparamagnetic nanoparticles may be provided by sol-gel technique [1]. Using this technological route authors obtained aggregate stable specimens starting to settle under the influence of constant magnetic field [4]. Aggregation and sedimentation processes were studied by MRI relaxation times' and AC signal resistivity measurements [1, 4].

2. Experimental results

In present work authors investigated colloidal solutions $\text{Fe}_m\text{O}_n\text{-SiO}_2$ derived by two different ways. The first one is based on magnetite precipitation in the presence of colloidal silica as described in [1] and the second one assumes magnetite precipitation followed by coating iron oxide particles by tetraetoxisilane at the alkaline aqueous medium. Analysis of particles' size distribution was made by AFM. The average diameter calculated using Gwyddion software equals about 15 nm for colloids obtained by both techniques. Magnetic properties were estimated measuring resistivity's change under the influence of constant magnetic field 500 A/m at AC signal by LCR-meter.

The study was partially supported by RFBR, research project No. 14-03-31534.

References

- [1] Bogachev Yu V, Chernenco Ju S, Gareev K G, Kononova I E, Matyushkin L B, Moshnikov V A, Nalimova S S 2014 Appl. Magn. Reson. **45** 329-337
- [2] Smolkova I S, Kazantseva N E, Makoveckaya K N, Smolka P, Saha P and Granov A M 2015 Mat. Sci. and Eng. C **48** 632–641
- [3] Kawai N, Kobayashi D, Yasui T, Umemoto Y, Mizuno K, Okada A, Tozawa K, Kobayashi T and Kohri K 2014 Vascular Cell **6** 15
- [4] Gareev K G, Kononova I E, Levitckii V S, Moshnikov V A and Nalimova S S 2014 J. of Phys.: Conf. Ser. **572** 012027

Cu/Diamond composite heat-conducting shims

E N Galashov¹, A A Yusuf¹ and E M Mandrik¹

¹ Department of Applied Physics, Scientific Research Department Novosibirsk State University, 2 Pirogov's Street, Novosibirsk 630090, Russia

Abstract. Composite material with high thermal conductivity was obtained by the method of thermal sintering of a diamond (50 - 75 %) with a size of 20 to 250 μm in a matrix of copper. Coefficient of thermal conductivity of copper diamond composite materials was measured and is $450 - 650 \text{ W}\cdot\text{m}^{-1}\cdot\text{K}^{-1}$. The coefficient of thermal expansion CTE was measured and is $5.5 - 7.5 \cdot 10^{-6}/^\circ\text{C}$. The obtained copper diamond composite materials are promising objects for use in THz and microwave devices.

1. Overview

For the manufacture of heat sinks working under extreme heat loads in various areas of technology (electronics, nuclear energy, particle accelerators), materials with high thermal conductivity are required [1]. This problem can be solved through the creation of composite materials based on diamond because diamond has a thermal conductivity $1000-2600 \text{ W}\cdot\text{m}^{-1}\cdot\text{K}^{-1}$ [2]. The manufacturing of products entirely of diamond is technically difficult, and they have a very high cost [3]. So now diamond-containing composite materials with dispersed diamond filler, in particular metal matrix Ag, Cu, Al, are being developed actively [4]. Diamond-metal composites with particles of a diamond of the 20-250 μm size with copper matrix have a high conductivity $600 - 950 \text{ W}\cdot\text{m}^{-1}\cdot\text{K}^{-1}$.

Along with the conductivity in the semiconductor device CTE is an important parameter. Semiconductor devices have a short lifespan if the heat sink substrate has a low thermal conductivity. Heat-conducting copper-diamond composites have CTE $5.5 - 10 \cdot 10^{-6}/^\circ\text{C}$ and they have a long lifespan.

2. Fabrication

We have developed the method of obtaining diamond-copper composites with high thermal conductivity. The diamonds are covered with tungsten coating by the method of vapor deposition of tungsten carbonyl. The thickness of the coating is $0.5 - 1 \mu\text{m}$. The coating composition may vary within $\text{W}-\text{W}_2\text{C}-\text{WC}$. Carbides provide adhesion of the coating to the diamond. Metallic tungsten and tungsten carbide are well moistened copper. Uncoated diamond is very poorly moistened by copper. In addition, tungsten and carbide are practically not dissolved in the melt of copper. Therefore, the tungsten coating on the diamond provides a copper-diamond composite by thermal sintering diamond in the matrix of copper.

Diamonds and copper were mixed and merged into a pill. The tablet was placed in the vacuum chamber of the furnace of the electrical resistance. The sintering temperature was 970°C . The sintering time was 1 hour.

3. Results

Copper diamond tablet was obtained. Pores are practically absent, the surface is smooth. The thickness of the tablets is 1 mm. Coefficient of thermal conductivity of copper diamond composite materials was measured and is $450 - 650 \text{ W} \cdot \text{m}^{-1} \cdot \text{K}^{-1}$. The coefficient of thermal expansion CTE was measured and is $5.5 - 7.5 \cdot 10^{-6} / ^\circ\text{C}$.

References

- [1] S.V. Kidalov, F.M. Shakhov 2009 *Materials* **2**, p 2467
- [2] J.S. Goela, S.L. Shinde 2006 *High Thermal Conductivity Materials*, Springer, N.Y., p 271
- [3] Synthetic CVD diamond products from Element Six <http://www.e6cvd.com>
- [4] ExtreMat —heat sink materials <http://www.extremat.org/heat-sink-materials?Edition=en>

Crystallite model of nanotube flow caused by soliton

O.A.Rodygina¹, S.A.Chivilikhin¹, I.Yu.Popov¹, V.V.Gusarov²

¹St. Petersburg National Research University of Information Technologies, Mechanics and Optics, Kronverkskiy, 49, St. Petersburg, 197101, Russia

²Ioffe Physical-Technical Institute RAS, Polytechnicheskaya, 26, St. Petersburg, Russia

Abstract. The fluid flow in nanotubes caused by a soliton in its wall and crystallite in the center of tube is considered.

1. Introduction

Fluid flow in nanostructures attracts great attention last decade due to its unusual properties and possible intriguing applications. At present there is no general theory in nanohydrodynamics (see, e.g., [1] - [4] and references therein). Recently, a model based on crystalline theory of liquid is suggested [5]. There is one interesting task more – how to create a flow inside a nanotube. A possible way is to initialize wall soliton which, in its turn, produce a flow inside the nanotube [6]. In the present paper we apply the crystallite model to this problem.

Namely, we consider soliton induced 3D flow in cylindrical nanotube with the crystallite in its center. The flow is described in the Stokes approximation:

$$\frac{\partial^2 v_z}{\partial z^2} + \frac{1}{r} \frac{\partial}{\partial r} \left(r \frac{\partial v_z}{\partial r} \right) = \frac{1}{\mu} \frac{\partial p}{\partial z}, \quad \frac{\partial^2 v_r}{\partial z^2} + \frac{1}{r} \frac{\partial}{\partial r} \left(r \frac{\partial v_r}{\partial r} \right) - \frac{1}{r^2} v_r = \frac{1}{\mu} \frac{\partial p}{\partial r}, \quad \frac{\partial v_z}{\partial z} + \frac{1}{r} \frac{\partial}{\partial r} (r v_r) = 0.$$

$$v_z|_{r=R} = 0, \quad v_z|_{r=R_c} = \frac{\partial h}{\partial t} \equiv -V \frac{\partial h}{\partial z}, \quad v_z|_{r=R_c} = V_c, \quad v_z|_{r=R_c} = 0,$$

where R , R_c are the nanotube and the crystallite radii, V , V_c are soliton and crystallite velocities $h(z)$ is the soliton profile.

2. Flow in nanotube and the crystallite velocity

We present the axisymmetric flow velocity between the nanotube wall and the crystallite using the stream function Ψ as follows

$$v_r = -\frac{1}{r} \frac{\partial \Psi}{\partial z}, \quad v_z = \frac{1}{r} \frac{\partial \Psi}{\partial r} + V_c \frac{\ln(R/r)}{\ln(R/R_c)} \quad (1)$$

The flow velocity, and, correspondingly, the stream function are related with the soliton profile:

$$\Psi(z, r) = \int_{-\infty}^{\infty} G(z - z', r) h(z') dz', \quad G(z, r) = \frac{V}{\pi} \int_0^{\infty} g_k(r) \cos(kz) dk, \quad (2)$$

where

$$g_k(r) = \frac{r(q_1 p_1 - q_2 p_2)}{\gamma(kR)(U_{11}(R)U_{22}(R) - U_{12}(R)U_{21}(R))},$$

$$q_1 = (U_{21}(R)I_0(kR) + U_{22}(R)K_0(kR)), \quad p_1 = (U_{11}(r)I_1(kr) + U_{12}(r)K_1(kr)),$$

$$q_2 = (U_{11}(R)I_0(kR) + U_{12}(R)K_0(kR)), \quad p_2 = (U_{21}(r)I_1(kr) + U_{22}(r)K_1(kr))$$

$$U_{11}(r) = -\frac{1}{k} \int_{R_c}^r \frac{I_1(kr')K_1(kr')dr'}{\gamma(kr')}, \quad U_{12}(r) = \frac{1}{k} \int_{R_c}^r \frac{I_1^2(kr')dr'}{\gamma(kr')},$$

$$U_{21}(r) = -\frac{1}{k} \int_{R_c}^r \frac{K_1^2(kr')dr'}{\gamma(kr')}, \quad U_{22}(r) = \frac{1}{k} \int_{R_c}^r \frac{I_1(kr')K_1(kr')dr'}{\gamma(kr')},$$

$$\gamma(kr) = I_1(kr)K_0(kr) - I_0(kr)K_1(kr),$$

where $I_{0,1}(x)$, $K_{0,1}(x)$ are modified Bessel and Macdonald functions.

To calculate the crystallite speed we consider the condition that the viscous friction force applied to the crystallite, is zero. It gives us

$$V_c = \frac{2VR_c}{\pi L} \ln\left(\frac{R}{R_c}\right) \int_0^\infty \frac{\sin(kL/2)h_k(q_1 I_1(kR_c) - q_2 K_1(kR_c))}{k\gamma(kR)(U_{11}(R)U_{22}(R) - U_{12}(R)U_{21}(R))} dk$$

The full stream function is $\Psi = \psi + \psi_0$, where ψ is determined by equation (2), and ψ_0 is as follows

$$\psi_0 = \frac{V_c}{4 \ln\left(\frac{R}{R_c}\right)} \left[r^2 \left(\ln\left(\frac{r}{R}\right) - 0.5 \right) - R_c^2 \left(\ln\left(\frac{R_c}{R}\right) - 0.5 \right) \right].$$

Thus, the model allows us to describe the mass transport in nanotube. It can be used in studying of nanopumping and chemical nanoreactors.

References

- [1] D.Li (Ed.) Encyclopedia of microfluidics and nanofluidics. New York, Springer, 2008
- [2] T.-D.Li, J.Gao, R.Szoszkeiwicz, U.Landnan, E.Riedo. Phys. Rev. B., 75, 115415/1-6 (2007)
- [3] I.Yu.Popov. Phys. Scripta. 83, 045601/1-3 (2011)
- [4] V.P.Maslov. Theor. Math. Phys. 153 (3), 1677-1696 (2007)
- [5] S.A.Chivilikhin, V.V.Gusarov, I.Yu.Popov, A.I.Svitenkov. Russian J. Math. Phys. 15 (3), 410-412 (2008).
- [6] M.B.Belonenko, S.A.Chivilikhin, I.Yu.Popov, O.A.Rodygina, V.V.Gusarov. EPL, 101, 6, 66001, (2013)

The conductivity of a thin semiconductor wire in the longitudinal magnetic field

O V Savenco, I A Kuznetsova

Physics department, Yaroslavl State University, ul. Sovetskaya 14, Yaroslavl, 150000, Russia

Abstract. The task of high-frequency conductivity of a thin semiconductor cylindrical wire round section at arbitrary temperature in the longitudinal magnetic field is solved by the kinetic method. The charge carrier reflection from wire inner surface is assumed to be diffuse. The ratio between the mean free path of charge carriers and the wire radius is supposed to be arbitrary. The calculations are made for the semiconductor with the spherically symmetric energy band. The comparative analysis of obtained results for the cases of degenerate and nondegenerate semiconductor are made.

The expression for the high-frequency conductivity of a thin semiconductor cylindrical wire round section in the longitudinal magnetic field is calculated by the kinetic method at arbitrary temperature. The similar task of thin wire conductivity calculation at the absence of magnetic field was considered in the work [1]. Wire radius is supposed to be smaller than skin layer depth for skin-effect disregarding. No restrictions are imposed on the ratio between the wire radius and the mean free path of charge carriers. Macroscopic electrodynamics is not applicable provided that the wire size is comparable with the mean free path of charge carriers. This task is solved by the kinetic method.

A homogeneous time-periodic electric field generates the high-frequency current within the wire. The non-equilibrium distribution function of charge carriers is found from the solution of the Boltzmann kinetic equation to the approximation of relaxation time and to the linear approximation in external field. The charge carrier reflection from the wire inner surface is assumed to be diffuse. The calculations are made for the semiconductor with the spherically symmetric energy band.

The wire integral conductivity was calculated by using found nonequilibrium distribution function. Two extreme cases of degenerate semiconductor (the case of metal) and nondegenerate semiconductor were considered. The comparative analysis of dimensionless integral conductivity module and dimensionless integral conductivity argument dependences on the dimensionless frequency of electric field, the dimensionless reciprocal mean free path of charge carriers and the dimensionless magnetic field induction was made for this extreme cases. Also the behaviour volume and surface contributions to the dimensionless integral conductivity of the metallic and semiconductor wire were considered.

It is shown that the volume contribution of wire integral conductivity grows with increasing of magnetic field induction. Under the influence of magnetic field the charge carriers move along a

trajectory, which can not intersect with the wire boundary. With increasing of magnetic field induction the amount of charge carriers with a trajectory not intersected the wire boundary increases.

The dependences of dimensionless integral conductivity module on dimensionless magnetic field induction have conductivity minimum more pronounced for the case of metal wire.

It is showed that the dimensionless integral conductivity argument of the semiconductor wire is more than that of the metal wire for the specified values of dimensionless parameters (electric field frequency and reciprocal mean free path of charge carriers). This difference enlarges with increasing of the mean free path of charge carriers. With growth of the dimensionless magnetic field induction the integral conductivity argument increases and converges to $\pi/2$.

References

- [1] Kuznetsova I A Yushkanov A A Khadchukaev R R 2009 *Phys. and Tech. of Semiconductors* **43** 645 – 50

MEMS switch with the active contact breaking mechanism

I V Uvarov, V V Naumov, O M Koroleva and I I Amirov

Yaroslavl Branch of the Institute of Physics and Technology, Institution of Russian Academy of Sciences, 150007, Universitetskaya Street 21, Yaroslavl, Russia

Abstract. Electrostatically actuated MEMS switch with resistive contact is represented. Movable electrode of the switch is a beam suspended by the torsion springs. Low stiffness of the springs allows to achieve low values of the actuation voltage. Main feature of the switch is a mechanism of active contact breaking, allowing to solve the problem of adhesive sticking of the beam to the signal electrode. Active opening of the switch is realized by the presence of two driving electrodes. The theoretical analysis, finite element simulation and experimental investigation of the switch characteristics are performed.

1. Introduction

Electrostatically actuated MEMS switches are widely used in various radio frequency and microwave systems [1]. They have advantages of low power consumption, small insertion losses in the closed state, high isolation in the opened state, low harmonic distortion, high radiation resistance, wide operating temperature range and the possibility of integration with CMOS circuits [2].

The one of main disadvantages of MEMS switches is the high actuation voltage, which is a few tens of volts [3]. The most effective way to make the actuation voltage lower is to reduce the stiffness of the movable electrode. However, in the vast majority of conventional switches the breaking of a contact between the movable electrode and the signal electrode is carried out by the force of elasticity (passive opening). Reducing the stiffness of the movable electrode increases the probability of its stiction to the signal electrode by forces of adhesion, and hence reduces the reliability of the switch. The design of the switch must contain mechanisms, which allow, if necessary, to overcome the adhesion forces and open the electrodes (active opening).

2. MEMS switch design and principle of operation

Switch design is schematically shown on figure 1. The movable electrode is a metallic beam, attached in the middle of its length to the torsion suspension. Driving and signal electrodes (also metallic) are situated under the each arm of the beam symmetrically with respect to the clamping points. Beam has the contact bumps on its bottom side above the signal electrodes. Bumps localize the area of contact of the beam with the signal electrode and prevent the contact of the beam with the gate electrode when triggered.

Initially the beam is in a horizontal position (figure 1). When the voltage is applied to the one of driving electrodes, beam bends towards the electrode under the electrostatic force and comes in contact with the signal electrode. When the driving voltage is removed, switch retains its state, because the torsion springs have low stiffness and cannot overcome the adhesion forces between the

beam and the signal electrode. To break the contact, driving electrode located under the raised arm of the beam is used.

3. Results and discussion

MEMS switches were fabricated by surface micromachining on thermally oxidized silicon wafers. Driving and signal electrodes had a thickness of 50 nm, material of electrodes was Cr. The length of the driving electrode was 40 μm . Springs were also made of Cr and had a thickness of 0.3 μm . Estimated stiffness of springs was $3.9 \cdot 10^{-9}$ N·m. Beam was made of Al and had a length of 100 μm , a width of 8 to 32 μm and a thickness of 2 μm . Sacrificial layer for the beam was the amorphous Si layer with the thickness of 0.5 μm . Deposition of materials was performed by magnetron sputtering method, the sacrificial layer was removed by etching in SF_6 plasma [4]. SEM image of the fabricated switch with the beam width of 16 μm is shown on figure 2.

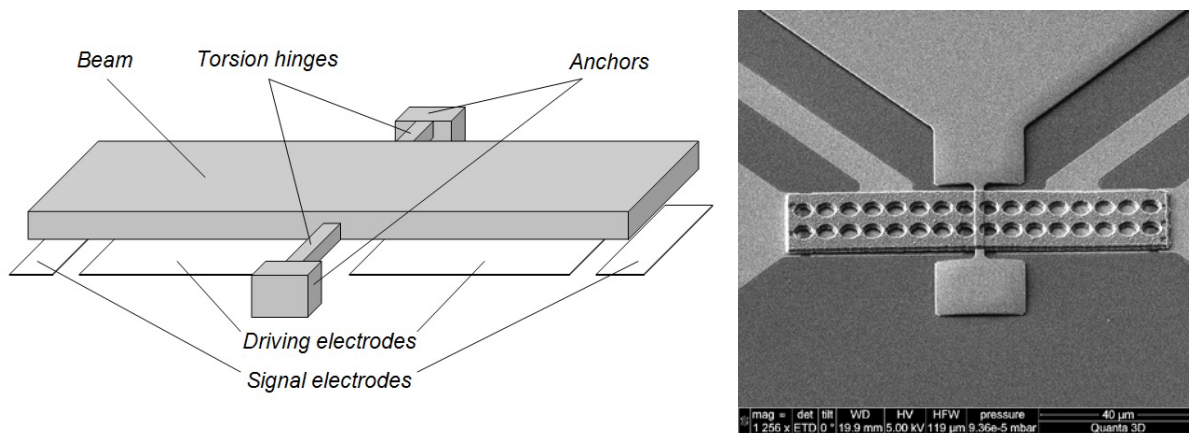


Figure 1. MEMS switch design.

Figure 2. SEM image of the switch.

Four types of switches with different beam widths were studied. According to analytical calculations [5], actuation voltage should be between 4.1 V in the case of a 32 μm beam width and 8.2 V for a 8 μm beam width. To account for the effect of fringing fields and perforation holes on the actuation voltage of the switch, simulations were performed using finite element method. According to simulation results, actuation voltage should be from 7.0 V to 12.8 V, depending on the beam width. Simulated actuation voltage exceeded the calculated values at 1.5-1.7 times. A possible reason for the excess was considering the perforation holes in the simulation.

The performance of the switch was measured at low frequency. The beam was grounded, DC voltage was applied to the driving electrodes, a small test signal was applied to the signal electrodes. Actuation of the switch was registered by the current flowing through the beam and the signal electrode. The experimental data are collected and compared to the theoretical predictions.

The reported study was supported by RFBR research project No. 14-07-31156 mol_a, by Facilities Sharing Centre “Diagnostics of Micro- and Nanostructures” and by the Ministry of education and science of Russian Federation.

References

- [1] Rebeiz G M 2003 *RF MEMS: Theory, Design, and Technology* (Hoboken, New Jersey: John Wiley & Sons, Inc.)
- [2] Dai C-L and Chen J-H 2006 *Microsyst. Technol.* **12** 1143
- [3] Sharma A K, Gautam A K, Farinelli P, Dutta A and Singh S G 2015 *J. Micromech. Microeng.* **25** 035014
- [4] Uvarov I V, Naumov V V and Selyukov R V 2014 *Proc. SPIE* **9440** 94400W
- [5] Degani O and Nemirovsky Y 2002 *J. Microelectromech. Syst.* **11** 20

Fabrication technology of CNT-Nickel Oxide based planar pseudocapacitor for MEMS and NEMS

I.M. Gavrilin², S.A. Gavrilov², D.G. Gromov², N.E. Gruzdev², A.A. Dronov²,
E.P. Kitsyuk¹, E.A. Lebedev², A.A. Pavlov³

¹Scientific Manufacturing Complex “Technological Centre”, 124498, Russia,
Moscow, Zelenograd, Bld. 5, Pas. 4806

²National Research University of Electronic Technology, 124498, Russia, Moscow,
Zelenograd, Bld. 5, Pas. 4806

³Institute of Nanotechnologies of Microelectronics Russian Academy of Sciences,
119991, Russia, Moscow, Leninsky Prospekt, 32A

Abstract. Fabrication technology of planar pseudocapacitor (PsC) based on carbon nanotube (CNT) forest, synthesized using plasma enhanced chemical vapor deposition (PECVD) method, covered with thin nickel oxide layer deposited by successive ionic layer adsorption and reaction (SILAR) method, is demonstrated. Dependences of device specific capacities from deposited oxide layers thickness is studied. It is shown that pseudocapacity of nickel oxide thin layer increases specific capacity of the CNT's based device up to 25 times.

1. Introduction

A rapid development of miniature electronics devices such as micro- and nanoelectromechanical systems, robots and implantable medical devices has significantly increased the demand for effective micro-sized energy storage devices. In this work we report on the planar pseudocapacitor based on CNT forest and nickel oxide - promising electrochemical energy storage device, which are in one hand combines significant energy and power density and long life cycle, and on the other hand the integral fabrication technology allows to implement on-chip energy sources directly on substrates.

2. Fabrication

Planar PsC based on the structure which consists of two nested into each other metal combs on the surface of the substrate. This structure allows to place two electrodes in the same planar surface and do not use separator. All experimental samples were prepared using standard integral technology and equipment.

The fabrication process began with wet cleaning and thermal oxidation of a bare silicon wafer to isolate the substrate from the electrodes. Then lithography was made to pattern two comb-like electrodes and pads. After that, Ti, TiN and Ni were evaporated onto the substrate with a thickness of 300 nm, 25 nm and 5 nm, respectively. Ti acts as the current collector material, TiN as the diffusion-barrier layer and Ni as the common catalyst of CNT forest growth. A photoresist lift-off followed to remove the metals on unwanted areas.

Vertically-aligned multi-wall carbon nanotubes were directly synthesized by PECVD method. For growing of carbon nanotubes it was needed to form a catalyst nanoclusters. It was performed by

thermal oxidizing of samples at 280°C in O₂ environment and annealing at 450°C in H₂ environment. Synthesis of multi-wall carbon nanotubes was carried out in gas mixture composition – C₂H₂, H₂ and NH₃. A temperature of substrate holder (500°C) was controlled by thermo sensor. Plasma energy generator creates of radio frequency (RF) with energies of 20 W and low frequency (LF) with energy 30 W. The operating pressure was 2 Torr. Synthesis for 3 minutes allows to receive 2 μm height CNT arrays.

To increase the PsC specific capacity CNT arrays were covered with a nickel oxide thin layer. The deposition of NiO onto the aligned CNT forest was done using the SILAR method. This is a stepwise chemical deposition technique based on immersion of the substrate into separately placed cationic and anionic precursors and rinsing after every immersion cycle with deionized water to avoid homogeneous precipitation. The cationic precursor for this study was a mixture of 0.01 M Ni(NO₃)₂*6H₂O and aqueous ammonia. Initially, precipitate of Ni(OH)₂ was formed from 0.01 M Ni(NO₃)₂*6H₂O, which was dissolved upon addition of ammonia to adjust the pH to 12, thereby forming hexaamminonickel (II) complex. The anionic precursor source was a hot water bath. When the substrate was immersed in the precursor solution (0.01 M Ni(NO₃)₂*6H₂O) at room temperature for 30 s, nickel ions were adsorbed onto the substrate surface. The substrate was transferred to the hot water bath at a temperature of 90°C for another 30 s to convert it into NiO, after which it was rinsed in deionized water for 30 s to remove the loosely bound or excess nickel hydroxyl ions. The SILAR steps were repeated for different number of cycles. After deposition, the samples were heat treated at 250 °C for 2 h in air.

In the last step 1 M aqueous solution of KOH was used as the electrolyte. Testing and measurement of electro-physical charge-discharge characteristics and cyclic voltammetry curves using potentiostat Elins P-30J were made. Charge and discharge current varied from 0.5 to 2 mA, and the voltage changed from 0 to 2 V. The scan rate during cyclic voltammetry ranged from 10 to 50 mV/sec.

CNT arrays structure and morphology were investigated and controlled using scanning electron microscope Agilent 8500 FE-SEM.

3. Results

We introduced the integral fabrication technology of planar PsC based on CNT arrays and nickel oxide thin layers deposition SILAR method. The influence of CNT's pre-treatment operations on the quality and morphology of the deposited layers was investigated.

The study of the PsC capacity dependence on the deposited nickel oxide layer thickness was produced. For these purposes the bulk experimental samples based on CNT's and oxide layers were made. Nickel oxide layer thickness was determined by the number of SILAR cycles. It was shown that with layers thickness increasing the device capacitance also increased. Capacitance value for the thickest oxide layer (20 SILAR cycles) was 25 times greater than that of devices based on pure CNT.

Further research and development should be directed towards to optimize the PC geometric dimensions, determine the oxide layers optimum thickness and to develop suitable the solid-state electrolyte.

Acknowledgments

This work was supported by the Ministry of education and science of the Russian Federation (Code: GP-1194).

Regimes of photon generation in dynamical Casimir effect under various resonance conditions

Levchenko A.V., Trifanov A.I.

ITMO University, 49 Kronverksky Avenue, Saint Petersburg, 197101, Russia

Abstract. We investigate spectral and statistical properties of the field generated in dynamical Casimir effect under various resonance conditions appeared from periodical motion of cavity boundary.

Dynamical Casimir effect (DCE) is the relativistic quantum parametric process by which the accelerated motion of the cavity boundaries excites vacuum fluctuations [1]. This process is accompanied by the generation of photons and intermode interaction. In spite of the fact that it requires relativistic velocities [2] at present there are experimental realization of DCE in superconducting schemes [3]. In [4] an effective Hamiltonian describing the evolution of the electromagnetic field in DCE, was presented. Particularly, for the case of one-dimensional rectangular cavity with perfectly conducting boundary it has the form:

$$H_{eff} = \sum_k \omega_k(t) a_k^\dagger a_k + i \sum_k \frac{\dot{q}(t)}{4q(t)} (a_k^{+2} - a_k^2) + \frac{i}{2} \sum_{j \neq k} (-1)^{j+k} \frac{kj}{j^2 - k^2} \left(\frac{k}{j}\right)^{1/2} \frac{\dot{q}(t)}{q(t)} (a_k^\dagger a_j^\dagger + a_k^\dagger a_j - a_j a_k - a_j^\dagger a_k). \quad (1)$$

Here $\omega_k(t)$ is spontaneous frequency of k-th intracavity mode, a_k is its annihilation operator, and $q(t)$ is time dependent boundary coordinate.

The aim of the presented work is investigation of spectral and statistical properties of DCE radiation under various resonant conditions. This conditions appears due to periodical law of boundary motion, which we define following [4] as

$$q(t) = L \exp\left(\frac{q_0 \cos \Omega t}{L}\right), \quad (2)$$

where L is the cavity length and q_0 initial boundary coordinate. In [4] it was only mentioned that the different regimes of photons generation and intermode interaction may occur and it depends on the choice of a particular resonant frequency of boundary motion. Here we investigate thoroughly three regimes of DCE field generation, which takes place when frequency "mechanical" frequency Ω takes the values $\omega_k = \frac{\pi ck}{L}$ ($c = 1$ is speed of light) of stationary cavity for $k = 1, 2$ and 4 .

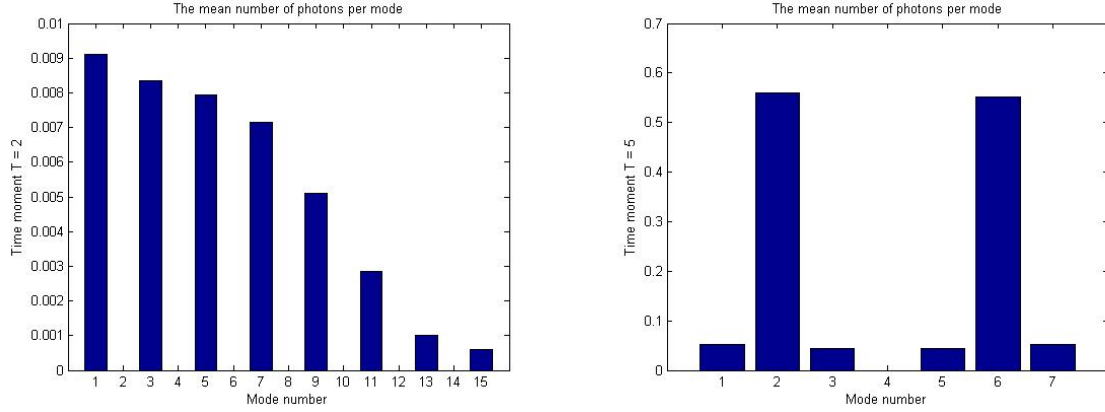


Figure 1. Photon generation in DCE; mean photon number per mode under the process described by Hamiltonians from Eq.(4) (left) at time $T = 2mcs$ and Eq.(5) (right) at time $T = 5mcs$

Using resonance condition $\Omega = \omega_1$ and rotating wave approximation (RWA) one can easily obtain resonance part of Eq. (1), namely:

$$H_{phm} = \frac{q_0\pi}{4L^2} \sum_k \sqrt{k(k+1)} (a_{k+1}^\dagger a_k + a_k^\dagger a_{k+1}). \quad (3)$$

This Hamiltonian has the form of that which describe phase modulation process. Under approximations of bounded spectrum it has an analytical solution for spectral problem. It is worthwhile to mention that there is no photon creation in this process.

Applying condition $\Omega = \omega_2$ together with RWA one can obtain the following Hamiltonian

$$H_{sms} = \frac{q_0\pi}{4L^2} (a_1^{\dagger 2} + a_1^2) + \frac{q_0\pi}{4L^2} \sum_k \sqrt{k(k+2)} (a_{k+2}^\dagger a_k + a_{k+2} a_k^\dagger), \quad (4)$$

which describes the process of photon creation in mode with $k = 1$ due to vacuum squeezing. We analyzed this process both theoretically and numerically. In particular the statistical properties of odd modes for single mode squeezing as a source of Casimir photons were investigated (since all even modes are in vacuum state).

Resonance condition $\Omega = \omega_4$ with applied RWA gives the following form of effective Hamiltonian

$$H_{mms} = \frac{q_0\pi}{2L^2} (a_2^{\dagger 2} + a_2^2) + \frac{\sqrt{3}q_0\pi}{4L^2} (a_1^\dagger a_3^\dagger + a_1 a_3) + \frac{q_0\pi}{L^2} \sum_k \sqrt{k(k+4)} (a_{k+4}^\dagger a_k + a_{k+4} a_k^\dagger). \quad (5)$$

There are two processes in this case which insert into photon generation: single mode squeezing (the first term) and multimode squeezing (second term). Under assumption of weak interaction between modes with numbers k and $k + 4$ spectral problem become solvable analytically. We analyze this solution and investigate statistical properties of intracavity DCE field.

References

- [1] Moore G 1970 *J. Math. Phys.* **11** 2679-2691.
- [2] Dodonov V V 2010 *Physica Scripta* **82** 038105
- [3] Wilson C M et al 2011 *Nature* **479** 376-379
- [4] Law C K 1994 *Phys. Rev. A* **49** 433-537

Force sensitive resistor on the base of metal-carbon structures

A Tikhomirov¹ and Y Izotov²

¹ Petrozavodsk State University, Department of Physics- Engineering, Researcher, Lenin Avenue 33, Russia.

² Petrozavodsk State University, Department of Physics- Engineering, Undergraduate student, Lenin Avenue 33, Russia.

Abstract. The aim of the work was to explore the opportunity of creation of force sensitive resistor on the base of metal-carbon structures in size hundreds of nanometers.

1. Introduction

Force sensors are very perspective direction at present. Using nanostructures it is possible to achieve the sensor sizes to 0.3 mm. Flexibility of the sensor is provided by a polymeric substrate. Researches of the sizes of nanoparticles metal-carbon for ensuring the best tensor effect were conducted. The aim of this work is to elaboration of the sensor with the acceptable properties for use as measurement of power loading.

2. Results and Discussion

The method of the electropulse category the nanopowders metal-carbon of structure used as a basis of this sensor was received. Samples of carbides of a titan and molybdenum were investigated. The greatest efficiency of the sensor it turned out at use molybdenum carbide. In figure 1 the structural scheme of a sensor is presented.

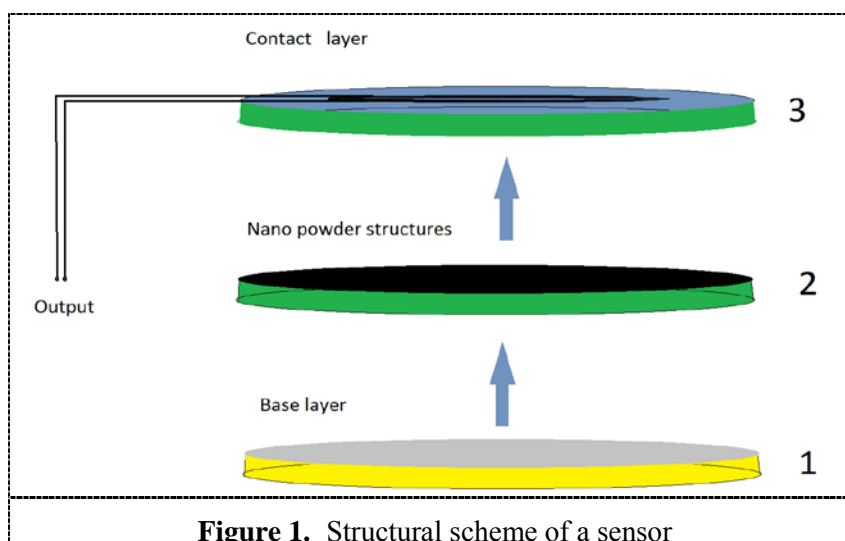
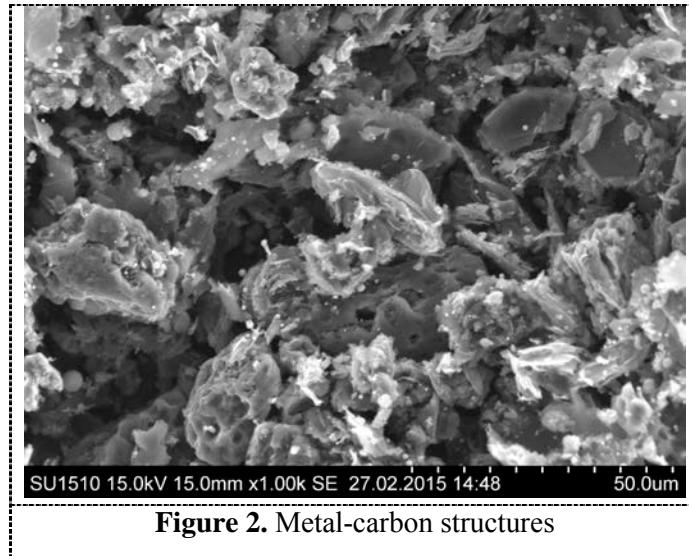


Figure 1. Structural scheme of a sensor

Where (1) is the lower layer deposited by nanopowder structures on top (2) which adjoins the contact layer (3). Metal-carbon structures explored on the scanning electronic microscope Hitachi SU1510 (Figure 2).



The average size of obtained structures is about 100 μm . On the basis of these structures the experimental example of force sensitive sensor has been created. In the result of the conducted research the dependence of electric resistant on the value of the external force has been found out.

References:

- [1] Vidal-Verdu, F., Barquero, M. J., Castellanos-Ramos, J., Navas-Gonzalez, R., Sanchez, J. A., Seron, J., & García-Cerezo, A. (2011). A large area tactile sensor patch based on commercial force sensors. *Sensors*, 11(5), 5489-5507.
- [2] Liu, H., Yang, S., Zhao, Y., Jiang, Z., Liu, Y., & Tian, B. (2013). A Micro-Force Sensor with Slotted-Quad-Beam Structure for Measuring the Friction in MEMS Bearings. *Sensors*, 13(10), 13178-13191.

Influence of ion irradiation on the resistive switching parameters of SiO_x-based thin-film structures

**D S Korolev, A N Mikhaylov, A I Belov, V A Sergeev, D V Efimovikh,
I N Antonov, E V Okulich, O N Gorshkov, A P Kasatkin and D I Tetelbaum**

Lobachevsky State University of Nizhni Novgorod, 23/3 Gagarin prospect, Nizhni Novgorod, 603950, Russia

Abstract. Influence of H⁺ and Ne⁺ ion irradiation on the bipolar resistive switching parameters of SiO_x-based thin-film memristor structures deposited by magnetron sputtering technique on the TiN/Ti metalized SiO₂/Si substrates has been studied. It is shown that the high-resistance memristor state reveals high tolerance to radiation exposure, whereas the low-resistance state is found to be sensitive to both ionizing and defect-producing ion irradiation.

1. Introduction

Memristor is a nonlinear resistor with memory [1] that can be implemented in a simple capacitor-like structure of the “metal-insulator-metal” (MIM) type [2]. One of the most commercially realizable applications of memristors is the creation on their basis of Resistive Random Access Memory (RRAM), the operating principle of which in a simple case is based on the use of two stable states of a material: high-resistance state (HRS) and low-resistance state (LRS). Switching between these states is achieved by the application of electric bias of certain polarity and value. Because of the simplicity of fabrication, scalability and low switching time, RRAM devices can replace in the nearest future the entire hierarchy of computer memory. The aim of this study is to reveal the radiation tolerance of RRAM devices to answer the question whether they are applicable in space and nuclear environments.

2. Experimental

Thin-film MIM structure was obtained on CMOS-compatible TiN (25 nm) / Ti (20 nm) / SiO₂ (30 nm) / Si substrate. SiO_x film (40 nm) was deposited using RF-magnetron sputtering system MagSputt 3G-2 (Torr International) from fused silica in the argon-oxygen gas mixture (50% oxygen content) at 300 °C. The top Au electrodes (40 nm) were deposited by DC sputtering using the same sputtering system. The Agilent B1500A semiconductor device analyzer was used to provide electroforming at negative bias of about 3-6 V and to measure the current-voltage (*I-V*) characteristics in the continuous sweeping regime. The sign of bias on the device corresponds to the potential of top electrode (Au) relative to the grounded bottom electrode (TiN). After electroforming and switching to both HRS and LRS, some of the MIM structures were irradiated by H⁺ and Ne⁺ ions (150 keV) with various doses.

3. Results and discussion

In the initial state, the MIM-structure shows typical characteristics of a capacitor with the silicon suboxide as dielectric layer. After electroforming, the current grows by several orders of magnitude

and the device begins to manifest reproducible bipolar resistive switching (RS) with the switching bias of 3-4 V and large number of switching cycles (more than 10^4) [3].

Due to the low thickness of MIM-structure, it is possible to use medium-energy ion irradiation to reproduce the effect of high energy space protons or other heavier particles like neutrons [4]. According to the SRIM calculations (www.srim.org) for the present MIM-structure, the inelastic energy losses in the case of 150-keV H^+ ions are about one order of magnitude higher than that for 10-MeV space protons. The corresponding elastic losses are about three orders of magnitude higher in the case of 150-keV Ne^+ defect-producing irradiation. The values of the LRS and HRS currents vs. the dose of ion irradiation are given in Figure 1. The LRS is found not to change up to the highest dose of proton irradiation ($1 \cdot 10^{16} \text{ cm}^{-2}$) that corresponds to the Ne^+ dose of $3.3 \cdot 10^{15} \text{ cm}^{-2}$, providing the inelastic losses being equal.

At the same time, when the memristor is irradiated in the HRS, there can be a spontaneous switching to LRS state during irradiation with both ionizing and defect-producing ions, however the HRS is always reproduced after the subsequent switching cycle. In the case of Ne^+ irradiation, some degradation of the HRS (decrease in resistance) is observed for the highest elastic loss value.

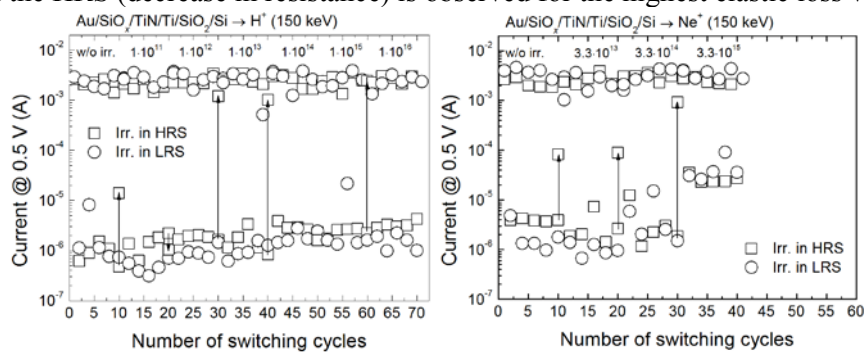


Figure 1. The dependencies of the LRS and HRS resistive states of $Au/SiO_x/TiN$ structures on the dose of proton and neon irradiation.

The nature of the observed reproducible bipolar resistive switching in SiO_x -based thin-film memristor structures can be related to the formation and local oxidation of silicon conducting channels (filaments) in the bulk of SiO_x layer [5]. Such filaments produced by breaking Si-O bonds under high electric stress can not be affected by ion irradiation in LRS, whereas the local dielectric interlayer formed in the site of filament oxidation can be sensitive to both ionizing and defect-producing irradiation, which leads to some observed HRS degradation.

4. Conclusions

The studied effect of medium-energy proton and neon ion irradiation allows to predict the high tolerance of the resistive switching parameters of SiO_x -based memristor structures to ionizing and defect-producing ion irradiation.

The work has been supported by the Ministry of Education and Science of the Russian Federation (RFMEFI57514X0029) and by the grant of the President of Russian Federation (MK-3714.2015.2).

References

- [1] Chua L 1971 *IEEE Transactions on Circuit Theory* **CT18** 507
- [2] Strukov D, Snider G, Stewart D and Williams R 2008 *Nature* **453** 80
- [3] Mikhaylov A N, Belov A I, Guseinov D V et al. 2015 *Mat. Sci. Eng. B* **194** 48
- [4] Tetelbaum D I, Guseinov D V, Vasiliev V K, Mikhaylov A N, Belov A I, Korolev D S, Obolensky S V and Kachemtsev A N 2014 *NIMB* **326** 41
- [5] Mehonic A, Cuffe S, Wojdak M, Hudziak S, Jambois O, Labbe C, Garrido B, Rizk R and Kenyon A 2012 *Journal of Applied Physics* **111** 074507

Microwave vortex field

D Poletaev

Department of Radiophysics and Electronics V.I. Vernadsky Crimean Federal University, Simferopol, Russia

Abstract. In this paper a method for the formation of microwave vortex field is proposed. A numerical simulation based on the finite element method is conducted. The conducted research confirms the possibility of the formation of a vortex field microwave near the open end of the circular waveguide. The calculations yielded a picture of the field distribution in the near and far zones.

1. Introduction

The vortex of space-time structure is typical for many physical processes. At the present time the attention of researchers working in the field of laser physics and coherent optics, attracted to field of light with helical perturbations of the wave front. Such perturbations are responsible for the propagation of a vortex of light energy – optical vortices. These physical phenomena are successfully used for the manipulation of micro-and nano-objects, the implementation of long-distance communications, sensing of the atmosphere and objects [1, 2]. Microwave electromagnetic waves are very similar to the light. It may be characterized by the Pointing vector and angular momentum.

There are a number of articles that tell about the successful formation of the vortex field microwave [3, 4]. So one of them used a spiral antenna, which allows to provide the necessary deformation of the wavefront. However, a disadvantage of this method is the inability to obtain significant power of the vortex field. It seems reasonable to propose a method for the generation of microwave vortex field.

The purpose of this paper is the analysis and numerical simulation of the formation of microwave vortex field near open end of the circular waveguide.

2. Theoretical part and simulation results

2.1. Theoretical data

In the microwave technique is widely used circular waveguide. The most interesting from a physical point of view, in terms of the application for the formation of optical vortices is type H₀₁ of magnetic wave. The main advantage of it is the low ohmic losses, due to only radial currents in the waveguide [4]. However, there are certain difficulties in excitation and isolation of this wave type in the waveguide. Electric power lines H₀₁ wave in a circular waveguide are a closed circle. Open end of the circular waveguide with this type of wave radiates into free space is the simplest antenna. Obviously, this method is not without drawbacks. However, at this stage analyze the possibility of formation of the vortex field, using a circular waveguide.

Building a model based on the general theory of the electromagnetic field and the apparatus of mathematical physics, in particular, the finite element method. In this case, the model space is divided into tetrahedra, values of the electric and magnetic fields are calculated at the vertices [5]. To establish

the existence of microwave vortex field is convenient to use directional patterns. They allow to get a complete picture of the field distribution in space.

Heterogeneity on the end of the waveguide is required to produce the phase shift. It may be a dielectric with the relative permittivity $\varepsilon > 1$. Empirically, the following structure as a half of a truncated cone with $\varepsilon = 5.5$ was chosen (Fig. 1). It allows optimal align the wave impedance of the waveguide and free space.

This heterogeneity makes it possible to shift the phase of the electric field vector, and introduce some screw dislocation in the field. Numerical simulation of circular waveguide with a radius of 19.3 mm and a half of a truncated cone with $\varepsilon = 5.5$ at the end of the frequency of 10 GHz, allowed to build the following pattern in the near field zone (20 mm) and far field zone (at infinity) (Fig. 1).

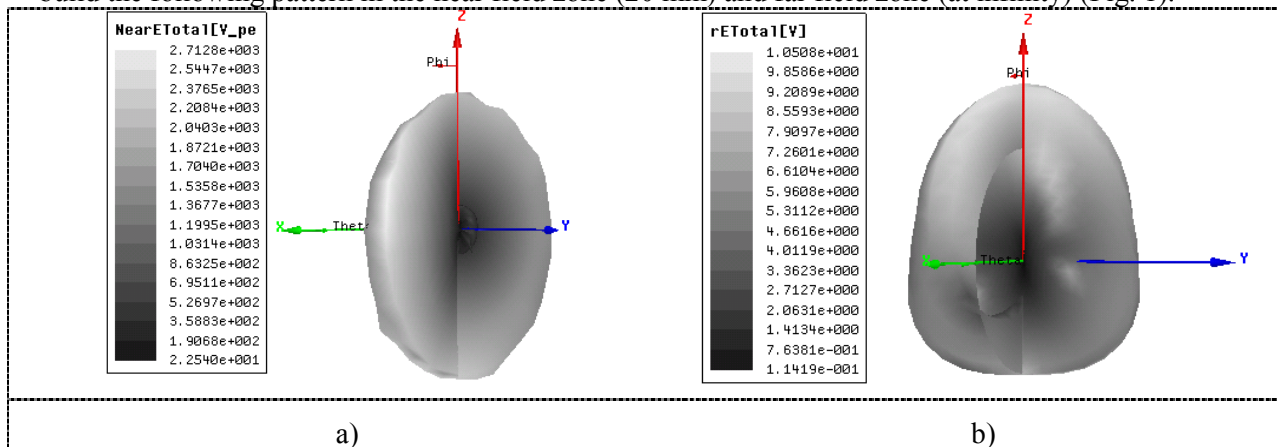


Fig. 1. Directional patterns from a circular waveguide with a half of a truncated cone at the end of a) the near field (20 mm), b) the far field (at infinity).

As can be seen from the diagrams (Fig. 1), this structure can form a vortex field in the far zone. Directional pattern (Fig. 1, b) is a spiral, which confirms the presence of a vortex field. Phase of the electric field changes not only in the time, but also in space.

2.2. Results and Discussion

The numerical simulation confirms the possibility of the formation of microwave vortex field near open end of the circular waveguide. The calculations allowed to establish a field distribution in the near and far zones.

References

- [1] Korolenko P.V. Optical vortices 1998 *Soros Educational Journal* **6** 133-143.
- [2] T.A. Fadeyeva, A.F. Rubass, B.V. Sokolenko and A.V. Volyar The vortex-beam precession in a rotating uniaxial crystal 2009 *J. Opt. Appl.* **11** 343-354.
- [3] Fabrizio T. Encoding many channels on the same frequency through radio vorticity: first experimental test 2012 *New J. Phys.* **14** 120-134.
- [4] L. Chen, C. Ong, C. Neo. 2004 *Microwave Electronics Measurement and Materials Characterization* (New York: John Wiley & Sons) pp 123-130.
- [5] Itoh T. 1989 *Numerical Techniques for Microwave and Millimeter-Wave Passive Structures* (New York: John Wiley & Sons) pp 333-35.

Effect of carbon-doping on magnetic properties of Mn/Si interface

M V Gomounova¹, G S Grebenyuk¹, I I Pronin¹, B V Senkovskiy²

¹ Ioffe Physical-Technical Institute, 26 Politekhnikeskaya, St Petersburg 194021, Russian Federation

² Institut für Festkörperphysik, Technische Universität Dresden, Helmholtzstrasse 10, Dresden 01069, Germany

The effect of carbon doping on both the Mn/Si interface formation and its ferromagnetic ordering has been studied by high-resolution photoelectron spectroscopy and magnetic linear dichroism (MLD) in angular distribution of Mn 3p photoelectrons. It is shown that manganese deposition on the Si(100) surface in vacuum as well as in the C₃H₆ atmosphere at room temperature results in the formation of an interfacial layer and a layer of silicon-manganese solid solution. The metal film begins to grow on the samples surface at coverage of 9 Å of Mn. The ferromagnetic ordering of the interface was observed after the deposition of ~6 Å of Mn in the system without carbon and ~4 Å in carbon doped system. The carbon also enhances the value of the MLD effect on the whole range of investigated manganese coverages.

Manganese silicides exhibit a great variety of physical properties and therefore are of significant basic and technological interest. They have already found wide application in microelectronics, optoelectronics and thermoelectrics [1]. The ultrathin magnetic films of these compounds are very promising for spintronics because they can be used for spinpolarized electrons injection in a semiconductor and can be easily integrated into the standard silicon-based technology. It is especially important that the films were ferromagnetic at room temperature. Despite that there is no any bulk Mn-Si phase with a Curie temperature above 50 K, it is known that ferromagnetism near and above room temperature occurs in diluted magnetic semiconductors Mn:Si and multilayer Mn/Si structures [2, 3]. The mechanism of this interesting phenomenon is not clear and still discussed. Different explanations of high-temperature ferromagnetism have been proposed as a consequence of the reduced coordination near surfaces and interfaces of silicon or due to presence of structural defects of the silicon lattice which occur in the process of preparation of the alloy [4]. Another possible reason is the presence of carbon in the grown manganese silicide film, which can result in anisotropic modification of the local structure around the Mn sites [5].

The aims of the present work were to study the initial growth of both pure and carbon-doped manganese silicide films and to confirm or refute the role of carbon doping in high-temperature ferromagnetism of the Mn/Si system.

The experiments were carried out in UHV using the Russian-German beamline at Helmholtz-Zentrum Berlin (HZB). The phase composition and the electronic structure of the interface were studied by high-resolution photoelectron spectroscopy. The magnetic properties of interface structures were analyzed by MLD in Mn 3p core-level photoemission. The use of these surface sensitive techniques in

the frame of a single experiment allows us to reveal specific features of the evolution of each system and establish correlations between their phase composition and magnetic properties. The silicides were grown on the atomically clean silicon surfaces Si(100) by solid-phase epitaxy. In the first experiment manganese was deposited on silicon in ultra-high vacuum while in the second one it was deposited in C_3H_6 atmosphere (10^{-7} mbar).

At room temperature the initial stages of the interface formation are similar for both investigated systems. The process starts with the formation of the interfacial layer and the Mn–Si solid solution. The pure manganese film in these systems begins to grow after the deposition of ~ 9 Å of Mn. Besides, the segregation of silicon is observed on the sample surfaces in the range of coverages up to ~ 15 Å for both systems, but in case of the carbon presence it is significantly lower than for pure manganese on silicon. During annealing the manganese film is transformed into the Mn–Si solid solution, MnSi metallic silicide and the $MnSi_{1.7}$ semiconductor silicide. In spite of the fact that formed phases are the same for both systems the thicknesses and temperature ranges differ from each other. So it can be concluded that carbon-doping has a significant impact on the phase composition of growing films.

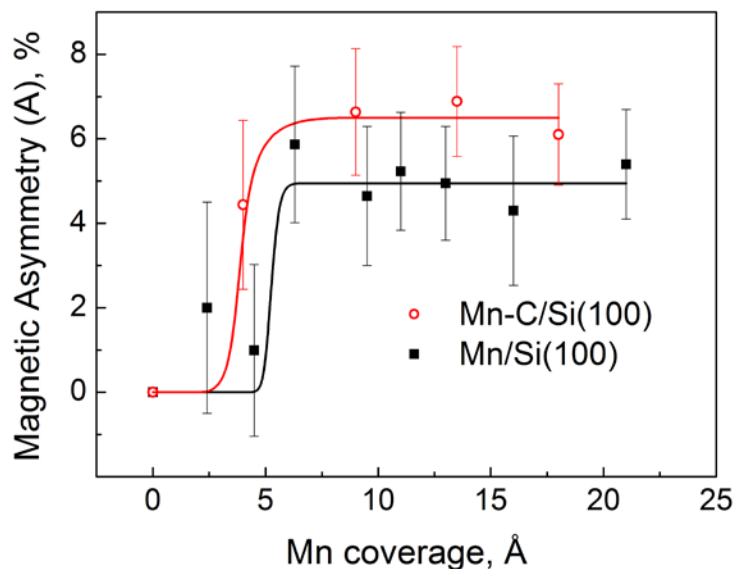


Figure 1. Magnetic asymmetry amplitude as a function of manganese coverage.

Magnetic properties of the interface are illustrated by Fig. 1, where the magnetic asymmetry amplitude (A) [6] of the MLD effect is shown as a function of Mn coverage. It is seen that the ferromagnetic ordering of the interface has a threshold nature and arises after the deposition of ~ 6 Å of Mn for Mn/Si system and of ~ 4 Å for carbon doped system. Thus, the presence of carbon enhances the high-temperature ferromagnetism in the Mn/Si(100) system.

We thank HZB for the allocation of synchrotron radiation beamtime. This work was partly supported by the Russian Foundation for Basic Research (grant № 13-02-00398).

- [1] Zhi-Qiang Zou, Gao-Ming Shi, Li-Min Sun, and Xiao-Yong Liu, 2013 J. Appl. Phys. **113**, 024305
- [2] B. A. Aronzon, V. V. Rylkov, S. N. Nikolaev, et al., 2011 Phys. Rev. B 84, 075209
- [3] S. Kahwaji, R. A. Gordon, E. D. Crozier, and T. L. Monchesky, 2012 Phys. Rev. B 85, 014405
- [4] E. Magnano, F. Bondino, C. Cepek, L. Sangaletti, M. C. Mozzati, and F. Parmigiani, 2012 J. Appl. Phys. 111, 013917
- [5] C. Surgers, M. Gajdzik, G. Fischer, H. V. Lohneysen, E. Welter, and K. Attenkofer, 2003 Phys. Rev. B 68, 174423
- [6] I. I. Pronin, M. V. Gomoyunova, D. E. Malygin, D. V. Vyalikh, Yu. S. Dedkov, and S. L. Molodtsov, 2008 J. Appl. Phys. 104, 104914

Model of quantum dot and resonant states for the Helmholtz resonator

A M Vorobiev¹ and I Yu Popov¹

¹ ITMO University, Kronverkskiy, 49, St. Petersburg, 197101, Russia

Abstract. The completeness of the system of resonant states for the operator extensions theory model of the Helmholtz resonator was proved. We deal with rectangular resonator with the Neumann boundary condition.

1. Introduction

Resonator with small boundary window is widely used model of a quantum dot weakly coupled with other parts of the nanosystem [1-3]. Completeness problem is very important when one tries to describe such system. It is this property, that allows one to use separation of variables and Fourier series. Particularly, the Laplace operator for bounded domain has purely discrete spectrum and complete system of eigenfunctions. But if one considers the Helmholtz resonator, i.e. the resonator coupled with the exterior through a small window, the situation changes. The eigenvalues and eigenstates transform, correspondingly, to resonances having non-zero imaginary part and to resonant states. The question about the resonant states system completeness was not earlier answered. In the present paper, we prove the completeness for a problem of such type.

2. The Laplacian on square domain perturbed by puncture on domain border

The Neumann Laplacian, $-\Delta$, acting on square domain $[0;1] \times [0;1]$, has the following eigenfunctions and eigenvalues:

$$\varphi_{n,m}(x, y) = 2 \cos(\pi n x) \cos(\pi m y), \quad \lambda_{n,m}^0 = (\pi n)^2 + (\pi m)^2.$$

To simulate coupling through small window with an exterior we use the model of point-like window [4]. We choose the window at $(x_1, y_1) = (0.5; 0)$ and construct a model by restriction-extension procedure [5]. We will consider perturbation of orthonormal system $\{\varphi_{n,m}(x, y)\}$ using the Green functions:

$$G^{in}(x, y, x_1, y_1, \lambda) = \sum_{n,m} \frac{\varphi_{n,m}(x, y) * \overline{\varphi_{n,m}(x_1, y_1)}}{\lambda_{n,m}^0 - \lambda} = \sum_{n:2,m} \frac{\varphi_{n,m}(x, y) * 2 * (-1)^{n/2}}{\lambda_{n,m}^0 - \lambda}.$$

The Green function for the exterior domain is another, but it has no singularities, that will matter for us. Formula for resonances from [6] is: $\sqrt{\lambda_{s,t}} = \sqrt{\lambda_{s,t}^0} - \frac{\pi * \psi_0^2}{4 * \sqrt{\lambda_{s,t}^0}} * \ln^{-1} \varepsilon - i * \frac{(\pi * \psi_0)^2}{8} * \ln^{-2} \varepsilon$. Here ε is a small parameter (in the corresponding realistic problem ε is the window width. Hence,

$$\lambda_{s,t}^0 - \lambda_{s,t} = \frac{\pi\psi_0^2}{2} * \ln^{-1}\varepsilon + i * \frac{\sqrt{\lambda_{s,t}^0(\pi * \psi_0)^2}}{4} * \ln^{-2}\varepsilon + o\left(\sqrt{\lambda_{s,t}^0}\right)$$

The perturbed functions $\{\psi_{s,t}(x, y)\}$ are described by the formula:

$$\psi_{s,t}(x, y) = c_{s,t} * \left(\varphi_{s,t}(x, y) + \alpha_{s,t} * G^{in}(x, y, x_1, y_1, \lambda_{s,t})\right),$$

$c_{s,t}$ is for normalization of ψ . $\alpha_{s,t}$ can be found from the coupling condition:

$$\alpha_{s,t} = \frac{-2 * (-1)^{s/2}}{\sum_{n:2,m} \left(\frac{4}{(\pi n)^2 + (\pi m)^2 - \lambda_{s,t}} - \frac{4}{(\pi n)^2 + (\pi m)^2 - k^2} \right) + F(k)}$$
 for $s : 2$ and $\alpha_{s,t} = 0$ for odd s .

$$c_{s,t} = \frac{1}{\sqrt{1 + \alpha_{s,t}^2 * \|G_{s,t}^{in}\|^2 + 2 * \alpha_{s,t} * \frac{2 * (-1)^{s/2}}{\frac{\pi * \psi_0^2}{2} * \ln^{-1}\varepsilon + i * \sqrt{\lambda_{s,t}^0} * \frac{(\pi * \psi_0)^2}{4} * \ln^{-2}\varepsilon}}}$$

We use the theorem [7] : If set $\{\varphi_{s,t}(x, y)\}$ is complete orthonormal system of functions and

$$\sum_{n,m} \|\psi_{n,m} - \varphi_{n,m}\|^2 < \infty,$$

then the set $\{\psi_{s,t}(x, y)\}$ forms a basis.

In our case this series is as follows:

$$\sum_{s,t} \|\varphi_{s,t}(x, y) * (c_{s,t} - 1) + c_{s,t} * \alpha_{s,t} * G_{s,t}^{in}(x, y)\|^2$$

Using the above obtained expressions for the coefficients, we prove the convergence of the series and, correspondingly, the completeness of the set of resonant states.

The work was partially financially supported by the Government of Russian Federation (grant 074-U01), by the Ministry of Science and Education of the Russian Federation (GOSZADANIE 2014/190, Project 14.Z50.31.0031), by grant MK-5001.2015.1 of the President of the Russian Federation.

References

- [1] Delerue, C., Lannoo M. Nanostructures: Theory and Modelling. Berlin: Springer. 2004.
- [2] Popov, I.Yu., Popova, S.L. Phys. Lett. A, 173 (1993), 484-488.
- [3] Wulf, U., Krahlich, M., Kučera, J., Richter, H., Höntschel, J. Nanosystems: Phys. Chem. Math. 4 (6) (2013), 800- 809.
- [4] Popov, I.Yu. Math. USSR Sbornik, 71 (1), (1992), 209--234.
- [5] Popov, I.Yu. J.Math.Phys. 41, 2000, 4391- 4405
- [6] Gadyl'shin R R Russ. Math. Surv. 52 (1) (1997), 1-72
- [7] Kato, T. Perturbation Theory for Linear Operators. Berlin: Springer. 1966.

On the spectrum discreteness of the quantum graph Hamiltonian with δ -coupling

M O Kovaleva¹, I Yu Popov¹

¹ITMO University, Kronverkskiy, 49, St. Petersburg, 197101, Russia

Abstract. A quantum graph with infinite leads (edges) or/and infinite chains of vertices such that neighbor ones are connected by finite number of edges and with δ -type conditions at the graph vertices is suggested. The Molchanov-type theorem for the quantum graph Hamiltonian spectrum discreteness is proved.

1. Introduction

Many important properties of nanosystems are predetermined by the spectrum of its Hamiltonian. There is an important characteristic, that is related with the basic properties of the corresponding physical system - type of the Hamiltonian spectrum. Particularly, spectrum discreteness shows the existence of only bound states of the corresponding system. As full general description of physical system is a very difficult problem, physicists prefer to use the model Hamiltonians. The most effective and widely used model is a model of quantum graph (see, e.g., [1], [2]). It is a metric graph with the Schrodinger operator defined at the edges (according the physical motivation) and some coupling conditions at the graph vertices that specify the transition probabilities across the vertices (see, e.g., [3,4]). The Hamiltonian spectrum discreteness condition for the potential was suggested by Molchanov in [5]. This condition becomes necessary and sufficient if we assume that the potential is bounded from below. Such consideration is closely related to the old problem starting from the Sturm theorem - the problem of zeros of eigenfunctions. At present, it is intensively investigated (see, e.g., [6]). The Courant theorem with the problem of nodal set counting is not solved in general case yet. The well known Molchanov's condition for the potential on the real half-axis (or axis) that guarantees the discreteness of the spectrum of the corresponding one-dimensional Hamiltonian is represented in [7,8]. The main goal of the work is to obtain the analogous condition for a special type quantum graph.

2. Molchanov-type theorem

Let Γ be a quantum graph, $V(\Gamma)$ is a set of it's vertices and $E(\Gamma)$ is a set of it's edges. Let also assume that the graph has finite number of infinite leads (edges) or/and infinite chains of vertices such that neighbor ones are connected by several (finite number) edges. We demand that the lengths of edges of these chains are bounded from below and above by some constants and attend that the periodicity or symmetry properties for this chain isn't needed. Moreover, we assume that after removing of these

infinite chains, the graph contains finite number of edges (may be, some of them have infinite lengths).

We assume the following equation at the edges:

$$(H - \lambda I)u(x) = -u''(x) - (\lambda - q(x))u(x) = 0.$$

We deal with the Dirichlet boundary condition at the boundary vertices of the graph and δ -type coupling at the internal graph vertices:

$$\sum_{e \in E_v} \frac{du}{dx_e}(v) = \beta_v u(v), \quad \beta_v < 0, \quad x \in V(\Gamma),$$

where E_v is a set of the edges containing vertex v , β_v , $\beta_v < 0$ are some real numbers. The main result of the paper is given in the following.

Theorem. Let $q(x)$ satisfy on Γ :

1. $q(x)$ is bounded from below, i.e. there exists such constant $c > 0$, that for every x the following inequality takes place: $q(x) > -c$.
2. For any fixed $w > 0$, for any path L on Γ , one has

$$\lim_{\text{dist}(x,v) \rightarrow \infty} \int_L q(x) dx = \infty, \quad x \in L, |L| = w.$$

Here v is some fixed vertex of Γ . Then, for every fixed λ any solution $u(x)$ of equation (1) has finite number of zeroes on Γ . While proving this Theorem we took into account two cases: when the graph has finite number of edges and when the graph has infinite leads (edges) and infinite chains of vertices such that neighbor ones are connected with finite number of edges. For the both cases the Theorem holds true. In conclusion, taking into account known the fact that sufficient spectrum discreteness condition is that for any fixed λ any solution u of the equation (1) has finite number of zeroes on Γ one comes to the conclusion that the Theorem gives us a sufficient condition for the discreteness of the quantum graph Hamiltonian spectrum.

The work was partially financially supported by the Government of Russian Federation (grant 074-U01), by the Ministry of Science and Education of the Russian Federation (GOSZADANIE 2014/190, Project 14.Z50.31.0031), by grant MK-5001.2015.1 of the President of the Russian Federation.

References

- [1] Kuchment P. 2002 Graph model of wave propagation in thin structures *Waves in Random Media* **12** (4), R1-R24.
- [2] Lobanov I.S. Trifanov A.I. and Trifanova E.S. 2013 Genetic algorithm for constructing graphene nanoribbon with given electronic transport properties. *Nanosystems: Phys. Chem. Math.* **4** (4), 512-523.
- [3] Exner P., Keating J. P., Kuchment P., Sunada T. and Teplyaev A. (eds.). 2008. *Analysis on Graphs and Its Applications*. Proc. Symp. Pure Math., 77 (Providence, RI: Amer. Math. Soc.)
- [4] Popov I. Yu., Skorynina A. N., and Blinova I. V.. 2014 On the existence of point spectrum for branching strips quantum graph. *J. Math. Phys.* **55**, 033504, doi: 10.1063/1.4867604
- [5] Molchanov A.M.. 1953 On conditions of spectrum discreteness for self-adjoint differential operators of second order. *Proc. Moscow Math. Soc.* **2**, 169-199.
- [6] Band R., Berkolaiko G., Raz H., Smilansky U.. 2012 The number of nodal domains on quantum graphs as a stability index of graph partitions. *Commun. Math. Phys.* **311**, 815–838. DOI: 10.1007/s00220-011-1384-9
- [7] Levitan B.M., Sargsyan I.S.. 1988 *Sturm-Liouville and Dirac operators*, (Moscow: Nauka).
- [8] Eckhardt J., Kostenko A., Malamud M. , G. Teschl. 2014 One-dimensional Schrödinger operators with δ' -interactions on Cantor-type sets. *J. Differential Equations* **257** 415–449

Hysteresis phenomenon of the field emission from carbon nanotube/polymer nanocomposite

S V Filippov^{1,2}, E O Popov^{1,2}, A G Kolosko^{1,3} and P A Romanov¹

¹A.F. Ioffe Physico-Technical Institute of Russian Academy of Sciences, ul. Polytechnitscheskaya 26, St.-Petersburg, 194021, Russia

²St. Petersburg State Polytechnical University, ul. Polytechnitscheskaya 29, St.-Petersburg, 195251, Russia

³The Bonch-Bruевич Saint-Petersburg State University of Telecommunications, pr. Bolshevikov 22, St.-Petersburg, 193232, Russia

Abstract. Using the high voltage scanning method and the technique of multichannel recording and processing of field emission (FE) characteristics in real time mode we found out some subtle effects on current voltage characteristics (IVC) of the multi-tip field emitters. We observed the direct and reverse hysteresis simultaneously in the same field emission experiment. Dependence of the form of IVC hysteresis on time of high voltage scanning was observed.

New nanocarbon composite field emitter materials are needed for high current density applications including microwave power amplifiers, miniature X-ray sources, compact mass-spectrometers and ion propulsions and others. Therefore the main task of vacuum nanoelectronics becomes the development of complex investigation of the multi-tip field emitters. Such procedures allow to perform quantitative comparative investigations of emitters operation in various conditions and power supply modes.

Now the number of works in which the high-voltage power units with program control by LabView are used is increasing. Use of various power supply allows not only to solve a series of practical questions on directional synthesis of new emission materials, but also to find out the new fundamental phenomena in emitters behavior. One of such phenomena is the hysteresis in the measured IVC observed in a number of publications [1-5]. This effect is usually explained by the processes of adsorption and desorption of the residual gases at the emitting centers [1-3]. But there are other possible explanations, which are described in various investigations of the different carbon nanostructures [4,5].

The basic approaches to preparing samples and our experiment technique are described in [6].

In figure 1 a small part of short and long sequences of step high voltage levels increase and decrease (on 10 s and 250 s on each branch) is shown. The cyclic applying of a high voltage leads to appreciable split of direct (increasing) and return (falling) voltage branches, a so-called direct hysteresis. The similar effect has been fixed on grafene sheets in [1-2]. However in the area of low currents at substantial growth of high voltage action duration an IVC bend leading the hysteresis to the 'eight' shape (it is similar in [5] for CNT) was observed (figure 2). We relate such behavior to mechanisms of emission centers self-heating.

On the contrary, processes of adsorption and desorption of residual gases is the basic mechanism in occurrence of a return hysteresis (observed, for example, in [4]). Such mode is observed at additional activation of the emitter at the raised voltages ('A' on figure 3). In this case the first IVC pass is presented on figure 4. The second pass (IVC loop) leads to restoration of IVC and occurrence of a

direct hysteresis at the further operation. Simultaneous existence of both direct and return hysteresis in one experiment was not described previously.

The investigations conducted by us are supported with the data on change of partial pressures (the mass spectrometer data) during field emission experiments.

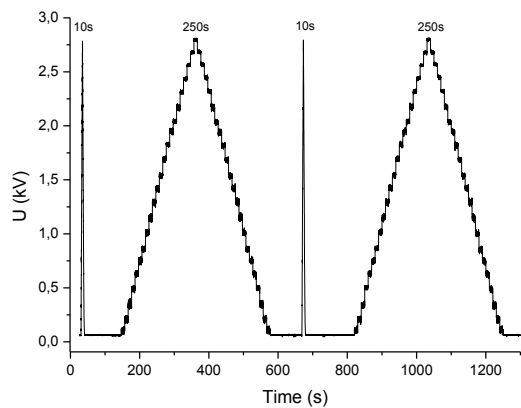


Figure 1. Example of a high voltage scanning for definition of results repeatability

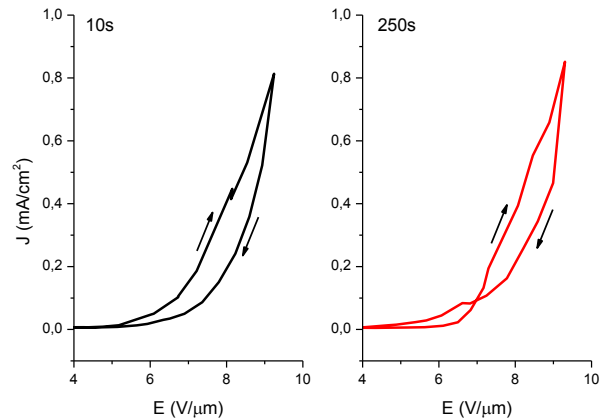


Figure 2. Hysteresis form change depending on duration of scanning (impulses 10s and 250s, accordingly Figure 1)

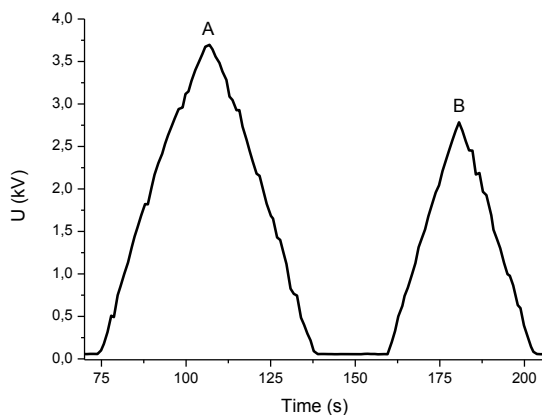


Figure 3. Sequence of slow pulse applied voltage

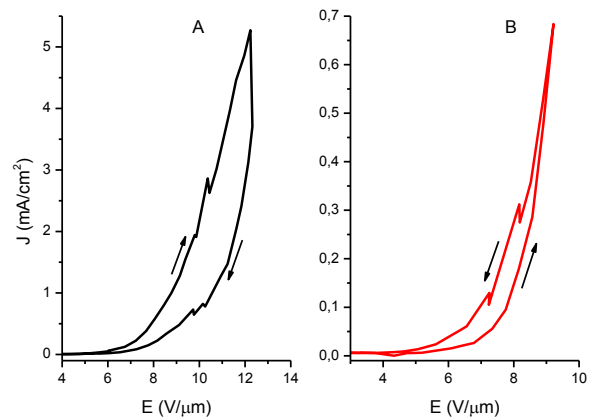


Figure 4. Change of IVC hysteresis direction after higher voltage applying

Acknowledgement

The work was carried out with the partial support of the Foundation for Assistance to Small Innovative Enterprises in Science and Technology (№0002235).

- [1] Chen J, Li J, Yang J, Yan X, Tay B-K and Xue Q 2011 Appl. Phys. Lett. **99** 173104
- [2] Li J, Yan X, Gou G, Wang Z and Chen J 2014 Phys. Chem. Chem. Phys. **16** 1850
- [3] Parveen S, Husain S, Kumar A, Ali J, Harsh and Husain M 2012 ISRN Nanomater. Article ID 971854, 5 p
- [4] Cahay M, Murray P T, Back T C, Fairchild S, Boeckl J, Bulmer J, Koziol K, Gruen G, Sparkes M, Orozco F and O'Neill W 2014 Appl. Phys. Lett. **105** 173107
- [5] Okotrub A V, Kuren'ya A G, Gusel'nikov A V, Kudashov A G, Bulusheva L G, Berdinskii A S, Ivanova Y A, Ivanov D K, Strel'tsov E A, Fink D, Petrov A V and Belonogov E K 2009 Nanotech. in Russia **4** 9-10 627
- [6] S V Filippov, E O Popov, A G Kolosko, P A Romanov 2014 J. of Phys.: Conf. Ser. **572** 012026

Changes in the density of states of the quantum well in a polar solvent

M. I. Zakirov

Taras Shevchenko National University of Kyiv, Kyiv 01601, Ukraine

Abstract. The work describes the assumption that the change in the density of states in nanocrystals when entering them in a polar solvent. It is assumed changes imaginary size of the potential well under the influence of an external field.

1. Introduction

Colloidal semiconductor nanoparticles have been studied extensively because of their novel optical properties and potential applications [1–5]. It is known that semiconductor nanoparticles exhibit quantum confinement effect when their sizes are comparable with the diameter of bulk excitons, leading to that the continuum of states are broken down into discrete states with an effective band gap blue-shift from that of bulk materials. Another interesting property that will be manifested in low dimensional structure is dielectric confinement effect. When organic molecules capped on semiconductor nanoparticles have a relatively smaller dielectric constant than that of the nanoparticles, the electric force lines emerging from charged particles within semiconductor nanoparticles pass through the surrounding medium, therefore, the screening effect is reduced and the Coulomb interaction between charged particles is enhanced. Such quantum confinement effect, as well as dielectric confinement effect, tailors the optical properties of semiconductor nanoparticles. Hence, it is critically important to synthesize the nanoparticles with a size comparable with Bohr radius and with a narrow size distribution in order to insure the occurrence of these two effects.

Change the optical properties of nanomaterials, when you change the environment in which they are placed noted by several authors [6, 7]. This and other works show that optical properties nanomaterials dependent for the environment.

2. Modeling

The paper shows a model to describe the changes in the properties of nanomaterials under the assumption introduction of the effective size of the system. Present nanocrystal as potential well with infinitely high walls (figure 1).

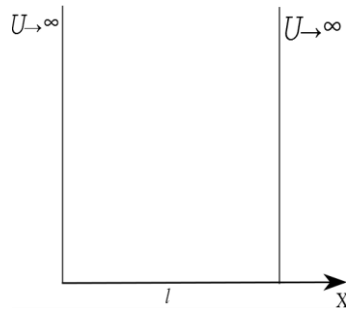


Figure 1. Simulated potential well

Where r – is a radius of nanoparticle, than the width potential well will $l=2r$. For simplification we take $r=l$.

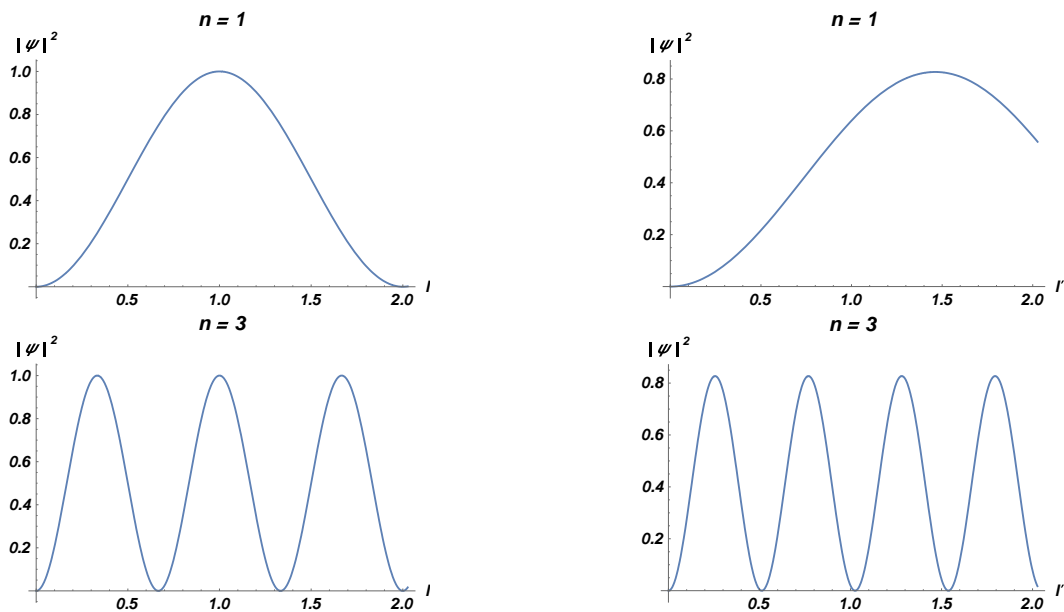
Then the solutions of the one-dimensional Schrödinger equation with the boundary conditions: $\Psi(0)=0$ and $\Psi(l)=0$ get the standard form of the wave function

$$\psi_n(x) = \sqrt{\frac{2}{l}} \sin \frac{\pi n}{l} x, n = 1, 2, 3 \dots \quad (1)$$

If introducing the particles into the polar solvent, the dipoles produce some electrostatic field. By considering effective distance of the field, the point at which the field decreases for ϵ once.

$$r_{ef} = \sqrt{\frac{1}{4\pi\epsilon\epsilon_0}} qe \quad (2)$$

where ϵ - dielectric constant of the material, q - charge produces a field. Now, the barrier has a fictive width $l'=l+2r_{ef}$. The solution of equation 1 shows how to change the probability of finding the particle in the management of the external field. The probability of the particle position shown in Fig. 2



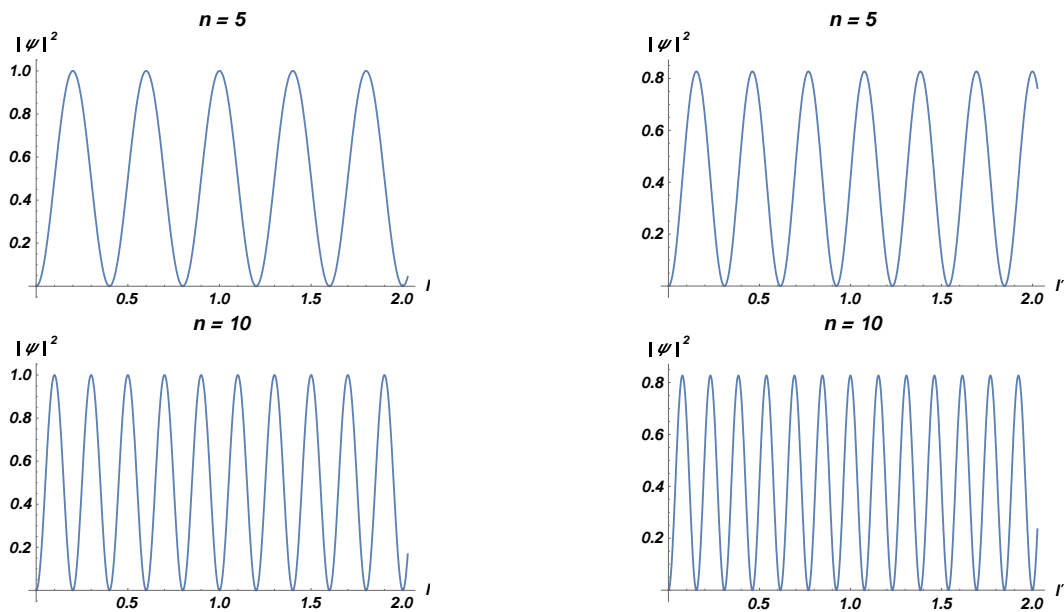


Figure 2. The probability of the particle's position according to n .

3. Conclusions

Thus, the work shows the change in the probability density in the potential well. Changes due the increase in size of potential well.

References

- [1] Bruchez Jr M, Moronne M, Gin P, Weiss S, Paul Alivisatos A. 1998 *Science* **281** 2013.
- [2] Soo YL, Ming ZH, Huang SW, Kao YH, Bhargava RN, Gallagher D. 1994 *Phys Rev B* **50** 7602.
- [4] Ito H, Takano T, Kuroda T, Minami F, Akinaga H. 1997 *J. Lumin* **72–74**. pp 106-107
- [5] Yu J, Liu H, Wang Y, Fernandez FE, Jia W, Sun L, et al. 1997 *Opt Lett* **22** 913.
- [6] S.K. Mehta, Sanjay Kumar, Michael Gradzielski 2011 *Journal of Colloid and Interface Science* **360** pp 497–507
- [7] Song Wei Lu, Burtrand I. Lee, Zhong Lin Wang, Wusheng Tong, Brent K. Wagner, Wounjhang Park, Christopher J. Summers 2000 *J. Lumin* **92** pp73-78

Phase diagram calculation of $A^{III}B^V$ binary solutions of the eutectic type in the generalized lattice model model

G A Panov and M A Zakharov

Department of Solid State Physics and Microelectronics, Novgorod State University, 173003, Novgorod the Great, Russia

Abstract. The present work is devoted to the phase diagrams calculation of $A^{III}B^V$ systems within the frame work of the generalized lattice model taking account of volume effects. The theoretically calculated phase diagram is compared with the corresponding experimental diagrams.

1. Introduction

Calculation of phase diagrams is one of the most interesting problem of physics of multicomponent systems. In particular, investigation of the thermodynamic properties and phase equilibria $A^{III}B^V$ binary systems is of great importance for micro- and nanoelectronics. The aim of this work is a theoretical calculation of the phase diagram of $A^{III}B^V$ binary systems (In–Sb, In–As, Al–P, Al–Sb) within the generalized lattice model [1].

2. Discussion of results

It is well known, that the phase diagrams of the In–Sb, In–As, Al–P, Al–Sb systems are eutectic type phase diagrams with one intermediate phase of constant composition. Method of calculation of phase diagrams of this type has been proposed in [2, 3] within the generalized lattice model.

Using the technique developed in [2, 3] calculation phase equilibria in the In–Sb, In–As, Al–P, Al–Sb systems was carried out (see, Fig. 1). The parameters of the model are correspond to theoretical calculations of the phase diagrams was obtained (see, Tab. 1). It should be noted here we use the notation introduced works [2, 3].

Table 1. Parameters of the generalized lattice model

N	<i>A-B</i>	$A_m B_n$	$T_A, ^\circ C$	$T_{AB}, ^\circ C$	$T_B, ^\circ C$	q_A	q_B
1	<i>In-Sb</i>	<i>InPb</i>	158.5	525.0	630.8	0.91	2.72
2	<i>In-As</i>	<i>InPb</i>	158.5	942.0	817.0	0.91	2.27
3	<i>Al-Sb</i>	<i>AlSb</i>	660.0	1058.0	630.0	1.38	2.72
4	<i>Al-P</i>	<i>AlSb</i>	660.0	2530.0	44.2	1.38	0.95
N	<i>A-B</i>	x_0	$T_0, ^\circ C$	\tilde{q}_{AB}	λ	$W/R, K$	
1	<i>In-InSb</i>	0.007	155.0	15.37	0.473	-1722	
	<i>InSb-Sb</i>	0.663	494.0	15.37	1.272	496	
2	<i>In-InAs</i>	0.003	155.2	13.99	0.045	-439	
	<i>InAs-As</i>	0.875	731.0	13.99	1.516	-1569	

3	<i>Al-ALSb</i>	0.004	657.0	23.53	0.178	-799
	<i>ALSb-Sb</i>	0.992	627.0	23.53	2.256	-6016
4	<i>Al-AIP</i>	0.001	659.7	18.00	0.162	-4459
	<i>AIP-P</i>	0.999	44.0	18.00	25.001	-4281

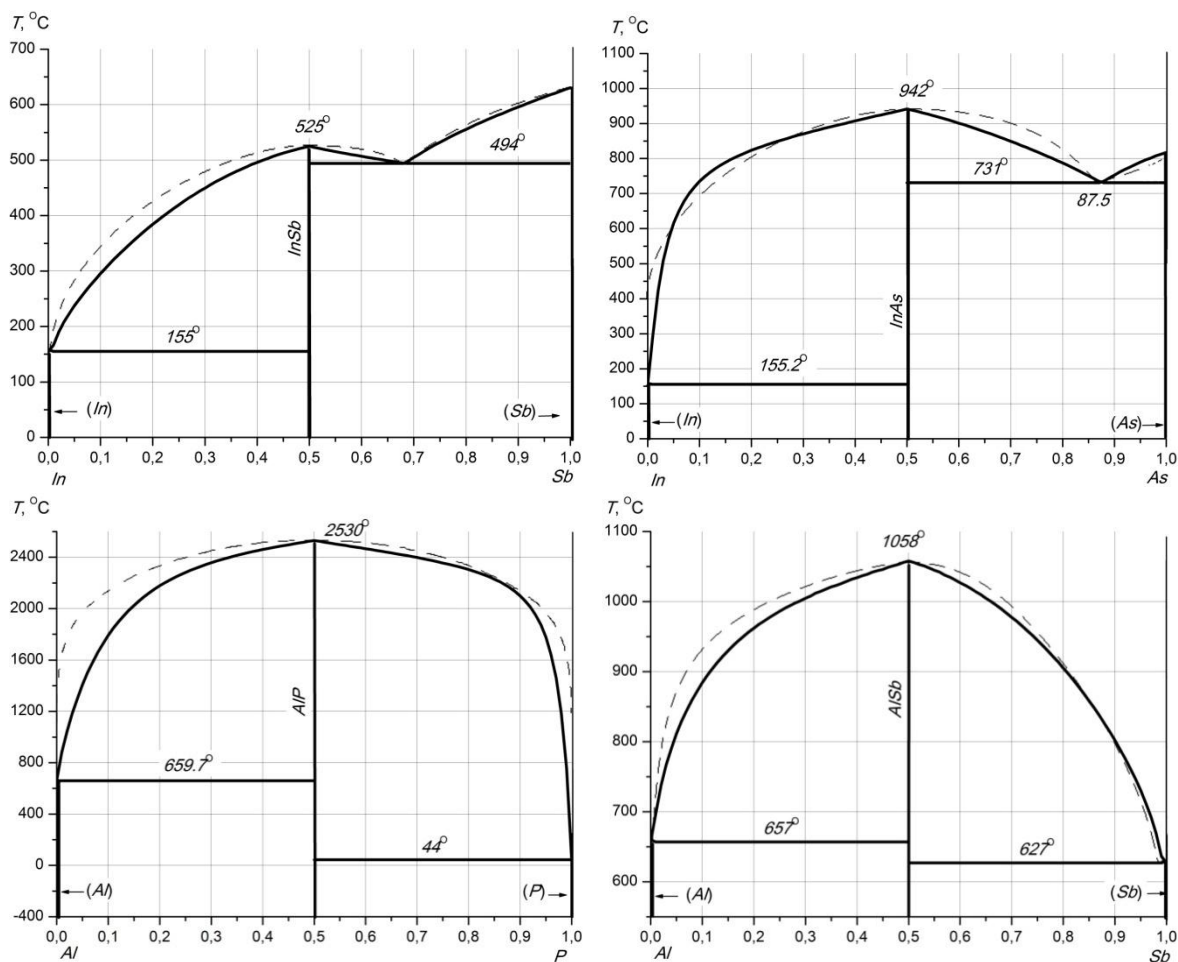


Figure 1. Phase diagrams of the the In–Sb, In–As, Al–P, Al–Sb systems. Dashed lines are the experimental data taken from [4]. Solid lines indicate the results obtained from theoretical calculations.

It can be seen from Figure 1 that the phase diagrams are consistent with the experimental data.

Acknowledgements. This work was supported by the Ministry of Education and Science of the Russian Federation in base part (project 1755).

References

- [1] Zakharov A Yu, Zakharov M A and Loginova O V 2004 *Int. J. Quant. Chem.* **100** 435
- [2] Zakharov M A 2007 *Phys. Solid State* **49** 2312
- [3] Panov G A and Zakharov M A 2013 *Journal of Physics: Conference Series* **461** 012003.
- [4] Liakishev N P 1996-2000 *Diagrams of binary metallic systems* (Moscow: Mashinostroenie) [In Russian]

Generalized Thomson Problem and its Applications in Carbon Nanotube Structures Design

A.N. Bondarenko, L.A. Kozinkin

Novosibirsk State University (NSU), Novosibirsk, Russia

Abstract. A practical numerical method for the rapid construction of nanotube caps is proposed. Founded upon the notion of lattice duality, the algorithm considers the face dual representation of a given nanotube which is used to solve an energy minimization problem analogous to The Thomson Problem. The developed iterative numerical algorithm enabled to perform theoretical research such as study of the number of solutions asymptotic dependence on the particle count. Based on presented method the framework for generating capped carbon nanotubes was created.

1. Introduction

What configuration of N unit point charges on a unit sphere minimizes the electrostatic potential energy of the system? The given problem was initially presented 1904 by Thomson and nowadays is one of the unsolved problems of the 20th Century. The development of numerical optimization methods for solving The Thomson Problem draws close attention of professionals due to its high complexity [1].

2. Applications

During the last decade a keen interest of researchers of various scientific fields is caused by design and study of the properties of nanomaterials. Nanomaterials are generally materials containing structural elements, that are not exceeding 100 nm along one dimension and thus developing entirely new properties.

Recently, increasing interest is caused by carbon nanotubes (CNTs) [2]. CNTs offer new opportunities for biological and medical applications: visualization of molecular, cellular and tissue structures, design of biosensors and its base electrodes, targeted delivery of various substances, radiation and photothermal therapy.

The most promising property of CNTs within biomedical applications area consist in its ability to penetrate into the various tissues of the body and transport large doses of agents, providing diagnostic and therapeutic effects [3].

3. Main result

We introduce a new statistical approach to the problem which allows to find not only ground state but also stable charges configurations and measure the degree of sustainability.

Based on the proposed algorithm and three-dimensional computer visualization the NanoCup software suite was created. NanoCup is a multifunctional application for the computer design

of low energy fullerene and capped nanotube structures. This software provides an ideal tool to accompany the study of the finite carbon molecules using atomistic computer simulation.

4. Conclusion

Despite the fact that numerical iterative methods aimed at The Thomson Problem solving are intensively developing in the last decade, the construction of the numerical algorithm that effectively enables to find all solutions for $N > 500$ is a desirable goal for many applied researcher. Perhaps, our research provides another step in the right direction.

References

- [1] Altschuler E L and Pérez-Garrido A 2005 *Physical Review E* **71** 047703
- [2] Mubarak N, Abdullah E, Jayakumar N and Sahu J 2014 *Journal of Industrial and Engineering Chemistry* **20** 1186–1197
- [3] Baeza A and Vallet-Regí M 2014 *Bio-and Bioinspired Nanomaterials* 23–48

Electron mobility in fully-depleted SOI films

E G Zaytseva, O V Naumova, B I Fomin, M A Ilitsky, V P Popov

Institute of Semiconductor Physics, SB RAS, Novosibirsk, 630090 Russia

Abstract. In this study the electron mobility μ_{eff} for fully depleted double-gate n^+-n-n^+ SOI MOSFETs was investigated at different modes of Si surface. It was shown that electron mobility $\mu_{\text{eff}}(N_e)$ dependencies is approximated by power functions $\mu_{\text{eff}}(N_e) \sim N_e^{-n}$, where the power n is determined by the mechanism of carrier scattering as for the field dependence of the mobility.

1. Introduction

Thin fully-depleted films of silicon-on-insulator (SOI) are important material for the micro- and nanoelectronics. One of the features of these films is so-called coupling-effect (the potential coupling of Si/SiO₂ interfaces) [1]. As the result of the coupling-effect, the parameters of FD SOI devices are dependent on the potentials of both interfaces. Carrier mobility is a fundamental characteristic and a main parameter of MOSFETs. In bulk MOSFETs with one Si/SiO₂ heterointerface, the field dependence of mobility is known to be used to describe the properties of Si/SiO₂ system. This dependence can be described by a power function $\mu_{\text{eff}}(E_{\text{eff}}) \sim E_{\text{eff}}^{-n}$, where n is determined by dominant scattering mechanisms [2]. However, it is difficult to determine the effective field in the FD SOI MOSFETs because in these structures the surface potential influences the carriers distribution in the film cross-section. The induced charge carrier mobility as function of their density $\mu_{\text{eff}}(N_e)$ instead of the field dependence of mobility has been proposed for determining the range of possible values of mobility and the dominant scattering mechanisms in the thin-film structures [3].

The aim of this research was to investigate the dependences $\mu_{\text{eff}}(N_e)$ of the electrons in fully-depleted SOI films in cases when the SOI film mode near one of its surfaces was varied from inversion to accumulation. Double-gate SOI MOSFETs were used in this research. The back gate (the substrate of SOI MOSFET) was biased (V_{bg}) to induce the electron channel near the interface Si/buried SiO₂. Top gate voltage (V_{tg}) was changed in wide range, to change mode of Si layer surface from inversion to accumulation.

2. Experiment

In the work, n-channel SOI MOSFETs were used. The transistors were fabricated on the n-type SOI films. Donor concentration N_d of the silicon layer was $(6-8) \cdot 10^{16} \text{ cm}^{-3}$. The silicon layer thicknesses t_{Si} were 30 nm (fully depleted, FD, SOI layer) or 400 nm (non-depleted SOI). The thicknesses of buried oxide t_{BOX} and of the gate oxide t_{ox} were 300 nm and 250 nm, respectively. The channel length L and width W were 10 μm and 3 μm , respectively. Details of the fabrication processes can be found in [4].

The top gate was separated from the regions of the drain and the source to avoid the formation of a conductivity channel from the top gate. The dependences of the drain current I_{ds} on the back gate

voltage V_{bg} were measurement at different V_{tg} . The mobility μ_{eff} and the density of induced electrons N_e were calculated from the obtained I_{ds} - V_{bg} dependences [3]. In the study, numerical simulation was made to determine the redistribution of electron density across the SOI film.

3. Results

Figure 1(a) shows the $\mu_{eff}(N_e)$ dependences for FD SOI MOSFET at different V_{tg} values. Insert shows $\mu_{eff}(N_e)$ and $\mu_{eff}(E_{eff})$ dependences for non-depleted SOI MOSFET. One can see that $\mu_{eff}(N_e)$ dependences follow power function $\mu_{eff}(N_e^{-n})$ with different n values. Figure 1(b) shows the change of n at $N_e=10^{12} \text{ cm}^{-2}$. The details of n variation at $N_e=10^{12} \text{ cm}^{-2}$ and at changing of film mode from inversion to accumulation are shown in figure 1b.

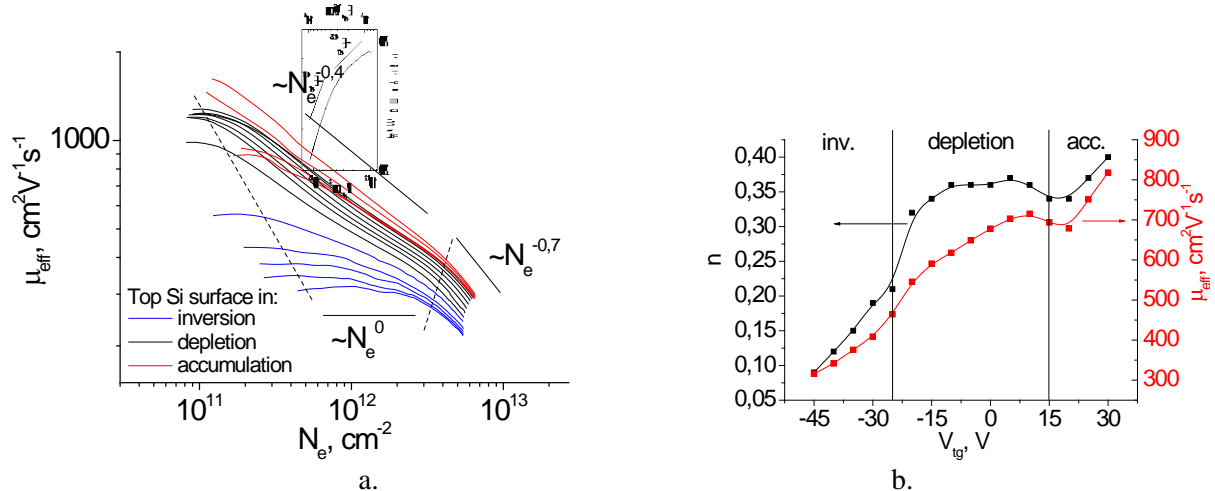


Figure 1. a) The dependences of the electron mobility on their density $\mu_{eff}(N_e)$ for FD SOI MOSFET at V_{tg} varied from -40 V to 30 V, $\Delta V_{TG}=5$ V. Insert shows μ_{eff} vs. N_e and E_{eff} (top scale) for non-depleted SOI MOSFETs; b) $\mu_{eff}(V_{tg})$ and $n(V_{tg})$ dependences calculated at $N_e=10^{12} \text{ cm}^{-2}$.

The $\mu_{eff}(V_{tg})$ and $n(V_{tg})$ dependences are non-monotonic functions of V_{tg} and V_{bg} . The reduction of n and μ_{eff} values was observed when $V_{tg} \geq V_{bg}$. It was found that for SOI films of 30 nm thickness, the bulk conductivity is observed when $V_{tg} \geq V_{bg}$. The different n values and the features of the $\mu_{eff}(V_{tg})$ and $n(V_{tg})$ dependences at different SOI film modes were explained by the redistribution of the electron density across the SOI film and by changing scattering mechanisms.

4. Conclusion

In FD SOI films it is reasonable to use the induced charge carrier mobility as function of their density $\mu_{eff}(N_e)$ instead of the field dependence of mobility $\mu_{eff}(E_{eff})$. The power n is determined by the dominant scattering mechanisms as for the field dependence of mobility.

5. Acknowledgments

The work is supported by using analyser Agilent B1500A “Center of shared scientific equipment” of Institute of Semiconductor Physics SB RAS.

References

- [1] Emenite S, Cristoloveanu S, Clerc R, Ohata A and Ghibaudo G, *Sol.-St. El.*, **51** 239 (2007)
- [2] Takagi S, Toriumi A, Iwase M and Tango H, *IEEE Trans. on el. dev.* **41** 2357 (1994)
- [3] Naumova O V, Zaytseva E G, Fomin B I, and Popov V P, *Semiconductors*, 2015 (in press)
- [4] Naumova O V, Fomin B I, Nasimov D A, Dudchenko N V, and all, *Sci. Technol.* **25** 055004 (7) (2010)

Electrophysical properties of thin films on the basis of phase change memory materials on the pseudobinary line GeTe-Sb₂Te₃

A O Yakubov^a and D Y Terekhov^b

Moscow State Institute of Electronic Technology (Technical University), 124498
Zelenograd, Russia

Abstract. Electrophysical and thermoelectric properties of thin films of materials on pseudobinary line GeTe-Sb₂Te₃ are investigated in this work. The temperature dependences of the resistivity are analyzed. The results of measurements of thermopower for thin films allowed to define the dominating p-type conductivity.

1. Introduction

Modern data storage devices are no longer satisfies the trends of productivity growth, and increasing level of miniaturization of electronic devices. In this connection the development of the next memory generation is urgent task, one of the most promising types of which is phase change memory (PCRAM - phase change random access memory). Chalcogenide semiconductors of Ge-Sb-Te (GST) system are most widely used as a programmable phase change memory material. In particular promising materials are those on the pseudobinary line GeTe-Sb₂Te₃, which are successfully applied in rewritable optical disks of different formats (for example, DVD-RW and Blu-Ray).

However, despite the successful commercial application of materials on the pseudobinary line Sb₂Te₃ - GeTe in optical storage devices, many fundamental and important practical issues related to the electrophysical properties of thin films, are not fully understood. Therefore, the aim of the work was to study the influence of the composition variation of thin films along the pseudobinary line GeTe-Sb₂Te₃ on the temperature dependences of the resistivities, the current-voltage characteristics, and the energy diagrams.

2. Experimental

GeSb₄Te₇, GeSb₂Te₄, and Ge₂Sb₂Te₅ thin films were used for the investigation of electrophysical and thermoelectric properties.

Planar semiconductor structures were fabricated for the investigation of electrophysical characteristics of chalcogenide thin films. Planar structures were fabricated as aluminum electrodes formed on the oxidized silicon substrate. Amorphous chalcogenide thin films were deposited above the interelectrode gap, which were then coated by the protective layer of SiO_x.

Electrophysical characteristics of thin film were investigated on a special stand, designed as a two-electrode circuit on the basis of voltage controlling unit NI6008, and picoammeter KEITHLEY 6486.

Studies of the thermal properties of thin films were carried out on a differential scanning calorimeter DSC-50 (Shimadzu).

The stand for measurements of thermoelectric power includes power supply Agilent E3647A, Multimeter HP 34401A, and Digital Thermometer DTI 1000.

3. Results and discussion

Analysis of the temperature dependences of resistivities of planar structures has shown that for all investigated compounds three ranges with common characteristic features for these dependences can be noticed. For the first range activation character of the conductivity in the amorphous state is observed, abrupt decrease of resistivity due to the phase transition occurs in the second range, and exponential dependences of the resistivity on the temperature, which are typical for chalcogenide films in a crystalline state were revealed in the third range.

Investigation of the current-voltage characteristics of the studied films showed that the I–V curves can be divided into three ranges with different dependencies between current and voltage: for the weak, medium and high electric fields.

The amorphous thin films of investigated materials have the temperature dependences of the resistivities close to exponential in the range from room temperature to 100 °C, which indicates on the activation nature of the conductivity typical for the disordered semiconductors.

Activation energies for the conductivities (σ) of the investigated materials were estimated from the σ versus $1/kT$ plots.

Thermopower coefficients for GST thin films were measured. The value of the Seebeck coefficient for GST225 thin films was 0.5 mV/K. The positive value of the thermopower coefficient indicates on the dominating hole-type conductivity.

Energy band diagrams for thin film materials in the amorphous states were analyzed. Investigation of the spectral characteristics of absorption coefficient for amorphous thin films (GST225, GST124 and GST147) showed the existence of ranges with exponential dependences, which indicates on the presence of the band tails in the mobility gap due to the optical transitions with participation of exponentially distributed states of the band tails. The obtained values of the Urbach parameters indicates that GST124 and GST147 thin films have less disordered structure in comparison with that of GST225.

For modeling of the dependences of σ versus $1/kT$ we used two-channel model proposed by P. Nagels, according to which conductivity is caused by the transfer of charge carriers by the delocalized states of the valence band and localized states of the valence band tail. So, for the description of the model the sum of two exponents characterizing the charge transport by these states was used.

Thus, the temperature dependences of the resistivities and current-voltage characteristics of amorphous thin films on the basis of the materials on the pseudobinary line GeTe-Sb₂Te₃ were investigated. The influence of the variation of composition on the film resistivities in the amorphous and crystalline states was determined. It was shown that the conductivity of the films is formed by the simultaneous contribution of carriers movement by the localized states of the valence band tail, and delocalized state of the valence band.

Problems of the experimental implementation of MTJ

L A Mazaletskiy^{1,2}, A S Rudy^{2,1}, O S Trushin^{2,1}, V V Naumov² and A A Mironenko²

¹ Department of Nanotechnology in Electronics, Yaroslavl State University, Sovetskaya Street 14, Yaroslavl 150003, Russia

² Yaroslavl Branch of the Institute of Physics and Technology, Russian Academy of Sciences, Universitetskaya Street 21, Yaroslavl 150007, Russia

Abstract. The results of experimental studies of MRAM technology based on standard spin-tunnel structures are presented. Basic steps of experimental fabrication of MRAM cell are considered. Experimental samples of MRAM cells with variable lateral sizes are fabricated. Current-voltage characteristics of the tunnel barriers are investigated. Main parameters of tunnel barriers are estimated from comparison of experimental data with the theory.

Magnetic Tunneling Junction (MTJ) is an important element of modern MRAM cell. It is believed that MRAM might be the next generation of computer memory. Therefore optimization of the technology for MTJ fabrication is of very important task. Achievement of high functional characteristics of MTJ requires intensive quality control at different stages of the technological route. In this work we discuss different aspects of quality control during this route. For this purpose we studied experimentally technology of typical MTJ fabrication.

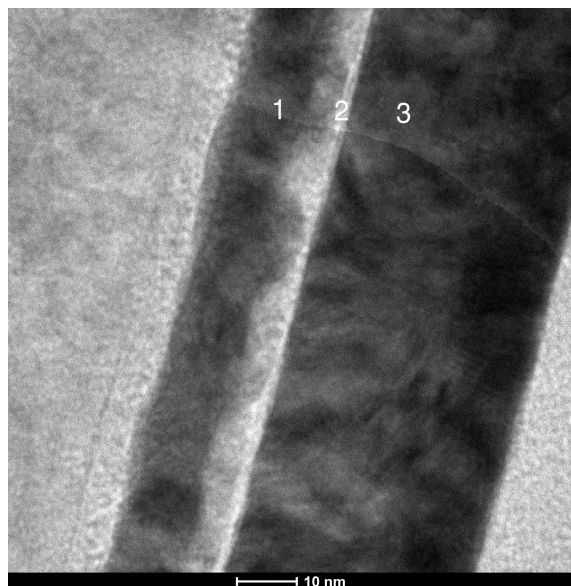


Figure 1. Cross-section of the spin-tunnel structure obtained using TEM. There are main functional layers shown: 1. FREE magnetic layer, 2. TUNNEL dielectric layer, 3. PINNED magnetic layer

Two kinds of spin-tunnel structures: symmetrical - CoFe(10 nm)/Al₂O₃(2 nm)/CoFe(30 nm)/SiO₂(200 nm)/Si and nonsymmetrical - Ta(3 nm)/FeMn(15 nm)/CoFe(5 nm)/Al₂O₃(3 nm)/CoFe(5 nm)/Ta(5 nm)/SiO₂(200 nm)/Si were deposited using RF magnetron sputtering at TETRA SCR-650 (Alcatel). Quality of multilayer structure has been studied using TEM. Cross-section of as deposited thin film structure is shown in figure 1. In this picture we see inhomogeneous interface between layers 1 and 2 due to possible oxygen diffusion.

Control of magnetic properties of those structures was done using Kerr-effect magnetometry. Hysteresis loop of as deposited structure is characterized by presence of typical steps, showing separate switching of two magnetic layers.

On the next stage multilayer structure has been subjected to photo-lithography processing to get MTJ patterning following well documented technology [1]. In this way MTJ junctions with different lateral dimensions (5x15 μm, 7x21 μm, 10x30 μm) were fabricated. Typical voltage-current characteristics of MTJ junctions of variable sizes are shown in figure 2. Results of experimental measurements were compared with the theoretical model [2] and from the approximation two parameters of the structure were estimated: $E_b = 2$ eV (height of energy barrier) and $d = 3.8$ nm (thickness of the barrier) [3]. This value of barrier thickness agrees well with the results of TEM analysis (3-5 nm).

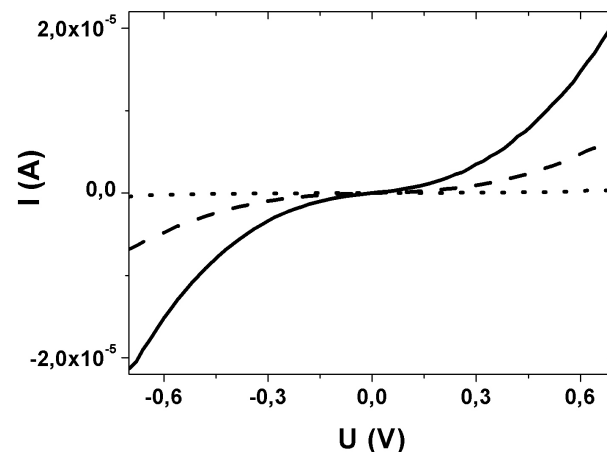


Figure 2. Voltage-Current characteristic of MTJ structure

In conclusion, we have studied typical MTJ fabrication process and developed methodology for quality control at different stages of technological route. These results might be useful for optimization of MRAM technology.

Acknowledgments

This work has been supported by grant of Russian Ministry of Education and Science (Agreement № 14.574.21.0099), program for fundamental research at the division of nanotechnology and informatics of RAS “Elements base for micro- nano-electronics and quantum computers, materials for micro- and nano-electronics, microchips techniques” project 1.11, and Russian Ministry of Education and Science state order 2014/258.

References

- [1] Gallagher W J, Parkin S S P, et.al. 1997 *J. Appl. Phys.* **81** 3741-3746
- [2] Simmons J G 1963 *J. Appl. Phys.* **34** 1793.
- [3] Trushin O S, Naumov V V, Mironenko A A and Mazaletskiy L A 2014 *J. Integral* **77** 10-11

Design and long-term monitoring of DSC/CIGS tandem solar module

M F Vildanova, A B Nikolskaia, S S Kozlov and O I Shevaleevskiy

Solar Photovoltaic Laboratory, Institute of Biochemical Physics, Russian Academy of Sciences, Kosygin St. 4, 119334, Moscow, Russia

Abstract. We report the results of metrological monitoring of the outdoor performance for the developed tandem DSC/CIGS modules. The outdoor test facility was located on the roof of the Institute of Biochemical Physics building in Moscow. The data obtained during the monitoring period has shown better performance characteristics of the designed tandem PV-modules over the conventional modules under real conditions with mostly cloudy weather and low light irradiation intensity.

1. Introduction

In our previous publications we have shown the advantages of the designed tandem dye-sensitized solar cells (TDSCs) for improving the energy conversion efficiency and light absorption characteristics by combining two stacked dye-sensitized solar cells (DSCs) with different sensitizers, absorbing light of the overlapped wavelength ranges [1, 2]. Later M. Graetzel and coworkers developed a new type of TDSC, where DSC cell was combined with a conventional Cu(Ga,In)Se₂ (CIGS) solid state cell with a total conversion efficiency exceeding 15% [3]. However, the reasonable advantage of DSC/CIGS tandem cell may rise not only from the improved performance characteristics, but also of the possibility to utilize both direct and diffuse light, while the average content of scattered irradiation in total irradiation during the year in Central Russia is about 55%.

2. Experimental

Mini DSC solar panels with the field size of 20x20 cm², were designed and fabricated in the Laboratory of Solar Photovoltaics and assembled with a commercial 0,9 m² CIGS panels into tandem DSC/CIGS solar module given in figure 1. We have also proposed a specific configuration of top DSC cells distribution for reaching the optimized effect of solar light utilization under varied wheather conditions.

The outdoor test facility provided a comparative monitoring of both commercial CIGS panels and tandem DSC/CIGS system with optimized configuration of the top mini panels. The PV-modules were grid-connected, thus the generated currents, voltage and power were monitored in parallel tests. A monitoring period was evaluated of 1 year to investigate a behavior under seasonal variations of the operating conditions.

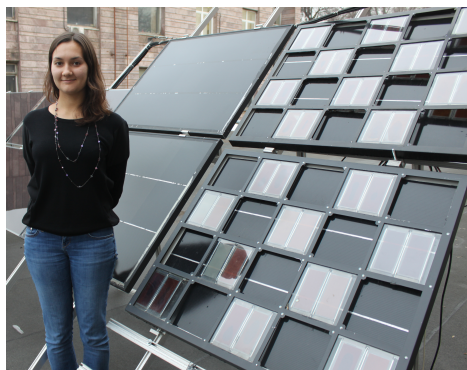


Figure 1. Tandem CIGS/DSC module with optimized top cell configuration and CIGS module (left), installed on the roof of the Institute of Biochemical Physics building.

The data obtained during the monitoring period confirmed better performance characteristics of specially designed tandem PV-modules over CIGS and DSCs when using in the real conditions with mostly cloudy weather and low light irradiation intensity. We have shown the ways how the total energy yield of a tandem system could be even more increased to reach a 50% improvement, compared to the conventional CIGS solar modules.

References

- [1] Chevaleyevski O, Larina L and Lim K S *Proc. of the 3rd World Conf. on Photovoltaic Energy Conversion (Osaka, Japan, 18-18 May 2003)* vol. 1 pp 23-26
- [2] Shevaleyevskiy O 2008 *Pure Appl. Chem.* **80** 2192
- [3] Liska P, Thampi K R, Graetzel M, Bremaud D, Rudmann D, Upadhyaya H M and Tiwari A N 2006 *Appl. Phys. Lett.* **88** 203103

Equation of state for simulation of nanosecond laser ablation aluminium in water and air.

R. Davydov, V. Antonov

Saint Petersburg State Polytechnical University, Saint Petersburg, Russia

Abstract. To analyze the physical processes at high energy densities, when laser is used, an adequate description the thermodynamic property of matter over a broad region of states including the normal conditions and plasma at high pressures and temperatures is required. For describing the thermodynamic properties of metals in nanoparticles production using laser ablation a semi-empirical equation of state model is proposed. To verify this model, an equation of state of aluminum was constructed. Using this equation was calculated ablation depths and crater profile for aluminum and compared with experimental data. Received results are in a good match with experiment.

There is a growing interest in the nanofabrication of materials and their applications in various fields of life and technology, such as electronics, energy generation, health care and storage. A great deal of progress in this field has relied on the use of lasers. Production of nanoparticles can be done in several ways; one of them is laser ablation. Evidence shows that this method is superior to other methods. Indeed, laser ablation in liquids, which consists of the pulverization of a solid target in liquid environment, gives a unique opportunity to solve the toxicity problems. In contrast to chemical nanofabrication methods, laser ablation can be performed in a clean, well-controlled environment, such as deionized water, giving rise to the production of ultrapure nanomaterial. The use of these particles decreases toxicity risks, which is especially important in vivo bio sensing and imaging applications.

To analyze the physical processes at high energy densities, when laser is used, an adequate description of the thermodynamic properties of matter over a broad region of states including the normal conditions and plasma at high pressures and temperatures is required. For that a semi-empirical equation of state model is proposed, based on Thomas–Fermi model with quantum, exchange and oscillation corrections.

To verify this model, an equation of state of aluminum was constructed. Using this equation was calculated ablation depths and crater profile for aluminum in air and water and compared with experimental data. Received results are in a good match with experiment.

Features of nuclear magnetic resonance signals registration in weak magnetic fields for the express - control of biological solutions and liquid medium by nuclear magnetic spectroscopy method

A. Karseev, V. Vologdin, V. Davydov

Saint Petersburg State Polytechnic University, Saint Petersburg, Russia

Abstract. In work, the method nuclear magnetic spectroscopy in weak magnetic fields is considered, and also the features of pilot studies of biological solutions and liquid medium are noted. The condensed medium relaxation constants measurement techniques in weak magnetic fields by method of a nuclear magnetic resonance for the express – control of their state on a research place are offered. Error of such methods doesn't exceed 1%.

Now one of high-precision analytical methods for research of the condensed medium is nuclear magnetic spectroscopy, which based on use of the phenomenon of the nuclear magnetic resonance (NMR) [1 - 3]. The nuclear magnetic resonance spectroscopy method is successfully applied in inorganic chemistry, in physics of a solid body, and in research of biological objects, including a pharmacy [1 - 3]. Unlike the infrared spectroscopy (IS), a NMR spectroscopy allows to receive fuller information about a molecular structure of studied chemical compounds. High resolution of the nuclear magnetic resonance method allows to use it for studying of intermolecular and intramolecular dynamics in liquid medium and to define constants of relaxations and chemical reactions speed.

The greatest practical application received some types of nuclear magnetic: a magnetic resonance on protons (^1H , ^2H), and also on kernels: carbon – 13 (^{13}C), fluorine – 19 (^{19}F), phosphorus – 31 (^{31}P), lithium – 7 (^7Li), sodium – 23 (^{23}Na), boron – 10 (^{10}B), nitrogen – 15 (^{15}N), etc. The only condition of the nuclear magnetic spectroscopy method application is existence in substance of the kernels having the magnetic moment. Now work of the most NMR spectrometers is based on signal registration by pulse methods (spin-echo Hanna and Kara – Pascrell, etc.). Pulse NMR spectrometers have magnetic systems with B_0 more than 7 T (working frequency is more than 300 MHz). In a high resolution NMR spectrometers the size of a magnetic field changes, in this case fields with induction not lower than 11 T are used. For researches of substances with complex structure, especially liquid medium (for example, biological solutions) the BRUKER company developed NMR spectrometer with superconducting magnets which working frequency equals to 1.82 GHz.

But now there is an actual problem which can be solved by means of spectrometry. It is fast and reliable express control of the condensed medium on a place of a sample of the studied substance capture. The reliable information about medium is required before using it for a various researches. The majority of laboratories aren't equipped with spectrometers or analyzers for full research of medium as these devices demand special service. Besides such researches cost rather much so they should be used only for abnormal state samples. This situation arises even more sharply when carrying out environmental monitoring with sampling in "manual", especially in difficult available places around water objects [1, 2]. Also the express – control is very demanded by industrial production of various solutions, liquid and viscous mixes.

Recently began to impose strict requirements to express-control methods. Research shouldn't change a chemical composition and physical structure of substance. It is necessary, for conformation of the deviation in researches of a test substance made by high resolution devices in stationary laboratories (for example, at customs control or quality check of production), and also for establishment of the possible reason which caused this deviation.

One of possible method of the express-control of biological solutions and liquid medium task is a method of nuclear-magnetic spectroscopy, which meets all requirements. In this case the nuclear magnetic resonance spectrometer has to be transferred easily and had a self-contained power supply (batteries). But, to provide mobility of the spectrometer, the signal of a nuclear magnetic resonance needs to be registered in a weak magnetic field ($B_0 \leq 0.1$ T – working frequency not higher than 4.2 MHz), as the main weight and the size of a spectrometer is defined by magnetic system and devices serving it. All this creates a set of features at research.

Use of pulse techniques and change of size of a magnetic field B_0 for registration of spectrum of the studied medium in this case is impossible [1, 2]. Therefore, the new scheme of the weak signals generator with high sensitivity (10^{-6}) was developed for registration of nuclear magnetic resonance signal by means of a modulation technique using the small volume of the studied medium. It is possible to determine constants of a relaxation T_1 and T_2 of the medium by the registered signal of a nuclear magnetic resonance [1 – 3]. By comparing measured T_1 and T_2 with the basic times the environment condition can be defined. As for researches the small volume of the liquid is used, its temperature is determined by the air temperature which is measured by standard devices. It allows to use a small-sized nuclear magnetic resonance spectrometer in the open air, in stationary nuclear magnetic resonances spectrometers measurements are taken at the stabilized temperature.

The other feature is that in a small-sized NMR spectrometer the permanent magnet which field doesn't demand stabilization is used is, but the automatic system of resonance frequency control – for changes of temperature conditions of signal registration is required. As it is required to investigate substances with various number of protons or kernels with the magnetic moments and various relaxation constants, it is necessary to carry out automatic control of all parameters of system with the maximum signal/noise ratio. The accounting of these and other features of nuclear magnetic resonance signal registration in weak magnetic fields allowed to take measurements of relaxation constants at air temperatures from 3 to 40 °C with an error of not higher than 1% in the following ranges: T_1 from 1 ms to 20 s, T_2 from 0.5 ms to 2.0 s.

References

- [1] Davydov V.V., Cheremiskina A.V., Velichko E.N. and Karseev A.Yu. 2014 *Journal of Physics: Conference Series* **541** 012006
- [2] Davydov V.V., Dudkin V.I. and Karseev A.Yu. 2014 *Measurement Techniques* vol 57 issue 8 pp 912 – 918
- [3] Davydov V.V., Velichko E.N., Dudkin V.I. and Karseev A.Yu. 2015 *Instruments and Experimental Techniques* vol 58 No 2 pp 62 – 66

Nanoimprinting and self-arrangement of silver nanoislands on glass surface

I Reduto¹, A Kamenskii², A Baklanov^{2,4}, S Chervinskii^{2,3}, and A Lipovskii^{1,2}

¹ St. Petersburg Academic University, 8/3 Khlopina, St. Petersburg, 194021 Russia

² St. Petersburg State Polytechnical University, 29 Polytechnicheskaya, St. Petersburg, 195251 Russia

³ University of Eastern Finland, P.O.Box 111 FI-80101 Joensuu, Finland

⁴ Ioffe Physical-Technical Institute, 26 Polytechnicheskaya, St. Petersburg, 194021 Russia

Abstract. A novel technique for structuring metal island films and formation of self-arranged groups of metal nanoislands, which is based on polarization and hydrogen annealing of ion-exchanged glasses, has been developed. Quantity and size of nanoislands in small groups can be given in a wide range via varying the mode of polarization and annealing in hydrogen. High temporal stability of the silver nanoislands has been demonstrated. This allows using the structures manufactured using developed technique in chemical and biological sensors of high spatial resolution.

1. Introduction

Silver nanoisland films can be used for luminescence enhancement, in photovoltaics, catalysis, surface-enhanced Raman spectroscopy, etc [1,2]. In case 2D structures are required, like e.g. in spatially selective Raman scattering based sensors, methods allowing precise structuring of metal island films or formation of separate groups of nanoislands should be designed [3]. We have proposed and developed a new approach to fabricate structured silver nanoisland films, that are groups of silver nanoislands, based on polarization and out-diffusion of the metal from a glass substrate [4,5].

2. Experiment

For the structuring of silver nanoisland films we used polarization of soda-lime glass, in which sodium ions were partly replaced with silver ones, with a profiled electrode (Fig. 1a). Applying of 500V voltage to the glass heated up to 250-350°C allowed us profiling the distribution of silver ions in the bulk of the glass (Fig. 1b). Thermal treatment of the polarized samples in hydrogen restored silver ions to neutral atoms, out-diffusion of which from the glass resulted in the formation of metal islands on the unpolarized regions of the glass surface (Fig. 1c). Structured glassy-carbon electrodes were used for the glass polarization (Fig. 2a).

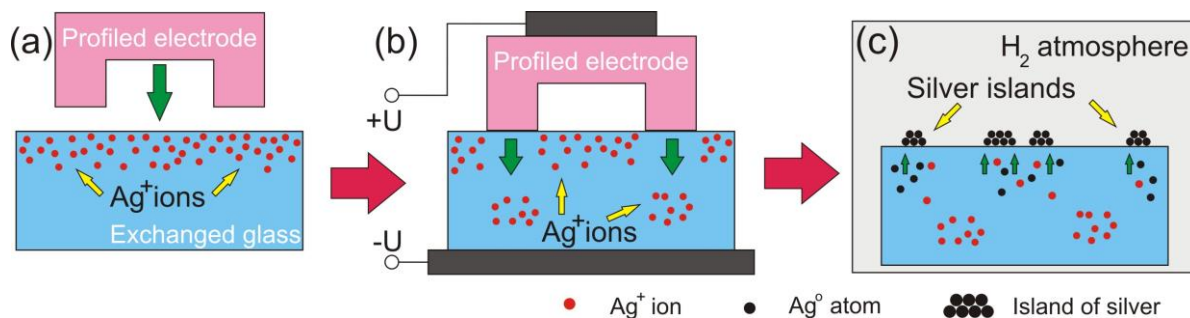


Figure 1. Schematic of metal island films nanostructuring: (a) ion exchanged glass and profiled electrode; (b) polarization of the ion exchanged glass; (c) annealing in hydrogen.

3. Results and discussion

Developed technique provides submicron-scale spatial resolution in fabrication of metal nanoislands and groups of the nanoislands with the specified number and size of islands in the groups. We have obtained the arrays of isolated islands of 200 nm in size and groups of several nanoislands as small as 50-60 nm in diameter while the distance between the islands varied from several to several tens of nanometers. The parameters of the fabricated structures were varied by using different electrodes and through the choice of conditions of polarization and annealing of the ion-exchanged glass samples in hydrogen (Fig. 2b,c,d).

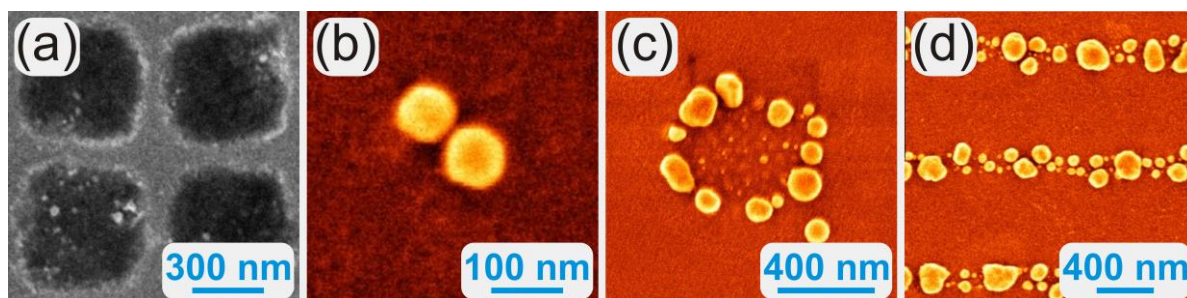


Figure 2. SEM image of one of the electrodes used for glass polarization (a) and SEM images of groups of silver nanoislands grown on the surface of the polarized glass, with different structures of electrode after annealing in hydrogen (b,c,d). The glass slide was ion-exchanged in the bath containing 5 wt.% of AgNO_3 and 95 wt.% of NaNO_3 at 325°C for 20 min, polarized for 60 sec at 300°C using 500V voltage and, finally, 3 sec (b) 60 sec (c) and 5 min (d) processed in hydrogen at 300°C .

References

- [1] Reduto I et al 2014 *J. Phys.: Conf. Ser.* **541** 012073
- [2] Chervinskii S et al 2014 *Nanoscale Research Letters* **9** 398
- [3] Yan B et al 2011 *J. Phys. Chem. C* **115** 24437
- [4] Chervinskii S et al 2013 *J. Appl. Phys.* **114** 224301
- [5] Redkov A et al 2014 *Nanoscale Research Letters* **9** 606

MODIFICATION OF PROPERTIES OF SILICON EPITAXIAL FILMS PROCESSING IN HYDROGEN PLASMA

O YuSmirnova¹ K A Solyanikova² A VErmakov³

¹Senior Lecturer, BSU Faculty of Physics, Minsk, BY

²Production Student, BSU Faculty of Physics, Minsk, BY

³Production Student, BSU Faculty of Physics, Minsk, BY

Abstract. Researches were the epitaxial layer thickness (55.2-64,8) microns is alloyed by phosphorus ($\rho = 1 \text{ Om.cm}$) processed in hydrogen plasma and implanted by protons. Revealed the new type of hydrogen-donor, which is formed without the subsequent heat treatment.

Researches were conducted on structures of Si/P +, processed in hydrogen plasma. Orientation a substrate $\langle 111 \rangle$, thickness is 510-540 microns. The epitaxial layer thickness (55.2-64,8) microns is alloyed by phosphorus ($\rho = 1 \text{ Om.cm}$). Processing of structures in hydrogen plasma was carried out at a temperature of 150 of 0C within 10 hours. Temperature dependences of concentration of electrons in the range of (2-300)K were defined from measurements of effect of the Hall. Ranges of combinational dispersion (KRS) were measured at the room temperature with use of the solid-state laser with the wavelength of 532 nanometers, the power brought to a sample of 2 MW. For comparison also Mo-Si Schottky's diodes implanted by hydrogen ions with energy 300 keV a dose of $1 \cdot 10^{15} \text{ cm}^{-2}$ were used. Distribution profiles the hydrogen-bearing of donors (N-donor) were defined from measurements of volts-faradnykh of characteristics.

In fig. 1 KRS range in initial (1) and the structure processed in N-plasma (2) Si/P + is presented. It is visible that after processing in a range there is a strip near 2140 cm^{-1} caused by oscillatory fashion of Si-H of the communication localized in extended defects. It agrees [2], such complexes are a basis for formation of N-donor of two types in the silicon irradiated with protons at the subsequent heat treatment in the range of (300-400) °C.

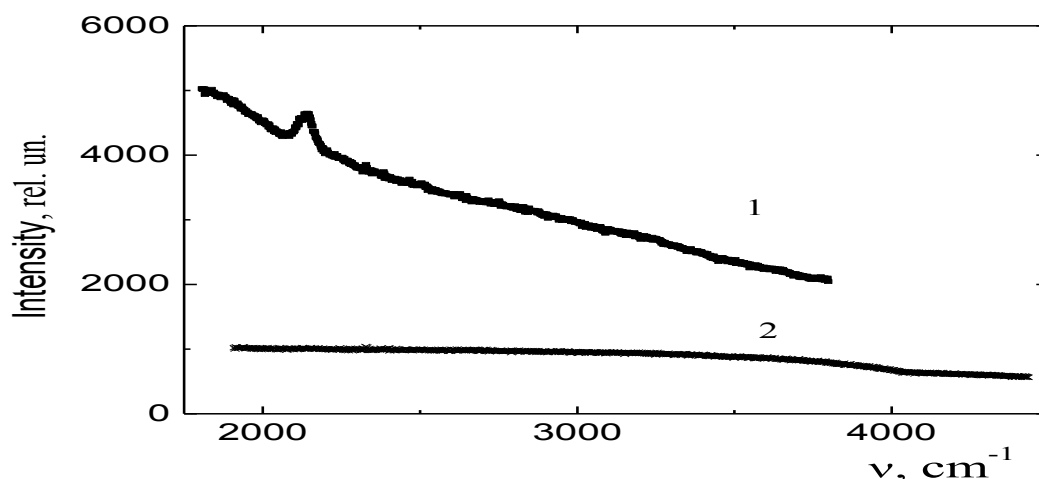


Fig. 1 Ranges of KRS in initial (2) and (1) silicon processed in N-plasma.

In fig. 2 temperature dependences of concentration of electrons are given in an epitaxial layer of Si/P +, processed in N-plasma.

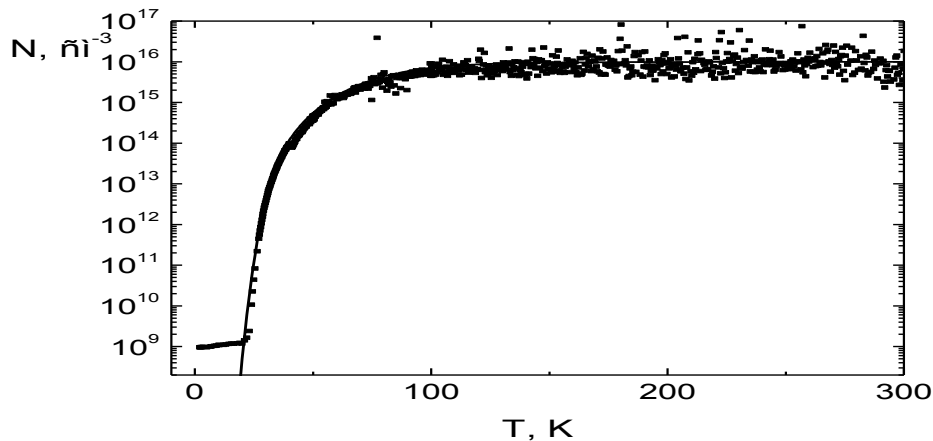


Fig. 2 Temperature dependence of concentration in the silicon processed in N-plasma.

Approximation of these data based on the single-level equation of a neutrality (the continuous line) is carried out at the following parameters – $N_d - N_a = 1 \cdot 10^{13} \text{ cm}^{-3}$ and $\Delta E = 0.045 \text{ eV}$. Concentration of electrons in the field of a starvation of impurity makes $1 \cdot 10^{16} \text{ cm}^{-3}$ that considerably exceeds the size of initial concentration of the alloying impurity of phosphorus $(2-3) \cdot 10^{15} \text{ cm}^{-3}$. On this basis, it is possible to assume that in an epitaxial layer of silicon when processing in plasma N-donor are formed. Besides the received value of energy of ionization is close to that for N-donor of the second type $\Delta E \approx 0.04 \text{ eV}$, found in [2]. However, in [2] it is postulated that a necessary condition of formation of N-donor is existence of high concentration of radiation defects (radiation by high-energy protons) and the subsequent heat treatment. Therefore, we conducted researches isochronous (20 min.) annealing of profiles of distribution of concentration of electrons in Schottky's diodes irradiated with protons with energy 300 keV .

Values of concentration of electrons in the maximum of profiles of distribution coinciding with the size of projective run of protons are presented during isochronous annealing. Excess concentration of electrons, in comparison with the initial level of an alloying, is observed only in the field of localization of the introduced hydrogen. Therefore, it is logical to assume that this effect is caused by formation of N-donor. As some stages of annealing are observed, at least, three types of N-donor are formed. And follows from that the first type of N-donor appears right after radiations without the subsequent heat treatment. In addition, its concentration approximately coincides with that for the N-donor who are formed in silicon after processing in hydrogen plasma. Stages of formation and annealing of N-donor of the second and third type coincide with that, established in [2].

Thus, in the silicon processed in hydrogen plasma and implanted by protons the new type of N-donor, which is formed without the subsequent heat treatment and, apparently, without participation of radiation defects is found.

References

- [1] Leitch A W R, Weber J, Alex V. Formation of hydrogen molecules in crystalline silicon/ Mat.Science and Eng. 1999. Vol.B58. P.6.
- [2] Laven J G, Job R, Schulze H I, Niedernostheide FG. Activation and dissipation of proton-induced donor profiles in silicon/ 2013.Vol.2(9). P.389

Excitation model of cardiac p cells of the cardiac conduction system

M Grigoriev and L Babich

Tomsk Polytechnic University, Tomsk, Russia

Abstract. The article considers elaboration of the mathematical model of cardiac electrical activity which will allow investigating excitation propagation processes at all sites of the cardiac conduction system.

1. The cardiac conduction system

There is a specific, anatomically separated master system in a human and animal heart. It comprises the sinoatrial and atrioventricular nodes, internodal atrial filaments, His bundle with left and right bands and Purkinje fibers. This system is formed by specific muscle cells which possess automatism properties and high (compared to non-specific muscle cells of atria and ventricles) excitation speed. A pulse is generated in P cells of the SA node (first-order pacemaker) which naturally sets the heart rhythm.

Then excitation is propagated to atrial surfaces resulting in their depolarization, following which it goes through internodal pathways to the AV node (second-order pacemaker) and excites (depolarizes) it. Afterwards the pulse is transferred along the His bundle and propagated to the right and left while exciting ventricular muscles [1].

Propagation of an electric pulse (action potential) in the conduction system as well as atrial and ventricular muscles is accompanied by depolarization and repolarization of corresponding cardiac cells. These processes are similar to action potential conduction in nerve cell processes [2] and primarily conditioned by conductance change of sodium, calcium and potassium ion channels in cell membranes under action of supraliminal stimulations.

2. Results of modelling

The equivalent electric diagram for the unit length of a cell membrane site in the cardiac conduction system can be expressed as five parallel branches. Three branches correspond to sodium, calcium and potassium ion channels. Electromotive forces (EMF) in these branches are determined by previous concentrations of corresponding ions inside and outside the cell, and their conductances G_K , G_{Ca} and G_{Na} are complex functions of the membrane potential and time [3]. These functions are different for various conduction system sites due to features of ion channels.

Based on the elaborated mathematical model, the digital model whereon mathematical experiments have been performed is implemented. Cell membrane potentials are selected as initial conditions for voltages.

To excite the cardiac conduction system, voltage of cardiac P cells is modeled with square-wave pulses, amplitudes of which are supraliminal values, and their frequency corresponds to heart rate. Individual results of mathematical experiments are shown on fig. 1.

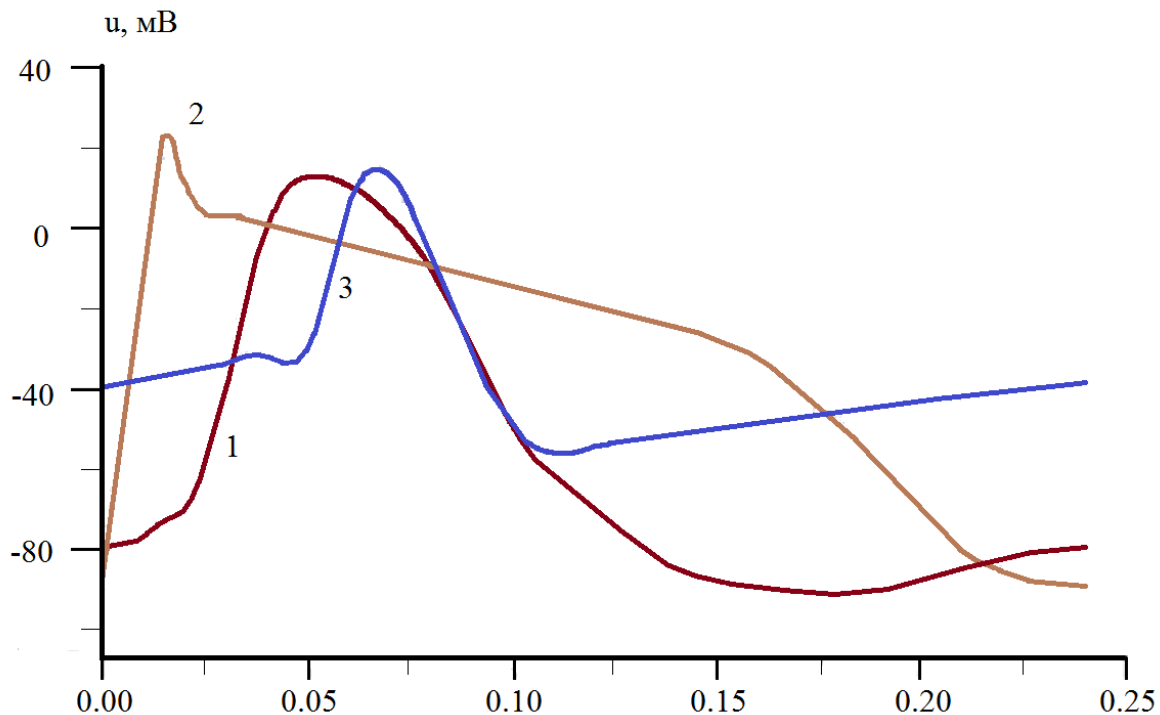


Fig. 1. Action potential curves for different sites of the cardiac conduction system: 1 – AV node site; 2 – His bundle site; 3 – site with P cells

Conclusions

The elaborated mathematical model allows investigating excitation propagation in a human heart and may be the element for generation of complex two-dimensional models as well as three-dimensional models in perspective.

References

- [1] Ganong W. Review of Medical Physiology // Translation from English – L.: BaK, 2002. – P. 784.
- [2] Horyachko V., Drohomiretska Kh., Kotsyuba M. Mathematical model of action potential propagation in neuron axon // VI International Workshop Computational Problems of Electrical Engineering. Proceedings. – Zakopane, Poland, September 1–4, 2004. – P. 137–138.
- [3] Coraboeuf E. Ionic basis of electrical activity in cardiac tissues // J. Physiol. – 1978. – Vol. 234(2). – P. H101-H116.

Two-dimensional porous anodic alumina for optoelectronics and photocatalytic application

L.S. Khoroshko, N.V. Gaponenko

Belarusian State University of Informatics and Radioelectronics
P. Browki Str., 6 Minsk 220013 Belarus

Abstract. Fabrication of porous anodic alumina film structures using anodizing, sol-gel synthesis and photolithography is reported. The structures receive interest as planar waveguides due to strong photoluminescence of the embedded trivalent lanthanides. Mesoporous structures comprising sol-gel derived titania in porous anodic alumina play a role of effective catalyst for water purification.

Porous anodic alumina is a unique honeycomb mesoscopic structure with open pore channels at the center of each cell; the cells are packed in honeycomb structure [1]. Such features render PAA as an appropriate structure for synthesis of diverse types of optically active species within the pore channels, using sol-gel technology [2–5]. The regularity of the open pore channels, the ability to tune the pore diameters in nanometer range, the reproducible growth and regular distribution of sol-gel derived films of the desired chemical composition in the tailored pores allow the fabrication of multifunctional film structures for diverse applications, like light-emitting multicolour images, X-ray converters, and mesoporous film catalyst. We investigate application of photolithography with electrochemistry and sol-gel synthesis with the aim of development planar waveguides doped with trivalent lanthanides and etched groves for patterning the thin film catalyst.

The use of electrochemical anodizing for fabrication of porous anodic alumina with the pore size not exceeding 50 nm, sol-gel synthesis and photolithography allow for fabrication of the film structures titania xerogel/porous anodic alumina in accordance with the photomask pattern without deposition of a metal mask (figure 1). Our recent results revealed that spin-on deposition of 8 layers of titania xerogels forms the smooth coating onto porous anodic alumina films 20–50 micron thick when size of the pores is not exceed 50 nm, making it possible further deposition of photomask and etching the groves. Presence of etched groves several mm in width enhance the photocatalytic activity of the structure titania xerogel/porous anodic alumina with respect of photodegradation of organic dye in water by a factor of 2.

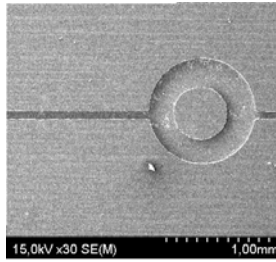


Figure 1. SEM image of the structure titania xerogel/PAA 20 micron thick, imitating the hollow waveguide connected to cylindrical microresonator. The structure was obtained using sequential fabrication of porous anodic alumina, deposition of titania xerogel, photolithography and chemical etching.

One of the reason of enhanced photoluminescence of lanthanides from these structures is multiple scattering of exciting light and anisotropy of photonic density of states in 2D PAA [6].

Taking into account strong photoluminescence of lanthanides from the structures xerogel/PAA and possibility of its photolithographic patterning, our current investigations relate to fabrication of planar optical amplifier doped with light-emitting lanthanides.

References

- [1] Thompson GE, Furneaux RC, Wood GC, Richardson JA, Goode JS 1978 *Nature* 272(5652) 433
- [2] Gaponenko NV 2001 *Synth. Met.* 124(1) 125
- [3] Gaponenko NV, Molchan IS, Thompson GE, Lambertini V, Repetto P 2003 *J. SID* 11(1) 27
- [4] Gaponenko NV, Kortov VS, Rudenko MV, Pustovarov VA, Zvonarev SV, Slesarev AI, Molchan IS, Thompson GE, Khoroshko LS, Prislopskii SYa 2012 *J. Appl. Phys.* 111 103101
- [5] Gaponenko NV, Kortov VS, Smirnova NP, Orekhovskaya TI, Nikolaenko IA, Pustovarov VA, Zvonarev SV, Slesarev AI, Linnik OP, Zhukovskii MA, Borisenko VE 2012 *Microelectron. Eng.* 90 131
- [6] Lutich AA, Gaponenko SV, Gaponenko NV, Molchan IS, Sokol VA and Parkhutik V 2004 *Nano Lett.* 4(9) 1755

Mathematical modeling of sedimentation process of nanoparticles in gradient medium

S I Ezhenkova, S A Chivilikhin

ITMO University, Kronverkskiy pr. 49, St.Petersburg 197101, Russian Federation

Abstract. We are building a mathematical model describing the motion of a light ray in a medium with a varying index of refraction formed by particles settling in a liquid. We have received a size distribution of particles settling in a liquid; calculated a trajectory of the light ray in the medium; investigated the dependence of the light ray's trajectory on the initial particles concentration; received solution of the equation of convective diffusion for nanoparticles.

In this paper we consider the gradient medium formed by particles settling in a liquid. For calculating the route of ray it uses the Fermat principle. Sedimentation process of nanoparticles is investigated in detail in [1,2], diffusion is investigated in [3].

Purpose of work is construct a mathematical model describing the sedimentation process of nanoparticles in the liquid and calculating the trajectory of ray's motion.

As object of research we take receptacle with liquid, which contains particles of different sizes. More heavy particles settle to the bottom, a lighter particles stay at the surface, and thus it is distributed over the depth and creating a gradient medium. A light ray falls on it, and we observe subsequent behavior of it.

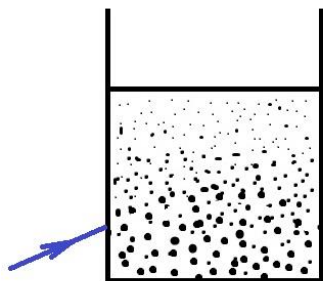


Fig.1. The object of modeling.

To find solution of the light ray's trajectory equation we consider time during light passages the finite size part of the way. According to Fermat's principle ray have to pass way with zero integral variation, and the function realizing the extremum of the integral have to satisfy the Euler equation.

As a result, we obtain the integral form of the ray's trajectory equation:

$$x = \int_0^z \frac{dz'}{\sqrt{z_0'^2 + 2(\hat{n}(z') - \hat{n}(0))}}, \quad (1)$$

where $\hat{n}(z')$ – the relative deviation of the refractive index.

Next, we consider a particles settling in a liquid with constant velocity. At first the ray's move in a liquid has been calculated without particle diffusion. We calculated radius of the particle, which had had depth z by the time t , then calculated the specific volume (volume of particles per unit volume) and the calculated perturbation of the refractive index, which has the following form:

$$\hat{n}(z) = \left(\frac{n_p}{n_0} - 1 \right) V_p(z, t), \quad (2)$$

where n_0 – refractive index at the initial time, n_p – refractive index medium formed settling particles.

We have got the trajectory chart of the light ray which indicates the ray's move and its deviation from more dense part of the medium:

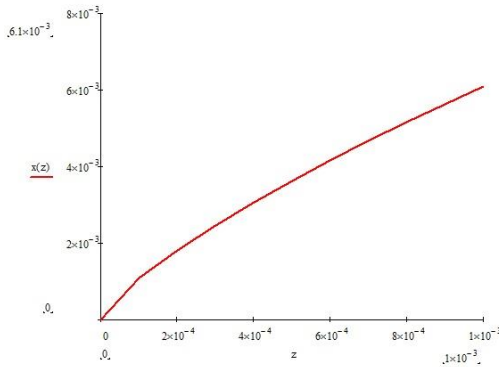


Fig.2. The trajectory of the light ray.

Currently, we investigated the ray's move in a liquid considering the Brownian diffusion of particles.

For convective diffusion equation

$$\frac{\partial f}{\partial t} + v \frac{\partial f}{\partial x} = D(R) \frac{\partial^2 f}{\partial x^2}, \quad (3)$$

solution was obtained (4), and, at the moment, is investigated analytically:

$$f(x, t) = f_0 - 2vf_0 \int_0^t \left[\frac{1}{\sqrt{\pi t'}} e^{-\frac{v^2 \sqrt{t'}}{4D} - \frac{x^2}{4Dt'}} - \frac{v}{\sqrt{D}} e^{-\frac{xv}{2D}} \operatorname{Erfc} \left(\frac{x}{2\sqrt{Dt'}} + \frac{v\sqrt{t'}}{2\sqrt{D}} \right) \right] dt', \quad (4)$$

where v – velocity of sedimentation, f_0 – cumulative distribution function at the initial time, D – diffusion, x – coordinate, t – time of sedimentation.

References

- [1] Suvankar Gangulya, Suman Chakraborty Sedimentation of nanoparticles in nanoscale colloidal suspensions. *Physics Letters A* **375** (2011) 2394–2399 .
- [2] Borries Demeler, Tich-Lam Nguyen, Gary E. Gorbet, Virgil Schirf, Emre H. Brookes, Paul Mulvaney, Ala'a O. El-Ballouli, Jun Pan, Osman M. Bakr, Aysha K. Demeler, Blanca I. Hernandez Uribe, Nabraj Bhattarai, and Robert L. Whetten Characterization of Size, Anisotropy, and Density Heterogeneity of Nanoparticles by Sedimentation Velocity. *Anal. Chem.* 2014, **86**, 7688–7695.
- [3]] Eun Chul Cho, Qiang Zhang, Younan Xia The effect of sedimentation and diffusion on cellular uptake of gold nanoparticles. DOI: 10.1038/NNANO.2011.58.
- [4] Southwell W.H. Ray Tracing in Gradient-Index Media. *J. Opt. Soc. Am.* -1982.

Study of micro- and nanomechanical oscillators based on crystalline and amorphous C and W nanowhiskers

S.Yu. Lukashenko¹, V. V. Lysak¹, I.D. Sapozhnikov³, I.S. Mukhin^{1,2},
A.O.Golubok^{1,3}

1 Department of material science and nanotechnology, ITMO University, 197101 Kronverkskiy pr., 49, Saint-Petersburg, Russian Federation

2 Laboratory of renewable energy source, St Petersburg Academic University RAS, 194021 Khlopina, 8/3, Saint-Petersburg, Russian Federation

3 Nanotechnology department, Institute of Analytical Instrumentation RAS, 198095 Ivan Chernykh, 31-33, Saint-Petersburg, Russian Federation

Abstract. Nanomechanical oscillators (NMO) on the basis of crystal W nanowhiskers (WNW) and amorphous C nanowhiskers (CNW) localized on the summits of W needles are created and studied. Trajectories of single and coupled resonant oscillations are visualized, resonant frequencies and quality factor of NMO are determined. Simulation of trajectories of coupled resonant oscillations of NMO is conducted. Results of calculations qualitatively correspond to the experimental data.

1. Introduction

Rapid development of nanotechnology methods in recent years makes nanomechanical oscillators (NMO) with small mass, high resonant frequency and high quality factor relatively accessible for both scientific research and practical applications. On the one hand, interest in NMO has purely scientific motivation given the possibility to research a fundamental physical problem concerning transition of a macroscopic object to the quantum state [1]. On the other hand, it is possible, using NMO, to conduct extremely-precise measurements of inertial mass, including determination of mass of single atoms and molecules [2], that being very attractive from the application-oriented viewpoint. Most studies in the field of NMO are usually dedicated to the research of oscillations of single micro- and nanoplates, nanobeams or nanowhiskers (NW) which are fixed on one or two ends. In this study we have researched oscillations of single amorphous C nanowhiskers (CNW) and crystal W micro- and nanowhiskers (WMW and WNW), and oscillations of more complex nanostructures which consist of CNW fixed on the summit of crystal WMW or WNW. These configurations may be considered as systems of coupled oscillators. Generally speaking, their behavior should differ from the behavior of single oscillators. To the best of our knowledge, such system of coupled NMOs has not been studied experimentally before.

2. Experimental setup

For the convenience of conducting research CNW are localized on the summits of W needles produced from polycrystal W wire with base diameter 150 μm with the use of method of electrochemical etching in 5% solution KOH. By changing parameters of the process of

electrochemical etching needles of gradual parabolic or sharp hyperbolic shape are created. Upper part of a needle of hyperbolic shape might have different geometrical dimensions depending on the etching modes and in fact is a WMW with cross section of around 4 μm and length of (400-600) μm or WNW with cross section of around 100 nm and length of (1-5) μm . Arrow-headed W wire is fixed on electromechanical transducer in the shape of piezoceramic tube which is located in the working chamber of SEM. Growth of CNW on the summit of W needle was conducted directly in the chamber of SEM with the use of focused electron beam [3]. Growth of CNW is conducted both on the needles of gradual parabolic shape and on the needles with WMW and WNW on the summits. Depending on the parameters of growth it was possible to create CNW of diameter (50-100) nm and length (0,5-3) μm . Structure of CNW and WNW is studied with the use of method of electron diffraction in the transmission electron microscope (TEM). It was established that CNW are in amorphous state, and WNW are in crystal state. In order to excite oscillations of NMO, oscillations of electromechanical transducer to which voltage from HF generator with frequency of 0 to 100 MHz is applied, is used. Excitation of NMO also is conducted by alternating electric field. In order to achieve that, second metal needle, to which alternating electric voltage from HF generator is applied, is made to approach CNW. Resonant frequencies of oscillations of NMO are determined through visualization of maximal amplitudes of oscillations with the use of SEM. On low frequencies, resonant oscillations of hard W wire are observed; on high frequencies, oscillations of NMO are observed.

3. Results and Discussions

Transverse oscillations of WMW, WNW and CNW are visualized in our experiments. Resonant oscillations of WMW are observed in three resonant modes with frequencies of around 30 kHz, 90 kHz, and 200 kHz, respectively. We have also managed to excite and visualize rotational mode of oscillations of WMW with frequency of around 100 kHz. Quality factor of such WMW was around 150. Frequencies of oscillations of first resonant modes of CNW and WNW are within (3 – 10) MHz depending on their geometrical dimensions. Quality factor of NMO is around 80. Coupled oscillations of NMO in the form of CNW grown on the summit of WNW are also visualized. In this case on the frequencies near the frequency of natural resonance of CNW the coupled resonance is observed as simultaneously increasing the amplitude of oscillations of both summit of WNW and summit of CNW. As far as the frequency is increased several such coupled resonances is observed. It should be noted that, on a trajectory of oscillations of CNW, “bundle” with zero amplitude of oscillations is observed. Location of that “bundle” changed with the change of frequency of oscillations. It was observed that quality of coupled resonant oscillations decreased to 30. Simulation of trajectory of oscillations of NMO conducted on the basis of coupled WNW and CNW is qualitatively congruent with the results of experiment.

4. Conclusions

Mechanical micro- and nanooscillators in the form of crystal and amorphous whiskers localized on the summits of metal needles are created and studied. Resonant frequencies and quality factor of single and coupled micro- and nanooscillators is measured. Revealed peculiarities in the trajectory of coupled resonant oscillations of nanooscillators on the basis of nanowhiskers qualitatively correspond to the results of simulation. Work carried out with the support of the leading universities of the Russian Federation (grant 074-U01), the Russian Foundation for Basic Research (14-02-31703 mol_a).

5. References

- [1] O’Connell A Hofheinz M 2010 *Nature* vol 464 pp 697-703
- [2] Jensen K Kwanpyo K 2008 *Nature Nanotech.* vol 3 pp 533-537
- [3] Fadeev I Zhukov M Dubrovskii V Golubok A 2015 *Ultramicroscopy* vol 148 pp 151-157

Reflectance anisotropy spectroscopy of plasmonic nanocluster arrays covering semiconductor surfaces

A V Korotchenkov^{1,2,3} and V A Kosobukin²

¹ St Petersburg Academic University of the Russian Academy of Sciences,
194021 Saint-Petersburg, Russia

² Ioffe Physical Technical Institute of the Russian Academy of Sciences,
194021 Saint-Petersburg, Russia

Abstract. The reflectance anisotropy of metal nanoparticles covering a semiconductor surface is theoretically studied. A model of ellipsoidal particles occupying a rectangular lattice is introduced to calculate the effective polarizability of dipole plasmons with account of their images. The theory explains the resonant anisotropy reflectance spectra observed for In nanoclusters on InAs(001) crystal surface. The plasmonic anisotropy parameters of both nanoparticles and lattice are estimated from the measured spectra.

Reflectance anisotropy spectroscopy (RAS) is a differential optical technique applied to study anisotropic surfaces of cubic semiconductors. It measures the differential signal at normal incidence

$$\frac{\Delta R}{R} = 2 \frac{R_x - R_y}{R_x + R_y} \quad (1)$$

depending on the energy of photons. The reflectivities R_x and R_y of linearly polarized light waves are measured along orthogonal in-surface axes x and y , being crystallographic $[110]$ and $[1\bar{1}0]$ axes for (001) crystal surface. Then, weak RAS signals ($\Delta R/R \sim 10^{-3}$) from semiconductor surfaces provide information on its atomic structure anisotropy [1].

When applied to a surface covered with metal nanoparticles, RAS demonstrates the plasmonic features disclosing the inherent anisotropy of nanocluster arrays [2]. We discuss consistency of the theory of plasmonic RAS with the experimental data for In nanoparticles on InAs(100) from [2]. It is essential that plasmonic RAS reveals a weak anisotropy of metal nanocluster arrays, which is hardly registered by the conventional image diagnostics.

Consider an interface between isotropic media whose permittivities are $\varepsilon_1 = \text{const}$ and ε_2 (semiconductor). A lattice of metal nanoparticles is located outside the semiconductor, at a distance $h \ll c/\omega$ from its surface. The reflectance of α -polarized normally incident light is

$$R_\alpha = \left| r^{(0)} + \Delta r_\alpha \right|^2, \quad (2)$$

where $r^{(0)}$ is the reflectivity from the interface without nanoparticles. The contribution

$$\Delta r_\alpha = \frac{2\pi i}{\sqrt{\varepsilon_1}} \frac{\omega}{c} \frac{\chi_\alpha}{A_x A_y} \left[\exp(-i\Phi) + r^{(0)} \exp(i\Phi) \right]^2, \quad (3)$$

where A_x and A_y are the periods of rectangular lattice and $\Phi = \sqrt{\varepsilon_1} \omega h / c$, is caused by nanoparticles, whose α -th component of effective plasmonic dipole polarizability is

$$\chi_\alpha = \left[\frac{1}{\chi_\alpha^{(0)}} - \frac{1}{\varepsilon_1} \left(S_\alpha^d + \frac{\varepsilon_1 - \varepsilon_2}{\varepsilon_1 + \varepsilon_2} S_\alpha^i \right) \right]^{-1}. \quad (4)$$

The polarizability of a single ellipsoidal particle with permittivity $\varepsilon(\omega)$ and depolarization factor N_α along semi-axes a_α is

$$\chi_\alpha^{(0)} = \frac{a_x a_y a_z}{3} \frac{\varepsilon - \varepsilon_1}{(\varepsilon - \varepsilon_1) N_\alpha + \varepsilon_1}. \quad (5)$$

The other term in (4) contains the sums over the lattice sites for the in-layer dipole S_α^d and image-dipole S_α^i interactions which define the local-field effects [3].

Theoretical spectra $\Delta R/R$ are calculated from Eq. (1) on substituting Eqs. (2) - (5). In the model of dipole oscillators, the plasmonic polarizability (4) is expressed as follows

$$\frac{\omega}{c} \frac{\chi_\alpha}{A_x A_y} \approx \frac{\Omega^2}{\omega_\alpha^2 - \omega^2 - i\omega\Gamma}. \quad (6)$$

This form can be applied to fit the measured spectra [2] and estimate the anisotropy of frequencies ω_x and ω_y which are interpreted using Eq. (4) for the in-surface plasmons of ellipsoidal particle arrays. To fit the experimental RAS data, the semi-axes of ellipsoids and the periods of lattice are used as variable anisotropy parameters.

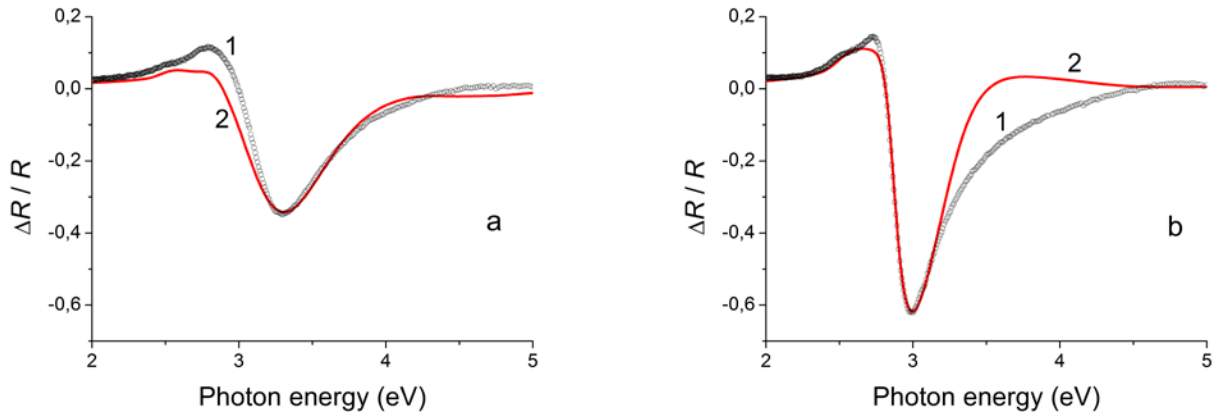


Figure 1. Plasmonic RAS data for two samples (a) and (b) of In nanoparticles covering InAs(001) surface. 1 – measured spectra from [2] and 2 – the spectra fitted within our theory.

The results of fitting are presented in Figs. 1(a) and 1(b) for two different samples In/InAs(001). For nearly spheroidal nanoparticles with $(a_x + a_y)/2a_z \approx 0.5$, the difference of resonant energies

$\hbar(\omega_x - \omega_y) = 0.19$ eV is obtained for Fig. 1(a) and $\hbar(\omega_x - \omega_y) = 0.08$ eV for Fig. 1(b). Using the fitted frequencies, the parameters $(a_x - a_y)/(a_x + a_y)$ of in-plane particle-shape anisotropy for the two samples is estimated to be a few per cent. Close estimation is obtained for the parameters $(A_x - A_y)/(A_x + A_y)$ being a measure of lattice (structure) anisotropy, cf. [2].

To conclude, we have demonstrated the ability of plasmonic resonant reflectance anisotropy spectroscopy to reveal anisotropy of metal nanocluster arrays. The mere fact of observing the RAS signal from indium nanoclusters formed on InAs surface is an implicit indication that a macroscopic anisotropy is present in the arrays. The proposed model allows us to estimate separately the related intra- and interparticle geometrical anisotropies. Therefore, the plasmonic RAS could be a tool for disclosing anisotropy of metal nanocluster arrays and optical characterization of them.

- [1] Weightman P, Martin D S, Cole R J, Farrel T, 2005 *Rep. Prog. Phys.* **68** 1251-1341
- [2] Berkovits V L, Kosobukin V A, Ulin V P, Gordeeva A B and Petrov V N 2013 *JETP Lett.* **98** 614-618
- [3] Kosobukin V A, 2012 *Phys. Solid State* **54** 2471-2480

Modeling, creation and study of highly efficient solar cells based on nitride nanowhiskers arrays grown on Si substrates

D A Kudryashov¹, A M Mozharov¹, I S Mukhin¹, G E Cirlin¹, J C Harmand² and M Tchernysheva²

¹ St.Petersburg Academic University, Khlopina 8/3, 194021, St. Petersburg, Russia

² CNRS-LPN, Route de Nozay, Marcoussis, 91460 France

Abstract. The tandem solar cell with a heterojunction “nanowires GaN – Si substrate” and high antireflection properties was grown by molecular beam epitaxy (MBE). For an increasing its efficiency it was simulated with a finite difference method. The carried out simulation showed that a maximum efficiency and a mean optical reflectance should be 13% and 4%, respectively.

1. Introduction

Highly efficient solar cells development and continuous search of new way for efficiency improvement are of interest for last few decades. Vertically aligned arrays of 1D nanostructures (nanowhiskers) due to their unusual properties are potential building block for optoelectronic devices, in particular solar cells. Arrays of nitride nanowhiskers (GaN, AlGaN, InGaN) grown by means of molecular beam epitaxy on silicon crystalline substrates are characterized with high crystalline quality and have low optical reflectance over the whole spectral range. An integrating of A_3B_5 and Si semiconductor technologies is a new priority research way of modern photovoltaic.

2. Modelling and Experiment

A photovoltaic cell based on Si substrate and arrays of n-GaN whiskers was simulated with finite difference method. It's showed that GaN whiskers / Si substrate interface formed heterojunction with high efficiency of separation of electron-hole pairs photogenerated in the substrate. The maximum of solar cell performance according to simulation was about 13%. The simulation showed that vertically aligned GaN whisker arrays with ITO as a top transparent contact have high antireflection properties and mean reflectance is about 4% over the whole spectral range.

The solar cell with n-type GaN whiskers was produced on n-type silicon substrate by molecular beam epitaxy. AlN porous thin film with 2-3 nm thickness was preliminary grown on a silicon substrate as a forming mask for GaN whiskers growth. Also we can consider this AlN film as a wideband window for charge carriers excited in the silicon substrate.

The top transparent contact of the solar cell was created from an ITO film with a 100 nm thickness by magnetron sputtering. Before this a PMMA layer was put on grown structure with a half whisker thickness. Before ITO sputtering the PMMA layer on a top of whiskers was removed by O_2 plasma.

The bottom contact was created from a silver paint. Produced prototype of a solar cell had efficiency about 2.4% and high antireflection properties.

3. Discussion

It was proposed that during growth GaN whiskers and AlN film were doped by Si atoms from the substrate while Si substrate was doped by metal atoms (Ga and Al). Therefore bases of whiskers and the AlN film had strongly n-type but silicon substrate had i-type near heterointerface. Existence of the potential barrier of the AlN film and i-type of silicon surface lead to a good separation of electrons in a conduction band and high solar cell open circuit voltage value for n-n junction (0.35 V). It was proposed that a main transport mechanism through the AlN film is tunneling and it limits the solar cell short-circuit current.

4. Summary

The solar cell with n-GaN/n-Si heterojunction was grown by MBE technique and it showed an efficiency at 2.4%. Simulation showed a maximum efficiency at 13% for n-GaN/p-Si heterojunction solar cell.

Conducted research demonstrates potential of creating of tandem solar cells with an increased efficiency based on planar A_3B_5 heterojunctional structures and whisker arrays matching to silicon substrate lattice parameters.

References

- [1] Y B Tang, Z H Chen, H S Song, C S Lee, H T Cong, H M Cheng, W J Zhang, I Bello and S T Lee 2008 *Nano Letters* **8-12** 4191
- [2] G E Cirlin, A D Bouravleuv, I P Soshnikov, Yu B Samsonenko, V G Dubrovskii, E M Arakcheeva, E M Tanklevskaya and P Werner 2010 *Nanoscale Research Letters* **5-2** 360
- [3] G E Cirlin, V G Dubrovskii, Yu B Samsonenko, A D Bouravleuv, K Durose, Y Y Proskuryakov, Budhikar Mendes, L Bowen, M A Kaliteevski, R A Abram and Dagou Zeze 2010 *Physical review B* **82-3** 035302

Research of materials for porous matrices in sol-gel systems based on silicon dioxide and metallic oxides

E.V. Maraeva¹, A.A. Bobkov¹, V.Ph. Markov², V.A. Moshnikov^{1,3}, S.S. Nalimova¹, L.V. Shaidadrov², A.V. Tretyakov²

¹ Saint Petersburg Electrotechnical University "LETI", ul. Prof. Popova, 5, 197376, Saint Petersburg, Russia

² Ural Federal University, ul. Mira, 19, 620002, Ekaterinburg, Russia

³ Peter the Great St.Petersburg Polytechnic University, 29, Polytechnicheskaya st., 195251, St.Petersburg, Russia

Abstract. In this study silicon dioxide – stannic oxide and silicon dioxide – zinc nanomaterials oxide were obtained through sol-gel technology. The results of nitrogen thermal desorption measurements, atomic force microscopy measurements and particle sizes measurements are discussed.

1. 1. Introduction

Currently, the “quantum dots – poromeric inert matrices” hybrid systems have become broadly used. The advantage of quantum dots in porous inert matrices is stability of sizes; in systems with quantum dots the density of radiating centers can be significantly higher than that in polycrystalline materials. Porous matrices must be optically and dielectrically transparent when photoluminescence particles are introduced into them. To develop electroluminescent structures, it is necessary to form highly-conductive wide-gap layers. In this respect the materials of sol-gel systems based on silicon dioxide and metallic oxides are most promising.

The purpose of this study is researching different stages of sol-gel synthesis of materials in silicon dioxide – stannic oxide and silicon dioxide – zinc oxide systems [1-4].

2. Experiment

In this study an inorganic salt $Zn(NO_3)_2 \cdot 6H_2O$ as the precursor of zinc oxide, $SnCl_2 \cdot 2H_2O$ as the precursor of stannic dioxide and tetraethoxysilane as the precursor of silicon dioxide were selected. To control properties of the synthesized nanomaterial surface, the nitrogen thermal desorption and atomic force microscopy were used.

AFM experiments were performed using NTEGRA-Therma nanolaboratory (NT-MDT, Zelenograd, Russia). Commercial etched silicon tips NSG 01 (NT-MDT, Zelenograd, Russia) with typical resonance frequency of 150 kHz were used as AFM probes. Specific surface area measurements were made using Sorbi № 4.1 (CJSC «META», Novosibirsk, Russia) that realizes physical adsorption of noble gas by the sample to be studied [5]. Sizes of particles in the solution were

analyzed with the Photocor Compact meter in the laboratory of Ural Federal University named after the first President of Russia B.N.Yeltsin.

3. Results and discussion

In the course of this study the samples of xerogels in the “silicon dioxide – stannic oxide” and “silicon dioxide – zinc oxide” systems were obtained, and specific influence of sol-gel synthesis conditions on the size of particles in sol solutions, on the specific surface area and morphology of samples surface was investigated. As an example figure 1 presents AFM images of 85% SiO₂ – 15% SnO₂ layer.

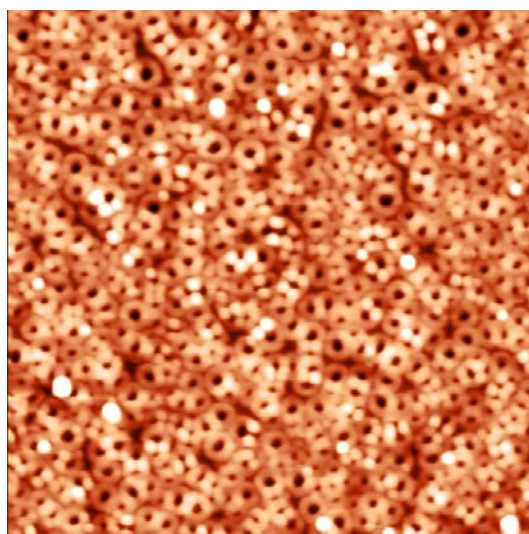


Figure 1. AFM images of 85% SiO₂ – 15% SnO₂ layer (scan size area is 10 * 10 μm)

It was determined that for the “silicon dioxide – stannic oxide” sol-gel system the smallest particles (10 nm) in solutions were observed when components ratio was 90% SnO₂ – 10% SiO₂. In case of “silicon dioxide – zinc oxide” system, the dependence of the size of particles in solution on sol aging time was analyzed. The results obtained allow for optimizing the conditions of production of xerogels with required parameters of pore structure.

Acknowledgments

The reported study was supported by project № NK 14-02-31680\14 (RFFI), by Russian Ministry of Education state task № 16.2112.2014 / K and also by program 211 of Russian Federation Government № 02. A 03.21.0006.

References

- [1] Maximov A I, Moshnikov V A, Tairov Yu M and Shilova O A 2008 *Basics of sol-gel technology of nanocomposites* (SPb: Elmor)
- [2] Gracheva I E, Moshnikov V A, Karpova S S, Maraeva E V 2011 *Journal of Physics: Conference Series* **291** 012017
- [3] Gracheva E I, Moshnikov V A, Maraeva E V, Karpova S S, Alexandrova O A, Alekseyev N I, Kuznetsov V V, Olchowik G, Semenov K N, Startseva A V, Sitnikov A V, Olchowik J M 2012 *Journal of Non-Crystalline Solids* **358** 433
- [4] Moshnikov V A, Gracheva I E, Kuznezov V V, Maximov A I, Karpova S S and Ponomareva A A 2010 *Journal of Non-Crystalline Solids* **356** 2020
- [5] Lenshin A S, Maraeva E V 2011 *Izvestiya of Saint-Petersburg Electrotechnical University* **6** 9

Investigation of experimental field emission data and classical theory conformity in real-time mode

P A Romanov¹, S V Filippov^{1,2}, E O Popov^{1,2} and A G Kolosko^{1,3}

¹A.F. Ioffe Physico-Technical Institute of Russian Academy of Sciences, ul. Polytechnitscheskaya 26, St.-Petersburg, 194021, Russia

²St. Petersburg State Polytechnical University, ul. Polytechnitscheskaya 29, St.-Petersburg, 195251, Russia

³The Bonch-Bruевич Saint-Petersburg State University of Telecommunications, pr. Bolshevikov 22, St.-Petersburg, 193232, Russia

Abstract An experimental set and a Labview-based software for real-time research of field emission were developed. The current-voltage characteristics (IVC) of field emitter based on carbon nanotube/polymer nanocomposite were received and analyzed using simple quantitative test for lack of classical field emission theory. The optimum sector of IVC was found to calculate characterization parameters of polymeric nanocomposite emission.

Multi-tip field emitters (MFE) have actual and potential uses as electron sources [1]. Investigation of its IVC is more important for MFE technology development. IVC can be converted into Fowler-Nordheim coordinates (FN-plot) and analysed using classical Fowler-Nordheim theory, then useful characterization parameters can be extracted, notably a typical field enhancement factor and a formal emission area. But if the emitter behaviour is non-classical, extracted numerical values may be spurious ones [2].

Our group developed a technique that opened up new opportunities for basic research of the behaviour of modern MFE. The technique contains original methods for online processing of IVC, including construction of a slope-interception diagram (SK-diagram), and extraction of microscopic emission parameters (field enhancement factor and estimated number of emission centers). Emission parameters are recorded during long-term operation of the sample, allowing assessment of its stability.

One of the last innovation is opportunity to check conformity of experimental IVC and classical emission theory in real-time mode. According to R. Forbes [3] idea we used a simple quantitative test with counting ranges of relative parameter f :

$$f_{low} = \frac{9,34}{x_2 \cdot \sqrt{\varphi} \cdot \frac{y_2 - y_1}{x_2 - x_1} \cdot \ln 10} \quad (1) \quad f_{up} = \frac{9,34}{x_1 \cdot \sqrt{\varphi} \cdot \frac{y_2 - y_1}{x_2 - x_1} \cdot \ln 10} \quad (2)$$

where x_1, x_2 – are the coordinates of X-axis of FN plot; y_1, y_2 – are the coordinates of Y-axis of FN plot; φ – is the Schottky-Nordheim barrier of zero-field height.

For extracted parameters f_{low} and f_{up} the conformity of experimental data with classical theory determined by finding them in field and thermal field emission ranges, given in [4].

As an object of research we used the polymeric nanocomposite 'polystyrene- single wall carbon nanotube emitter' (PC-SWCNT). Length of tubes is up to 10 μm , diameter - is up to 2 nm (Novosibirsk production). The process of drawing of emission film on a substrate is described in detail in [5].

Figure 1(a) shows voltage and current pulses used for fast IVC plotting. Sector of curve between the blue and green markers is used for FN-plot. The optimal straight line FN-plot is presented on figure 1(b). In last case experimental data passed the test.

Figure 2(a) shows dependence of parameters f_{low} and f_{up} on lower range current value (green marker on figure 1(a)). Figure 2(b) presents the interface of Labview-based software with typical parameter f (there is an occurrence when FN-plot fails the test).

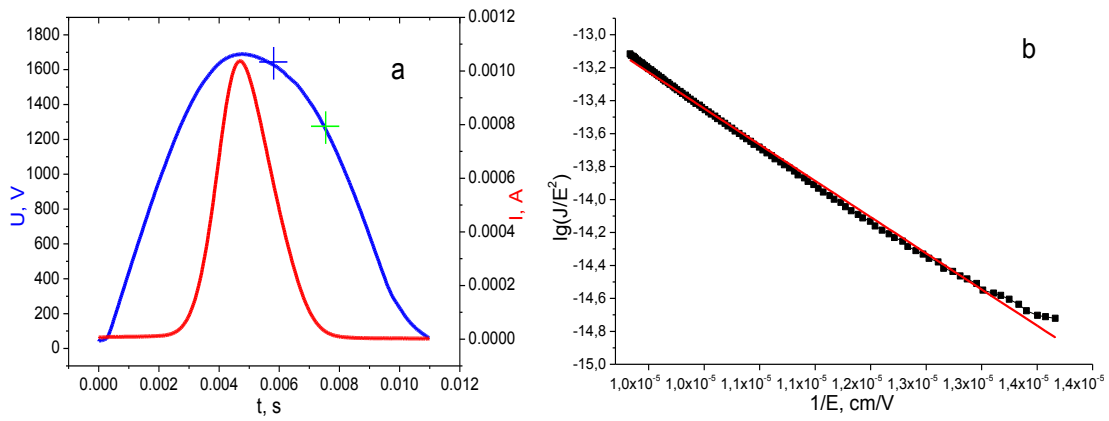


Figure 1. The voltage and current pulses for fast IVC plotting (a) and typical FN-plot (b)

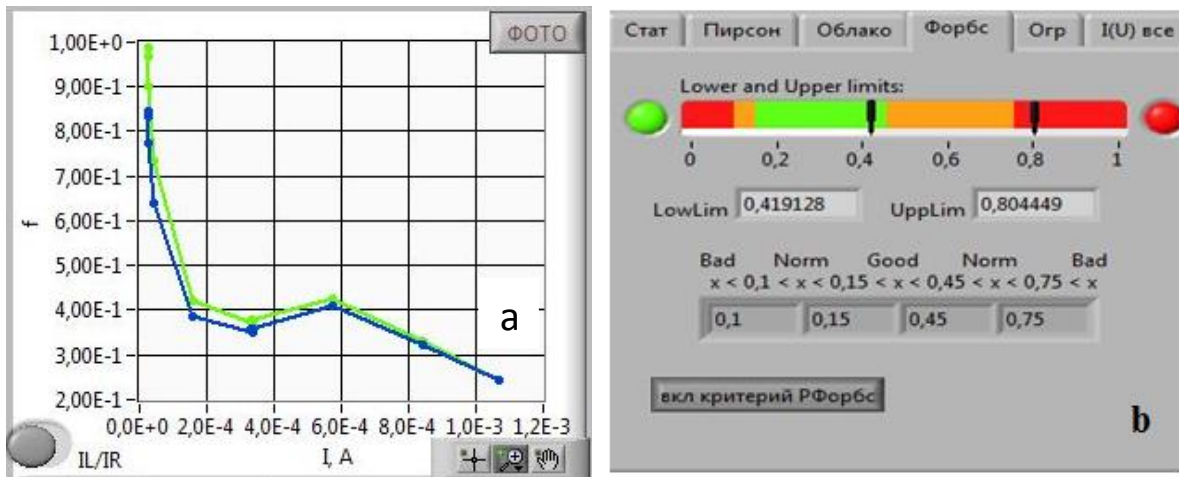


Figure 2. The dependence of parameters f_{low} and f_{up} on lower range value of a current (a); the interface of Labview-based software, illustrating the calculation of the parameter f (b)

As can be seen from figure 2 with changing of the length of the FN-plot, the parameters f_{low} and f_{up} one after another pass through the region of experimental results in conformity with the classical theory, and in current range [50 ÷ 150 uA] these parameters almost match each other. We assume that effective emission parameters of the sample should be calculated at the length of FN-plot not lower then several tens of uA.

The work was carried out with the partial support of the Foundation for Assistance to Small Innovative Enterprises in Science and Technology (№0002235).

- [1] Egorov N V, Sheshin E P. *Field emission. Principles and instruments*. 2011. 528 p
- [2] Forbes R G 2012 *Nanotechnology* **23** 095706
- [3] Forbes R G 2013 *Proc R Soc A* **469** 20130271
- [4] Murphy E L, Good R H 1956 *Phys. Rev.* **102** 1464
- [5] Kolosko A G, Ershov M V, Filippov S V, Popov E O 2013 *Tech. Phys. Lett.* **39** 5 484

A theory of spectral properties of disordered metal-semiconductor nanocomposites

N A Olekhno^{1,2}, Y M Beltukov^{2,3} and D A Parshin¹

¹Saint Petersburg State Polytechnical University, 195251 Saint Petersburg, Russia

²Ioffe Institute, 194021 Saint Petersburg, Russia

³Université Montpellier II, CNRS, Montpellier 34095, France

Abstract. Random LC -networks are widely used to describe optical properties of disordered metal-dielectric nanocomposites. In such networks inductive bonds correspond to metal regions, while capacitive bonds represent dielectric. We show that parallel LC -circuits better describe metallic regions where values of L and C depend on a network lattice parameter and plasma frequency of metal. Spectral properties of disordered metal-dielectric and metal-heavily doped semiconductor composites are studied in a framework of this generalized LC -model. We derive analytical expressions for dependence of eigenfrequencies of metal-dielectric composites on permittivity of dielectric and relation between eigenfrequencies of metal-semiconductor composites before and after metal-dielectric transition in semiconductor. Obtained results are illustrated by numerical simulations.

1. Introduction

Disordered composites consisting of nanosize grains of noble metals placed into a dielectric matrix attract considerable attention because of their interesting optical properties associated with plasmon resonances, including second harmonic generation, enhanced optical absorption and surface-enhanced Raman scattering [1].

Discretized Maxwell equations in quasistatic approximation of metal regions with Drude-permittivity $\varepsilon_m(\omega) = 1 - \omega_p^2/\omega^2$ correspond to a cubic lattice of parallel LC -circuits with $L_m = 4\pi c^2/(a\omega_p^2)$ and $C_m = a/(4\pi)$, where ω_p is a plasma frequency of metal, a is a lattice parameter of discretization network and c is the speed of light. In the following we consider the units where $c = 1$. Dielectric regions correspond to a cubic lattice of capacitors $C_d = a\varepsilon_d/(4\pi)$ if permittivity ε_d is approximately constant in optical region. Thus, continuous heterogeneous medium is replaced by a discrete network with LC - and C -bonds. In literature the approximation when LC -bonds are replaced to L -bonds is extensively studied [1, 2]. However it is valid only for a low frequencies $\omega \ll \omega_p$ and the properties of the general case remain unclear.

Resonances in such networks could be studied in terms of generalized eigenvalue problem [3]

$$\sum_j K_{ij}\varphi_j - \omega^2 \sum_j C_{ij}\varphi_j = 0, \quad (1)$$

where i and j enumerate sites of a network, K is a matrix of inverse inductances $1/L_{ij}$ between sites of network and C is a matrix of capacitances C_{ij} . Eigenvalues ω^2 correspond to a squares

of resonant frequencies of a system and eigenvectors φ describe distribution of potential at the sites of network for eigenmodes.

Capacitances of dielectric C_d depend on the permittivity ε_d , therefore eigenfrequencies ω also depend on ε_d . We can rewrite eigenvalue problem (1) as

$$|K - \mu C_0| = 0, \quad (2)$$

where the matrix $C_0 = \omega_p^2(C_m + C_d/\varepsilon_d)$ does not depend on the permittivity ε_d . Now eigenvalues μ in the Eq. (2) do not depend on the permittivity ε_d and have form

$$\mu = \frac{\varepsilon_d(\omega/\omega_p)^2}{1 + (\varepsilon_d - 1)(\omega/\omega_p)^2}. \quad (3)$$

Therefore the eigenfrequency ω can be expressed in the permittivity ε_d and eigenvalue μ

$$\omega = \frac{\omega_p}{\sqrt{\varepsilon_d(1 - \mu)/\mu + 1}}. \quad (4)$$

For example, surface plasmon in spherical granule has $\mu = 1/3$ which gives the well-known result $\omega = \omega_p/\sqrt{2\varepsilon_d + 1}$.

Another case which attracts attention is a composite of metal and doped semiconductor [4] which could be considered as a mixture of two Drude-metals. Eigenvalue problem (1) in this case reduces to a form

$$|K_1 - \xi(K_1 + K_2)| = 0 \quad (5)$$

where K_1 and K_2 are matrices of inverse inductances of metal and semiconductor respectively, and eigenvalues

$$\xi = \frac{(\omega/\omega_{p2})^2 - 1}{(\omega_{p1}/\omega_{p2})^2 - 1} \quad (6)$$

include plasma frequencies of metal ω_{p1} and semiconductor ω_{p2} . Usually ω_{p1} correspond to ultraviolet or visible range, while ω_{p2} — to THz or infrared.

By establishing correspondence between problems (2) and (5) one can obtain the expression which connect the eigenfrequencies of a metal-semiconductor composite when semiconductor acts as dielectric and after it exhibits metal-dielectric transition (for example, after heating of an initial composite)

$$\omega = \omega_{p2} \sqrt{1 - \mu(1 - \omega_{p1}^2/\omega_{p2}^2)} \quad (7)$$

where ω is a frequencies of eigenmodes of metal-semiconductor composite with semiconductor acting as metal and μ is a spectrum of composite with semiconductor acting as dielectric.

2. Acknowledgements

We are very grateful to Prof. V. I. Kozub for many fruitful discussions. NAO and YMB thank Dynasty Foundation for financial support.

References

- [1] Sarychev A K, Shalaev V M 2000 *Physics Reports* **335** 275
- [2] Jonckheere Th and Luck J M 1998 *J. Phys. A* **31** 3687
- [3] Olekhno N A, Beltukov Y M and Parshin D A 2014 *J. Phys. Conf. Ser.* **572** 012037
- [4] Naik G V and Boltasseva A 2010 *Phys. Status Solidi RRL* **4** 295

THz radiation under noncentral propagation of electrons through periodical channel

A A Ponomarenko¹, A A Tishchenko¹, K V Lekomtsev² and M N Strikhanov¹

¹National Research Nuclear University MEPhI, Moscow, Russia

²High Energy Accelerator Research Organization (KEK), Tsukuba, Japan

Abstract. Radiation from noncentral electrons moving through channel with variable radius in the THz region is investigated using Particle In Cell (PIC) solver of the Computer Simulation Technology (CST) software package. Radiation which arises due to noncentral electrons propagation is compared with radiation from central electrons propagation. Theoretical model describing noncentral propagation is discussed.

1. Introduction

There is a variety of possible schemes for generation of electromagnetic radiation in the THz (terahertz) frequency range. The most powerful THz sources can be based on relativistic electron bunches with a huge number of electrons, up to 10^{10} and more in the each bunch. In order not to damage the target one should use the electrons moving near the target surface. Different radiation schemes are possible here: synchrotron radiation (very bright, but the facilities are very big and expensive), undulator radiation (electrons move through the space with periodically changing magnetic field; the well-known example of the kind is Free Electron Laser), and polarization radiation, mainly Cerenkov radiation (CR), and Smith-Purcell (SPR) radiation. CR is known to be an effective radiation source in THz region [1]. In our previous article it was shown that SPR can also used as a good source of THz [2]. CR and SPR permit to make comparatively compact THz radiation source.

2. CST simulation of noncentral propagation

As we mentioned before in our previous article we investigated bunch of electrons moving through the channel with variable radius (figure 1), where radiation arises due to Cerenkov and Smith-Purcell mechanisms.

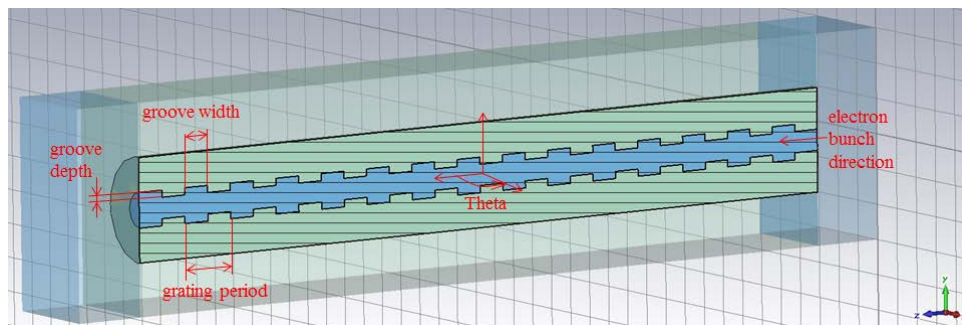


Figure 1. Scheme of THz source.

In that article we considered electrons propagate at distance y of axis of dielectric channel, because it is interesting from experimental point of view. The radiation occurs due to polarization of channel material by electrons Coulomb field. Simulation was performed using Particle In Cell (PIC) solver of Computer Simulation Technology (CST) software where $\gamma = 16$, $\varepsilon = 3.75$, $\omega = 300 \text{ GHz}$, groove width $l = 0.75 \text{ mm}$, groove depth $a = 0.3 \text{ mm}$, grating period $d = 1.5 \text{ mm}$.

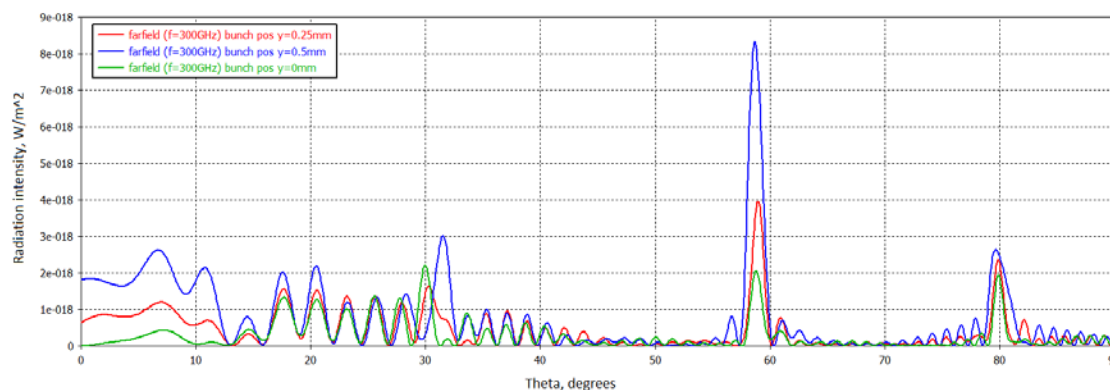


Figure 2. Dependence intensity on theta for different distances between axis and electrons. Spectral-angular dependence on theta (figure 3) has several maxima, which correspond to SPR and CR peaks. Another interesting fact that if we increase the distance between bunch and axis, the radiation intensity also increases.

3. Discussion

Noncentral propagation of bunch of electrons through the channel was investigated. Influence of distance between bunch and axis on intensity of radiation was shown.

References

- [1] Zrelov B P, Cerenkov radiation and its application in high-energy, *Atomizdat*, 1968
- [2] Ponomarenko A A, Ryazanov M I, Strikhanov M N and Tishchenko A A 2013 Terahertz radiation from electrons moving through a waveguide with variable radius, based on Smith-Purcell and Cherenkov mechanisms *NIM B* **309** 223

Spectral correlations of phase modulated entangled photons

Sheremetyev V.O., Trifanov A.I.

ITMO University, Kronverksky 49, Saint-Petersburg, 197101, Russia

Abstract. We investigate spectral properties of entangled photons in EPR-pair, which interacts with phase modulators. In three mode approximation we got the exact analytical expressions for their common state evolution and calculated probabilities of coincidence between detectors clicks.

Phase modulation (PM) process for the quantized radiation is being actively investigated due to the development of quantum communication systems. The foundation in this area was formed in works [1], [2] and [3], where different approaches were suggested. Various correlations between entangled photons which undergoes PM were investigated in [4, 5]. Statistical properties of field quantum state interacted with PM were studied in detail in [3].

In our scheme polarization entangled photons (with horizontal H and vertical V states of polarizations) are generated due to spontaneous down-conversion process (see fig.(1)) and transmitted to the detector part with optical waveguides in use. Passing through these waveguides photons interact with PM's φ_1 and φ_2 setting in each channel. Just after this interaction these photons are detected by detectors D_1 and D_2 . Restricted by three mode approximation we analyze probabilities of single and double clicks of detectors, monitoring each of these three modes (l , m and r). The aim of this work is to investigate nonlocal modulation of entangled photon pair and calculate conditional states of modes in one channel using the measurement data from another.

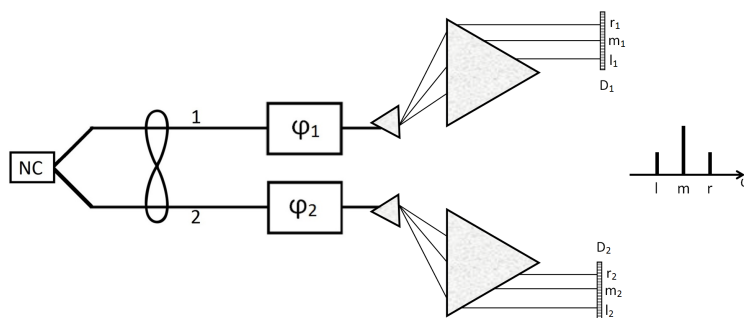


Figure 1. Nonlocal phase modulation of entangled photons generated by nonlinear crystal (NC). Each photon in EPR-pair is transmitted by optical waveguide and interacts with phase modulator. After that the probability of detectors clicks coincidence is monitored

We assume the following polarization entangled state transmitted in channels 1 and 2

$$|\Psi_0\rangle = \frac{1}{\sqrt{2}} [|010\rangle_{1H}|000\rangle_{1V}|000\rangle_{2H}|010\rangle_{2V} + |000\rangle_{1H}|010\rangle_{1V}|010\rangle_{2H}|000\rangle_{2V}], \quad (1)$$

where $|ijk\rangle = |i\rangle_l |j\rangle_m |k\rangle_r$, $i, j, k \in \{0, 1\}$, l, m , and r are indexes of the modes. Under the assumption that PM's do not recognize state of polarization we calculated action of α -th modulator on initial state $|010\rangle_{\alpha\beta}$ as follows:

$$U(t)|010\rangle_{\alpha\beta} = \left(ie^{-i\tilde{\Omega}t} e^{i\varphi} \sin(2\Gamma t) \right) |100\rangle_{\alpha\beta} + \left(\sqrt{2} e^{-2i\tilde{\Omega}t} \cos(2\Gamma t) \right) |010\rangle_{\alpha\beta} + \left(ie^{-3i\tilde{\Omega}t} e^{-i\varphi} \sin(2\Gamma t) \right) |001\rangle_{\alpha\beta}, \quad (2)$$

Here $\alpha \in \{1, 2\}$, $\beta \in \{H, V\}$, φ is modulator phase, $\Gamma = \left| \frac{2\gamma}{3} \right|$, γ is parameter of mode interaction, $\tilde{\Omega}$ is modulation frequency and Ω is frequency difference between adjacent optical modes [3].

	l_1	m_1	r_1
l_2	$\frac{1}{4} \sin^4(2\Gamma t)$	$\frac{1}{2} \sin^2(2\Gamma t) \cos^2(2\Gamma t)$	$\frac{1}{4} \sin^4(2\Gamma t)$
m_2	$\frac{1}{2} \sin^2(2\Gamma t) \cos^2(2\Gamma t)$	$\cos^4(2\Gamma t)$	$\frac{1}{2} \sin^2(2\Gamma t) \cos^2(2\Gamma t)$
r_2	$\frac{1}{4} \sin^4(2\Gamma t)$	$\frac{1}{2} \sin^2(2\Gamma t) \cos^2(2\Gamma t)$	$\frac{1}{4} \sin^4(2\Gamma t)$

Table 1. Second order correlation matrix

In Table 1 we show joint probabilities for detection photons in the corresponding detectors

$$P_{x_\alpha y_{\bar{\alpha}}} = \left\langle a_{x_\alpha}^\dagger a_{x_\alpha} a_{y_{\bar{\alpha}}}^\dagger a_{y_{\bar{\alpha}}} \right\rangle = \langle \Psi_0 | U(t)^\dagger a_{x_\alpha}^\dagger a_{x_\alpha} a_{y_{\bar{\alpha}}}^\dagger a_{y_{\bar{\alpha}}} U(t) | \Psi_0 \rangle, \quad (3)$$

where $x, y \in \{l, m, r\}$, $\bar{\alpha} = 2$ when $\alpha = 1$ and $\bar{\alpha} = 1$ when $\alpha = 2$, a_{x_α} is annihilation operator for mode indexed x in detector D_α . In case of detector l_1 is clicking, one can obtain the probability distribution of clicking for detectors in second channel (the first column). Also for other detectors clicking we can obtain the similar probability distributions.

In summary, this work reports analytical description in three mode approximation of entangled state phase modulation. Obtained analytical results are used in discussion about quantum key distribution systems.

References

- [1] Pegg D T and Barnett S M 1989 *Phys. Rev. A* **39** 1665-1675
- [2] Kolchin P, et. al. 2008 *Phys. Rev. Lett.* **101**, 103601
- [3] Miroshnichenko G P *Proc. Int. Conf. on Math. Chall. of Quant. Transp. in Nanosystems* (Saint-Petersburg)
- [4] Harris S E 2008 *Phys. Rev A* **78** 021807(R)
- [5] Sensarn S 2009 *Phys. Rev. Letters* **103** 163601

The flow reactor system for in-line synthesis of semiconductor nanoparticles

O A Ryzhov¹, L B Matyushkin²

¹ Student, St. Petersburg State Electrotechnical University “LETI”, Pr. Popova 5, St. Petersburg, 197376 Russia

² Postgraduate, St. Petersburg State Electrotechnical University “LETI”, Pr. Popova 5, St. Petersburg, 197376 Russia

Abstract. A flow reactor nanoparticle synthesis technique is proposed as replacement for «hot injection» synthesis of semiconductor nanocrystals in a glass flask. The main advantages are possibility of continuous nanoparticles production, technology flexibility and lower cost of the final products in comparison with currently applied methods.

1. Introduction

The classical synthesis in a chemical glass flask allows to obtain a variety of nanoparticle types with different functional properties: luminescent quantum dots [1], magnetic structures [2], plasmonic active elements [3] *etc.* In some of these methods materials are synthesized at room temperature, while others require a heating step. For instance, in the case of “hot-injection” synthesis of colloidal quantum dots temperatures about 200–300°C are used. Dividing nanoparticles nucleation and their growth allows to obtain monodisperse nanoparticles. However, in the case of chemical flask it is impossible to separate these stages completely, because the reaction takes place in a restricted volume. This technique also limits the product yield – a single synthesis gives only a limited amount of particles, and for large quantities it must be repeated many times. This factor limits the creation of industrial systems for production of colloidal quantum dots and hinders development of their applications.

2. Experiment

In comparison with traditional chemical synthesis in a flask, a flow chemistry nanoparticle synthesis is performed in a stream of fluid flowing in a narrow capillary. Precursors can be solutions of water-soluble salts or organic compounds in a nonpolar medium. There are two organic immiscible fluids in our system: one fluid serves as the liquid carrier with good wetting of capillary wall, while the other consists of precursor solution drops which are distributed in the flow of medium. Syringe pumps are used for setting of components (carrier and precursors) transfer rates. Number of pumps equals to the number of independent components that are placed in corresponding syringes.

Our system works as follows: 1) the precursors A and B are moved by syringe pumps to the mixing cell, 2) the mixed solution gets into a coil with a temperature T_n corresponding to the nucleation of nanocrystals, 3) the core particles solution flows into the coil with a temperature T_g corresponding to

the particles growth stage, 4) in the last step the solutions are selected and cooled to room temperature. Time control of the particle growth is determined by the flow rate of carrier fluid. Due to the immiscible nature of the carrier and the solvent, the liquids separate into two layers of different density, so nanoparticles are isolated from the solvent by standard flocculation technique by polar liquid such as acetone or methanol.

At the last stage and each of the intermediate steps the solutions can be tested by optical spectroscopy. For this purpose we have developed a compact optical spectrophotometer Eltech-M-14 allowing to obtain *in situ* luminescence spectra. The syringe pumps flow rate and the heating devices temperatures T_n and T_g are controlled by computer program, microcontroller board and several additional printed circuit boards created ourselves.

3. Results

The reactor uses the principle of separation of nucleation and growth of nanoparticles. The offered technique increases the production rate, makes synthesis more reproducible and reduces the reagents consumption. Such system allows to obtain nanoparticles of metal chalcogenides A^2B^6 , A^4B^6 .

Acknowledgements

The authors acknowledge financial support from the Russian Research Foundation (project 14-15-00324).

References

- [1] Mikhailov I I *et al* 2014 *Functional Materials* 21, №2, pp 186-189
- [2] Bogachev Yu V *et al* 2014 *Applied Magnetic Resonance*, 45, № 4, pp. 329-337
- [3] Viazmitinov D V, Matyushkin L B and Maximov A I 2014 *J. Phys.: Conf. Ser* 541 p. 012015

The characteristics of semiconductor-to-metal transition in VO₂ of different morphology

Petukhova Yu.V., Osmolovskaya O.M., Osmolovsky M.G.

Saint Petersburg State University, Institute of chemistry, 198504, Russia, Saint Petersburg, Petrodvorets, Universitetsky pr. 26

Abstract. Vanadium dioxide nanoparticles (NPs) of different morphologies were obtained using the hydrothermal technique. Their shape and size were studied by SEM, XRD and SSA estimation. The functional properties, structural changes and thermal behaviour of samples obtained were investigated to clarify the SMPT peculiarities. It is shown that the introduction of a doping element changes a mechanism of the nanoparticles growth and so that the SMPT becomes less expressed. The detailed study of SMPT in undoped VO₂ showed the steps of the transition process. The testing of VO₂ coating on glass for «smart» windows was successfully performed.

1. Introduction

Bulk vanadium dioxide undergoes a semiconductor-to-metal phase transition (SMPT) at 340 K resulting in an abrupt change of magnetic, electrical and optical properties. Due to this fact, VO₂ becomes a perspective material for optical switchers and IR sensors [1], «smart» covers for windows [2], electrical switchers and elements of energy-independent memory [3]. What is more, vanadium dioxide has a rutile structure so that the different ions are able to intercalate easily into the lattice. Therefore, this material can be used as an electrode material for Li-ions batteries [4].

It is known that application of VO₂ depends on characteristics of SMPT which in its turn were effected by VO₂ morphology. As we have shown before the temperature of the transition can be lowered by doping [5]. But there is one more way to regulate morphology of the product obtained. The introduction of a chelating agent leads to change in a growth mechanism and thereby influences on particles size and shape.

So the hydrothermal synthesis of undoped and Fe and Cr-doped VO₂ particles in presence and in absence of the chelating agent and their physico-chemical and functional characteristics are reported.

2. Experimental

The morphology of powders obtained was analyzed by XRD, SEM and SSA estimation, and electrical properties were studied by impedance spectroscopy. The temperature dependence of magnetization was measured by VSM. The detailed investigation of SMPT in undoped VO₂ was conducted by DSC and XRD at temperatures ranges 7 – 400 K. The IR transmittance of VO₂ coating on glass at temperature range 279 – 333 K was studied by IR spectroscopy.

3. Results and discussion

3.1. The regulation of NPs morphology by variation of synthesis conditions

It is shown that the particles shape changes from ribbons and microplates obtained before with large amounts of dopant [5] to carambola-like and sponge-like spheres with the chelating agent and smooth hollow spheres without one. The tendency of nanoparticle formation both for Fe and Cr-doped samples is mostly the same.

An undoped VO₂ synthesized without the chelating agent represents rods with 80 nm thick and 1 μm length.

3.2. The dependence of SMPT characteristics on the morphology of VO₂

From the magnetic and electrical properties of doped vanadium dioxide it is found that the SMPT become less expressed and the temperature of the transition decreases to 200 K with the chelating agent and 150 K without one compared to the bulk material. There is no difference appeared between samples with varied amount of doping element which means that the characteristics of SMPT depend on morphology of the sample but not the quantity of dopant. The shape of doped samples makes them perspective for Li-ion batteries.

The detailed study of SMPT in undoped VO₂ has shown the abrupt change in magnetic characteristics near 280 K and the crystalline structure modification near room temperature. The thermal effects of transition and decrease in IR-transmittance were observed at about 310 K. It means that the transition consists of several steps appearing on different levels of structural organization. Thereby the SMPT takes place in temperature range which is convenient for “smart” cover application. The decrease in IR transmittance of VO₂ coating on glass above the room temperature was shown.

References

- [1] X. Chen, Q. Lv, Theoretical analysis on the switching speed and driving power dissipation for optical switch based on VO₂ thin film, *Optik - International Journal for Light and Electron Optics*, 2013, V. 124, I. 7, P. 579-582.
- [2] Z. Huang, C. Chen, C. Lv, S. Chen, Tungsten-doped vanadium dioxide thin films on borosilicate glass for smart window application, *Journal of Alloys and Compounds*, 2013, V.564, P. 158-161.
- [3] A. Velichko, A. Pergament, V. Putrolaynen, O. Berezina, G. Stefanovich, Effect of memory electrical switching in metal/vanadium oxide/silicon structures with VO₂ films obtained by the sol-gel method, *Materials Science in Semiconductor Processing*, 2015, V. 29, P. 315-320.
- [4] C. Nethravathi, B. Viswanath, J. Michael, M. Rajamath, Hydrothermal synthesis of a monoclinic VO₂ nanotube-graphene hybrid for use as cathode material in lithium ion batteries, *Carbon*, 2012, V. 50, P. 4839-4846.
- [5] Yu.V. Petukhova, O.M. Osmolovskaya, A.V. Fedorova, M.G. Osmolowsky, Magnetic behavior of doped VO₂ nanoparticles, *Bulletin of the Russian Academy of Science: Physics*, 2014, V. 78, №4, P. 325 – 327.

Acknowledgements

Scientific researches were performed at the Centre of X-ray Diffraction Studies, Centre for Geo-Environmental Research and Modelling (GEOMODEL), Innovate Technologies of Composite Nanomaterials, Center of Thermal Analysis and Calorimetry and Center of Chemical Analysis and Materials Research of St. Petersburg State University.

Modelling of field emitter array characteristics in diode system

K A Nikiforov and M F Sayfullin

Saint Petersburg State University, Universitetskii prospekt 35, 198504 Saint-Petersburg, Russia

Abstract. Mathematical model of diode system based on field emitter array (FEA) cathode with cylindrical sharp-edge emitters is presented. Macro- and microscopic distributions of electric field over the FEA surface are calculated. Microscopic electric fields are compared for different locations on the edges of emitters in FEA.

Electric field on emitters depends on their location relative to the boundary of the FEA [1-3]. Therefore emission from different emitters varies. The effectiveness of the FEA is determined by the emission current density magnitude and uniformity of its distribution over the FEA surface. Emission current density depends on the magnitude of the electric field, so the most important factors affecting the performance of the cathode are macroscale homogeneity of the field distribution over the FEA surface and its maximum microscale enhancement at the emission surface.

The main problem of this paper is to calculate the electric field in the diode with the FEA cathode, as well as the definition by the methods of mathematical modeling [4] of system geometric parameters to ensure the greatest uniformity of macroscopic electric field distribution. Thus, research is aimed at improving the efficiency of the FEA cathode.

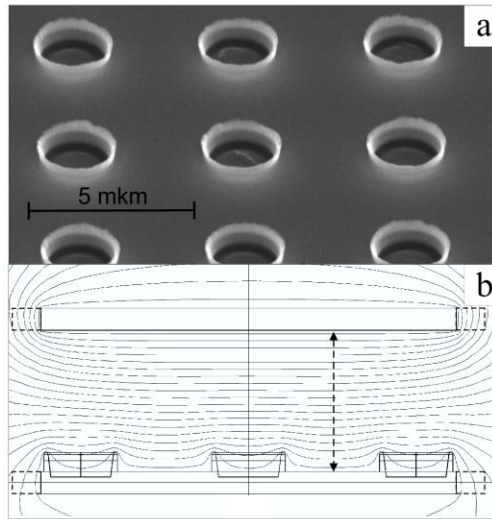


Figure 1. a) The SEM image of the FEA surface. b) Model structure of the array and the equipotential lines of the electric field in the cross section of a plane diode system. The dotted line shows the variable geometrical model parameters.

Acknowledgments

Financial support has been obtained from RFBR (13-01-00150) and partially from SPbSU (9.38.673.2013). Research was carried out using computational resources provided by Resource Center "Computer Center of SPbU" (<http://cc.spbu.ru/en>) and using experimental equipment of the Interdisciplinary Resource Center for Nanotechnology of St. Petersburg State University.

- [1] Sayfullin M F and Nikiforov K A 2014 *J. Phys.: Conf. Ser.* **541** 012020
- [2] Nikiforov K A, Antonova L I, Egorov N V, Trofimov V V, Makeev V V, Ogurtsov O F 2012 *RuPAC 2012 Contributions to the Proc. of 23 Russian Particle Accelerator Conf. (St. Petersburg)*, (Cern: JACoW) p 218
- [3] Sayfullin M, Nikiforov K 2014 Fringe field effect study of a field emitter array *2014 Tenth Int. Vacuum Electron Sources Conf. (Saint Petersburg)* (Piscataway: IEEE)
- [4] Nikiforov K A, Egorov N V Program complex for vacuum nanoelectronics finite element simulations 2012 *RuPAC 2012 Contributions to the Proc. of 23 Russian Particle Accelerator Conf. (St. Petersburg)*, (Cern: JACoW) p 409

Theoretical investigation of sedimentation process for nanoparticles statistical ensemble

K D Mukhina, S A Chivilikhin

ITMO University, 49 Kronverkskiy pr., Saint-Petersburg, 197101, Russia

Abstract. In this paper the sedimentation process of nanoparticles, which have distribution in sizes, was studied. The mathematical model under consideration gives a rise of velocity which resembles Rayleigh-Taylor instability. The numerical solution is consistent with results predicted by the model. The maximum value of concentration, where instability does not occur, was found.

Sedimentation of particles in a fluid environment is a familiar phenomenon in nature and has important technical applications. This process in suspension was studied rather well [1-3]. The Rayleigh-Taylor instability (or RT instability) can be observed in a lot of situations in astrophysics, for instance supernova's explosion, in physics of plasma, also in electro- and magneto- hydrodynamics and nanohydrodynamics [4].

The major objective of this study is to investigate the sedimentation process of nanoparticles statistical ensemble where particles had some distribution in size. In this paper the term 'nanoparticles' will be used to described nano-sized balls which don't interact with each other.

The sedimentation process of nanoparticles was modeled in a gravity field (see Figure 1). System is unlimited in horizontal direction and consists of gas and dust. Upper half-space contains mix of gas and dust, the lower half-space contains gas only. Particles of dust have some distribution in sizes with density function f_0 . Origin point is located on the border of dusted area. Z-axis is directed to the ground.

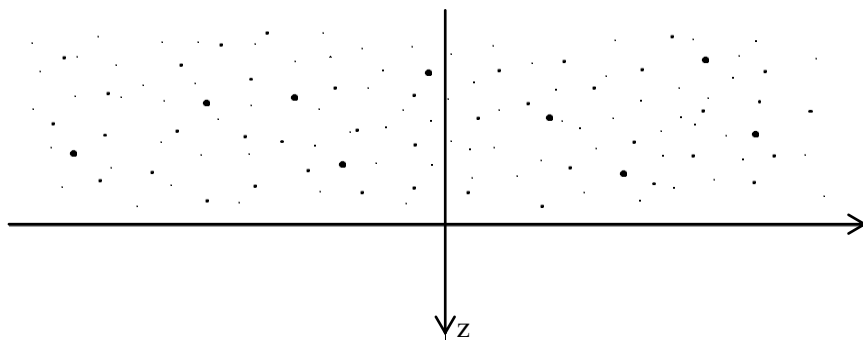


Figure 1. The scheme of the problem. Z-axis is directed as a gravity force.

In case of moving gas, dust gets gas velocity immediately. In vertical direction, velocity contains velocity of gas and velocity of dust in zeroth-order approximation. Using Navier–Stokes equations and kinetic equation, the system of equations describing the given model was completed:

$$\begin{cases} \frac{\partial \hat{f}}{\partial t} + \gamma R^2 \frac{\partial \hat{f}}{\partial z} + \hat{v}_z \frac{\partial f^{(0)}}{\partial z} = 0 \\ \rho \frac{\partial \hat{v}_z}{\partial t} = \mu \left(\frac{\partial^2 \hat{v}_z}{\partial z^2} + \frac{\partial^2 \hat{v}_z}{\partial y^2} + \frac{\partial^2 \hat{v}_z}{\partial x^2} \right) - \frac{\partial \hat{p}}{\partial z} + \int_0^\infty 6\pi\mu R \gamma R^2 \hat{f} dR \\ \frac{\partial^2 \hat{p}}{\partial x^2} + \frac{\partial^2 \hat{p}}{\partial y^2} + \frac{\partial^2 \hat{p}}{\partial z^2} = \int_0^\infty 6\pi\mu R \gamma R^2 \frac{\partial \hat{f}_k}{\partial z} dR \end{cases}$$

Solving this system we get mathematical expression for Z-component of velocity. The concentration value can be found by using numerical solution:

$$V_{j,n+1} = V_{j,n} + \nu \Delta t \left(\frac{V_{j+1,n} + V_{j-1,n} - 2V_{j,n} - k^2 V_{j,n}}{(\Delta z)^2} \right) + \frac{k \Delta t}{2} e^{k \cdot j \Delta z} \sum_{j'=j}^{\infty} e^{-k \cdot j' \Delta z} \frac{J(j')}{\rho} \Delta z + \frac{k \Delta t}{2} e^{-k \cdot j \Delta z} \sum_{j'=0}^j e^{k \cdot j' \Delta z} \frac{J(j')}{\rho} \Delta z$$

The charts below show velocity's behavior with different concentration of particles. It is clear that after certain level of concentration was reached, velocity has a sudden rise which can be explained by the instability similar to RT instability. The minimum value of concentration, where instability is appearing, is $n_0 = 3 \cdot 10^{10} m^{-3}$.

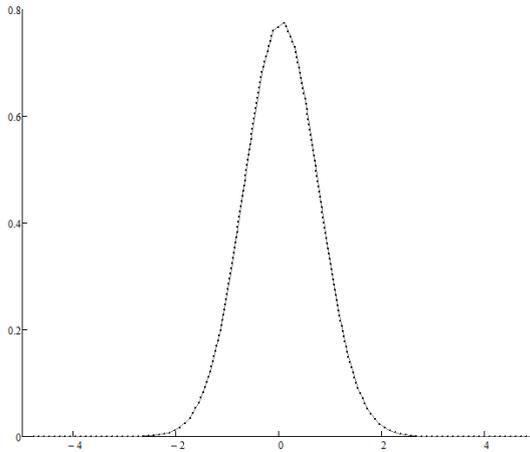


Figure 2. Comparing Fourier transform of velocity's Z-component dependence from coordinate with and without perturbation; $\nu = 10^{-6}$; $\gamma = 2.173 \cdot 10^6$; $n_0 = 10^{10}$

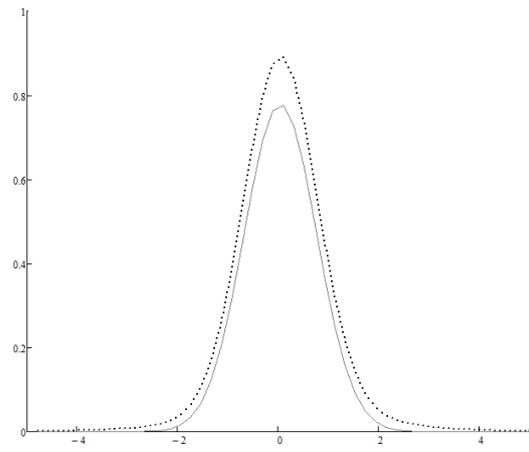


Figure 3. Comparing Fourier transform of velocity's Z-component dependence from coordinate with and without perturbation; $\nu = 10^{-6}$; $\gamma = 2.173 \cdot 10^6$; $n_0 = 10^{16}$

References

- [1] Völtz C, Pesch W and I Rehberg 2001 Rayleigh-Taylor instability in a sedimenting suspension *Phys. Rev. E.* **65** p 1–7.
- [2] Glowinski R, Pan T W and Joseph D D 2001 *J. Fluid Mech.* **434** p 23–37
- [3] Suvankar Ganguly and Suman Chakraborty 2011 Sedimentation of nanoparticles in nanoscale colloidal suspensions *Physics Letters A* **375** p 2394
- [4] Kadau K 2004 et. al. Nanohydrodynamics Simulations: An Atomic View of the Rayleigh-Taylor Instability *Proc. Nat. Acad. Sci.* **101** (16) p 5851–55

High Resolution Fourier Transform Spectrum of C₂H₄ in the Region of 2500 - 3000 cm⁻¹

Yu.S. Aslapovskaya¹, A.L. Litvinovskaya²,

¹ Physical and Technical Institute, Tomsk Polytechnic University, 634050, Tomsk, Russia

² Physics Department, Tomsk State University, 634050, Tomsk, Russia

Abstract. The article describes the results of high-precision ro-vibrational analysis of the ethylene molecule. The study of the state 3v₇ in the range of 2500 - 3000 cm⁻¹ was performed for the first time. Analysis was made on the basis of the new ground state parameters.

Ethylene - the most produced organic compound in the world. It is the base product in industrial chemistry. Ethylene is released into the atmosphere chemical and petrochemical industries. Thus ethylene emissions in the atmosphere affect the generation of ozone formation and global climate. Ethylene is one of the most relevant objects of study in astrophysics (it was found in the atmospheres of the planets Jupiter, Saturn, Titan, as well as in interstellar space) as well as in interstellar space. Ethylene is used as raw material for the production of acetaldehyde and synthetic ethanol. At high concentrations, ethylene has a narcotic effect on the person.

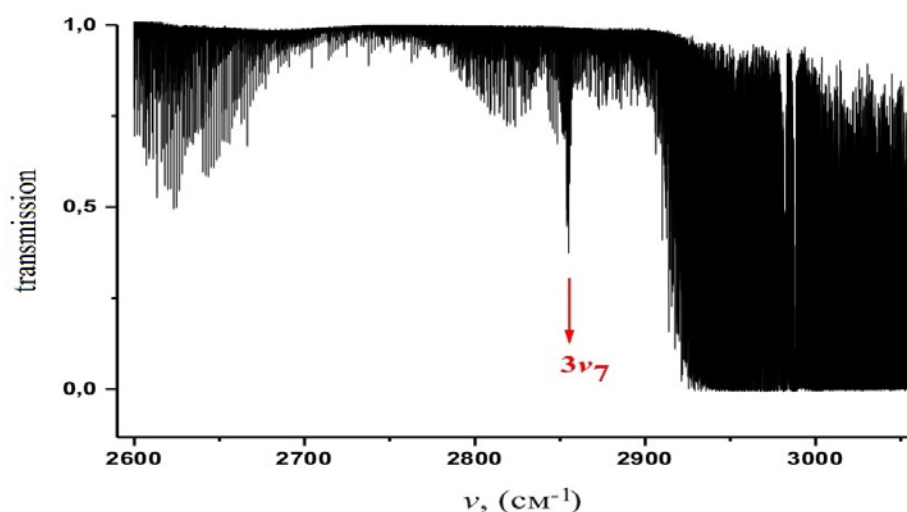


Figure 1. Spectrum of C₂H₄ in the region of 2500 – 3000 cm⁻¹.

Thus, for many years the ethylene molecule is the subject of extensive experimental as well as theoretical research (ref. [1],[2]). The present analysis is part of the spectroscopic high-resolution study of the ethylene molecule in the region of 2500 – 3000 cm⁻¹. It is known that the molecule has a symmetry D_{2h} allowed transitions from the ground vibrational state in the upper vibrational states can have one of three types of symmetry B_{1u}, B_{2u}, or B_{3u}.

This work is devoted to analysis of the rotational structure of 3v₇ excited vibrational state with B_{1u} symmetry. It is known that this band no one studied earlier. The experimental work was performed in the Infrared Laboratory of Oulu, Finland and the Braunschweig University, Germany. Spectrum in the range 2500 – 3000 cm⁻¹ with high accuracy was recorded with a Bruker IFS-120 HR Fourier Transform spectrometer.

C₂H₄ is an asymmetric top molecule, therefore, in our study we used Watson's Hamiltonian [3]:

$$\begin{aligned}
 H^{vv} = & E^v + \left[A^v - \frac{1}{2}(B^v + C^v) \right] J_z^2 + \frac{1}{2}(B^v + C^v) J^2 + \frac{1}{2}(B^v + C^v) J_{xy}^2 \\
 & - \Delta_K^v J_z^4 - \Delta_{JK}^v J_z^2 J^2 - \Delta_K^v J^2 - \delta_K^v \left[J_z^2, J_{xy}^2 \right]_+ - 2\delta_J^v J^2 J_{xy}^2 \\
 & + H_K^v J_z^6 + H_{KJ}^v J_z^4 J^2 + H_{JK}^v J_z^2 J^4 + H_J^v J^6 \\
 & + \left[h_K^v J_z^4 + h_{JK}^v J_z^2 J^2 + h_J^v J^4, J_{xy}^2 \right]_+ + L_K^v J_z^8 + L_{KKJ}^v J_z^6 J^2 + L_{JK}^v J_z^4 J^4 \\
 & + L_{JJK}^v J_z^2 J^6 + L_J^v J_z^8 + \left[J_K^v J_z^6 + J_{KJ}^v J_z^4 J^2 + J_{JK}^v J_z^2 J^4 + J_J^v J^6, J_{xy}^2 \right]_+ \\
 & + P_K^v J_z^{10} + P_{KKJ}^v J_z^8 J^2 + P_{KJ}^v J_z^6 J^4 + P_{JK}^v J_z^4 J^6 + \\
 & + S_K^v J_z^{12} + S_{KKJ}^v J_z^{10} J^2 + \dots,
 \end{aligned}$$

where $J_{xy}^2 = J_x^2 - J_y^2$, $[A, B]_{\pm} = AB + BA$

Analysis band 3v₇ was made on the basis of the ground state parameters are taken from ref. [4].

As the result, 241 transitions with J^{max}=25 and Ka^{max}=7 were assigned to the 3v₇ band. The set of parameters obtained from the fit allow us to reproduce the experimental data with an accuracy close to experimental uncertainties.

Reference

- [1] Duncan J. L., Robertson G. E. Vibrational anharmonicity in ethylenic Compounds. J. Mol. Spectrosc., 145: 25, 1-26 l (1991)
- [2] Lorono G. High-resolution spectroscopy and preliminary global analysis of C–H stretching vibrations of C₂H₄ in the 3000 and 6000 cm⁻¹ regions / G. Lorono, V. Boudon, M. Loete, M. Rotger, M.-T. Bourgeois, K. Didriche, M. Herman, V. A. Kapitanov, Yu. N. Ponomarev, A. A. Solodov, A. M. Solodov, T. M. Petrova // JQSRT–T. – 111 – C. 2265–2278 (2010)
- [3] Watson. J.K.G. Determination of centrifugal coefficients of asymmetric – top molecules, J. Chem. Phys.,46: 1935-1949 (1967)
- [4] Ulenikov O.N. High resolution spectroscopic study of C₂H₄: Re-analysis of the ground state and v₄, v₇, v₁₀, and v₁₂ vibrational bands / O.N. Ulenikov, O.V. Gromova, Yu. S. Aslapovskaya, V.-M. Horneman // J. QSRT– T. 118, – C. 14 – 25 (2013)

New type of high efficiency silicon multijunction solar cells

I.A. Morozov¹ A.S. Gudovskikh^{1,2} T.N. Berezovskaya¹ D. A. Kudryashov¹

¹Saint-Petersburg Academic University - Nanotechnology Research and Education Centre RAS,

194021, St. Petersburg, Russia

²Saint-Petersburg Electrotechnical University "LETI"

197376, St.-Petersburg, Russia.

Abstract. The aim of this study is to explore the possibility of creating a tandem a-Si:H/c-Si solar cell completely based on silicon due to formation of the top junction with the developed surface relief in the form of periodic columnar structure. The theoretical calculations showed that the use of advanced surface topography can increase by factor of 1.5 the value of the short circuit current of the top junction based on a-Si:H p-i-n structures - necessary condition for currents match between the top and bottom junctions. The effect of the p-i-n structure thickness, the distance between c-Si wires and their diameter was calculated. A technology for forming of the columnar periodic structure on the surface of silicon wafers have been developed. Two methods for obtaining the columnar structure were considered such as a liquid etching method using silver as a catalyst in etching and a dry etching method using micron sized polystyrene spheres as a mask. The structural and optical properties of the developed structures were investigated.

Dry etching results

Preparation of substrate surface, application of polystyrene spheres and etching were performed. The ordered columnar structure on the Si substrate can be achieved by etching as seen from the electron microscope photographs presented in fig1 and fig.2.

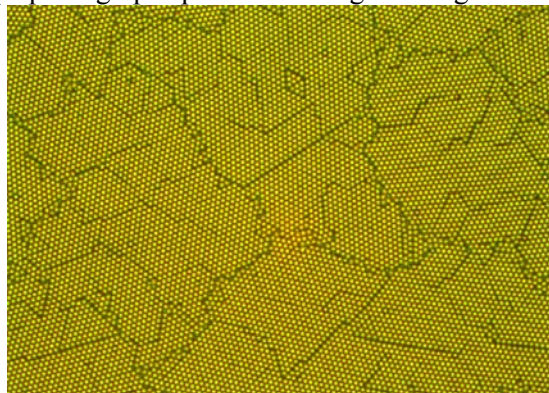


Figure 1. C-Si surface with polystyrene spheres with a diameter of 1 micron 100 times magnification.

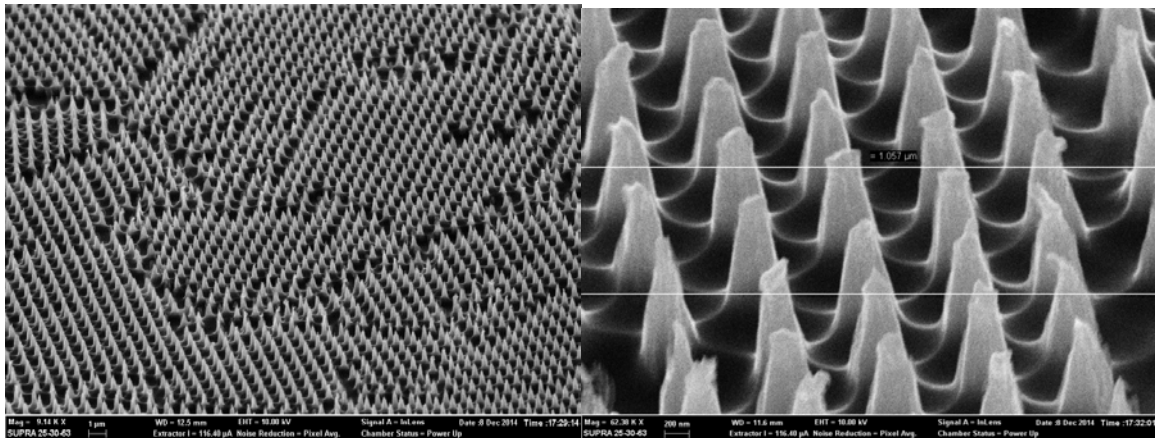


Figure 2. SEM image of periodic structures

Theoretical study

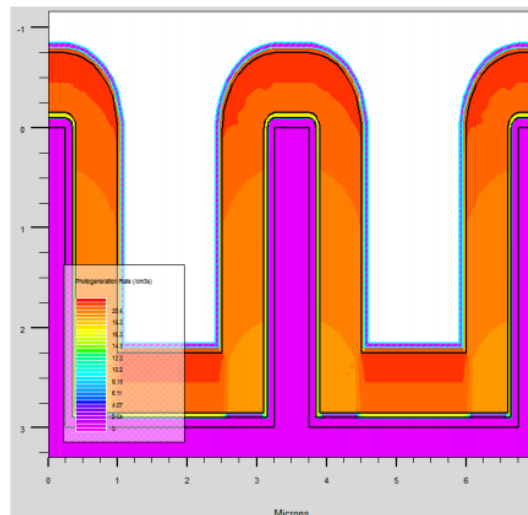


Figure 3 Model of solar cell with columnar structure

To assess the influence of the parameters of the periodic structure on the photovoltaic properties the theoretical calculations of the two-dimensional model with the columnar structure heterostructures were performed. The simulation was carried out using Silvaco-TCAD software package. The calculation demonstrates the possibility to increase the short-circuit current of pin solar cells formed on nanostructured silicon substrate by **factor of 1.5**.

Light in moving medium

Petrenko S.A., Trifanov A.I.

Saint Petersburg National Research University of Information Technologies,
Mechanics and Optics, Kronverksky, 49, Saint Petersburg, 197101, Russia

Abstract. Behavior of light in moving medium with very large permittivity is investigated. As was shown by Leohardt[1] medium moving faster than speed of light in this medium acts as parametric amplifier. We derive Hamiltonian for one-dimensional medium moving with arbitrary speed $u(x)$ and examine properties of such system after quantization procedure.

When light propagates in medium which at some point is moving in the opposite direction with greater velocity than speed of light, analogue of black hole is formed because of inability of light to get beyond this point. As was shown in [2] black holes has tight correspondence to several other parametric amplification processes capable of photon generation from vacuum state. Such properties are main subject of our interest in presented research.

The one dimensional medium moves from right to left with speed $u(x)$. In co-moving frame of reference (in which speed of the medium is zero at every point) Lagrangian density has form

$$\mathcal{L} = \frac{\epsilon\epsilon_0}{2}((\partial_t A)^2 - c'^2(\partial_x A)^2), \quad (1)$$

where $c'^2 = \frac{c^2}{\epsilon}$ is the speed of light in medium. After transformation to laboratory frame Lagrangian density can be expressed as

$$\mathcal{L} = \frac{1}{2}((\partial_t A + u \partial_x A)(\partial_t A + u \partial_x A) - c'^2(\frac{1}{1 + u'(x)t} \partial_x A)^2), \quad (2)$$

where A is vector-potential of the field.

To derive time-independent Hamiltonian we have to agree with locally constant speed approximation, where $u'(x) = 0$. Following the formalism of [3] we then take Fourier transform of A (express it as combination of plain waves)

$$A(x, t) = \int_{\mathbb{R}} q_{\alpha}(t) \exp(-i\alpha x) d\alpha \quad (3)$$

and derive Hamiltonian:

$$H_x(t) = \int_{\mathbb{R}} \frac{p_{\alpha} p_{-\alpha}}{2} + \frac{c'^2 \alpha^2}{2} q_{\alpha} q_{-\alpha} - i\alpha u(x) p_{\alpha} q_{-\alpha} d\alpha, \quad (4)$$

where

$$p_{\alpha} = \frac{\partial L}{\partial \dot{q}_{\alpha}} = \dot{q}_{\alpha} + \mathcal{R}_{\alpha\beta} q_{\beta}, \quad \mathcal{R}_{\alpha\beta} = -i\beta u(x) \delta(\alpha + \beta). \quad (5)$$

Then pairs of self-adjoint coordinates and momenta are introduced:

$$\begin{aligned} Q_\alpha^{(r)} &= \frac{1}{2}(q_\alpha + q_{-\alpha}), & Q_\alpha^{(i)} &= \frac{i}{2}(q_\alpha - q_{-\alpha}) \\ P_\alpha^{(r)} &= \frac{1}{2}(p_\alpha + p_{-\alpha}), & P_\alpha^{(i)} &= \frac{i}{2}(p_\alpha - p_{-\alpha}). \end{aligned}$$

and after secondary quantization Hamiltonian is expressed in terms of creation and annihilation operators ($\omega_\alpha = \alpha c'$)

$$a_\alpha = \frac{\omega_\alpha Q_\alpha^{(r)} + iP_\alpha^{(i)}}{\sqrt{2\omega_\alpha}}, \quad b_\alpha = \frac{\omega_\alpha Q_\alpha^{(i)} + iP_\alpha^{(r)}}{\sqrt{2\omega_\alpha}}. \quad (6)$$

as follows

$$\begin{aligned} \hat{H}_x &= \int_0^\infty -\frac{\omega_\alpha}{2} ((\hat{a}_\alpha^\dagger - \hat{a}_\alpha)^2 + (\hat{b}_\alpha^\dagger - \hat{b}_\alpha)^2) + \frac{\omega_\alpha}{2} ((\hat{a}_\alpha^\dagger + \hat{a}_\alpha)^2 + (\hat{b}_\alpha^\dagger + \hat{b}_\alpha)^2) \\ &\quad + i\alpha u(x) \left[(\hat{a}_\alpha^\dagger - \hat{a}_\alpha)(\hat{b}_\alpha^\dagger + \hat{b}_\alpha) - (\hat{b}_\alpha^\dagger - \hat{b}_\alpha)(\hat{a}_\alpha^\dagger + \hat{a}_\alpha) \right] d\alpha. \end{aligned}$$

Using this Hamiltonian we investigate statistical and spectral properties of pulse of electromagnetic field propagating in the medium. Particularly, we study vacuum squeezing and photons creation out of vacuum near the analogue of event horizon, where $u(x) = -c'$.

References

- [1] Leonhardt U 2003 *Rept.Prog.Phys.* **66** 1207-1250
- [2] Nation, P. D. and Johansson, J. R. and Blencowe, M. P. and Nori, Franco 2012 *Rev. Mod. Phys.* **84** 1-24
- [3] Schützhold R Plunien G and Soff G 1998 *Phys. Rev. A* **57** 2311-2318

Modes of silver nanoisland film growth on the surface of ion-exchanged glass

A Kamenskii¹, I Reduto^{1,2}, J Kobert² and A Lipovskii^{1,2}

¹St.Petersburg State Polytechnical University, 29 Polytechnicheskaya, St. Petersburg, 195251 Russia

²St. Petersburg Academic University, 8/3 Khlopina, St. Petersburg, 194021 Russia

Abstract. The behavior of silver nanoisland film growth on the surface of ion-exchanged glasses processed in air and hydrogen atmosphere is compared. The films grown in air degrade with the increase of processing time because of oxidizing of the film. The growth of the film in hydrogen atmosphere tends to saturate with time due to the decrease in the flow of atomic silver towards the glass surface. This is because of the formation and growth of silver nanoparticles in the bulk of the glass, these nanoparticles being the preferable sink for silver atoms. The delay in the growth of the films on the surface of poled glasses is registered.

1. Introduction

Metal island films are of interest during last decades because of high local electric field formed in the vicinity of metal nanoparticles if such a film is irradiated with a light waves, wavelength of which is close to the wavelength of surface plasmon resonance (SPR) in the nanoparticles or groups of nanoparticles. The enhancement of the electric field is responsible for high optical nonlinearity, better catalytic abilities of the films, high efficiency of Raman scattering in the agent deposited onto the film and other related phenomena.

2. Experiment

In the experiments we studied the growth of silver nanoisland film (SNF) on the surface of ion-exchanged glass in the course of out-diffusion of neutral silver from the glass matrix enriched with silver ions by silver-sodium ion exchange processing as described elsewhere [1,2]. The glass was ion-exchanged in the bath containing 5 wt.% of AgNO₃ and 95 wt.% of NaNO₃ at 325°C for 20 min. We used atomic force microscopy (AFM) and optical absorption spectroscopy to compare the growth of SNF on the glasses thermally processed in air and hydrogen atmosphere, on the ion-exchanged glasses stored in air and in nitrogen atmosphere at room temperature, and on the surface of thermally poled ion-exchanged glasses annealed in hydrogen.

3. Results and discussion

Thermal processing of the glasses in the air resulted in the growth of SNF, which was evidenced by the formation and growth of optical absorption peak corresponding to the SPR in the silver nanoislands (Figure 1). Here one can see that the increase in the SPR absorption magnitude is followed by its degradation. AFM measurements (Figure 2a,b) shows that longer processing in air results both in decreasing surface concentration of the nanoislands and their average size. This allows concluding that the most probable reason of the degradation is the oxidation/sulfidation of silver nanoparticles and back diffusion of silver in the glass matrix.

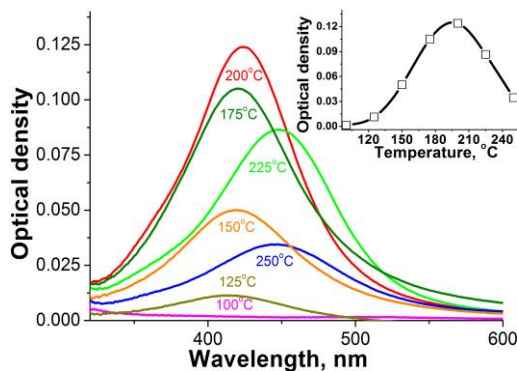


Figure 1. The absorption spectra of the SNF on ion-exchanged glass annealed at different temperatures for 10 minutes in air. Inset: the height of the SPR absorption peak vs processing temperature.

This occurs only in a very thin layer beneath the glass surface since MIF formed in hydrogen atmosphere did not demonstrate any change, contrary, they were highly stable at room temperature that allows concluding about the absence of silver ions and atoms in the subsurface layer of glasses processed in hydrogen.

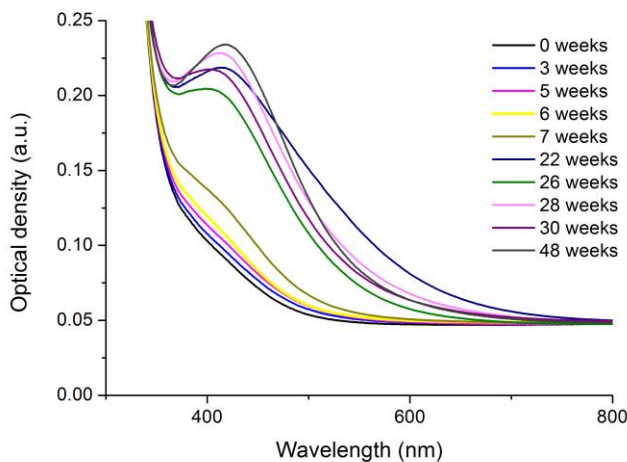


Figure 3. The absorption spectra of the ion-exchanged glass annealed at room temperature for 3-48 weeks in air.

atoms to reach the glass surface, and then just makes formation of silver nanoparticles in the bulk of the glass more preferable than growth of the nanoislands since the nanoparticles are stronger sink for silver atoms than distant surface of the glass.

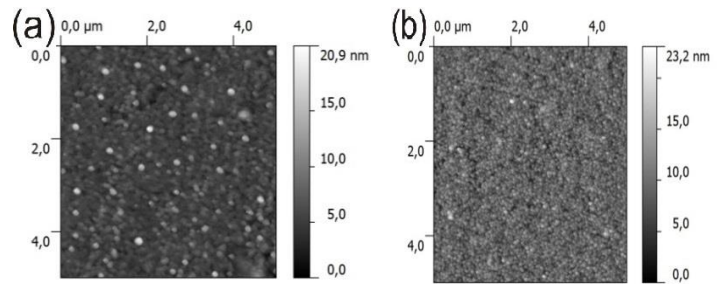


Figure 2. AFM images of MIF formed after 10 minute processing of ion-exchanged glass in air atmosphere at 150°C (a) and 250°C (b) [3].

It is essential that ion-exchanged glasses kept in air at room temperature have also demonstrated the growth of MIF (Figure 3), which is definitely because of water vapors in-diffusion, silver reduction and out diffusion.

Processing of the glass samples in hydrogen resulted in a monotonous growth of the SPR absorption peak with the increase of the processing temperature. However at higher temperatures temporal dependence of the peak magnitude showed saturation (Figure 3) that was because of the nanoparticles growing in the bulk of the glass, which behaved as powerful sink for silver atoms. Measured with AFM lateral size of silver nanoislands varied from 20 to 400 nm depending on the mode of hydrogen anneal. Studied of the growth of silver nanoislands on the surfaces of ion exchanged glasses after thermal poling demonstrated delay or complete suppression of the nanoisland growth. This is because of burying of silver ions in poling which first results in just increasing the time necessary for hydrogen to reach silver ions and for silver

References

- [1] Zhurikhina V, Brunkov P, Melehin V, Kaplas T et al 2012 *Nanoscale Research Letters* **7** 676
- [2] Chervinskii S, Sevriuk V, Reduto I, Lipovskii A 2013 *J. Appl. Phys.* **114** 224301
- [3] Reduto I, Chervinskii S, Matikainen A, Baklanov A et al 2014 *J. Phys.: Conf. Ser.* **541** 01207

Single-walled carbon nanotubes: from synthesis to applications

Evgenia Gilshteyn¹, Alexey Tsapenko¹, Albert G. Nasibulin^{1,2}

¹ Skolkovo Institute of Science and Technology, 100 Novaya st., Skolkovo, Moscow Region, 143025, Russia

² Department of Applied Physics and Centre for New Materials, Aalto University, PO Box 15100, 00076 Aalto, Espoo, Finland

Abstract. Carbon nanotubes (CNTs) are a unique family of materials exhibiting diverse useful chemical and physical properties. The CNTs and especially single-walled CNTs (SWCNTs) were found to have exceptional mechanical, thermal and electronic properties. Among different routes to synthesize SWCNTs, an aerosol CVD method is one of the most promising. This method allows growing high quality and cleaning SWCNTs with certain diameters and lengths. This paper reviews the latest results obtained by two different aerosol synthesis methods elaborated in our group.

CNTs can be easily deposited onto practically any substrate, including temperature nontolerant polymers, so that time-consuming steps of CNT purification from the catalyst and support, dispersion and deposition processes are avoided. Supplementary advantages of the aerosol method are possibilities to on-line control of the CNT quality and separate individual and bundled CNTs. This continuous aerosol CVD process is one of the most promising and powerful methods for the high-yield synthesis at controlled conditions [1].

This paper reviews the latest results obtained by two different aerosol synthesis methods elaborated in our group. In the first method, catalyst particles were produced by evaporating catalyst material from resistively heated Fe wire (a hot wire generator, HWG method) [2]. The second method is based on ferrocene vapor decomposition in carbon monoxide atmosphere [3]. We report the investigations of the mechanism of single-walled carbon nanotube formation [4, 5] and charging of CNTs in the gas phase due to the bundling process [6]. The paper also discusses the discovery and growth mechanism of a novel hybrid material, NanoBuds [7], SWCNTs with covalently attached fullerenes. Direct integration of the CNTs produced by the aerosol methods into different applications, especially for high-performance flexible electronics, is discussed [8, 9]. Produced SWCNT/polyethylene composite films have exhibited excellent optical and electrical properties as well as high mechanical flexibility. It was found

that the electrical conductivity of the SWCNT films could be significantly improved by ethanol densification and chemical doping. SWCNT/polyethylene thin films demonstrated excellent cold electron field emission properties. We have fabricated state-of-the-art key components from the same single component multifunctional SWNT material for several high-impact application areas: high efficiency nanoparticle filters with a figure of merit of 147 Pa^{-1} , transparent and conductive electrodes with a sheet resistance of $84 \text{ } \Omega/\square$ and a transmittance of 90%, electrochemical sensors with extremely low detection limits below 100 nM, and polymer-free saturable absorbers for ultrafast femtosecond lasers. Furthermore, the films are demonstrated as the main components in gas flowmeters, gas heaters and transparent thermo acoustic loudspeakers.

- [1] Anisimov, A.S., Nasibulin, A.G., Jiang, H., Launois, P., Cambedouzou, J., Shandakov, S.D., Kauppinen, E.I. (2010). Mechanistic investigations of single-walled carbon nanotube synthesis by ferrocene vapor decomposition in carbon monoxide. *Carbon*, 48, 380-388.
- [2] Nasibulin, A.G., Moisala, A., Brown, D.P., Jiang, H., & Kauppinen, E.I. (2005). A Novel Aerosol Method for Single Walled Carbon Nanotube Synthesis. *Chem. Phys. Lett.*, 402, 227-232.
- [3] Moisala, A., Nasibulin, A.G., Brown, D.P., Jiang, H., Khriachtchev, L., & Kauppinen, E.I. (2006). Single-walled Carbon Nanotube Synthesis Using Ferrocene and Iron Pentacarbonyl in a Laminar Flow Reactor. *Chem. Eng. Sci.*, 61, 4393-4402.
- [4] Nasibulin, A.G., Queipo, P., Shandakov, S.D., Brown, D.P., Jiang, H., Pikhitsa, P.V., Tolochko, O.V., & Kauppinen, E.I. (2006). Studies on mechanism of single-walled carbon nanotube formation. *J. Nanosci. Nanotech.*, 6, 1233-1246.
- [5] Nasibulin, A.G., & Shandakov, S.D. (2010). Aerosol synthesis of carbon nanotubes. In *Aerosols: Science and Technology* (Edited Agranovski, I.), *Aerosols: Science and Technology* (pp. 65-89). Wiley-VCH, City.
- [6] Nasibulin, A.G., Shandakov, S.D., Anisimov, A.S., Gonzalez, D., Jiang, H., Pudas, M., Queipo, P., & Kauppinen, E.I. (2008). Charging of Aerosol Products during Ferrocene Vapor Decomposition in N₂ and CO Atmospheres. *J. Phys. Chem. C*, 112, 5762-5769.
- [7] Nasibulin, A.G., Pikhitsa, P.V., Jiang, H., Brown, D.P., Krashennnikov, A.V., Anisimov, A.S., Queipo, P., Moisala, A., Gonzalez, D., Lientschnig, G., Hassanien, A., Shandakov, S.D., Lolli, G., Resasco, D.E., Choi, M., Tomanek, D., & Kauppinen, E.I. (2007). A Novel Hybrid Carbon Material. *Nat. Nanotechnol.*, 2, 156-161.
- [8] Kaskela, A., Nasibulin, A.G., Zavodchikova, M.Y., Aitchison, B., Papadimitratos, A., Tian, Y., Zhu, Z., Jiang, H., Brown, D.P., Zakhidov, A., & Kauppinen, E.I. (2010). Aerosol Synthesized SWCNT Networks with Tuneable Conductivity and Transparency by Dry Transfer Technique. *Nano Lett.*, 10, 4349-4355.
- [9] Sun, D.-M., Timmermans, M.Y., Nasibulin, A.G., Kauppinen, E.I., Kishimoto, S., Mizutani, T., & Ohno, Y. (2011). High-performance carbon nanotube thin-film transistors and logic circuits on flexible substrate. *Nat. Nanotechnol.*, 6, 156-161.

Investigation of the dielectric properties of composites based on silicon dioxide with carbon nanotubes

A A Goshev¹, M K Eseev¹, C S Osokin¹, S N Kapustin¹

¹Northern Arctic Federal University named after M.V. Lomonosov, Severnaya Dvina Emb. 17, 163002, Arkhangelsk, Russia

Abstract. This paper presents the results of an experimental study of conductive and dielectric properties of nanocomposites in the radio frequency electric field. Matrix composite - is silica powder. Filler - a dispersed aqueous solution of multilayer carbon nanotubes having different concentrations. The study found that in addition to the standard behavior of the electrical characteristics of nanocomposites with increasing concentration there is an optimum concentration of carbon nanotubes at which greatly increased conductivity and absorption of electromagnetic radiation in the material. This can be used to enhance the functionality of nanocomposites.

1. Introduction

Recently, active research composite materials which include nanostructures, in particular, carbon nanotubes (CNTs) as filler. Due to the large surface area of the CNT, as well as significant differences of the physical properties of nano-objects from macrostate material properties of the nanocomposites are not additive properties of each phase and can be radically different from those of each of its components [1]. In the review [2] provides data on the study of the electrical properties of nanocomposites with CNT. Particularly urgent task is to study the strongly nonlinear dependence of properties of the composite on the concentration of the filler, which is necessary for the selection of the optimum functional properties of materials (strength, thermal, dielectric and other characteristics). In the literature [3] presents data on the influence of impurities on the dielectric properties of CNTs of different composites at microwave frequencies associated with the search for promising materials for "stealth" -technologies. The aim of this work is an experimental study of the dielectric properties of nanocomposites with a matrix of silica-reinforced filled multi-walled CNTs at different concentrations and determine the role of the CNT in the scattering and absorption of electromagnetic radiation in the range of extra-long and medium radio waves.

2. The frequency dependence of the electrical properties of the nanocomposite

As a n experiment performed in the composite SiO₂ (matrix) reinforced with carbon multiwalled nanotubes with an aspect ratio of 10²-10³, obtained CVD-method. After setting the humidity of 35% sample was placed in the measuring cell, which is a parallel-plate capacitor. Study of electrical properties of the composites produced in electric fields at frequencies of 25 Hz-1 MHz using

¹ Northern Arctic Federal University, Severnaya Dvina Emb. 17, 163002, Arkhangelsk, Russia.

immittance meter E7-20. The measurement results at room temperature for a real (ϵ'), the imaginary (ϵ'') the permittivity and the conductivity (σ) are given in Table 1.

Table 1. The dependence of the electrical properties of the silicon dioxide powder concentration of carbon nanotubes at a frequency of 25 Hz.

Concentration CNT/H ₂ O, %	$\epsilon', 10^6$	$\epsilon'', 10^6$	$\sigma, 10^{-3} \text{ Sm cm}^{-1}$
0	1.42	5.14	7.15
0.01	6.99	0.43	0.59
0.05	8.81	41.95	58
0.1	0.7	1.46	2.03
0.5	0.12	0.13	0.18

The results of measurements found that the percolation threshold for the material less than 0.01% by weight content of CNTs. Noted optimum value CNT concentration (0.05%) at which the conductivity increases sharply, and the absorption properties of the sample. It is known that the change in concentration of CNTs leads to a nonlinear modification of the functional properties of nanomaterials. In [4] noted this dependence for the mechanical properties. It can be concluded that such a non-linear dependence on concentration is a consequence of the decrease in aggregation of CNTs bundles and clusters. This leads to a more uniform distribution of the CNTs by volume of the composite and raising effect of CNTs on the dielectric properties of the sample. To verify this assumption is supposed to study these materials by means of positron annihilation spectroscopy [5].

3. Conclusions

In conclusion, we formulate the main conclusions and results.

- The frequency dependence of the dielectric properties of the material dioxide matrix filled in the form of a solution of various concentrations of CNTs.
- Spotted nonlinear dependence of the dielectric properties of the concentration and found the optimal concentration of CNT to change the permittivity and conductivity of the material.

4. Acknowledgement

This work was supported by the project the Ministry of Education of the Russian Federation №3635 "Investigation of the properties nanocomposites with controlled modification of the structure reinforced with carbon nanotubes".

5. References

- [1] Rakov E G 2013 *Russ. Chem. Rev.* **82** 538
- [2] Eletsii A V, Knizhnik A A, Potapkin B V, Kenny J M 2015 *Phys. Usp.* **58** in print
- [3] Usanov D A, Skripal' A V, Romanov A V 2011 *Tech. Phys.* **56** 102
- [4] Kablov E N, Kondrashov S V, Yurkov G Yu *Nanotechnologies in Russia* 2013 **8** 163
- [5] Sidorin A A, Meshkov I, Ahmanova E, Eseev M, Kobets A, Lokhmatov V, Pavlov V, Rudakov A and Yakovenko S 2013 *Mater. Sci. Forum* **733** 322

Atomic force microscopy of lead sulphide – cadmium sulphide solid solutions layers obtained by chemical bath deposition

E.V. Maraeva¹, L.N. Maskaeva², V.Ph. Markov², V. A. Moshnikov^{1,3}, S.S. Tulenin², N.A. Forostyanaya²

¹ Saint Petersburg Electrotechnical University "LETI", ul. Prof. Popova, 5, 197376, Saint Petersburg, Russia

² Ural Federal University, ul. Mira, 19, 620002, Ekaterinburg, Russia

³ St. Petersburg Polytechnic University, 29, Polytechnicheskaya st., 195251, St. Petersburg, Russia

Abstract. In this study lead sulphide – cadmium sulphide based layers were obtained through chemical deposition of water solutions. The article discusses the results of surface investigations with the use of atomic force microscopy.

1. Introduction

Currently, the technology of hydrochemical deposition of films of metallic sulphides [1-4] is especially attractive as far as such method of synthesis is relatively simple from technological point of view and effective at the same time; in comparison with vacuum thermal evaporation [5-7] it does not require expensive equipment.

The purpose of this study is research of morphology of the surface of hydrochemically deposited layers of lead sulphide – cadmium sulphide using optical and atomic force microscopy (AFM).

2. Experiment

In this study lead sulphide – cadmium sulphide based layers were obtained through chemical deposition of water solutions using the following precursors: lead acetate $\text{Pb}(\text{CH}_3\text{COO})_2$; sodium citrate Na_3Cit ; cadmium chloride CdCl_2 ; thiourea $(\text{NH}_2)_2\text{CS}$. The pH level was adjusted by adding water solution of ammonia NH_4OH . The volumes of solutions and volume of water added into reactor were calculated according to law of mass action depending on expected content of cadmium sulphide in the solid solution. Deposition was made on the vitroceraic-based substrate within 2 hours at temperature of 80°C.

AFM experiments were performed using NTEGRA-Therma nanolaboratory (NT-MDT, Zelenograd, Russia). Commercial etched silicon tips NSG 01 (NT-MDT, Zelenograd, Russia) with typical resonance frequency of 150 kHz were used as AFM probes.

3. Results and discussion

As a result, a set of samples of solid solutions with different contents of cadmium sulphide was obtained, and properties of their surface were examined by analyzing the substrate area. The layers obtained were 100 to 500 nm thick depending on the original mix proportion.

It was discovered that regardless the proportion in original mix of solutions the most homogeneous film was formed in the center of substrate. Figure 1 presents AFM images of layers being obtained from water solutions with cadmium (a) and without adding cadmium (b).

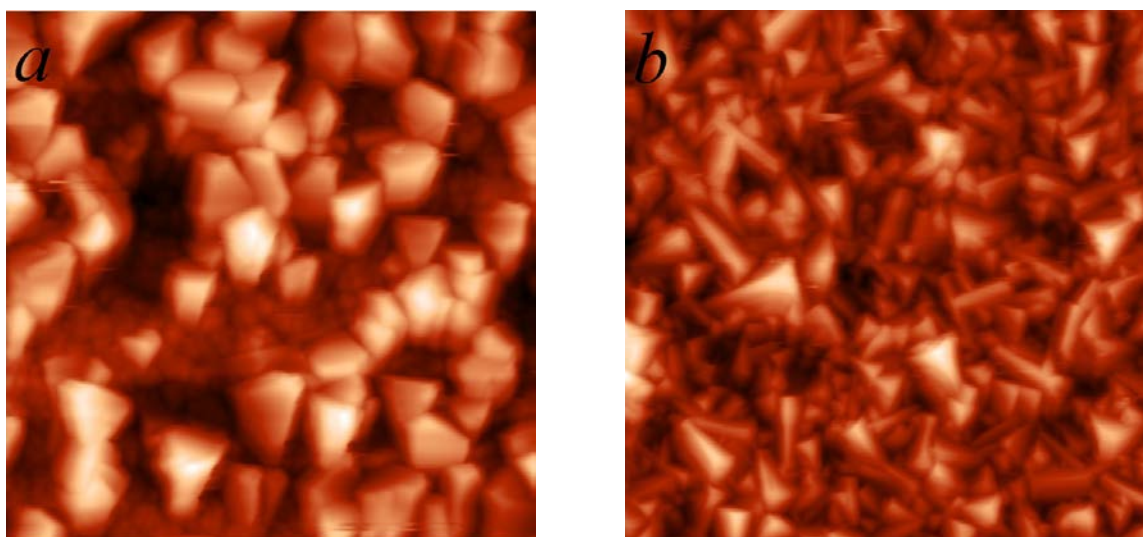


Figure 1. AFM images of layers being obtained with cadmium (a) and without adding cadmium (b) (scan size area is $10 * 10 \mu\text{m}$)

If the film of undiluted lead sulphide was formed (without adding cadmium), the surface was represented by a coupled system of irregular shaped crystallites, the height of the pattern varied from 100 to 300 nm at the film edge and from 100 to 500 nm in its center. If solid solutions were formed, a large amount of hexagonal agglomerates, grid-like in some cases, were observed on the surface.

Acknowledgments

The reported study was supported by project "Preparation and study of porous systems, functionalized nanomaterials, applications in photonics, sensor technology and medicine" (under the Russian Ministry of Education state task № 16.2112.2014 / K) and also by program 211 of Russian Federation Government № 02. A 03.21.0006.

References

- [1] Markov V, Maskayeva L, Ivanov P 2006 *Hydrochemical deposition of metallic sulphide films: simulation and experiment* (Ekaterinburg)
- [2] Markov V F, Maskayeva L N, Kitaev G A 2000 *Inorganic Materials* **36** 1194
- [3] Markov V F, Maskayeva L N 2010 *Russian Journal of Physical Chemistry A*. **84** 1288
- [4] Katysheva A S, Markov V F, Maskayeva L N 2013 *Russian Journal of Inorganic Chemistry* **58** 833
- [5] Chesnokova D B, Moshnikov V A, Gamarts A E, Maraeva E V, Aleksandrova O A, Kuznetsov V V 2010 *Journal of Non-Crystalline Solids* **356** 2010
- [6] Moshnikov V A, Gamarts A E, Chesnokova D B, Maraeva E V 2011 *Inorganic Materials*. **47** 18
- [7] Maraeva E V, Moshnikov V A, Tairov Y M 2013 *Semiconductors* **47** 1422

Laser cutting of GaN/Al₂O₃ structures

O S Medvedev¹, O Khait², S Yu Kurin³, A S Usikov^{4,5}, B P Papchenko⁴, H Helava⁵, and Yu N Makarov^{3,5}

¹St. Petersburg State University, Universitetskaya nab. 7-9, St. Petersburg 199034, Russia

²Multitech Ltd., Rizhsky pr. 26, St. Petersburg 190103, Russia

³Nitride Crystals Group Ltd., pr. Engel'sa 27, St. Petersburg 194156, Russia

⁴University ITMO, Kronverkskiy pr. 49, St. Petersburg 197101, Russia

⁵Nitride Crystals Inc., 181 E Industry Court, Suite B, Deer Park, NY 11729, USA

Abstract. We report on laser cutting process developed for GaN/Al₂O₃ structures. The impact of laser cutting on the mechanical properties of GaN/Al₂O₃ structures has been studied.

Post-growth treatment is an essential part of manufacturing process of semiconductor devices. It largely determines their performance. One of the most important procedures is to divide the epitaxial structures into chips while keeping crack-free, clean, smooth chip surface. We report on laser cutting process developed for GaN/Al₂O₃ structures that have a wide range of applications (e.g. UV LEDs, lasers, photodiodes, solar cells). Specifically, we study the impact of laser cutting on the mechanical properties of GaN/Al₂O₃ structures.

GaN/Al₂O₃ structures were grown by hydride vapor phase epitaxy (HVPE) on c-plane (0001) Al₂O₃ substrates in a horizontal quartz reactor [1]. It is important to note that we used single side polished (SSP) Al₂O₃ substrates for HVPE growth runs whereas in the process of laser cutting the structures grown on double side polished (DSP) Al₂O₃ substrates are commonly used. On the one hand, it required fine-tuning of the laser cutting mode, on the other hand, it allowed us to grow low-cost GaN/Al₂O₃ structures since the cost of SSP substrates is much lower than that of DSP ones.

In order to divide GaN/Al₂O₃ structures into chips a 1.06 μm laser operated in a pulsed mode with a pulse energy of 2 mJ in a 15-ns pulse was used.

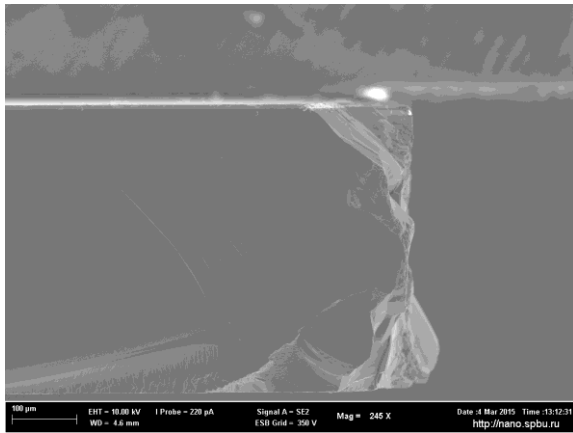


Figure 1. SEM image of the cleaved edge of GaN/Al₂O₃ structure.

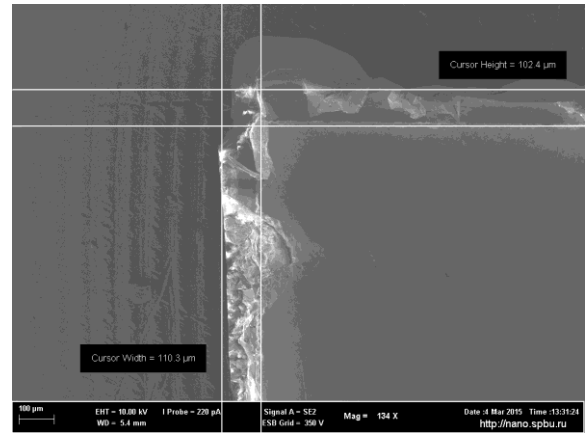


Figure 2. Planar view of GaN/Al₂O₃ structure near the edge exposed to laser cutting.

The main conclusions are given below:

1. Cracks formed by laser cutting are not observed (figure 1).
2. Laser cut thickness is about 100 µm (figure 2); the width of the cleaved region is about 30 µm.
3. Heavily contaminated areas are not detected.
4. The morphology of the laser cuts is different on *a-m* planes.

Acknowledgments

Work at University ITMO was supported by the Ministry of Education and Science of Russian Federation within the grant agreement 14.575.21.0054 (unique identifier of research activities is RFMEFI57514X0054).

References

- [1] Kurin S, Antipov A, Barash, I, Roenkov A et al. 2014 *Phys. Status Solidi C* **11** 813-816

Synthesis of luminescent ceramics from alumina nanopowder

A.N Kiryakov, D.V. Ananchenko, V.S. Kortov and S.V. Zvonarev
Ural Federal University, Yekaterinburg, 62000 Russia

Abstract. The effect of high-temperature synthesis conditions in a reducing medium on the structure and cathodoluminescence of ceramics made of compacted $\alpha\text{-Al}_2\text{O}_3$ powder is the focus of this work. The possibility of using oxygen-deficient alumina ceramics as a functional material in plasma- and optical electronics, as well as solid dosimetry of radiations is discussed.

1. Introduction

Numerous studies show that anion-defective $\alpha\text{-Al}_2\text{O}_3$ single crystals synthesized in a highly reducing medium have a high photon yield of luminescence when exposed to an electron beam, in particular [1]. Luminescent properties of oxygen-deficient single alumina crystals depend on the concentration of oxygen vacancies that form charge carrier trapping centers and participate in recombination processes. Highly sensitive detectors of ionizing radiations have been created on the basis of anion-defective $\alpha\text{-Al}_2\text{O}_3$ single crystals. Alongside with that, applications of oxygen-deficient alumina can be extended through using nanopowders and thin-layer ceramics as phosphors in electronic beam tubes, plasma panels and optical electronic devices. However, the techniques of obtaining luminescent ceramics from alumina nanopowder have been little studied. The purpose of this work was to research the effects of synthesis conditions (temperature, annealing time) on the structure and cathodoluminescence of the ceramics made of alumina nanopowder.

2. Materials and Methods

$\alpha\text{-Al}_2\text{O}_3$ nanopowder with high purity (99,99%) and a grain size of 50-70 nm was used to produce compacts by uniaxial pressing at a pressure of 1,000 kg/cm². The compacts were 40 mg in mass, 5 mm in diameter and 1.3 mm thick. They were annealed in vacuum ($\sim 10^{-4}$ Pa) in an electric furnace at the temperature range of 1,000-1,600 °C for various periods of time. Alongside with the samples, graphite rods were placed in the vacuum chamber to make a highly reducing medium at heating. The reducing medium is necessary for oxygen vacancies to emerge in the samples. Pulsed cathodoluminescence (PCL) in the ceramics was excited with an electron beam with the pulse length of 2 ns, electron energy of 130 keV, and the flux density of 60 A/cm². A change in the structure of the samples after annealing was controlled with SEM. SIAMS method and equipment were used to study size-distributions of crystal grains.

3. Results

PCL was not registered in the produced compacts before annealing. After annealing at T=1,300 °C, a band with the maximum at 420 nm associated with glowing of F-centers emerged in the PCL spectrum [2]. The centers are formed by oxygen vacancies with two trapped electrons. Fig.1 shows a change in the intensity of the band of F-centers depending on the synthesis temperature. It can be seen that the

PCL intensity increases with a growing temperature. A similar result was observed at varying the time periods of the samples annealing at a fixed temperature. At $T=1,600\text{ }^{\circ}\text{C}$ the PCL intensity increased four-fold with a growing annealing time from 60 to 300 min. All the mentioned PCL changes appear if the synthesis of ceramics occurs at the presence of graphite. Heating of the samples in vacuum without graphite weakens the effects of the changes in PCL intensity tenfold.

High-temperature synthesis of luminescent ceramics is accompanied by the increase in their densities and particle sizes. Fig. 2 shows the size distributions of particles in the ceramics synthesized at the temperatures of $1,300\text{ }^{\circ}\text{C}$. A growing synthesis temperature causes an increase in particle sizes up to several hundred nanometers. It also leads to a decrease in their sizes due to sintering and thermal etching of the samples. The described processes occur most explicitly at $T>1300\text{ }^{\circ}\text{C}$.

4. Conclusion

The performed studies allowed us to define the optimal conditions of synthesis of luminescent ceramics made of alumina nanopowder and to outline their possible applications.

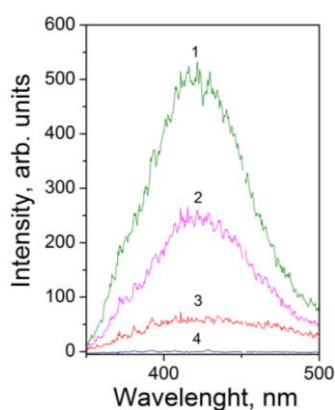


Figure 1. PCL spectra of the ceramics synthesized for 1 hour at various temperatures: 1- $1,660\text{ }^{\circ}\text{C}$, 2 – $1,500\text{ }^{\circ}\text{C}$, 3 – $1,300\text{ }^{\circ}\text{C}$. Curve 4 for the sample synthesized in vacuum without graphite at $T=1,600\text{ }^{\circ}\text{C}$.

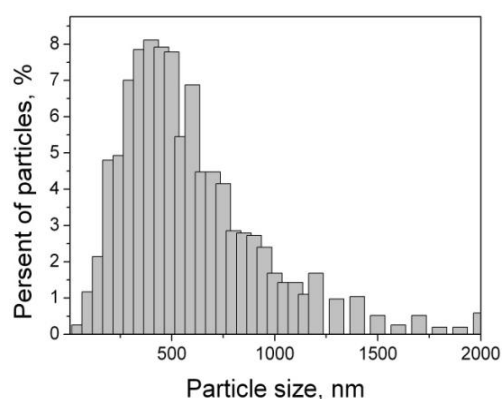


Figure 2. Size distribution of particles in the ceramics synthesized at $1,300\text{ }^{\circ}\text{C}$ for 1 hour

Acknowledgments

The work has been done as a part of the government task (№3.2016.2014/K) of the Ministry of Education and Science of the Russian Federation.

References

- [1] Kortov V.S. 2007 Radiat. Meas. **42**, 576
- [2] Zvonarev S.V., Kortov V.S., Stang T.V., Ananchenko D.V. and Petrovykh K.A. Applied Radiation and Isotopes. 2015 **95**, 44

Elastic moduli of alumina nanoceramics

J A Perevozchikova¹, E A Buntov, A F Zatsepin and V S Kortov

Ural Federal University named after the first President of Russia Boris Yeltsin, 19 Mira Street, Yekaterinburg, 620002, Russia

Abstract. In this study we investigated the physico-mechanical properties of alumina nanoceramics, that is used in micro- and optoelectronics chips as substrates. The elastic characteristics (Young's modulus E , shear modulus G , Poisson's ratio ν) are determined by measuring the longitudinal and transverse wave velocities. The results suggest that the nanoceramics have unique properties that can be used in the future in microelectronics to improve the stability of chips and optimization of production technology.

1. Introduction

Currently, nanostructured materials that have special electrical, optical and mechanical properties represent considerable interest for micro- and optoelectronics. Studied in this work nanoceramics are used in microelectronics for chip substrates. For the stable operation of the device, it must be combined the electrical with any physical and mechanical properties, that can be obtained by measuring the speed of sound. In this work, we determined the elastic characteristics (Young's modulus E , shear modulus G , Poisson's ratio ν) of nanoceramics based on Al_2O_3 .

2. Samples and Methods

In this study we investigated three samples of nanoceramics with alumina nanostructured phase received from Zelenograd factory of electronic instrumentation "Elion". For certification of the samples it was carried out X-ray analysis, which showed that the main phase is $\alpha\text{-Al}_2\text{O}_3$, and the average size of coherent scattering regions 100-150 nm. The scanning electron microscopy showed that the particle size of Sample 1 was 70-200 nm, sample 2 was crystalline and had particle size 1-3 micron, and the particle size of the sample 3 was 80-200 nm.

Determining the propagation velocity of the longitudinal waves carried out on the device consisting of two piezoelectric transducers (5 MHz). One of them was used as the signal source and the other was the receiver. The sample was put between them. The signal received by the second transducer was registered by a personal computer. Using a special program written in LabView, there was calculated value of the longitudinal ultrasonic velocity in the sample.

The size of nanoceramics sample was quite small, that is why a scheme was developed that allows single point measurements, in which the transverse wave reflected perpendicularly from the sample face in order to determine the velocity of shear waves. We used a special form aluminum prism that conducts transverse waves. Measurements were performed using ultrasonic flaw detector PCUS 10 in pulse mode and the inclined transducer with 65° angle and 5 MHz frequency.

3. Results

The results are shown in Table 1. Values of the elastic characteristics were calculated according to well known formulas [1-3].

Table 1. The properties of nanoceramics.

	Sample 1	Sample 2	Sample 3
Density ρ, kg/m³	3746	3762	3756
Longitudinal waves velocity C_l, km/s	10	9.9	8.7
Shear waves velocity C_t, km/s	4.2	4.1	5
Young's modulus E, GPa	170	162	229
Shear modulus G, GPa	61	58	90
Poisson's ratio ν	0.39	0.4	0.28

The sample 1 and the sample 2 are made in a single technology, but differ in particle size. The interesting relations of the acoustic parameters depending on the density are observed. The value of the longitudinal waves velocity decreases with increasing density that is not typical for a normal dependency. For the sample with a smaller particle size Young's and shear moduli are greater than in macrocrystalline.

Comparing the samples with nanometer sized particles (sample 1 and sample 3), with a slight increase of density it is observed anomalous dependence of the values of longitudinal wave velocities and significantly increase Young's and shear moduli and Poisson's ratio decreases. Perhaps this is due to the high porosity of the sample 3. The transverse velocities increase with increasing density. In this case there is no anomaly.

4. Conclusion

In this study we investigated the physico-mechanical properties of aluminum oxide nanoceramics. The findings suggest that the nanoceramics have unique properties that can be used in the future in microelectronics to improve the stability of chips and optimization of production technology.

Acknowledgments

This work is supported by the Ministry of Education and Science of the Russian Federation.

References

- [1] Mason U 1966 *Physical Acoustics. The methods and tools for ultrasound studies* (Moscow: Mir)
- [2] Klyuev V V 2004 *Non-Destructive Testing: A Guide to 7 volumes* vol 3 (Moscow: Mashinostroenie)
- [3] Rinkevich A B, Perov D V, Samoilovich M I and Klescheva S M 2010 Elastic properties and heat capacity of opal matrices and related 3D-nanocomposite materials *Phys. Sol. State* **52** 2570–76

Specialized probes with nanowhisker structures for high resolution magnetic force microscopy

M.V. Zhukov¹, K.I. Belousov¹, A.M. Mozharov², I.S. Mukhin^{1,2}, A.O. Golubok^{1,3}

¹ Department of material science and nanotechnology, ITMO University, 197101 Kronverkskiy pr., 49, Saint-Petersburg, Russian Federation

² Laboratory of renewable energy source, St Petersburg Academic University RAS, 194021 Khlopina, 8/3, Saint-Petersburg, Russian Federation

³ Nanotechnology department, Institute of Analytical Instrumentation RAS, 198095 Ivan Chernykh, 31-33, Saint-Petersburg, Russian Federation

Abstract. Creation and study of specialized single nanowhisker probes with magnetic coating are performed for high-precision imaging of various objects by means of atomic force and magnetic force microscopy. Thin layers of Ni and Co are deposited on the surface of nanowhisker structures to perform visualization of magnetic fields on the sample surface, in particular, structure of pits on a hard disk drive (HDD). It is revealed that probes with nanowhisker structures covered with magnetic coating demonstrate a higher spatial resolution and contrast of magnetic fields visualization compared to standard magnetic probes due to their high aspect ratio.

1. Introduction

Scanning probe microscopy (SPM) is one of the main methods of high precision material investigation and modification with nanometer resolution according to wide range of different SPM techniques. The advantage of SPM is ability to visualize geometric dimensions of the surface of various materials as well as to perform the measurement of mechanical properties, the spatial distribution of adhesion forces, electric and magnetic fields on the surface of samples.

Magnetic force microscopy (MFM) should be also distinguish as one of promising technique in nanotechnology due to its ability to perform both highly accurate reading of magnetic fields distribution [1] and recording of magnetic information [2]. The important role of nanoprobe for MFM resolution should be noted. Indeed, geometric parameters and the type of the probe determine the sensitivity of this method, the resulting resolution and contrast of obtained images.

The aim of this study is to create a new type of magnetic probes based on whisker structures, including the simulation of magnetic probes with different geometric shapes.

2. Experimental setup

Producing of nanowhisker structures on the tops of probes and control of their parameters were performed by means of scanning electron microscope CrossBeam Neon 40 (Carl Zeiss, Germany). Studies of the possibilities of nanowhisker probes were carried out on SPM complex Ntegra Aura (NT-MDT, Russia).

Deposition of magnetic materials (Ni, Co) on the top of the pyramid surface of probes were produced by laser ablation and electron sputtering with Auto 500 Edwards (BOC Edw., England).

3. Results and Discussions

Investigation of the probe with nanowhiskers (NW) in the air was carried out in tapping mode, increasing the stability of NW probes and reducing damaging effects of the probe to the sample. Study of micro- and nanostructures of test lattice TGQ01 with calibrated geometric characteristics demonstrated a two-fold decreasing of broadening on vertical steps projection of the surface using NW probes compared to standard probes. Furthermore, imaging of nanoscale channels in electron resist PMMA on Si substrate revealed improvement of penetration ability using NW probes. The phenomenon of lateral resolution and penetration ability improvement in case of NW probes can be explained by the high aspect ratio of nanowhisiker structures (length to diameter ratio).

Distribution of magnetic fields on test specimens in the form of segments of a magnetic hard disk (HDD) was investigated with standard and specialized NW probes whose surfaces were coated with thin layers of magnetic material (Ni, Co). Magnetic fields study was performed with two-pass method. On the first pass information about topological features was obtained, while the second pass at a height of 10 nm from the sample surface gave information about magnetic fields according to probe oscillation phase shift. The magnetic probe oscillates at the resonant frequency ($f_0 \approx 133$ kHz) during the distribution of magnetic fields measurement. The presence of magnetic field provides additional damping effect influenced on a phase shift between the driving force and the vibrations of the probe.

Our investigation showed that a NW probe allows obtaining better contrast of MFM phase in comparison with a standard probe. It should be noticed that so-called "cross effect" linked with influence of magnetic probe on sample magnetic field distribution was observed. The phenomenon of "cross effect" is more significant in case of the NW probes compared to standard probes that can be associated with a higher sensitivity of the NW probe due to the peculiarities of its geometry.

Numerical simulation of magnetic probes with different geometry was carried out. The simulation confirmed that NW magnetic probes are more sensitive in comparison with MFM standard probes.

4. Conclusions

Magnetic probes on the basis of whisker structures were created and studied. The approbation of these probes was carried out on test lattice TGQ01 with calibrated geometric parameters, artificial channels in PMMA resist and magnetic disks. The simulation of MFM images was performed for magnetic probes with different geometry. A comparison of the results obtained by standard magnetic probes and specialized magnetic NW probes was carried out. Both theoretically and experimentally data showed that magnetic NW probes significantly improves the sensitivity, contrast and spatial resolution of magnetic force microscopy.

Work was carried out with the support of the leading universities of the Russian Federation (grant 074-U01), the Russian Foundation for Basic Research (14-02-31703 mol_a), and program U.M.N.I.K.

References

- [1] M.R. Koblischka, U. Hartmann, T. Sulzbach 2003 Improvements of the lateral resolution of the MFM technique *Thin Solid Films* Vol. 428 pp. 93–97.
- [2] Yu. P. Ivanov, A. I. Il'in, E. V. Pustovalov, L. A. Chebotkevich 2010 Influence of induced anisotropy on the processes of magnetization reversal of cobalt circular nanodots *Physics of the Solid State* Vol. 52 issue 8 pp 1694-1700.

Formation of metallic nanostructures on the surface of ion-exchange glass by focused electron beam

F E Komissarenko¹, M V Zhukov¹, I S Mukhin^{1,2}, A O Golubok^{1,3} and A I Sidorov¹

¹ ITMO University, 49 Kronverksky pr., 197101 St. Petersburg, Russian Federation

² St. Petersburg Academic University – Nanotechnology Research and Education Centre RAS, 8/3 ul. Khlopina, 195220 St. Petersburg, Russian Federation

³ Nanotechnology Department, Institute for Analytical Instrumentation RAS, 31-33 ul. Ivana Chernykh, 198095 Saint-Petersburg, Russian Federation

Abstract. This paper presents a new method for formation of metallic nanostructures on the surface of ion-exchange glass. The method is based on the interaction of a focused electron beam with ions in ion-exchange glass. In experiments nanostructures with different shapes were obtained, depending on the electrons irradiation conditions.

1. Introduction

Currently, metal nanostructures of different configurations are widely used in photonics. They are used in devices such as plasmon waveguides, microresonators, concentrators of surface plasmon waves, and also they are of interest for optical measurements, for example, by amplifying the light signal of the studied objects (surface enhanced Raman spectroscopy) [1]. Existing methods of obtaining such nanosystems include various types of lithography, chemical methods, deposition and epitaxial methods.

2. Experiment

This paper presents a method for creating nanoscale metal structures on the surface of ion-exchange glasses. The method is based on the interaction of a focused electron beam with ions in glass and gives opportunity to produce metal structures of various shapes. In the experiments we used Soda-lime glass with the composition of $\text{SiO}_2\text{-Na}_2\text{O-MgO-Al}_2\text{O}_3$, in which Ag^+ ions were introduced by ion-exchange mechanism. Aluminum film with thickness of 90 nm was deposited on the surface of prepared glass for charges drain when glass is irradiated by electrons. Focused electron beam exposure was carried out using a scanning electron microscope Carl Zeiss CrossBeam Neon 40 with Raith Elphy Plus lithography attachment. On the sample surface pattern with an array of disks with a diameter of 200 nm and period of 600 nm was exposed. In experiments we used different exposure parameters: acceleration voltage, beam current and dose. After irradiation, the aluminum layer was removed with a ten percent solution of KOH. Next, the surface of glass was studied with a scanning electron microscope and with a scanning probe microscope NT-MDT Ntegra Aura. Metal structures were formed in the irradiated areas on the glass surface, and shapes of these structures were circles,

triangles, rectangles or polygons depending on the exposure regime. The study of nanostructures carried out by atomic force microscopy showed that the height of structures was 40 nm. It was also found that obtained nanostructures were inhomogeneous and formed from the multiple clusters. Creation of metallic structures using proposed method is reproducible.

3. Discussion

Formation of metallic structures on the glass surface is explained as follows. Under electron beam irradiation negatively charged region is formed near the glass surface due to the accumulation of thermalized electrons. Positively charged silver and sodium ions migrate to that area, reduce to neutral atoms after interaction with electrons and emerge on the glass surface, forming clusters, and combining in structures at locations where the current density of the electron beam was maximized. [2]

4. Summary

A new method of the formation of metallic nanostructures on the surface of ion-exchange glasses was presented. Structure formation occurs due to the interaction of a focused electron beam and free metal ions in glass. This method of metallic nanostructures producing can be used in the fabrication of plasmon devices on glass, because it has the advantages of electron beam lithography (high resolution) while being productive due to small number of process steps.

Work was carried out with the support of the leading universities of the Russian Federation (grant 074-U01).

References

- [1] Zayats A V, Smolyaninov I I and Maradudin A A, 2005 *Phys. Rep.* **408** 131
- [2] Brunov V S, Podsvirov O A, Sidorov A I and Churaev D V 2014 *Technical Physics* **59** 1215–19

Energetics of H₂ generation from aqueous electrolytes using GaN electrodes

A M Puzyk¹, M V Puzyk¹, A S Usikov^{2,3}, S Yu Kurin⁴, I A Ermakov², D S Kovalev², B P Papchenko², Yu N Makarov^{3,4}, N M Shmidt⁵

¹ Herzen University, Nab. r. Moyki 48, St. Petersburg 194186, Russia

² University ITMO, Kronverkskiy pr. 49, St. Petersburg 197101, Russia

³ Nitride Crystals Inc., 181 E Industry Court, Suite B, Deer Park, NY 11729, USA,

⁴ Nitride Crystals Group Ltd., pr. Engel'sa 27, St. Petersburg 194156, Russia

⁵ Ioffe Physical Technical Institute, Polytekhnicheskaya 26, St. Petersburg 194021, Russia

Abstract. An application of GaN layers grown by HVPE on sapphire substrates for water splitting and hydrogen gas generation is discussed. Specifics of water electrolysis using different electrolytes and corrosion stability of the GaN materials are also considered.

The XXI century has begun from the maximally high prices on the main energy sources, such as petroleum and gas. In spite of a growing demand to the energy sources for a sustainable the global petroleum-based industry is more and more disruptive from an ecological viewpoint, and alternative sources of energy must be developed. The major interest in semiconductor electrodes immersed into an electrolyte is due to the photoelectrochemical properties of the semiconductor electrolyte interface under solar irradiation [1]. Solar energy is an inexhaustible natural resource that produces a power striking the earth surface of about 0.9-1.0 kW/m². Thus, one of the trends for an alternative power source is to develop photoelectrochemical cells (PECE) for water splitting into H₂ and O₂ gases under a sunlight using semiconductor electrodes. Note that water recourses are almost unlimited, H₂ gas is an environmentally pure fuel because the only combustion product is water; and H₂ has the highest specific heat among all chemical compounds.

In this paper, we report on the H₂ generation from water using n-type GaN as a working photoelectrode. We evaluate energetic of hydrogen reduction in water solutions of various pH-electrolytes (NaOH, Na₂SO₄, H₂SO₄) on GaN under conditions of external electrical power and solar irradiation.

5-7 μm thick GaN layers, which subsequently were used as working electrodes, were grown by hydride vapor phase epitaxy (HVPE) on c-plane (0001) sapphire substrates in a horizontal quartz reactor [2]. The first layers (tens of nanometers) AlN и AlGaN were used as thin buffer layers prior to GaN growth.

The substrate orientation made it possible to cut a 2-inch wafer into six sectors. These sectors were used for contact deposition electrode preparation. As contacts, either Ti/Ni/Au thin films were evaporated on select areas of the electrode or an indium droplet contact was deposited into the

electrode using microsoldering-iron. A wire welding completed the electrode fabrication. The contact pads and contact wire were protected by chemical-resistant varnish (wax).

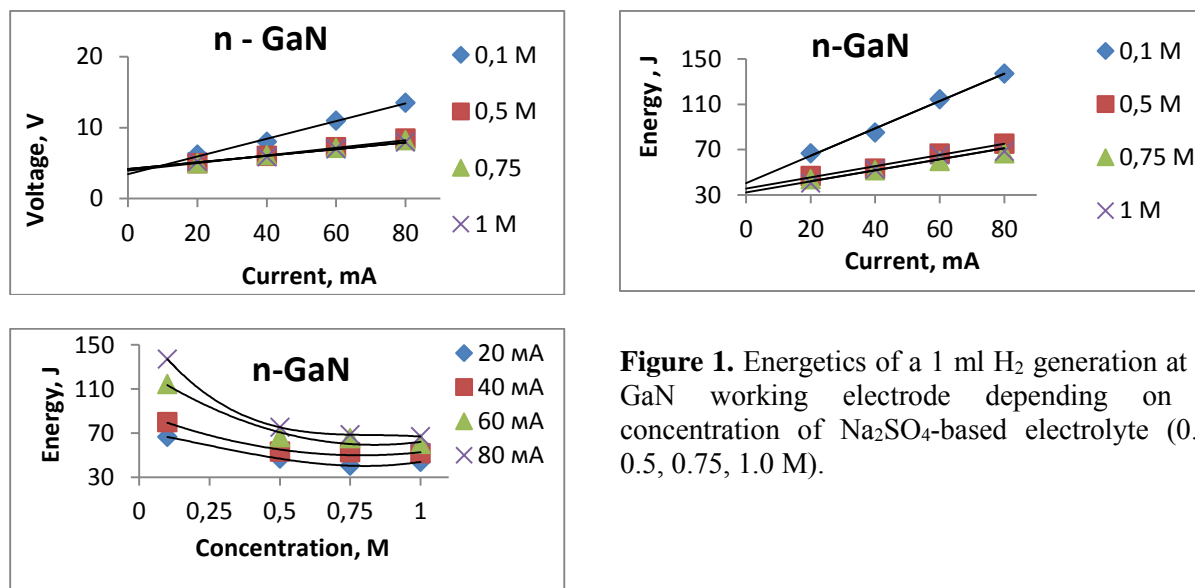


Figure 1. Energetics of a 1 ml H₂ generation at n-GaN working electrode depending on a concentration of Na₂SO₄-based electrolyte (0.1, 0.5, 0.75, 1.0 M).

First, over potential on GaN working electrodes needed for H₂ generation was measured using different aqua electrolytes and an external power source. The aqueous contact area of the GaN electrode was about 2.5-3 cm². Pt plate (4 cm²) was used as the counter-electrode. The reference electrode was made of Ag/AgCl/KCl (potassium-chloride-saturated silver-chloride electrode). Potential of hydrogen reduction at GaN electrode (Na₂SO₄-based electrolyte, pH=7) was -0.80 V that is on -0.40 V lower (over potential) than that at Pt. The over potentials measured on GaN electrode in other electrolytes were -0.4 V (H₂SO₄, pH=1) and -1.20 V (KOH, pH=14). The over potentials could be due to a potential barrier for carriers on the GaN/electrolyte interface, higher specific resistivity and worse current spreading on the GaN electrode. Optimization of the GaN electrode contact configuration is required.

Then, the effectiveness of water electrolysis with GaN working electrodes was studied. Figure 1 shows I-V characteristics and energy consumption of a 1 ml H₂ generation using Na₂SO₄-based electrolyte. Graduated test tube was used to collect generated hydrogen. The energy consumption showed sublinear dependencies at low concentration of the electrolyte. It seems to reflect band bending effect on the electrode surface that creates an energy barrier in n-GaN to be overcome by electrons to participate in the redox reaction in the electrolyte. Corrosion of n-GaN working electrode using as cathode or anode was not observed.

Photoelectrochemical experiments for H₂ generation were performed with Xenon light bulb (100 mW/cm²) or 365 nm UV LED and external power source. Hydrogen formation was observed at Pt cathode using n-GaN as photoanode. The experiments have shown doping and crystalline quality of the GaN electrodes need to be optimized. More results and discussions will be presented.

Acknowledgments

Work at University ITMO was supported by the Ministry of Education and Science of Russian Federation within the grant agreement 14.575.21.0054 (unique identifier of research activities is RFMEFI57514X0054).

References

- [1] Walter M G, Warren E L, McKone J R, Boettcher S W et al. 2010 *Chem. Rev.* **110** 6446–6473
- [2] Kurin S, Antipov A, Barash I, Roenkov et al. 2014 *Phys. Status Solidi C* **11** 813-816

ISBN 978-5-906433-08-4

